Physics Reference Manual

Version: geant4 9.1 (14 December, 2007)

Contents

Part I

Introduction

Chapter 1

Introduction

1.1 Scope of This Manual

The Physics Reference Manual provides detailed explanations of the physics implemented in the Geant4 toolkit. The manual's purpose is threefold:

- to present the theoretical formulation, model, or parameterization of the physics interactions included in Geant4,

- to describe the probability of the occurrence of an interaction and the sampling mechanisms required to simulate it, and

- to serve as a reference for toolkit users and developers who wish to consult the underlying physics of an interaction.

This manual does not discuss code implementation or how to use the implemented physics interactions in a simulation. These topics are discussed in the User's Guide for Application Developers. Details of the object-oriented design and functionality of the Geant4 toolkit are given in the User's Guide for Toolkit Developers. The Installation Guide for Setting up Geant4 in Your Computing Environment describes how to get the Geant4 code, install it, and run it.

1.2 Definition of Terms

Several terms used throughout the Physics Reference Manual have specific meaning within Geant4, but are not well-defined in general usage. The definitions of these terms are given here.

- **process** - a C++ class which describes how and when a specific kind of physical interaction takes place along a particle track. A given particle type typically has several processes assigned to it. Occaisionally "process" refers to the interaction which the process class describes.

- **model** - a C++ class whose methods implement the details of an interaction, such as its kinematics. One or more models may be assigned to each process. In sections discussing the theory of an interaction, "model" may refer to the formulae or parameterization on which the model class is based.

- **Geant3** - a physics simulation tool written in Fortran, and the predecessor of Geant4. Although many references are made to Geant3, no knowledge of it is required to understand this manual.

1.3   Status of this document

4.12.01 created by D.H. Wright

Chapter 2

Monte Carlo Methods

The Geant4 toolkit uses a combination of the composition and rejection Monte Carlo methods. Only the basic formalism of these methods is outlined here. For a complete account of the Monte Carlo methods, the interested user is referred to the publications of Butcher and Messel, Messel and Crawford, or Ford and Nelson [1, 2, 3].

Suppose we wish to sample x in the interval $[x_1, \ x_2]$ from the distribution $f(x)$ and the *normalised* probability density function can be written as :

$$f(x) = \sum_{i=1}^{n} N_i f_i(x) g_i(x) \tag{2.1}$$

where $N_i > 0$, $f_i(x)$ are *normalised* density functions on $[x_1, \ x_2]$, and $0 \leq g_i(x) \leq 1$.

According to this method, x can sampled in the following way:

1. select a random integer $i \in \{1, 2, \cdots n\}$ with probability proportional to N_i

2. select a value x_0 from the distribution $f_i(x)$

3. calculate $g_i(x_0)$ and accept $x = x_0$ with probability $g_i(x_0)$;

4. if x_0 is rejected restart from step 1.

It can be shown that this scheme is correct and the mean number of tries to accept a value is $\sum_i N_i$.

In practice, a good method of sampling from the distribution $f(x)$ has the following properties:

- all the subdistributions $f_i(x)$ can be sampled easily;

- the rejection functions $g_i(x)$ can be evaluated easily/quickly;

- the mean number of tries is not too large.

Thus the different possible decompositions of the distribution $f(x)$ are not equivalent from the practical point of view (e.g. they can be very different in computational speed) and it can be useful to optimise the decomposition. A remark of practical importance : if our distribution is not normalised

$$\int_{x_1}^{x_2} f(x)dx = C > 0$$

the method can be used in the same manner; the mean number of tries in this case is $\sum_i N_i/C$.

2.1   Status of this document

18.01.02 created by M.Maire.

Bibliography

[1] J.C. Butcher and H. Messel. *Nucl. Phys. 20* 15 (1960)

[2] H. Messel and D. Crawford. *Electron-Photon shower distribution, Pergamon Press* (1970)

[3] R. Ford and W. Nelson. *SLAC-265, UC-32* (1985)

[4] Particle Data Group. Rev. of Particle Properties. *Eur. Phys. J. C15. (2000) 1.* http://pdg.lbl.gov

Chapter 3

Transportation

The transportation process is responsible for determining the geometrical limits of a step. It calculates the length of step with which a track will cross into another volume. When the track actually arrives at a boundary, the transportation process locates the next volume that it enters.

If the particle is charged and there is an electromagnetic (or potentially other) field, it is responsible for propagating the particle in this field. It does this according to an equation of motion. This equation can be provided by Geant4, for the case a magnetic or EM field, or can be provided by the user for other fields.

The transportation updates the time of flight of a particle, utilising its initial velocity.

Some additional details on motion in fields:

In order to intersect the model Geant4 geometry of a detector or setup, the curved trajectory followed by a charged particle is split into 'chords segments'. A chord is a straight line segment between two trajectory points. Chords are created utilizing a criterion for the maximum estimated distance between a curve point and the chord. This distance is also known as the sagitta.

The equations of motions are solved utilising Runge Kutta methods. Runge Kutta methods of different can be utilised for fields depending on the numerical method utilised for approximating the field. Specialised methods for near-constant magnetic fields are under development.

Part II

Particle Decay

Chapter 4

Decay

The decay of particles in flight and at rest is simulated by the *G4Decay* class.

4.1 Mean Free Path for Decay in Flight

The mean free path λ is calculated for each step using

$$\lambda = \gamma \beta c \tau$$

where τ is the lifetime of the particle and

$$\gamma = \frac{1}{\sqrt{1 - \beta^2}}.$$

β and γ are calculated using the momentum at the beginning of the step. The decay time in the rest frame of the particle (proper time) is then sampled and converted to a decay length using β.

4.2 Branching Ratios and Decay Channels

G4Decay selects a decay mode for the particle according to branching ratios defined in the *G4DecayTable* class, which is a member of the *G4ParticleDefinition* class. Each mode is implemented as a class derived from *G4VDecayChannel* and is responsible for generating the secondaries and the kinematics of the decay. In a given decay channel the daughter particle momenta are calculated in the rest frame of the parent and then boosted into the laboratory frame. Polarization is not currently taken into account for either the parent or its daughters.

A large number of specific decay channels may be required to simulate an experiment, ranging from two-body to many-body decays and $V - A$ to semi-leptonic decays. Most of these are covered by the five decay channel classes provided by Geant4:

G4PhaseSpaceDecayChannel	: phase space decay
G4DalitzDecayChannel	: dalitz decay
G4MuonDecayChannel	: muon decay
G4TauLeptonicDecayChannel	: tau leptonic decay
G4KL3DecayChannel	: semi-leptonic decays of kaon .

4.2.1   G4PhaseSpaceDecayChannel

The majority of decays in Geant4 are implemented using the *G4PhaseSpaceDecayChannel* class. It simulates phase space decays with isotropic angular distributions in the center-of-mass system. Three private methods of *G4PhaseSpaceDecayChannel* are provided to handle two-, three- and N-body decays:

TwoBodyDecayIt()
ThreeBodyDecayIt()
ManyBodyDecayIt()

Some examples of decays handled by this class are:

$$\pi^0 \to \gamma\gamma,$$

$$\Lambda \to p\pi^-$$

and

$$K^0{}_L \to \pi^0\pi^+\pi^-.$$

4.2.2   G4DalitzDecayChannel

The Dalitz decay

$$\pi^0 \to \gamma + e^+ + e^-$$

and other Dalitz-like decays, such as

$$K^0{}_L \to \gamma + e^+ + e^-$$

and

$$K^0{}_L \to \gamma + \mu^+ + \mu^-$$

9

are simulated by the *G4DalitzDecayChannel* class. In general, it handles any decay of the form

$$P^0 \rightarrow \gamma + l^+ + l^-,$$

where P^0 is a spin-0 meson of mass M and $l^\pm$ are leptons of mass m. The angular distribution of the γ is isotropic in the center-of-mass system of the parent particle and the leptons are generated isotropically and back-to-back in their center-of-mass frame. The magnitude of the leptons' momentum is sampled from the distribution function

$$f(t) = (1 - \frac{t}{M^2})^3 (1 + \frac{2m^2}{t})\sqrt{1 - \frac{4m^2}{t}},$$

where t is the square of the sum of the leptons' energy in their center-of-mass frame.

4.2.3 Muon Decay

G4MuonDecayChannel simulates muon decay according to $V - A$ theory. Neglecting the electron mass, the electron energy is sampled from the following distribution:

$$d\Gamma = \frac{G_F{}^2 m_\mu{}^5}{192\pi^3} 2\epsilon^2 (3 - 2\epsilon)$$

where: Γ : decay rate
             ϵ : $= E_e/E_{max}$
             E_e : electron energy
             E_{max} : maximum electron energy $= m_\mu/2$

The momenta of the two neutrinos are not sampled from their $V - A$ distributions. Instead they are generated back-to-back and isotropically in the neutrinos' center-of-mass frame, with the magnitude of the neutrino momentum chosen to conserve energy in the decay. The two neutrinos are then boosted opposite to the momentum of the decay electron. This approximation is sufficient for most simulations because the neutrino is usually not observed in any detector.

Currently, neither the polarization of the muon or the electron is considered in this class.

4.2.4 Leptonic Tau Decay

G4TauLeptonicDecayChannel simulates leptonic tau decays according to $V-A$ theory. This class is valid for both

$$\tau^{\pm} \rightarrow e^{\pm} + \nu_{\tau} + \nu_e$$

and

$$\tau^{\pm} \rightarrow \mu^{\pm} + \nu_{\tau} + \nu_{\mu}$$

modes.

The energy spectrum is calculated without neglecting lepton mass as follows:

$$d\Gamma = \frac{G_F{}^2 m_\tau{}^3}{24\pi^3} p_l E_l (3E_l m_\tau{}^2 - 4E_l{}^2 m_\tau - 2m_\tau m_l{}^2)$$

where:
Γ : decay rate
E_l : daughter lepton energy (total energy)
p_l : daughter lepton momentum
m_l : daughter lepton mass

As in the case of muon decay, the energies of the two neutrinos are not sampled from their $V-A$ spectra, but are calculated so that energy and momentum are conserved. Polarization of the τ and final state leptons is not taken into account in this class.

4.2.5 Kaon Decay

The class *G4KL3DecayChannel* simulates the following four semi-leptonic decay modes of the kaon:

$$
\begin{array}{lll}
K^{\pm}{}_{e3} & : & K^{\pm} \rightarrow \pi^0 + e^{\pm} + \nu \\
K^{\pm}{}_{\mu3} & : & K^{\pm} \rightarrow \pi^0 + \mu^{\pm} + \nu \\
K^0{}_{e3} & : & K^0_L \rightarrow \pi^{\pm} + e^{\mp} + \nu \\
K^0{}_{\mu3} & : & K^0_L \rightarrow \pi^{\pm} + \mu^{\mp} + \nu
\end{array}
$$

Assuming that only the vector current contributes to $K \rightarrow l\pi\nu$ decays, the matrix element can be described by using two dimensionless form factors, f_+ and f_-, which depend only on the momentum transfer $t = (P_K - P_\pi)^2$. The Dalitz plot density used in this class is as follows [1]:

$$\rho\left(E_\pi, E_\mu\right) \propto f_+^2\left(t\right)[A + B\xi\left(t\right) + C\xi\left(t\right)^2]$$

11

where:
$$A = m_K(2E_\mu E_\nu - m_K E'_\pi) + m_\mu{}^2(\tfrac{1}{4}E'_\pi - E_\nu)$$
$$B = m_\mu{}^2(E_\nu - \tfrac{1}{2}E'_\pi)$$
$$C = \tfrac{1}{4}m_\mu{}^2 E'_\pi$$
$$E'_\pi = E_\pi{}^{max} - E_\pi$$

Here $\xi(t)$ is the ratio of the two form factors

$$\xi(t) = f_-(t)/f_+(t).$$

$f_+(t)$ is assumed to depend linearly on t, i.e.

$$f_+(t) = f_+(0)[1 + \lambda_+(t/m_\pi{}^2)]$$

and $f_-(t)$ is assumed to be constant due to time reversal invariance.

Two parameters, λ_+ and $\xi(0)$ are then used for describing the Dalitz plot density in this class. The values of these parameters are taken to be the world average values given by the Particle Data Group [2].

4.3   Status of this document

10.04.02 re-written by D.H. Wright
02.04.02 editing by Hisaya Kurashige
14.11.01 editing by Hisaya Kurashige

Bibliography

[1] L.M. Chounet, J.M. Gaillard, and M.K. Gaillard, Phys. Reports 4C, 199 (1972).

[2] *Review of Particle Physics* The European Physical Journal C, 15 (2000).

Part III

Electromagnetic Interactions

Chapter 5

Particle Transport

5.1 The Interaction Length or Mean Free Path

1) In a simple material the number of atoms per volume is:

$$n = \frac{\mathcal{N}\rho}{A}$$

where:

$\mathcal{N}$ Avogadro's number

ρ density of the medium

A mass of a mole

2) In a compound material the number of atoms per volume of the ith element is:

$$n_i = \frac{\mathcal{N}\rho w_i}{A_i}$$

where:

$\mathcal{N}$ Avogadro's number

ρ density of the medium

w_i proportion by mass of the ith element

A_i mass of a mole of the ith element

3) The **mean free path** of a process, λ, also called the **interaction length**, can be given in terms of the total cross section :

$$\lambda(E) = \left(\sum_i [n_i \cdot \sigma(Z_i, E)] \right)^{-1}$$

where $\sigma(Z, E)$ is the total cross section per atom of the process and $\sum_i$ runs over all elements composing the material.

$\sum_i [n_i \sigma(Z_i, E)]$ is also called the *macroscopic cross section*. The mean free path is the inverse of the macroscopic cross section.

Cross sections per atom and mean free path values are tabulated during initialisation.

5.2 Determination of the Interaction Point

The mean free path, λ, of a particle for a given process depends on the medium and cannot be used directly to sample the probability of an interaction in a heterogeneous detector. The number of mean free paths which a particle travels is:

$$n_\lambda = \int_{x_1}^{x_2} \frac{dx}{\lambda(x)},$$

(5.1)

which is independent of the material traversed. If n_r is a random variable denoting the number of mean free paths from a given point to the point of interaction, it can be shown that n_r has the distribution function:

$$P(n_r < n_\lambda) = 1 - e^{-n_\lambda}$$

(5.2)

The total number of mean free paths the particle travels before reaching the interaction point, n_λ, is sampled at the beginning of the trajectory as:

$$n_\lambda = -\log(\eta)$$

(5.3)

where η is a random number uniformly distributed in the range $(0, 1)$. n_λ is updated after each step Δx according the formula:

$$n'_\lambda = n_\lambda - \frac{\Delta x}{\lambda(x)}$$

(5.4)

until the step originating from $s(x) = n_\lambda \cdot \lambda(x)$ is the shortest and this triggers the specific process.

The short description given above is the *differential approach* to particle transport, which is used in most simulation codes ([1],[2]). In this approach besides the other (*discrete*) processes the continuous energy loss imposes a limit on the stepsize too, because the cross sections depend of the energy of the particle. Then it is assumed that the step is small enough so that the particle cross sections remain approximately constant during the step. In principle one must use very small steps in order to insure an accurate simulation, but computing time increases as the stepsize decreases. A good compromise is to limit the stepsize in Geant4 by not allowing the stopping range of the particle to decrease by more than 20 % during the step. This condition works well for particles with kinetic energies > 0.5 MeV, but for lower energies it can give very short step sizes. To cure this problem a lower limit on the stepsize is also introduced.

5.3   Updating the Particle Lifetime

The proper and laboratory times of the particle should be updated after each step. In the laboratory system:

$$\Delta t_{lab} = \frac{\Delta x}{0.5(v_0 + v)} \tag{5.5}$$

where

Δx	step travelled by the particle
v_0	particle velocity at the beginning of the step
v	particle velocity at the end of the step

This expression is a good approximation if the velocity is not allowed to change too much during the step.

5.4   Status of this document

09.10.98 created by L. Urbán.
27.07.01 minor revisions by M. Maire
01.12.03 integral method subsection added by V. Ivanchenko
12.08.04 splitted and partly moved in introduction by M. Maire
25.12.06 minor revision by V. Ivanchenko

Bibliography

[1] W.R. Nelson et al. the EGS4 Code System. SLAC-Report-265, December 1985.

[2] GEANT3 manual, CERN Program Library Long Writeup W5013 (October 1994).

Chapter 6

Gamma Incident

6.1 Introduction

All processes of gamma interaction with media in Geant4 are happen at the end of the step, so are following $G4VDiscreteProcess$ interface. There are a number of similar functions for discrete electromagnetic processes and in the Standard electromagnetic (EM) package an additional base classes are designed to provide common computations [1].

6.1.1 General Interfaces

Common calculations are performed in the class $G4VEmProcess$ in which the following public methods are implemented:

- PrintInfoDefinition;

- PreparePhysicsTable;

- BuildPhysicsTable;

- PostStepDoIt;

- StorePhysicsTable;

- RetrievePhysicsTable;

- MeanFreePath;

- PostStepGetPhysicalInteractionLength;

- MicroscopicCrossSection;

- AddEmModel;

- SetEmModel;

- UpdateEmModel;

- SelectModelForMaterial;

- LambdaTable;

There are many Get/Set and other accessors methods implemented for this base class. Any derive class need to have an implementation of pure virtual methods:

- IsApplicable;

- PrintInfo;

- InitialiseProcess;

This interface is used by the following processes:

- G4ComptonScattering;

- G4CoulombScattering;

- G4GammaConversion;

- G4eplusAnnihilation (additionally AtRest methods are provided);

- G4eeToHadrons;

- G4PolarizedCompton;

- G4PolarizedGammaConversion;

- G4PolarizedPhotoElectricEffect;

- G4eplusPolarizedAnnihilation (additionally AtRest methods are provided);

These processes mainly provide initialization and also some generic functions like *PostStepDoIt*. The physics models are implemented using the *G4VEmModel* interface. Because a model is defined to be active over a given energy range and for a defined set of *G4Region*s, an energy loss process can have one or several models defined for a particle and *G4Region*. The following models are available for above list of processes:

- G4KleinNishinaCompton;

- G4PEEffectModel;

- G4CoulombScatteringModel;

- G4eCoulombScatteringModel;

- G4BetheHeitlerModel;

- G4eeToHadronsModel;

- G4DummyModel (zero cross section, no secondaries);

Some processes do not follow described interfaces but provide direct implementations of the basic *G4VDiscreteProcess* process:

- G4GammaConversionToMuons;

- G4AnnihiToMuPair;

- G4ScreenedNuclearRecoil;

- G4Cerenkov;

- G4Scintillation;

- G4SynchrotronRadiation;

6.1.2 Status of this document

06.12.07 created by V.Ivanchenko

Bibliography

[1] H. Burkhardt et al., Geant4 standard electromagnetic package for HEP applications. *Nuclear Science Symposium Conference Record 2004, IEEE, Volume 3, Oct 2004. pp. 1907-1910.*

6.2 PhotoElectric effect

The photoelectric effect is the ejection of an electron from a material after a photon has been absorbed by that material. It is simulated by using a parameterized photon absorption cross section to determine the mean free path, atomic shell data to determine the energy of the ejected electron, and the K-shell angular distribution to sample the direction of the electron.

6.2.1 Cross Section and Mean Free Path

The parameterization of the photoabsorption cross section proposed by Biggs et al. [1] was used :

$$\sigma(Z, E_\gamma) = \frac{a(Z, E_\gamma)}{E_\gamma} + \frac{b(Z, E_\gamma)}{E_\gamma^2} + \frac{c(Z, E_\gamma)}{E_\gamma^3} + \frac{d(Z, E_\gamma)}{E_\gamma^4} \qquad (6.1)$$

Using the least-squares method, a separate fit of each of the coefficients a, b, c, d to the experimental data was performed in several energy intervals [2]. As a rule, the boundaries of these intervals were equal to the corresponding photoabsorption edges.

In a given material the mean free path, λ, for a photon to interact via the photoelectric effect is given by :

$$\lambda(E_\gamma) = \left(\sum_i n_{ati} \cdot \sigma(Z_i, E_\gamma) \right)^{-1} \qquad (6.2)$$

where n_{ati} is the number of atoms per volume of the ith element of the material. The cross section and mean free path are discontinuous and must be computed 'on the fly' from the formulas 6.1 and 6.2.

6.2.2 Final State

Choosing an Element

The binding energies of the shells depend on the atomic number Z of the material. In compound materials the ith element is chosen randomly according to the probability:

$$Prob(Z_i, E_\gamma) = \frac{n_{ati}\sigma(Z_i, E_\gamma)}{\sum_i [n_{ati} \cdot \sigma_i(E_\gamma)]}.$$

22

Shell

A quantum can be absorbed if $E_\gamma > B_{shell}$ where the shell energies are taken from `G4AtomicShells` data: the closest available atomic shell is chosen. The photoelectron is emitted with kinetic energy :

$$T_{photoelectron} = E_\gamma - B_{shell}(Z_i) \tag{6.3}$$

Theta Distribution of the Photoelectron

The polar angle of the photoelectron is sampled from the Sauter-Gavrila distribution (for K-shell) [3], which is correct only to zero order in αZ :

$$\frac{d\sigma}{d(\cos\theta)} \sim \frac{\sin^2\theta}{(1-\beta\cos\theta)^4} \left\{ 1 + \frac{1}{2}\gamma(\gamma-1)(\gamma-2)(1-\beta\cos\theta) \right\} \tag{6.4}$$

where β and γ are the Lorentz factors of the photoelectron.
$\cos\theta$ is sampled from the probability density function :

$$f(\cos\theta) = \frac{1-\beta^2}{2\beta}\frac{1}{(1-\beta\cos\theta)^2} \quad \implies \quad \cos\theta = \frac{(1-2r)+\beta}{(1-2r)\beta+1} \tag{6.5}$$

The rejection function is :

$$g(\cos\theta) = \frac{1-\cos^2\theta}{(1-\beta\cos\theta)^2}\left[1+b(1-\beta\cos\theta)\right] \tag{6.6}$$

with $b = \gamma(\gamma-1)(\gamma-2)/2$
It can be shown that $g(\cos\theta)$ is positive $\forall\cos\theta \in [-1, +1]$, and can be majored by :

$$\begin{aligned} gsup &= \gamma^2\left[1+b(1-\beta)\right] \text{ if } \gamma \in\,]1,2] \\ &= \gamma^2\left[1+b(1+\beta)\right] \text{ if } \gamma > 2 \end{aligned} \tag{6.7}$$

The efficiency of this method is $\sim 50\%$ if $\gamma < 2$, $\sim 25\%$ if $\gamma \in [2,\ 3]$.

Relaxation

In the current implementation the relaxation of the atom is not simulated, but instead is counted as a local energy deposit.

6.2.3 Status of this document

09.10.98 created by M.Maire.
08.01.02 updated by mma
22.04.02 re-worded by D.H. Wright
02.05.02 modifs in total cross section and final state (mma)
15.11.02 introduction added by D.H. Wright

Bibliography

[1] Biggs F., and Lighthill R., Preprint Sandia Laboratory, SAND 87-0070 (1990)

[2] Grichine V.M., Kostin A.P., Kotelnikov S.K. et al., Bulletin of the Lebedev Institute no. 2-3, 34 (1994).

[3] Gavrila M. Phys.Rev. 113, 514 (1959).

6.3 Compton scattering

6.3.1 Cross Section and Mean Free Path

Cross Section per Atom

When simulating the Compton scattering of a photon from an atomic electron, an empirical cross section formula is used, which reproduces the cross section data down to 10 keV:

$$\sigma(Z, E_\gamma) = \left[P_1(Z) \frac{\log(1 + 2X)}{X} + \frac{P_2(Z) + P_3(Z)X + P_4(Z)X^2}{1 + aX + bX^2 + cX^3} \right].$$ (6.8)

Here,

$$
\begin{aligned}
Z &= \text{atomic number of the medium} \\
E_\gamma &= \text{energy of the photon} \\
X &= E_\gamma/mc^2 \\
m &= \text{electron mass} \\
P_i(Z) &= Z(d_i + e_i Z + f_i Z^2).
\end{aligned}
$$

The values of the parameters can be found within the method which computes the cross section per atom. A fit of the parameters was made to over 511 data points [1, 2] chosen from the intervals

$$1 \leq Z \leq 100$$

and

$$E_\gamma \in [10 \text{ keV}, 100 \text{ GeV}].$$

The accuracy of the fit was estimated to be

$$\frac{\Delta\sigma}{\sigma} = \begin{cases} \approx 10\% & \text{for } E_\gamma \simeq 10 \text{ keV} - 20 \text{ keV} \\ \leq 5 - 6\% & \text{for } E_\gamma > 20 \text{ keV} \end{cases}$$

Mean Free Path

In a given material the mean free path, λ, for a photon to interact via Compton scattering is given by

$$\lambda(E_\gamma) = \left(\sum_i n_{ati} \cdot \sigma_i(E_\gamma) \right)^{-1}$$ (6.9)

where n_{ati} is the number of atoms per volume of the ith element of the material.

6.3.2 Sampling the Final State

The quantum mechanical Klein-Nishina differential cross section per atom is [3] :

$$\frac{d\sigma}{d\epsilon} = \pi r_e^2 \frac{m_e c^2}{E_0} Z \left[\frac{1}{\epsilon} + \epsilon\right] \left[1 - \frac{\epsilon \sin^2 \theta}{1 + \epsilon^2}\right] \qquad (6.10)$$

where
$$
\begin{aligned}
r_e &= \text{classical electron radius} \\
m_e c^2 &= \text{electron mass} \\
E_0 &= \text{energy of the incident photon} \\
E_1 &= \text{energy of the scattered photon} \\
\epsilon &= E_1/E_0 \ .
\end{aligned}
$$
Assuming an elastic collision, the scattering angle θ is defined by the Compton formula:

$$E_1 = E_0 \frac{m_e c^2}{m_e c^2 + E_0(1 - \cos\theta)}. \qquad (6.11)$$

Sampling the Photon Energy

The value of ϵ corresponding to the minimum photon energy (backward scattering) is given by

$$\epsilon_0 = \frac{m_e c^2}{m_e c^2 + 2E_0}, \qquad (6.12)$$

hence $\epsilon \in [\epsilon_0, 1]$. Using the combined composition and rejection Monte Carlo methods described in [4, 5, 6] one may set

$$\Phi(\epsilon) \simeq \left[\frac{1}{\epsilon} + \epsilon\right]\left[1 - \frac{\epsilon \sin^2 \theta}{1 + \epsilon^2}\right] = f(\epsilon){\cdot}g(\epsilon) = [\alpha_1 f_1(\epsilon) + \alpha_2 f_2(\epsilon)]{\cdot}g(\epsilon), \quad (6.13)$$

where
$$
\begin{aligned}
\alpha_1 &= \ln(1/\epsilon_0) &;& \quad f_1(\epsilon) = 1/(\alpha_1 \epsilon) \\
\alpha_2 &= (1 - \epsilon_0^2)/2 &;& \quad f_2(\epsilon) = \epsilon/\alpha_2.
\end{aligned}
$$
f_1 and f_2 are probability density functions defined on the interval $[\epsilon_0, 1]$, and

$$g(\epsilon) = \left[1 - \frac{\epsilon}{1 + \epsilon^2} \sin^2 \theta\right]$$

is the rejection function $\forall \epsilon \in [\epsilon_0, 1] \Longrightarrow 0 < g(\epsilon) \leq 1$.

Given a set of 3 random numbers r, r', r'' uniformly distributed on the interval [0,1], the sampling procedure for ϵ is the following:

1. decide whether to sample from $f_1(\epsilon)$ or $f_2(\epsilon)$:
   if $r < \alpha_1/(\alpha_1 + \alpha_2)$ select $f_1(\epsilon)$, otherwise select $f_2(\epsilon)$

2. sample ϵ from the distributions corresponding to f_1 or f_2:
   for $f_1 : \epsilon = \epsilon_0^{r'} \qquad (\equiv \exp(-r'\alpha_1))$
   for $f_2 : \epsilon^2 = \epsilon_0^2 + (1 - \epsilon_0^2)r'$

3. calculate $\sin^2\theta = t(2-t)$ where $t \equiv (1 - \cos\theta) = m_e c^2 (1 - \epsilon)/(E_0\epsilon)$

4. test the rejection function:
   if $g(\epsilon) \geq r''$ accept ϵ, otherwise go to step 1.

Compute the Final State Kinematics

After the successful sampling of ϵ, the polar angles of the scattered photon with respect to the direction of the parent photon are generated. The azimuthal angle, ϕ, is generated isotropically and θ is as defined in the previous section. The momentum vector of the scattered photon, $\overrightarrow{P_{\gamma 1}}$, is then transformed into the `World` coordinate system. The kinetic energy and momentum of the recoil electron are then

$$
\begin{aligned}
T_{el} &= E_0 - E_1 \\
\overrightarrow{P_{el}} &= \overrightarrow{P_{\gamma 0}} - \overrightarrow{P_{\gamma 1}}.
\end{aligned}
$$

6.3.3 Validity

The differential cross-section is valid only for those collisions in which the energy of the recoil electron is large compared to its binding energy (which is ignored). However, as pointed out by Rossi [7], this has a negligible effect because of the small number of recoil electrons produced at very low energies.

6.3.4 Status of this document

09.10.98 created by M.Maire.
14.01.02 minor revision (mma)
22.04.02 reworded by D.H. Wright
18.03.04 include references for total cross section (mma)

Bibliography

[1] Hubbell, Gimm and Overbo. *J. Phys. Chem. Ref. Data 9* 1023 (1980)

[2] H. Storm and H.I. Israel *Nucl. Data Tables A7* 565 (1970)

[3] O. Klein and Y. Nishina. *Z. Physik 52* 853 (1929)

[4] J.C. Butcher and H. Messel. *Nucl. Phys. 20* 15 (1960)

[5] H. Messel and D. Crawford. *Electron-Photon shower distribution, Pergamon Press* (1970)

[6] R. Ford and W. Nelson. *SLAC-265, UC-32* (1985)

[7] B. Rossi. *High energy particles, Prentice-Hall* 77-79 (1952)

6.4 Gamma Conversion into an Electron - Positron Pair

6.4.1 Cross Section and Mean Free Path

Cross Section per Atom

The total cross-section per atom for the conversion of a gamma into an (e^+, e^-) pair has been parameterized as

$$\sigma(Z, E_\gamma) = Z(Z+1) \left[F_1(X) + F_2(X)\, Z + \frac{F_3(X)}{Z} \right], \qquad (6.14)$$

where E_γ is the incident gamma energy and $X = \ln(E_\gamma / m_e c^2)$. The functions F_n are given by

$$
\begin{aligned}
F_1(X) &= a_0 + a_1 X + a_2 X^2 + a_3 X^3 + a_4 X^4 + a_5 X^5 \qquad (6.15) \\
F_2(X) &= b_0 + b_1 X + b_2 X^2 + b_3 X^3 + b_4 X^4 + b_5 X^5 \\
F_3(X) &= c_0 + c_1 X + c_2 X^2 + c_3 X^3 + c_4 X^4 + c_5 X^5,
\end{aligned}
$$

with the parameters a_i, b_i, c_i taken from a least-squares fit to the data [1]. Their values can be found in the function which computes formula 6.14. This parameterization describes the data in the range

$$1 \leq Z \leq 100$$

and

$$E_\gamma \in [1.5 \text{ MeV}, 100 \text{ GeV}].$$

The accuracy of the fit was estimated to be $\frac{\Delta \sigma}{\sigma} \leq 5\%$ with a mean value of $\approx 2.2\%$. Above 100 GeV the cross section is constant. Below $E_{low} = 1.5$ MeV the extrapolation

$$\sigma(E) = \sigma(E_{low}) \cdot \left(\frac{E - 2 m_e c^2}{E_{low} - 2 m_e c^2} \right)^2 \qquad (6.16)$$

is used.

Mean Free Path

In a given material the mean free path, λ, for a photon to convert into an (e^+, e^-) pair is

$$\lambda(E_\gamma) = \left(\sum_i n_{ati} \cdot \sigma(Z_i, E_\gamma) \right)^{-1} \qquad (6.17)$$

29

where n_{ati} is the number of atoms per volume of the ith element of the material.

6.4.2   Final State

Choosing an Element

The differential cross section depends on the atomic number Z of the material in which the interaction occurs. In a compound material the element i in which the interaction occurs is chosen randomly according to the probability

$$Prob(Z_i, E_\gamma) = \frac{n_{ati}\sigma(Z_i, E_\gamma)}{\sum_i [n_{ati} \cdot \sigma_i(E_\gamma)]}. \tag{6.18}$$

Corrected Bethe-Heitler Cross Section

As written in [2], the Bethe-Heitler formula corrected for various effects is

$$\begin{aligned}
\frac{d\sigma(Z, \epsilon)}{d\epsilon} &= \alpha r_e^2 Z[Z + \xi(Z)] \left\{ [\epsilon^2 + (1 - \epsilon)^2] \left[\Phi_1(\delta(\epsilon)) - \frac{F(Z)}{2} \right] \right. \\
&\left. + \frac{2}{3}\epsilon(1 - \epsilon) \left[\Phi_2(\delta(\epsilon)) - \frac{F(Z)}{2} \right] \right\}
\end{aligned} \tag{6.19}$$

where α is the fine-structure constant and r_e the classical electron radius. Here $\epsilon = E/E_\gamma$, E_γ is the energy of the photon and E is the total energy carried by one particle of the (e^+, e^-) pair. The kinematical limits of ϵ are therefore

$$\frac{m_e c^2}{E_\gamma} = \epsilon_0 \leq \epsilon \leq 1 - \epsilon_0. \tag{6.20}$$

Screening Effect   The *screening variable*, δ, is a function of ϵ

$$\delta(\epsilon) = \frac{136}{Z^{1/3}} \frac{\epsilon_0}{\epsilon(1 - \epsilon)}, \tag{6.21}$$

and measures the 'impact parameter' of the projectile. Two screening functions are introduced in the Bethe-Heitler formula :

$$\begin{aligned}
\text{for } \delta \leq 1 \quad \Phi_1(\delta) &= 20.867 - 3.242\delta + 0.625\delta^2 \\
\Phi_2(\delta) &= 20.209 - 1.930\delta - 0.086\delta^2 \\
\text{for } \delta > 1 \quad \Phi_1(\delta) &= \Phi_2(\delta) = 21.12 - 4.184\ln(\delta + 0.952).
\end{aligned} \tag{6.22}$$

Because the formula 6.19 is symmetric under the exchange $\epsilon \leftrightarrow (1 - \epsilon)$, the range of ϵ can be restricted to

$$\epsilon \in [\epsilon_0, 1/2]. \tag{6.23}$$

Born Approximation The Bethe-Heitler formula is calculated with plane waves, but Coulomb waves should be used instead. To correct for this, a *Coulomb correction function* is introduced in the Bethe-Heitler formula :

$$\text{for } E_\gamma \ < 50 \text{ MeV} : \quad F(z) = \ 8/3 \ln Z \tag{6.24}$$
$$\text{for } E_\gamma \ \geq 50 \text{ MeV} : \quad F(z) = \ 8/3 \ln Z + 8 f_c(Z)$$

with

$$f_c(Z) \ = \ (\alpha Z)^2 \left[\frac{1}{1 + (\alpha Z)^2} \right. \tag{6.25}$$
$$\left. + 0.20206 - 0.0369(\alpha Z)^2 + 0.0083(\alpha Z)^4 - 0.0020(\alpha Z)^6 + \cdots \right].$$

It should be mentioned that, after these additions, the cross section becomes negative if

$$\delta > \delta_{max}(\epsilon_1) = \exp\left[\frac{42.24 - F(Z)}{8.368} \right] - 0.952. \tag{6.26}$$

This gives an additional constraint on ϵ :

$$\delta \leq \delta_{max} \implies \epsilon \geq \epsilon_1 = \frac{1}{2} - \frac{1}{2}\sqrt{1 - \frac{\delta_{min}}{\delta_{max}}} \tag{6.27}$$

where

$$\delta_{min} = \delta\left(\epsilon = \frac{1}{2}\right) = \frac{136}{Z^{1/3}} \, 4\epsilon_0 \tag{6.28}$$

has been introduced. Finally the range of ϵ becomes

$$\epsilon \in [\epsilon_{min} = \max(\epsilon_0, \epsilon_1), \ 1/2]. \tag{6.29}$$
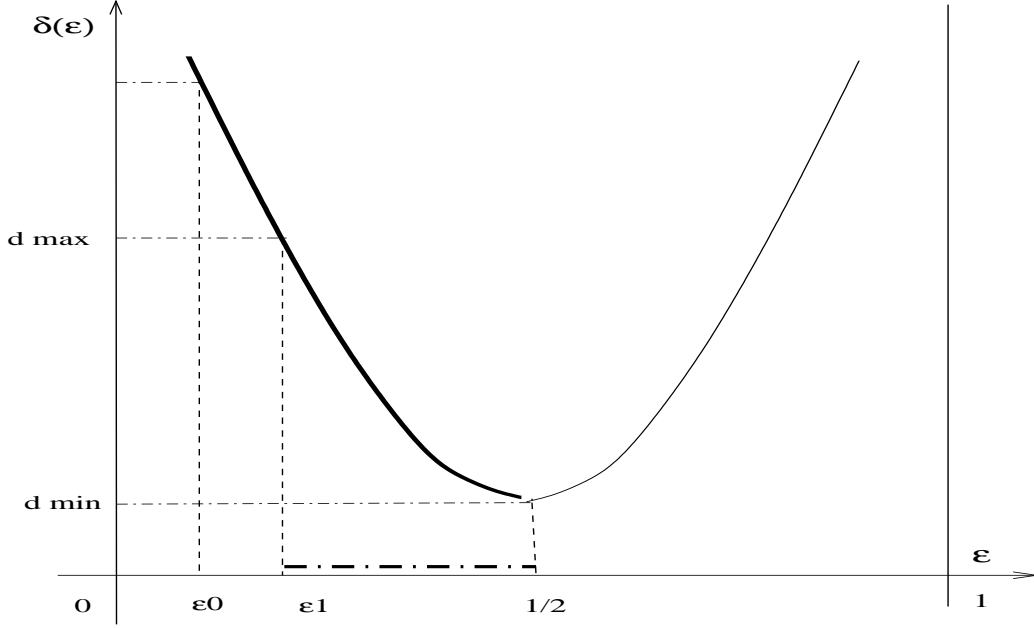
Gamma Conversion in the Electron Field   The electron cloud gives an additional contribution to pair creation, proportional to Z (instead of Z^2). This is taken into account through the expression

$$\xi(Z) = \frac{\ln(1440/Z^{2/3})}{\ln(183/Z^{1/3}) - f_c(Z)}. \tag{6.30}$$

Factorization of the Cross Section ϵ is sampled using the techniques of 'composition+rejection', as treated in [3, 4, 5]. First, two auxiliary screening functions should be introduced:

$$
\begin{aligned}
F_1(\delta) &= 3\Phi_1(\delta) - \Phi_2(\delta) - F(Z) \\
F_2(\delta) &= \frac{3}{2}\Phi_1(\delta) - \frac{1}{2}\Phi_2(\delta) - F(Z)
\end{aligned} \tag{6.31}
$$

It can be seen that $F_1(\delta)$ and $F_2(\delta)$ are decreasing functions of δ, $\forall \delta \in [\delta_{min}, \delta_{max}]$. They reach their maximum for $\delta_{min} = \delta(\epsilon = 1/2)$:

$$
\begin{aligned}
F_{10} &= \max F_1(\delta) = F_1(\delta_{min}) \\
F_{20} &= \max F_2(\delta) = F_2(\delta_{min}).
\end{aligned} \tag{6.32}
$$

After some algebraic manipulations the formula 6.19 can be written :

$$
\begin{aligned}
\frac{d\sigma(Z,\epsilon)}{d\epsilon} &= \alpha r_e^2 Z[Z + \xi(Z)]\frac{2}{9}\left[\frac{1}{2} - \epsilon_{min}\right] \\
&\quad \times \left[N_1\ f_1(\epsilon)\ g_1(\epsilon) + N_2\ f_2(\epsilon)\ g_2(\epsilon)\right],
\end{aligned} \tag{6.33}
$$

32

where

$$N_1 = \left[\frac{1}{2} - \epsilon_{min}\right]^2 F_{10} \qquad f_1(\epsilon) = \frac{3}{\left[\frac{1}{2}-\epsilon_{min}\right]^3} \left[\frac{1}{2} - \epsilon\right]^2 \qquad g_1(\epsilon) = \frac{F_1(\epsilon)}{F_{10}}$$

$$N_2 = \frac{3}{2} F_{20} \qquad f_2(\epsilon) = \text{const} = \frac{1}{\left[\frac{1}{2}-\epsilon_{min}\right]} \qquad g_2(\epsilon) = \frac{F_2(\epsilon)}{F_{20}}.$$

$f_1(\epsilon)$ and $f_2(\epsilon)$ are probability density functions on the interval $\epsilon \in [\epsilon_{min}, 1/2]$ such that

$$\int_{\epsilon_{min}}^{1/2} f_i(\epsilon) \, d\epsilon = 1$$

, and $g_1(\epsilon)$ and $g_2(\epsilon)$ are valid rejection functions: $0 < g_i(\epsilon) \le 1$.

Sampling the Energy   Given a triplet of uniformly distributed random numbers (r_a, r_b, r_c) :

1. use r_a to choose which decomposition term in 6.33 to use:

$$\text{if } r_a < N_1/(N_1 + N_2) \to f_1(\epsilon) \, g_1(\epsilon) \text{ otherwise } \to f_2(\epsilon) \, g_2(\epsilon) \quad (6.34)$$

2. sample ϵ from $f_1(\epsilon)$ or $f_2(\epsilon)$ with r_b :

$$\epsilon = \frac{1}{2} - \left(\frac{1}{2} - \epsilon_{min}\right) r_b^{1/3} \quad \text{or} \quad \epsilon = \epsilon_{min} + \left(\frac{1}{2} - \epsilon_{min}\right) r_b \quad (6.35)$$

3. reject ϵ if $g_1(\epsilon)$ or $g_2(\epsilon) < r_c$

NOTE : below $E_\gamma = 2$ MeV it is enough to sample ϵ uniformly on $[\epsilon_0, \ 1/2]$, without rejection.

Charge   The charge of each particle of the pair is fixed randomly.

Polar Angle of the Electron or Positron

The polar angle of the electron (or positron) is defined with respect to the direction of the parent photon. The energy-angle distribution given by Tsai [6] is quite complicated to sample and can be approximated by a density function suggested by Urban [7] :

$$\forall u \in [0, \ \infty[\ \ f(u) = \frac{9a^2}{9+d} \left[u \exp(-au) + d \, u \exp(-3au)\right] \quad (6.36)$$

with

$$a = \frac{5}{8} \quad d = 27 \qquad \text{and } \theta_{\pm} = \frac{mc^2}{E_{\pm}} \, u. \tag{6.37}$$

A sampling of the distribution 6.36 requires a triplet of random numbers such that

$$\text{if } r_1 < \frac{9}{9+d} \rightarrow u = \frac{-\ln(r_2 r_3)}{a} \quad \text{otherwise } u = \frac{-\ln(r_2 r_3)}{3a}. \tag{6.38}$$

The azimuthal angle ϕ is generated isotropically.

Final State   The e^+ and e^- momenta are assumed to be coplanar with the parent photon. This information, together with energy conservation, is used to calculate the momentum vectors of the (e^+, e^-) pair and to rotate them to the global reference system.

6.4.3   Status of this document

12.01.02 created by M.Maire.
21.03.02 corrections in angular distribution (mma)
22.04.02 re-worded by D.H. Wright

Bibliography

[1] J.H.Hubbell, H.A.Gimm, I.Overbo *Jou. Phys. Chem. Ref. Data 9:1023* (1980)

[2] W. Heitler *The Quantum Theory of Radiation, Oxford University Press* (1957)

[3] R. Ford and W. Nelson. *SLAC-210, UC-32* (1978)

[4] J.C. Butcher and H. Messel. *Nucl. Phys. 20* 15 (1960)

[5] H. Messel and D. Crawford. *Electron-Photon shower distribution, Pergamon Press* (1970)

[6] Y. S. Tsai, *Rev. Mod. Phys. 46* 815 (1974), Y. S. Tsai, *Rev. Mod. Phys. 49* 421 (1977)

[7] L.Urban in GEANT3 writeup, section PHYS-211. *Cern Program Library* (1993)

6.5 Gamma Conversion into a Muon - Antimuon Pair

The class `G4GammaConversionToMuons` simulates the process of gamma conversion into muon pairs. Given the photon energy and Z and A of the material in which the photon converts, the probability for the conversions to take place is calculated according to a parameterized total cross section. Next, the sharing of the photon energy between the μ^+ and μ^- is determined. Finally, the directions of the muons are generated. Details of the implementation are given below and can be also found in [1].

6.5.1 Cross Section and Energy Sharing

In the field of the nucleus, muon pair production on atomic electrons, $\gamma + e \rightarrow e + \mu^+ + \mu^-$, has a threshold of $2m_\mu(m_\mu + m_e)/m_e \approx 43.9$ GeV . Up to several hundred GeV this process has a much lower cross section than the corresponding process on the nucleus. At higher energies, the cross section on atomic electrons represents a correction of $\sim 1/Z$ to the total cross section.

For the approximately elastic scattering considered here, momentum, but no energy, is transferred to the nucleon. The photon energy is fully shared by the two muons according to

$$E_\gamma = E_\mu^+ + E_\mu^- \tag{6.39}$$

or in terms of energy fractions

$$x_+ = \frac{E_\mu^+}{E_\gamma}, \qquad x_- = \frac{E_\mu^-}{E_\gamma}, \qquad x_+ + x_- = 1 \ .$$

The differential cross section for electromagnetic pair creation of muons in terms of the energy fractions of the muons is

$$\frac{d\sigma}{dx_+} = 4\,\alpha\,Z^2\,r_c^2\left(1 - \frac{4}{3}\,x_+x_-\right)\log(W) \ , \tag{6.40}$$

where Z is the charge of the nucleus, r_c is the classical radius of the particles which are pair produced (here muons) and

$$W = W_\infty\,\frac{1 + (D_n\sqrt{e} - 2)\,\delta\,/m_\mu}{1 + B\,Z^{-1/3}\,\sqrt{e}\,\delta\,/m_e} \tag{6.41}$$

where

$$W_\infty = \frac{B\,Z^{-1/3}}{D_n}\,\frac{m_\mu}{m_e} \qquad \delta = \frac{m_\mu^2}{2\,E_\gamma\,x_+x_-} \qquad \sqrt{e} = 1.6487\ldots .$$

35

$$\text{For hydrogen} \quad B = 202.4 \quad D_n = \quad 1.49$$
$$\text{and for all other nuclei} \quad B = 183 \quad D_n = \quad 1.54\, A^{0.27}. \quad (6.42)$$

These formulae are obtained from the differential cross section for muon bremsstrahlung [2] by means of crossing relations. The formulae take into account the screening of the field of the nucleus by the atomic electrons in the Thomas-Fermi model, as well as the finite size of the nucleus, which is essential for the problem under consideration. The above parameterization gives good results for $E_\gamma \gg m_\mu$. The fact that it is approximate close to threshold is of little practical importance. Close to threshold, the cross section is small and the few low energy muons produced will not travel very far. The cross section calculated from Eq. (6.40) is positive for $E_\gamma > 4m_\mu$ and

$$x_{\min} \leq x \leq x_{\max} \quad \text{with} \quad x_{\min} = \frac{1}{2} - \sqrt{\frac{1}{4} - \frac{m_\mu}{E_\gamma}} \qquad x_{\max} = \frac{1}{2} + \sqrt{\frac{1}{4} - \frac{m_\mu}{E_\gamma}} \,, \tag{6.43}$$

except for very asymmetric pair-production, close to threshold, which can easily be taken care of by explicitly setting $\sigma = 0$ whenever $\sigma < 0$.

Note that the differential cross section is symmetric in x_+ and x_- and that

$$x_+ x_- = x - x^2$$

where x stands for either x_+ or x_-. By defining a constant

$$\sigma_0 = 4\,\alpha\,Z^2\,r_c^2 \log(W_\infty) \tag{6.44}$$

the differential cross section Eq. (6.40) can be rewritten as a normalized and symmetric as function of x:

$$\frac{1}{\sigma_0} \frac{d\sigma}{dx} = \left[1 - \frac{4}{3}\,(x - x^2) \right] \frac{\log W}{\log W_\infty} \,. \tag{6.45}$$

This is shown in Fig. 6.1 for several elements and a wide range of photon energies. The asymptotic differential cross section for $E_\gamma \to \infty$

$$\frac{1}{\sigma_0} \frac{d\sigma_\infty}{dx} = 1 - \frac{4}{3}\,(x - x^2)$$

is also shown.
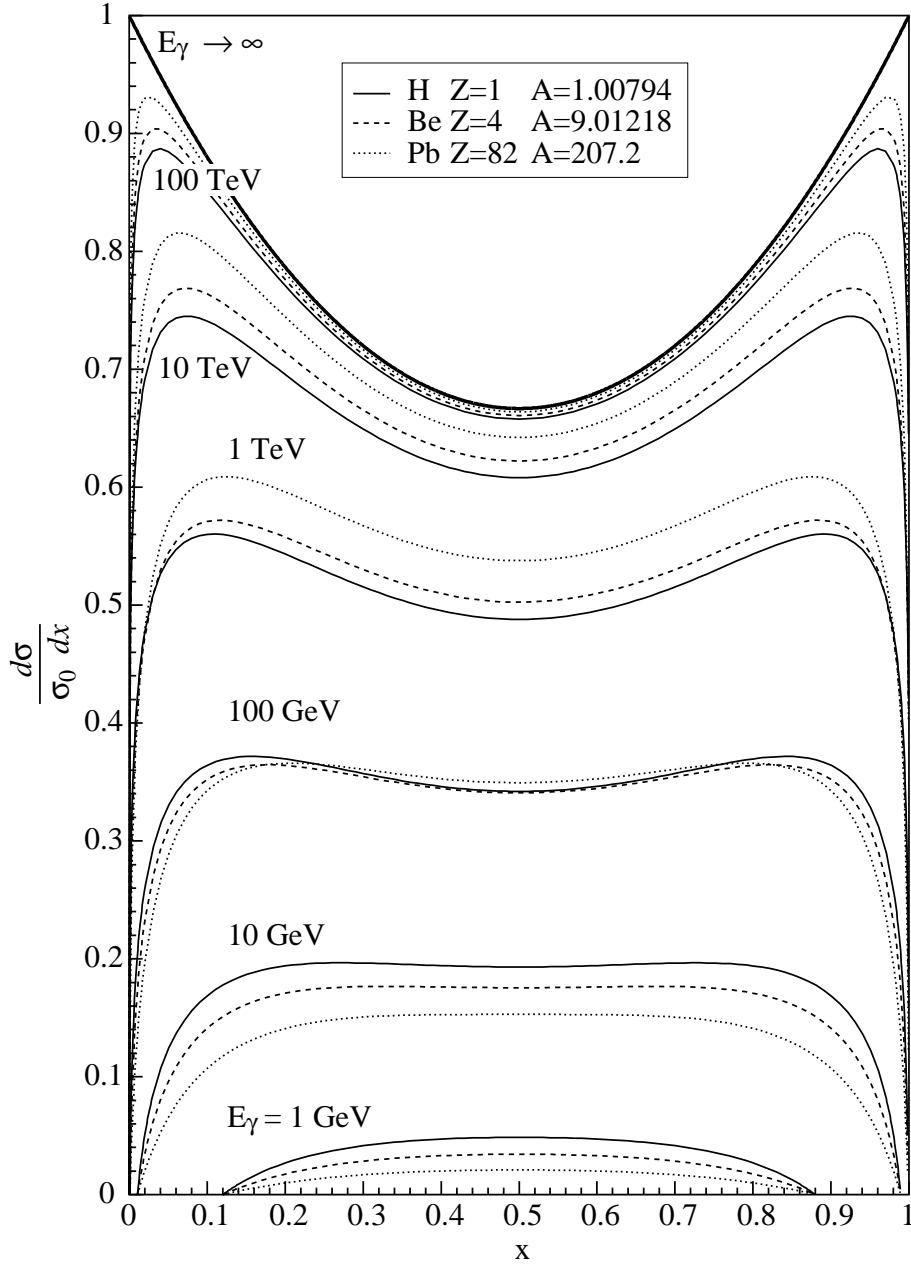
Figure 6.1: Normalized differential cross section for pair production as a function of x, the energy fraction of the photon energy carried by one of the leptons in the pair. The function is shown for three different elements, hydrogen, beryllium and lead, and for a wide range of photon energies.

37

6.5.2 Parameterization of the Total Cross Section

The total cross section is obtained by integration of the differential cross section Eq. (6.40), that is

$$\sigma_{\text{tot}}(E_\gamma) = \int_{x_{\min}}^{x_{\max}} \frac{d\sigma}{dx_+} \, dx_+ = 4 \, \alpha \, Z^2 \, r_c^2 \int_{x_{\min}}^{x_{\max}} \left(1 - \frac{4}{3} \, x_+ x_- \right) \log(W) \, dx_+ \, . \tag{6.46}$$

W is a function of (x_+, E_γ) and (Z, A) of the element (see Eq. (6.41)). Numerical values of W are given in Table 6.1.

Table 6.1: Numerical values of W for $x_+ = 0.5$ for different elements.

E_γ GeV	W for H	W for Be	W for Cu	W for Pb
1	2.11	1.594	1.3505	5.212
10	19.4	10.85	6.803	43.53
100	191.5	102.3	60.10	332.7
1000	1803	919.3	493.3	1476.1
10000	11427	4671	1824	1028.1
∞	28087	8549	2607	1339.8

Values of the total cross section obtained by numerical integration are listed in Table 6.2 for four different elements. Units are in μbarn, where $1 \, \mu\text{barn} = 10^{-34} \, \text{m}^2$.

Table 6.2: Numerical values for the total cross section

E_γ GeV	σ_{tot}, H μbarn	σ_{tot}, Be μbarn	σ_{tot}, Cu μbarn	σ_{tot}, Pb μbarn
1	0.01559	0.1515	5.047	30.22
10	0.09720	1.209	49.56	334.6
100	0.1921	2.660	121.7	886.4
1000	0.2873	4.155	197.6	1476
10000	0.3715	5.392	253.7	1880
∞	0.4319	6.108	279.0	2042

Well above threshold, the total cross section rises about linearly in $\log(E_\gamma)$ with the slope

$$W_M = \frac{1}{4 \, D_n \, \sqrt{e} \, m_\mu} \tag{6.47}$$
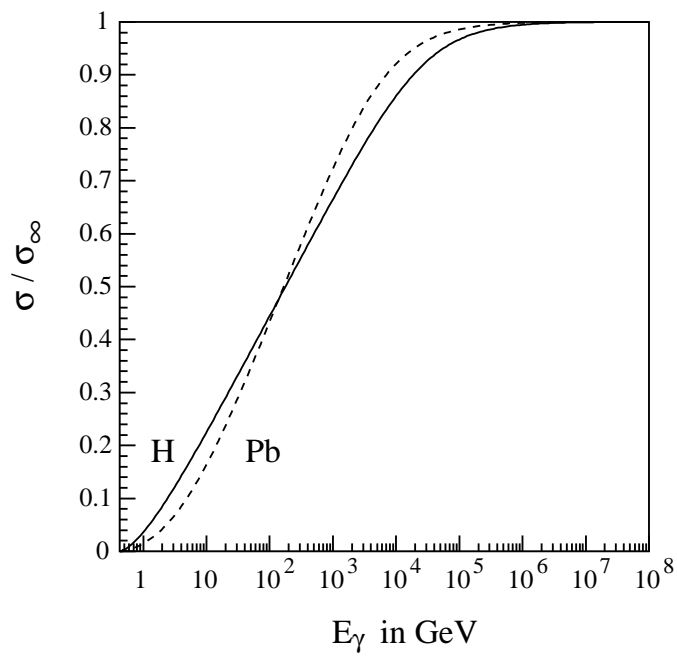
Figure 6.2: Total cross section for the Bethe-Heitler process $\gamma \to \mu^+\mu^-$ as a function of the photon energy E_γ in hydrogen and lead, normalized to the asymptotic cross section σ_∞.

until it saturates due to screening at σ_∞. Fig. 6.2 shows the normalized cross section where

$$\sigma_\infty = \frac{7}{9}\,\sigma_0 \qquad \text{and} \qquad \sigma_0 = 4\,\alpha\,Z^2\,r_c^2\,\log(W_\infty)\ . \qquad (6.48)$$

Numerical values of W_M are listed in Table 6.3.

Table 6.3: Numerical values of W_M.

Element	W_M
	1/GeV
H	0.963169
Be	0.514712
Cu	0.303763
Pb	0.220771

The total cross section can be parameterized as

$$\sigma_{\text{par}} = \frac{28\,\alpha\,Z^2\,r_c^2}{9}\,\log(1 + W_M C_f E_g)\ , \qquad (6.49)$$

with

$$E_g = \left(1 - \frac{4m_\mu}{E_\gamma}\right)^t \left(W_{\text{sat}}^s + E_\gamma^s\right)^{1/s}\ . \qquad (6.50)$$

and

$$W_{\text{sat}} = \frac{W_\infty}{W_M} = B\,Z^{-1/3}\,\frac{4\,\sqrt{e}\,m_\mu^2}{m_e}\ .$$

The threshold behavior in the cross section was found to be well approximated by $t = 1.479 + 0.00799 D_n$ and the saturation by $s = -0.88$. The agreement at lower energies is improved using an empirical correction factor, applied to the slope W_M, of the form

$$C_f = \left[1 + 0.04\log\left(1 + \frac{E_c}{E_\gamma}\right)\right]\ ,$$

where

$$E_c = \left[-18. + \frac{4347.}{B\,Z^{-1/3}}\right]\ \text{GeV}\ .$$

A comparison of the parameterized cross section with the numerical integration of the exact cross section shows that the accuracy of the parametrization is better than 2%, as seen in Fig. 6.3.
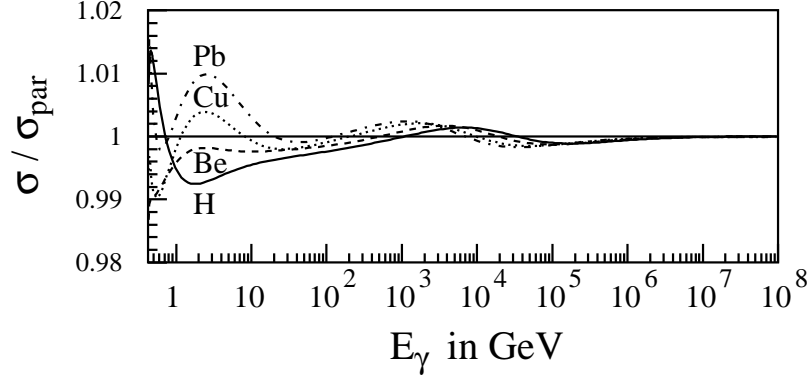
Figure 6.3: Ratio of numerically integrated and parametrized total cross sections as a function of E_γ for hydrogen, beryllium, copper and lead.

6.5.3 Multi-differential Cross Section and Angular Variables

The angular distributions are based on the multi-differential cross section for lepton pair production in the field of the Coulomb center

$$\frac{d\sigma}{dx_+\,du_+\,du_-\,d\varphi} = \frac{4\,Z^2\alpha^3}{\pi}\,\frac{m_\mu^2}{q^4}\,u_+\,u_-$$

$$\left\{\frac{u_+^2 + u_-^2}{(1 + u_+^2)\,(1 + u_-^2)} - 2x_+x_-\right.$$

$$\left.\left[\frac{u_+^2}{(1 + u_+^2)^2} + \frac{u_-^2}{(1 + u_-^2)^2}\right] - \frac{2u_+u_-(1 - 2x_+x_-)\cos\varphi}{(1 + u_+^2)\,(1 + u_-^2)}\right\}\,. \qquad (6.51)$$

Here

$$u_\pm = \gamma_\pm\theta_\pm \quad , \qquad \gamma_\pm = \frac{E_\mu^\pm}{m_\mu} \quad , \qquad q^2 = q_\parallel^2 + q_\perp^2 \quad , \qquad (6.52)$$

where

$$q_\parallel^2 = q_{\min}^2\,(1 + x_-u_+^2 + x_+u_-^2)^2\,,$$
$$q_\perp^2 = m_\mu^2\left[(u_+ - u_-)^2 + 2\,u_+u_-(1 - \cos\varphi)\right]\,. \qquad (6.53)$$

q^2 is the square of the momentum $\mathbf{q}$ transferred to the target and $q_\parallel^2$ and $q_\perp^2$ are the squares of the components of the vector $\mathbf{q}$, which are parallel and perpendicular to the initial photon momentum, respectively. The minimum momentum transfer is $q_{\min} = m_\mu^2/(2E_\gamma\,x_+x_-)$.

41

The muon vectors have the components

$$
\begin{aligned}
\mathbf{p}_+ &= p_+ \left(\; \sin\theta_+ \cos(\varphi_0 + \varphi/2) , \quad \sin\theta_+ \sin(\varphi_0 + \varphi/2) , \, \cos\theta_+ \right) , \\
\mathbf{p}_- &= p_- \left(-\sin\theta_- \cos(\varphi_0 - \varphi/2) , \; -\sin\theta_- \sin(\varphi_0 - \varphi/2) , \, \cos\theta_- \right) ,
\end{aligned}
\tag{6.54}
$$

where $p_\pm = \sqrt{E_\pm^2 - m_\mu^2}$. The initial photon direction is taken as the z-axis. The cross section of Eq. (6.51) does not depend on φ_0. Because of azimuthal symmetry, φ_0 can simply be sampled at random in the interval $(0, 2\pi)$.

Eq. (6.51) is too complicated for efficient Monte Carlo generation. To simplify, the cross section is rewritten to be symmetric in u_+, u_- using a new variable u and small parameters ξ, β, where $u_\pm = u \pm \xi/2$ and $\beta = u\varphi$. When higher powers in small parameters are dropped, the differential cross section in terms of u, ξ, β becomes

$$
\frac{d\sigma}{dx_+ \, d\xi \, d\beta \, u du} = \frac{4\,Z^2\alpha^3}{\pi} \frac{m_\mu^2}{\left(q_\parallel^2 + m_\mu^2(\xi^2 + \beta^2)\right)^2}
\tag{6.55}
$$
$$
\left\{ \xi^2 \left[\frac{1}{(1+u^2)^2} - 2\,x_+ x_- \frac{(1-u^2)^2}{(1+u^2)^4} \right] + \frac{\beta^2(1 - 2x_+ x_-)}{(1+u^2)^2} \right\} ,
$$

where, in this approximation,

$$
q_\parallel^2 = q_{\min}^2 \, (1+u^2)^2 .
$$

For Monte Carlo generation, it is convenient to replace (ξ, β) by the polar coordinates (ρ, ψ) with $\xi = \rho\cos\psi$ and $\beta = \rho\sin\psi$. Integrating Eq. 6.55 over ψ and using symbolically du^2 where $du^2 = 2u\,du$ yields

$$
\frac{d\sigma}{dx_+ \, d\rho \, du^2} = \frac{4Z^2\alpha^3}{m_\mu^2} \frac{\rho^3}{(q_\parallel^2/m_\mu^2 + \rho^2)^2} \left\{ \frac{1 - x_+ x_-}{(1+u^2)^2} - \frac{x_+ x_-(1-u^2)^2}{(1+u^2)^4} \right\} .
\tag{6.56}
$$

Integration with logarithmic accuracy over ρ gives

$$
\int \frac{\rho^3 \, d\rho}{(q_\parallel^2/m_\mu^2 + \rho^2)^2} \approx \int\limits_{q_\parallel/m_\mu}^{1} \frac{d\rho}{\rho} = \log\left(\frac{m_\mu}{q_\parallel} \right) .
\tag{6.57}
$$

Within the logarithmic accuracy, $\log(m_\mu/q_\parallel)$ can be replaced by $\log(m_\mu/q_{\min})$, so that

$$
\frac{d\sigma}{dx_+ \, du^2} = \frac{4\,Z^2\alpha^3}{m_\mu^2} \left\{ \frac{1 - x_+ x_-}{(1+u^2)^2} - \frac{x_+ x_-(1-u^2)^2}{(1+u^2)^4} \right\} \log\left(\frac{m_\mu}{q_{\min}} \right) .
\tag{6.58}
$$

Making the substitution $u^2 = 1/t - 1$, $du^2 = -dt/t^2$ gives

$$\frac{d\sigma}{dx_+ \, dt} = \frac{4 \, Z^2 \alpha^3}{m_\mu^2} \left[1 - 2 \, x_+ x_- + 4 \, x_+ x_- t \, (1-t)\right] \log\left(\frac{m_\mu}{q_{\min}}\right). \qquad (6.59)$$

Atomic screening and the finite nuclear radius may be taken into account by multiplying the differential cross section determined by Eq. (6.56) with the factor

$$\left(F_a(q) - F_n(q)\right)^2 , \qquad (6.60)$$

where F_a and F_n are atomic and nuclear form factors. Please note that after integrating Eq. 6.56 over ρ, the q-dependence is lost.

6.5.4 Procedure for the Generation of Muon - Antimuon Pairs

Given the photon energy E_γ and Z and A of the material in which the γ converts, the probability for the conversions to take place is calculated according to the parametrized total cross section Eq. (6.49). The next step, determining how the photon energy is shared between the μ^+ and μ^-, is done by generating x_+ according to Eq. (6.40). The directions of the muons are then generated via the auxilliary variables t, ρ, ψ. In more detail, the final state is generated by the following five steps, in which $R_{1,2,3,4,...}$ are random numbers with a flat distribution in the interval [0,1]. The generation proceeds as follows.

1) Sampling of the positive muon energy $E_\mu^+ = x_+ \, E_\gamma$.
This is done using the rejection technique. x_+ is first sampled from a flat distribution within kinematic limits using

$$x_+ = x_{\min} + R_1(x_{\max} - x_{\min})$$

and then brought to the shape of Eq. (6.40) by keeping all x_+ which satisfy

$$\left(1 - \frac{4}{3} x_+ x_-\right) \frac{\log(W)}{\log(W_{\max})} < R_2 \, .$$

Here $W_{\max} = W(x_+ = 1/2)$ is the maximum value of W, obtained for symmetric pair production at $x_+ = 1/2$. About 60% of the events are kept in this step. Results of a Monte Carlo generation of x_+ are illustrated in Fig. 6.4. The shape of the histograms agrees with the differential cross section illustrated in Fig. 6.1.
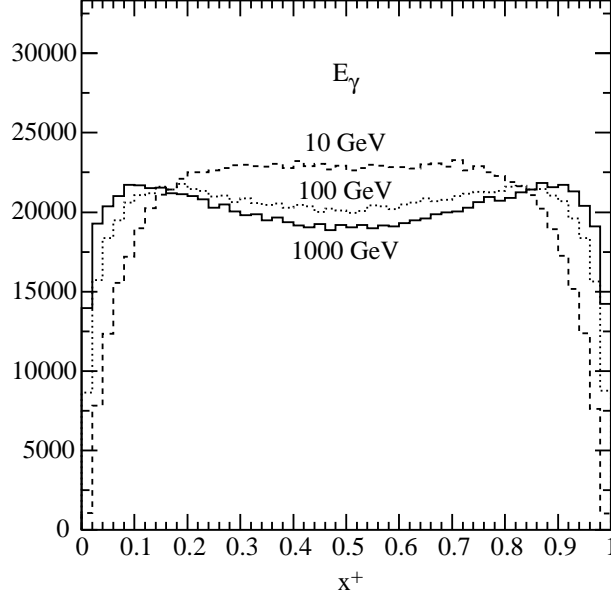
Figure 6.4: Histogram of generated x_+ distributions for beryllium at three different photon energies. The total number of entries at each energy is 10^6.

2) Generate $t(= \frac{1}{\gamma^2\theta^2+1})$.
The distribution in t is obtained from Eq.(6.59) as

$$f_1(t)\, dt = \frac{1 - 2\, x_+x_- + 4\, x_+x_- t\, (1-t)}{1 + C_1/t^2}\, dt, \quad 0 < t \le 1\,. \qquad (6.61)$$

with form factors taken into account by

$$C_1 = \frac{(0.35\, A^{0.27})^2}{x_+x_-\, E_\gamma/m_\mu}\,. \qquad (6.62)$$

In the interval considered, the function $f_1(t)$ will always be bounded from above by

$$\max[f_1(t)] = \frac{1 - x_+x_-}{1 + C_1}\,.$$

For small x_+ and large E_γ, $f_1(t)$ approaches unity, as shown in Fig. 6.5.
The Monte Carlo generation is done using the rejection technique. About 70% of the generated numbers are kept in this step. Generated t-distributions are shown in Fig. 6.6.

3) Generate ψ by the rejection technique using t generated in the previous step for the frequency distribution

$$f_2(\psi) = \Big[1 - 2\, x_+x_- + 4\, x_+x_- t\, (1-t)\, (1+\cos(2\psi))\Big], \qquad 0 \le \psi \le 2\pi\,. \quad (6.63)$$

44
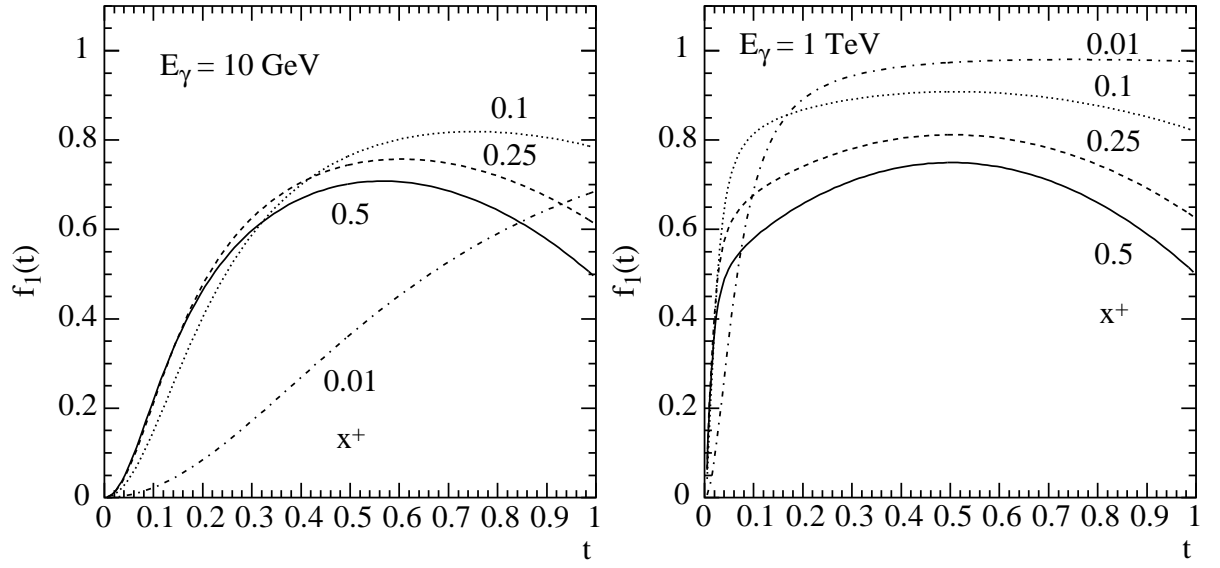
Figure 6.5: The function $f_1(t)$ at $E_\gamma = 10\,\text{GeV}$ (left) and $E_\gamma = 1\,\text{TeV}$ (right) in beryllium for different values of x_+.
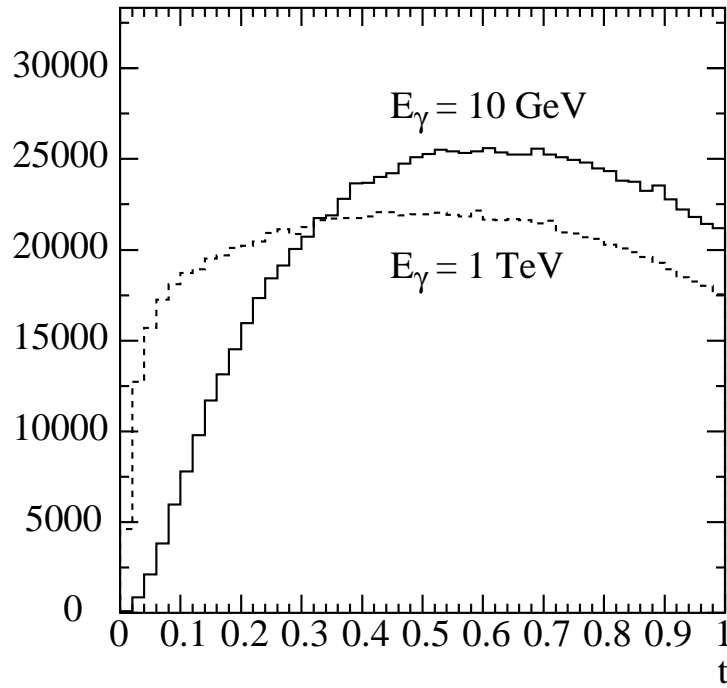
Figure 6.6: Histograms of generated t distributions for $E_\gamma = 10\,\text{GeV}$ (solid line) and $E_\gamma = 100\,\text{GeV}$ (dashed line) with 10^6 events each.
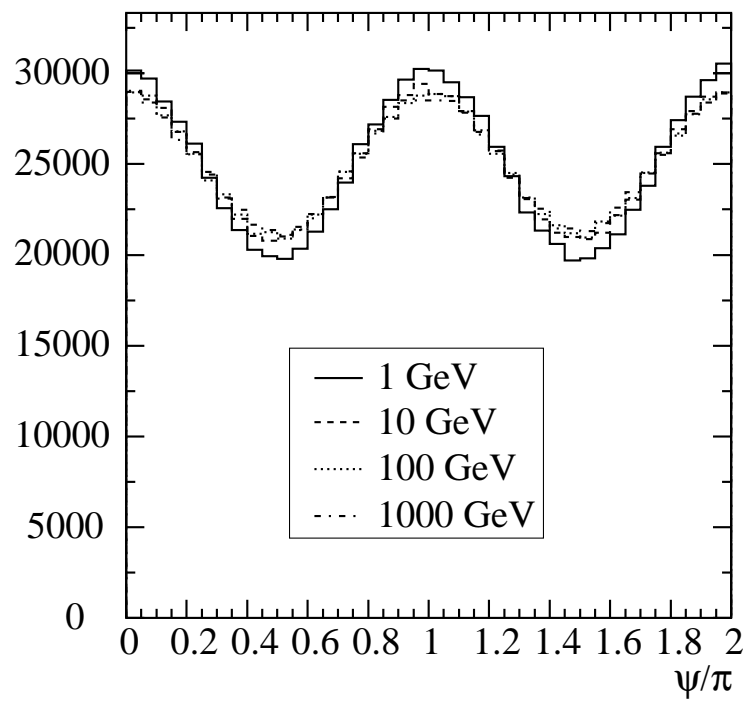
Figure 6.7: Histograms of generated ψ distributions for beryllium at four different photon energies.

The maximum of $f_2(\psi)$ is

$$\max[f_2(\psi)] = 1 - 2\,x_+x_-\,[1 - 4\,t\,(1 - t)]\,. \tag{6.64}$$

Generated distributions in ψ are shown in Fig. 6.7.

4) Generate ρ.
The distribution in ρ has the form

$$f_3(\rho)\,d\rho = \frac{\rho^3\,d\rho}{\rho^4 + C_2}\,, \qquad 0 \le \rho \le \rho_{\max}\,, \tag{6.65}$$

where

$$\rho_{\max}^2 = \frac{1.9}{A^{0.27}}\left(\frac{1}{t} - 1\right), \tag{6.66}$$

and

$$C_2 = \frac{4}{\sqrt{x_+x_-}}\left[\left(\frac{m_\mu}{2E_\gamma x_+x_-\,t}\right)^2 + \left(\frac{m_e}{183\,Z^{-1/3}\,m_\mu}\right)^2\right]^2\,. \tag{6.67}$$

The ρ distribution is obtained by a direct transformation applied to uniform random numbers R_i according to

$$\rho = [C_2(\exp(\beta\,R_i) - 1)]^{1/4}\,, \tag{6.68}$$

where

$$\beta = \log\left(\frac{C_2 + \rho_{\max}^4}{C_2}\right)\,. \tag{6.69}$$

Generated distributions of ρ are shown in Fig. 6.8
5) Calculate θ_+, θ_- and φ from t, ρ, ψ with

$$\gamma_\pm = \frac{E_\mu^\pm}{m_\mu} \qquad \text{and} \qquad u = \sqrt{\frac{1}{t} - 1}\,. \tag{6.70}$$

according to

$$\theta_+ = \frac{1}{\gamma_+}\left(u + \frac{\rho}{2}\cos\psi\right), \quad \theta_- = \frac{1}{\gamma_-}\left(u - \frac{\rho}{2}\cos\psi\right) \quad \text{and} \quad \varphi = \frac{\rho}{u}\sin\psi\,. \tag{6.71}$$

The muon vectors can now be constructed from Eq. (6.54), where φ_0 is chosen randomly between 0 and 2π. Fig. 6.9 shows distributions of θ_+ at different photon energies (in beryllium). The spectra peak around $1/\gamma$ as expected.

The most probable values are $\theta_+ \sim m_\mu/E_\mu^+ = 1/\gamma_+$. In the small angle approximation used here, the values of θ_+ and θ_- can in principle be any
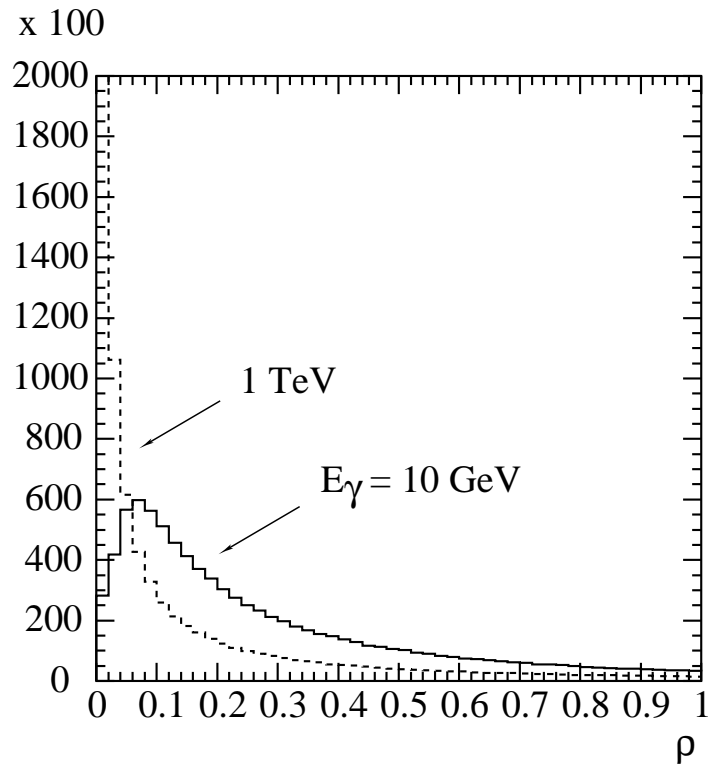
Figure 6.8: Histograms of generated ρ distributions for beryllium at two different photon energies. The total number of entries at each energy is 10^6.
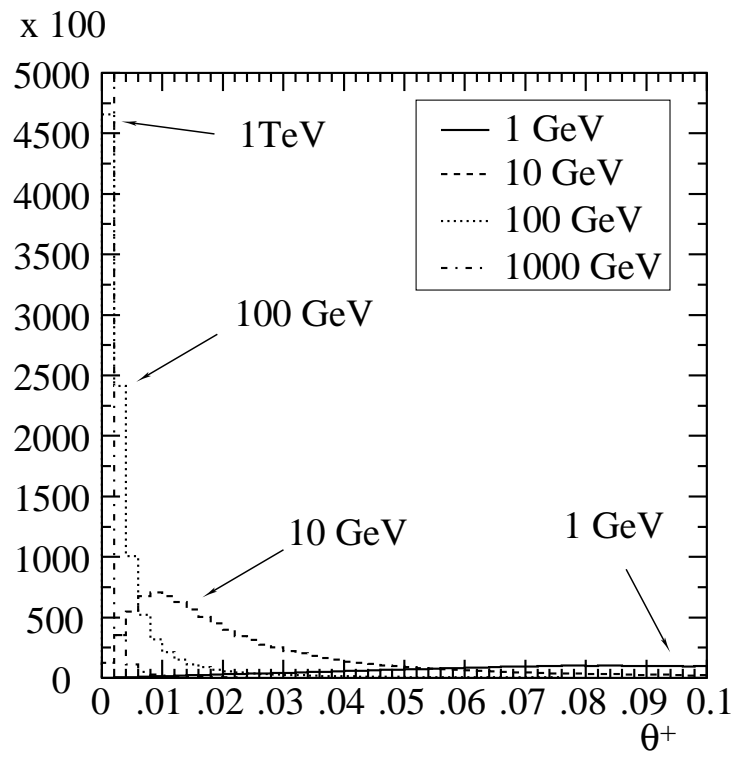
Figure 6.9: Histograms of generated θ_+ distributions at different photon energies.

49
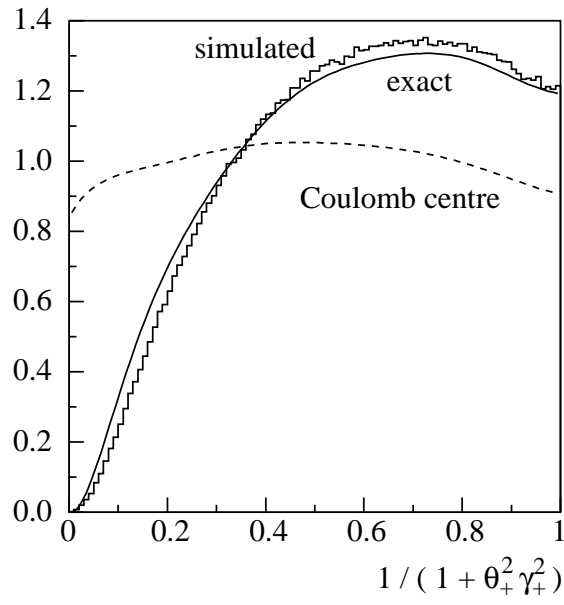
Figure 6.10: Angular distribution of positive (or negative) muons. The solid curve represents the results of the exact calculations. The histogram is the simulated distribution. The angular distribution for pairs created in the field of the Coulomb centre (point-like target) is shown by the dashed curve for comparison.
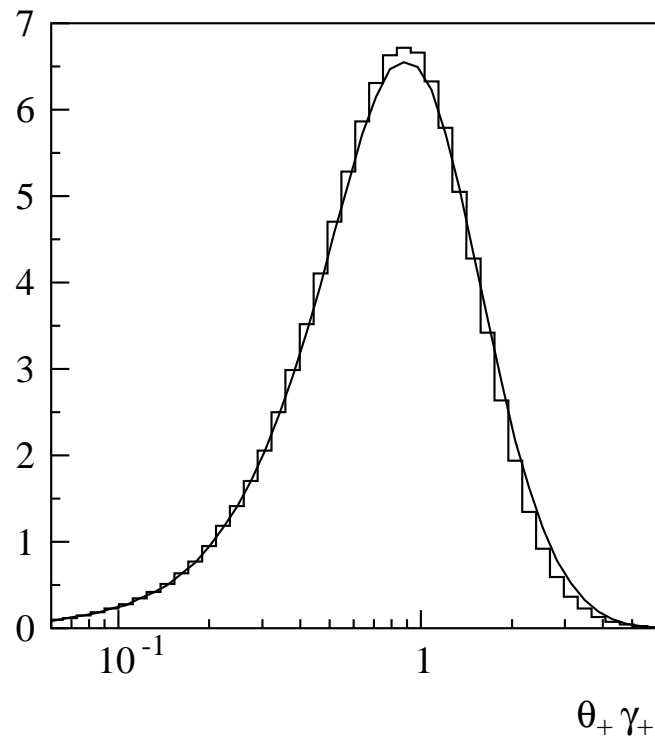
Figure 6.11: Angular distribution in logarithmic scale. The curve corresponds to the exact calculations and the histogram is the simulated distribution.
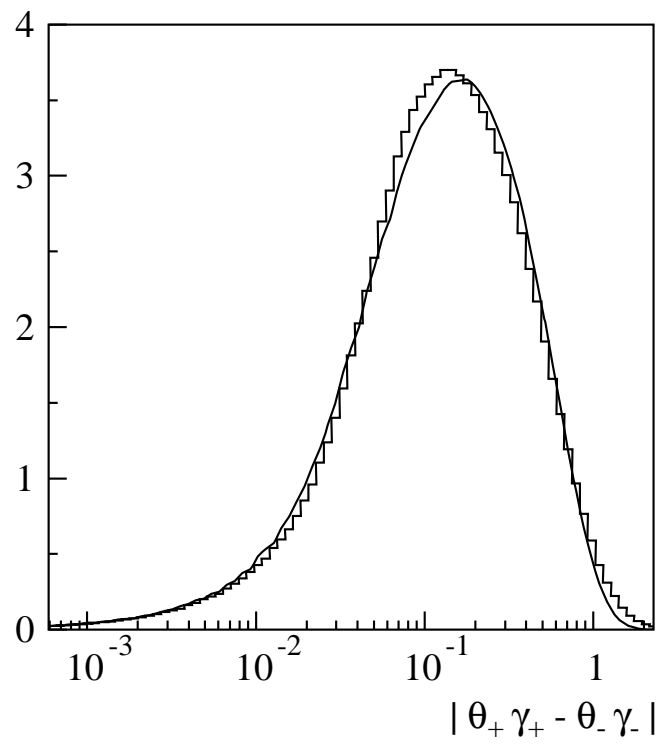
Figure 6.12: Distribution of the difference of transverse momenta of positive and negative muons (with logarithmic x-scale).

positive value from 0 to ∞. In the simulation, this may lead (with a very small probability, of the order of m_μ/E_γ) to unphysical events in which θ_+ or θ_- is greater than π. To avoid this, a limiting angle $\theta_{\text{cut}} = \pi$ is introduced, and the angular sampling repeated, whenever $\max(\theta_+, \theta_-) > \theta_{\text{cut}}$.

Figs. 6.10, 6.11 and 6.12 show distributions of the simulated angular characteristics of muon pairs in comparison with results of exact calculations. The latter were obtained by means of numerical integration of the squared matrix elements with respective nuclear and atomic form factors. All these calculations were made for iron, with $E_\gamma = 10\,\text{GeV}$ and $x_+ = 0.3$. As seen from Fig. 6.10, wide angle pairs (at low values of the argument in the figure) are suppressed in comparison with the Coulomb center approximation. This is due to the influence of the finite nuclear size which is comparable to the inverse mass of the muon. Typical angles of particle emission are of the order of $1/\gamma_\pm = m_\mu/E_\mu^\pm$ (Fig. 6.11). Fig. 6.12 illustrates the influence of the momentum transferred to the target on the angular characteristics of the produced pair. In the frame of the often used model which neglects target recoil, the pair particles would be symmetric in transverse momenta, and coplanar with the initial photon.

6.5.5 Status of this document

28.05.02 created by H.Burkhardt.
01.12.02 re-worded by D.H. Wright

Bibliography

[1] H. Burkhardt, S. Kelner, and R. Kokoulin, "Monte Carlo Generator for Muon Pair Production". CERN-SL-2002-016 (AP) and CLIC Note 511, May 2002.

[2] S. R. Kelner, R. P. Kokoulin, and A. A. Petrukhin, "About cross section for high energy muon bremsstrahlung,". Moscow Phys. Eng. Inst. 024-95, 1995. 31pp.

Chapter 7

Common to All Charged Particles

7.1 Computing the Mean Energy Loss

Energy loss processes are very similar for $e+/e-$, $\mu+/\mu-$ and charged hadrons, so a common description for them was a natural choice in Geant4. Any energy loss process must calculate the continuous and discrete energy loss in a material. Below a given energy threshold the energy loss is continuous and above it the energy loss is simulated by the explicit production of secondary particles - gammas, electrons, and positrons.

7.1.1 Method

Let

$$\frac{d\sigma(Z, E, T)}{dT}$$

be the differential cross-section per atom (atomic number Z) for the ejection of a secondary particle with kinetic energy T by an incident particle of total energy E moving in a material of density ρ. The value of the *kinetic energy cut-off* or *production threshold* is denoted by T_{cut}. Below this threshold the soft secondaries ejected are simulated as continuous energy loss by the incident particle, and above it they are explicitly generated. The mean rate of energy loss is given by:

$$\frac{dE_{soft}(E, T_{cut})}{dx} = n_{at} \cdot \int_0^{T_{cut}} \frac{d\sigma(Z, E, T)}{dT} T \, dT \qquad (7.1)$$

where n_{at} is the number of atoms per volume in the material. The total cross section per atom for the ejection of a secondary of energy $T > T_{cut}$ is

$$\sigma(Z, E, T_{cut}) = \int_{T_{cut}}^{T_{max}} \frac{d\sigma(Z, E, T)}{dT} \, dT \qquad (7.2)$$

where T_{max} is the maximum energy transferable to the secondary particle. If there are several processes providing energy loss for a given particle, then the total continuous part of the energy loss is the sum:

$$\frac{dE_{soft}^{tot}(E, T_{cut})}{dx} = \sum_i \frac{dE_{soft,i}(E, T_{cut})}{dx}. \qquad (7.3)$$

These values are pre-calculated during the initialization phase of GEANT4 and stored in the dE/dx table. Using this table the ranges of the particle in given materials are calculated and stored in the *Range* table. The *Range* table is then inverted to provide the *InverseRange* table. At run time, values of the particle's continuous energy loss and range are obtained using these

tables. Concrete processes contributing to the energy loss are not involved in the calculation at that moment. In contrast, the production of secondaries with kinetic energies above the production threshold is sampled by each concrete energy loss process.

The default energy interval for these tables extends from 100 eV to 100 TeV and the default number of bins is 120. For muon energy loss processes models are valid for higher energies and this interval can be extended up to 1000 PeV. Note that this extension should be done for all three processes which contribute to muon energy loss.

7.1.2   Implementation Details

Common calculations are performed in the class $G4VEnergyLossProcess$ in which the following public methods are implemented:

- PrintInfoDefinition;
- PreparePhysicsTable;
- BuildPhysicsTable;
- AlongStepDoIt;
- PostStepDoIt;
- StorePhysicsTable;
- RetrievePhysicsTable;
- MeanFreePath;
- GetContinuousStepLimit;
- SampleSubCutSecondaries;
- GetDEDXDispersion;
- AlongStepGetPhysicalInteractionLength;
- PostStepGetPhysicalInteractionLength;
- MicroscopicCrossSection;
- AddEmModel;
- SetEmModel;

- UpdateEmModel;

- SetFluctModel;

- BuildDEDXTable;

- BuildLambdaTable;

There are many Get/Set and other accessors methods implemented for this base class. Any derive class need to have an implementation of pure virtual methods:

- IsApplicable;

- PrintInfo;

- InitialiseEnergyLossProcess;

This interface is used by the following processes:

- G4eIonisation;

- G4eBremsstrahlung;

- G4hIonisation;

- G4hhIonisation;

- G4ionIonisation;

- G4ionGasIonisation;

- G4mplIonisation;

- G4MuIonisation;

- G4MuBremsstrahlung;

- G4ePolarizedBremsstrahlung;

- G4ePolarizedIonisation.

These processes mainly provide initialization and also some generic functions like *AlongStepDoIt* and *PostStepDoIt*. The physics models are implemented using the $G4VEmModel$ interface. Because a model is defined to be active over a given energy range and for a defined set of $G4Region$s, an energy loss process can have one or several models defined for a particle and $G4Region$. The following models are available:

- G4BetheBlochModel;

- G4BetheBlochNoDeltaModel;

- G4BraggModel;

- G4BraggIonModel;

- G4BraggNoDeltaModel;

- G4MollerBhabhaModel;

- G4PAIModel;

- G4PAIPhotonModel;

- G4mplIonisationModel;

- G4eBremmstrahlungModel;

- G4MuBetheBlochModel;

- G4MuBremmstrahlungModel;

- G4MuPairProductionModel;

- G4ePolarizedBremsstrahlungModel;

- G4PolarizedMollerBhabhaModel.

Step-size Limit Due to Continuous Energy Loss

Continuous energy loss imposes a limit on the step-size because of the energy dependence of the cross sections. It is generally assumed in MC programs [1] that the cross sections are approximately constant along a step, i.e. the step size should be small enough, so that the change in cross section along the step is also small. In principle one must use very small steps in order to insure an accurate simulation, however the computing time increases as the step-size decreases.

The exact solution is available inside Geant4 Standard EM package (see next chapter 7.3) but is is not implemented yet for all physics processes. A good compromise is to limit the step-size by not allowing the stopping range of the particle to decrease by more than ~ 20 % during the step. This condition works well for particles with kinetic energies > 1 MeV, but for lower energies it gives too short step-sizes, so must be relaxed. To solve this problem a lower limit on the step-size was introduced. A smooth *StepFunction*,

with 2 parameters, controls the step size. At high energy the maximum step size is defined by Step/Range $\sim \alpha_R$ (parameter *dRoverRange*). By default $\alpha_R = 0.2$. As the particle travels the maximum step size decreases gradually until the range becomes lower than ρ_R (parameter *finalRange*). Default *finalRange* $\rho_R = 1mm$. For the case of a particle range $R > \rho_R$ the *StepFunction* provides limit for the step size ΔS_{lim} by the following formula:

$$\Delta S_{lim} = \alpha_R R + \rho_R(1 - \alpha_R)\left(2 - \frac{\rho_R}{R}\right). \tag{7.4}$$

In the opposite case of a small range $\Delta S_{lim} = R$. The figure below shows the ratio step/range as a function of range if step limitation is determined only by the expression (7.4).
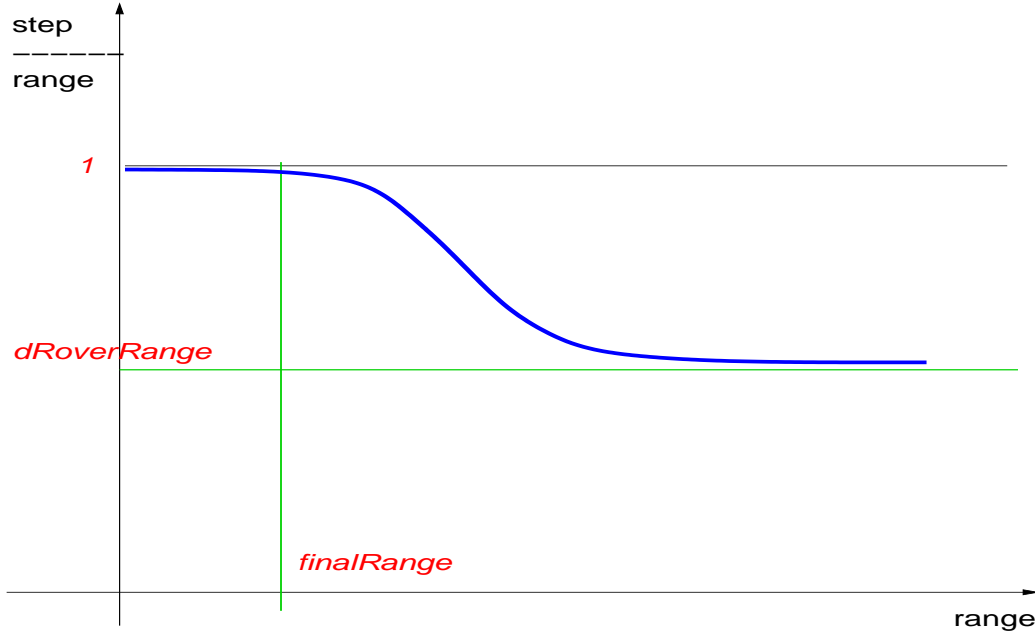
The parameters of *StepFunction* can be overwritten using an UI command:

/process/eLoss/StepFunction 0.2 1 mm

Energy Loss Computation

The computation of the *mean energy loss* after a given step is done by using the dE/dx, *Range*, and *InverseRange* tables. The dE/dx table is used if the energy deposition (ΔT) is less than allowed limit $\Delta T < \xi T_0$, where ξ is *linearLossLimit* parameter (by default $\xi = 0.05$), T_0 is the kinetic energy

of the particle. In that case

$$\Delta T = \frac{dE}{dx}\Delta s, \tag{7.5}$$

where ΔT is the energy loss, Δs is the *true step length*. When a larger percentage of energy is lost, the mean loss can be written as

$$\Delta T = T_0 - f_T(r_0 - \Delta s) \tag{7.6}$$

where r_0 the range at the beginning of the step, the function $f_T(r)$ is the inverse of the *Range* table (i.e. it gives the kinetic energy of the particle for a range value of r) .

After the mean energy loss has been calculated, the process computes the *actual* energy loss, i.e. the loss with fluctuations. The fluctuation is computed from a model described in Section 7.2.

7.1.3 Energy Loss by Heavy Charged Particles

To save memory in the case of positively charged hadrons energy loss, dE/dx, *Range* and *InverseRange* tables are constructed only for *protons*. The energy loss for other positively charged heavy, charged particles is computed from these tables at the *scaled kinetic energy* T_{scaled} :

$$T_{scaled} = q_{eff}^2 T \frac{M_{proton}}{M_{particle}}, \tag{7.7}$$

where T is the kinetic energy of the particle, q_{eff} its effective change in units of positron charge, M_{proton} and $M_{particle}$ are the masses of the proton and particle. For a hadron q_{eff} is equal to the hadron charge, for a slow ion effective charge is different from the charge of the ion's nucleus, because of electron exchange between transporting ion and the media. The effective charge approach is used to describe this effect [2]. The scaling relation (7.7) is valid for any combination of two heavy charged particles with accuracy corresponding to high order mass, charge and spin corrections [3]. To reduce systematics due to these corrections for negatively changed hadrons the same scaling is performed using tables of the anti-proton, for K^+ and π^+ the tables for pi^+ are used, for K^- and π^- the tables for pi^- respectively. Note, that original tables are also computed for electron, positron and muons.

7.1.4 Status of this document

09.10.98 created by L. Urbán
01.12.03 revised by V.Ivanchenko

02.12.03 spelling and grammar check by D.H. Wright
09.12.05 minor update by V.Ivanchenko
14.06.07 formula of StepFunction (mma)
15.06.07 updated last sub-charter, list of processes and models by V.Ivanchenko

Bibliography

[1] GEANT3 manual *Cern Program Library Long Writeup W5013 (1994)*

[2] J.F. Ziegler and J.M. Manoyan, *Nucl. Instr. and Meth. B35 (1988) 215.*

[3] ICRU (A. Allisy et al), Stopping Powers and Ranges for Protons and Alpha Particles, *ICRU Report 49, 1993.*

7.2 Energy loss fluctuations

7.2.1 Fluctuations in thick absorbers

The total continuous energy loss of charged particles is a stochastic quantity with a distribution described in terms of a straggling function. The straggling is partially taken into account in the simulation of energy loss by the production of δ-electrons with energy $T > T_c$. However, continuous energy loss also has fluctuations. Hence in the current GEANT4 implementation two different models of fluctuations are applied depending on the value of the parameter κ which is the lower limit of the number of interactions of the particle in a step. The default value chosen is $\kappa = 10$. In the case of a high range cut (i.e. energy loss without delta ray production) for thick absorbers the following condition should be fulfilled:

$$\Delta E > \kappa \, T_{max} \tag{7.8}$$

where ΔE is the mean continuous energy loss in a track segment of length s, and T_{max} is the maximum kinetic energy that can be transferred to the atomic electron. If this condition holds the fluctuation of the total (unrestricted) energy loss follows a Gaussian distribution. It is worth noting that this condition can be true only for heavy particles, because for electrons, $T_{max} = T/2$, and for positrons, $T_{max} = T$, where T is the kinetic energy of the particle. In order to simulate the fluctuation of the continuous (restricted) energy loss, the condition should be modified. After a study, the following conditions have been chosen:

$$\Delta E > \kappa \, T_c \tag{7.9}$$

and

$$T_{max} <= 2 \, T_c \tag{7.10}$$

where T_c is the cut kinetic energy of δ-electrons. For thick absorbers the straggling function approaches the Gaussian distribution with Bohr's variance [4]:

$$\Omega^2 = 2\pi r_e^2 m_e c^2 N_{el} \frac{Z_h^2}{\beta^2} T_c s \left(1 - \frac{\beta^2}{2} \right), \tag{7.11}$$

where r_e is the classical electron radius, N_{el} is the electron density of the medium, Z_h is the charge of the incident particle in units of positron charge, and β is the relativistic velocity.

7.2.2 Fluctuations in thin absorbers

If the conditions 7.9 and 7.10 are not satisfied the model of energy fluctuations in thin absorbers is applied. The formulae used to compute the energy loss fluctuation (straggling) are based on a very simple physics model of the atom. It is assumed that the atoms have only two energy levels with binding energies E_1 and E_2. The particle-atom interaction can be an excitation with energy loss E_1 or E_2, or ionization with energy loss distributed according to a function $g(E) \sim 1/E^2$:

$$\int_{E_0}^{T_{up}} g(E) \, dE = 1 \implies g(E) = \frac{E_0 T_{up}}{T_{up} - E_0} \frac{1}{E^2}.$$ (7.12)

The macroscopic cross section for excitation ($i = 1, 2$) is

$$\Sigma_i = C \frac{f_i}{E_i} \frac{\ln[2mc^2 \ (\beta\gamma)^2/E_i] - \beta^2}{\ln[2mc^2 \ (\beta\gamma)^2/I] - \beta^2} \ (1 - r)$$ (7.13)

and the ionization cross section is

$$\Sigma_3 = C \frac{T_{up} - E_0}{E_0 T_{up} \ln(\frac{T_{up}}{E_0})} \ r$$ (7.14)

where E_0 denotes the ionization energy of the atom, I is the mean ionization energy, T_{up} is the production threshold for delta ray production (or the maximum energy transfer if this value smaller than the production threshold), E_i and f_i are the energy levels and corresponding oscillator strengths of the atom, and C and r are model parameters. The oscillator strengths f_i and energy levels E_i should satisfy the constraints

$$f_1 + f_2 = 1$$ (7.15)

$$f_1 \cdot lnE_1 + f_2 \cdot lnE_2 = lnI.$$ (7.16)

The cross section formulae 7.13,7.14 and the sum rule equations 7.15,7.16 can be found e.g. in Ref. [1]. The model parameter C can be defined in the following way. The numbers of collisions (n_i, $i = 1, 2$ for excitation and 3 for ionization) follow the Poisson distribution with a mean value $\langle n_i \rangle$. In a step of length Δx the mean number of collisions is given by

$$\langle n_i \rangle = \Delta x \ \Sigma_i$$ (7.17)

The mean energy loss in a step is the sum of the excitation and ionization contributions and can be written as

$$\frac{dE}{dx} \cdot \Delta x = \left\{ \Sigma_1 E_1 + \Sigma_2 E_2 + \int_{E_0}^{T_{up}} Eg(E)dE \right\} \Delta x.$$ (7.18)

From this, using eq. 7.13 - 7.16, one can see that

$$C = dE/dx. \tag{7.19}$$

The other parameters in the fluctuation model have been chosen in the following way. $Z \cdot f_1$ and $Z \cdot f_2$ represent in the model the number of loosely/tightly bound electrons

$$f_2 = 0 \quad for \quad Z = 1 \tag{7.20}$$

$$f_2 = 2/Z \quad for \quad Z \geq 2 \tag{7.21}$$

$$E_2 = 10 \text{ eV } Z^2 \tag{7.22}$$

$$E_0 = 10 \text{ eV }. \tag{7.23}$$

Using these parameter values, E_2 corresponds approximately to the K-shell energy of the atoms (and $Zf_2 = 2$ is the number of K-shell electrons). The parameters f_1 and E_1 can be obtained from Eqs. 7.15 and 7.16. The parameter r is the only variable in the model which can be tuned. This parameter determines the relative contribution of ionization and excitation to the energy loss. Based on comparisons of simulated energy loss distributions to experimental data, its value has been parametrized as

$$r = 0.03 + 0.23 \cdot ln(ln(\frac{T_{up}}{I})) \tag{7.24}$$

Sampling the energy loss. The energy loss is computed in the model under the assumption that the step length (or relative energy loss) is small and, in consequence, the cross section can be considered constant along the step. The loss due to the excitation is

$$\Delta E_{exc} = n_1 E_1 + n_2 E_2 \tag{7.25}$$

where n_1 and n_2 are sampled from a Poisson distribution. The energy loss due to ionization can be generated from the distribution $g(E)$ by the inverse transformation method :

$$u = F(E) = \int_{E_0}^{E} g(x) dx \tag{7.26}$$

$$E = F^{-1}(u) = \frac{E_0}{1 - u \frac{T_{up} - E_0}{T_{up}}} \tag{7.27}$$

where u is a uniformly distributed random number $\in [0, 1]$. The contribution coming from the ionization will then be

$$\Delta E_{ion} = \sum_{j=1}^{n3} \frac{E_0}{1 - u_j \frac{T_{up} - E_0}{T_{up}}} \tag{7.28}$$

where n_3 is the number of ionizations sampled from the Poisson distribution. The total energy loss in a step will be $\Delta E = \Delta E_{exc} + \Delta E_{ion}$ and the energy loss fluctuation comes from fluctuations in the number of collisions n_i and from the sampling of the ionization loss.

Thick layers   If the mean energy loss and step are in the range of validity of the Gaussian approximation of the fluctuation, the much faster Gaussian sampling is used to compute the actual energy loss.

Conclusions   This simple model of energy loss fluctuations is rather fast and can be used for any thickness of material. This has been verified by performing many simulations and comparing the results with experimental data, such as those in Ref.[2].

As the limit of validity of Landau's theory is approached, the loss distribution approaches the Landau form smoothly.

7.2.3   Status of this document

30.01.02 created by L. Urbán.
28.08.02 updated by V.Ivanchenko.
17.08.04 moved to common to all charged particles (mma)
04.12.04 spelling and grammar check by D.H. Wright
04.05.05 updated by L. Urbán.
09.12.05 updated by V.Ivanchenko.
29.03.07 updated by L. Urbán.

Bibliography

[1] H.Bichsel *Rev.Mod.Phys. 60 (1988) 663*

[2] K.Lassila-Perini, L.Urbán *Nucl.Inst.Meth. A362(1995) 416*

[3] GEANT3 manual *Cern Program Library Long Writeup W5013 (1994)*

[4] ICRU (A. Allisy et al), Stopping Powers and Ranges for Protons and Alpha Particles, ICRU Report 49, 1993.

7.3 Correcting the cross section for energy variation

As described in Sections 7.1 and 5.2 the step size limitation is provided by energy loss processes in order to insure the precise calculation of the probability of particle interaction. It is generally assumed in Monte Carlo programs that the particle cross sections are approximately constant during a step, hence the reaction probability p at the end of the step can be expressed as

$$p = 1 - \exp\left(-ns\sigma(E_i)\right), \tag{7.29}$$

where n is the density of atoms in the medium, s is the step length, E_i is the energy of the incident particle at the beginning of the step, and $\sigma(E_i)$ is the reaction cross section at the beginning of the step.

However, it is possible to sample the reaction probability from the exact expression

$$p = 1 - \exp\left(-\int_{E_i}^{E_f} n\sigma(E)ds\right), \tag{7.30}$$

where E_f is the energy of the incident particle at the end of the step, by using the integral approach to particle transport. This approach is available for processes implemented via the $G4VEnergyLossProcess$ and $G4VEmProcess$ interfaces.

The Monte Carlo method of integration is used for sampling the reaction probability [1]. It is assumed that during the step the reaction cross section smaller, than some value $\sigma(E) < \sigma_m$. The mean free path for the given step is computed using σ_m. If the process is chosen as the process happens at the step, the sampling of the final state is performed only with the probability $p = \sigma(E_f)/\sigma_m$, alternatively no interaction happen and tracking of the particle is continued. To estimate the maximum value σ_m for the given tracking step at Geant4 initialisation the energy E_m of absoluted maximum σ_{max} of the cross section for given material is determined and stored. If at the tracking time particle energy $E < E_m$, then $\sigma_m = \sigma(E)$. For higher initial energies if $\xi E > E_m$ then $\sigma_m = min(\sigma(E), \sigma(\xi E))$. In the opposit case $\sigma_m = \sigma_{max}$. Here ξ is a parameter of the algorithm. Its optimal value is connected with the value of the $dRoverRange$ parameter (see sub-chapter 7.1), by default $\xi = 1 - \alpha_R = 0.8$. Note, that described method is precise if the cross section has only one maximum, which is a typical case for electromagnetic processes.

The integral variant of step limitation is the default for the $G4eIonisation$, $G4eBremsstrahlung$ and some otehr process but is not automatically activated for others. To do so the boolean UI command can be used:

/process/eLoss/integral true

The integral variant of the energy loss sampling process is less dependent on values of the production cuts [2] and allows to have less step limitation, however it should be applied on a case-by-case basis because may require extra CPU.

7.3.1 Status of this document

01.12.03 integral method subsection added by V. Ivanchenko
17.08.04 moved to common to all charged particles by M. Maire
25.11.06 revision by V. Ivanchenko

Bibliography

[1] V.N.Ivanchenko et al., Proc. of Int. Conf. MC91: Detector and event simulation in high energy physics, Amsterdam 1991, pp. 79-85. (HEP INDEX 30 (1992) No. 3237).

[2] V.N.Ivanchenko. Geant4 Workshop (TRIUMF, Canada, 2003) http://www.triumf.ca/ geant4-03/talks/04-Thursday-AM-1/02-V.Ivanchenko/eloss03.ppt

7.4 Conversion from range cut to kinetic energy cut

In Geant4 charged particles are tracked to the end of their range. The differential cross section of δ-electron productions and bremsstrahlung grow rapidly when secondary energy decrease. If all secondary particles will be tracked the CPU performance of any Monte Carlo code will be pure. The traditional solution is to use cuts. The specific of Geant4 [1] is that user provides value of cut in term of *cut in range*, which is unique for defined *G4Region* or for the complete geometry.

Range is used, rather than energy, as a more natural concept for designing a coherent policy for different particles and materials. Definition of the certain value of the *cut in range* means the requirement for precision of spatial radioactive dose deposition. This conception is more strict for a simulation code and provides less handles for user to modify final results. At the same time, it ensures that simulation validated in one geometry is valid also for the other geometries.

The value of cut is defined only for electrons, positrons and gamma. At the beginning of initialization of Geant4 physics the conversion from unique *cut in range* to cuts in kinetic energy for each *G4MaterialCutsCouple* [2] is performed. At that moment no energy loss or range table is created, so computation should be performed using original formulas. For electrons and positrons ionization above $10 keV$ a simplified Berger-Seltzer energy loss formula () is used, in which the density correction term is omitted. The contribution of the bremsstrahlung is added using empirical parameterized formula. For $T < 10 keV$ the linear dependence of ionization losses on electron velocity is assumed, bremsstrahlung contribution is neglected. Using these simplified formulas that energy loss vector for each *G4Element* is built. From this vector the range vector for the given material is constructed. The stopping range is defined as

$$R(T) = \int_0^T \frac{1}{(dE/dx)} \, dE. \tag{7.31}$$

The integration has been done analytically for the low energy part and numerically above an energy limit $1\ keV$. Using this table for each *cut in range* the corresponding kinetic energy can be found out. If obtained *cutinenergy* cannot be below the parameter *lowlimit* (default $1\ keV$). If in specific application lower cut is required, then the allowed energy cut needs to be extended:

G4ProductionCutsTable::GetProductionCutsTable()→SetEnergyRange(lowlimit,highlimit);

In contrary to electrons, gammas has no range, so some approximation should be used for range to energy conversion. An approximate empirical formula is used to compute the *absorption cross section* of a photon in an element σ_{abs}. Here, the *absorption cross section* means the sum of the cross sections of the gamma conversion, Compton scattering and photoelectric effect. These processes are the "destructive" processes for photons: they destroy the photon or decrease its energy. The coherent or Rayleigh scattering changes the direction of the gamma only; its cross section is not included in the *absorption cross section.*

The `AbsorptionLength` L_{abs} vector is calculated for every material as :

$$L_{abs} = 5/\sigma_{abs}. \tag{7.32}$$

The factor 5 comes from the requirement that the probability of having no 'destructive' interaction should be small, hence

$$\exp(-L_{abs}\sigma_{abs}) = \exp(-5) = 6.7 \times 10^{-3}. \tag{7.33}$$

The photon cross section for a material has a minimum at a certain energy E_{min}. Correspondingly L_{abs} has a maximum at $E = E_{min}$, the value of the maximal L_{abs} is the biggest "meaningful" cut in absorption length. If the cut given by the user is bigger than this maximum, a warning is printed and the cut in kinetic energy is set to the *highlimit.*

The conversion from range to energy can be studied using *G4EmCalculator* class. This class allows access or recalculation of energy loss, ranges and other values. It can be instantiated and at any place of user code and can be used after initialisation of Physics Lists:

G4EmCalculator calc;
calc.ComputeEnergyCutFromRangeCut(range, particle, material);

here particle and material may be string names or corresponding const pointers to *G4ParticleDefinition* and *G4Material.*

7.4.1   Status of this document

 9.10.98 created by L. Urbán.
27.07.01 minor revision M.Maire
17.08.04 moved to common to all charged particles (mma)
04.12.04 minor re-wording by D.H. Wright
18.05.07 rewritten by V. Ivanchenko

Bibliography

[1] Geant4 Collaboration (S. Agostinelli et al.), Nucl. Instr. Meth. A506 (2003) 250.

[2] j. Allison et al., IEEE Trans. Nucl. Sci., 53 (2006) 270.

7.5 Multiple Scattering

Geant4 uses a new model to simulate the multiple scattering (MSC) of charged particles in matter [1]. The model (*G4UrbanMscModel*) simulates the scattering of the particle after a given step, and also computes the path length correction and the lateral displacement. It does not use the Moliere formalism [2].

7.5.1 Introduction

MSC simulation algorithms can be classified as either *detailed* or *condensed*. In the detailed algorithms, all the collisions/interactions experienced by the particle are simulated. This simulation can be considered as exact; it gives the same results as the solution of the transport equation. However, it can be used only if the number of collisions is not too large, a condition fulfilled only for special geometries (such as thin foils), or low enough kinetic energies. For larger kinetic energies the average number of collisions is very large and the detailed simulation becomes very inefficient. High energy simulation codes use condensed simulation algorithms, in which the global effects of the collisions are simulated at the end of a track segment. The global effects generally computed in these codes are the net displacement, energy loss, and change of direction of the charged particle. These quantities are computed from the multiple scattering theories used in the codes. The accuracy of the condensed simulations is limited by the approximations of the multiple scattering theories.

Most particle physics simulation codes use the multiple scattering theories of Molière [2], Goudsmit and Saunderson [4] and Lewis [3]. The theories of Molière and Goudsmit-Saunderson give only the angular distribution after a step, while the Lewis theory computes the moments of the spatial distribution as well. None of these MSC theories gives the probability distribution of the spatial displacement. Therefore each of the MSC simulation codes incorporates its own algorithm to determine the spatial displacement of the charged particle after a given step. These algorithms are not exact, of course, and are responsible for most of the uncertainties in the MSC codes. Therefore the simulation results can depend on the value of the step length and generally one has to select the value of the step length carefully.

A new class of MSC simulation, the *mixed* simulation algorithms (see e.g.[5]), appeared in the literature recently. The mixed algorithm simulates the *hard* collisions one by one and uses a MSC theory to treat the effects of the *soft*

collisions at the end of a given step. Such algorithms can prevent the number of steps from becoming too large and also reduce the dependence on the step length.

The MSC model used in Geant4 belongs to the class of condensed simulations. It uses model functions to determine the angular and spatial distributions after a step. The functions have been chosen in such a way as to give the same moments of the (angular and spatial) distributions as the Lewis theory [3].

7.5.2 Definition of Terms

In simulation, a particle is transported by steps through the detector geometry. The shortest distance between the endpoints of a step is called the *geometrical path length*, z. In the absence of a magnetic field, this is a straight line. For non-zero fields, z is the shortest distance along a curved trajectory. Constraints on z are imposed when particle tracks cross volume boundaries. The path length of an actual particle, however, is usually longer than the geometrical path length, due to physical interactions like multiple scattering. This distance is called the *true path length*, t. Constraints on t are imposed by the physical processes acting on the particle.

The properties of the multiple scattering process are completely determined by the *transport mean free paths*, λ_k, which are functions of the energy in a given material. The k-th transport mean free path is defined as

$$\frac{1}{\lambda_k} = 2\pi n_a \int_{-1}^{1} [1 - P_k(cos\chi)] \frac{d\sigma(\chi)}{d\Omega} d(cos\chi) \qquad (7.34)$$

where $d\sigma(\chi)/d\Omega$ is the differential cross section of the scattering, $P_k(cos\chi)$ is the k-th Legendre polynomial, and n_a is the number of atoms per volume.

Most of the mean properties of MSC computed in the simulation codes depend only on the first and second transport mean free paths. The mean value of the geometrical path length (first moment) corresponding to a given true path length t is given by

$$\langle z \rangle = \lambda_1 \left[1 - \exp\left(-\frac{t}{\lambda_1} \right) \right] \qquad (7.35)$$

Eq. 7.35 is an exact result for the mean value of z if the differential cross section has axial symmetry and the energy loss can be neglected. The transformation between true and geometrical path lengths is called the *path length*

correction. This formula and other expressions for the first moments of the spatial distribution were taken from either [5] or [6], but were originally calculated by Goudsmit and Saunderson [4] and Lewis [3].

At the end of the true step length, t, the scattering angle is θ. The mean value of $cos\theta$ is

$$\langle cos\theta \rangle = \exp\left[-\frac{t}{\lambda_1}\right] \tag{7.36}$$

The variance of $cos\theta$ can be written as

$$\sigma^2 = \langle cos^2\theta \rangle - \langle cos\theta \rangle^2 = \frac{1 + 2e^{-2\kappa\tau}}{3} - e^{-2\tau} \tag{7.37}$$

where $\tau = t/\lambda_1$ and $\kappa = \lambda_1/\lambda_2$.

The mean lateral displacement is given by a more complicated formula [5], but this quantity can also be calculated relatively easily and accurately. The square of the *mean lateral displacement* is

$$\langle x^2 + y^2 \rangle = \frac{4\lambda_1^2}{3} \left[\tau - \frac{\kappa + 1}{\kappa} + \frac{\kappa}{\kappa - 1}e^{-\tau} - \frac{1}{\kappa(\kappa - 1)}e^{-\kappa\tau}\right] \tag{7.38}$$

Here it is assumed that the initial particle direction is parallel to the the z axis.

The lateral correlation is determined by the equation

$$\langle xv_x + yv_y \rangle = \frac{2\lambda_1}{3} \left[1 - \frac{\kappa}{\kappa - 1}e^{-\tau} + \frac{1}{\kappa - 1}e^{-\kappa\tau}\right] \tag{7.39}$$

where v_x and v_y are the x and y components of the direction unit vector. This equation gives the correlation strength between the final lateral position and final direction.

The transport mean free path values have been calculated by Liljequist et al. [7], [8] for electrons and positrons in the kinetic energy range 100 eV - 20 MeV in 15 materials. The MSC model in Geant4 uses these values for kinetic energies below 10 MeV. For high energy particles (above 10 MeV) the transport mean free path values have been taken from a paper of R.Mayol and F.Salvat ([9]). When necessary, the model linearly interpolates or extrapolates the transport cross section, $\sigma_1 = 1/\lambda_1$, in atomic number Z and in the square of the particle velocity, β^2. The ratio κ is a very slowly varying function of the energy: $\kappa > 2$ for $T >$ a few keV, and $\kappa \to 3$ for very high energies (see [6]).

Hence, a constant value of 2.5 is used in the model.

Nuclear size effects are negligible for low energy particles and they are accounted for in the Born approximation in [9], so there is no need for extra corrections of this kind in the model.

7.5.3 Path Length Correction

As mentioned above, the path length correction refers to the transformation true path length $\longrightarrow$ geometrical path length and its inverse. The true path length $\longrightarrow$ geometrical path length transformation is given by Eq. 7.35 if the step is small and the energy loss can be neglected. If the step is not small the energy dependence makes the transformation more complicated. For this case Eqs. 7.36,7.35 should be modified as

$$\langle cos\theta \rangle = \exp \left[- \int_0^t \frac{du}{\lambda_1(u)} \right] \tag{7.40}$$

$$\langle z \rangle = \int_0^t \langle cos\theta \rangle_u \, du \tag{7.41}$$

where θ is the scattering angle, t and z are the true and geometrical path lengths, and λ_1 is the transport mean free path.

In order to compute Eqs. 7.40,7.41 the t dependence of the transport mean free path must be known. λ_1 depends on the kinetic energy of the particle which decreases along the step. All computations in the model use a linear approximation for this t dependence:

$$\lambda_1(t) = \lambda_{10}(1 - \alpha t) \tag{7.42}$$

Here λ_{10} denotes the value of λ_1 at the start of the step, and α is a constant. It is worth noting that Eq. 7.42 is *not* a crude approximation. It is rather good at low (< 1 MeV) energy. At higher energies the step is generally much smaller than the range of the particle, so the change in energy is small and so is the change in λ_1. Using Eqs. 7.40 - 7.42 the explicit formula for $\langle cos\theta \rangle$ and $\langle z \rangle$ are :

$$\langle cos\theta \rangle = (1 - \alpha t)^{\frac{1}{\alpha \lambda_{10}}} \tag{7.43}$$

$$\langle z \rangle = \frac{1}{\alpha(1 + \frac{1}{\alpha \lambda_{10}})} \left[1 - (1 - \alpha t)^{1 + \frac{1}{\alpha \lambda_{10}}} \right] \tag{7.44}$$

The value of the constant α can be expressed using λ_{10} and λ_{11} where λ_{11} is the value of the transport mean free path at the end of the step

$$\alpha = \frac{\lambda_{10} - \lambda_{11}}{t\lambda_{10}} \tag{7.45}$$

At low energies ($T_{kin} < M$, M - particle mass) α has a simpler form:

$$\alpha = \frac{1}{r_0} \tag{7.46}$$

where r_0 denotes the range of the particle at the start of the step.
It can easily be seen that for a small step (i.e. for a step with small relative energy loss) the formula of $\langle z \rangle$ is

$$\langle z \rangle = \lambda_{10} \left[1 - \exp\left(-\frac{t}{\lambda_{10}} \right) \right] \tag{7.47}$$

Eq. 7.44 or 7.47 gives the mean value of the geometrical step length for a given true step length.

The actual geometrical path length is sampled in the model according to the simple probability density function defined for $v = z/t \in [0, 1]$:

$$f(v) = (k + 1)(k + 2)v^k(1 - v) \tag{7.48}$$

The value of the exponent k is computed from the requirement that $f(v)$ must give the same mean value for $z = vt$ as Eq. 7.44 or 7.47. Hence

$$k = \frac{3\langle z \rangle - t}{t - \langle z \rangle} \tag{7.49}$$

The value of $z = vt$ is sampled using $f(v)$ if $k > 0$, otherwise $z = \langle z \rangle$ is used.

The geometrical path length $\longrightarrow$ true path length transformation is performed using the mean values. The transformation can be written as

$$t(z) = \langle t \rangle = -\lambda_1 \log\left(1 - \frac{z}{\lambda_1} \right) \tag{7.50}$$

if the geometrical step is small and

$$t(z) = \frac{1}{\alpha} \left[1 - (1 - \alpha w z)^{\frac{1}{w}} \right] \tag{7.51}$$

where

$$w = 1 + \frac{1}{\alpha\lambda_{10}}$$

if the step is not small, i.e. the energy loss should be taken into account.

This transformation is needed when the particle arrives at a volume boundary, causing the step to be geometry-limited. In this case the true path length should be computed in order to have the correct energy loss of the particle after the step.

7.5.4   Angular Distribution

The quantity $u = cos\theta$ is sampled according to a model function $g(u)$. The shape of this function has been chosen such that Eqs. 7.36 and 7.37 are satisfied. The functional form of g is

$$g(u) = pg_1(u) + (1 - p)g_2(u) \tag{7.52}$$

where $0 \leq p \leq 1$, and the g_i are simple functions of $u = cos\theta$, normalized over the range $u \in [-1,\ 1]$. The functions g_i have been chosen as

$$g_1(u) = C_1 \ \ e^{-a(1-u)} \qquad\qquad -1 \leq u \leq 1 \tag{7.53}$$

$$g_2(u) = C_2 \ \ \frac{1}{(b-u)^2} \qquad\qquad -1 \leq u \leq 1 \tag{7.54}$$

where $a > 0$ and $b > 1$ are model parameters, and the C_i are normalization constants. It is worth noting that for small scattering angles, θ, $g_1(u)$ is nearly Gaussian ($exp(-\theta^2/2\theta_0^2)$) if $\theta_0^2 \approx 1/a$, while $g_2(u)$ has a Rutherford-like tail for large θ .

7.5.5   Determination of the Model Parameters

The parameters a, b and p are not independent.
A constraint comes from the requirement that $g(u)$ must give the same mean value for u as the theory:

$$q\{p\langle u\rangle_1 + (1-p)\langle u\rangle_2\} = \langle cos\theta\rangle \tag{7.55}$$

where $\langle u\rangle_i$ denotes the mean value of u computed from the distribution $g_i(u)$.

The parameter a was chosen according to a modified Highland-Lynch-Dahl formula for the width of the angular distribution [10], [11].

$$a = \frac{0.5}{1 - cos(\theta_0)} \tag{7.56}$$

where θ_0 is

$$\theta_0 = \frac{13.6 MeV}{\beta cp} z_{ch} \sqrt{\frac{t}{X_0}} \left[1 + h_c \ln\left(\frac{t}{X_0}\right) \right] \tag{7.57}$$

when the original Highland-Lynch-Dahl formula is used. Here $\theta_0 = \theta_{plane}^{rms}$ is the width of the approximate Gaussian projected angle distribution, p, βc and z_{ch} are the momentum, velocity and charge number of the incident particle, and t/X_0 is the true path length in radiation length unit. The correction term $h_c = 0.038$ in the formula. This value of θ_0 is from a fit to the Molière distribution for singly charged particles with $\beta = 1$ for all Z, and is accurate to 11 % or better for $10^{-3} \leq t/X_0 \leq 100$ (see e.g. Rev. of Particle Properties, section 23.3).

The model uses a slightly modified Highland-Lynch-Dahl formula to compute θ_0. The modification is that different correction terms h_c are used for electrons/positrons , muons and for heavier particles (hadrons). The numerical value of the parameters can be found in the code.

The parameter b is set to

$$b = 1/\langle cos\theta \rangle \tag{7.58}$$

This value of b ensures that Eq. 7.37 is satisfied in a good approximation.

It should be noted that in this model there is no step limitation originating from the multiple scattering process. Another important feature of this model is that the sum of the 'true' step lengths of the particle, that is, the total true path length, does not depend on the length of the steps. Most algorithms used in simulations do not have these properties.

In the case of heavy charged particles (μ, π, p, etc.) the mean transport free path is calculated from the electron or positron λ_1 values with a 'scaling' applied. This is possible because the transport mean free path λ_1 depends only on the variable $P\beta c$, where P is the momentum, and βc is the velocity of the particle.

In its present form the model samples the path length correction and angular distribution from model functions, while for the lateral displacement and the lateral correlation only the mean values are used and all the other correlations

are neglected. However, the model is general enough to incorporate other random quantities and correlations in the future.

7.5.6 The MSC Process in Geant4

The step length of the particles is determined by the physics processes or the geometry of the detectors. The tracking/stepping algorithm checks all the step lengths demanded by the (continuous or discrete) physics processes and determines the minimum of these step lengths.

Then, this minimum step length must be compared with the length determined by the geometry of the detectors and one has to select the minimum of the 'physics step length' and the 'geometrical step length' as the actual step length.

This is the point where the MSC model comes into the game. All the physics processes use the true path length t to sample the interaction point, while the step limitation originated from the geometry is a geometrical path length z. The MSC algorithm transforms the 'physics step length' into a 'geometrical step length' before the comparison of the two lengths. This 't'→'z' transformation can be called the inverse of the path length correction.

After the actual step length has been determined and the particle relocation has been performed the MSC performs the transformation 'z'→'t', because the energy loss and scattering computation need the true step length 't'.

The scattering angle θ of the particle after the step of length 't' is sampled according to the model function given in Eq. 7.52 . The azimuthal angle ϕ is generated uniformly in the range $[0, 2\pi]$.

After the simulation of the scattering angle, the lateral displacement is computed using Eq. 7.38. Then the correlation given by Eq. 7.39 is used to determine the direction of the lateral displacement. Before 'moving' the particle according to the displacement a check is performed to ensure that the relocation of the particle with the lateral displacement does not take the particle beyond the volume boundary.

7.5.7 Step Limitation Algorithm

In Geant4 the boundary crossing is treated by the transportation process. The transportation ensures that the particle does not penetrate in a new

volume without stopping at the boundary, it restricts the step size when the particle leaves a volume. However, this step restriction can be rather weak in big volumes and this fact can result a not very good angular distribution after the volume. At the same time, there is no similar step limitation when a particle enters a volume and this fact does not allow a good backscattering simulation for low energy particles. Low energy particles penetrate too deeply into the volume in the first step and then - because of energy loss - they are not able to reach again the boundary in backward direction.

A very simple step limitation algorithm has been implemented in the MSC code to cure this situation. At the start of a track or after entering in a new volume, the algorithm restricts the step size to a value

$$f_r \cdot max\{r, \lambda_1\} \tag{7.59}$$

where r is the range of the particle, f_r is a parameter $\in [0, 1]$, taking the max of r and λ_1 is an empirical choice. The value of f_r is constant for low energy particles while for particles with $\lambda_1 > \lambda_{lim}$ an effective value is used given by the scaling equation

$$f_{reff} = f_r \cdot \left[1 - sc + sc * \frac{\lambda_1}{\lambda_{lim}} \right] \tag{7.60}$$

(The numerical values $sc = 0.25$ and $\lambda_{lim} = 1 \ mm$ are used in the equation.) In order not to use very small - unphysical - step sizes a lower limit is given for the step size as

$$tlimitmin = max \left[\frac{\lambda_1}{nstepmax}, \lambda_{elastic} \right] \tag{7.61}$$

with $nstepmax = 25$ and $\lambda_{elastic}$ is the elastic mean free path of the particle (see later).

It can be easily seen that this kind of step limitation poses a real constraint only for low energy particles.

In order to prevent a particle from crossing a volume in just one step, an additional limitation is imposed: after entering a volume the step size cannot be bigger than

$$\frac{d_{geom}}{f_g} \tag{7.62}$$

where d_{geom} is the distance to the next boundary (in the direction of the particle) and f_g is a constant parameter. A similar restriction at the start of

a track is

$$\frac{2d_{geom}}{f_g} \qquad (7.63)$$

The choice of the parameters f_r and f_g is also related to performance. By default $f_r = 0.02$ and $f_g = 2.5$ are used, but these may be set to any other value in a simple way. One can get an approximate simulation of the backscattering with the default value, while if a better backscattering simulation is needed it is possible to get it using a smaller value for f_r. However, this model is very simple and it can only approximately reproduce the backscattering data.

7.5.8   Boundary Crossing Algorithm

A special stepping algorithm has been implemented recently (Autumn 2006) in order to improve the simulation around interfaces. This algorithm does not allow 'big' last steps in a volume and 'big' first steps in the next volume. The step length of these steps around a boundary crossing can not be bigger than the mean free path of the elastic scattering of the particle in the given volume (material). After these small steps the particle scattered according to a single scattering law (i.e. there is no multiple scattering very close to the boundary or at the boundary).

The key parameter of the algorithm is the variable called $skin$. The algorithm is not active for $skin \leq 0$, while for $skin > 0$ it is active in layers of thickness $skin \cdot \lambda_{elastic}$ before boundary crossing and of thickness $(skin - 1) \cdot \lambda_{elastic}$ after boundary crossing (for $skin = 1$ there is only one small step just before the boundary). In this active area the particle performs steps of length $\lambda_{elastic}$ (or smaller if the particle reaches the boundary traversing a smaller distance than this value).

The scattering at the end of a small step is single or plural and for these small steps there are no path length correction and lateral displacement computation. In other words the program works in this thin layer in 'microscopic mode'.

The elastic mean free path can be estimated as

$$\lambda_{elastic} = \lambda_1 \cdot rat\,(T_{kin}) \qquad (7.64)$$

where $rat(T_{kin})$ a simple empirical function computed from the elastic and first transport cross section values of Mayol and Salvat [9]

$$rat\left(T_{kin}\right) = \frac{0.001(MeV)^2}{T_{kin}\left(T_{kin} + 10MeV\right)} \qquad (7.65)$$

T_{kin} is the kinetic energy of the particle.

At the end of a small step the number of scatterings is sampled according to the Poissonian distribution with a mean value $t/\lambda_{elastic}$ and in the case of plural scattering the final scattering angle is computed by summing the contributions of the individual scatterings.

The single scattering is determined by the distribution

$$g(u) = C\frac{1}{(1 + 0.5a^2 - u)^2} \qquad (7.66)$$

where $u = \cos(\theta)$, a is the screening parameter, C is a normalization constant. The form of the screening parameter is

$$a = \frac{\alpha Z^{1/3}}{\sqrt{(\tau(\tau + 2))}} \qquad (7.67)$$

where Z is the atomic number, τ is the kinetic energy measured in particle mass units, α is a constant. It can be shown easily that the function $g(u)$ for small scattering angle θ is equivalent to the well known screened Rutherford scattering formula :

$$\tilde{g}(\theta)\ d\Omega = \tilde{C}\frac{\theta\ d\theta}{(a^2 + \theta^2)^2} \qquad (7.68)$$

7.5.9 Implementation Details

The concrete implementation of described algorithms of simulation is provided in *G4UrbanMscModel* class which inherit from *G4VEmModel* interface. Because multiple scattering is very similar for different particles the base class *G4VMultipleScattering* was created to collect and provide significant features of the calculations which are common to different particle types.

In the `AlongStepGetPhysicalInteractionLength` method the minimum step size due to the physics processes is compared with the step size constraints imposed by the transportation process and the geometry. In order to do this, the 't' step → 'z' step transformation must be performed. Therefore, the method should be invoked after the `GetPhysicalInteractionLength` methods of other physics processes, but before the same method of the transportation process. The reason for this ordering is that the physics processes

81

'feel' the true path length t traveled by the particle, while the transportation process (geometry) uses the z step length.

At this point the program also checks whether the particle has entered a new volume. If it has, the particle steps cannot be bigger than $t_{lim} = f_r \ max(r, \lambda)$. This step limitation is governed by the physics, because t_{lim} depends on the particle energy and the material.

The `PostStepGetPhysicalInteractionLength` method of the multiple scattering process simply sets the force flag to 'Forced' in order to ensure that `PostStepDoIt` is called at every step. It also returns a large value for the interaction length so that there is no step limitation at this level.

The `AlongStepDoIt` function of the process performs the inverse, 'z' $\rightarrow$ 't' transformation. This function should be invoked after the `AlongStepDoIt` method of the transportation process, that is, after the particle relocation is determined by the geometrical step length, but before applying any other physics `AlongStepDoIt`.

The `PostStepDoIt` method of the process samples the scattering angle and performs the lateral displacement when the particle is not near a boundary.

There are two processes *G4MultipleScattering* and *G4hMultipleScattering*, which inherit from *G4VMultipleScattering* and use the same model *G4UrbanMscModel* but different default values of parameters of the model (Table 7.1). Note, that there is three types of step limitation by multiple scattering process:

- `Minimal` - only f_r parameter is used, was used for g4 7.1 release;

- `UseSafety` or $skin = 0$ - uses particle range and geometrical safety;

- `UseDistanceToBoundary` - uses particle range, geometrical safety and linear distance to geometrical boundary.

The parameters of the model can be changed via public functions of the base class *G4VMultipleSacttering*. They can be changed for all multiple scattering processes simultaneously via *G4EmProcessOptions* class or via Geant4 UI commands. The following commands are available:

/process/msc/StepLimit UseDistanceToBoundary
/process/msc/LateralDisplacement false
/process/msc/RangeFactor 0.02
/process/msc/GeomFactor 2.5

parameter	G4MultipleScattering	G4hMultipleScattering	ions
StepLimitType	fUseSafety	fMinimal	fMinimal
skin	0	0	0
f_r	0.02	0.2	0.2
f_g	2.5	0.1	0.1
LateralDisplacement	true	true	false

Table 7.1: The default values of parameters of *G4UrbanMscModel* for different processes: in first two coulombs for all particles except ions, in the last coulomb for ions.

/process/msc/Skin 2

7.5.10   Status of this document

09.10.98 created by L. Urbán.
15.11.01 major revision by L. Urbán.
18.04.02 updated by L. Urbán.
25.04.02 re-worded by D.H. Wright
07.06.02 major revision by L. Urbán.
18.11.02 updated by L. Urbán, now it describes the new angle distribution.
05.12.02 grammar check and parts re-written by D.H. Wright
13.11.03 revision by L. Urbán.
01.12.03 revision by V. Ivanchenko.
17.05.04 revision by L.Urbán.
01.12.04 updated by L.Urbán.
18.03.05 sampling z + mistyping corrections (mma)
22.06.05 grammar, spelling check by D.H. Wright
12.12.05 revised by L. Urbán, according Msc version in Geant4 V8.0
14.12.05 updated Implementation Details (mma)
08.06.06 revised by L. Urbán, according Msc version in Geant4 V8.1
25.11.06 revised by L. Urbán, according Msc version in Geant4 V8.2
29.03.07 revised by L. Urbán, for Geant4 V8.3
13.06.07 modified introduction (mma)
17.06.07 explain effective fr (L. Urbán)
25.06.07 update description of options (V. Ivanchenko)
05.12.07 revised by L. Urbán, for Geant4 V9.1

Bibliography

[1] L. Urban, A multiple scattering model, *CERN-OPEN-2006-077, Dec 2006. 18 pp.*

[2] G.Z. Molière *Z. Naturforsch. 3a (1948) 78.*

[3] H.W. Lewis. *Phys. Rev. 78 (1950) 526.*

[4] S. Goudsmit and J.L. Saunderson. *Phys. Rev. 57 (1940) 24.*

[5] J.M. Fernandez-Varea et al. *NIM B73 (1993) 447.*

[6] I. Kawrakow and A.F. Bielajew *NIM B 142 (1998) 253.*

[7] D. Liljequist and M. Ismail. *J.Appl.Phys. 62 (1987) 342.*

[8] D. Liljequist et al. *J.Appl.Phys. 68 (1990) 3061.*

[9] R. Mayol and F. Salvat *At.Data and Nucl.Data Tables 65 (1997) 55..*

[10] V.L. Highland *NIM 129 (1975) 497.*

[11] G.R. Lynch and O.I. Dahl *NIM B58 (1991) 6.*

[12] G. Shen et al. *Phys. Rev. D 20 (1979) 1584.*

[13] D. Attwood et al. *NIM B 251 (2006) 41.*

7.6 Single Scattering

Single elastic scattering process is an alternative to the multiple scattering process. The advantage of the single scattering process is in possibility of usage of theory based cross sections, in contrary to the Geant4 multiple scattering model [1], which uses a number of phenomenological approximations on top of Lewis theory. The process $G4CoulombScattering$ was created for simulation of single scattering of muons, it also applicable with some physical limitations to electrons, muons and ions. Because each of elastic collisions are simulated the number of steps of charged particles significantly increasing in comparison with the multiple scattering approach, correspondingly its CPU performance is pure. However, in low-density media (vacuum, low-density gas) multiple scattering may provide wrong results and single scattering processes is more adequate.

7.6.1 Coulomb Scattering

The single scattering model of Wentzel [2] is used in many of multiple scattering models including Penelope code [4]. The Wentzel for describing elastic scattering of particles with charge ze ($z = -1$ for electron) by atomic nucleus with atomic number Z based on simplified scattering potential

$$V(r) = \frac{zZe^2}{r} exp(-r/R),\tag{7.69}$$

where the exponential factor tries to reproduce the effect of screening. The parameter R is a screening radius, which may be estimated from Thomas-Fermi model of the atom

$$R = 0.885Z^{-1/3}r_B,\tag{7.70}$$

where r_B is the Bohr radius. In the first Born approximation the elastic scattering cross section $\sigma^{(W)}$ can be obtained as

$$\frac{d\sigma^{(W)}(\theta)}{d\Omega} = \frac{zZe^2}{(p\beta c)^2}\frac{1}{(2A + 1 - cos\theta)^2},\tag{7.71}$$

where p is the momentum and β is the velocity of the projectile particle. The screening parameter A according to Moliere and Bethe [3]

$$A = \left(\frac{\hbar}{2pR}\right)^2 (1.13 + 3.76(\alpha Z/\beta)^2),\tag{7.72}$$

where α is a fine structure constant and the factor in brackets is used to take into account second order corrections to the first Born approximation.

The total elastic cross section σ can be expressed via Wentzel cross section (7.71)

$$\frac{d\sigma(\theta)}{d\Omega} = \frac{d\sigma^{(W)}(\theta)}{d\Omega}\left(\frac{1}{(1 + \frac{(qR_N)^2}{12})^2} + \frac{1}{Z}\right), \qquad (7.73)$$

where q is momentum transfer to the nucleus, R_N is nuclear radius. This term takes into account nuclear size effect [5], the second term takes into account scattering off electrons. The results of simulation with the single scattering model (Fig.7.1) are competitive with the results of the multiple scattering.
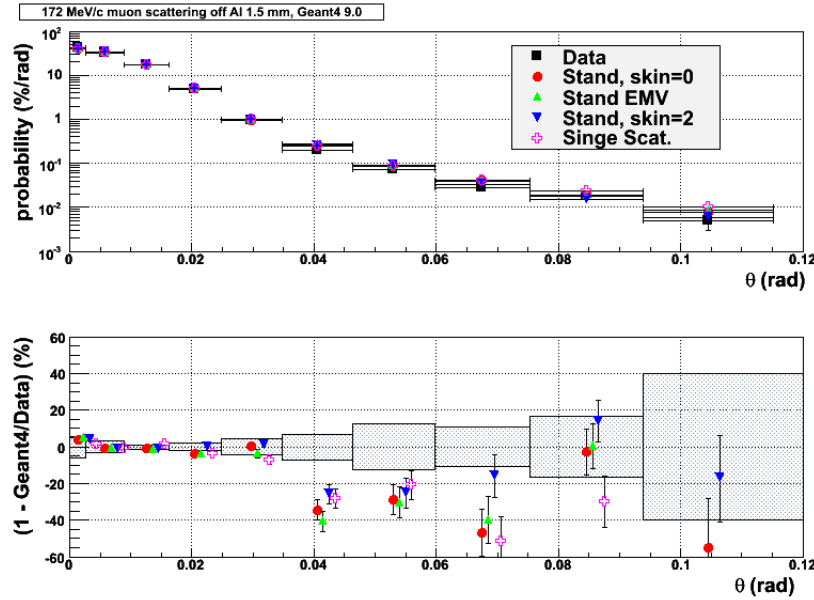
Figure 7.1: Scattering of muons off 1.5 mm aluminum foil: data [6] - black squares; simulation - colored markers corresponding different options of multiple scattering and single scattering model; in the bottom plot - relative difference between the simulation and the data in percents; hashed area demonstrates one standard deviation of the data.

7.6.2 Implementation Details

The total cross section of the process is obtained as a result of integration of the differential cross section (7.73). The first term of this cross section

is integrated in the interval $(0, \pi)$. The second term in the smaller interval $(0, \theta_m)$, where θ_m is the maximum scattering angle off electrons, which is determined using the cut value for the delta electron production. Before sampling of angular distribution the random choice is performed between scattering off the nucleus and off electrons.

7.6.3 Status of this document

06.12.07 created by V. Ivanchenko

Bibliography

[1] L. Urban, A multiple scattering model, *CERN-OPEN-2006-077, Dec 2006. 18 pp.*

[2] G. Wentzel, *Z. Phys. 40 (1927) 590.*

[3] H.A. Bethe, *Phys. Rev. 89 (1953) 1256.*

[4] J.M. Fernandez-Varea et al. *NIM B 73 (1993) 447.*

[5] A.V. Butkevich et al., *NIM A 488 (2002) 282.*

[6] D. Attwood et al. *NIM B 251 (2006) 41.*

7.7 Ion Scattering

The necessity of accurately computing the characteristics of interatomic scattering arises in many disciplines in which energetic ions pass through materials. Traditionally, solutions to this problem not involving hadronic interactions have been dominated by the multiple scattering, which is reasonably successful, but not very flexible. In particular, it is relatively difficult to introduce into such a system a particular screening function which has been measured for a specific atomic pair, rather than the universal functions which are applied. In many problems of current interest, such as the behavior of semiconductor device physics in a space environment, nuclear reactions, particle showers, and other effects are critically important in modeling the full details of ion transport. The process $G4ScreenedNuclearRecoil$ provides simulation of ion elastic scattering [1].

7.7.1 Method

The method used in this computation is a variant of a subset of the method described in Ref.[2]. A very short recap of the basic material is included here. The scattering of two atoms from each other is assumed to be a completely classical process, subject to an interatomic potential described by a potential function

$$V(r) = \frac{Z_1 Z_2 e^2}{r} \phi\left(\frac{r}{a}\right) \tag{7.74}$$

where Z_1 and Z_2 are the nuclear proton numbers, e^2 is the electromagnetic coupling constant ($q_e^2/4\pi\epsilon_0$ in SI units), r is the inter-nuclear separation, ϕ is the screening function describing the effect of electronic screening of the bare nuclear charges, and a is a characteristic length scale for this screening. In most cases, ϕ is a universal function used for all ion pairs, and the value of a is an appropriately adjusted length to give reasonably accurate scattering behavior. In the method described here, there is no particular need for a universal function ϕ, since the method is capable of directly solving the problem for most physically plausible screening functions. It is still useful to define a typical screening length a in the calculation described below, to keep the equations in a form directly comparable with our previous work even though, in the end, the actual value is irrelevant as long as the final function $\phi(r)$ is correct. From this potential $V(r)$ one can then compute the classical scattering angle from the reduced center-of-mass energy $\varepsilon \equiv E_c a/Z_1 Z_2 e^2$ (where E_c is the kinetic energy in the center-of-mass frame) and reduced

88

impact parameter $\beta \equiv b/a$

$$\theta_c = \pi - 2\beta \int_{x_0}^{\infty} f(z)\, dz/z^2 \qquad (7.75)$$

where

$$f(z) = \left(1 - \frac{\phi(z)}{z\,\varepsilon} - \frac{\beta^2}{z^2}\right)^{-1/2} \qquad (7.76)$$

and x_0 is the reduced classical turning radius for the given ε and β.

The problem, then, is reduced to the efficient computation of this scattering integral. In our previous work, a great deal of analytical effort was included to proceed from the scattering integral to a full differential cross section calculation, but for application in a Monte-Carlo code, the scattering integral $\theta_c(Z_1, Z_2, E_c, b)$ and an estimated total cross section $\sigma_0(Z_1, Z_2, E_c)$ are all that is needed. Thus, we can skip algorithmically forward in the original paper to equations 15-18 and the surrounding discussion to compute the reduced distance of closest approach x_0. This computation follows that in the previous work exactly, and will not be reintroduced here.

For the sake of ultimate accuracy in this algorithm, and due to the relatively low computational cost of so doing, we compute the actual scattering integral (as described in equations 19-21 of [2]) using a Lobatto quadrature of order 6, instead of the 4th order method previously described. This results in the integration accuracy exceeding that of any available interatomic potentials in the range of energies above those at which molecular structure effects dominate, and should allow for future improvements in that area. The integral α then becomes (following the notation of the previous paper)

$$\alpha \approx \frac{1 + \lambda_0}{30} + \sum_{i=1}^{4} w_i'\, f\left(\frac{x_0}{q_i}\right) \qquad (7.77)$$

where

$$\lambda_0 = \left(\frac{1}{2} + \frac{\beta^2}{2\,x_0^2} - \frac{\phi'(x_0)}{2\,\varepsilon}\right)^{-1/2} \qquad (7.78)$$

$w_i' \in [0.03472124,\ 0.1476903,\ 0.23485003,\ 0.1860249]$
$q_i \in [0.9830235,\ 0.8465224,\ 0.5323531,\ 0.18347974]$
Then

$$\theta_c = \pi - \frac{\pi\beta\alpha}{x_0} \qquad (7.79)$$

The other quantity required to implement a scattering process is the total scattering cross section σ_0 for a given incident ion and a material through

89

which the ion is propagating. This value requires special consideration for a process such as screened scattering. In the limiting case that the screening function is unity, which corresponds to Rutherford scattering, the total cross section is infinite. For various screening functions, the total cross section may or may not be finite. However, one must ask what the intent of defining a total cross section is, and determine from that how to define it.

In Geant4, the total cross section is used to determine a mean-free-path l_μ which is used in turn to generate random transport distances between discrete scattering events for a particle. In reality, where an ion is propagating through, for example, a solid material, scattering is not a discrete process but is continuous. However, it is a useful, and highly accurate, simplification to reduce such scattering to a series of discrete events, by defining some minimum energy transfer of interest, and setting the mean free path to be the path over which statistically one such minimal transfer has occurred. This approach is identical to the approach developed for the original TRIM code [3]. As long as the minimal interesting energy transfer is set small enough that the cumulative effect of all transfers smaller than that is negligible, the approximation is valid. As long as the impact parameter selection is adjusted to be consistent with the selected value of l_μ, the physical result isn't particularly sensitive to the value chosen.

Noting, then, that the actual physical result isn't very sensitive to the selection of l_μ, one can be relatively free about defining the cross section σ_0 from which l_μ is computed. The choice used for this implementation is fairly simple. Define a physical cutoff energy E_{min} which is the smallest energy transfer to be included in the calculation. Then, for a given incident particle with atomic number Z_1, mass m_1, and lab energy E_{inc}, and a target atom with atomic number Z_2 and mass m_2, compute the scattering angle θ_c which will transfer this much energy to the target from the solution of

$$E_{min} = E_{inc} \frac{4\,m_1\,m_2}{(m_1 + m_2)^2}\,\sin^2\frac{\theta_c}{2} \qquad (7.80)$$

. Then, noting that α from eq. 7.77 is a number very close to unity, one can solve for an approximate impact parameter b with a single root-finding operation to find the classical turning point. Then, define the total cross section to be $\sigma_0 = \pi b^2$, the area of the disk inside of which the passage of an ion will cause at least the minimum interesting energy transfer. Because this process is relatively expensive, and the result is needed extremely frequently, the values of $\sigma_0(E_{inc})$ are precomputed for each pairing of incident ion and target atom, and the results cached in a cubic-spline interpolation table. However, since the actual result isn't very critical, the cached results can be stored in a very coarsely sampled table without degrading the calculation at

all, as long as the values of the l_μ used in the impact parameter selection are rigorously consistent with this table.

The final necessary piece of the scattering integral calculation is the statistical selection of the impact parameter b to be used in each scattering event. This selection is done following the original algorithm from TRIM, where the cumulative probability distribution for impact parameters is

$$P(b) = 1 - \exp\left(\frac{-\pi\, b^2}{\sigma_0}\right) \tag{7.81}$$

where $N\, \sigma_0 \equiv 1/l_\mu$ where N is the total number density of scattering centers in the target material and l_μ is the mean free path computed in the conventional way. To produce this distribution from a uniform random variate r on (0,1], the necessary function is

$$b = \sqrt{\frac{-\log r}{\pi\, N\, l_\mu}} \tag{7.82}$$

This choice of sampling function does have the one peculiarity that it can produce values of the impact parameter which are larger than the impact parameter which results in the cutoff energy transfer, as discussed above in the section on the total cross section, with probability $1/e$. When this occurs, the scattering event is not processed further, since the energy transfer is below threshold. For this reason, impact parameter selection is carried out very early in the algorithm, so the effort spent on uninteresting events is minimized.

The above choice of impact sampling is modified when the mean-free-path is very short. If $\sigma_0 > \pi \left(\frac{l}{2}\right)^2$ where l is the approximate lattice constant of the material, as defined by $l = N^{-1/3}$, the sampling is replaced by uniform sampling on a disk of radius $l/2$, so that

$$b = \frac{l}{2}\sqrt{r} \tag{7.83}$$

This takes into account that impact parameters larger than half the lattice spacing do not occur, since then one is closer to the adjacent atom. This also derives from TRIM.

One extra feature is included in our model, to accelerate the production of relatively rare events such as high-angle scattering. This feature is a cross-section scaling algorithm, which allows the user access to an unphysical control of the algorithm which arbitrarily scales the cross-sections for a selected fraction of interactions. This is implemented as a two-parameter

adjustment to the central algorithm. The first parameter is a selection frequency f_h which sets what fraction of the interactions will be modified. The second parameter is the scaling factor for the cross-section. This is implemented by, for a fraction f_h of interactions, scaling the impact parameter by $b' = b/\sqrt{scale}$. This feature, if used with care so that it does not provide excess multiple-scattering, can provide between 10 and 100-fold improvements to event rates. If used without checking the validity by comparing to un-adjusted scattering computations, it can also provide utter nonsense.

7.7.2 Implementation Details

The coefficients for the summation to approximate the integral for α in eq.(7.77) are derived from the values in Abramowitz & Stegun [4], altered to make the change-of-variable used for this integral. There are two basic steps to the transformation. First, since the provided abscissas x_i and weights w_i are for integration on [-1,1], with only one half of the values provided, and in this work the integration is being carried out on [0,1], the abscissas are transformed as:

$$y_i \in \left\{ \frac{1 \mp x_i}{2} \right\} \tag{7.84}$$

Then, the primary change-of-variable is applied resulting in:

$$q_i = \cos \frac{\pi\, y_i}{2} \tag{7.85}$$

$$w_i' = \frac{w_i}{2} \sin \frac{\pi\, y_i}{2} \tag{7.86}$$

except for the first coefficient w_1' where the sin() part of the weight is taken into the limit of λ_0 as described in eq.(7.78). This value is just $w_1' = w_1/2$.

7.7.3 Status of this document

06.12.07 created by V. Ivanchenko from paper of M.H. Mendenhall and R.A. Weller
06.12.07 further edited by M. Mendenhall to bring contents of paper up-to-date with current implementation.

Bibliography

[1] M.H. Mendenhall, R.A. Weller, An algorithm for computing screened Coulomb scattering in Geant4, *Nucl. Instr. Meth. B 227 (2005) 420.*

[2] M.H. Mendenhall, R.A. Weller, Algorithms for the rapid computation of classical cross sections for screened coulomb collisions, *Nucl. Instr. Meth. in Physics Res. B58 (1991) 11.*

[3] J.P. Biersack, L.G. Haggmark, A Monte Carlo computer program for the transport of energetic ions in amorphous targets, *Nucl. Instr. Meth. in Physics Res. 174 (1980) 257.*

[4] M. Abramowitz, I. Stegun (Eds.), Handbook of Mathematical Functions, *Dover, New York, 1965, pp. 888, 920.*

7.8 Transition radiation

7.8.1 The Relationship of Transition Radiation to X-ray Cherenkov Radiation

X-ray transition radiation (XTR) occurs when a relativistic charged particle passes from one medium to another of a different dielectric permittivity. In order to describe this process it is useful to begin with an explanation of X-ray Cherenkov radiation, which is closely related.

The mean number of X-ray Cherenkov radiation (XCR) photons of frequency ω emitted into an angle θ per unit distance along a particle trajectory is [1]

$$\frac{d^3 \bar{N}_{xcr}}{\hbar d\omega \, dx \, d\theta^2} = \frac{\alpha}{\pi \hbar c} \frac{\omega}{c} \theta^2 \text{Im} \left\{ Z \right\}. \tag{7.87}$$

Here the quantity Z is introduced as the *complex formation zone* of XCR in the medium:

$$Z = \frac{L}{1 - i\dfrac{L}{l}}, \quad L = \frac{c}{\omega} \left[\gamma^{-2} + \frac{\omega_p^2}{\omega^2} + \theta^2 \right]^{-1}, \quad \gamma^{-2} = 1 - \beta^2. \tag{7.88}$$

with l and ω_p the photon absorption length and the plasma frequency, respectively, in the medium. For the case of a transparent medium, $l \to \infty$ and the complex formation zone reduces to the *coherence length L* of XCR. The coherence length roughly corresponds to that part of the trajectory in which an XCR photon can be created.

Introducing a complex quantity Z with its imaginary part proportional to the absorption cross-section ($\sim l^{-1}$) is required in order to account for absorption in the medium. Usually, $\omega_p^2/\omega^2 \gg c/\omega l$. Then it can be seen from Eqs. 7.87 and 7.88 that the number of emitted XCR photons is considerably suppressed and disappears in the limit of a transparent medium. This is caused by the destructive interference between the photons emitted from different parts of the particle trajectory.

The destructive interference of X-ray Cherenkov radiation is removed if the particle crosses a boundary between two media with different dielectric permittivities, ϵ, where

$$\epsilon = 1 - \frac{\omega_p^2}{\omega^2} + i\frac{c}{\omega l}. \tag{7.89}$$

Here the standard high-frequency approximation for the dielectric permittivity has been used. This is valid for energy transfers larger than the K-shell excitation potential.

If layers of media are alternated with spacings of order L, the X-ray radiation yield from a trajectory of unit length can be increased by roughly l/L times. The radiation produced in this case is called X-ray transition radiation (XTR).

7.8.2 Calculating the X-ray Transition Radiation Yield

Using the methods developed in Ref. [2] one can derive the relation describing the mean number of XTR photons generated per unit photon frequency and θ^2 *inside* the radiator for a general XTR radiator consisting of n different absorbing media with fluctuating thicknesses:

$$\frac{d^2 \bar{N}_{in}}{\hbar d\omega\, d\theta^2} = \frac{\alpha}{\pi \hbar c^2} \omega \theta^2 \text{Re} \left\{ \sum_{i=1}^{n-1} (Z_i - Z_{i+1})^2 + \right. \tag{7.90}$$

$$+ \; 2\sum_{k=1}^{n-1}\sum_{i=1}^{k-1} (Z_i - Z_{i+1}) \left[\prod_{j=i+1}^{k} F_j \right] (Z_k - Z_{k+1}) \left. \right\}, \; F_j = \exp\left[-\frac{t_j}{2Z_j}\right].$$

In the case of gamma distributed gap thicknesses (foam or fiber radiators) the values F_j, $(j = 1, 2)$ can be estimated as:

$$F_j = \int_0^\infty dt_j \left(\frac{\nu_j}{\bar{t}_j}\right)^{\nu_j} \frac{t_j^{\nu_j - 1}}{\Gamma(\nu_j)} \exp\left[-\frac{\nu_j t_j}{\bar{t}_j} - i\frac{t_j}{2Z_j}\right] = \left[1 + i\frac{\bar{t}_j}{2Z_j \nu_j}\right]^{-\nu_j}, \tag{7.91}$$

where Z_j is the complex formation zone of XTR (similar to relation 7.88 for XCR) in the j-th medium [2, 6]. Γ is the Euler gamma function, $\bar{t}_j$ is the mean thickness of the j-th medium in the radiator and $\nu_j > 0$ is the parameter roughly describing the relative fluctuations of t_j. In fact, the relative fluctuation is $\delta t_j / \bar{t}_j \sim 1/\sqrt{\nu_j}$.

In the particular case of n foils of the first medium (Z_1, F_1) interspersed with gas gaps of the second medium (Z_2, F_2), one obtains:

$$\frac{d^2 \bar{N}_{in}}{\hbar d\omega\, d\theta^2} = \frac{2\alpha}{\pi \hbar c^2} \omega \theta^2 \text{Re} \left\{ \langle R^{(n)} \rangle \right\}, \quad F = F_1 F_2, \tag{7.92}$$

$$\langle R^{(n)} \rangle = (Z_1 - Z_2)^2 \left\{ n\frac{(1 - F_1)(1 - F_2)}{1 - F} + \frac{(1 - F_1)^2 F_2 [1 - F^n]}{(1 - F)^2} \right\}. \tag{7.93}$$

Here $\langle R^{(n)} \rangle$ is the stack factor reflecting the radiator geometry. The integration of (7.92) with respect to θ^2 can be simplified for the case of a regular radiator $(\nu_{1,2} \to \infty)$, transparent in terms of XTR generation media, and

$n \gg 1$ [3]. The frequency spectrum of emitted XTR photons is given by:

$$\frac{d\bar{N}_{in}}{\hbar d\omega} = \int_0^{\sim 10\gamma^{-2}} d\theta^2 \frac{d^2\bar{N}_{in}}{\hbar d\omega \, d\theta^2} = \frac{4\alpha n}{\pi\hbar\omega}(C_1 + C_2)^2$$

$$\cdot \sum_{k=k_{min}}^{k_{max}} \frac{(k - C_{min})}{(k - C_1)^2(k + C_2)^2} \sin^2\left[\frac{\pi t_1}{t_1 + t_2}(k + C_2)\right],$$

(7.94)

$$C_{1,2} = \frac{t_{1,2}(\omega_1^2 - \omega_2^2)}{4\pi c\omega}, \quad C_{min} = \frac{1}{4\pi c}\left[\frac{\omega(t_1 + t_2)}{\gamma^2} + \frac{t_1\omega_1^2 + t_2\omega_2^2}{\omega}\right].$$

The sum in (7.94) is defined by terms with $k \geq k_{min}$ corresponding to the region of $\theta \geq 0$. Therefore k_{min} should be the nearest to C_{min} integer $k_{min} \geq C_{min}$. The value of k_{max} is defined by the maximum emission angle $\theta_{max}^2 \sim 10\gamma^{-2}$. It can be evaluated as the integer part of

$$C_{max} = C_{min} + \frac{\omega(t_1 + t_2)}{4\pi c}\frac{10}{\gamma^2}, \quad k_{max} - k_{min} \sim 10^2 \div 10^3 \gg 1.$$

Numerically, however, only a few tens of terms contribute substantially to the sum, that is, one can choose $k_{max} \sim k_{min} + 20$. Equation (7.94) corresponds to the spectrum of the total number of photons emitted inside a regular transparent radiator. Therefore the mean interaction length, λ_{XTR}, of the XTR process in this kind of radiator can be introduced as:

$$\lambda_{XTR} = n(t_1 + t_2)\left[\int_{\hbar\omega_{min}}^{\hbar\omega_{max}} \hbar d\omega \frac{d\bar{N}_{in}}{\hbar d\omega}\right]^{-1},$$

where $\hbar\omega_{min} \sim 1$ keV, and $\hbar\omega_{max} \sim 100$ keV for the majority of high energy physics experiments. Its value is constant along the particle trajectory in the approximation of a transparent regular radiator. The spectrum of the total number of XTR photons *after* regular transparent radiator is defined by (7.94) with:

$$n \to n_{eff} = \sum_{k=0}^{n-1} \exp[-k(\sigma_1 t_1 + \sigma_2 t_2)] = \frac{1 - \exp[-n(\sigma_1 t_1 + \sigma_2 t_2)]}{1 - \exp[-(\sigma_1 t_1 + \sigma_2 t_2)]},$$

where σ_1 and σ_2 are the photo-absorption cross-sections corresponding to the photon frequency ω in the first and the second medium, respectively. With this correction taken into account the XTR absorption in the radiator (7.94) corresponds to the results of [4]. In the more general case of the flux of XTR

photons *after* a radiator, the XTR absorption can be taken into account with a calculation based on the stack factor derived in [5]:

$$
\begin{aligned}
\langle R_{flux}^{(n)} \rangle &= (L_1 - L_2)^2 \left\{ \frac{1 - Q^n}{1 - Q} \frac{(1 + Q_1)(1 + F) - 2F_1 - 2Q_1 F_2}{2(1 - F)} \right. \\
&+ \left. \frac{(1 - F_1)(Q_1 - F_1)F_2(Q^n - F^n)}{(1 - F)(Q - F)} \right\},
\end{aligned}
\tag{7.95}
$$

$$
Q = Q_1 \cdot Q_2, \quad Q_j = \exp\left[-t_j/l_j\right] = \exp\left[-\sigma_j t_j\right], \quad j = 1, 2.
$$

Both XTR energy loss (7.93) and flux (7.95) models can be implemented as a discrete electromagnetic process (see below).

7.8.3 Simulating X-ray Transition Radiation Production

A typical XTR radiator consits of many (~ 100) boundaries between different materials. To improve the tracking performance in such a volume one can introduce an artificial material [6], which is the geometrical mixture of foil and gas contents. Here is an example:

```
// In DetectorConstruction of an application
// Preparation of mixed radiator material
foilGasRatio  = fRadThickness/(fRadThickness+fGasGap);
foilDensity   = 1.39*g/cm3;     // Mylar
gasDensity    = 1.2928*mg/cm3 ; // Air
totDensity    = foilDensity*foilGasRatio +
                gasDensity*(1.0-foilGasRatio);
fractionFoil =  foilDensity*foilGasRatio/totDensity;
fractionGas  =  gasDensity*(1.0-foilGasRatio)/totDensity;
G4Material* radiatorMat = new G4Material("radiatorMat",
                                          totDensity,
                                          ncomponents = 2 );
radiatorMat->AddMaterial( Mylar, fractionFoil );
radiatorMat->AddMaterial( Air,   fractionGas  );
G4cout << *(G4Material::GetMaterialTable()) << G4endl;
// materials of the TR radiator
fRadiatorMat = radiatorMat;   // artificial for geometry
fFoilMat     = Mylar;
fGasMat      = Air;
```

This artificial material will be assigned to the logical volume in which XTR will be generated:

```
solidRadiator = new G4Box("Radiator",
                          1.1*AbsorberRadius ,
                          1.1*AbsorberRadius,
                          0.5*radThick        );
logicRadiator = new G4LogicalVolume( solidRadiator,
                                     fRadiatorMat,  // !!!
                                     "Radiator");
physiRadiator = new G4PVPlacement(0,
                                  G4ThreeVector(0,0,zRad),
                                  "Radiator", logicRadiator,
                                  physiWorld, false, 0       );
```

XTR photons generated by a relativistic charged particle intersecting a radiator with $2n$ interfaces between different media can be simulated by using the following algorithm. First the total number of XTR photons is estimated using a Poisson distribution about the mean number of photons given by the following expression:

$$\bar{N}^{(n)} = \int_{\omega_1}^{\omega_2} d\omega \int_0^{\theta_{max}^2} d\theta^2 \frac{d^2 \bar{N}^{(n)}}{d\omega\, d\theta^2} = \frac{2\alpha}{\pi c^2} \int_{\omega_1}^{\omega_2} \omega d\omega \int_0^{\theta_{max}^2} \theta^2 d\theta^2 \mathrm{Re}\left\{\langle R^{(n)}\rangle\right\}.$$

Here $\theta_{max}^2 \sim 10\gamma^{-2}$, $\hbar\omega_1 \sim 1$ keV, $\hbar\omega_2 \sim 100$ keV, and $\langle R^{(n)}\rangle$ correspond to the geometry of the experiment. For events in which the number of XTR photons is not equal to zero, the energy and angle of each XTR quantum is sampled from the integral distributions obtained by the numerical integration of expression (7.92). For example, the integral energy spectrum of emitted XTR photons, $\bar{N}_{>\omega}^{(n)}$, is defined from the following integral distribution:

$$\bar{N}_{>\omega}^{(n)} = \frac{2\alpha}{\pi c^2} \int_\omega^{\omega_2} \omega d\omega \int_0^{\theta_{max}^2} \theta^2 d\theta^2 \mathrm{Re}\left\{\langle R^{(n)}\rangle\right\}.$$

In GEANT4 XTR generation *inside* or *after* radiators is described as a discrete electromagnetic process. It is convenient for the description of tracks in magnetic fields and can be used for the cases when the radiating charge experiences a scattering inside the radiator. The base class G4VXTRenergyLoss is responsible for the creation of tables with integral energy and angular distributions of XTR photons. It also contains the PostDoIt function providing XTR photon generation and motion (if fExitFlux=true) through a XTR radiator to its boundary. Particular models like G4RegularXTRadiator implement the pure virtual function GetStackFactor, which calculates the response of the XTR radiator reflecting its geometry. Included below are some comments for the declaration of XTR in a user application.

In the physics list one should pass to the XTR process additional details of the XTR radiator involved:

```
// In PhysicsList of an application
else if (particleName == "e-")  // Construct processes for electron with XTR
{
   pmanager->AddProcess(new G4MultipleScattering, -1, 1,1 );
   pmanager->AddProcess(new G4eBremsstrahlung(),  -1,-1,1 );
   pmanager->AddProcess(new Em10StepCut(),        -1,-1,1 );
// in regular radiators:
   pmanager->AddDiscreteProcess(
   new G4RegularXTRadiator         // XTR dEdx in general regular radiator
// new G4XTRRegularRadModel        - XTR flux after general regular radiator
// new G4TransparentRegXTRadiator  - XTR dEdx in transparent
//                                   regular radiator
// new G4XTRTransparentRegRadModel - XTR flux after transparent
//                                   regular radiator
                      (pDet->GetLogicalRadiator(), // XTR radiator

                       pDet->GetFoilMaterial(), // real foil
                       pDet->GetGasMaterial(),  // real gas
                       pDet->GetFoilThick(),    // real geometry
                       pDet->GetGasThick(),
                       pDet->GetFoilNumber(),
                       "RegularXTRadiator"));
// or for foam/fiber radiators:
   pmanager->AddDiscreteProcess(
   new G4GammaXTRadiator    - XTR dEdx in general foam/fiber radiator
// new G4XTRGammaRadModel   - XTR flux after general foam/fiber radiator
                      ( pDet->GetLogicalRadiator(),
                        1000.,
                        100.,
                        pDet->GetFoilMaterial(),
                        pDet->GetGasMaterial(),
                        pDet->GetFoilThick(),
                        pDet->GetGasThick(),
                        pDet->GetFoilNumber(),
                        "GammaXTRadiator"));
}
```

Here for the foam/fiber radiators the values 1000 and 100 are the ν parameters (which can be varied) of the Gamma distribution for the foil and gas gaps,

respectively. Classes G4TransparentRegXTRadiator and G4XTRTransparentRegRadModel correspond (7.94) to n and n_{eff}, respectively.

7.8.4 Status of this document

18.11.05 modified by V.Grichine
29.11.02 re-written by D.H. Wright
29.05.02 created by V.Grichine

Bibliography

[1] V.M. Grichine, *Nucl. Instr. and Meth.*, **A482** (2002) 629.

[2] V.M. Grichine, *Physics Letters*, **B525** (2002) 225-239

[3] G.M. Garibyan, *Sov. Phys. JETP* **32** (1971) 23.

[4] C.W. Fabian and W. Struczinski *Physics Letters*, **B57** (1975) 483.

[5] G.M. Garibian, L.A. Gevorgian, and C. Yang, *Sov. Phys.- JETP, 39 (1975) 265.*

[6] J. Apostolakis, S. Giani, V. Grichine et al., *Comput. Phys. Commun.* **132** (2000) 241.

7.9 Scintillation

Every scintillating material has a characteristic light yield, Y $(photons/MeV)$, and an intrinsic resolution which generally broadens the statistical distribution, $\sigma_i/\sigma_s > 1$, due to impurities which are typical for doped crystals like NaI(Tl) and CsI(Tl). The average yield can have a non-linear dependence on the local energy deposition. Scintillators also have a time distribution spectrum with one or more exponential decay time constants, τ_i, with each decay component having its intrinsic photon emission spectrum. These are empirical parameters typical for each material.

The generation of scintillation light can be simulated by sampling the number of photons from a Poisson distribution. This distribution is based on the energy lost during a step in a material and on the scintillation properties of that material. The frequency of each photon is sampled from the empirical spectra. The photons are generated evenly along the track segment and are emitted uniformly into 4π with a random linear polarization.

7.9.1 Status of this document

07.12.98 created by P.Gumplinger

7.10 Čerenkov Effect

The radiation of Čerenkov light occurs when a charged particle moves through a dispersive medium faster than the speed of light in that medium. A dispersive medium is one whose index of refraction is an increasing function of photon energy. Two things happen when such a particle slows down:

1. a cone of Čerenkov photons is emitted, with the cone angle (measured with respect to the particle momentum) decreasing as the particle loses energy;

2. the momentum of the photons produced increases, while the number of photons produced decreases.

When the particle velocity drops below the local speed of light, photons are no longer emitted. At that point, the Čerenkov cone collapses to zero.

In order to simulate Čerenkov radiation the number of photons per track length must be calculated. The formulae used for this calculation can be found below and in [1, 2]. Let n be the refractive index of the dielectric material acting as a radiator. Here $n = c/c'$ where c' is the group velocity of light in the material, hence $1 \leq n$. In a dispersive material n is an increasing function of the photon energy ϵ $(dn/d\epsilon \geq 0)$. A particle traveling with speed $\beta = v/c$ will emit photons at an angle θ with respect to its direction, where θ is given by

$$\cos\theta = \frac{1}{\beta n}.$$

From this follows the limitation for the momentum of the emitted photons:

$$n(\epsilon_{min}) = \frac{1}{\beta}.$$

Photons emitted with an energy beyond a certain value are immediately re-absorbed by the material; this is the window of transparency of the radiator. As a consequence, all photons are contained in a cone of opening angle $\cos\theta_{max} = 1/(\beta n(\epsilon_{max}))$.

The average number of photons produced is given by the relations :

$$
\begin{aligned}
dN &= \frac{\alpha z^2}{\hbar c} \sin^2\theta \, d\epsilon dx = \frac{\alpha z^2}{\hbar c}\left(1 - \frac{1}{n^2\beta^2}\right) d\epsilon dx \\
&\approx 370 z^2 \frac{photons}{eV\ cm}\left(1 - \frac{1}{n^2\beta^2}\right) d\epsilon dx
\end{aligned}
$$

and the number of photons generated per track length is

$$\frac{dN}{dx} \approx 370z^2 \int_{\epsilon_{min}}^{\epsilon_{max}} d\epsilon \left(1 - \frac{1}{n^2\beta^2}\right) = 370z^2 \left[\epsilon_{max} - \epsilon_{min} - \frac{1}{\beta^2} \int_{\epsilon_{min}}^{\epsilon_{max}} \frac{d\epsilon}{n^2(\epsilon)}\right]$$

.

The number of photons produced is calculated from a Poisson distribution with a mean of $\langle n \rangle = $ StepLength dN/dx. The energy distribution of the photon is then sampled from the density function

$$f(\epsilon) = \left[1 - \frac{1}{n^2(\epsilon)\beta^2}\right]$$

.

7.10.1 Status of this document

07.12.98 created by P.Gumplinger
11.12.01 SI units (mma)
08.05.02 re-written by D.H. Wright

Bibliography

[1] J.D.Jackson, Classical Electrodynamics, John Wiley and Sons (1998)

[2] D.E. Groom et al. Particle Data Group . Rev. of Particle Properties.
Eur. Phys. J. C15,1 (2000) http://pdg.lbl.gov/

7.11 Photoabsorption Ionization Model

7.11.1 Cross Section for Ionizing Collisions

The Photoabsorption Ionization (PAI) model describes the ionization energy loss of a relativistic charged particle in matter. For such a particle, the differential cross section $d\sigma_i/d\omega$ for ionizing collisions with energy transfer ω can be expressed most generally by the following equations [1]:

$$\frac{d\sigma_i}{d\omega} = \frac{2\pi Z e^4}{mv^2} \left\{ \frac{f(\omega)}{\omega \left|\varepsilon(\omega)\right|^2} \left[\ln \frac{2mv^2}{\omega \left|1 - \beta^2 \varepsilon\right|} - \frac{\varepsilon_1 - \beta^2 \left|\varepsilon\right|^2}{\varepsilon_2} \arg(1 - \beta^2 \varepsilon^*) \right] + \frac{\tilde{F}(\omega)}{\omega^2} \right\}, \qquad (7.96)$$

$$\tilde{F}(\omega) = \int_0^\omega \frac{f(\omega')}{\left|\varepsilon(\omega')\right|^2} d\omega',$$

$$f(\omega) = \frac{m\omega\varepsilon_2(\omega)}{2\pi^2 Z N \hbar^2}.$$

Here m and e are the electron mass and charge, $\hbar$ is Planck's constant, $\beta = v/c$ is the ratio of the particle's velocity v to the speed of light c, Z is the effective atomic number, N is the number of atoms (or molecules) per unit volume, and $\varepsilon = \varepsilon_1 + i\varepsilon_2$ is the complex dielectric constant of the medium. In an isotropic non-magnetic medium the dielectric constant can be expressed in terms of a complex index of refraction, $n(\omega) = n_1 + in_2$, $\varepsilon(\omega) = n^2(\omega)$. In the energy range above the first ionization potential I_1 for all cases of practical interest, and in particular for all gases, $n_1 \sim 1$. Therefore the imaginary part of the dielectric constant can be expressed in terms of the photoabsorption cross section $\sigma_\gamma(\omega)$:

$$\varepsilon_2(\omega) = 2n_1 n_2 \sim 2n_2 = \frac{N\hbar c}{\omega}\sigma_\gamma(\omega).$$

The real part of the dielectric constant is calculated in turn from the dispersion relation

$$\varepsilon_1(\omega) - 1 = \frac{2N\hbar c}{\pi} V.p. \int_0^\infty \frac{\sigma_\gamma(\omega')}{\omega'^2 - \omega^2} d\omega',$$

where the integral of the pole expression is considered in terms of the principal value. In practice it is convenient to calculate the contribution from the continuous part of the spectrum only. In this case the normalized photoabsorption cross section

$$\tilde{\sigma}_\gamma(\omega) = \frac{2\pi^2 \hbar e^2 Z}{mc} \sigma_\gamma(\omega) \left[\int_{I_1}^{\omega_{max}} \sigma_\gamma(\omega') d\omega' \right]^{-1} , \quad \omega_{max} \sim 100 \ keV$$

is used, which satisfies the quantum mechanical sum rule [2]:

$$\int_{I_1}^{\omega_{max}} \tilde{\sigma}_\gamma(\omega') d\omega' = \frac{2\pi^2 \hbar e^2 Z}{mc}.$$

The differential cross section for ionizing collisions is expressed by the photoabsorption cross section in the continuous spectrum region:

$$\begin{aligned}
\frac{d\sigma_i}{d\omega} &= \frac{\alpha}{\pi\beta^2} \left\{ \frac{\tilde{\sigma}_\gamma(\omega)}{\omega \left| \varepsilon(\omega) \right|^2} \left[\ln \frac{2mv^2}{\omega \left| 1 - \beta^2 \varepsilon \right|} - \right. \right. \\
&\quad \left. \left. - \frac{\varepsilon_1 - \beta^2 \left| \varepsilon \right|^2}{\varepsilon_2} \arg(1 - \beta^2 \varepsilon^*) \right] + \frac{1}{\omega^2} \int_{I_1}^{\omega} \frac{\tilde{\sigma}_\gamma(\omega')}{\left| \varepsilon(\omega') \right|^2} d\omega' \right\} , \quad (7.97)
\end{aligned}$$

$$\varepsilon_2(\omega) = \frac{N\hbar c}{\omega} \tilde{\sigma}_\gamma(\omega),$$

$$\varepsilon_1(\omega) - 1 = \frac{2N\hbar c}{\pi} V.p. \int_{I_1}^{\omega_{max}} \frac{\tilde{\sigma}_\gamma(\omega')}{\omega'^2 - \omega^2} d\omega'.$$

For practical calculations using Eq. 7.96 it is convenient to represent the photoabsorption cross section as a polynomial in ω^{-1} as was proposed in [3]:

$$\sigma_\gamma(\omega) = \sum_{k=1}^{4} a_k^{(i)} \omega^{-k},$$

where the coefficients, $a_k^{(i)}$ result from a separate least-squares fit to experimental data in each energy interval i. As a rule the interval borders are equal to the corresponding photoabsorption edges. The dielectric constant can now be calculated analytically with elementary functions for all ω, except near the photoabsorption edges where there are breaks in the photoabsorption cross section and the integral for the real part is not defined in the sense of the principal value.

The third term in Eq. (7.96), which can only be integrated numerically, results in a complex calculation of $d\sigma_i/d\omega$. However, this term is dominant

for energy transfers $\omega > 10\ keV$, where the function $|\varepsilon(\omega)|^2 \sim 1$. This is clear from physical reasons, because the third term represents the Rutherford cross section on atomic electrons which can be considered as quasifree for a given energy transfer [4]. In addition, for high energy transfers, $\varepsilon(\omega) = 1 - \omega_p^2/\omega^2 \sim 1$, where ω_p is the plasma energy of the material. Therefore the factor $|\varepsilon(\omega)|^{-2}$ can be removed from under the integral and the differential cross section of ionizing collisions can be expressed as:

$$\frac{d\sigma_i}{d\omega} = \frac{\alpha}{\pi\beta^2\,|\varepsilon(\omega)|^2} \left\{ \frac{\tilde{\sigma}_\gamma(\omega)}{\omega} \left[\ln \frac{2mv^2}{\omega\,|1 - \beta^2\varepsilon|} - \frac{\varepsilon_1 - \beta^2\,|\varepsilon|^2}{\varepsilon_2} \arg(1 - \beta^2\varepsilon^*) \right] + \frac{1}{\omega^2} \int_{I_1}^{\omega} \tilde{\sigma}_\gamma(\omega')d\omega' \right\}. \quad (7.98)$$

This is especially simple in gases when $|\varepsilon(\omega)|^{-2} \sim 1$ for all $\omega > I_1$ [4].

7.11.2 Energy Loss Simulation

For a given track length the number of ionizing collisions is simulated by a Poisson distribution whose mean is proportional to the total cross section of ionizing collisions:

$$\sigma_i = \int_{I_1}^{\omega_{max}} \frac{d\sigma(\omega')}{d\omega'} d\omega'.$$

The energy transfer in each collision is simulated according to a distribution proportional to

$$\sigma_i(> \omega) = \int_{\omega}^{\omega_{max}} \frac{d\sigma(\omega')}{d\omega'} d\omega'.$$

The sum of the energy transfers is equal to the energy loss. PAI ionisation is implemented according to the model approach (class G4PAIModel) allowing a user to select specific models in different regions. Here is an example physics list:

```
const G4RegionStore* theRegionStore = G4RegionStore::GetInstance();
G4Region* gas = theRegionStore->GetRegion("VertexDetector");
...
if (particleName == "e-")
{
  G4eIonisation* eion = new G4eIonisation();
  G4PAIModel*    pai = new G4PAIModel(particle,
```

```
                                    "PAIModel");
    // set energy limits where 'pai' is active
    pai->SetLowEnergyLimit(0.1*keV);
    pai->SetHighEnergyLimit(100.0*TeV);

    // here 0 is the highest priority in region 'gas'
    eion->AddEmModel(0,pai,pai,gas);

    pmanager->AddProcess(eion,-1, 2, 2);
    pmanager->AddProcess(new G4MultipleScattering, -1, 1,1);
    pmanager->AddProcess(new G4eBremsstrahlung,-1,1,3);
  }
```

It shows how to select the G4PAIModel to be the preferred ionisation model for electrons in a G4Region named VertexDetector. The first argument in AddEmModel is 0 which means highest priority.

The class G4PAIPhotonModel generates both δ-electrons and photons as secondaries and can be used for more detailed descriptions of ionisation space distribution around the particle trajectory.

7.11.3   Status of this document

01.12.05 expanded discussion by V. Grichine
08.05.02 re-written by D.H. Wright
16.11.98 created by V. Grichine

Bibliography

[1] Asoskov V.S., Chechin V.A., Grichine V.M. at el, Lebedev Institute annual report, v. 140, p. 3 (1982)

[2] Fano U., and Cooper J.W. Rev.Mod.Phys., v. 40, p. 441 (1968)

[3] Biggs F., and Lighthill R., Preprint Sandia Laboratory, SAND 87-0070 (1990)

[4] Allison W.W.M., and Cobb J. Ann.Rev.Nucl.Part.Sci., v.30,p.253 (1980)

7.12 Photoabsorption Cross Section at Low Energies

7.12.1 Method

The photoabsorption cross section, $\sigma_\gamma(\omega)$, where ω is the photon energy, is used in Geant4 for the description of the photo-electric effect, X-ray transportation and ionization effects in very thin absorbers. As mentioned in the discussion of photoabsorption ionization (see section 7.11), it is convenient to represent the cross section as a polynomial in ω^{-1} [1] :

$$\sigma_\gamma(\omega) = \sum_{k=1}^{4} a_k^{(i)} \omega^{-k}. \qquad (7.99)$$

Using cross sections from the original Sandia data tables, calculations of primary ionization and energy loss distributions produced by relativistic charged particles in gaseous detectors show clear disagreement with experimental data, especially for gas mixtures which include xenon.

Therefore a special investigation was performed [2] by fitting the coefficients $a_k^{(i)}$ to modern data from synchrotron radiation experiments in the energy range of $10 - 50 \ eV$. The fits were performed for elements typically used in detector gas mixtures: hydrogen, fluorine, carbon, nitrogen and oxygen. Parameters for these elements were extracted from data on molecular gases such as N_2, O_2, CO_2, CH_4, and CF_4 [3, 4]. Parameters for the noble gases were found using data given in the tables [5, 6].

7.12.2 Status of this document

18.11.98 created by V. Grichine
10.05.02 re-written by D.H. Wright

Bibliography

[1] Biggs F., and Lighthill R., Preprint Sandia Laboratory, SAND 87-0070 (1990)

[2] Grichine V.M., Kostin A.P., Kotelnikov S.K. et al., Bulletin of the Lebedev Institute no. 2-3, 34 (1994).

[3] Lee L.C. et al., J.Q.S.R.T., v. 13, p. 1023 (1973).

[4] Lee L.C. et al., Journ. of Chem. Phys., v. 67, p. 1237 (1977).

[5] G.V. Marr and J.B. West, Atom. Data Nucl. Data Tabl., v. 18, p. 497 (1976).

[6] J.B. West and J. Morton, Atom. Data Nucl. Data Tabl., v. 30, p. 253 (1980).

Chapter 8

Electron and Positron Incident

8.1 Ionization

8.1.1 Method

The *G4eIonisation* class provides the continuous and discrete energy losses of electrons and positrons due to ionization in a material according to the approach described in Section 7.1. The value of the maximum energy transferable to a free electron T_{max} is given by the following relation:

$$T_{max} = \begin{cases} E - mc^2 & for \ \ e^+ \\ (E - mc^2)/2 & for \ \ e^- \end{cases} \tag{8.1}$$

where mc^2 is the electron mass. Above a given threshold energy the energy loss is simulated by the explicit production of delta rays by Möller scattering (e^-e^-), or Bhabha scattering (e^+e^-). Below the threshold the soft electrons ejected are simulated as continuous energy loss by the incident $e^{\pm}$.

8.1.2 Continuous Energy Loss

The integration of 7.1 leads to the Berger-Seltzer formula [1]:

$$\frac{dE}{dx}\bigg]_{T<T_{cut}} = 2\pi r_e^2 mc^2 n_{el} \frac{1}{\beta^2} \left[\ln \frac{2(\gamma+1)}{(I/mc^2)^2} + F^{\pm}(\tau, \tau_{up}) - \delta \right] \tag{8.2}$$

with

r_e	classical electron radius: $e^2/(4\pi\epsilon_0 mc^2)$
mc^2	mass energy of the electron
n_{el}	electron density in the material
I	mean excitation energy in the material
γ	E/mc^2
β^2	$1 - (1/\gamma^2)$
τ	$\gamma - 1$
T_{cut}	minimum energy cut for δ -ray production
τ_c	T_{cut}/mc^2
τ_{max}	maximum energy transfer: τ for e^+, $\tau/2$ for e^-
τ_{up}	$\min(\tau_c, \tau_{max})$
δ	density effect function.

In an elemental material the electron density is

$$n_{el} = Z \, n_{at} = Z \, \frac{\mathcal{N}_{av}\rho}{A}.$$

111

$\mathcal{N}_{av}$ is Avogadro's number, ρ is the material density, and A is the mass of a mole. In a compound material

$$n_{el} = \sum_i Z_i \, n_{ati} = \sum_i Z_i \frac{\mathcal{N}_{av} w_i \rho}{A_i},$$

where w_i is the proportion by mass of the ith element, with molar mass A_i. The mean excitation energies I for all elements are taken from [2]. The functions $F^{\pm}$ are given by :

$$F^+(\tau, \tau_{up}) = \ln(\tau \tau_{up})$$
$$- \frac{\tau_{up}^2}{\tau} \left[\tau + 2\tau_{up} - \frac{3\tau_{up}^2 y}{2} - \left(\tau_{up} - \frac{\tau_{up}^3}{3} \right) y^2 - \left(\frac{\tau_{up}^2}{2} - \tau \frac{\tau_{up}^3}{3} + \frac{\tau_{up}^4}{4} \right) y^3 \right] \tag{8.3}$$

$$F^-(\tau, \tau_{up}) = -1 - \beta^2 \tag{8.4}$$
$$+ \ln \left[(\tau - \tau_{up}) \tau_{up} \right] + \frac{\tau}{\tau - \tau_{up}} + \frac{1}{\gamma^2} \left[\frac{\tau_{up}^2}{2} + (2\tau + 1) \ln \left(1 - \frac{\tau_{up}}{\tau} \right) \right]$$

where $y = 1/(\gamma + 1)$.

The density effect correction is calculated according to the formalism of Sternheimer [3]:
x is a kinetic variable of the particle : $x = \log_{10}(\gamma\beta) = \ln(\gamma^2 \beta^2)/4.606$, and $\delta(x)$ is defined by

$$\begin{array}{lll}
\text{for} \quad x < x_0 : & \delta(x) = 0 & \\
\text{for} \quad x \in [x_0, \, x_1] : & \delta(x) = 4.606x - C + a(x_1 - x)^m & (8.5) \\
\text{for} \quad x > x_1 : & \delta(x) = 4.606x - C &
\end{array}$$

where the matter-dependent constants are calculated as follows:

$$\begin{array}{rcl}
h\nu_p & = & \text{plasma energy of the medium} \; = \sqrt{4\pi n_{el} r_e^3} mc^2/\alpha = \sqrt{4\pi n_{el} r_e} \hbar c \\
C & = & 1 + 2\ln(I/h\nu_p) \\
x_a & = & C/4.606 \\
a & = & 4.606(x_a - x_0)/(x_1 - x_0)^m \\
m & = & 3.
\end{array}$$
$$\tag{8.6}$$

For condensed media

$$\begin{array}{ll}
I < 100\,\text{eV} & \left\{ \begin{array}{llll}
\text{for } C \le 3.681 & x_0 = 0.2 & & x_1 = 2 \\
\text{for } C > 3.681 & x_0 = 0.326C - 1.0 & x_1 = 2
\end{array} \right. \\[1em]
I \ge 100\,\text{eV} & \left\{ \begin{array}{llll}
\text{for } C \le 5.215 & x_0 = 0.2 & & x_1 = 3 \\
\text{for } C > 5.215 & x_0 = 0.326C - 1.5 & x_1 = 3
\end{array} \right.
\end{array}$$

and for gaseous media

$$
\begin{array}{llll}
\text{for} & C < 10. & x_0 = 1.6 & x_1 = 4 \\
\text{for} & C \in [10.0, \ 10.5[& x_0 = 1.7 & x_1 = 4 \\
\text{for} & C \in [10.5, \ 11.0[& x_0 = 1.8 & x_1 = 4 \\
\text{for} & C \in [11.0, \ 11.5[& x_0 = 1.9 & x_1 = 4 \\
\text{for} & C \in [11.5, \ 12.25[& x_0 = 2. & x_1 = 4 \\
\text{for} & C \in [12.25, \ 13.804[& x_0 = 2. & x_1 = 5 \\
\text{for} & C \geq 13.804 & x_0 = 0.326C - 2.5 & x_1 = 5.
\end{array}
$$

8.1.3 Total Cross Section per Atom and Mean Free Path

The total cross section per atom for Möller scattering (e^-e^-) and Bhabha scattering (e^+e^-) is obtained by integrating Eq. 7.2. In GEANT4 T_{cut} is always 1 keV or larger. For delta ray energies much larger than the excitation energy of the material $(T \gg I)$, the total cross section becomes [1] for Möller scattering,

$$
\sigma(Z, E, T_{cut}) = \frac{2\pi r_e^2 Z}{\beta^2(\gamma - 1)} \times \tag{8.7}
$$
$$
\left[\frac{(\gamma - 1)^2}{\gamma^2} \left(\frac{1}{2} - x \right) + \frac{1}{x} - \frac{1}{1 - x} - \frac{2\gamma - 1}{\gamma^2} \ln \frac{1 - x}{x} \right],
$$

and for Bhabha scattering (e^+e^-),

$$
\sigma(Z, E, T_{cut}) = \frac{2\pi r_e^2 Z}{(\gamma - 1)} \times \tag{8.8}
$$
$$
\left[\frac{1}{\beta^2} \left(\frac{1}{x} - 1 \right) + B_1 \ln x + B_2(1 - x) - \frac{B_3}{2}(1 - x^2) + \frac{B_4}{3}(1 - x^3) \right].
$$

Here

$$
\begin{array}{llll}
\gamma &=& E/mc^2 & B_1 &=& 2 - y^2 \\
\beta^2 &=& 1 - (1/\gamma^2) & B_2 &=& (1 - 2y)(3 + y^2) \\
x &=& T_{cut}/(E - mc^2) & B_3 &=& (1 - 2y)^2 + (1 - 2y)^3 \\
y &=& 1/(\gamma + 1) & B_4 &=& (1 - 2y)^3.
\end{array}
$$

The above formulae give the total cross section for scattering above the threshold energies

$$
T_{\text{Moller}}^{\text{thr}} = 2T_{cut} \qquad \text{and} \qquad T_{\text{Bhabha}}^{\text{thr}} = T_{cut}. \tag{8.9}
$$

In a given material the mean free path is then

$$
\lambda = (n_{at} \cdot \sigma)^{-1} \quad or \quad \lambda = \left(\sum_i n_{ati} \cdot \sigma_i \right)^{-1}. \tag{8.10}
$$

113

8.1.4 Simulation of Delta-ray Production

Differential Cross Section

For $T \gg I$ the differential cross section per atom becomes [1] for Möller scattering,

$$
\frac{d\sigma}{d\epsilon} = \frac{2\pi r_e^2 Z}{\beta^2(\gamma - 1)} \times \tag{8.11}
$$
$$
\left[\frac{(\gamma - 1)^2}{\gamma^2} + \frac{1}{\epsilon}\left(\frac{1}{\epsilon} - \frac{2\gamma - 1}{\gamma^2}\right) + \frac{1}{1 - \epsilon}\left(\frac{1}{1 - \epsilon} - \frac{2\gamma - 1}{\gamma^2}\right) \right]
$$

and for Bhabha scattering,

$$
\frac{d\sigma}{d\epsilon} = \frac{2\pi r_e^2 Z}{(\gamma - 1)} \left[\frac{1}{\beta^2 \epsilon^2} - \frac{B_1}{\epsilon} + B_2 - B_3 \epsilon + B_4 \epsilon^2 \right]. \tag{8.12}
$$

Here $\epsilon = T/(E - mc^2)$. The kinematical limits of ϵ are

$$
\epsilon_0 = \frac{T_{cut}}{E - mc^2} \leq \epsilon \leq \frac{1}{2} \quad \text{for } e^- e^- \qquad\qquad \epsilon_0 = \frac{T_{cut}}{E - mc^2} \leq \epsilon \leq 1 \quad \text{for } e^+ e^-.
$$

Sampling

The delta ray energy is sampled according to methods discussed in Chapter 2. Apart from normalization, the cross section can be factorized as

$$
\frac{d\sigma}{d\epsilon} = f(\epsilon)g(\epsilon). \tag{8.13}
$$

For $e^- e^-$ scattering

$$
f(\epsilon) = \frac{1}{\epsilon^2}\frac{\epsilon_0}{1 - 2\epsilon_0} \tag{8.14}
$$
$$
g(\epsilon) = \frac{4}{9\gamma^2 - 10\gamma + 5}\left[(\gamma - 1)^2 \epsilon^2 - (2\gamma^2 + 2\gamma - 1)\frac{\epsilon}{1 - \epsilon} + \frac{\gamma^2}{(1 - \epsilon)^2} \right] \tag{8.15}
$$

and for $e^+ e^-$ scattering

$$
f(\epsilon) = \frac{1}{\epsilon^2}\frac{\epsilon_0}{1 - \epsilon_0} \tag{8.16}
$$
$$
g(\epsilon) = \frac{B_0 - B_1 \epsilon + B_2 \epsilon^2 - B_3 \epsilon^3 + B_4 \epsilon^4}{B_0 - B_1 \epsilon_0 + B_2 \epsilon_0^2 - B_3 \epsilon_0^3 + B_4 \epsilon_0^4}. \tag{8.17}
$$

Here $B_0 = \gamma^2/(\gamma^2 - 1)$ and all other quantities have been defined above.

To choose ϵ, and hence the delta ray energy,

1. ϵ is sampled from $f(\epsilon)$

2. the rejection function $g(\epsilon)$ is calculated using the sampled value of ϵ

3. ϵ is accepted with probability $g(\epsilon)$.

After the successful sampling of ϵ, the direction of the ejected electron is generated with respect to the direction of the incident particle. The azimuthal angle ϕ is generated isotropically and the polar angle θ is calculated from energy-momentum conservation. This information is used to calculate the energy and momentum of both the scattered incident particle and the ejected electron, and to transform them to the global coordinate system.

8.1.5   Status of this document

9.10.98 created by L. Urbán.
29.07.01 revised by M.Maire.
13.12.01 minor cosmetic by M.Maire.
24.05.02 re-written by D.H. Wright.
01.12.03 revised by V. Ivanchenko.

Bibliography

[1] H.Messel and D.F.Crawford. Pergamon Press,Oxford,1970.

[2] ICRU Report No. 37 (1984)

[3] R.M.Sternheimer. Phys.Rev. B3 (1971) 3681.

8.2 Bremsstrahlung

The class $G4eBremsstrahlung$ provides the energy loss of electrons and positrons due to the radiation of photons in the field of a nucleus according to the approach described in Section 7.1. Above a given threshold energy the energy loss is simulated by the explicit production of photons. Below the threshold the emission of soft photons is treated as a continuous energy loss. In GEANT4 the Landau-Pomeranchuk-Migdal effect has also been implemented.

8.2.1 Cross Section and Energy Loss

$d\sigma(Z,T,k)/dk$ is the differential cross section for the production of a photon of energy k by an electron of kinetic energy T in the field of an atom of charge Z. If k_c is the energy cut-off below which the soft photons are treated as continuous energy loss, then the mean value of the energy lost by the electron is

$$E_{Loss}^{brem}(Z,T,k_c) = \int_0^{k_c} k\frac{d\sigma(Z,T,k)}{dk}dk. \qquad (8.18)$$

The total cross section for the emission of a photon of energy larger than k_c is

$$\sigma_{brem}(Z,T,k_c) = \int_{k_c}^{T} \frac{d\sigma(Z,T,k)}{dk}dk. \qquad (8.19)$$

Parameterization of the Energy Loss and Total Cross Section

The cross section and energy loss due to bremsstrahlung have been parameterized using the EEDL (Evaluated Electrons Data Library) data set [1] as input.
The following parameterization was chosen for the electron bremsstrahlung cross section :

$$\sigma(Z,T,k_c) = Z(Z+\xi_\sigma)(1-c_{sigh}Z^{1/4})\left[\frac{T}{k_c}\right]^\alpha \frac{f_s}{N_{Avo}} \qquad (8.20)$$

where f_s is a polynomial in $x = lg(T)$ with Z-dependent coefficients for $x < x_l$, $f_s = 1$ for $x \geq x_l$, $\xi_\sigma, c_{sigh}, \alpha$ are constants, N_{Avo} is the Avogadro number. For the case of low energy electrons ($T \leq T_{lim} = 10MeV$) the above expression should be multiplied by

$$\left(\frac{T_{lim}}{T}\right)^{c_l} \cdot \left(1 + \frac{a_l}{\sqrt{Z}T}\right), \tag{8.21}$$

with constant c_l, a_l parameters.

The energy loss parameterization is the following :

$$E_{Loss}^{brem}(Z,T,k_c) = \frac{Z(Z+\xi_l)(T+m)^2}{(T+2m)} \left[\frac{k_c}{T}\right]^\beta (2 - c_{lh}Z^{\frac{1}{4}}) \frac{a + b\frac{T}{T_{lim}}}{1 + c\frac{T}{T_{lim}}} \frac{f_l}{N_{Avo}} \tag{8.22}$$

where m is the mass of the electron, $\xi_l, \beta, c_{lh}, a, b, c$ are constants, f_l is a polynomial in $x = lg(T)$ with Z-dependent coefficients for $x < x_l$, $f_l = 1$ for $x \geq x_l$. For low energies this expression should be divided by

$$\left(\frac{T_{lim}}{T}\right)^{c_l} \tag{8.23}$$

and if $T < k_c$ the expression should be multiplied by

$$\left(\frac{T}{k_c}\right)^{a_l} \tag{8.24}$$

with some constants c_l, a_l. The numerical values of the parameters and the coefficients of the polynomyals f_s and f_l can be found in the class code.

The errors of the parameterizations (8.20) and (8.22) were estimated to be

$$\frac{\Delta\sigma}{\sigma} = \begin{cases} 6 - 8\% & \text{for} \quad T \leq 1MeV \\ \leq 4 - 5\% & \text{for} \quad 1MeV < T \end{cases}$$

$$\frac{\Delta E_{Loss}^{brem}}{E_{Loss}^{brem}} = \begin{cases} 8 - 10\% & \text{for} \quad T \leq 1MeV \\ 5 - 6\% & \text{for} \quad 1MeV < T. \end{cases}$$

When running GEANT4, the energy loss due to soft photon bremsstrahlung is tabulated at initialization time as a function of the medium and of the energy, as is the mean free path for discrete bremsstrahlung.

Corrections for e^+e^- Differences

The preceding section has dealt exclusively with electrons. One might expect that positrons could be treated the same way. According to reference

[9] however, the differences between the radiative loss of positrons and electrons are considerable and cannot be disregarded. The ratio of the radiative energy loss for positrons to that for electrons obeys a simple scaling law, is a function only of the quantity T/Z^2.

The radiative energy loss for electrons or positrons is given by

$$-\frac{1}{\rho}\left(\frac{dE}{dx}\right)^{\pm}_{rad} = \frac{N_{Av}\alpha r_e^2}{A}(T+m)Z^2\Phi^{\pm}_{rad}(Z,T)$$

$$\Phi^{\pm}_{rad}(Z,T) = \frac{1}{\alpha r_e^2 Z^2(T+m)}\int_0^T k\frac{d\sigma^{\pm}}{dk}dk$$

and it is the ratio

$$\eta = \frac{\Phi^+_{rad}(Z,T)}{\Phi^-_{rad}(Z,T)} = \eta\left(\frac{T}{Z^2}\right)$$

that obeys the scaling law.

The authors have calculated this function in the range $10^{-7} \leq \frac{T}{Z^2} \leq 0.5$, where the kinetic energy T is expressed in MeV. Their *data* can be fairly accurately reproduced using a parametrization:

$$\eta = \begin{cases} 0 & \text{if} & x \leq -8 \\ \frac{1}{2} + \frac{1}{\pi}\arctan\left(a_1 x + a_3 x^3 + a_5 x^5\right) & \text{if} & -8 < x < 9 \\ 1 & \text{if} & x \geq 9 \end{cases}$$

where

$$x = \log\left(C\frac{T}{Z^2}\right) \text{(T in GeV)}$$
$$C = 7.5221 \times 10^6$$
$$a_1 = 0.415$$
$$a_3 = 0.0021$$
$$a_5 = 0.00054.$$

The e^+e^- energy loss difference is not purely a low-energy phenomenon (at least for high Z), as shown in Table 8.1.
The scaling property will be used to obtain the positron energy loss and discrete bremsstrahlung from the corresponding electron values. However,

$\frac{T}{Z^2}(GeV)$	T	η	$\left(\frac{rad.\ loss}{total\ loss}\right)_{e^-}$
10^{-9}	$\sim 7keV$	~ 0.1	$\sim 0\%$
10^{-8}	$67keV$	~ 0.2	$\sim 1\%$
2×10^{-7}	$1.35MeV$	~ 0.5	$\sim 15\%$
2×10^{-6}	$13.5MeV$	~ 0.8	$\sim 60\%$
2×10^{-5}	$135.MeV$	~ 0.95	$> 90\%$

Table 8.1: ratio of the e^+e^- radiative energy loss in lead (Z=82).

while scaling holds for the ratio of the total radiative energy losses, it is significantly broken for the photon spectrum in the screened case. That is,

$$\frac{\Phi^+}{\Phi^-} = \eta\left(\frac{T}{Z^2}\right) \qquad\qquad \frac{\frac{d\sigma^+}{dk}}{\frac{d\sigma^-}{dk}} = \text{does not scale .}$$

For the case of a point Coulomb charge, scaling would be restored for the photon spectrum. In order to correct for non-scaling, it is useful to note that in the photon spectrum from bremsstrahlung reported in [9]:

$$\frac{d\sigma^\pm}{dk} = S^\pm\left(\frac{k}{T}\right) \qquad \frac{S^+(k)}{S^-(k)} \leq 1 \qquad S^+(1) = 0 \qquad S^-(1) > 0$$

One can further assume that

$$\frac{d\sigma^+}{dk} = f(\epsilon)\frac{d\sigma^-}{dk}, \qquad\qquad \epsilon = \frac{k}{T} \qquad\qquad (8.25)$$

and require

$$\int_0^1 f(\epsilon)d\epsilon = \eta \qquad\qquad (8.26)$$

in order to approximately satisfy the scaling law for the ratio of the total radiative energy loss. From the photon spectra the boundary conditions

$$\left.\begin{array}{l} f(0) = 1 \\ f(1) = 0 \end{array}\right\} \qquad \text{for all } Z, T \qquad\qquad (8.27)$$

may be inferred. Choosing a simple function for f

$$f(\epsilon) = C(1-\epsilon)^\alpha \qquad\qquad C, \alpha > 0, \qquad\qquad (8.28)$$

the conditions (8.26), (8.27) lead to:

$$\begin{aligned} C &= 1 \\ \alpha &= \frac{1}{\eta} - 1 \qquad\qquad (\alpha > 0 \text{ because } \eta < 1) \\ f(\epsilon) &= (1-\epsilon)^{\frac{1}{\eta}-1}. \end{aligned}$$

119

Now the weight factors F_l and F_σ for the positron continuous energy loss and the discrete bremsstrahlung cross section can be defined:

$$F_l = \frac{1}{\epsilon_0} \int_0^{\epsilon_0} f(\epsilon)d\epsilon \qquad\qquad F_\sigma = \frac{1}{1-\epsilon_0} \int_{\epsilon_0}^1 f(\epsilon)d\epsilon \quad (8.29)$$

where $\epsilon_0 = \frac{k_c}{T}$ and k_c is the photon cut. In this scheme the positron energy loss and discrete bremsstrahlung can be calculated as:

$$\left(-\frac{dE}{dx}\right)^+ = F_l \left(-\frac{dE}{dx}\right)^- \qquad\qquad \sigma_{brems}^+ = F_\sigma \sigma_{brems}^-$$

In this approximation the photon spectra are identical, therefore the same sampling is used for generating e^- or e^+ bremsstrahlung. The following relations hold:

$$\begin{aligned}
F_\sigma &= \eta(1-\epsilon_0)^{\frac{1}{\eta}-1} < \eta \\
\epsilon_0 F_l + (1-\epsilon_0)F_\sigma &= \eta \qquad\qquad\qquad \text{from the def (8.29)} \\
\Rightarrow F_l &= \eta\frac{1-(1-\epsilon_0)^{\frac{1}{\eta}}}{\epsilon_0} > \eta\frac{1-(1-\epsilon_0)}{\epsilon_0} = \eta \qquad \Rightarrow \left\{ \begin{array}{l} F_l > \eta \\ F_\sigma < \eta \end{array} \right.
\end{aligned}$$

which is consistent with the spectra. The effect of the difference in e^- and e^+ bremsstrahlung can also be seen in electromagnetic shower development when the primary energy is not too high.

Landau Pomeranchuk Migdal (LPM) effect

The LPM effect (see for example [3, 4]) is the suppression of photon production due to the multiple scattering of the electron. If an electron undergoes multiple scattering while traversing the so called "formation zone", the bremsstrahlung amplitudes from before and after the scattering can interfere, reducing the probability of bremsstrahlung photon emission (a similar suppression occurs for pair production). The suppression becomes significant for photon energies below a certain value, given by

$$\frac{k}{E} < \frac{E}{E_{LPM}}, \tag{8.30}$$

where

k	photon energy
E	electron energy
E_{LPM}	characteristic energy for LPM effect (depend on the medium).

The value of the LPM characteristic energy can be written as

$$E_{LPM} = \frac{\alpha m^2 X_0}{2hc},$$ (8.31)

where

α	fine structure constant
m	electron mass
X_0	radiation length in the material
h	Planck constant
c	velocity of light in vacuum.

The LPM suppression of the photon spectrum is given by the formula

$$S_{LPM} = \sqrt{\frac{E_{LPM} \cdot k}{E^2}},$$ (8.32)

while the dielectric suppression (included already in the parameterizations) can be written as

$$S_p = \frac{k^2}{k^2 + C_p \cdot E^2},$$ (8.33)

where the quantity C_p is given by

$$C_p = \frac{r_0 \lambda_e^2 n}{\pi}.$$ (8.34)

In eq. 8.34 the parameters are

r_0	classical electron radius
λ_e	electron Compton wavelength
n	electron density in the material.

Both suppression effects reduce the effective formation length of the photon, so the suppressions *do not simply multiply*. For the total suppression S the following equation holds (see [3])

$$\frac{1}{S} = 1 + \frac{1}{S_p} + \frac{S}{S_{LPM}^2}$$ (8.35)

which can be solved easily for S

$$S = \frac{\sqrt{S_{LPM}^4 \cdot (1 + \frac{1}{S_p})^2 + 4 \cdot S_{LPM}^2} - S_{LPM}^2 \cdot (1 + \frac{1}{S_p})}{2}.$$ (8.36)

The LPM effect was implemented by applying to the energy loss a factor $\frac{S}{S_p}$, which depends on the energy and material. This is done at initialization time by computing the correction factor

$$f_c = \frac{\int_0^{k_{cut}} n_\gamma(k) \cdot \frac{S}{S_p} dk}{\int_0^{k_{cut}} n_\gamma(k) dk},$$ (8.37)

where $n_\gamma(k)$ is the photon spectrum. A similar correction has not been applied to the total cross section given by the parameterization 8.20. Instead the LPM effect is included in the photon generation algorithm.

8.2.2 Simulation of Discrete Bremsstrahlung

The energy of the final state photons is sampled according to the spectrum [5] of Seltzer and Berger. They have calculated the bremsstrahlung spectra for materials with atomic numbers Z = 6, 13, 29, 47, 74 and 92 in the electron kinetic energy range 1 keV - 10 GeV. Their tabulated results have been used as input in a fit of the parameterized function

$$S(x) = Ck\frac{d\sigma}{dk},$$

which will be used to form the rejection function for the sampling process. The parameterization can be written as

$$S(x) = \begin{cases} (1 - a_h\epsilon)F_1(\delta) + b_h\epsilon^2 F_2(\delta) & T \geq 1MeV \\ 1 + a_l x + b_l x^2 & T < 1MeV \end{cases}$$ (8.38)

where

C		normalization constant
k		photon energy
T, E		kinetic and total energy of the primary electron
x	$=$	$\frac{k}{T}$
ϵ	$=$	$\frac{k}{E} = x\frac{T}{E}$

and $a_{h,l}$ and $b_{h,l}$ are the parameters to be fitted. The $F_i(\delta)$ screening functions depend on the screening variable

δ	$=$	$\frac{136m_e}{Z^{1/3}E}\frac{\epsilon}{1-\epsilon}$	
$F_1(\delta)$	$=$	$F_0(42.392 - 7.796\delta + 1.961\delta^2 - F)$	$\delta \leq 1$
$F_2(\delta)$	$=$	$F_0(41.734 - 6.484\delta + 1.250\delta^2 - F)$	$\delta \leq 1$
$F_1(\delta)$	$=$	$F_2(\delta) = F_0(42.24 - 8.368\ln(\delta + 0.952) - F)$	$\delta > 1$
F_0	$=$	$\frac{1}{42.392 - F}$	
F	$=$	$4\ln Z - 0.55(\ln Z)^2.$	

The "high energy" ($T > 1$ MeV) formula is essentially the Coulomb-corrected, screened Bethe-Heitler formula (see e.g. [10, 11, 6]). However, Eq. (8.38) differs from Bethe-Heitler in two ways:

1. a_h, b_h depend on T and on the atomic number Z, whereas in the Bethe-Heitler spectrum they are fixed ($a_h = 1$, $b_h = 0.75$);

2. the function F is not the same as that in the Bethe-Heitler cross-section; the present function gives a better behavior in the high frequency limit, i.e. when $k \to T$ ($x \to 1$).

The T and Z dependence of the parameters are described by the equations:

$$
\begin{aligned}
a_h &= 1 + \frac{a_{h1}}{u} + \frac{a_{h2}}{u^2} + \frac{a_{h3}}{u^3} \\
b_h &= 0.75 + \frac{b_{h1}}{u} + \frac{b_{h2}}{u^2} + \frac{b_{h3}}{u^3} \\
a_l &= a_{l0} + a_{l1}u + a_{l2}u^2 \\
b_l &= b_{l0} + b_{l1}u + b_{l2}u^2 \\
\text{with} \\
u &= \ln\left(\frac{T}{m_e}\right)
\end{aligned}
$$

The parameters $a_{hi}, b_{hi}, a_{li}, b_{li}$ are polynomials of second order in the variable:

$$v = [Z(Z+1)]^{1/3}.$$

In the limiting case $T \to \infty$, $a_h \to 1, b_h \to 0.75$, Eq. (8.38) gives the Bethe-Heitler cross section.

There are altogether 36 linear parameters in the formulae and their values are given in the code. This parameterization reproduces the Seltzer-Berger tables to within 2-3 % on average, with the maximum error being less than 10-12 %. The original tables, on the other hand, agree well with the experimental data and theoretical (low- and high-energy) results (< 10 % below 50 MeV and < 5 % above 50 MeV).

Apart from the normalization the cross section differential in photon energy can be written as

$$\frac{d\sigma}{dk} = \frac{1}{\ln\frac{1}{x_c}}\frac{1}{x}g(x) = \frac{1}{\ln\frac{1}{x_c}}\frac{1}{x}\frac{S(x)}{S_{max}}$$

where $x_c = k_c/T$ and k_c is the photon cut-off energy below which the bremsstrahlung is treated as a continuous energy loss. Using this decomposition of the cross section and two random numbers r_1, r_2 uniformly distributed in $[0, 1]$, the sampling of x is done as follows:

1. sample x from

$$\frac{1}{\ln \frac{1}{x_c}} \frac{1}{x} \qquad \text{setting} \qquad x = e^{r_1 \ln x_c}$$

2. calculate the rejection function $g(x)$ and:

   - if $r_2 > g(x)$ reject x and go back to 1;
   - if $r_2 \le g(x)$ accept x.

The application of the dielectric suppression [8] and the LPM effect requires that ϵ also be sampled. First, the rejection function must be multiplied by a suppression factor

$$C_M(\epsilon) = \frac{1 + C_0/\epsilon_c^2}{1 + C_0/\epsilon^2}$$

where

$$C_0 = \frac{n r_0 \lambda^2}{\pi}, \qquad \epsilon_c = \frac{k_c}{E}$$

n electron density in the medium

r_0 classical electron radius

λ reduced Compton wavelength of the electron.

Apart from the Migdal correction factor, this is simply expression 8.33 . This correction decreases the cross-section for low photon energies.

While sampling ϵ, the suppression factor $f_{LPM} = \frac{S}{S_p}$ is also used as a rejection function in order to take into account the LPM effect. Here the supression factor is compared to a random number r uniformly distributed in the interval $[0, 1]$. If $f_{LPM} \ge r$ the simulation continues, otherwise the bremsstrahlung process concludes *without photon production*. It can be seen that this procedure performs the LPM suppression correctly.

After the successful sampling of ϵ, the polar angles of the radiated photon are generated with respect to the parent electron's momentum. It is difficult to

find simple formulae for this angle in the literature. For example the double differential cross section reported by Tsai [12, 13] is

$$
\begin{aligned}
\frac{d\sigma}{dkd\Omega} &= \frac{2\alpha^2 e^2}{\pi km^4} \left\{ \left[\frac{2\epsilon - 2}{(1+u^2)^2} + \frac{12u^2(1-\epsilon)}{(1+u^2)^4} \right] Z(Z+1) \right. \\
&\quad + \left. \left[\frac{2 - 2\epsilon - \epsilon^2}{(1+u^2)^2} - \frac{4u^2(1-\epsilon)}{(1+u^2)^4} \right] \left[X - 2Z^2 f_c((\alpha Z)^2) \right] \right\} \\
u &= \frac{E\theta}{m} \\
X &= \int_{t_{min}}^{m^2(1+u^2)^2} \left[G_Z^{el}(t) + G_Z^{in}(t) \right] \frac{t - t_{min}}{t^2} dt \\
G_Z^{el,in}(t) &\quad \text{atomic form factors} \\
t_{min} &= \left[\frac{km^2(1+u^2)}{2E(E-k)} \right]^2 = \left[\frac{\epsilon m^2(1+u^2)}{2E(1-\epsilon)} \right]^2 .
\end{aligned}
$$

The sampling of this distribution is complicated. It is also only an approximation to within a few percent, due at least to the presence of the atomic form factors. The angular dependence is contained in the variable $u = E\theta m^{-1}$. For a given value of u the dependence of the shape of the function on Z, E and $\epsilon = k/E$ is very weak. Thus, the distribution can be approximated by a function

$$
f(u) = C \left(ue^{-au} + due^{-3au} \right) \tag{8.39}
$$

where

$$
C = \frac{9a^2}{9+d} \qquad a = 0.625 \qquad d = 27
$$

where E is in GeV. While this approximation is good at high energies, it becomes less accurate around a few MeV. However in that region the ionization losses dominate over the radiative losses.

The sampling of the function $f(u)$ can be done with three random numbers r_i, uniformly distributed on the interval [0,1]:

1. choose between ue^{-au} and due^{-3au}:

$$
b = \begin{cases} a & \text{if} \quad r_1 < 9/(9+d) \\ 3a & \text{if} \quad r_1 \geq 9/(9+d) \end{cases}
$$

2. sample ue^{-bu}:

$$
u = -\frac{\log(r_2 r_3)}{b}
$$

$$P = \int_{u_{max}}^{\infty} f(u)\, du$$

E (MeV)	P(%)
0.511	3.4
0.6	2.2
0.8	1.2
1.0	0.7
2.0	< 0.1

Table 8.2: Angular sampling efficiency

3. check that:

$$u \le u_{max} = \frac{E\pi}{m}$$

otherwise go back to 1.

The probability of failing the last test is reported in table 8.2.

The function $f(u)$ can also be used to describe the angular distribution of the photon in μ bremsstrahlung and to describe the angular distribution in photon pair production.

The azimuthal angle ϕ is generated isotropically. Along with θ, this information is used to calculate the momentum vectors of the radiated photon and parent recoiled electron, and to transform them to the global coordinate system. The momentum transfer to the atomic nucleus is neglected.

8.2.3   Status of this document

09.10.98 created by L. Urbán.
21.03.02 modif in angular distribution (M.Maire)
27.05.02 re-written by D.H. Wright
01.12.03 minor update by V. Ivanchenko
20.05.04 updated by L.Urban
09.12.05 minor update by V. Ivanchenko
15.03.07 modify definition of Elpm (mma)

Bibliography

[1] S.T.Perkins, D.E.Cullen, S.M.Seltzer, UCRL-50400 Vol.31

[2] GEANT3 manual ,CERN Program Library Long Writeup W5013 (October 1994).

[3] V.M.Galitsky and I.I.Gurevich. Nuovo Cimento 32 (1964) 1820.

[4] P.L. Anthony et al. SLAC-PUB-7413/LBNL-40054 (February 1997)

[5] S.M.Seltzer and M.J.Berger. Nucl.Inst.Meth. 80 (1985) 12.

[6] W.R. Nelson et al.:The EGS4 Code System. *SLAC-Report-265 , December 1985*

[7] H.Messel and D.F.Crawford. Pergamon Press,Oxford,1970.

[8] A.B. Migdal. Phys.Rev. 103. (1956) 1811.

[9] L. Kim et al. Phys. Rev. A33 (1986) 3002.

[10] R.W. Williams, Fundamental Formulas of Physics, vol.2., Dover Pubs. (1960).

[11] J. C. Butcher and H. Messel. Nucl.Phys. 20. (1960) 15.

[12] Y-S. Tsai, Rev. Mod. Phys. 46. (1974) 815.

[13] Y-S. Tsai, Rev. Mod. Phys. 49. (1977) 421.

8.3 Positron - Electron Annihilation

8.3.1 Introduction

The process `G4eplusAnnihilation` simulates the in-flight annihilation of a positron with an atomic electron. As is usually done in shower programs [1], it is assumed here that the atomic electron is initially free and at rest. Also, annihilation processes producing one, or three or more, photons are ignored because these processes are negligible compared to the annihilation into two photons [1, 2].

8.3.2 Cross Section and Mean Free Path

Cross Section per Atom

The annihilation in flight of a positron and electron is described by the cross section formula of Heitler [3, 1]:

$$\sigma(Z, E) \;=\; \frac{Z\pi r_e^2}{\gamma + 1} \left[\frac{\gamma^2 + 4\gamma + 1}{\gamma^2 - 1} \ln\left(\gamma + \sqrt{\gamma^2 - 1}\right) - \frac{\gamma + 3}{\sqrt{\gamma^2 - 1}} \right] \quad (8.40)$$

where

$$
\begin{aligned}
E &= \text{total energy of the incident positron} \\
\gamma &= E/mc^2 \\
r_e &= \text{classical electron radius}
\end{aligned}
$$

Mean Free Path

In a given material the mean free path, λ, for a positron to be annihilated with an electron is given by

$$\lambda(E) = \left(\sum_i n_{ati} \cdot \sigma(Z_i, E) \right)^{-1} \quad (8.41)$$

where n_{ati} is the number of atoms per volume of the ith element composing the material.

8.3.3 Sampling the final state

The final state of the $e + e-$ annihilation process

$$e^+ \; e^- \rightarrow \gamma_a \; \gamma_b$$

is simulated by first determining the kinematic limits of the photon energy and then sampling the photon energy within those limits using the differential cross section. Conservation of energy-momentum is then used to determine the directions of the final state photons.

Kinematic Limits

If the incident e^+ has a kinetic energy T, then the total energy is $E_e = T + mc^2$ and the momentum is $Pc = \sqrt{T(T + 2mc^2)}$. The total available energy is $E_{tot} = E_e + mc^2 = E_a + E_b$ and momentum conservation requires $\vec{P} = \vec{P}_{\gamma_a} + \vec{P}_{\gamma_b}$. The fraction of the total energy transferred to one photon (say γ_a) is

$$\epsilon = \frac{E_a}{E_{tot}} \equiv \frac{E_a}{T + 2mc^2}. \tag{8.42}$$

The energy transfered to γ_a is largest when γ_a is emitted in the direction of the incident e^+. In that case $E_{amax} = (E_{tot} + Pc)/2$. The energy transfered to γ_a is smallest when γ_a is emitted in the opposite direction of the incident e^+. Then $E_{amin} = (E_{tot} - Pc)/2$. Hence,

$$\epsilon_{max} = \frac{E_a\mathsf{max}}{E_{tot}} = \frac{1}{2}\left[1 + \sqrt{\frac{\gamma - 1}{\gamma + 1}}\right] \tag{8.43}$$

$$\epsilon_{min} = \frac{E_a\mathsf{min}}{E_{tot}} = \frac{1}{2}\left[1 - \sqrt{\frac{\gamma - 1}{\gamma + 1}}\right] \tag{8.44}$$

where $\gamma = (T + mc^2)/mc^2$. Therefore the range of ϵ is $[\epsilon_{min} ; \epsilon_{max}]$ ($\equiv [\epsilon_{min} ; 1 - \epsilon_{min}]$).

Sampling the Gamma Energy

A short overview of the sampling method is given in Chapter 2.

The differential cross section of the two-photon positron-electron annihilation can be written as [3, 1]:

$$\frac{d\sigma(Z, \epsilon)}{d\epsilon} = \frac{Z\pi r_e^2}{\gamma - 1}\frac{1}{\epsilon}\left[1 + \frac{2\gamma}{(\gamma + 1)^2} - \epsilon - \frac{1}{(\gamma + 1)^2}\frac{1}{\epsilon}\right] \tag{8.45}$$

where Z is the atomic number of the material, r_e the classical electron radius, and $\epsilon \in [\epsilon_{min} ; \epsilon_{max}]$. The differential cross section can be decomposed as

$$\frac{d\sigma(Z, \epsilon)}{d\epsilon} = \frac{Z\pi r_e^2}{\gamma - 1}\alpha f(\epsilon)g(\epsilon) \tag{8.46}$$

where

$$\begin{aligned}
\alpha &= \ln(\epsilon_{max}/\epsilon_{min}) \\
f(\epsilon) &= \frac{1}{\alpha\epsilon} \quad\quad\quad\quad\quad\quad\quad\quad\quad\quad\quad\quad\quad\quad (8.47) \\
g(\epsilon) &= \left[1 + \frac{2\gamma}{(\gamma+1)^2} - \epsilon - \frac{1}{(\gamma+1)^2}\frac{1}{\epsilon} \right] \equiv 1 - \epsilon + \frac{2\gamma\epsilon - 1}{\epsilon(\gamma+1)^2} \quad (8.48)
\end{aligned}$$

Given two random numbers $r, r' \in [0, 1]$, the photon energies are chosen as follows:

1. sample ϵ from $f(\epsilon): \epsilon = \epsilon_{min}\left(\frac{\epsilon_{max}}{\epsilon_{min}}\right)^r$

2. test the rejection function: if $g(\epsilon) \geq r'$ accept ϵ, otherwise return to step 1.

Then the photon energies are $E_a = \epsilon E_{tot}$ $\quad\quad$ $E_b = (1 - \epsilon)E_{tot}$.

Computing the Final State Kinematics

If θ is the angle between the incident e^+ and γ_a, then from energy-momentum conservation,

$$\cos\theta = \frac{1}{Pc}\left[T + mc^2\frac{2\epsilon - 1}{\epsilon} \right] = \frac{\epsilon(\gamma+1) - 1}{\epsilon\sqrt{\gamma^2 - 1}}. \quad\quad (8.49)$$

The azimuthal angle, ϕ, is generated isotropically and the photon momentum vectors, $\vec{P}_{\gamma_a}$ and $\vec{P}_{\gamma_b}$, are computed from energy-momentum conservation and transformed into the lab coordinate system.

Annihilation at Rest

The method `AtRestDoIt` treats the special case when a positron comes to rest before annihilating. It generates two photons, each with energy $k = mc^2$ and an isotropic angular distribution.

8.3.4   Status of this document

09.10.98 created by M.Maire.
01.08.01 minor corrections (mma)
09.01.02 MeanFreePath (mma)
01.12.02 Re-written by D.H. Wright

Bibliography

[1] R. Ford and W. Nelson. *SLAC-265, UC-32* (1985)

[2] H. Messel and D. Crawford. *Electron-Photon shower distribution, Pergamon Press* (1970)

[3] W. Heitler. *The Quantum Theory of Radiation, Clarendon Press, Oxford* (1954)

8.4 Positron - Electron Annihilation into Muon - Anti-muon

The class `G4AnnihiToMuPair` simulates the electromagnetic production of muon pairs by the annihilation of high-energy positrons with atomic electrons. Details of the implementation are given below and can also be found in Ref. [1].

8.4.1 Total Cross Section

The annihilation of positrons and target electrons producing muon pairs in the final state ($e^+e^- \rightarrow \mu^+\mu^-$) may give an appreciable contribution to the total number of muons produced in high-energy electromagnetic cascades. The threshold positron energy in the laboratory system for this process with the target electron at rest is

$$E_{\text{th}} = 2m_\mu^2/m_e - m_e \approx 43.69 \, \text{GeV} \,, \tag{8.50}$$

where m_μ and m_e are the muon and electron masses, respectively. The total cross section for the process on the electron is

$$\sigma = \frac{\pi \, r_\mu^2}{3} \xi \left(1 + \frac{\xi}{2}\right) \sqrt{1 - \xi} \,, \tag{8.51}$$

where $r_\mu = r_e \, m_e/m_\mu$ is the classical muon radius, $\xi = E_{\text{th}}/E$, and E is the total positron energy in the laboratory frame. In Eq. 8.51, approximations are made that utilize the inequality $m_e^2 \ll m_\mu^2$.

The cross section as a function of the positron energy E is shown in Fig.8.1. It has a maximum at $E = 1.396 \, E_{\text{th}}$ and the value at the maximum is $\sigma_{\text{max}} = 0.5426 \, r_\mu^2 = 1.008 \, \mu\text{b}$.

8.4.2 Sampling of Energies and Angles

It is convenient to simulate the muon kinematic parameters in the center-of-mass (c.m.) system, and then to convert into the laboratory frame.

The energies of all particles are the same in the c.m. frame and equal to

$$E_{\text{cm}} = \sqrt{\frac{1}{2} \, m_e(E + m_e)} \,. \tag{8.52}$$

The muon momenta in the c.m. frame are $P_{\text{cm}} = \sqrt{E_{\text{cm}}^2 - m_\mu^2}$. In what follows, let the cosine of the angle between the c.m. momenta of the μ^+ and e^+ be denoted as $x = \cos\theta_{\text{cm}}$.
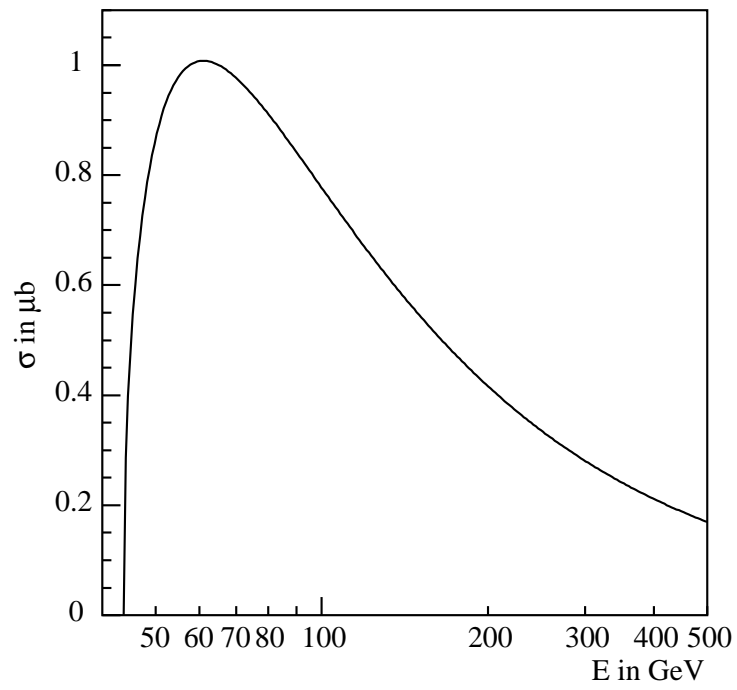
Figure 8.1: Total cross section for the process $e^+e^- \rightarrow \mu^+\mu^-$ as a function of the positron energy E in the laboratory system.

133

From the differential cross section it is easy to derive that, apart from normalization, the distribution in x is described by

$$f(x)\,dx = (1 + \xi + x^2\,(1 - \xi))\,dx\,, \quad -1 \leq x \leq 1\,. \qquad (8.53)$$

The value of this function is contained in the interval $(1+\xi) \leq f(x) \leq 2$ and the generation of x is straightforward using the rejection technique. Fig. 8.2 shows both generated and analytic distributions.
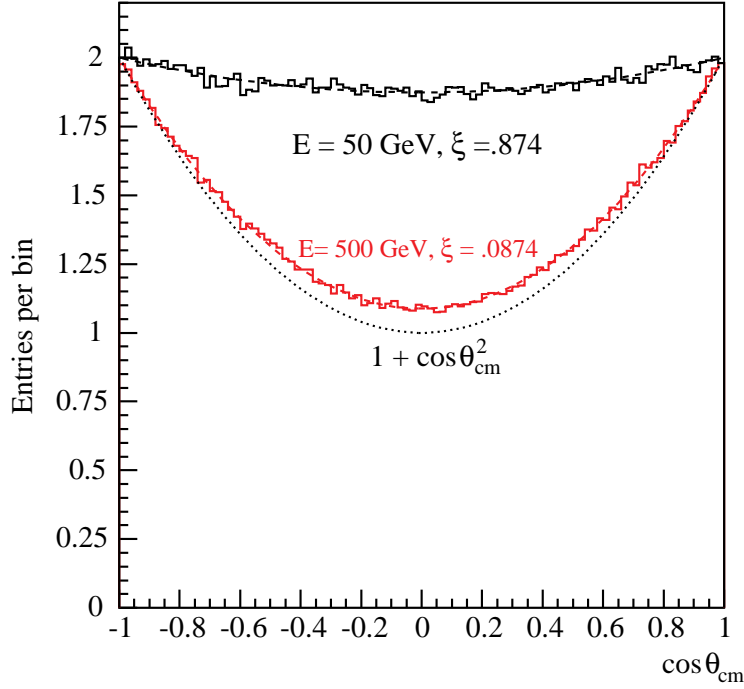
Figure 8.2: Generated histograms with 10^6 entries each and the expected $\cos\theta_{\mathrm{cm}}$ distributions (dashed lines) at $E = 50$ and $500\,\mathrm{GeV}$ positron energy in the lab frame. The asymptotic $1 + \cos\theta_{\mathrm{cm}}^2$ distribution valid for $E \to \infty$ is shown as dotted line.

The transverse momenta of the μ^+ and μ^- particles are the same, both in the c.m. and the lab frame, and their absolute values are equal to

$$P_\perp = P_{\mathrm{cm}}\,\sin\theta_{\mathrm{cm}} = P_{\mathrm{cm}}\,\sqrt{1 - x^2}\,. \qquad (8.54)$$

The energies and longitudinal components of the muon momenta in the lab system may be obtained by means of a Lorentz transformation. The velocity and Lorentz factor of the center-of-mass in the lab frame may be written as

$$\beta = \sqrt{\frac{E - m_e}{E + m_e}}\,, \quad \gamma \equiv \frac{1}{\sqrt{1 - \beta^2}} = \sqrt{\frac{E + m_e}{2m_e}} = \frac{E_{\mathrm{cm}}}{m_e}\,. \qquad (8.55)$$

The laboratory energies and longitudinal components of the momenta of the positive and negative muons may then be obtained:

$$E_+ = \gamma \left(E_{\mathrm{cm}} + x\,\beta\,P_{\mathrm{cm}} \right), \quad P_{+\parallel} = \gamma \left(\beta E_{\mathrm{cm}} + x\,P_{\mathrm{cm}} \right), \qquad (8.56)$$

$$E_- = \gamma \left(E_{\mathrm{cm}} - x\,\beta\,P_{\mathrm{cm}} \right), \quad P_{-\parallel} = \gamma \left(\beta E_{\mathrm{cm}} - x\,P_{\mathrm{cm}} \right). \qquad (8.57)$$

Finally, for the vectors of the muon momenta one obtains:

$$\mathbf{P}_+ = \left(+P_\perp \cos\varphi, +P_\perp \sin\varphi, P_{+\parallel} \right), \qquad (8.58)$$

$$\mathbf{P}_- = \left(-P_\perp \cos\varphi, -P_\perp \sin\varphi, P_{-\parallel} \right), \qquad (8.59)$$

where φ is a random azimuthal angle chosen between 0 and $2\,\pi$. The z-axis is directed along the momentum of the initial positron in the lab frame.

The maximum and minimum energies of the muons are given by

$$E_{\max} \approx \frac{1}{2}\,E \left(1 + \sqrt{1-\xi} \right), \qquad (8.60)$$

$$E_{\min} \approx \frac{1}{2}\,E \left(1 - \sqrt{1-\xi} \right) = \frac{E_{\mathrm{th}}}{2 \left(1 + \sqrt{1-\xi} \right)}. \qquad (8.61)$$

The fly-out polar angles of the muons are approximately

$$\theta_+ \approx P_\perp/P_{+\parallel}, \quad \theta_- \approx P_\perp/P_{-\parallel}\,; \qquad (8.62)$$

the maximal angle $\theta_{\max} \approx \dfrac{m_e}{m_\mu}\,\sqrt{1-\xi}$ is always small compared to 1.

Validity

The process described is assumed to be purely electromagnetic. It is based on virtual γ exchange, and the Z-boson exchange and $\gamma - Z$ interference processes are neglected. The Z-pole corresponds to a positron energy of $E = M_Z^2/2m_e = 8136\,\mathrm{TeV}$. The validity of the current implementation is therefore restricted to initial positron energies of less than about $1000\,\mathrm{TeV}$.

8.4.3   Status of this document

05.02.03 created by H.Burkhardt
14.04.03 minor re-wording by D.H. Wright

Bibliography

[1] H. Burkhardt, S. Kelner, and R. Kokoulin, "Production of muon pairs in annihilation of high-energy positrons with resting electrons," CERN-AB-2003-002 (ABP) and CLIC Note 554, January 2003.

8.5 Positron - Electron Annihilation into Hadrons

8.5.1 Introduction

The process `G4eeToHadrons` simulates the in-flight annihilation of a positron with an atomic electron into hadrons. It is assumed here that the atomic electron is initially free and at rest. Currently only two-pion production is available with a validity range up to 1 TeV.

8.5.2 Cross Section and Mean Free Path

The annihilation of positrons and target electrons producing pion pairs in the final state ($e^+e^- \to \pi^+\pi^-$) may give an appreciable contribution to electron-jet conversion at the LHC, and for the increasing total number of muons produced in the beam pipe of the linear collider [1]. The threshold positron energy in the laboratory system for this process with the target electron at rest is

$$E_{\text{th}} = 2m_\pi^2/m_e - m_e \approx 70.35 \,\text{GeV} , \tag{8.63}$$

where m_π and m_e are the pion and electron masses, respectively. The total cross section is dominated by the reaction

$$e^+e^- \to \rho\gamma \to \pi^+\pi^-\gamma, \tag{8.64}$$

where γ is a radiative photon and $\rho(770)$ is a well known vector meson. This radiative correction is essential, because it significantly modifies the shape of the resonance. Details of the theory are described in [2], in which the main term and the leading α^2 corrections are taken into account.

8.5.3 Sampling the final state

The final state of the $e + e-$ annihilation process 8.64 is simulated by first determining the kinematic limits of the photon energy in the center of mass system and then sampling the photon energy within those limits using the differential cross section. Conservation of energy-momentum is then used to determine the four-momentum of the pion final state. Then the backward transformation to the laboratory system is performed.

8.5.4 Status of this document

09.12.05 created by V.Ivanchenko

Bibliography

[1] A.G. Bogdanov et al., IEEE-NSS-33-179 conference Record, 2004, accepted by IEEE Transaction.

[2] M. Benayoun et al., Mod. Phys. Lett. A14, 2605 (1999).

8.6 Synchrotron Radiation

8.6.1 Photon spectrum

Synchrotron radiation photons are emitted by relativistic charged particles traveling in magnetic fields. The properties of synchrotron radiation are well understood and described in textbooks [1, 2, 3].

In the simplest case, we have an electron of momentum p moving perpendicular to a homogeneous magnetic field B. The magnetic field will keep the particle on a circular path, with radius

$$\rho = \frac{p}{e\,B} = \frac{m\gamma\beta c}{e\,B}\,. \quad \text{Numerically we have} \quad \rho[\text{m}] = p[\text{GeV/c}]\,\frac{3.336\,\text{m}}{B[\text{T}]}\,. \tag{8.65}$$

In general, there will be an arbitrary angle θ between the local magnetic field $\mathbf{B}$ and momentum vector $\mathbf{p}$ of the particle. The motion has a circular component in the plane perpendicular to the magnetic field, and in addition a constant momentum component parallel to the magnetic field. For a constant homogeneous field, the resulting trajectory is a helix.

The critical energy of the synchrotron radiation can be calculated using the radius ρ of Eq.8.65 and angle θ or the magnetic field perpendicular to the particle direction $B_\perp = B\sin\theta$ according to

$$E_c = \frac{3}{2}\,\hbar c\,\frac{\gamma^3 \sin\theta}{\rho} = \frac{3\,\hbar}{2\,m}\,\gamma^2\,eB_\perp\,. \tag{8.66}$$

Half of the synchrotron radiation power is radiated by photons above the critical energy.

With x we denote the photon energy E_γ, expressed in units of the critical energy E_c

$$x = \frac{E_\gamma}{E_c}\,. \tag{8.67}$$

The photon spectrum (number of photons emitted per path length s and relative energy x) can be written as

$$\frac{d^2 N}{ds\,dx} = \frac{\sqrt{3}\,\alpha}{2\pi}\,\frac{eB_\perp}{mc}\int_x^\infty K_{5/3}(\xi)\,d\xi \tag{8.68}$$

where $\alpha = e^2/\,4\pi\epsilon_0\hbar c$ is the dimensionless electromagnetic coupling (or fine structure) constant and $K_{5/3}$ is the modified Bessel function of the third kind.

The number of photons emitted per unit length and the mean free path λ between two photon emissions is obtained by integration over all photon

energies. Using

$$\int_0^\infty dx \int_x^\infty K_{5/3}(\xi)\, d\xi = \frac{5\pi}{3} \tag{8.69}$$

we find that

$$\frac{dN}{ds} = \frac{5\,\alpha}{2\sqrt{3}} \frac{eB_\perp}{m\beta c} = \frac{1}{\lambda}\,. \tag{8.70}$$

Here we are only interested in ultra-relativistic ($\beta \approx 1$) particles, for which λ only depends on the field B and not on the particle energy. We define a constant λ_B such that

$$\lambda = \frac{\lambda_B}{B_\perp} \qquad \text{where} \quad \lambda_B = \frac{2\sqrt{3}}{5} \frac{m\,c}{\alpha\,e} = 0.16183\,\text{Tm}\,. \tag{8.71}$$

As an example, consider a $10\,\text{GeV}$ electron, travelling perpendicular to a $1\,\text{T}$ field. It moves along a circular path of radius $\rho = 33.356\,\text{m}$. For the Lorentz factor we have $\gamma = 19569.5$ and $\beta = 1 - 1.4 \times 10^{-9}$. The critical energy is $E_c = 66.5\,\text{keV}$ and the mean free path between two photon emissions is $\lambda = 0.16183\,\text{m}$.

8.6.2 Validity

The spectrum given in Eq. 8.68 can generally be expected to provide a very accurate description for the synchrotron radiation spectrum generated by GeV electrons in magnetic fields.

Here we discuss some known limitations and possible extensions.

For particles traveling on a circular path, the spectrum observed in one location will in fact not be a continuous spectrum, but a discrete spectrum, consisting only of harmonics or modes n of the revolution frequency. In practice, the mode numbers will generally be too high to make this a visible effect. The critical mode number corresponding to the critical energy is $n_c = 3/2\,\gamma^3$. $10\,\text{GeV}$ electrons for example have $n_c \approx 10^{13}$.

Synchrotron radiation can be neglected for slower particles and only becomes relevant for ultra-relativistic particles with $\gamma > 10^3$. Using $\beta = 1$ introduces an uncertainty of about $1/2\gamma^2$ or less than 5×10^{-7}.

It is rather straightforward to extend the formulas presented here to particles other than electrons, with arbitrary charge q and mass m, see [4]. The number of photons and the power scales with the square of the charge.

The standard synchrotron spectrum of Eq. 8.68 is only valid as long as the photon energy remains small compared to the particle energy [5, 6]. This is a very safe assumption for GeV electrons and standard magnets with fields of order of Tesla.

An extension of synchrotron radiation to fields exceeding several hundred Tesla, such as those present in the beam-beam interaction in linear-colliders, is also known as beamstrahlung. For an introduction see [7].

The standard photon spectrum applies to homogeneous fields and remains a good approximation for magnetic fields which remain approximately constant over a the length ρ/γ, also known as the formation length for synchrotron radiation. Short magnets and edge fields will result instead in more energetic photons than predicted by the standard spectrum.

We also note that short bunches of many particles will start to radiate coherently like a single particle of the equivalent charge at wavelengths which are longer than the bunch dimensions.

Low energy, long-wavelength synchrotron radiation may destructively interfere with conducting surfaces [8].

The soft part of the synchrotron radiation spectrum emitted by charged particles travelling through a medium will be modified for frequencies close to and lower than the plasma frequency [9].

8.6.3 Direct inversion and generation of the photon energy spectrum

The task is to find an algorithm that effectively transforms the flat distribution given by standard pseudo-random generators into the desired distribution proportional to the expressions given in Eqs. 8.68, 8.72. The transformation is obtained from the inverse F^{-1} of the cumulative distribution function $F(x) = \int_0^x f(t)dt$.

Leaving aside constant factors, the probability density function relevant for the photon energy spectrum is

$$\mathrm{SynRad}(x) = \int_x^\infty K_{5/3}(t)dt \ . \tag{8.72}$$

Numerical methods to evaluate $K_{5/3}$ are discussed in [10]. An efficient algorithm to evaluate the integral SynRad using Chebyshev polynomials is described in [11]. This has been used in an earlier version of the Monte Carlo generator for synchrotron radiation using approximate transformations and the rejection method [12].

The cumulative distribution function is the integral of the probability density function. Here we have

$$\mathrm{SynRadInt}(z) = \int_z^\infty \mathrm{SynRad}(x)\,dx \ , \tag{8.73}$$

with normalization

$$\text{SynRadInt}(0) = \int_0^\infty \text{SynRad}(x)\, dx = \frac{5\pi}{3}, \qquad (8.74)$$

such that $\frac{3}{5\pi}\text{SynRadInt}(x)$ gives the fraction of photons above x.

It is possible to directly obtain the desired distribution with a fast and accurate algorithm using an analytical description based on simple transformations and Chebyshev polynomials. This approach is used here.

We now describe in some detail how the analytical description was obtained. For more details see [13].

It turned out to be convenient to start from the normalized complement rather then Eq. 8.73 directly, that is

$$\text{SynFracInt}(x) = \frac{3}{5\pi} \int_0^x \int_x^\infty K_{5/3}(t)dt\, dx = 1 - \frac{3}{5\pi}\text{SynRadInt}(x), \quad (8.75)$$

which gives the fraction of photons below x.

Figure 8.3 shows on the left hand side $y = \text{SynFracInt(x)}$ and on the right hand side the inverse $x = \text{InvSynFracInt}(y)$ together with simple approximate functions. We can see, that SynFracInt can be approximated by $x^{1/3}$ for small arguments, and by $1 - e^{-x}$ for large x. Consequently, we have for the inverse, $\text{InvSynFracInt}(y)$, which can be approximated for small y by y^3 and for large y by $-\log(1-y)$.

Good convergence for $\text{InvSynFracInt}(y)$ was obtained using Chebyshev polynomials combined with the approximate expressions for small and large arguments. For intermediate values, a Chebyshev polynomial can be used directly. Table 8.3 summarizes the expressions used in the different intervals.

Table 8.3: InvSynFracInt.

y	$x = \text{InvSynFracInt}(y)$
$y < 0.7$	$y^3\,\text{P}_{\text{Ch}}(y)$
$0.7 \le y \le 0.9999$	$\text{P}_{\text{Ch}}(y)$
$y > 0.9999$	$-\log(1-y)\text{P}_{\text{Ch}}(-\log(1-y))$

The procedure for Monte Carlo simulation is to generate y at random uniformly distributed between 0 at 1, as provided by standard random generators, and then to calculate the energy x in units of the critical energy according to $x = \text{InvSynFracInt}(y)$.

The numerical accuracy of the energy spectrum presented here is about 14 decimal places, close to the machine precision. Fig. 8.4 shows a comparison of generated and expected spectra. A Geant4 display of an electron moving in a magnetic field radiating synchrotron photons is presented in Fig. 8.5
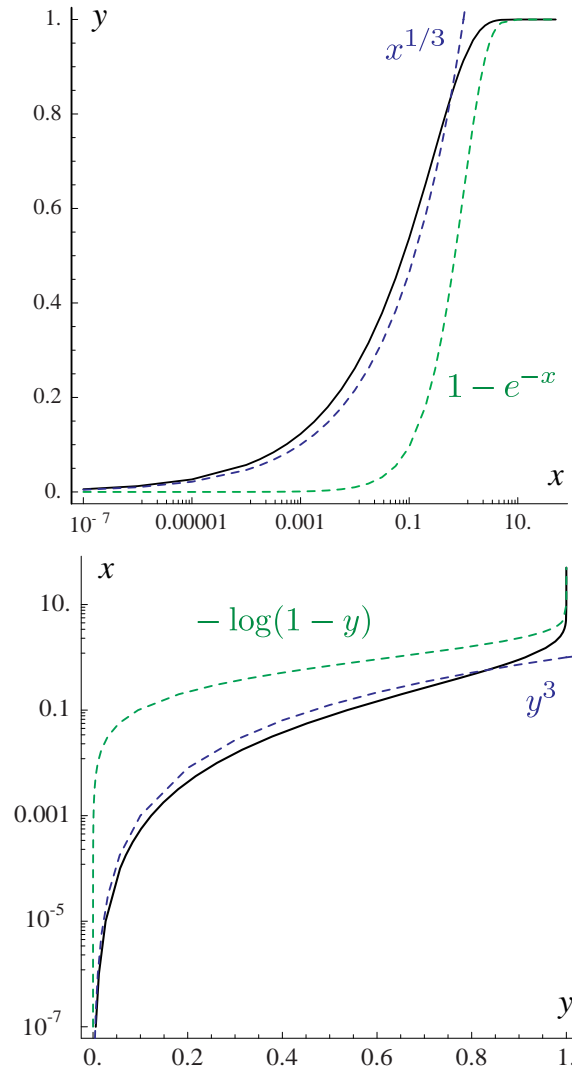
Figure 8.3: SynFracInt (left) and its inverse InvSynFracInt (right), on a $\log x$ scale. The functions $x^{1/3}$, y^3 and $1 - e^{-x}$, $-\log(1-y)$ are shown as dashed lines.

143
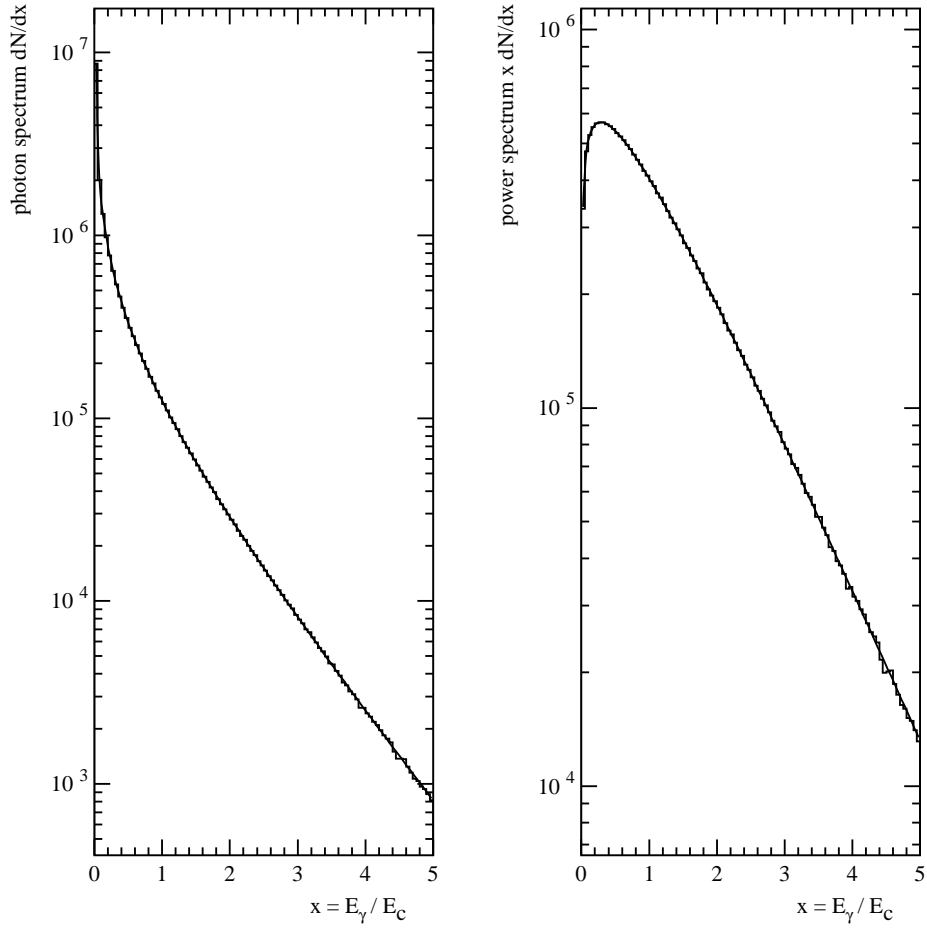
Figure 8.4: Comparison of the exact (smooth curve) and generated (histogram) spectra for 2×10^7 events. The photon spectrum is shown on the left and the power spectrum on the right side.
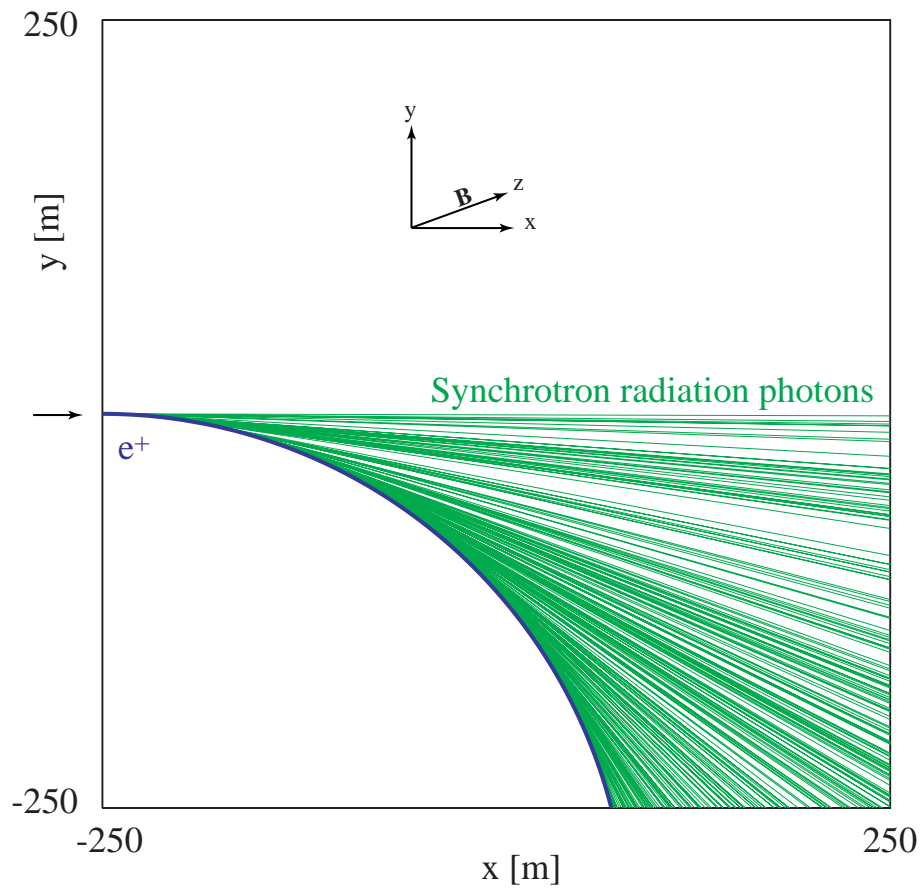
Figure 8.5: Geant4 display. 10 GeV e$^+$ moving initially in x-direction, bends downwards on a circular path by a 0.1 T magnetic field in z-direction.

8.6.4 Properties of the photon energy and power spectra

The normalised probability function describing the photon energy spectrum is

$$n_\gamma(x) = \frac{3}{5\pi} \int_x^\infty K_{5/3}(t)dt \; . \tag{8.76}$$

$n_\gamma(x)$ gives the fraction of photons in the interval x to $x + dx$, where x is the photon energy in units of the critical energy.

The first moment or mean value is

$$\mu = \int_0^\infty x \, n_\gamma(x) \, dx = \frac{8}{15\sqrt{3}} \; . \tag{8.77}$$

implying that the mean photon energy is $\frac{8}{15\sqrt{3}} = 0.30792$ of the critical energy.

The second moment about the mean, or variance, is

$$\sigma^2 = \int_0^\infty (x - \mu)^2 \, n_\gamma(x) \, dx = \frac{211}{675} \; , \tag{8.78}$$

and the r.m.s. value of the photon energy spectrum is $\sigma = \sqrt{\frac{211}{675}} = 0.5591$.

The normalised power spectrum is

$$P_\gamma(x) = \frac{9\sqrt{3}}{8\pi} x \int_x^\infty K_{5/3}(t)dt \; . \tag{8.79}$$

$P_\gamma(x)$ gives the fraction of the power which is radiated in the interval x to $x + dx$.

Half of the power is radiated below the critical energy

$$\int_0^1 P_\gamma(x) \, dx = 0.5000 \tag{8.80}$$

The mean value of the power spectrum is

$$\mu = \int_0^\infty x \, P_\gamma(x) \, dx = \frac{55}{24\sqrt{3}} = 1.32309 \; . \tag{8.81}$$

The variance is

$$\sigma^2 = \int_0^\infty (x - \mu)^2 \, P_\gamma(x) \, dx = \frac{2351}{1728} \; , \tag{8.82}$$

and the r.m.s. width is $\sigma = \sqrt{\frac{2351}{1728}} = 1.16642$.

8.6.5 Status of this document

08.06.06 created by H. Burkhardt

Bibliography

[1] A.A.Sokolov and I.M.Ternov, *Radiation from Relativistic Electrons*, Amer. Inst of Physics, 1986.

[2] J. Jackson, *Classical Electrodynamics.* John Wiley & Sons, third ed., 1998.

[3] A. Hofmann, *The Physics of Synchrotron Radiation.* Cambridge University Press, 2004.

[4] H. Burkhardt, "Reminder of the Edge Effect in Synchrotron Radiation", LHC Project Note 172, CERN Geneva 1998.

[5] F. Herlach, R. McBroom, T. Erber, J. .Murray, and R. Gearhart, "Experiments with Megagauss targets at SLAC", IEEE Trans Nucl Sci, NS 18, 3 (1971) 809-814.

[6] T. Erber, G. B. Baumgartner, D. White, and H. G. Latal, "Megagauss Bremsstrahlung and Radiation Reaction", in *Batavia 1983, proceedings, High Energy Accelerators*, 372-374.

[7] P. Chen, "An Introduction to Beamstrahlung and Disruption", in *Frontiers of Particle Beams*, M. Month and S. Turner, eds., Lecture Notes in Physics 296, pp. 481–494. Springer-Verlag, 1986.

[8] J. B. Murphy, S. Krinsky, and R. L. Gluckstern, "Longitudinal wakefield for an electron moving on a circular orbit", *Part. Acc.* 57 (1997) 9.

[9] V. M. Grichine, "Radiation of accelerated charge in absorbing medium", CERN-OPEN-2002-056.

[10] Y. Luke, "The special functions and their approximations", New York, NY: Academic Press, 1975.- 585 p.

[11] H.H.Umstätter. CERN/PS/SM/81-13, CERN Geneva 1981.

[12] H. Burkhardt, "Monte Carlo Generator for Synchrotron Radiation", LEP Note 632, CERN, December, 1990.

[13] H. Burkhardt, "Monte Carlo Generation of the Energy Spectrum of Synchrotron Radiation", to be published as CERN-AB and EuroTeV report.

Chapter 9

Charged Hadron Incident

9.1 Hadron and Ion Ionization

9.1.1 Method

The class *G4hIonisation* provides the continuous energy loss due to ionization and simulates the 'discrete' part of the ionization, that is, delta rays produced by charged hadrons. The class *G4ionIonisation* is intended for the simulation of energy loss by positive ions with change greater than unit. Inside these classes the following models are used:

- *G4BetherBlochModel* (valid for protons with $T > 2 \ MeV$)

- *G4BraggModel* (valid for protons with $T < 2 \ MeV$)

- *G4BraggIonModel* (valid for protons with $T < 2 \ MeV$)

The scaling relation (7.7) is a basic conception for the description of ionization of heavy charged particles. It is used both in energy loss calculation and in determination of the validity range of models. Namely the $T_p = 2MeV$ limit for protons is scaled for a particle with mass M_i by the ratio of the particle mass to the proton mass $T_i = T_p M_p / M_i$.

For all ionization models the value of the maximum energy transferable to a free electron T_{max} is given by the following relation [1]:

$$T_{max} = \frac{2m_e c^2 (\gamma^2 - 1)}{1 + 2\gamma(m_e/M) + (m_e/M)^2}, \tag{9.1}$$

where m_e is the electron mass and M is the mass of the incident particle. The method of calculation of the continuous energy loss and the total cross-section are explained below.

9.1.2 Continuous Energy Loss

The integration of 7.1 leads to the Bethe-Bloch restricted energy loss ($T < T_{cut}$ formula [1], which is modified taken into account various corrections [2]:

$$\frac{dE}{dx} = 2\pi r_e^2 mc^2 n_{el} \frac{z^2}{\beta^2} \left[\ln\left(\frac{2mc^2 \beta^2 \gamma^2 T_{up}}{I^2} \right) - \beta^2 \left(1 + \frac{T_{up}}{T_{max}} \right) - \delta - \frac{2C_e}{Z} + F \right] \tag{9.2}$$

where

$$
\begin{array}{ll}
r_e & \text{classical electron radius:} \quad e^2/(4\pi\epsilon_0 mc^2) \\
mc^2 & \text{mass-energy of the electron} \\
n_{el} & \text{electrons density in the material} \\
I & \text{mean excitation energy in the material} \\
Z & \text{atomic number of the material} \\
z & \text{charge of the hadron in units of the electron change} \\
\gamma & E/mc^2 \\
\beta^2 & 1 - (1/\gamma^2) \\
T_{up} & \min(T_{cut}, T_{max}) \\
\delta & \text{density effect function} \\
C_e & \text{shell correction function} \\
F & \text{high order corrections}
\end{array}
$$

In a single element the electron density is

$$
n_{el} = Z\, n_{at} = Z\, \frac{\mathcal{N}_{av}\rho}{A}
$$

($\mathcal{N}_{av}$: Avogadro number, ρ: density of the material, A: mass of a mole). In a compound material

$$
n_{el} = \sum_i Z_i\, n_{ati} = \sum_i Z_i\, \frac{\mathcal{N}_{av} w_i \rho}{A_i}.
$$

w_i is the proportion by mass of the ith element, with molar mass A_i.

The mean excitation energy I for all elements is tabulated according to the ICRU recommended values [3].

Shell Correction

$2C_e/Z$ is the so-called *shell correction term* which accounts for the fact of interaction of atomic electrons with atomic nucleus. This term more visible at low energies and for heavy atoms. The classical expression for the term [4] is used

$$
C = \sum C_\nu(\theta_\nu, \eta_\nu), \quad \nu = K, L, M, ..., \quad \theta = \frac{J_\nu}{\epsilon_\nu}, \quad \eta_\nu = \frac{\beta^2}{\alpha^2 Z_\nu^2}, \tag{9.3}
$$

where α is the fine structure constant, β is the hadron velocity, J_ν is the ionisation energy of the shell ν, ϵ_ν is Bohr ionisation energy of the shell ν, Z_ν is the effective charge of the shell ν. First terms C_K and C_L can

be analytically computed in using an assumption non-relativistic hydrogenic wave functions [5, 6]. The results [7] of tabulation of these computations in the interval of parameters $\eta_\nu = 0.005 \div 10$ and $\theta_\nu = 0.25 \div 0.95$ are used directly. For higher values of η_ν the parameterization [7] is applied:

$$C_\nu = \frac{K_1}{\eta} + \frac{K_2}{\eta^2} + \frac{K_3}{\eta^3}, \qquad (9.4)$$

where coefficients K_i provide smooth shape of the function. The effective nuclear charge for the L-shell can be reproduced as $Z_L = Z - d$, d is a parameter shown in Table 9.24. For outer shells the calculations are not available, so

Z	3	4	5	6	7	8	9	>9
d	1.72	2.09	2.48	2.82	3.16	3.53	3.84	4.15

Table 9.1: Effective nuclear charge for the L-shell [4].

L-shell parameterization is used and the following scaling relation [4, 8] is applied:

$$C_\nu = V_\nu C_L(\theta_L, H_\nu \eta_L), \quad V_\nu = \frac{n_\nu}{n_L}, \quad H_\nu = \frac{J_\nu}{J_L}, \qquad (9.5)$$

where V_ν is a vertical scaling factor proportional to number of electrons at the shell n_ν. The contribution of the shell correction term is about 10% for protons at $T = 2 MeV$.

Density Correction

δ is a correction term which takes into account the reduction in energy loss due to the so-called *density effect*. This becomes important at high energies because media have a tendency to become polarized as the incident particle velocity increases. As a consequence, the atoms in a medium can no longer be considered as isolated. To correct for this effect the formulation of Sternheimer [9] is used:
x is a kinetic variable of the particle : $x = \log_{10}(\gamma\beta) = \ln(\gamma^2\beta^2)/4.606$, and $\delta(x)$ is defined by

$$
\begin{array}{lll}
\text{for} & x < x_0 : & \delta(x) = 0 \\
\text{for} & x \in [x_0, \ x_1] : & \delta(x) = 4.606x - C + a(x_1 - x)^m \\
\text{for} & x > x_1 : & \delta(x) = 4.606x - C
\end{array} \qquad (9.6)
$$

where the matter-dependent constants are calculated as follows:

$$
\begin{aligned}
h\nu_p &= \quad \text{plasma energy of the medium} \ = \sqrt{4\pi n_{el} r_e^3} mc^2/\alpha = \sqrt{4\pi n_{el} r_e}\, \hbar c \\
C &= \quad 1 + 2\ln(I/h\nu_p) \\
x_a &= \quad C/4.606 \\
a &= \quad 4.606(x_a - x_0)/(x_1 - x_0)^m \\
m &= \quad 3.
\end{aligned}
\tag{9.7}
$$

For condensed media

$$
\begin{aligned}
I < 100\,\text{eV} &\left\{
\begin{array}{llll}
\text{for } C \le 3.681 & x_0 = 0.2 & x_1 = 2 \\
\text{for } C > 3.681 & x_0 = 0.326C - 1.0 & x_1 = 2
\end{array}\right. \\
I \ge 100\,\text{eV} &\left\{
\begin{array}{llll}
\text{for } C \le 5.215 & x_0 = 0.2 & x_1 = 3 \\
\text{for } C > 5.215 & x_0 = 0.326C - 1.5 & x_1 = 3
\end{array}\right.
\end{aligned}
$$

and for gaseous media

$$
\begin{array}{llll}
\text{for} & C < 10. & x_0 = 1.6 & x_1 = 4 \\
\text{for} & C \in [10.0,\ 10.5[& x_0 = 1.7 & x_1 = 4 \\
\text{for} & C \in [10.5,\ 11.0[& x_0 = 1.8 & x_1 = 4 \\
\text{for} & C \in [11.0,\ 11.5[& x_0 = 1.9 & x_1 = 4 \\
\text{for} & C \in [11.5,\ 12.25[& x_0 = 2. & x_1 = 4 \\
\text{for} & C \in [12.25,\ 13.804[& x_0 = 2. & x_1 = 5 \\
\text{for} & C \ge 13.804 & x_0 = 0.326C - 2.5 & x_1 = 5.
\end{array}
$$

High Order Corrections

High order corrections term to Bethe-Bloch formula (9.2) can be expressed as

$$
F = G - S + 2(zL_1 + z^2 L_2),
\tag{9.8}
$$

where G is the Mott correction term, S is the finite size correction term, L_1 is the Barkas correction, L_2 is the Bloch correction. The Mott term [2] describes the close-collision corrections tend to become more important at large velocities and higher charge of projectile. The Fermi result is used:

$$
G = \pi \alpha z \beta.
\tag{9.9}
$$

The Barkas correction term describes distant collisions. The parameterization of Ref. is expressed in the form:

$$
L_1 = \frac{1.29 F_A(b/x^{1/2})}{Z^{1/2} x^{3/2}}, \quad x = \frac{\beta^2}{Z\alpha^2},
\tag{9.10}
$$

Z	1 (H_2 gas)	1	2	3 - 10	11 - 17	18	19 - 25	26 - 50	> 50
d	0.6	1.8	0.6	1.8	1.4	1.8	1.4	1.35	1.3

Table 9.2: Scaled minimum impact parameter b [4].

where F_A is tabulated function [10], b is scaled minimum impact parameter shown in Table 9.2. This and other corrections depending on atomic properties are assumed to be additive for mixtures and compounds. For the Bloch correction term the classical expression [4] is following:

$$z^2 L_2 = -y^2 \sum_{n=1}^{\infty} \frac{1}{n(n^2 + y^2)}, \quad y = \frac{z\alpha}{\beta}. \tag{9.11}$$

The finite size correction term takes into account the space distribution of charge of the projectile particle. For muon it is zero, for hadrons this term become visible at energies above few hundred GeV and the following parameterization [2] is used:

$$S = ln(1 + q), \quad q = \frac{2m_e T_{max}}{\varepsilon^2}, \tag{9.12}$$

where T_{max} is given in relation (9.1), ε is proportional to the inverse effective radius of the projectile (Table 9.3). All these terms break scaling relation

mesons, spin = 0 ($\pi^{\pm}$, $K^{\pm}$)	0.736 GeV
baryons, spin = 1/2	0.843 GeV
ions	0.843 $A^{1/3}$ GeV

Table 9.3: The values of the ε parameter for different particle types.

(7.7) if the projectile particle charge differs from ± 1. To take this circumstance into account in $G4ionIonisation$ process at initialisation time the term F is ignored for the computation of the dE/dx table. At run time this term is taken into account by adding to the mean energy loss a value

$$\Delta T' = 2\pi r_e^2 mc^2 n_{el} \frac{z^2}{\beta^2} F \Delta s, \tag{9.13}$$

where Δs is the *true step length* and F is the high order correction term (9.8).

Parameterizations at Low Energies

For scaled energies below $T_{lim} = 2 \, MeV$ shell correction becomes very large and precision of the Bethe-Bloch formula degrades, so parameterisation of

evaluated data for stopping powers at low energies is required. These parameterisations for all atoms is available from ICRU'49 report [4]. The proton parametrisation is used in *G4BraggModel*, which is included by default in the process *G4hIonisation*. The alpha particle parameterisation is used in the *G4BraggIonModel*, which is included by default in the process *G4ionIonisation*. To provide a smooth transition between low-energy and high-energy models the modified energy loss expression is used for high energy

$$S(T) = S_H(T) + (S_L(T_{lim}) - S_H(T_{lim}))\frac{T_{lim}}{T}, \ \ T > T_{lim}, \tag{9.14}$$

where S is smoothed stopping power, S_H is stopping power from formula (9.2) and S_L is the low-energy parameterisation.

The precision of Bethe-Bloch formula for $T > 10MeV$ is within 2%, below the precision degrades and at $1keV$ only 20% may be garanteed. In the energy interval $1 - 10MeV$ the quality of description of the stopping power varied from atom to atom. To provide more stable and precise parameterisation the data from the NIST databases are included inside the standard package. These data are provided for 74 materials of the NIST material database [11]. The data from the PSTAR database are included into *G4BraggModel*. The data from the ASTAR database are included into *G4BraggIonModel*. So, if Geant4 material is defined as a NIST material, than NIST data are used for low-energy parameterisation of stopping power. If material is not from the NIST database, then the ICRU'49 parameterisation is used.

Nuclear Stopping

For scaled energies below $T_{lim} = 2MeV$ the contribution of non-ionizing energy loss needs to be taken into account. The additional energy loss due to *nuclear stopping power* $\Delta T_N \Delta s$ is added the the energy loss. The process *G4ionIonisation* has a flag, which allows to switch on or off this correction. For that the method

G4ionIonisation::ActivateNuclearStopping(G4bool)

can be used. By default this correction is active and the ICRU'49 parameterisation [4] is used.

9.1.3 Total Cross Section per Atom and Mean Free Path

For $T \gg I$ the differential cross section can be written as

$$\frac{d\sigma}{dT} = 2\pi r_e^2 mc^2 Z \frac{z_p^2}{\beta^2} \frac{1}{T^2} \left[1 - \beta^2 \frac{T}{T_{max}} + \frac{T^2}{2E^2} \right] \tag{9.15}$$

[1]. In GEANT4 $T_{cut} \geq 1$ keV. Integrating from T_{cut} to T_{max} gives the total cross section per atom :

$$\sigma(Z, E, T_{cut}) = \frac{2\pi r_e^2 Z z_p^2}{\beta^2} mc^2 \times \tag{9.16}$$
$$\left[\left(\frac{1}{T_{cut}} - \frac{1}{T_{max}} \right) - \frac{\beta^2}{T_{max}} \ln \frac{T_{max}}{T_{cut}} + \frac{T_{max} - T_{cut}}{2E^2} \right]$$

The last term is for spin $1/2$ only. In a given material the mean free path is:

$$\lambda = (n_{at} \cdot \sigma)^{-1} \quad or \quad \lambda = \left(\sum_i n_{ati} \cdot \sigma_i \right)^{-1} \tag{9.17}$$

The mean free path is tabulated during initialization as a function of the material and of the energy for all kinds of charged particles.

9.1.4 Simulating Delta-ray Production

A short overview of the sampling method is given in Chapter 2. Apart from the normalization, the cross section 9.15 can be factorized :

$$\frac{d\sigma}{dT} = f(T)g(T) \quad with \quad T \in [T_{cut}, \ T_{max}] \tag{9.18}$$

where

$$f(T) = \left(\frac{1}{T_{cut}} - \frac{1}{T_{max}} \right) \frac{1}{T^2} \tag{9.19}$$

$$g(T) = 1 - \beta^2 \frac{T}{T_{max}} + \frac{T^2}{2E^2}. \tag{9.20}$$

The last term in $g(T)$ is for spin $1/2$ only. The energy T is chosen by

1. sampling T from $f(T)$

2. calculating the rejection function $g(T)$ and accepting the sampled T with a probability of $g(T)$.

After the successful sampling of the energy, the direction of the scattered electron is generated with respect to the direction of the incident particle. The azimuthal angle ϕ is generated isotropically. The polar angle θ is calculated from energy-momentum conservation. This information is used to calculate the energy and momentum of both scattered particles and to transform them into the *global* coordinate system.

Ion Effective Charge

As ions penetrate matter they exchange electrons with the medium. In the implementation of *G4ionIonisation* the effective charge approach is used [12]. A state of equilibrium between the ion and the medium is assumed, so that the ion's effective charge can be calculated as a function of its kinetic energy in a given material. Before and after each step the dynamic charge of the ion is recalculated and saved in *G4DynamicParticle*, where it can be used not only for energy loss calculations but also for the sampling of transportation in an electromagnetic field.

The ion effective charge is expressed via the ion charge z_i and the fractional effective charge of ion γ_i:

$$z_{eff} = \gamma_i z_i. \tag{9.21}$$

For helium ions fractional effective charge is parameterized for all elements

$$(\gamma_{He})^2 = \left(1 - \exp\left[-\sum_{j=0}^{5} C_j Q^j\right]\right)\left(1 + \frac{7 + 0.05Z}{1000}\exp(-(7.6 - Q)^2)\right)^2,$$
$$Q = \max(0, \ln T), \tag{9.22}$$

where the coefficients C_j are the same for all elements, and the helium ion kinetic energy T is in keV/amu.

The following expression is used for heavy ions [13]:

$$\gamma_i = \left(q + \frac{1-q}{2}\left(\frac{v_0}{v_F}\right)^2 \ln\left(1 + \Lambda^2\right)\right)\left(1 + \frac{(0.18 + 0.0015Z)\exp(-(7.6 - Q)^2)}{Z_i^2}\right), \tag{9.23}$$

where q is the fractional average charge of the ion, v_0 is the Bohr velocity, v_F is the Fermi velocity of the electrons in the target medium, and Λ is the term taking into account the screening effect:

$$\Lambda = 10\frac{v_F}{v_0}\frac{(1-q)^{2/3}}{Z_i^{1/3}(6+q)}. \tag{9.24}$$

The Fermi velocity of the medium is of the same order as the Bohr velocity, and its exact value depends on the detailed electronic structure of the medium. The expression for the fractional average charge of the ion is the following:

$$q = [1 - \exp(0.803y^{0.3} - 1.3167y^{0.6} - 0.38157y - 0.008983y^2)], \qquad (9.25)$$

where y is a parameter that depends on the ion velocity v_i

$$y = \frac{v_i}{v_0 Z^{2/3}} \left(1 + \frac{v_F^2}{5v_i^2}\right). \qquad (9.26)$$

The parametrisation of the effective charge of the ion applied if the kinetic energy is below limit value

$$T < 10z_i \frac{M_i}{M_p} \, MeV, \qquad (9.27)$$

where M_i is the ion mass and M_p is the proton mass.

9.1.5   Status of this document

09.10.98 created by L. Urbán.
14.12.01 revised by M.Maire
29.11.02 re-worded by D.H. Wright
01.12.03 revised by V. Ivanchenko
21.06.07 revised by V. Ivanchenko

Bibliography

[1] W.-M. Yao et al., Jour. of Phys. G33 (2006) 1.

[2] S.P. Ahlen, Rev. Mod. Phys. 52 (1980) 121.

[3] ICRU (A. Allisy et al), Stopping Powers for Electrons and Positrons, ICRU Report 37, 1984.

[4] ICRU (A. Allisy et al), Stopping Powers and Ranges for Protons and Alpha Particles, ICRU Report 49, 1993.

[5] M.C. Walske, Phys. Rev. 88 (1952) 1283.

[6] M.C. Walske, Phys. Rev. 181 (1956) 940.

[7] G.S. Khandelwal, Nucl. Phys. A116 (1968) 97.

[8] H. Bichsel, Phys. Rev. A46 (1992) 5761.

[9] R.M. Sternheimer. Phys.Rev. B3 (1971) 3681.

[10] J.C. Ashley, R.H. Ritchie and W. Brandt, Phys. Rev. A8 (1973) 2402.

[11] http://physics.nist.gov/PhysRevData/contents-radi.html

[12] J.F. Ziegler, J.P. Biersack, U. Littmark, The Stopping and Ranges of Ions in Solids. Vol.1, Pergamon Press, 1985.

[13] W. Brandt and M. Kitagawa, Phys. Rev. B25 (1982) 5631.

Chapter 10

Muon Incident

10.1 Muon Ionization

The class *G4MuIonisation* provides the continuous energy loss due to ionization and simulates the 'discrete' part of the ionization, that is, delta rays produced by muons. Inside this class the following models are used:

- *G4BraggModel* (valid for protons with $T < 0.2\ MeV$)

- *G4BetherBlochModel* (valid for protons with $0.2\ MeV < T < 1\ GeV$)

- *G4MuBetherBlochModel* (valid for protons with $T > 1\ GeV$)

The limit energy $0.2\ MeV$ is equivalent to the proton limit energy $2MeV$ because of scaling relation (7.7), which allows simulation for muons with energy below $1\ GeV$ in the same way as for point-like hadrons with spin $1/2$ described in the section 7.1.

For higher energies the *G4MuBetherBlochModel* is applied, in which leading radiative corrections are taken into account [1]. Simple analytical formula for the cross section, derived with the logarithmic are used. Calculation results appreciably differ from usual elastic $\mu - e$ scattering in the region of high energy transfers $m_e << T < T_{max}$ and give non-negligible correction to the total average energy loss of high-energy muons. The total cross section is written as following:

$$\sigma(E, \epsilon) = \sigma_{BB}(E, \epsilon)\left[1 + \frac{\alpha}{2\pi}ln\left(1 + \frac{2\epsilon}{m_e}\right)ln\left(\frac{4m_e E(E - \epsilon)}{m_\mu^2(2\epsilon + m_e)}\right)\right], \quad (10.1)$$

here $\sigma(E, \epsilon)$ is the differential cross sections, $\sigma(E, \epsilon)_{BB}$ is the Bethe-Bloch cross section (9.15), m_e is the electron mass, m_μ is the muon mass, E is the muon energy, ϵ is the energy transfer, $\epsilon = \omega + T$, where T is the electron kinetic energy and ω is the energy of radiative gamma.

For computation of the truncated mean energy loss (7.1) the partial integration of the expression (10.1) is performed

$$S(E, \epsilon_{up}) = S_{BB}(E, \epsilon_{up}) + S_{RC}(E, \epsilon_{up}), \quad \epsilon_{up} = min(\epsilon_{max}, \epsilon_{cut}), \quad (10.2)$$

where term S_{BB} is the Bethe-Bloch truncated energy loss (9.2) for the interval of energy transfer $(0 - \epsilon_{up})$ and term S_{RC} is a correction due to radiative effects. The function become smooth after log-substitution and is computed by numerical integration

$$S_{RC}(E, \epsilon_{up}) = \int_{\ln \epsilon_1}^{\ln \epsilon_{up}} \epsilon^2(\sigma(E, \epsilon) - \sigma_{BB}(E, \epsilon))d(\ln \epsilon), \quad (10.3)$$

161

where lower limit ϵ_1 does not effect result of integration in first order and in the class *G4MuBetheBlochModel* the default value $\epsilon_1 = 100keV$ is used.

For computation of the discrete cross section (7.2) another substitution is used in order to perform numerical integration of a smooth function

$$\sigma(E) = \int_{1/\epsilon_{max}}^{1/\epsilon_{up}} \epsilon^2 \sigma(E, \epsilon) d(1/\epsilon). \tag{10.4}$$

The sampling of energy transfer is performed between $1/\epsilon_{up}$ and $1/\epsilon_{max}$ using rejection constant for the function $\epsilon^2 \sigma(E, \epsilon)$. After the successful sampling of the energy transfer, the direction of the scattered electron is generated with respect to the direction of the incident particle. The energy of radiative gamma is neglected. The azimuthal electron angle ϕ is generated isotropically. The polar angle θ is calculated from energy-momentum conservation. This information is used to calculate the energy and momentum of both scattered particles and to transform them into the *global* coordinate system.

10.1.1 Status of this document

09.10.98 created by L. Urbán.
14.12.01 revised by M.Maire
30.11.02 re-worded by D.H. Wright
01.12.03 revised by V. Ivanchenko
22.06.07 rewritten by V. Ivanchenko

Bibliography

[1] S.R. Kelner, R.P. Kokoulin, A.A. Petrukhin, Phys. Atomic Nuclei 60 (1997) 576.

10.2 Bremsstrahlung

Bremsstrahlung dominates other muon interaction processes in the region of catastrophic collisions ($v \geq 0.1$), that is at "moderate" muon energies above the kinematic limit for knock–on electron production. At high energies ($E \geq 1$ TeV) this process contributes about 40% of the average muon energy loss.

10.2.1 Differential Cross Section

The differential cross section for muon bremsstrahlung (in units of $cm^2/(g \ GeV)$) can be written as

$$
\begin{aligned}
\frac{d\sigma(E,\epsilon,Z,A)}{d\epsilon} &= \frac{16}{3}\alpha N_A (\frac{m}{\mu}r_e)^2 \frac{1}{\epsilon A} Z(Z\Phi_n + \Phi_e)(1 - v + \frac{3}{4}v^2) \\
&= 0 \quad \text{if} \quad \epsilon \geq \epsilon_{\max} = E - \mu, \quad\quad\quad (10.5)
\end{aligned}
$$

where μ and m are the muon and electron masses, Z and A are the atomic number and atomic weight of the material, and N_A is Avogadro's number. If E and T are the initial total and kinetic energy of the muon, and ϵ is the emitted photon energy, then $\epsilon = E - E'$ and the relative energy transfer $v = \epsilon/E$.

Φ_n represents the contribution of the nucleus and can be expressed as

$$
\begin{aligned}
\Phi_n &= \ln \frac{BZ^{-1/3}(\mu + \delta(D'_n\sqrt{e} - 2))}{D'_n(m + \delta\sqrt{e}BZ^{-1/3})}; \\
&= 0 \quad \text{if} \quad \text{negative.}
\end{aligned}
$$

Φ_e represents the contribution of the electrons and can be expressed as

$$
\begin{aligned}
\Phi_e &= \ln \frac{B'Z^{-2/3}\mu}{\left(1 + \frac{\delta\mu}{m^2\sqrt{e}}\right)(m + \delta\sqrt{e}B'Z^{-2/3})}; \\
&= 0 \quad \text{if} \quad \epsilon \geq \epsilon'_{\max} = E/(1 + \mu^2/2mE); \\
&= 0 \quad \text{if} \quad \text{negative.}
\end{aligned}
$$

In Φ_n and Φ_e, for all nuclei except hydrogen,

$$
\begin{aligned}
\delta &= \mu^2\epsilon/2EE' = \mu^2 v/2(E - \epsilon); \\
D'_n &= D_n^{(1-1/Z)}, \quad D_n = 1.54A^{0.27}; \\
B &= 183, \quad B' = 1429, \quad \sqrt{e} = 1.648(721271).
\end{aligned}
$$

For hydrogen (Z=1) $B = 202.4$, $B' = 446$, $D'_n = D_n$.

These formulae are taken mostly from Refs. [1] and [2]. They include improved nuclear size corrections in comparison with Ref. [3] in the region $v \sim 1$ and low Z. Bremsstrahlung on atomic electrons (taking into account target recoil and atomic binding) is introduced instead of a rough substitution $Z(Z+1)$. A correction for processes with nucleus excitation is also included [4].

Applicability and Restrictions of the Method

The above formulae assume that:

1. $E \gg \mu$, hence the ultrarelativistic approximation is used;
2. $E \le 10^{20}$ eV; above this energy, LPM suppression can be expected;
3. $v \ge 10^{-6}$; below 10^{-6} Ter-Mikaelyan suppression takes place. However, in the latter region the cross section of muon bremsstrahlung is several orders of magnitude less than that of other processes.

The Coulomb correction (for high Z) is not included. However, existing calculations [5] show that for muon bremsstrahlung this correction is small.

10.2.2   Continuous Energy Loss

The restricted energy loss for muon bremsstrahlung $(dE/dx)_{\mathrm{rest}}$ with relative transfers $v = \epsilon/(T + \mu) \le v_{\mathrm{cut}}$ can be calculated as follows :

$$\left(\frac{dE}{dx}\right)_{\mathrm{rest}} = \int_0^{\epsilon_{\mathrm{cut}}} \epsilon\, \sigma(E, \epsilon)\, d\epsilon = (T + \mu) \int_0^{v_{\mathrm{cut}}} \epsilon\, \sigma(E, \epsilon)\, dv\,.$$

If the user cut $v_{\mathrm{cut}} \ge v_{\mathrm{max}} = T/(T + \mu)$, the total average energy loss is calculated. Integration is done using Gaussian quadratures, and binning provides an accuracy better than about 0.03% for $T = 1$ GeV, $Z = 1$. This rapidly improves with increasing T and Z.

10.2.3   Total Cross Section

The integration of the differential cross section over $d\epsilon$ gives the total cross section for muon bremsstrahlung:

$$\sigma_{\mathrm{tot}}(E, \epsilon_{\mathrm{cut}}) = \int_{\epsilon_{\mathrm{cut}}}^{\epsilon_{\mathrm{max}}} \sigma(E, \epsilon) d\epsilon = \int_{\ln v_{\mathrm{cut}}}^{\ln v_{\mathrm{max}}} \epsilon\sigma(E, \epsilon) d(\ln v), \qquad (10.6)$$

where $v_{\mathrm{max}} = T/(T + \mu)$. If $v_{\mathrm{cut}} \ge v_{\mathrm{max}}$, $\sigma_{\mathrm{tot}} = 0$.

10.2.4 Sampling

The photon energy ϵ_p is found by numerically solving the equation :

$$P = \int_{\epsilon_p}^{\epsilon_{\max}} \sigma(E, \epsilon, Z, A) \, d\epsilon \Big/ \int_{\epsilon_{\text{cut}}}^{\epsilon_{\max}} \sigma(E, \epsilon, Z, A) \, d\epsilon \ .$$

Here P is the random uniform probability, $\epsilon_{\max} = T$, and $\epsilon_{\text{cut}} = (T + \mu) \cdot v_{\text{cut}}$. $v_{min.cut} = 10^{-5}$ is the minimal relative energy transfer adopted in the algorithm.

For fast sampling, the solution of the above equation is tabulated at initialization time for selected Z, T and P. During simulation, this table is interpolated in order to find the value of ϵ_p corresponding to the probability P.

The tabulation routine uses accurate functions for the differential cross section. The table contains values of

$$x_p = \ln(v_p/v_{\max})/\ln(v_{\max}/v_{\text{cut}}), \tag{10.7}$$

where $v_p = \epsilon_p/(T + \mu)$ and $v_{\max} = T/(T + \mu)$. Tabulation is performed in the range $1 \leq Z \leq 128$, $1 \leq T \leq 1000$ PeV, $10^{-5} \leq P \leq 1$ with constant logarithmic steps. Atomic weight (which is a required parameter in the cross section) is estimated here with an iterative solution of the approximate relation:

$$A = Z \left(2 + 0.015 \, A^{2/3}\right).$$

For $Z = 1$, $A = 1$ is used.

To find x_p (and thus ϵ_p) corresponding to a given probability P, the sampling method performs a linear interpolation in $\ln Z$ and $\ln T$, and a cubic, 4 point Lagrangian interpolation in $\ln P$. For $P \leq P_{\min}$, a linear interpolation in (P, x) coordinates is used, with $x = 0$ at $P = 0$. Then the energy ϵ_p is obtained from the inverse transformation of 10.7 :

$$\epsilon_p = (T + \mu) v_{\max} (v_{\max}/v_{\text{cut}})^{x_p}$$

The algorithm with the parameters described above has been tested for various Z and T. It reproduces the differential cross section to within 0.2 – 0.7 % for $T \geq 10$ GeV. The average total energy loss is accurate to within 0.5%. While accuracy improves with increasing T, satisfactory results are also obtained for $1 \leq T \leq 10$ GeV.

It is important to note that this sampling scheme allows the generation of ϵ_p for different user cuts on v which are above $v_{\text{min.cut}}$. To perform such a simulation, it is sufficient to define a new probability variable

$$P' = P \, \sigma_{\text{tot}} \, (v_{\text{user.cut}})/\sigma_{\text{tot}}(v_{\text{min.cut}})$$

and use it in the sampling method. Time consuming re-calculation of the 3-dimensional table is therefore not required because only the tabulation of $\sigma_{\text{tot}}(v_{\text{user.cut}})$ is needed.

The small-angle, ultrarelativistic approximation is used for the simulation (with about 20% accuracy at $\theta \leq \theta^* \approx 1$) of the angular distribution of the final state muon and photon. Since the target recoil is small, the muon and photon are directed symmetrically (with equal transverse momenta and coplanar with the initial muon):

$$p_{\perp\mu} = p_{\perp\gamma}, \quad \text{where} \quad p_{\perp\mu} = E'\theta_\mu, \quad p_{\perp\gamma} = \epsilon\theta_\gamma. \qquad (10.8)$$

θ_μ and θ_γ are muon and photon emission angles. The distribution in the variable $r = E\theta_\gamma/\mu$ is given by

$$f(r)dr \sim rdr/(1 + r^2)^2. \qquad (10.9)$$

Random angles are sampled as follows:

$$\theta_\gamma = \frac{\mu}{E}r \quad \theta_\mu = \frac{\epsilon}{E'}\theta_\gamma, \qquad (10.10)$$

where

$$r = \sqrt{\frac{a}{1-a}}, \quad a = \xi \frac{r_{\max}^2}{1 + r_{\max}^2}, \quad r_{\max} = \min(1, E'/\epsilon) \cdot E\,\theta^*/\mu,$$

and ξ is a random number uniformly distributed between 0 and 1.

10.2.5 Status of this document

09.10.98 created by R.Kokoulin and A.Rybin
17.05.00 updated by S.Kelner, R.Kokoulin and A.Rybin
30.11.02 re-written by D.H. Wright

Bibliography

[1] S.R.Kelner, R.P.Kokoulin, A.A.Petrukhin. Preprint MEPhI 024-95, Moscow, 1995; CERN SCAN-9510048.

[2] S.R.Kelner, R.P.Kokoulin, A.A.Petrukhin. Phys. Atomic Nuclei, **60** (1997) 576.

[3] A.A.Petrukhin, V.V.Shestakov. Canad.J.Phys., **46** (1968) S377.

[4] Yu.M.Andreyev, L.B.Bezrukov, E.V.Bugaev. Phys. Atomic Nuclei, **57** (1994) 2066.

[5] Yu.M.Andreev, E.V.Bugaev, Phys. Rev. D, **55** (1997) 1233.

10.3 Positron - Electron Pair Production by Muons

Direct electron pair production is one of the most important muon interaction processes. At TeV muon energies, the pair production cross section exceeds those of other muon interaction processes over a range of energy transfers between 100 MeV and $0.1E_\mu$. The average energy loss for pair production increases linearly with muon energy, and in the TeV region this process contributes more than half the total energy loss rate.

To adequately describe the number of pairs produced, the average energy loss and the stochastic energy loss distribution, the differential cross section behavior over an energy transfer range of 5 MeV $\leq \epsilon \leq 0.1 \cdot E_\mu$ must be accurately reproduced. This is is because the main contribution to the total cross section is given by transferred energies 5 MeV $\leq \epsilon \leq 0.01 \cdot E_\mu$, and because the contribution to the average muon energy loss is determined mostly in the region $0.001 \cdot E_\mu \leq \epsilon \leq 0.1 \cdot E_\mu$.

For a theoretical description of the cross section, the formulae of Ref. [1] are used, along with a correction for finite nuclear size [2]. To take into account electron pair production in the field of atomic electrons, the inelastic atomic form factor contribution of Ref. [3] is also applied.

10.3.1 Differential Cross Section

Definitions and Applicability

In the following discussion, these definitions are used:

- m and μ are the electron and muon masses, respectively

- $E \equiv E_\mu$ is the total muon energy, $E = T + \mu$

- Z and A are the atomic number and weight of the material

- ϵ is the total pair energy or, approximately, the muon energy loss $(E - E')$

- $v = \epsilon/E$

- $e = 2.718\ldots$

- $A^\star = 183$.

The formula for the differential cross section applies when:

- $E_\mu \gg \mu$ ($E \geq 2 - 5$ GeV) and $E_\mu \leq 10^{15} - 10^{17}$ eV. If muon energies exceed this limit, the LPM (Landau Pomeranchuk Migdal) effect may become important, depending on the material

- the muon energy transfer ϵ lies between $\epsilon_{\min} = 4\,m$ and $\epsilon_{\max} = E_\mu - \frac{3\sqrt{e}}{4}\,\mu\,Z^{1/3}$, although the formal lower limit is $\epsilon \gg 2\,m$, and the formal upper limit requires $E'_\mu \gg \mu$.

- $Z \leq 40 - 50$. For higher Z, the Coulomb correction is important but has not been sufficiently studied theoretically.

Formulae

The differential cross section for electron pair production by muons $\sigma(Z, A, E, \epsilon)$ can be written as :

$$\sigma(Z, A, E, \epsilon) = \frac{4}{3\pi}\,\frac{Z(Z+\zeta)}{A}\,N_A\,(\alpha r_0)^2\,\frac{1-v}{\epsilon}\int_0^{\rho_{\max}} G(Z, E, v, \rho)\,d\rho,$$
$$(10.11)$$

where

$$G(Z, E, v, \rho) = \Phi_e + (m/\mu)^2 \Phi_\mu,$$
$$\Phi_{e,\mu} = B_{e,\mu} L'_{e,\mu}$$

and

$$\Phi_{e,\mu} = 0 \quad \text{whenever} \quad \Phi_{e,\mu} < 0.$$

B_e and B_μ do not depend on Z, A, and are given by

$$B_e = [(2+\rho^2)(1+\beta) + \xi(3+\rho^2)]\ln\left(1+\frac{1}{\xi}\right) + \frac{1-\rho^2-\beta}{1+\xi} - (3+\rho^2);$$

$$B_e \approx \frac{1}{2\xi}[(3-\rho^2) + 2\beta(1+\rho^2)] \quad \text{for} \quad \xi \geq 10^3;$$

$$B_\mu = \left[(1+\rho^2)\left(1+\frac{3\beta}{2}\right) - \frac{1}{\xi}(1+2\beta)(1-\rho^2)\right]\ln(1+\xi)$$
$$+ \frac{\xi(1-\rho^2-\beta)}{1+\xi} + (1+2\beta)(1-\rho^2);$$

$$B_\mu \approx \frac{\xi}{2}[(5-\rho^2) + \beta(3+\rho^2)] \quad \text{for} \quad \xi \leq 10^{-3};$$

Also,

169

$$\xi = \frac{\mu^2 v^2}{4m^2} \frac{(1-\rho^2)}{(1-v)}; \quad \beta = \frac{v^2}{2(1-v)};$$

$$L'_e = \ln \frac{A^* Z^{-1/3} \sqrt{(1+\xi)(1+Y_e)}}{1 + \dfrac{2m\sqrt{e}A^* Z^{-1/3}(1+\xi)(1+Y_e)}{Ev(1-\rho^2)}}$$

$$- \frac{1}{2} \ln \left[1 + \left(\frac{3mZ^{1/3}}{2\mu} \right)^2 (1+\xi)(1+Y_e) \right];$$

$$L'_\mu = \ln \frac{(\mu/m)A^* Z^{-1/3} \sqrt{(1+1/\xi)(1+Y_\mu)}}{1 + \dfrac{2m\sqrt{e}A^* Z^{-1/3}(1+\xi)(1+Y_\mu)}{Ev(1-\rho^2)}}$$

$$- \ln \left[\frac{3}{2} Z^{1/3} \sqrt{(1+1/\xi)(1+Y_\mu)} \right].$$

For faster computing, the expressions for $L'_{e,\mu}$ are further algebraically transformed. The functions $L'_{e,\mu}$ include the nuclear size correction [2] in comparison with parameterization [1] :

$$Y_e = \frac{5 - \rho^2 + 4\beta(1+\rho^2)}{2(1+3\beta)\ln(3+1/\xi) - \rho^2 - 2\beta(2-\rho^2)};$$

$$Y_\mu = \frac{4 + \rho^2 + 3\beta(1+\rho^2)}{(1+\rho^2)(\frac{3}{2}+2\beta)\ln(3+\xi) + 1 - \frac{3}{2}\rho^2};$$

$$\rho_{\max} = [1 - 6\mu^2/E^2(1-v)]\sqrt{1-4m/Ev}.$$

Comment on the Calculation of the Integral $\int d\rho$ in Eq. 10.11

The integral $\int\limits_0^{\rho_{\max}} G(Z,E,v,\rho)\,d\rho$ is computed with the substitutions:

$$
\begin{aligned}
t &= \ln(1-\rho), \\
1 - \rho &= \exp(t), \\
1 + \rho &= 2 - \exp(t), \\
1 - \rho^2 &= e^t(2 - e^t).
\end{aligned}
$$

After that,

$$\int_0^{\rho_{\max}} G(Z,E,v,\rho)\,d\rho = \int_{t_{\min}}^0 G(Z,E,v,\rho)\,e^t\,dt, \qquad (10.12)$$

170

where

$$t_{\min} = \ln \frac{\dfrac{4m}{\epsilon} + \dfrac{12\mu^2}{EE'}\left(1 - \dfrac{4m}{\epsilon}\right)}{1 + \left(1 - \dfrac{6\mu^2}{EE'}\right)\sqrt{1 - \dfrac{4m}{\epsilon}}}.$$

To compute the integral of Eq. 10.12 with an accuracy better than 0.5%, Gaussian quadrature with $N = 8$ points is sufficient.

The function $\zeta(E, Z)$ in Eq. 10.11 serves to take into account the process on atomic electrons (inelastic atomic form factor contribution). To treat the energy loss balance correctly, the following approximation, which is an algebraic transformation of the expression in Ref. [3], is used:

$$\zeta(E, Z) = \frac{0.073 \ln \dfrac{E/\mu}{1 + \gamma_1 Z^{2/3} E/\mu} - 0.26}{0.058 \ln \dfrac{E/\mu}{1 + \gamma_2 Z^{1/3} E/\mu} - 0.14};$$

$$\zeta(E, Z) = 0 \quad \text{if the numerator is negative.}$$

For $E \le 35\,\mu$, $\zeta(E, Z) = 0$. Also $\gamma_1 = 1.95 \cdot 10^{-5}$ and $\gamma_2 = 5.30 \cdot 10^{-5}$.

The above formulae make use of the Thomas-Fermi model which is not good enough for light elements. For hydrogen $(Z = 1)$ the following parameters must be changed:

$A^* = 183 \;\Rightarrow\; 202.4$;

$\gamma_1 = 1.95 \cdot 10^{-5} \;\Rightarrow\; 4.4 \cdot 10^{-5}$;

$\gamma_2 = 5.30 \cdot 10^{-5} \;\Rightarrow\; 4.8 \cdot 10^{-5}$.

10.3.2   Total Cross Section and Restricted Energy Loss

If the user's cut for the energy transfer ϵ_{cut} is greater than $\epsilon_{\min}$, the process is represented by continuous restricted energy loss for interactions with $\epsilon \le \epsilon_{\text{cut}}$, and discrete collisions with $\epsilon > \epsilon_{\text{cut}}$. Respective values of the total cross section and restricted energy loss rate are defined as:

$$\sigma_{\text{tot}} = \int_{\epsilon_{\text{cut}}}^{\epsilon_{\max}} \sigma(E, \epsilon)\, d\epsilon; \quad (dE/dx)_{\text{restr}} = \int_{\epsilon_{\min}}^{\epsilon_{\text{cut}}} \epsilon\, \sigma(E, \epsilon)\, d\epsilon.$$

For faster computing, $\ln \epsilon$ substitution and Gaussian quadratures are used.

10.3.3 Sampling of Positron - Electron Pair Production

The e^+e^- pair energy ϵ_P, is found numerically by solving the equation

$$P = \int_{\epsilon_P}^{\epsilon_{\max}} \sigma(Z, A, T, \epsilon)d\epsilon \quad / \int_{cut}^{\epsilon_{\max}} \sigma(Z, A, T, \epsilon)d\epsilon \qquad (10.13)$$

or

$$1 - P = \int_{cut}^{\epsilon_P} \sigma(Z, A, T, \epsilon)d\epsilon \quad / \int_{cut}^{\epsilon_{\max}} \sigma(Z, A, T, \epsilon)d\epsilon \qquad (10.14)$$

To reach high sampling speed, solutions of Eqs. 10.13, 10.14 are tabulated at initialization time. Two 3-dimensional tables (referred to here as A and B) of $\epsilon_P(P, T, Z)$ are created, and then interpolation is used to sample ϵ_P. The number and spacing of entries in the table are chosen as follows:

- a constant increment in $\ln T$ is chosen such that there are four points per decade in the range $T_{\min} - T_{\max}$. The default range of muon kinetic energies in Geant4 is $T = 1\,\text{GeV} - 1000\,\text{PeV}$.

- a constant increment in $\ln Z$ is chosen. The shape of the sampling distribution does depend on Z, but very weakly, so that eight points in the range $1 \leq Z \leq 128$ are sufficient. There is practically no dependence on the atomic weight A.

- for probabilities $P \leq 0.5$, Eq. 10.13 is used and Table A is computed with a constant increment in $\ln P$ in the range $10^{-7} \leq P \leq 0.5$. The number of points in $\ln P$ for Table A is about 100.

- for $P \geq 0.5$, Eq. 10.14 is used and Table B is computed with a constant increment in $\ln(1 - P)$ in the range $10^{-5} \leq (1 - P) \leq 0.5$. In this case 50 points are sufficient.

The values of $\ln(\epsilon_P - cut)$ are stored in both Table A and Table B.

To create the "probability tables" for each (T, Z) pair, the following procedure is used:

- a temporary table of ~ 2000 values of $\epsilon \cdot \sigma(Z, A, T, \epsilon)$ is constructed with a constant increment (~ 0.02) in $\ln \epsilon$ in the range $(cut, \epsilon_{\max})$. ϵ is taken in the middle of the corresponding bin in $\ln \epsilon$.

- the accumulated cross sections

$$\sigma_1 = \int_{\ln \epsilon}^{\ln \epsilon_{\max}} \epsilon\, \sigma(Z, A, T, \epsilon)\, d(\ln \epsilon)$$

172

and

$$\sigma_2 = \int_{\ln(cut)}^{\ln \epsilon} \epsilon \, \sigma(Z, A, T, \epsilon) \, d(\ln \epsilon)$$

are calculated by summing the temporary table over the values above $\ln \epsilon$ (for σ_1) and below $\ln \epsilon$ (for σ_2) and then normalizing to obtain the accumulated probability functions.

- finally, values of $\ln(\epsilon_P - cut)$ for corresponding values of $\ln P$ and $\ln(1 - P)$ are calculated by linear interpolation of the above accumulated probabilities to form Tables A and B. The monotonic behavior of the accumulated cross sections is very useful in speeding up the interpolation procedure.

The random transferred energy corresponding to a probability P, is then found by linear interpolation in $\ln Z$ and $\ln T$, and a cubic interpolation in $\ln P$ for Table A or in $\ln(1-P)$ for Table B. For $P \leq 10^{-7}$ and $(1-P) \leq 10^{-5}$, linear extrapolation using the entries at the edges of the tables may be safely used. Electron pair energy is related to the auxiliary variable $x = \ln(\epsilon_P - cut)$ found by the trivial interpolation $\epsilon_P = e^x + cut$.

Similar to muon bremsstrahlung (section 10.2), this sampling algorithm does not re-initialize the tables for user cuts greater than cut_{min}. Instead, the probability variable is redefined as

$$P' = P\sigma_{\text{tot}}(cut_{user})/\sigma_{\text{tot}}(cut_{min}),$$

and P' is used for sampling.

In the simulation of the final state, the muon deflection angle (which is of the order of m/E) is neglected. The procedure for sampling the energy partition between e^+ and e^- and their emission angles is similar to that used for the $\gamma \rightarrow e^+ e^-$ conversion.

10.3.4   Status of this document

12.10.98 created by R.Kokoulin and A.Rybin
18.05.00 edited by S.Kelner, R.Kokoulin, and A.Rybin
27.01.03 re-written by D.H. Wright

Bibliography

[1] R.P.Kokoulin and A.A.Petrukhin, Proc. 11th Intern. Conf. on Cosmic Rays, Budapest, 1969 [Acta Phys. Acad. Sci. Hung.,**29, Suppl.4**, p.277, 1970].

[2] R.P.Kokoulin and A.A.Petrukhin, Proc. 12th Int. Conf. on Cosmic Rays, Hobart, 1971, **vol.6**, p.2436.

[3] S.R.Kelner, Phys. Atomic Nuclei, **61** (1998) 448.

10.4 Muon Photonuclear Interaction

The inelastic interaction of muons with nuclei is important at high muon energies ($E \geq 10$ GeV), and at relatively high energy transfers ν ($\nu/E \geq 10^{-2}$). It is especially important for light materials and for the study of detector response to high energy muons, muon propagation and muon-induced hadronic background. The average energy loss for this process increases almost lineary with energy, and at TeV muon energies constitutes about 10% of the energy loss rate.

The main contribution to the cross section $\sigma(E, \nu)$ and energy loss comes from the low Q^2–region ($Q^2 \ll 1$ GeV^2). In this domain, many simplifications can be made in the theoretical consideration of the process in order to obtain convenient and simple formulae for the cross section. Most widely used are the expressions given by Borog and Petrukhin [1], and Bezrukov and Bugaev [2]. Results from these authors agree within 10% for the differential cross section and within about 5% for the average energy loss, provided the same photonuclear cross section, $\sigma_{\gamma N}$, is used in the calculations.

10.4.1 Differential Cross Section

The Borog and Petrukhin formula for the cross section is based on:

- Hand's formalism [3] for inelastic muon scattering,

- a semi-phenomenological inelastic form factor, which is a Vector Dominance Model with parameters estimated from experimental data, and

- nuclear shadowing effects with a reasonable theoretical parameterization [4].

For $E \geq 10$ GeV, the Borog and Petrukhin cross section (cm^2/g GeV), differential in transferred energy, is

$$\sigma(E, \nu) = \Psi(\nu)\Phi(E, v), \tag{10.15}$$

$$\Psi(\nu) = \frac{\alpha}{\pi} \frac{A_{\text{eff}} N_{AV}}{A} \sigma_{\gamma N}(\nu) \frac{1}{\nu}, \tag{10.16}$$

$$\Phi(E, v) = v - 1 + \left[1 - v + \frac{v^2}{2}\left(1 + \frac{2\mu^2}{\Lambda^2}\right)\right] \ln \frac{\dfrac{E^2(1-v)}{\mu^2}\left(1 + \dfrac{\mu^2 v^2}{\Lambda^2(1-v)}\right)}{1 + \dfrac{Ev}{\Lambda}\left(1 + \dfrac{\Lambda}{2M} + \dfrac{Ev}{\Lambda}\right)}, \tag{10.17}$$

175

where ν is the energy lost by the muon, $v = \nu/E$, and μ and M are the muon and nucleon (proton) masses, respectively. Λ is a Vector Dominance Model parameter in the inelastic form factor which is estimated to be $\Lambda^2 = 0.4\,\text{GeV}^2$.

For A_{eff}, which includes the effect of nuclear shadowing, the parameterization [4]

$$A_{\text{eff}} = 0.22A + 0.78A^{0.89} \tag{10.18}$$

is chosen.

A reasonable choice for the photonuclear cross section, $\sigma_{\gamma N}$, is the parameterization obtained by Caldwell et al. [5] based on the experimental data on photoproduction by real photons:

$$\sigma_{\gamma N} = (49.2 + 11.1 \ln K + 151.8/\sqrt{K}) \cdot 10^{-30}\text{cm}^2 \quad K \ \text{in GeV.} \tag{10.19}$$

The upper limit of the transferred energy is taken to be $\nu_{\max} = E - M/2$. The choice of the lower limit $\nu_{\min}$ is less certain since the formula 10.15, 10.16, 10.17 is not valid in this domain. Fortunately, $\nu_{\min}$ influences the total cross section only logarithmically and has no practical effect on the average energy loss for high energy muons. Hence, a reasonable choice for $\nu_{\min}$ is 0.2 GeV.

In Eq. 10.16, A_{eff} and $\sigma_{\gamma N}$ appear as factors. A more rigorous theoretical approach may lead to some dependence of the shadowing effect on ν and E; therefore in the differential cross section and in the sampling procedure, this possibility is forseen and the atomic weight A of the element is kept as an explicit parameter.

The total cross section is obtained by integration of Eq. 10.15 between $\nu_{\min}$ and $\nu_{\max}$; to facilitate the computation, a $\ln(\nu)$–substitution is used.

10.4.2 Sampling

Sampling the Transferred Energy

The muon photonuclear interaction is always treated as a discrete process with its mean free path determined by the total cross section. The total cross section is obtained by the numerical integration of Eq. 10.15 within the limits $\nu_{\min}$ and $\nu_{\max}$. The process is considered for muon energies $1\text{GeV} \leq$ T $\leq 1000\text{PeV}$, though it should be noted that above 100 TeV the extrapolation (Eq. 10.19) of $\sigma_{\gamma N}$ may be too crude.

The random transferred energy, ν_p, is found from the numerical solution of the equation :

$$P = \int_{\nu_p}^{\nu_{\max}} \sigma(E,\nu)d\nu \bigg/ \int_{\nu_{\min}}^{\nu_{\max}} \sigma(E,\nu)d\nu . \qquad (10.20)$$

Here P is the random uniform probability, with $\nu_{\max} = E - M/2$ and $\nu_{\min} = 0.2$ GeV.

For fast sampling, the solution of Eq. 10.20 is tabulated at initialization time. During simulation, the sampling method returns a value of ν_p corresponding to the probability P, by interpolating the table. The tabulation routine uses Eq. 10.15 for the differential cross section. The table contains values of

$$x_p = \ln(\nu_p/\nu_{\max})/\ln(\nu_{\max}/\nu_{\min}), \qquad (10.21)$$

calculated at each point on a three-dimensional grid with constant spacings in $\ln(T)$, $\ln(A)$ and $\ln(P)$. The sampling uses linear interpolations in $\ln(T)$ and $\ln(A)$, and a cubic interpolation in $\ln(P)$. Then the transferred energy is calculated from the inverse transformation of Eq. 10.21, $\nu_p = \nu_{\max}(\nu_{\max}/\nu_{\min})^{x_p}$. Tabulated parameters reproduce the theoretical dependence to better than 2% for $T > 1$ GeV and better than 1% for $T > 10$ GeV.

Sampling the Muon Scattering Angle

According to Refs. [1, 6], in the region where the four-momentum transfer is not very large $(Q^2 \leq 3\mathrm{GeV}^2)$, the t – dependence of the cross section may be described as:

$$\frac{d\sigma}{dt} \sim \frac{(1 - t/t_{\max})}{t(1 + t/\nu^2)(1 + t/m_0^2)}[(1-y)(1 - t_{\min}/t) + y^2/2], \qquad (10.22)$$

where t is the square of the four-momentum transfer, $Q^2 = 2(EE' - PP'\cos\theta - \mu^2)$. Also, $t_{\min} = (\mu y)^2/(1 - y)$, $y = \nu/E$ and $t_{\max} = 2M\nu$. $\nu = E - E'$ is the energy lost by the muon and E is the total initial muon energy. M is the nucleon (proton) mass and $m_0^2 \equiv \Lambda^2 \simeq 0.4$ GeV^2 is a phenomenological parameter determing the behavior of the inelastic form factor. Factors which depend weakly, or not at all, on t are omitted.

To simulate random t and hence the random muon deflection angle, it is convenient to represent Eq. 10.22 in the form :

$$\sigma(t) \sim f(t)g(t), \qquad (10.23)$$

where

$$f(t) = \frac{1}{t(1 + t/t_1)}, \tag{10.24}$$

$$g(t) = \frac{1 - t/t_{\max}}{1 + t/t_2} \cdot \frac{(1 - y)(1 - t_{\min}/t) + y^2/2}{(1 - y) + y^2/2},$$

and

$$t_1 = \min(\nu^2, m_0^2) \quad t_2 = \max(\nu^2, m_0^2). \tag{10.25}$$

t_P is found analytically from Eq. 10.24 :

$$t_P = \frac{t_{\max} t_1}{(t_{\max} + t_1) \left[\dfrac{t_{\max}(t_{\min} + t_1)}{t_{\min}(t_{\max} + t_1)} \right]^P - t_{\max}},$$

where P is a random uniform number between 0 and 1, which is accepted with probability $g(t)$. The conditions of Eq. 10.25 make use of the symmetry between ν^2 and m_0^2 in Eq. 10.22 and allow increased selection efficiency, which is typically ≥ 0.7. The polar muon deflection angle θ can easily be found from [1]

$$\sin^2(\theta/2) = \frac{t_P - t_{\min}}{4\,(EE' - \mu^2) - 2\,t_{\min}}.$$

The hadronic vertex is generated by the hadronic processes taking into account the four-momentum transfer.

10.4.3 Status of this document

12.10.98 created by R.Kokoulin, A.Rybin.
18.05.00 edited by S.Kelner, R.Kokoulin, and A.Rybin.
07.12.02 re-worded by D.H. Wright
30.08.04 correction of eq. 8.24 (to 1/sqrt) from H. Araujo

Bibliography

[1] V.V.Borog and A.A.Petrukhin, Proc. 14th Int.Conf. on Cosmic Rays, Munich,1975, **vol.6**, p.1949.

[2] L.B.Bezrukov and E.V.Bugaev, Sov. J. Nucl. Phys., **33**, 1981, p.635.

---

[1]This convenient formula has been shown to the authors by D.A. Timashkov.

[3] L.N.Hand. Phys. Rev., **129**, 1834 (1963).

[4] S.J.Brodsky, F.E.Close and J.F.Gunion, Phys. Rev. **D6**, 177 (1972).

[5] D.O. Caldwell et al., Phys. Rev. Lett., **42**, 553 (1979).

[6] V.V.Borog, V.G.Kirillov-Ugryumov, A.A.Petrukhin, Sov. J. Nucl. Phys., **25**, 1977, p.46.

Chapter 11

Polarized Electron/Positron/Gamma Incident

11.1 Introduction

With the EM polarization extension it is possible to track polarized particles (leptons and photons). Special emphasis will be put in the proper treatment of polarized matter and its interaction with longitudinal polarized electrons/positrons or circularly polarized photons, which is for instance essential for the simulation of positron polarimetry. The implementation is base on Stokes vectors [1]. Further details can be found in [2].

In its current state, the following polarization dependent processes are considered

- Bhabha/Møller scattering,

- Positron Annihilation,

- Compton scattering,

- Pair creation,

- Bremsstrahlung.

Several simulation packages for the realistic description of the development of electromagnetic showers in matter have been developed. A prominent example of such codes is EGS (Electron Gamma Shower)[3]. For this simulation framework extensions with the treatment of polarized particles exist [4, 5, 6]; the most complete has been developed by K. Flöttmann [4]. It is based on the matrix formalism [1], which enables a very general treatment of polarization. However, the Flöttmann extension concentrates on evaluation of polarization transfer, i.e. the effects of polarization induced asymmetries are neglected, and interactions with polarized media are not considered.

Another important simulation tool for detector studies is GEANT3 [7]. Here also some effort has been made to include polarization [8, 9], but these extensions are not publicly available.

In general the implementation of polarization in this EM polarization library follows very closely the approach by K. Flöttmann [4]. The basic principle is to associate a *Stokes vector* to each particle and track the mean polarization from one interaction to another. The basics for this approach is the matrix formalism as introduced in [1].

11.1.1 Stokes vector

The *Stokes vector* [10, 1] is a rather simple object (in comparison to e.g. the spin density matrix), three real numbers are sufficient for the characterization

of the polarization state of any single electron, positron or photon. Using *Stokes vectors* **all** possible polarization states can be described, i.e. circular and linear polarized photons can be handled with the same formalism as longitudinal and transverse polarized electron/positrons.

The *Stokes vector* can be used also for beams, in the sense that it defines a mean polarization.

In the EM polarization library the Stokes vector is defined as follows:

	Photons	Electrons
ξ_1	linear polarization	polarization in x direction
ξ_2	linear polarization but $\pi/4$ to right	polarization in y direction
ξ_3	circular polarization	polarization in z direction

This definition is assumed in the *particle reference frame*, i.e. with the momentum of the particle pointing to the z direction, cf. also next section about coordinate transformations. Correspondingly a 100% longitudinally polarized electron or positron is characterized by

$$\boldsymbol{\xi} = \begin{pmatrix} 0 \\ 0 \\ \pm 1 \end{pmatrix},$$

(11.1)

where ± 1 corresponds to spin parallel (anti parallel) to particle's momentum. Note that this definition is similar, but not identical to the definition used in McMaster [1].

Many scattering cross sections of polarized processes using Stokes vectors for the characterization of initial and final states are available in [1]. In general a differential cross section has the form

$$\frac{d\sigma(\boldsymbol{\zeta}^{(1)}, \boldsymbol{\zeta}^{(2)}, \boldsymbol{\xi}^{(1)}, \boldsymbol{\xi}^{(2)})}{d\Omega} ,$$

(11.2)

i.e. it is a function of the polarization states of the initial particles $\boldsymbol{\zeta}^{(1)}$ and $\boldsymbol{\zeta}^{(2)}$, as well as of the polarization states of the final state particles $\boldsymbol{\xi}^{(1)}$ and $\boldsymbol{\xi}^{(2)}$ (in addition to the kinematic variables E, θ, and ϕ).

Consequently, in a simulation we have to account for

- Asymmetries:

  Polarization of beam ($\boldsymbol{\zeta}^{(1)}$) and target ($\boldsymbol{\zeta}^{(2)}$) can induce azimuthal and polar asymmetries, and may also influence on the total cross section (Geant4: GetMeanFreePath()).

- Polarization transfer / depolarization effects

  The dependence on the final state polarizations defines a possible transfer from initial polarization to final state particles.

11.1.2 Transfer matrix

Using the formalism of McMaster, differential cross section and polarization transfer from the initial state ($\boldsymbol{\zeta}^{(1)}$) to one final state particle ($\boldsymbol{\xi}^{(1)}$) are combined in an interaction matrix T:

$$\begin{pmatrix} O \\ \boldsymbol{\xi}^{(1)} \end{pmatrix} = T \begin{pmatrix} I \\ \boldsymbol{\zeta}^{(1)} \end{pmatrix} , \tag{11.3}$$

where I and O are the incoming and outgoing currents, respectively. In general the 4×4 matrix T depends on the target polarization $\boldsymbol{\zeta}^{(2)}$ (and of course on the kinematic variables E, θ, ϕ). Similarly one can define a matrix defining the polarization transfer to second final state particle like

$$\begin{pmatrix} O \\ \boldsymbol{\xi}^{(2)} \end{pmatrix} = T' \begin{pmatrix} I \\ \boldsymbol{\zeta}^{(1)} \end{pmatrix} . \tag{11.4}$$

In this framework the transfer matrix T is of the form

$$T = \begin{pmatrix} S & A_1 & A_2 & A_3 \\ P_1 & M_{11} & M_{21} & M_{31} \\ P_2 & M_{12} & M_{22} & M_{32} \\ P_3 & M_{13} & M_{23} & M_{33} \end{pmatrix} . \tag{11.5}$$

The matrix elements T_{ij} can be identified as (unpolarized) differential cross section (S), polarized differential cross section (A_j), polarization transfer (M_{ij}), and (de)polarization (P_i). In the Flöttmann extension the elements A_j and P_i have been neglected, thus concentrating on polarization transfer only. Using the full matrix takes now all polarization effects into account.

The transformation matrix, i.e. the dependence of the mean polarization of final state particles, can be derived from the asymmetry of the differential cross section w.r.t. this particular polarization. Where the asymmetry is defined as usual by

$$A = \frac{\sigma(+1) - \sigma(-1)}{\sigma(+1) + \sigma(-1)} . \tag{11.6}$$

The mean final state polarizations can be determined coefficient by coefficient.

In general, the differential cross section is a linear function of the polarizations, i.e.

$$
\begin{aligned}
\frac{d\sigma(\boldsymbol{\zeta}^{(1)}, \boldsymbol{\zeta}^{(2)}, \boldsymbol{\xi}^{(1)}, \boldsymbol{\xi}^{(2)})}{d\Omega} = \quad & \Phi_{(\zeta^{(1)},\zeta^{(2)})} + \boldsymbol{A}_{(\zeta^{(1)},\zeta^{(2)})} \cdot \boldsymbol{\xi}^{(1)} + \boldsymbol{B}_{(\zeta^{(1)},\zeta^{(2)})} \cdot \boldsymbol{\xi}^{(2)} \\
& + \boldsymbol{\xi}^{(1)^T} M_{(\zeta^{(1)},\zeta^{(2)})} \, \boldsymbol{\xi}^{(2)} \quad\quad\quad (11.7)
\end{aligned}
$$

In this form, the mean polarization of the final state can be read off easily, and one obtains

$$
\langle \boldsymbol{\xi}^{(1)} \rangle = \frac{1}{\Phi_{(\zeta^{(1)},\zeta^{(2)})}} \boldsymbol{A}_{(\zeta^{(1)},\zeta^{(2)})} \text{ and} \quad\quad (11.8)
$$

$$
\langle \boldsymbol{\xi}^{(2)} \rangle = \frac{1}{\Phi_{(\zeta^{(1)},\zeta^{(2)})}} \boldsymbol{B}_{(\zeta^{(1)},\zeta^{(2)})} \, . \quad\quad (11.9)
$$

Note, that the *mean* polarization states do not depend on the correlation matrix $M_{(\zeta^{(1)},\zeta^{(2)})}$. In order to account for correlation one has to generate *single* particle Stokes vector explicitly, i.e. on an event by event basis. However, this implementation generates *mean* polarization states, and neglects correlation effects.

11.1.3 Coordinate transformations

Three different coordinate systems are used in the evaluation of polarization states:

- **World frame**

  The geometry of the target, and the momenta of all particles in Geant4 are noted in the world frame X, Y, Z (the *global reference frame*, GRF). It is the basis of the calculation of any other coordinate system.

- **Particle frame**

  Each particle is carrying its own coordinate system. In this system the direction of motion coincides with the z-direction. Geant4 provides a transformation from any particle frame to the World frame by the method `G4ThreeMomemtum::rotateUz()`. Thus, the y-axis of the *particle reference frame* (PRF) lies in the X-Y-plane of the world frame.

  The Stokes vector of any moving particle is defined w.r.t. the corresponding particle frame. Particles at rest (e.g. electrons of a media) use the world frame as particle frame.
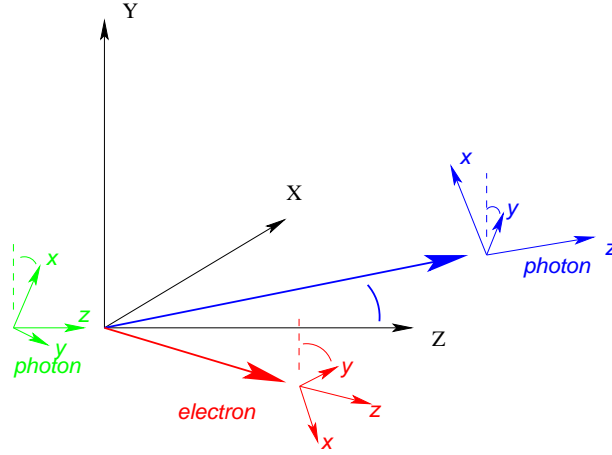
Figure 11.1: The *interaction frame* and the *particle frames* for the example of Compton scattering. The momenta of all participating particle lie in the x-z-plane, the scattering plane. The incoming photon gives the z direction. The outgoing photon is defined as *particle 1* and gives the x-direction, perpendicular to the z-axis. The y-axis is then perpendicular to the scattering plane and completes the definition of a right handed coordinate system called *interaction frame*. The *particle frame* is defined by the Geant4 routine `G4ThreeMomemtum::rotateUz()`.

- **Interaction frame**

  For the evaluation of the polarization transfer another coordinate system is used, defined by the scattering plane, cf. fig. 11.1. There the z-axis is defined by the direction of motion of the incoming particle. The scattering plane is spanned by the z-axis and the x-axis, in a way, that the direction of *particle 1* has a positive x component. The definition of *particle 1* depends on the process, for instance in Compton scattering, the outgoing photon is referred as *particle 1*[1].

All frames are right handed.

11.1.4   Polarized beam and material

Polarization of beam particles is well established. It can be used for simulating low-energy Compton scattering of linear polarized photons. The interpretation as Stokes vector allows now the usage in a more general framework. The polarization state of a (initial) beam particle can be fixed using standard

---

[1]Note, for an incoming particle travelling on the Z-axis (of GRF), the y-axis of the PRF of both outgoing particles is parallel to the y-axis of the *interaction frame*.

the ParticleGunMessenger class. For example, the class `G4ParticleGun` provides the method `SetParticlePolarization()`, which is usually accessable via

```
/gun/polarization <Sx> <Sy> <Sz>
```

in a macro file.

In addition for the simulation of polarized media, a possibility to assign Stokes vectors to physical volumes is provided by a new class, the so-called *G4PolarizationManager*. The procedure to assign a polarization vector to a media, is done during the *detector construction*. There the *logical volumes* with certain polarization are made known to *polarization manager*. One example `DetectorConstruction` might look like follows:

```
G4double Targetthickness = .010*mm;
G4double Targetradius    = 2.5*mm;

G4Tubs *solidTarget =
  new G4Tubs("solidTarget",
             0.0,
             Targetradius,
             Targetthickness/2,
             0.0*deg,
             360.0*deg );

G4LogicalVolume * logicalTarget =
  new G4LogicalVolume(solidTarget,
                      iron,
                      "logicalTarget",
                      0,0,0);

G4VPhysicalVolume *  physicalTarget =
  new G4PVPlacement(0,G4ThreeVector(0.*mm, 0.*mm, 0.*mm),
                    logicalTarget,
                    "physicalTarget",
                    worldLogical,
                    false,
                    0);

G4PolarizationManager * polMgr = G4PolarizationManager::GetInstance();
polMgr->SetVolumePolarization(logicalTarget,G4ThreeVector(0.,0.,0.08));
```

Once a logical volume is known to the `G4PolarizationManager`, its polarization vector can be accessed from a macro file by its name, e.g. the polarization of the logical volume called "logicalTarget" can be changed via

```
/polarization/volume/set logicalTarget 0. 0. -0.08
```

Note, the polarization of a material is stated in the world frame.

11.1.5   Status of this document

20.11.06 created by A.Schälicke

Bibliography

[1] W. H. McMaster, Rev. Mod. Phys. **33** (1961) 8; and references therein.

[2] K. Laihem, PhD thesis, Humboldt University Berlin, Germany, (2007).

[3] W. R. Nelson, H. Hirayama, D. W. O. Rogers, SLAC-R-0265.

[4] K. Flöttmann, PhD thesis, DESY Hamburg (1993); DESY-93-161.

[5] Y. Namito, S. Ban, H. Hirayama, Nucl. Instrum. Meth. A **332** (1993) 277.

[6] J. C. Liu, T. Kotseroglou, W. R. Nelson, D. C. Schultz, SLAC-PUB-8477.

[7] R. Brun, M. Caillat, M. Maire, G. N. Patrick, L. Urban, CERN-DD/85/1.

[8] G. Alexander *et al.*, SLAC-TN-04-018, SLAC-PROPOSAL-E-166.

[9] J. Hoogduin, PhD thesis, Rijksuniversiteit Groningen (1997).

[10] G. Stokes, Trans. Cambridge Phil. Soc. **9** (1852) 399.

11.2 Ionization

11.2.1 Method

The class *G4ePolarizedIonization* provides continuous and discrete energy losses of polarized electrons and positrons in a material. It evaluates polarization transfer and – if the material is polarized – asymmetries in the explicit delta rays production. The implementation baseline follows the approach derived for the class *G4eIonization* described in sections 7.1 and 8.1. For continuous energy losses the effects of a polarized beam or target are negligible provided the separation cut T_{cut} is small, and are therefore not considered separately. On the other hand, in the explicit production of delta rays by Møller or Bhabha scattering, the effects of polarization on total cross section and mean free path, on distribution of final state particles and the average polarization of final state particles are taken into account.

11.2.2 Total cross section and mean free path

Kinematics of Bhabha and Møller scattering is fixed by initial energy

$$\gamma = \frac{E_{k_1}}{mc^2} \tag{11.10}$$

and variable

$$\epsilon = \frac{E_{p_2} - mc^2}{E_{k_1} - mc^2}, \tag{11.11}$$

which is the part of kinetic energy of initial particle carried out by scatter. Lower kinematic limit for ϵ is 0, but in order to avoid divergencies in both total and differential cross sections one sets

$$\epsilon_{min} = x = \frac{T_{min}}{E_{k_1} - mc^2}, \tag{11.12}$$

where T_{min} has meaning of minimal kinetic energy of secondary electron. And, $\epsilon_{\text{max}} = 1(1/2)$ for Bhabha(Møller) scatterings.

Total Møller cross section

The total cross section of the polarized Møller scattering can be expressed as follows

$$\sigma_{pol}^M = \frac{2\pi\gamma^2 r_e^2}{(\gamma-1)^2(\gamma+1)} \left[\sigma_0^M + \zeta_3^{(1)}\zeta_3^{(2)}\sigma_L^M + \left(\zeta_1^{(1)}\zeta_1^{(2)} + \zeta_2^{(1)}\zeta_2^{(2)} \right) \sigma_T^M \right], \tag{11.13}$$

where the r_e is classical electron radius, and

$$
\begin{aligned}
\sigma_0^M &= -\frac{1}{1-x} + \frac{1}{x} - \frac{(\gamma-1)^2}{\gamma^2}\left(\frac{1}{2} - x\right) + \frac{2 - 4\gamma}{2\gamma^2}\ln\left(\frac{1-x}{x}\right) \\
\sigma_L^M &= \frac{(-3 + 2\gamma + \gamma^2)(1 - 2x)}{2\gamma^2} + \frac{2\gamma(-1 + 2\gamma)}{2\gamma^2}\ln\left(\frac{1-x}{x}\right) \\
\sigma_T^M &= \frac{2(\gamma-1)(2x-1)}{2\gamma^2} + \frac{(1 - 3\gamma)}{2\gamma^2}\ln\left(\frac{1-x}{x}\right)
\end{aligned}
\tag{11.14}
$$

Total Bhabha cross section

The total cross section of the polarized Bhabha scattering can be expressed as follows

$$
\sigma_{pol}^B = \frac{2\pi r_e^2}{\gamma - 1}\left[\sigma_0^B + \zeta_3^{(1)}\zeta_3^{(2)}\sigma_L^B + \left(\zeta_1^{(1)}\zeta_1^{(2)} + \zeta_2^{(1)}\zeta_2^{(2)}\right)\sigma_T^B\right],
\tag{11.15}
$$

where

$$
\begin{aligned}
\sigma_0^B &= \frac{1-x}{2(\gamma-1)x} + \frac{2(-1 + 3x - 6x^2 + 4x^3)}{3(1+\gamma)^3} \\
&\quad + \frac{-1 - 5x + 12x^2 - 10x^3 + 4x^4}{2(1+\gamma)x} + \frac{-3 - x + 8x^2 - 4x^3 - \ln(x)}{(1+\gamma)^2} \\
&\quad + \frac{3 + 4x - 9x^2 + 3x^3 - x^4 + 6x\ln(x)}{3x} \\
\sigma_L^B &= \frac{2(1 - 3x + 6x^2 - 4x^3)}{3(1+\gamma)^3} + \frac{-14 + 15x - 3x^2 + 2x^3 - 9\ln(x)}{3(1+\gamma)} \\
&\quad + \frac{5 + 3x - 12x^2 + 4x^3 + 3\ln(x)}{3(1+\gamma)^2} + \frac{7 - 9x + 3x^2 - x^3 + 6\ln(x)}{3} \\
\sigma_T^B &= \frac{2(-1 + 3x - 6x^2 + 4x^3)}{3(1+\gamma)^3} + \frac{-7 - 3x + 18x^2 - 8x^3 - 3\ln(x)}{3(1+\gamma)^2} \\
&\quad + \frac{5 + 3x - 12x^2 + 4x^3 + 9\ln(x)}{6(1+\gamma)}
\end{aligned}
\tag{11.16}
$$

Mean free path

With the help of the total polarized Møller cross section one can define a longitudinal asymmetry A_L^M and the transverse asymmetry A_T^M, by

$$
A_L^M = \frac{\sigma_L^M}{\sigma_0^M} \qquad \text{and} \qquad A_T^M = \frac{\sigma_T^M}{\sigma_0^M}.
$$

Similarly, using the polarized Bhabha cross section one can introduce a longitudinal asymmetry A_L^B and the transverse asymmetry A_T^B via

$$A_L^B = \frac{\sigma_L^B}{\sigma_0^B} \qquad \text{and} \qquad A_T^B = \frac{\sigma_T^B}{\sigma_0^B} .$$

These asymmetries are depicted in figures 11.2 and 11.3 respectively.

If both beam and target are polarized the mean free path as defined in section 8.1 has to be modified. In the class *G4ePolarizedIonization* the polarized mean free path λ^{pol} is derived from the unpolarized mean free path λ^{unpol} via

$$\lambda^{\mathrm{pol}} = \frac{\lambda^{\mathrm{unpol}}}{1 + \zeta_3^{(1)}\zeta_3^{(2)} A_L + \left(\zeta_1^{(1)}\zeta_1^{(2)} + \zeta_2^{(1)}\zeta_2^{(2)} \right) A_T} \tag{11.17}$$

11.2.3 Sampling the final state

Differential cross section

The polarized differential cross section is rather complicated, the full result can be found in [1, 2, 3]. In *G4PolarizedMollerCrossSection* the complete result is available taking all mass effects into account, only binding effects are neglected. Here we state only the ultra-relativistic approximation (URA), to show the general dependencies.

$$\frac{d\sigma_{URA}^M}{d\epsilon d\varphi} = \frac{r_\epsilon^2}{\gamma + 1} \times$$

$$\left[\frac{(1 - \epsilon + \epsilon^2)^2}{4\,(\epsilon - 1)^2\,\epsilon^2} + \zeta_3^{(1)}\zeta_3^{(2)} \frac{2 - \epsilon + \epsilon^2}{-4\,\epsilon(1 - \epsilon)} + \left(\zeta_2^{(1)}\zeta_2^{(2)} - \zeta_1^{(1)}\zeta_1^{(2)} \right) \frac{1}{4} \right.$$

$$\left. + \left(\xi_3^{(1)}\zeta_3^{(1)} - \xi_3^{(2)}\zeta_3^{(2)} \right) \frac{1 - \epsilon + 2\,\epsilon^2}{4\,(1 - \epsilon)\,\epsilon^2} + \left(\xi_3^{(2)}\zeta_3^{(1)} - \xi_3^{(1)}\zeta_3^{(2)} \right) \frac{2 - 3\,\epsilon + 2\,\epsilon^2}{4\,(1 - \epsilon)^2\,\epsilon} \right] \tag{11.18}$$

The corresponding cross section for Bhabha cross section is implemented in *G4PolarizedBhabhaCrossSection*. In the ultra-relativistic approximation it
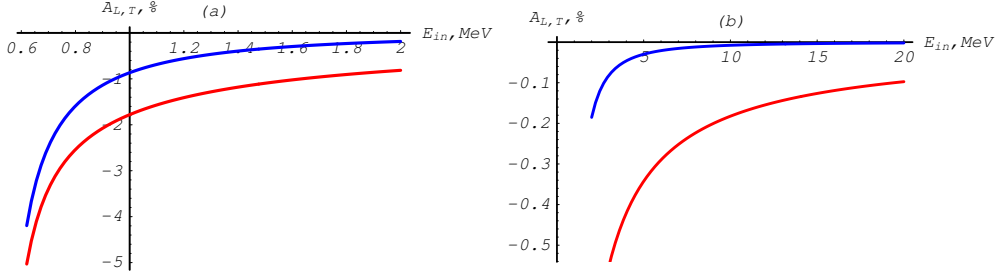
Figure 11.2: Møller total cross section asymmetries depending on the total energy of the incoming electron, with a cut-off $T_{\text{cut}} = 1\text{keV}$. Transverse asymmetry is plotted in blue, longitudinal asymmetry in red. Left part, between 0.5 MeV and 2 MeV, right part up to 10 MeV.
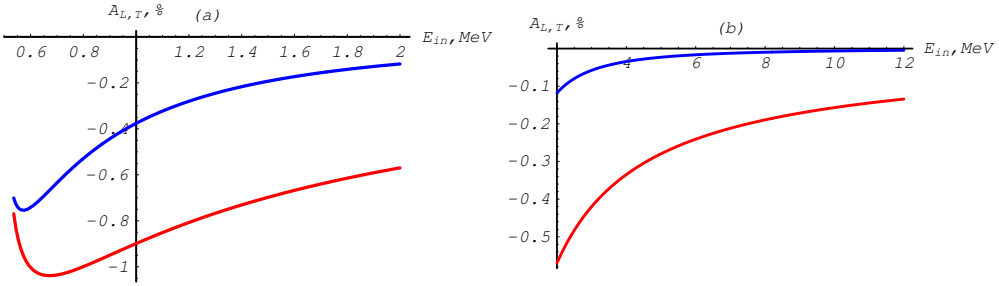
Figure 11.3: Bhabha total cross section asymmetries depending on the total energy of the incoming positron, with a cut-off $T_{\text{cut}} = 1\text{keV}$. Transverse asymmetry is plotted in blue, longitudinal asymmetry in red. Left part, between 0.5 MeV and 2 MeV, right part up to 10 MeV.

reads

$$\frac{d\sigma_{URA}^B}{d\epsilon d\varphi} = \frac{r_\epsilon{}^2}{\gamma - 1} \times$$

$$\left[\frac{(1 - \epsilon + \epsilon^2)^2}{4\,\epsilon^2} + \zeta_3^{(1)}\zeta_3^{(2)}\frac{(\epsilon - 1)\,(2 - \epsilon + \epsilon^2)}{4\,\epsilon} + \left(\zeta_2^{(1)}\zeta_2^{(2)} - \zeta_1^{(1)}\zeta_1^{(2)}\right)\frac{(1 - \epsilon)^2}{4} \right.$$

$$\left. + \left(\xi_3^{(1)}\zeta_3^{(1)} - \xi_3^{(2)}\zeta_3^{(2)}\right)\frac{1 - 2\,\epsilon + 3\,\epsilon^2 - 2\,\epsilon^3}{4\,\epsilon^2} + \left(\xi_3^{(2)}\zeta_3^{(1)} - \xi_3^{(1)}\zeta_3^{(2)}\right)\frac{2 - 3\,\epsilon + 2\,\epsilon^2}{4\epsilon} \right]$$

$$(11.19)$$

where
$$
\begin{aligned}
r_e &= \text{classical electron radius} \\
\gamma &= E_{k_1}/m_e c^2 \\
\epsilon &= (E_{p_1} - m_e c^2)/(E_{k_1} - m_e c^2) \\
E_{k_1} &= \text{energy of the incident electron/positron} \\
E_{p_1} &= \text{energy of the scattered electron/positron} \\
m_e c^2 &= \text{electron mass} \\
\boldsymbol{\zeta}^{(1)} &= \text{Stokes vector of the incoming electron/positron} \\
\boldsymbol{\zeta}^{(2)} &= \text{Stokes vector of the target electron} \\
\boldsymbol{\xi}^{(1)} &= \text{Stokes vector of the outgoing electron/positron} \\
\boldsymbol{\xi}^{(2)} &= \text{Stokes vector of the outgoing (2nd) electron .}
\end{aligned}
$$

Sampling

The delta ray is sampled according to methods discussed in Chapter 2. After exploitation of the symmetry in the Møller cross section under exchanging ϵ versus $(1 - \epsilon)$, the differential cross section can be approximated by a simple function $f^M(\epsilon)$:

$$
f^M(\epsilon) = \frac{1}{\epsilon^2} \frac{\epsilon_0}{1 - 2\epsilon_0} \tag{11.20}
$$

with the kinematic limits given by

$$
\epsilon_0 = \frac{T_{\text{cut}}}{E_{k_1} - m_e c^2} \leq \epsilon \leq \frac{1}{2} \tag{11.21}
$$

A similar function $f^B(\epsilon)$ can be found for Bhabha scattering:

$$
f^B(\epsilon) = \frac{1}{\epsilon^2} \frac{\epsilon_0}{1 - \epsilon_0} \tag{11.22}
$$

with the kinematic limits given by

$$
\epsilon_0 = \frac{T_{\text{cut}}}{E_{k_1} - m_e c^2} \leq \epsilon \leq 1 \tag{11.23}
$$

The kinematic of the delta ray production is constructed by the following steps:

1. ϵ is sampled from $f(\epsilon)$

2. calculate the differential cross section, depending on the initial polarizations $\boldsymbol{\zeta}^{(1)}$ and $\boldsymbol{\zeta}^{(2)}$.

3. ϵ is accepted with the probability defined by ratio of the differential cross section over the approximation function.

4. The φ is diced uniformly.

5. φ is determined from the differential cross section, depending on the initial polarizations $\boldsymbol{\zeta}^{(1)}$ and $\boldsymbol{\zeta}^{(2)}$

Note, for initial states without transverse polarization components, the φ distribution is always uniform. In figure 11.4 the asymmetries indicate the influence of polarization. In general the effect is largest around $\epsilon = \frac{1}{2}$.
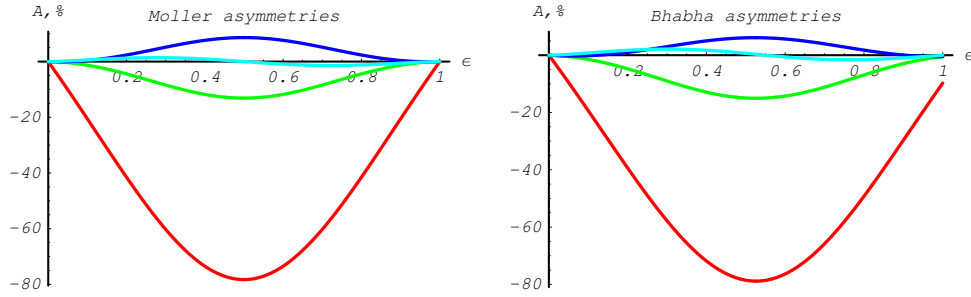
Figure 11.4: Differential cross section asymmetries in% for Møller (left) and Bhabha (right) scattering (red - $A_{ZZ}(\epsilon)$, green - $A_{XX}(\epsilon)$, blue - $A_{YY}(\epsilon)$, lightblue - $A_{ZX}(\epsilon)$)

After both ϕ and ϵ are known, the kinematic can be constructed fully. Using momentum conservation the momenta of the scattered incident particle and the ejected electron are constructed in global coordinate system.

Polarization transfer

After the kinematics is fixed the polarization properties of the outgoing particles are determined. Using the dependence of the differential cross section on the final state polarization a mean polarization is calculated according to method described in section 11.1.

The resulting polarization transfer functions $\xi_3^{(1,2)}(\epsilon)$ are depicted in figures 11.5 and 11.6.

11.2.4   Status of this document

20.11.06 created by P.Starovoitov
21.02.07 minor update by A.Schälicke
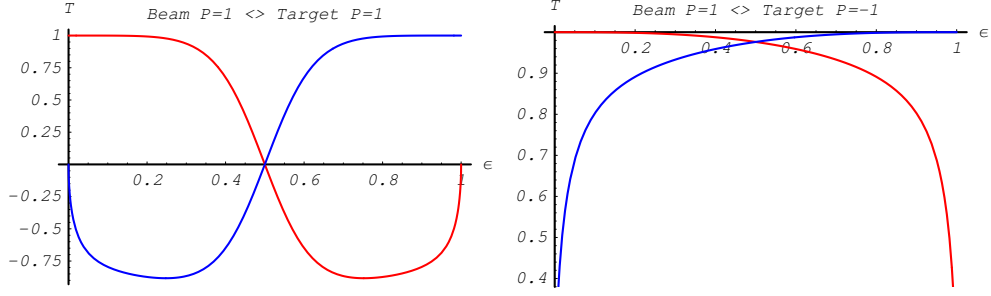
Figure 11.5: Polarization transfer functions in Møller scattering. Longitudinal polarization $\xi_3^{(2)}$ of electron with energy E_{p_2} in blue; longitudinal polarization $\xi_3^{(1)}$ of second electron in red. Kinetic energy of incoming electron $T_{k_1} = 10\text{MeV}$

.
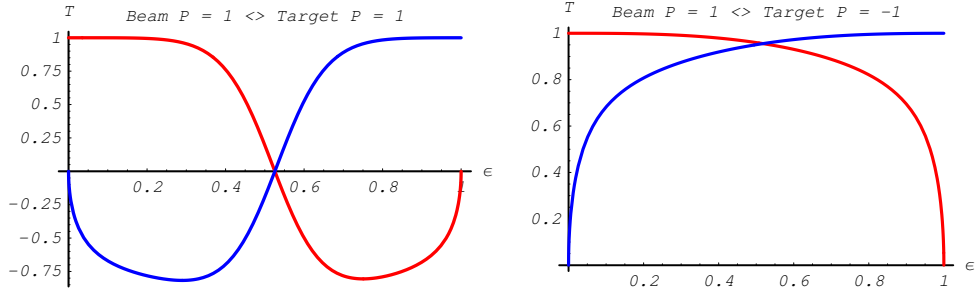
Figure 11.6: Polarization Transfer in Bhabha scattering. Longitudinal polarization $\xi_3^{(2)}$ of electron with energy E_{p_2} in blue; longitudinal polarization $\xi_3^{(1)}$ of scattered positron. Kinetic energy of incoming positron $T_{k_1} = 10\text{MeV}$

.

Bibliography

[1] P. Starovoitov *et.al.*, in preparation.

[2] G. W. Ford, C. J. Mullin, Phys. Rev. **108** (1957) 477.

[3] P. Stehle, Phys. Rev. **110** (1958) 1458.

11.3 Positron - Electron Annihilation

11.3.1 Method

The class *G4eplusPolarizedAnnihilation* simulates annihilation of polarized positrons with electrons in a material. The implementation baseline follows the approach derived for the class *G4eplusAnnihilation* described in section 8.3. It evaluates polarization transfer and – if the material is polarized – asymmetries in the produced photons. Thus, it takes the effects of polarization on total cross section and mean free path, on distribution of final state photons into account. And calculates the average polarization of these generated photons. The material electrons are assumed to be free and at rest.

11.3.2 Total cross section and mean free path

Kinematics of annihilation process is fixed by initial energy

$$\gamma = \frac{E_{k_1}}{mc^2} \qquad (11.24)$$

and variable

$$\epsilon = \frac{E_{p_1}}{E_{k_1} + mc^2}, \qquad (11.25)$$

which is the part of total energy available in initial state carried out by first photon. This variable has the following kinematical limits

$$\frac{1}{2}\left(1 - \sqrt{\frac{\gamma - 1}{\gamma + 1}}\right) < \epsilon < \frac{1}{2}\left(1 + \sqrt{\frac{\gamma - 1}{\gamma + 1}}\right). \qquad (11.26)$$

Total Cross Section

The total cross section of the annihilation of a polarized e^+e^- pair into two photons could be expressed as follows

$$\sigma_{pol}^A = \frac{\pi r_e^2}{\gamma + 1}\left[\sigma_0^A + \zeta_3^{(1)}\zeta_3^{(2)}\sigma_L^A + \left(\zeta_1^{(1)}\zeta_1^{(2)} + \zeta_2^{(1)}\zeta_2^{(2)}\right)\sigma_T^A\right], \qquad (11.27)$$

where

$$\sigma_0^A = \frac{-\left(3 + \gamma\right)\sqrt{-1 + \gamma^2} + \left(1 + \gamma\left(4 + \gamma\right)\right)\ln(\gamma + \sqrt{-1 + \gamma^2})}{4\left(\gamma^2 - 1\right)} \qquad (11.28)$$

$$\sigma_L^A = \frac{-\sqrt{-1+\gamma^2}\,(5+\gamma\,(4+3\,\gamma)) + (3+\gamma\,(7+\gamma+\gamma^2))\,\ln(\gamma+\sqrt{\gamma^2-1})}{4\,(\gamma-1)^2\,(1+\gamma)}$$

(11.29)

$$\sigma_T^A = \frac{(5+\gamma)\,\sqrt{-1+\gamma^2} - (1+5\,\gamma)\,\ln(\gamma+\sqrt{-1+\gamma^2})}{4\,(-1+\gamma)^2\,(1+\gamma)}$$

(11.30)

Mean free path

With the help of the total polarized annihilation cross section one can define a longitudinal asymmetry A_L^A and the transverse asymmetry A_T^A, by

$$A_L^A = \frac{\sigma_L^A}{\sigma_0^A} \qquad \text{and} \qquad A_T^A = \frac{\sigma_T^A}{\sigma_0^A}\,.$$

These asymmetries are depicted in figure 11.7.

If both incident positron and target electron are polarized the mean free path as defined in section 8.3 has to be modified. The polarized mean free path λ^{pol} is derived from the unpolarized mean free path λ^{unpol} via

$$\lambda^{\text{pol}} = \frac{\lambda^{\text{unpol}}}{1 + \zeta_3^{(1)}\zeta_3^{(2)}\,A_L + \left(\zeta_1^{(1)}\zeta_1^{(2)} + \zeta_2^{(1)}\zeta_2^{(2)}\right)\,A_T}$$

(11.31)
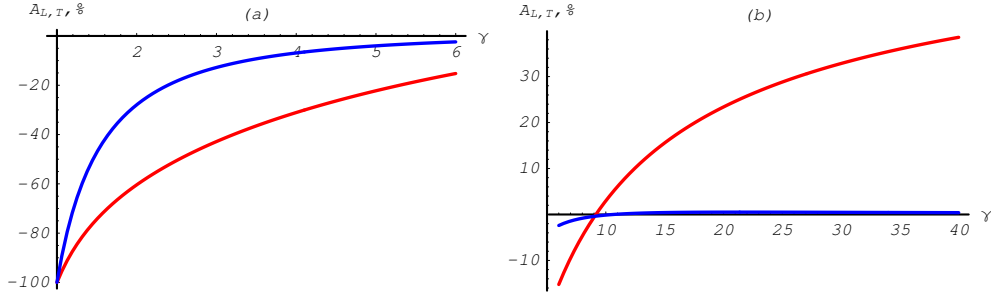
Figure 11.7: Annihilation total cross section asymmetries depending on the total energy of the incoming positron E_{k_1}. The transverse asymmetry is shown in blue, the longitudinal asymmetry in red.

11.3.3 Sampling the final state

Differential Cross Section

The fully polarized differential cross section is implemented in the class *G4PolarizedAnnihilationCrossSection*, which takes all mass effects into account, but binding effects are neglected [1, 2]. In the ultra-relativistic approximation (URA) and concentrating on longitudinal polarization states only the cross section is rather simple:

$$
\frac{d\sigma_{URA}^A}{d\epsilon d\varphi} = \frac{r_e^2}{\gamma - 1} \times \left(\frac{1 - 2\,\epsilon + 2\,\epsilon^2}{8\,\epsilon - 8\,\epsilon^2} \left(1 + \zeta_3^{(1)}\zeta_3^{(2)} \right) \right.
$$
$$
\left. + \frac{(1 - 2\,\epsilon)\left(\zeta_3^{(1)} + \zeta_3^{(2)}\right)\left(\xi_3^{(1)} - \xi_3^{(2)}\right)}{8\,(\epsilon - 1)\,\epsilon} \right) \quad (11.32)
$$

where r_e = classical electron radius
γ = $E_{k_1}/m_e c^2$
E_{k_1} = energy of the incident positron
$m_e c^2$ = electron mass
$\boldsymbol{\zeta}^{(1)}$ = Stokes vector of the incoming positron
$\boldsymbol{\zeta}^{(2)}$ = Stokes vector of the target electron
$\boldsymbol{\xi}^{(1)}$ = Stokes vector of the 1st photon
$\boldsymbol{\xi}^{(2)}$ = Stokes vector of the 2nd photon .

Sampling

The photon energy is sampled according to methods discussed in Chapter 2. After exploitation of the symmetry in the Annihilation cross section under exchanging ϵ versus $(1-\epsilon)$, the differential cross section can be approximated by a simple function $f(\epsilon)$:

$$
f(\epsilon) = \frac{1}{\epsilon} \ln^{-1}\left(\frac{\epsilon_{\max}}{\epsilon_{\min}} \right) \quad (11.33)
$$

with the kinematic limits given by

$$
\epsilon_{\min} = \frac{1}{2}\left(1 - \sqrt{\frac{\gamma - 1}{\gamma + 1}} \right) ,
$$
$$
\epsilon_{\max} = \frac{1}{2}\left(1 + \sqrt{\frac{\gamma - 1}{\gamma + 1}} \right) . \quad (11.34)
$$

The kinematic of the two photon final state is constructed by the following steps:

Figure 11.8: Annihilation differential cross section in arbitrary units. Black line corresponds to unpolarized cross section; red line – to the antiparallel spins of initial particles, and blue line – to the parallel spins. Kinetic energy of the incoming positron $T_{k_1} = 10\text{MeV}$.

1. ϵ is sampled from $f(\epsilon)$

2. calculate the differential cross section, depending on the initial polarizations $\boldsymbol{\zeta}^{(1)}$ and $\boldsymbol{\zeta}^{(2)}$.

3. ϵ is accepted with the probability defined by the ratio of the differential cross section over the approximation function $f(\epsilon)$.

4. The φ is diced uniformly.

5. φ is determined from the differential cross section, depending on the initial polarizations $\boldsymbol{\zeta}^{(1)}$ and $\boldsymbol{\zeta}^{(2)}$.

A short overview over the sampling method is given in Chapter 2. In figure 11.9 the asymmetries indicate the influence of polarization for an 10MeV incoming positron. The actual behavior is very sensitive to the energy of the incoming positron.

Polarization transfer

After the kinematics is fixed the polarization of the outgoing photon is determined. Using the dependence of the differential cross section on the final state polarizations a mean polarization is calculated for each photon according to method described in section 11.1.

Figure 11.9: Annihilation differential cross section asymmetries in%. Red line corrsponds to $A_{ZZ}(\epsilon)$, green line – $A_{XX}(\epsilon)$, blue line – $A_{YY}(\epsilon)$, lightblue line – $A_{ZX}(\epsilon)$). Kinetic energy of the incoming positron $T_{k_1} = 10$MeV.

The resulting polarization transfer functions $\xi^{(1,2)}(\epsilon)$ are depicted in figure 11.10.
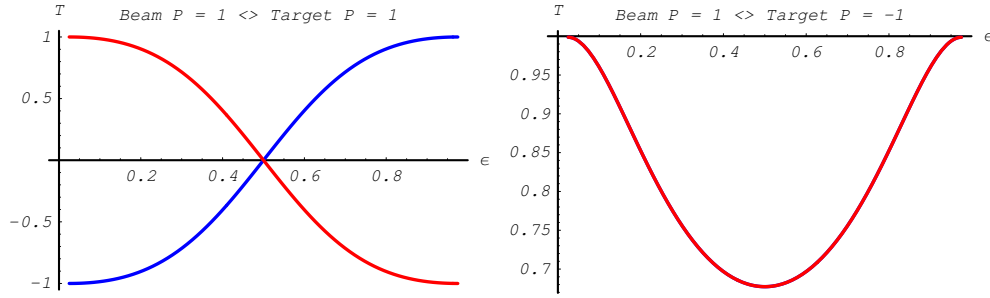
Figure 11.10: Polarization Transfer in annihilation process. Blue line corresponds to the circular polarization $\xi_3^{(1)}$ of the photon with energy $m(\gamma + 1)\epsilon$; red line – circular polarization $\xi_3^{(2)}$ of the photon photon with energy $m(\gamma + 1)(1 - \epsilon)$.

11.3.4 Annihilation at Rest

The method `AtRestDoIt` treats the special case where a positron comes to rest before annihilating. It generates two photons, each with energy $E_{p_{1/2}} = mc^2$ and an isotropic angular distribution. Starting with the differential cross section for annihilation with positron and electron spins opposed and parallel,

199

respectively,[2]

$$d\sigma_1 = \sim \frac{(1-\beta^2) + \beta^2(1-\beta^2)(1-\cos^2\theta)^2}{(1-\beta^2\cos^2\theta)^2} d\cos\theta \qquad (11.35)$$

$$d\sigma_2 = \sim \frac{\beta^2(1-\cos^4\theta)}{(1-\beta^2\cos^2\theta)^2} d\cos\theta \qquad (11.36)$$

In the limit $\beta \to 0$ the cross section $d\sigma_1$ becomes one, and the cross section $d\sigma_2$ vanishes. For the opposed spin state, the total angular momentum is zero and we have a uniform photon distribution. For the parallel case the total angular momentum is 1. Here the two photon final state is forbidden by angular momentum conservation, and it can be assumed that higher order processes (e.g. three photon final state) play a dominant role. However, in reality 100% polarized electron targets do not exist, consequently there are always electrons with opposite spin, where the positron can annihilate with. Final state polarization does not play a role for the decay products of a spin zero state, and can be safely neglected. (Is set to zero)

11.3.5   Status of this document

20.11.06 created by P.Starovoitov
21.02.07 minor update by A.Schälicke

Bibliography

[1] P. Starovoitov *et.al.*, in preparation.

[2] L. A. Page, Phys. Rev. **106** (1957) 394-398.

11.4 Polarized Compton scattering

11.4.1 Method

The class *G4PolarizedCompton* simulates Compton scattering of polarized photons with (possibly polarized) electrons in a material. The implementation follows the approach described for the class *G4ComptonScattering* introduced in section 6.3. Here the explicit production of a Compton scattered photon and the ejected electron is considered taking the effects of polarization on total cross section and mean free path as well as on the distribution of final state particles into account. Further the average polarizations of the scattered photon and electron are calculated. The material electrons are assumed to be free and at rest.

11.4.2 Total cross section and mean free path

Kinematics of the Compton process is fixed by the initial energy

$$X = \frac{E_{k_1}}{mc^2} \tag{11.37}$$

and the variable

$$\epsilon = \frac{E_{p_1}}{E_{k_1}}, \tag{11.38}$$

which is the part of total energy avaible in initial state carried out by scattered photon, and the scattering angle

$$\cos\theta = 1 - \frac{1}{X}\left(\frac{1}{\epsilon} - 1\right) \tag{11.39}$$

The variable ϵ has the following limits:

$$\frac{1}{1 + 2X} < \epsilon < 1 \tag{11.40}$$

Total Cross Section

The total cross section of Compton scattering reads

$$\sigma_{pol}^C = \frac{\pi\, r_e{}^2}{X^2\,(1 + 2\,X)^2}\left[\sigma_0^C + \zeta_3^{(1)}\zeta_3^{(2)}\sigma_L^C\right] \tag{11.41}$$

where

$$\sigma_0^C = \frac{2\,X\,(2 + X\,(1 + X)\,(8 + X)) - (1 + 2\,X)^2\,(2 + (2 - X)\,X)\,\ln(1 + 2\,X)}{X} \tag{11.42}$$

and

$$\sigma_L^C = 2\,X\,(1 + X\,(4 + 5\,X)) - (1 + X)\,(1 + 2\,X)^2\,\ln(1 + 2\,X) \qquad (11.43)$$
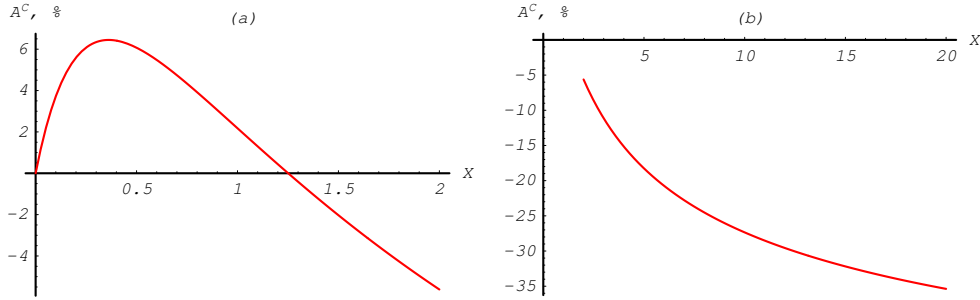
Figure 11.11: Compton total cross section asymmetry depending on the energy of incoming photon. Left part, between 0 and ~ 1 MeV, right part – up to 10MeV.

Mean free path

When simulating the Compton scattering of a photon with an atomic electron, an empirical cross section formula is used, which reproduces the cross section data down to 10 keV (see section 6.3). If both, beam and target, are polarized this mean free path has to be corrected.

In the class *G4ComptonScattering* the polarized mean free path λ^{pol} is defined on the basis of the the unpolarized mean free path λ^{unpol} via

$$\lambda^{\mathrm{pol}} = \frac{\lambda^{\mathrm{unpol}}}{1 + \zeta_3^{(1)}\zeta_3^{(2)}\,A_L^C} \qquad (11.44)$$

where

$$A_L^C = \frac{\sigma_L^A}{\sigma_0^A} \qquad (11.45)$$

is the expected asymmetry from the the total polarized Compton cross section given above. This asymmetry is depicted in figure 11.11.

11.4.3 Sampling the final state

Differential Compton Cross Section

In the ultra-relativistic approximation the dependence of the differential cross section on the longitudinal/circular degree of polarization is very simple. It

202
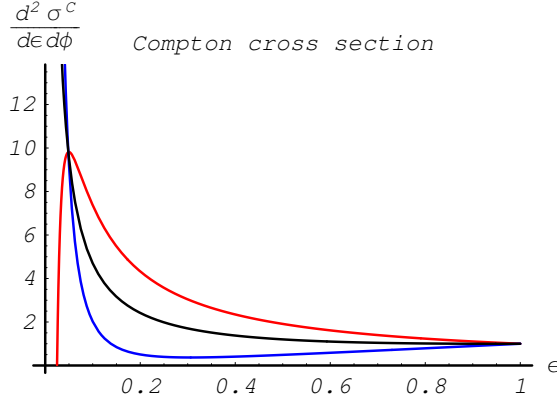
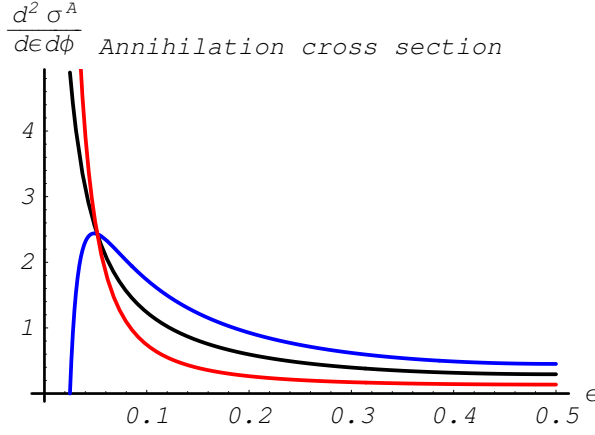Figure 11.12: Compton scattering differential cross section in arbitrary units. Black line corresponds to the unpolarized cross section; red line – to the antiparallel spins of initial particles, and blue line – to the parallel spins. Energy of the incoming photon $E_{k_1} = 10\text{MeV}$.

reads

$$\frac{d\sigma^C_{URA}}{ded\varphi} = \frac{r_e^2}{X} \left(\frac{\epsilon^2 + 1}{2\,\epsilon} + \frac{\epsilon^2 - 1}{2\,\epsilon} \left(\zeta_3^{(1)} \zeta_3^{(2)} + \zeta_3^{(2)} \xi_3^{(1)} - \zeta_3^{(1)} \xi_3^{(2)} \right) \right.$$

$$\left. + \frac{\epsilon^2 + 1}{2\,\epsilon} \left(\zeta_3^{(1)} \xi_3^{(1)} - \zeta_3^{(2)} \xi_3^{(2)} \right) \right) \qquad (11.46)$$

where r_e =   classical electron radius
$\quad\quad\;\; X$ = $E_{k_1}/m_e c^2$
$\quad\quad\;\; E_{k_1}$ =   energy of the incident photon
$\quad\quad\;\; m_e c^2$ =   electron mass

The fully polarized differential cross section is available in the class *G4PolarizedComptonCrossS...* It takes all mass effects into account, but binding effects are neglected [1, 2]. The cross section dependence on ϵ for right handed circularly polarized photons and longitudinally polarized electrons is plotted in figure 11.12

Sampling

The photon energy is sampled according to methods discussed in Chapter 2. The differential cross section can be approximated by a simple function $\Phi(\epsilon)$:

$$\Phi(\epsilon) = \frac{1}{\epsilon} + \epsilon \qquad (11.47)$$

203
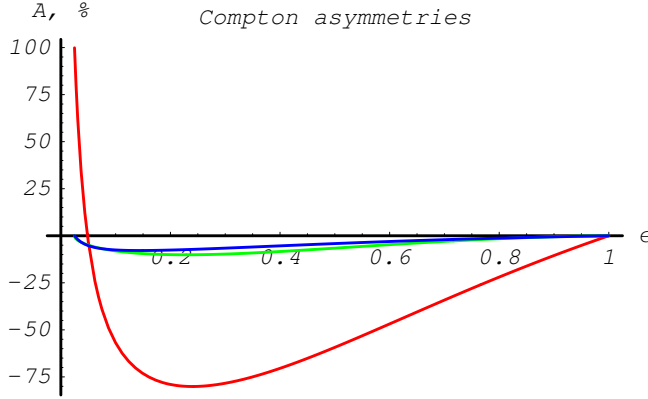
Figure 11.13: Compton scattering differential cross section asymmetries in%. Red line corresponds to the asymmetry due to circular photon and longitudinal electron initial state polarization, green line – due to circular photon and transverse electron initial state polarization, blue line – due to linear photon and transverse electron initial state polarization.

with the kinematic limits given by

$$\epsilon_{\min} = \frac{1}{1 + 2X} \tag{11.48}$$

$$\epsilon_{\max} = 1 \tag{11.49}$$

The kinematic of the scattered photon is constructed by the following steps:

1. ϵ is sampled from $\Phi(\epsilon)$

2. calculate the differential cross section, depending on the initial polarizations $\boldsymbol{\zeta}^{(1)}$ and $\boldsymbol{\zeta}^{(2)}$, which the correct normalization.

3. ϵ is accepted with the probability defined by ratio of the differential cross section over the approximation function.

4. The φ is diced uniformly.

5. φ is determined from the differential cross section, depending on the initial polarizations $\boldsymbol{\zeta}^{(1)}$ and $\boldsymbol{\zeta}^{(2)}$.

In figure 11.13 the asymmetries indicate the influence of polarization for an 10MeV incoming positron. The actual behavior is very sensitive to energy of the incoming positron.

Polarization transfer

After the kinematics is fixed the polarization of the outgoing photon is determined. Using the dependence of the differential cross section on the final state polarizations a mean polarization is calculated for each photon according to the method described in section 11.1.
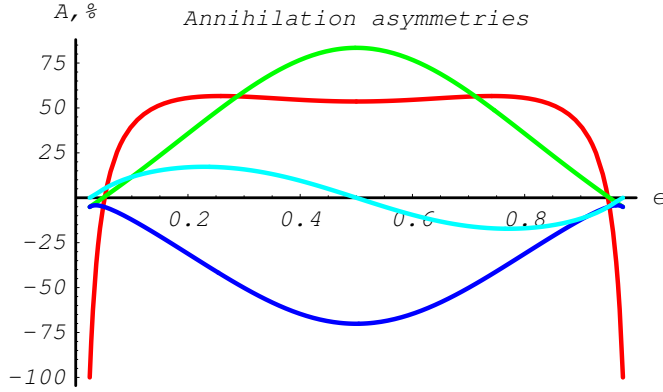
The resulting polarization transfer functions $\xi^{(1,2)}(\epsilon)$ are depicted in figure 11.14.
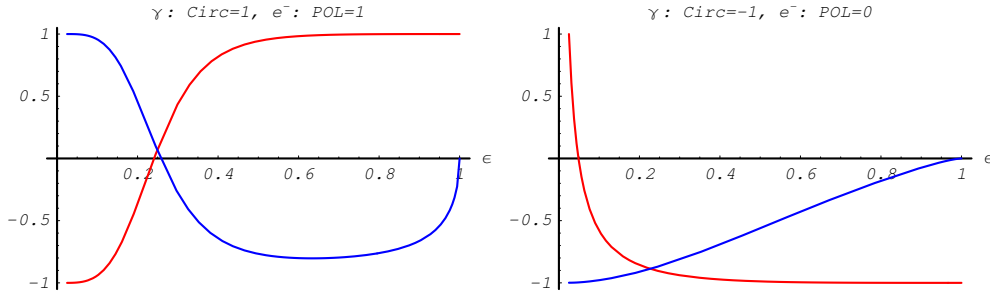
Figure 11.14: Polarization Transfer in Compton scattering. Blue line corresponds to the longitudinal polarization $\xi_3^{(2)}$ of the electron, red line – circular polarization $\xi_3^{(1)}$ of the photon.

11.4.4   Status of this document

20.11.06 created by P.Starovoitov
21.02.07 corrected cross section and some minor update by A.Schälicke

Bibliography

[1] P. Starovoitov *et.al.*, in preparation.

[2] F.W. Lipps, H.A. Tolhoek, Physica **20** (1954) 85; F.W. Lipps, H.A. Tolhoek, Physica **20** (1954) 395.

11.5 Polarized Bremsstrahlung for electron and positron

11.5.1 Method

The polarized version of Bremsstrahlung is based on the unpolarized cross section. Energy loss, mean free path, and distribution of explicitly generated final state particles are treated by the unpolarized version *G4eBremsstrahlung*. For details consult section 8.2.

The remaining task is to attribute polarization vectors to the generated final state particles, which is discussed in the following.

11.5.2 Polarization in gamma conversion and bremsstrahlung

Gamma conversion and bremsstrahlung are cross-symmetric processes (i.e. the Feynman diagram for electron bremsstrahlung can be obtained from the gamma conversion diagram by flipping the incoming photon and outgoing positron lines) and their cross sections closely related. For both processes, the interaction occurs in the field of the nucleus and the total and differential cross section are polarization independent. Therefore, only the polarization transfer from the polarized incoming particle to the outgoing particles is taken into account.
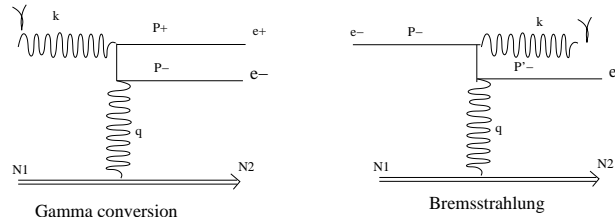
Figure 11.15: Feynman diagrams of Gamma conversion and bremsstrahlung processes.

For both processes, the scattering can be formulated by:

$$\mathcal{K}_1(k_1, \boldsymbol{\zeta}^{(1)}) + \mathcal{N}_1(k_{\mathcal{N}_1}, \boldsymbol{\zeta}^{(\mathcal{N}_1)}) \longrightarrow \mathcal{P}_1(p_1, \boldsymbol{\xi}^{(1)}) + \mathcal{P}_2(p_2, \boldsymbol{\xi}^{(2)}) + \mathcal{N}_2(p_{\mathcal{N}_2}, \boldsymbol{\xi}^{(\mathcal{N}_2)})$$
$$(11.50)$$

Where $\mathcal{N}_1(k_{\mathcal{N}_1}, \boldsymbol{\zeta}^{(\mathcal{N}_1)})$ and $\mathcal{N}_2(p_{\mathcal{N}_2}, \boldsymbol{\xi}^{(\mathcal{N}_2)})$ are the initial and final state of the field of the nucleus respectively assumed to be unchanged, at rest and unpolarized. This leads to $k_{\mathcal{N}_1} = k_{\mathcal{N}_2} = 0$ and $\boldsymbol{\zeta}^{(\mathcal{N}_1)} = \boldsymbol{\xi}^{(\mathcal{N}_2)} = 0$

In the case of gamma conversion process:
$\mathcal{K}_1(k_1, \boldsymbol{\zeta}^{(1)})$ is the incoming photon initial state with momentum k_1 and polarization state $\boldsymbol{\zeta}^{(1)}$.
$\mathcal{P}_1(p_1, \boldsymbol{\xi}^{(1)})$ and $\mathcal{P}_2(p_2, \boldsymbol{\xi}^{(2)})$ are the two photons final states with momenta p_1 and p_2 and polarization states $\boldsymbol{\xi}^{(1)}$ and $\boldsymbol{\xi}^{(2)}$.
In the case of bremsstrahlung process:
$\mathcal{K}_1(k_1, \boldsymbol{\zeta}^{(1)})$ is the incoming lepton $e^-(e^+)$ initial state with momentum k_1 and polarization state $\boldsymbol{\zeta}^{(1)}$.
$\mathcal{P}_1(p_1, \boldsymbol{\xi}^{(1)})$ is the lepton $e^-(e^+)$ final state with momentum p_1 and polarization state $\boldsymbol{\xi}^{(1)}$.
$\mathcal{P}_2(p_2, \boldsymbol{\xi}^{(2)})$ is the bremsstrahlung photon in final state with momentum p_2 and polarization state $\boldsymbol{\xi}^{(2)}$.

11.5.3 Polarization transfer from the lepton $e^-(e^+)$ to a photon

The polarization transfer from an electron (positron) to a photon in a bremsstrahlung process was first calculated by Olsen and Maximon [1] taking into account both Coulomb and screening effects. In the Stokes vector formalism, the $e^-(e^+)$ polarization state can be transformed to a photon polarization finale state by means of interaction matrix T_γ^b. It defined via

$$\begin{pmatrix} O \\ \boldsymbol{\xi}^{(2)} \end{pmatrix} = T_\gamma^b \begin{pmatrix} 1 \\ \boldsymbol{\zeta}^{(1)} \end{pmatrix}, \qquad (11.51)$$

and

$$T_\gamma^b \approx \begin{pmatrix} 1 & 0 & 0 & 0 \\ D & 0 & 0 & 0 \\ 0 & 0 & 0 & 0 \\ 0 & T & 0 & L \end{pmatrix}, \qquad (11.52)$$

where

$$I = (\epsilon_1^2 + \epsilon_2^2)(3 + 2\Gamma) - 2\epsilon_1\epsilon_2(1 + 4u^2\hat{\xi}^2\Gamma) \qquad (11.53)$$

$$D = \left\{ 8\epsilon_1\epsilon_2 u^2\hat{\xi}^2\Gamma \right\}/I \qquad (11.54)$$

$$T = \left\{ -4k\epsilon_2\hat{\xi}(1 - 2\hat{\xi})u\Gamma \right\}/I \qquad (11.55)$$

$$L = k\{(\epsilon_1^2 + \epsilon_2^2)(3 + 2\Gamma) - 2\epsilon_2(1 + 4u^2\hat{\xi}^2\Gamma)\}/I \qquad (11.56)$$

and

ϵ_1 Total energy of the incoming lepton $e^+(e^-)$ in units mc^2

ϵ_2 Total energy of the outgoing lepton $e^+(e^-)$ in units mc^2

k $= (\epsilon_1 - \epsilon_2)$, the energy of the bremsstrahlung photon in units of mc^2

$\boldsymbol{p}$ Electron (positron) initial momentum in units mc

$\boldsymbol{k}$ Bremsstrahlung photon momentum in units mc

$\boldsymbol{u}$ Component of $\boldsymbol{p}$ perpendicular to $\boldsymbol{k}$ in units mc and $u = |\boldsymbol{u}|$

$\hat{\xi}$ $= 1/(1 + u^2)$

Coulomb and screening effects are contained in Γ, defined as follows

$$\Gamma = \ln\left(\frac{1}{\delta}\right) - 2 - f(Z) + \mathcal{F}\left(\frac{\hat{\xi}}{\delta}\right) \quad \text{for } \Delta \le 120 \qquad (11.57)$$

$$\Gamma = \ln\left(\frac{111}{\hat{\xi}Z^{\frac{1}{3}}}\right) - 2 - f(z) \quad \text{for } \Delta \ge 120 \qquad (11.58)$$

with

$$\Delta = \frac{12Z^{\frac{1}{3}}\epsilon_1\epsilon_2\hat{\xi}}{121k} \quad \text{with } Z \text{ the atomic number and } \delta = \frac{k}{2\epsilon_1\epsilon 2}(11.59)$$

$f(Z)$ is the coulomb correction term derived by Davies, Bethe and Maximon [6]. $\mathcal{F}(\hat{\xi}/\delta)$ contains the screening effects and is zero for $\Delta \le 0.5$ (No screening effects). For $0.5 \le \Delta \le 120$ (intermediate screening) it is a slowly decreasing function. The $\mathcal{F}(\hat{\xi}/\delta)$ values versus Δ are given in table 11.1 and used with a linear interpolation in between.

The polarization vector of the incoming $e^-(e^+)$ must be rotated into the frame defined by the scattering plane (x-z-plane) and the direction of the outgoing photon (z-axis). The resulting polarization vector of the bremsstrahlung photon is also given in this frame. Using Eq. (11.51) and the transfer matrix given by Eq. (11.52) the bremsstrahlung photon polarization state in the Stokes formalism [2, 3] is given by

$$\xi^{(2)} = \begin{pmatrix} \xi_1^{(2)} \\ \xi_2^{(2)} \\ \xi_3^{(2)} \end{pmatrix} \approx \begin{pmatrix} D \\ 0 \\ \zeta_1^{(1)}L + \zeta_2^{(1)}T \end{pmatrix} \qquad (11.60)$$

11.5.4   Remaining polarization of the lepton after emitting a bremsstrahlung photon

The $e^-(e^+)$ polarization final state after emitting a bremsstrahlung photon can be calculated using the interaction matrix T_l^b which describes the lepton

Table 11.1: $\mathcal{F}(\hat{\xi}/\delta)$ for intermediate values of the screening factor [7].

Δ	$-\mathcal{F}\left(\hat{\xi}/\delta\right)$	Δ	$-\mathcal{F}\left(\hat{\xi}/\delta\right)$
0.5	0.0145	40.0	2.00
1.0	0.0490	45.0	2.114
2.0	0.1400	50.0	2.216
4.0	0.3312	60.0	2.393
8.0	0.6758	70.0	2.545
15.0	1.126	80.0	2.676
20.0	1.367	90.0	2.793
25.0	1.564	100.0	2.897
30.0	1.731	120.0	3.078
35.0	1.875		

depolarization. The polarization vector for the outgoing $e^-(e^+)$ is not given by Olsen and Maximon. However, their results can be used to calculate the following transfer matrix [4, 5].

$$\begin{pmatrix} O \\ \boldsymbol{\xi}^{(1)} \end{pmatrix} = T_l^b \begin{pmatrix} 1 \\ \boldsymbol{\zeta}^{(1)} \end{pmatrix} \tag{11.61}$$

$$T_l^b \approx \begin{pmatrix} 1 & 0 & 0 & 0 \\ D & M & 0 & E \\ 0 & 0 & M & 0 \\ 0 & F & 0 & M+P \end{pmatrix} \tag{11.62}$$

where

$$I = (\epsilon_1^2 + \epsilon_2^2)(3 + 2\Gamma) - 2\epsilon_1\epsilon_2(1 + 4u^2\hat{\xi}^2\Gamma) \tag{11.63}$$

$$F = \epsilon_2 \left\{ 4k\hat{\xi}u(1 - 2\hat{\xi})\Gamma \right\}/I \tag{11.64}$$

$$E = \epsilon_1 \left\{ 4k\hat{\xi}u(2\hat{\xi} - 1)\Gamma \right\}/I \tag{11.65}$$

$$M = \left\{ 4k\epsilon_1\epsilon_2(1 + \Gamma - 2u^2\hat{\xi}^2\Gamma) \right\}/I \tag{11.66}$$

$$P = \left\{ k^2(1 + 8\Gamma(\hat{\xi} - 0.5)^2 \right\}/I \tag{11.67}$$

and

209

ϵ_1 Total energy of the incoming e^+/e^- in units mc^2
ϵ_2 Total energy of the outgoing e^+/e^- in units mc^2
k $= (\epsilon_1 - \epsilon_2)$, energy of the photon in units of mc^2
$\boldsymbol{p}$ Electron (positron) initial momentum in units mc
$\boldsymbol{k}$ Photon momentum in units mc
$\boldsymbol{u}$ Component of $\boldsymbol{p}$ perpendicular to $\boldsymbol{k}$ in units mc and $u = |\boldsymbol{u}|$

Using Eq. (11.61) and the transfer matrix given by Eq. (11.62) the $e^-(e^+)$ polarization state after emitting a bremsstrahlung photon is given in the Stokes formalism by

$$\xi^{(1)} = \begin{pmatrix} \xi_1^{(1)} \\ \xi_2^{(1)} \\ \xi_3^{(1)} \end{pmatrix} \approx \begin{pmatrix} \zeta_1^{(1)} M + \zeta_3^{(1)} E \\ \zeta_2^{(1)} M \\ \zeta_3^{(1)}(M + P) + \zeta_1^{(1)} F \end{pmatrix} . \qquad (11.68)$$

11.5.5   Status of this document

20.11.06 created by K.Laihem
21.02.07 minor update by A.Schälicke

Bibliography

[1] H. Olsen and L.C. Maximon. Photon and electron polarization in high-energy bremsstrahlung and pair production with screening. Physical Review, 114:887-904, 1959.

[2] W.H. McMaster. Polarization and the Stokes parameters. American Journal of Physics, 22(6):351-362, 1954.

[3] W.H. McMaster. Matrix representation of polarization. Reviews of Modern Physics, 33(1):8-29, 1961.

[4] K. Flöttmann. Investigations toward the development of polarized and unpolarized high intensity positron sources for linear colliders. PhD thesis, Universitat Hamburg, 1993.

[5] Hoogduin, Johannes Marinus. Electron, positron and photon polarimetry. PhD thesis, Rijksuniversiteit Groningen 1997.

[6] H. Davies, H.A. Bethe and L.C. Maximon. Theory of Bremsstrahlung and Pair Production. II. Integral Cross Section for Pair Production. Physical Review, 93(4):788-795, 1954.

[7] H.W. Koch and J.W. Motz. Bremsstrahlung cross-section formulas and related data. Review Mod. Phys., 31(4):920-955, 1959.

[8] K. Laihem, PhD thesis, Humboldt University Berlin, Germany, (2007).

11.6 Polarized Gamma conversion into an electron–positron pair

11.6.1 Method

The polarized version of gamma conversion is based on the EM standard process *G4GammaConversion*. Mean free path and the distribution of explicitly generated final state particles are treated by this version. For details consult section 6.4.

The remaining task is to attribute polarization vectors to the generated final state leptons, which is discussed in the following.

11.6.2 Polarization transfer from the photon to the two leptons

Gamma conversion process is essentially the inverse process of Bremsstrahlung and the interaction matrix is obtained by inverting the rows and columns of the bremsstrahlung matrix and changing the sign of ϵ_2, cf. section 11.5. It follows from the work by Olsen and Maximon [1] that the polarization state $\xi^{(1)}$ of an electron or positron after pair production is obtained by

$$\begin{pmatrix} O \\ \boldsymbol{\xi}^{(1)} \end{pmatrix} = T_l^p \begin{pmatrix} 1 \\ \boldsymbol{\zeta}^{(1)} \end{pmatrix} \tag{11.69}$$

and

$$T_l^p \approx \begin{pmatrix} 1 & D & 0 & 0 \\ 0 & 0 & 0 & T \\ 0 & 0 & 0 & 0 \\ 0 & 0 & 0 & L \end{pmatrix}, \tag{11.70}$$

where

$$I = (\epsilon_1^2 + \epsilon_2^2)(3 + 2\Gamma) + 2\epsilon_1\epsilon_2(1 + 4u^2\hat{\xi}^2\Gamma) \tag{11.71}$$

$$D = \left\{ -8\epsilon_1\epsilon_2 u^2 \hat{\xi}^2 \Gamma \right\} / I \tag{11.72}$$

$$T = \left\{ -4k\epsilon_2\hat{\xi}(1 - 2\hat{\xi})u\Gamma \right\} / I \tag{11.73}$$

$$L = k\{(\epsilon_1^2 + \epsilon_2^2)(3 + 2\Gamma) - 2\epsilon_2(1 + 4u^2\hat{\xi}^2\Gamma)\}/I \tag{11.74}$$

and

ϵ_1	total energy of the first lepton $e^+(e^-)$ in units mc^2
ϵ_2	total energy of the second lepton $e^-(e^+)$ in units mc^2
$k = (\epsilon_1 + \epsilon_2)$	energy of the incoming photon in units of mc^2
$\boldsymbol{p}$	electron=positron initial momentum in units mc
$\boldsymbol{k}$	photon momentum in units mc
$\boldsymbol{u}$	electron/positron initial momentum in units mc
u	$= |\boldsymbol{u}|$

Coulomb and screening effects are contained in Γ, defined in section 11.5.

Using Eq. (11.69) and the transfer matrix given by Eq. (11.70) the polarization state of the produced $e^-(e^+)$ is given in the Stokes formalism by:

$$\xi^{(1)} = \begin{pmatrix} \xi_1^{(1)} \\ \xi_2^{(1)} \\ \xi_3^{(1)} \end{pmatrix} \approx \begin{pmatrix} \zeta_3^{(1)}T \\ 0 \\ \zeta_3^{(1)}L \end{pmatrix} \qquad (11.75)$$

11.6.3 Status of this document

20.11.06 created by K.Laihem
21.02.07 minor update by A.Schälicke

Bibliography

[1] H. Olsen and L.C. Maximon. Photon and electron polarization in high-energy bremsstrahlung and pair production with screening. Physical Review, 114:887-904, 1959.

[2] K. Laihem, PhD thesis, Humboldt University Berlin, Germany, (2007).

11.7 Polarized Photoelectric Effect

11.7.1 Method

This section describes the basic formulas of polarization transfer in the photoelectric effect class (*G4PolarizedPhotoElectricEffect*). The photoelectric effect is the emission of electrons from matter upon the absorption of electromagnetic radiation, such as ultraviolet radiation or x-rays. The energy of the photon is completely absorbed by the electron and, if sufficient, the electron can escape from the material with a finite kinetic energy. A single photon can only eject a single electron, as the energy of one photon is only absorbed by one electron. The electrons that are emitted are often called photoelectrons. If the photon energy is higher than the binding energy the remaining energy is transferred to the electron as a kinetic energy

$$E_{kin}^{e^-} = k - B_{shell} \tag{11.76}$$

In Geant4 the photoelectric effect process is taken into account if:

$$k > B_{shell} \tag{11.77}$$

Where k is the incoming photon energy and B_{shell} the electron binding energy provided by the class *G4AtomicShells*.

The polarized version of the photoelectric effect is based on the EM standard process *G4PhotoElectricEffect*. Mean free path and the distribution of explicitly generated final state particles are treated by this version. For details consult section 6.2.

The remaining task is to attribute polarization vectors to the generated final state electron, which is discussed in the following.

11.7.2 Polarization transfer

The polarization state of an incoming polarized photon is described by the Stokes vector $\vec{\zeta}^{(1)}$. The polarization transfer to the photoelectron can be described in the Stokes formalism using the same approach as for the Bremsstrahlung and gamma conversion processes, cf. 11.5 and 11.6. The relation between the photoelectron's Stokes parameters and the incoming photon's Stokes parameters is described by the interaction matrix T_l^p derived from H. Olsen [1] and reviewed by H.W McMaster [2]:

$$\begin{pmatrix} I' \\ \vec{\xi}^{(1)} \end{pmatrix} = T_l^p \begin{pmatrix} I_0 \\ \vec{\zeta}^{(1)} \end{pmatrix} \tag{11.78}$$

214

In general, for the photoelectric effect as a two-body scattering, the cross section should be correlated with the spin states of the incoming photon and the target electron. In our implementation the target electron is not polarized and only the polarization transfer from the photon to the photoelectron is taken into account. In this case the cross section of the process remains polarization independent. To compute the matrix elements we take advantage of the available kinematic variables provided by the generic *G4PhotoelectricEffect* class. To compute the photoelectron spin state (Stokes parameters), four main parameters are needed:

- The incoming photon Stokes vector $\vec{\zeta}^{(1)}$

- The incoming photon's energy k.

- the photoelectron's kinetic energy $E_{kin}^{e^-}$ or the Lorentz factors β and γ.

- The photoelectron's polar angle θ or $\cos\theta$.

The interaction matrix derived by H. Olsen [1] is given by:

$$
T_l^P = \begin{pmatrix} 1+D & -D & 0 & 0 \\ 0 & 0 & 0 & B \\ 0 & 0 & 0 & 0 \\ 0 & 0 & 0 & A \end{pmatrix} \tag{11.79}
$$

Where

$$
D = \frac{1}{k}\left[\frac{2}{k\epsilon(1-\beta\cos\theta)} - 1\right] \tag{11.80}
$$

$$
A = \frac{\epsilon}{\epsilon+1}\left[\frac{2}{k\epsilon} + \beta\cos\theta + \frac{2}{k\epsilon^2(1-\beta\cos\theta)}\right] \tag{11.81}
$$

$$
B = \frac{\epsilon}{\epsilon+1}\beta\sin\theta\left[\frac{2}{k\epsilon(1-\beta\cos\theta)} - 1\right] \tag{11.82}
$$

Using Eq. (11.78) and the transfer matrix given by Eq. (11.79) the polarization state of the produced e^- is given in the Stokes formalism by:

$$
\vec{\xi}^{(1)} = \begin{pmatrix} \xi_1^{(1)} \\ \xi_2^{(1)} \\ \xi_3^{(1)} \end{pmatrix} = \begin{pmatrix} \zeta_3^{(1)}B \\ 0 \\ \zeta_3^{(1)}A \end{pmatrix} \tag{11.83}
$$

From equation (11.83) one can see that a longitudinally (transversally) polarized photoelectron can only be produced if the incoming photon is circularly polarized.

11.7.3 Status of this document

20.11.07 created by K.Laihem
03.12.07 minor update by A.Schälicke

Bibliography

[1] H. Olsen, Kgl. N. Videnskab. Selskabs Forh. 31, Nos 11, 11a (1958).

[2] W.H. McMaster. Matrix representation of polarization. Reviews of Modern Physics, 33(1):8-29, 1961.

[3] K. Laihem, PhD thesis, Humboldt University Berlin, Germany, (2007).

Chapter 12

Low Energy Extensions

12.1 Introduction

Additional electromagnetic physics processes for photons, electrons, hadrons and ions have been implemented in Geant4 in order to extend the validity range of particle interactions to lower energies than those available in the standard Geant4 electromagnetic processes [1, 2, 3]. Because atomic shell structure is more important in most cases at low energies than it is at higher energies, the low energy processes make direct use of shell cross section data. The standard processes, which are optimized for high energy physics applications, rely on parameterizations of these data.

The low energy processes include the photo-electric effect, Compton scattering, Rayleigh scattering, gamma conversion, bremsstrahlung and ionization. Fluorescence of excited atoms is also considered.

Some features common to all low energy processes currently implemented in Geant4 are summarized in this section. Subsequent sections provide more detailed information for each process.

12.1.1 Physics

The low energy processes of Geant4 represent electromagnetic interactions at lower energies than those covered by the equivalent Geant4 standard electromagnetic processes.

The current implementation of low energy processes is valid for energies down to 250 eV (and can be used up to approximately 100 GeV), unless differently specified. It covers elements with atomic number between 1 and 99.

All processes involve two distinct phases:

- the calculation and use of total cross sections, and

- the generation of the final state.

Both phases are based on the theoretical models and on exploitation of evaluated data.

12.1.2 Data Sources

The data used for the determination of cross-sections and for sampling of the final state are extracted from a set of publicly distributed evaluated data libraries:

- EPDL97 (Evaluated Photons Data Library) [4];

- EEDL (Evaluated Electrons Data Library) [5];

- EADL (Evaluated Atomic Data Library) [6];

- stopping power data [7, 8, 9, 10];

- binding energy values based on data of Scofield [11].

Evaluated data sets are produced through the process of critical comparison, selection, renormalization and averaging of the available experimental data, normally complemented by model calculations. These libraries provide the following data relevant for the simulation of Geant4 low energy processes:

- total cross-sections for photoelectric effect, Compton scattering, Rayleigh scattering, pair production and bremsstrahlung,

- subshell integrated cross sections for photo-electric effect and ionization,

- energy spectra of the secondaries for electron processes,

- scattering functions for the Compton effect,

- form factors for Rayleigh scattering,

- binding energies for electrons for all subshells,

- transition probabilities between subshells for fluorescence and the Auger effect, and

- stopping power tables.

The energy range covered by the data libraries extends from 100 GeV down to 1 eV for Rayleigh and Compton effects, down to the lowest binding energy for each element for photo-electric effect and ionization, and down to 10 eV for bremsstrahlung.

12.1.3   Distribution of the Data Sets

The author of EPDL97 [4], who is also responsible for the EEDL [5] and EADL [6] data libraries, Dr. Red Cullen, has kindly permitted the libraries and their related documentation to be distributed with the Geant4 toolkit. The data are reformatted for Geant4 input. They can be downloaded from the source code section of the Geant4 page: http://cern.ch/geant4/geant4.html.

The EADL, EEDL and EPDL97 data-sets are also available from several public distribution centres in a format different from the one used by Geant4 [12].

Stopping power data are taken from publications [7, 8, 9, 10].

12.1.4 Calculation of Total Cross Sections

The energy dependence of the total cross section is derived for each process from the evaluated data libraries. Since the libraries provide cross sections for a set of discrete incident energies, the total cross section at a given energy, E, is obtained by interpolation according to the formula [13]:

$$\log(\sigma(E)) = \frac{log(\sigma_1)log(E_2/E) + log(\sigma_2)log(E/E_1)}{log(E_2/E_1)} \quad (12.1)$$

where E_1 and E_2 are respectively the closest lower and higher energy for which data (σ_1 and σ_2) are available.

For each process a production threshold energy is defined; by default it is set to the low end of the energy validity range of the process (250 eV in the current implementation), but a higher or lower value can be set by the user.

For a particle of energy E, the mean free path for interacting via a given process is calculated as:

$$\lambda = \frac{1}{\Sigma_i \sigma_i(E) \cdot n_i} \quad (12.2)$$

where $\sigma_i(E)$ is the microscopic integrated cross-section of the process considered at energy E, and n_i is the atomic density of the $i - th$ element contributing to the material composition. The sum runs over all the elements of which the material is composed. The cross sections are determined as described in this section. An exception to this method is the implementation of the chemical effect on hadron/ion stopping powers for a set of materials.

12.1.5 Sampling of Relevant Physics Quantities

The final state products of the processes are generated by sampling relevant physical quantities, such as energies and angular distributions of secondaries, from distributions derived from theoretical models and evaluated data. The energy dependence of the parameters which characterize the distributions is taken into account either by direct interpolation of the data available in the libraries, or by interpolation of values obtained from fits to the data.

When generating the final state, an atom of the material in which the interaction occurs is randomly selected and atomic de-excitation is simulated.

Secondaries which would be produced with energies below their user defined production threshold are not created and their energy is deposited locally.

12.1.6   Status of the document

30.09.1999 created by Alessandra Forti
07.02.2000 modified by Véronique Lefébure
08.03.2000 reviewed by Petteri Nieminen and Maria Grazia Pia
04.12.2001 reviewed by Vladimir Ivanchenko
26.01.2003 minor re-write by D.H. Wright .

Bibliography

[1] "Geant4 Low Energy Electromagnetic Models for Electrons and Photons", J.Apostolakis et al., CERN-OPEN-99-034(1999), INFN/AE-99/18(1999)

[2] V.N. Ivanchenko et al., GEANT4 Simulation of Energy Losses of Slow Hadrons, CERN-99-121, INFN/AE-99/20, (September 1999).

[3] S. Giani et al., GEANT4 Simulation of Energy Losses of Ions, CERN-99-300, INFN/AE-99/21, (November 1999).

[4] "EPDL97: the Evaluated Photon Data Library, '97 version", D.Cullen, J.H.Hubbell, L.Kissel, UCRL–50400, Vol.6, Rev.5

[5] "Tables and Graphs of Electron-Interaction Cross-Sections from 10 eV to 100 GeV Derived from the LLNL Evaluated Electron Data Library (EEDL), Z=1-100" S.T.Perkins, D.E.Cullen, S.M.Seltzer, UCRL-50400 Vol.31

[6] "Tables and Graphs of Atomic Subshell and Relaxation Data Derived from the LLNL Evaluated Atomic Data Library (EADL), Z=1-100" S.T.Perkins, D.E.Cullen, M.H.Chen, J.H.Hubbell, J.Rathkopf, J.Scofield, UCRL-50400 Vol.30

[7] H.H. Andersen and J.F. Ziegler, The Stopping and Ranges of Ions in Matter. Vol.3, Pergamon Press, 1977.

[8] J.F. Ziegler, The Stopping and Ranges of Ions in Matter. Vol.4, Pergamon Press, 1977.

[9] J.F. Ziegler, J.P. Biersack, U. Littmark, The Stopping and Ranges of Ions in Solids. Vol.1, Pergamon Press, 1985.

[10] ICRU (A. Allisy et al), Stopping Powers and Ranges for Protons and Alpha Particles, ICRU Report 49, 1993.

[11] J.H. Scofield, "Radiative Transitions", in "Atomic Inner-Shell Processes", B.Crasemann ed. (Academic Press, New York, 1975),pp.265-292.

[12] http://www.nea.fr/html/dbdata/nds_evaluated.htm

[13] "New Photon, Positron and Electron Interaction Data for Geant in Energy Range from 1 eV to 10 TeV", J. Stepanek, Draft to be submitted for publication

12.2 Compton Scattering

12.2.1 Total Cross Section

The total cross section for the Compton scattering process is determined from the data as described in section 12.1.4.

12.2.2 Sampling of the Final State

For low energy incident photons, the simulation of the Compton scattering process is performed according to the same procedure used for the "standard" Compton scattering simulation, with the addition that Hubbel's atomic form factor [1] or scattering function, SF, is taken into account. The angular and energy distribution of the incoherently scattered photon is then given by the product of the Klein-Nishina formula $\Phi(\epsilon)$ and the scattering function, $SF(q)$ [2]

$$P(\epsilon, q) = \Phi(\epsilon) \times SF(q). \tag{12.3}$$

ϵ is the ratio of the scattered photon energy E', and the incident photon energy E. The momentum transfer is given by $q = E \times \sin^2(\theta/2)$, where θ is the polar angle of the scattered photon with respect to the direction of the parent photon. $\Phi(\epsilon)$ is given by

$$\Phi(\epsilon) \cong [\frac{1}{\epsilon} + \epsilon][1 - \frac{\epsilon}{1 + \epsilon^2} sin^2\theta]. \tag{12.4}$$

The effect of the scattering function becomes significant at low energies, especially in suppressing forward scattering [2].

The sampling method of the final state is based on composition and rejection Monte Carlo methods [3, 4, 5], with the SF function included in the rejection function

$$g(\epsilon) = \left[1 - \frac{\epsilon}{1 + \epsilon^2} \sin^2\theta\right] \times SF(q), \tag{12.5}$$

with $0 < g(\epsilon) < Z$. Values of the scattering functions at each momentum transfer, q, are obtained by interpolating the evaluated data for the corresponding atomic number, Z.

The polar angle θ is deduced from the sampled ϵ value. In the azimuthal direction, the angular distributions of both the scattered photon and the recoil electron are considered to be isotropic [6].

Since the incoherent scattering occurs mainly on the outermost electronic subshells, the binding energies can be neglected, as stated in reference [6].

223

The momentum vector of the scattered photon, $\overrightarrow{P'_\gamma}$, is transformed into the `World` coordinate system. The kinetic energy and momentum of the recoil electron are then

$$
\begin{aligned}
T_{el} &= E - E' \\
\overrightarrow{P_{el}} &= \overrightarrow{P_\gamma} - \overrightarrow{P'_\gamma}.
\end{aligned}
$$

12.2.3   Status of the document

30.09.1999 created by Alessandra Forti
07.02.2000 modified by Véronique Lefébure
08.03.2000 reviewed by Petteri Nieminen and Maria Grazia Pia
26.01.2003 minor re-write by D.H. Wright

Bibliography

[1] "Summary of Existing Information on the Incoherent Scattering of Photons particularly on the Validity of the Use of the Incoherent Scattering Function", Radiat. Phys. Chem. Vol. 50, No 1, pp 113-124 (1997)

[2] "A simple model of photon transport", D.E. Cullen, Nucl. Instr. Meth. in Phys. Res. B 101(1995)499-510

[3] J.C. Butcher and H. Messel. *Nucl. Phys. 20* 15 (1960)

[4] H. Messel and D. Crawford. *Electron-Photon shower distribution, Pergamon Press* (1970)

[5] R. Ford and W. Nelson. *SLAC-265, UC-32* (1985)

[6] "New Photon, Positron and Electron Interaction Data for Geant in Energy Range from 1 eV to 10 TeV", J. Stepanek, Draft to be submitted for publication

12.3 Compton Scattering by Linearly Polarized Gamma Rays

12.3.1 The Cross Section

The quantum mechanical Klein - Nishina differential cross section for polarized photons is [Heitler 1954]:

$$\frac{d\sigma}{d\Omega} = \frac{1}{4}r_0^2 \frac{h\nu^2}{h\nu_o^2}\frac{h\nu_o^2}{h\nu^2}\left[\frac{h\nu_o}{h\nu} + \frac{h\nu}{h\nu_o} - 2 + 4cos^2\Theta\right]$$

where Θ is the angle between the two polarization vectors. In terms of the polar and azimuthal angles (θ, ϕ) this cross section can be written as

$$\frac{d\sigma}{d\Omega} = \frac{1}{2}r_0^2 \frac{h\nu^2}{h\nu_o^2}\frac{h\nu_o^2}{h\nu^2}\left[\frac{h\nu_o}{h\nu} + \frac{h\nu}{h\nu_o} - 2cos^2\phi sin^2\theta\right]$$

.

12.3.2 Angular Distribution

The integration of this cross section over the azimuthal angle produces the standard cross section. The angular and energy distribution are then obtained in the same way as for the standard process. Using these values for the polar angle and the energy, the azimuthal angle is sampled from the following distribution:

$$P(\phi) = 1 - \frac{a}{b}cos^2\phi$$

where $a = sin^2\theta$ and $b = \epsilon + 1/\epsilon$. ϵ is the ratio between the scattered photon energy and the incident photon energy.

12.3.3 Polarization Vector

The components of the vector polarization of the scattered photon are calculated from

$$\vec{\epsilon'}_\perp = \frac{1}{N}\left(\hat{j}cos\theta - \hat{k}sin\theta sin\phi\right)sin\beta$$

$$\vec{\epsilon'}_\parallel = \left[N\hat{i} - \frac{1}{N}\hat{j}sin^2\theta sin\phi cos\phi - \frac{1}{N}\hat{k}sin\theta cos\theta cos\phi\right]cos\beta$$

where

$$N = \sqrt{1 - sin^2\theta cos^2\phi}.$$

$cos\beta$ is calculated from $cos\Theta = Ncos\beta$, while $cos\Theta$ is sampled from the Klein - Nishina distribution.

The binding effects and the Compton profile are neglected. The kinetic energy and momentum of the recoil electron are then

$$T_{el} = E - E'$$
$$\vec{P_{el}} = \vec{P_\gamma} - \vec{P'_\gamma}.$$

The momentum vector of the scattered photon $\vec{P_\gamma}$ and its polarization vector are transformed into the `World` coordinate system. The polarization and the direction of the scattered gamma in the final state are calculated in the reference frame in which the incoming photon is along the z-axis and has its polarization vector along the x-axis. The transformation to the `World` coordinate system performs a linear combination of the initial direction, the initial poalrization and the cross product between them, using the projections of the calculated quantities along these axes.

12.3.4 Unpolarized Photons

A special treatment is devoted to unpolarized photons. In this case a random polarization in the plane perpendicular to the incident photon is selected.

12.3.5 Status of this document

18.06.2001 created by Gerardo Depaola and Francesco Longo
10.06.2002 revision by Francesco Longo
26.01.2003 minor re-wording and correction of equations by D.H. Wright

Bibliography

[1] W. Heitler *The Quantum Theory of Radiation, Oxford Clarendom Press* (1954)

12.4 Rayleigh Scattering

12.4.1 Total Cross Section

The total cross section for the Rayleigh scattering process is determined from the data as described in section 12.1.4.

12.4.2 Sampling of the Final State

The coherent scattered photon angle θ is sampled according to the distribution obtained from the product of the Rayleigh formula $(1 + \cos^2 \theta) \sin \theta$ and the square of Hubbel's form factor $FF^2(q)$ [1] [2]

$$\Phi(E, \theta) = [1 + \cos^2 \theta] \sin \theta \times FF^2(q), \qquad (12.6)$$

where $q = 2E \sin(\theta/2)$ is the momentum transfer.

Form factors introduce a dependency on the initial energy E of the photon that is not taken into account in the Rayleigh formula. At low energies, form factors are isotropic and do not affect angular distribution, while at high energies they are forward peaked.

The sampling procedure is as follows [3]:

1. $cos\theta$ is chosen from a uniform distribution between -1 and 1

2. the form factor FF is extracted from the data table for the considered element, using logarithmic data interpolation, for $q = 2E \cdot \sin(\theta/2)$

3. if the value obtained for $\Phi(E, \theta)$ is larger than a random number uniformly distributed between 0 and Z^2, the procedure is repeated from step 1, otherwise θ is taken as the photon scattering angle with respect to its incident direction.

4. the azimuthal direction of the scattered photon is chosen at random.

12.4.3 Status of this document

30.09.1999 created by Alessandra Forti
07.02.2000 modified by Véronique Lefébure
08.03.2000 reviewed by Petteri Nieminen and Maria Grazia Pia
10.06.2002 modified by Francesco Longo and Gerardo Depaola
26.01.2003 minor re-write and correction of equations by D.H. Wright

Bibliography

[1] "Relativistic Atom Form Factors and Photon Coherent Scattering Cross Sections", J.H. Hubbell et al., J.Phys.Chem.Ref.Data, 8,69(1979)

[2] "A simple model of photon transport", D.E. Cullen, Nucl. Instr. Meth. in Phys. Res. B 101(1995)499-510

[3] "New Photon, Positron and Electron Interaction Data for Geant in Energy Range from 1 eV to 10 TeV", J. Stepanek, Draft to be submitted for publication

12.5 Gamma Conversion

12.5.1 Total cross-section

The total cross-section of the Gamma Conversion process is determined from the data as described in section 12.1.4.

12.5.2 Sampling of the final state

For low energy incident photons, the simulation of the Gamma Conversion final state is performed according to [1].

The secondary $e^\pm$ energies are sampled using the Bethe-Heitler cross-sections with Coulomb correction.

The Bethe-Heitler differential cross-section with the Coulomb correction for a photon of energy E to produce a pair with one of the particles having energy ϵE (ϵ is the fraction of the photon energy carried by one particle of the pair) is given by [2]:

$$\frac{d\sigma(Z, E, \epsilon)}{d\epsilon} = \frac{r_0^2 \alpha Z(Z + \xi(Z))}{E^2} \left[(\epsilon^2 + (1 - \epsilon)^2) \left(\Phi_1(\delta) - \frac{F(Z)}{2} \right) + \right.$$
$$\left. + \frac{2}{3}\epsilon(1 - \epsilon) \left(\Phi_2(\delta) - \frac{F(Z)}{2} \right) \right]$$

where $\Phi_i(\delta)$ are the screening functions depending on the screening variable δ [1].

The value of ϵ is sampled using composition and rejection Monte Carlo methods [1, 3, 4].

After the successful sampling of ϵ, the process generates the polar angles of the electron with respect to an axis defined along the direction of the parent photon. The electron and the positron are assumed to have a symmetric angular distribution. The energy-angle distribution is given by[5]:

$$\frac{d\sigma}{dpd\Omega} = \frac{2\alpha^2 e^2}{\pi k m^4} \left[\left(\frac{2x(1 - x)^2}{(1 + l)} - \frac{12lx(1 - x)}{(1 + l)^4} \right) (Z^2 + Z) + \right.$$
$$\left. + \left(\frac{2x^2 - 2x + 1}{(1 + l)^2} + \frac{4lx(1 - x)}{(1 + l)^4} \right) (X - 2Z^2 f((\alpha Z)^2)) \right]$$

where k is the photon energy, p the momentum and E the energy of the electron of the $e^\pm$ pair $x = E/k$ and $l = E^2\theta^2/m^2$. The sampling of this cross-section is obtained according to [1].

The azimuthal angle ϕ is generated isotropically.

This information together with the momentum conservation is used to calculate the momentum vectors of both decay products and to transform them to the GEANT coordinate system. The choice of which particle in the pair is the electron/positron is made randomly.

12.5.3   Status of the document

18.06.2001 created by Francesco Longo

Bibliography

[1] Urban L., in Brun R. et al. (1993), *Geant. Detector Description and Simulation Tool*, CERN Program Library, section `Phys/211`

[2] R. Ford and W. Nelson., *SLAC-210, UC-32* (1978)

[3] J.C. Butcher and H. Messel. *Nucl. Phys. 20* 15 (1960)

[4] H. Messel and D. Crawford. *Electron-Photon shower distribution, Pergamon Press* (1970)

[5] Y. S. Tsai, *Rev. Mod. Phys. 46* 815 (1974), Y. S. Tsai, *Rev. Mod. Phys. 49* 421 (1977)

12.6 Photoelectric effect

12.6.1 Total cross-section

The total photoelectric cross-section at a given energy, E, is calculated as described in section 12.1.4. Note that for this process the *MeanFreePathTable* is not built, since the cross-section is not a smooth function of the energy, therefore in all calculations the cross-section is used directly.

12.6.2 Sampling of the final state

The incident photon is absorbed and an electron is emitted.

The electron kinetic energy is the difference between the incident photon energy and the binding energy of the electron before the interaction. The sub-shell, from which the electron is emitted, is randomly selected according to the relative cross-sections of all subshells, determined at the given energy, T, by interpolating the evaluated cross-section data from the EPDL97 data bank [1].

The interaction leaves the atom in an excited state. The deexcitation of the atom is simulated as described in section 12.9.

12.6.3 Angular distribution of the emmited photoelectron

Three models are available to describe the direction of the emmited photoelectron: G4PhotoElectricAngularGeneratorSimple, G4PhotoElectricAngularGeneratorSauterGavrila and G4PhotoElectricAngularGeneratorPolarized.

G4PhotoElectricAngularGeneratorSimple

The default model assumes that the photoelectron direction is emmited in the same direction as the incident photon.

G4PhotoElectricAngularGeneratorSauterGavrila

This model implements the Sauter–Gavrilla distribution has presented in the Standard Photoelectric effect.

G4PhotoElectricAngularGeneratorPolarized

This model models the double differential cross section (for angles θ and ϕ) and thus it is capable of account for polarization of the incident photon.

The developed generator was based in the research of Sauter in 1931[2]. The Sauter's formula was recalculated by Gavrila in 1959 for the K-shell [3] and in 1961 for the L-shells [4]. These new double differential formulas have some limitations, $\alpha Z \ll 1$ and have a range between $0.1 < \beta < 0.99$ c.

K–shell

The double differential photoeffect for K–shell can be written as [3]:

$$\frac{d\sigma}{d\omega}(\theta, \phi) = \frac{4}{m^2} \alpha^6 Z^5 \frac{\beta^3(1-\beta^2)^3}{[1-(1-\beta^2)^{1/2}]} \left(F\left(1 - \frac{\pi\alpha Z}{\beta}\right) + \pi\alpha Z G \right) \quad (12.7)$$

where

$$
\begin{aligned}
F &= \frac{\sin^2\theta \cos^2\phi}{(1-\beta\cos\theta)^4} - \frac{1-(1-\beta^2)^{1/2}}{2(1-\beta^2)} \frac{\sin^2\theta \cos^2\phi}{(1-\beta\cos\theta)^3} \\
&\quad + \frac{\left[1-(1-\beta^2)^{1/2}\right]^2}{4(1-\beta^2)^{3/2}} \frac{\sin^2\theta}{(1-\beta\cos\theta)^3}
\end{aligned}
$$

$$
\begin{aligned}
G &= \frac{[1-(1-\beta^2)^{1/2}]^{1/2}}{2^{7/2}\beta^2(1-\beta\cos\theta)^{5/2}} \left[\frac{4\beta^2}{(1-\beta^2)^{1/2}} \frac{\sin^2\theta \cos^2\phi}{1-\beta\cos\theta} + \frac{4\beta}{1-\beta^2} \cos\theta \cos^2\phi - \right. \\
&\quad - 4\frac{1-(1-\beta^2)^{1/2}}{1-\beta^2}(1-\cos^2\phi) - \beta^2 \frac{1-(1-\beta^2)^{1/2}}{1-\beta^2} \frac{\sin^2\theta}{1-\beta\cos\theta} - \\
&\quad + \left. 4\beta^2\frac{1-(1-\beta^2)^{1/2}}{(1-\beta^2)^{3/2}} - 4\beta\frac{\left[1-(1-\beta^2)^{1/2}\right]^2}{(1-\beta^2)^{3/2}} \right] \\
&\quad + \frac{1-(1-\beta^2)^{1/2}}{4\beta^2(1-\beta\cos\theta)^2} \left[\frac{\beta}{1-\beta^2} - \frac{2}{1-\beta^2}\cos\theta\cos^2\phi + \frac{1-(1-\beta^2)^{1/2}}{(1-\beta^2)^{3/2}}\cos\theta \right. \\
&\quad - \left. \beta\frac{1-(1-\beta^2)^{1/2}}{(1-\beta^2)^{3/2}} \right]
\end{aligned}
$$

where β is the electron velocity, α is the fine–structure constant, Z is the atomic number of the material and θ, ϕ are the emission angles with respect to the electron initial direction.

L1–shell

The double differential photoeffect distribution for L1–shell is the same as for K–shell despising a constant [4]:

$$B = \xi\frac{1}{8} \quad (12.8)$$

where ξ is equal to 1 when working with unscreened Coulomb wave functions as it is done in this development.

The generation of the photoelectron distribution

Since the polarized Gavrila cross–section is a 2–dimensional non–factorized distribution an acceptance–rejection technique was the adopted [5]. For the Gravrila distribution, two functions were defined $g_1(\phi)$ and $g_2(\theta)$:

$$g_1(\phi) = a \tag{12.9}$$

$$g_2(\theta) = \frac{\theta}{1 + c\theta^2} \tag{12.10}$$

such that:

$$Ag_1(\phi)g_2(\theta) \geq \frac{d^2\sigma}{d\phi d\theta} \tag{12.11}$$

where A is a global constant. The method used to calculate the distribution is the same as the one used in Low Energy 2BN Bremsstrahlung Generator, being the difference $g_1(\phi) = a$.

12.6.4 Status of the document

30.09.1999 created by Alessandra Forti
07.02.2000 modified by Véronique Lefébure
08.03.2000 reviewed by Petteri Nieminen and Maria Grazia Pia
13.05.2002 modified by Vladimir Ivanchenko 01.05.2006 modified by Ana Farinha, Andreia Trindade, Luís Peralta and Pedro Rodrigues

Bibliography

[1] "EPDL97: the Evaluated Photon Data Library, '97 version", D.Cullen, J.H.Hubbell, L.Kissel, UCRL–50400, Vol.6, Rev.5

[2] "K–Shell Photoelectric Cross Sections from 200 keV to 2 MeV", R H Pratt, R D Levee, R L Pexton and W Aron, Phys. Rev. 134 (1964) 4A

[3] "Relativistic K–Shell Photoeffect", M. Gavrila, Phys. Rev. 113 (1959) 2

[4] "Relativistic L–Shell Photoeffect", M. Gavrila, Phys. Rev. 124 (1961) 4

[5] "Monte Carlo Generation of 2BNBremsstrahlung Distribution", L. Peralta, P. Rodrigues, A. Trindade CERN EXT–2004–039 (July, 2003)

12.7 Bremsstrahlung

The class G4LowEnergyBremsstrahlung calculates the continuous energy loss due to low energy gamma emission and simulates the gamma production by electrons. The gamma production threshold for a given material ω_c is used to separate the continuous and the discrete parts of the process. The energy loss of an electron with the incident energy T are expressed via the integrand over energy of the gammas:

$$\frac{dE}{dx} = \sigma(T) \frac{\int_{0.1eV}^{\omega_c} t \frac{d\sigma}{d\omega} d\omega}{\int_{0.1eV}^{T} \frac{d\sigma}{d\omega} d\omega}, \qquad (12.12)$$

where $\sigma(T)$ is the total cross-section at a given incident kinetic energy, T, $0.1eV$ is the low energy limit of the EEDL data. The production cross-section is a complimentary function:

$$\sigma = \sigma(T) \frac{\int_{\omega_c}^{T} \frac{d\sigma}{d\omega} d\omega}{\int_{0.1eV}^{T} \frac{d\sigma}{d\omega} d\omega}. \qquad (12.13)$$

The total cross-section, σ_s, is obtained from an interpolation of the evaluated cross-section data in the EEDL library [1], according to the formula (12.1) in Section 12.1.4.

The EEDL data [1] of total cross-sections are parametrised [2] according to (12.1). The probability of the emission of a photon with energy, ω, considering an electron of incident kinetic energy, T, is generated according to the formula:

$$\frac{d\sigma}{d\omega} = \frac{F(x)}{x}, \quad \text{with} x = \frac{\omega}{T}. \qquad (12.14)$$

The function, $F(x)$, describing energy spectra of the outcoming photons is taken from the EEDL library. For each element 15 points in x from 0.01 to 1 are used for the linear interpolation of this function. The function F is normalised by the condition $F(0.01) = 1$. The energy distributions of the emitted photons available in the EEDL library are for only a few incident electron energies (about 10 energy points between 10 eV and 100 GeV). For other energies a logarithmic interpolation formula (12.1) is used to obtain values for the function, $F(x)$. For high energies, the spectral function is very close to:

$$F(x) = 1 - x + 0.75x^2. \qquad (12.15)$$

12.7.1 Bremsstrahlung angular distributions

The angular distribution of the emitted photons with respect to the incident electron can be sampled according to three alternative generators described below. The direction of the outcoming electron is determined from the energy-momentum balance. This generators are currently implemented in G4ModifiedTsai, G4Generator2BS and G4Generator2BN classes.

G4ModifiedTsai

The angular distribution of the emitted photons is obtained from a simplified [3] formula based on the Tsai cross-section [4], which is expected to become isotropic in the low energy limit.

G4Generator2BS

In G4Generator2BS generator, the angular distribution of the emitted photons is obtained from the 2BS Koch and Motz bremsstrahlung double differential cross-section [5]:

$$
\begin{aligned}
d\sigma_{k,\theta} \;=\; & \frac{4Z^2 r_0^2}{137} \frac{dk}{k} y\, dy \left\{ \frac{16y^2 E}{(y^2+1)^4 E_0} - \right. \\
& \left. \frac{(E_0+E)^2}{(y^2+1)^2 E_0^2} + \left[\frac{E_0^2 + E^2}{(y^2+1)^2 E_0^2} - \frac{4y^2 E}{(y^2+1)^4 E_0} \right] lnM(y) \right\}
\end{aligned}
$$

where k the photon energy, θ the emission angle, E_0 and E are the initial and final electron energy in units of $m_e c^2$, r_0 is the classical electron radius and Z the atomic number of the material. y and $M(y)$ are defined as:

$$
y \;=\; E_0 \theta
$$

$$
\frac{1}{M(y)} \;=\; \left(\frac{k}{2E_0 E} \right)^2 + \left(\frac{Z^{1/3}}{111(y^2+1)} \right)^2
$$

The adopted sampling algorithm is based on the sampling scheme developed by A. F. Bielajew et al. [6], and latter implemented in EGS4. In this sampling algorithm only the angular part of 2BS is used, with the emitted photon energy, k, determined by GEANT4 $\left(\frac{d\sigma}{dk} \right)$ differential cross-section.

G4Generator2BN

The angular distribution of the emitted photons is obtained from the 2BN Koch and Motz bremsstrahlung double differential cross-section [5] that can be written as:

$$d\sigma_{k,\theta} = \frac{Z^2 r_0^2}{8\pi 137} \frac{dk}{k} \frac{p}{p_0} d\Omega_k \left\{ \frac{8\sin^2\theta(2E_0^2 - 1)}{p_0^2\Delta_0^4} - \right.$$

$$\frac{2(5E_0^2 + 2EE_0 + 3)}{p_0^2\Delta_0^2} - \frac{2(p_0^2 - k^2)}{Q^2\Delta_0} + \frac{4E}{p_2^2\Delta_0} + \frac{L}{pp_0}$$

$$\left[\frac{4E_0\sin^2\theta(3k - p_0^2 E)}{p_0^2\Delta^4} + \frac{4E_0^2(E_0^2 + E^2)}{p_0^2\Delta_0^2} + \right.$$

$$\left. \frac{2 - 2(E_0^2 - 3EE_0 + E^2)}{p_0^2\Delta_0^2} + \frac{2k(E_0^2 + EE_0 - 1)}{p_0^2\Delta_0} \right]$$

$$\left. - \left(\frac{4\epsilon}{p\Delta 0} \right) + \left(\frac{\epsilon^Q}{pQ} \right) \left[\frac{4}{\Delta_0^2} - \frac{6k}{\Delta_0} - \frac{2k(p_0^2 - k^2)}{Q^2\Delta_0} \right] \right\}$$

in which:

$$L = \ln\left[\frac{EE_0 - 1 + pp_0}{EE_0 - 1 - pp_0} \right]$$

$$\Delta_0 = E_0 - p_0\cos\theta$$

$$Q^2 = p_0^2 + k^2 - 2p_0 k\cos\theta$$

$$\epsilon = \ln\left[\frac{E + p}{E - p} \right] \qquad \epsilon^Q = \ln\left[\frac{Q + p}{Q - p} \right]$$

where k is the photon energy, θ the emission angle and (E_0, p_0) and (E, p) are the total (energy, momentum) of the electron before and after the radiative emission, all in units of $m_e c^2$.

Since the 2BN cross–section is a 2-dimensional non-factorized distribution an acceptance-rejection technique was the adopted. For the 2BN distribution, two functions $g_1(k)$ and $g_2(\theta)$ were defined:

$$g_1(k) = k^{-b} \qquad g_2(\theta) = \frac{\theta}{1 + c\theta^2} \qquad (12.16)$$

such that:

$$Ag_1(k)g_2(\theta) \geq \frac{d\sigma}{dk d\theta} \qquad (12.17)$$

where A is a global constant to be completed. Both functions have an analytical integral G and an analytical inverse G^{-1}. The b parameter of $g_1(k)$ was empirically tuned and set to 1.2. For positive θ values, $g_2(\theta)$ has a maximum at $\frac{1}{\sqrt{(c)}}$. c parameter controls the function global shape and it was used to tune $g_2(\theta)$ according to the electron kinetic energy.

To generate photon energy k according to g_1 and θ according to g_2 the inverse-transform method was used. The integration of these functions gives

$$G_1 = C_1 \int_{k_{min}}^{k_{max}} k'^{-b} dk' = C_1 \frac{k^{1-b} - k_{min}^{1-b}}{1-b} \qquad (12.18)$$

$$G_2 = C_2 \int_0^\theta \frac{\theta'}{1+c\theta'^2} d\theta' = C_2 \frac{\log(1+c\theta^2)}{2c} \qquad (12.19)$$

where C_1 and C_2 are two global constants chosen to normalize the integral in the overall range to the unit. The photon momentum k will range from a minimum cut value k_{min} (required to avoid infrared divergence) to a maximum value equal to the electron kinetic energy E_k, while the polar angle ranges from 0 to π, resulting for C_1 and C_2:

$$C_1 = \frac{1-b}{E_k^{1-b}} \qquad C_2 = \frac{2c}{\log(1+c\pi^2)} \qquad (12.20)$$

k and θ are then sampled according to:

$$k = \left[\frac{1-b}{C_1}\xi_1 + k_{min}^{1-b} \right] \qquad \theta = \sqrt{\frac{\exp\left(\frac{2c\xi_2}{C_1}\right)}{2c}} \qquad (12.21)$$

where ξ_1 and ξ_2 are uniformly sampled in the interval (0,1). The event is accepted if:

$$uAg_1(k)g_2(\theta) \leq \frac{d\sigma}{dkd\theta} \qquad (12.22)$$

where u is a random number with uniform distribution in (0,1). The A and c parameters were computed in a logarithmic grid, ranging from 1 keV to 1.5 MeV with 100 points per decade. Since the $g_2(\theta)$ function has a maximum at $\theta = \frac{1}{\sqrt{c}}$, the c parameter was computed using the relation $c = \frac{1}{\theta_{max}}$. At the point (k_{min}, θ_{max}) where k_{min} is the k cut value, the double differential cross-section has its maximum value, since it is monotonically decreasing in k and thus the global normalization parameter A is estimated from the relation:

$$Ag_1(k_{min})g_2(\theta_{max}) = \left(\frac{d^2\sigma}{dkd\theta} \right)_{max} \qquad (12.23)$$

where $g_1(k_{min})g_2(\theta_{max}) = \frac{k_{min}^{-b}}{2\sqrt{c}}$. Since A and c can only be retrieved for a fixed number of electron kinetic energies there exists the possibility that $Ag_1(k_{min})g_2(\theta_{max}) \leq \left(\frac{d^2\sigma}{dkd\theta} \right)_{max}$ for a given E_k. This is a small violation that

can be corrected introducing an additional multiplicative factor to the A parameter, which was empirically determined to be 1.04 for the entire energy range.

Comparisons between Tsai, 2BS and 2BN generators

The currently available generators can be used according to the user required precision and timing requirements. Regarding the energy range, validation results indicate that for lower energies ($\leq$ 100 keV) there is a significant deviation on the most probable emission angle between Tsai/2BS generators and the 2BN generator - Figure 12.1. The 2BN generator maintains however a good agreement with Kissel data [7], derived from the work of Tseng and co-workers [8], and it should be used for energies between 1 keV and 100 keV [9]. As the electron kinetic energy increases, the different distributions tend to overlap and all generators present a good agreement with Kissel data.
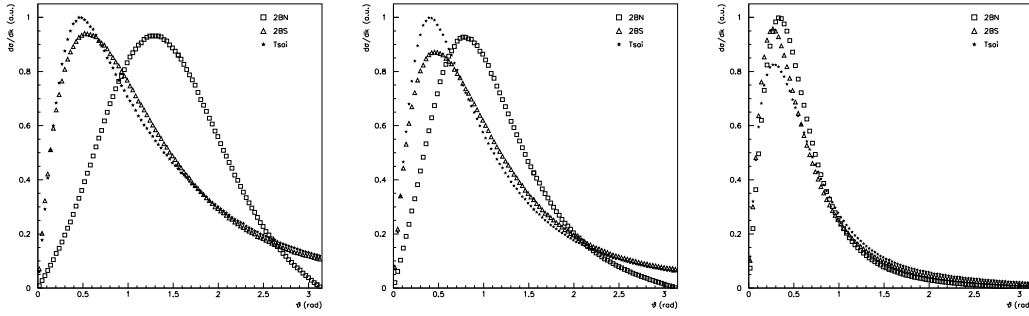
Figure 12.1: Comparison of polar angle distribution of bremsstrahlung photons ($k/T = 0.5$) for 10 keV (*left*) and 100 keV (*middle*) and 500 keV (*right*) electrons in silver, obtained with Tsai, 2BS and 2BN generator

In figure 12.2 the sampling efficiency for the different generators are presented. The sampling generation efficiency was defined as the ratio between the number of generated events and the total number of trials. As energies increases the sampling efficiency of the 2BN algorithm decreases from 0.65 at 1 keV electron kinetic energy down to almost 0.35 at 1 MeV. For energies up to 10 keV the 2BN sampling efficiency is superior or equivalent to the one of the 2BS generator. These results are an indication that precision simulation of low energy bremsstrahlung can be obtained with little performance degradation. For energies above 500 keV, Tsai generator can be used,

retaining a good physics accuracy and a sampling efficiency superior to the 2BS generator.
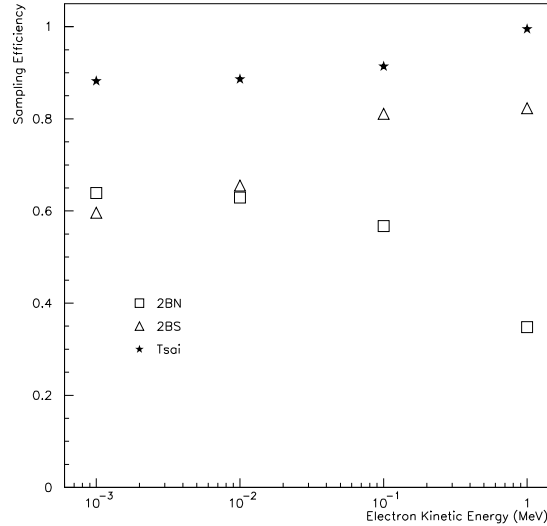
Figure 12.2: Sampling efficiency for Tsai generator, 2BS and 2BN Koch and Motz generators.

12.7.2 Status of the document

30.09.1999 created by Alessandra Forti
07.02.2000 modified by Véronique Lefébure
08.03.2000 reviewed by Petteri Nieminen and Maria Grazia Pia
05.12.2001 modified by Vladimir Ivanchenko
13.05.2002 modified by Vladimir Ivanchenko
24.11.2003 modified by Andreia Trindade, Pedro Rodrigues and Luis Peralta

Bibliography

[1] "Geant4 Low Energy Electromagnetic Models for Electrons and Photons", J.Apostolakis et al., CERN-OPEN-99-034(1999), INFN/AE-99/18(1999)

[2] "Tables and Graphs of Electron-Interaction Cross-Sections from 10 eV to 100 GeV Derived from the LLNL Evaluated Electron Data Library (EEDL), Z=1-100" S.T.Perkins, D.E.Cullen, S.M.Seltzer, UCRL-50400 Vol.31

[3] "GEANT, Detector Description and Simulation Tool", CERN Application Software Group, CERN Program Library Long Writeup W5013

[4] "Pair production and bremsstrahlung of charged leptons", Y. Tsai, Rev. Mod. Phys., Vol.46, 815(1974), Vol.49, 421(1977)

[5] "Bremsstrahlung Cross-Section Formulas and Related Data", H. W. Koch and J. W. Motz, Rev. Mod. Phys., Vol.31, 920(1959)

[6] "Improved bremsstrahlung photon angular sampling in the EGS4 code system", A. F. Bielajew, R. Mohan and C.-S. Chui, Report NRCC/PIRS-0203 (1989)

[7] "Bremsstrahlung from electron collisions with neutral atoms", L. Kissel, C. A. Quarls and R. H. Pratt, At. Data Nucl. Data Tables, Vol. 28, 382(1983)

[8] "Electron bremsstrahlung angular distributions in the 1-500 keV energy range", H. K. Tseng, R. H. Pratt and C. M. Lee , Phys. Rev. A, Vol. 19, 187(1979)

[9] "GEANT4 Applications and Developments for Medical Physics Experiments", P. Rodrigues et al. IEEE 2003 NSS/MIC Conference Record

12.8 Electron ionisation

The class G4LowEnergyIonisation calculates the continuous energy loss due to electron ionisation and simulates δ-ray production by electrons. The *delta*-electron production threshold for a given material, T_c, is used to separate the continuous and the discrete parts of the process. The energy loss of an electron with the incident energy, T, is expressed via the sum over all atomic shells, s, and the integral over the energy, t, of *delta*-electrons:

$$\frac{dE}{dx} = \sum_s \left(\sigma_s(T) \frac{\int_{0.1eV}^{T_c} t \frac{d\sigma}{dt} dt}{\int_{0.1eV}^{T_{max}} \frac{d\sigma}{dt} dt} \right), \qquad (12.24)$$

where $T_{max} = 0.5T$ is the maximum energy transfered to a δ-electron, $\sigma_s(T)$ is the total cross-section for the shell, s, at a given incident kinetic energy, T, and $0.1eV$ is the low energy limit of the EEDL data. The δ-electron production cross-section is a complimentary function:

$$\sigma(T) = \sum_s \left(\sigma_s(T) \frac{\int_{T_c}^{T_{max}} \frac{d\sigma}{dt} dt}{\int_{0.1eV}^{T_{max}} \frac{d\sigma}{dt} dt} \right). \qquad (12.25)$$

The partial sub-shell cross-sections, σ_s, are obtained from an interpolation of the evaluated cross-section data in the EEDL library [1], according to the formula (12.1) in Section 12.1.4.

The probability of emission of a δ-electron with kinetic energy, t, from a sub-shell, s, of binding energy, B_s, as the result of the interaction of an incoming electron with kinetic energy, T, is described by:

$$\frac{d\sigma}{dt} = \frac{P(x)}{x^2}, \quad \text{with} x = \frac{t + B_s}{T + B_s}, \qquad (12.26)$$

where the parameter x is varied from $x_{min} = (0.1eV + B_s)/(T + B_s)$ to 0.5. The function, $P(x)$, is parametrised differently in 3 regions of x: from x_{min} to x_1 the linear interpolation with linear scale of 4 points is used; from x_1 to x_2 the linear interpolation with logarithmic scale of 16 points is used; from x_2 to 0.5 the following interpolation is applied:

$$P(x) = 1 - gx + (1 - g)x^2 + \frac{x^2}{1 - x}(\frac{1}{1 - x} - g) + A * (0.5 - x)/x, \quad (12.27)$$

where A is a fit coefficient, g is expressed via the gamma factor of the incoming electron:

$$g = (2\gamma - 1)/\gamma^2. \qquad (12.28)$$

For the high energy case ($x >> 1$) the formula (12.27) is transformed to the Möller electron-electron scattering formula [2, 3].

The value of the coefficient, A, for each element is obtained as a result of the fit on the spectrum from the EEDL data for those energies which are available in the database. The values of x_1 and x_2 are chosen for each atomic shell according to the spectrum of δ-electrons in this shell. Note that x_1 corresponds to the maximum of the spectrum, if the maximum does not coincide with x_{min}. The dependence of all 24 parameters on the incident energy, T, is evaluated from a logarithmic interpolation (12.1).

The sampling of the final state proceeds in three steps. First a shell is randomly selected, then the energy of the *delta*-electron is sampled, finally the angle of emission of the scattered electron and of the δ-ray is determined by energy-momentum conservation taken into account electron motion on the atomic orbit.

The interaction leaves the atom in an excited state. The deexcitation of the atom is simulated as described in section 12.9. Sampling of the excitations is carried out for both the continuous and the discrete parts of the process.

12.8.1   Status of the document

30.09.1999 created by Alessandra Forti
07.02.2000 modified by Véronique Lefébure
08.03.2000 reviewed by Petteri Nieminen and Maria Grazia Pia
05.12.2001 modified by Vladimir Ivanchenko
13.05.2002 modified by Vladimir Ivanchenko

Bibliography

[1] "Tables and Graphs of Electron-Interaction Cross-Sections from 10 eV to 100 GeV Derived from the LLNL Evaluated Electron Data Library (EEDL), Z=1-100" S.T.Perkins, D.E.Cullen, S.M.Seltzer, UCRL-50400 Vol.31

[2] GEANT3 manual ,CERN Program Library Long Writeup W5013 (October 1994).

[3] H.Messel and D.F.Crawford. Pergamon Press,Oxford,1970.

12.9 Atomic relaxation

The atomic relaxation can be triggered by other electromagnetic interactions such as the photoelectric effect or ionisation, which leave the atom in an excited state.

The Livermore Evaluation Atomic Data Library EADL [1] contains data to describe the relaxation of atoms back to neutrality after they are ionised.

It is assumed that the binding energy of all subshells are the same for neutral ground state atoms as for ionised atoms [1].

The data in EADL includes the radiative and non-radiative transition probabilities for each sub-shell of each element, for Z=1 to 100. The atom has been ionised by a process that has caused an electron to be ejected from an atom, leaving a vacancy or "hole" in a given subshell. The EADL data are then used to calculate the complete radiative and non-radiative spectrum of X-rays and electrons emitted as the atom relaxes back to neutrality.

Non-radiative de-excitation can occur via the Auger effect (the initial and secondary vacancies are in different shells) or Coster-Kronig effect (transitions within the same shell).

12.9.1 Fluorescence

The simulation procedure for the fluorescence process is the following:

1. If the vacancy subshell is not included in the data, a photon is emitted in a random direction in 4π with an energy equal to the corresponding binding energy, and the procedure is terminated.

2. If the vacancy subshell is included in the data, an outer subshell is randomly selected taking into account the relative transition probabilities for all possible outer subshells.

3. In the case where the energy corresponding to the selected transition is larger than a user defined cut value (equal to zero by default), a photon particle is created and emitted in a random direction in 4π, with an energy equal to the transition energy.

4. the procedure is repeated from step 1, for the new vacancy subshell.

The final local energy deposit is the difference between the binding energy of the initial vacancy subshell and the sum of all transition energies which were taken by fluorescence photons. The atom is assumed to be initially ionised with an electric charge of $+1e$.

Sub-shell data are provided in the EADL data bank [1] for Z=1 through 100. However, transition probabilities are only explicitly included for Z=6 through 100, from the subshells of the K, L, M, N shells and some O sub-shells. For subshells O,P,Q: transition probabilities are negligible (of the order of 0.1%) and smaller than the precision with which they are known. Therefore, for the time being, for Z=1 through 5, only a local energy deposit corresponding to the binding energy B of an electron in the ionised subshell is simulated. For subshells of the O, P, and Q shells, a photon is emitted with that energy B.

12.9.2 Auger process

The Auger effect is complimentary to fluorescence, hence the simulation process is the same as for the fluorescence, with the exception that two random shells are selected, one for the transition electron that fills the original vacancy, and the other for selecting the shell generating the Auger electron.

Subshell data are provided in the EADL data bank [1] for $Z = 6$ through 100. Since in EADL no data for elements with $Z < 5$ are provided, Auger effects are only considered for $5 < Z < 100$ and always due to the EADL data tables, only for those transitions which have a probabiliy to occur $> 0.1\%$ of the total non-radiative transition probability. EADL probability data used are, however, normalized to one for Fluorescence + Auger.

12.9.3 Status of the document

08.02.2000 created by Véronique Lefébure
08.03.2000 reviewed by Petteri Nieminen and Maria Grazia Pia
05.06.2002 added Auger Effect description by Alfonso Mantero

Bibliography

[1] "Tables and Graphs of Atomic Subshell and Relaxation Data Derived from the LLNL Evaluated Atomic Data Library (EADL), Z=1-100" S.T.Perkins, D.E.Cullen, M.H.Chen, J.H.Hubbell, J.Rathkopf, J.Scofield, UCRL-50400 Vol.30

[2] "A simple model of photon transport", D.E. Cullen, Nucl. Instr. Meth. in Phys. Res. B 101(1995)499-510

[3] "A program to determine the radiation spectra due to a single atomic-subshell ionisation by a particle or due to deexcitation or decay of radionuclides", J. Stepanek, Comp. Phys. Comm. 106(1997)237-257

12.10 Hadron and Ion Ionisation

The class `G4hLowEnergyIonisation` calculates the continuous energy loss due to ionisation and simulates the δ-ray production by charged hadrons or ions. This represents an extension of the Geant4 physics models down to low energy [1, 2].

12.10.1 Delta-ray production

In Geant4, δ-rays are generated generally only above a threshold energy, T_c, the value of which depends on atomic parameters and the cut value, T_{cut}, calculated from the unique *cut in range* parameter for all charged particles in all materials. The total cross-section for the production of a δ-ray electron of kinetic energy $T > T_c$ by a particle of kinetic energy E is:

$$\sigma(E, T_c) = \int_{T_c}^{T_{max}} \frac{d\sigma(E, T)}{dT} dT \quad \text{with } T_c = \min(\max(I, T_{cut}), T_{max}) \tag{12.29}$$

where I is the mean excitation potential of the atom (the formulae of this charter are precise if $T \gg I$), T_{max} is the maximum energy transferable to the free electron

$$T_{max} = \frac{2m_e c^2(\gamma^2 - 1)}{1 + 2\gamma(m_e/M) + (m_e/M)^2} \tag{12.30}$$

with m_e the electron mass, M the mass of the incident particle, and γ is the relativistic factor. For heavy charged particles the differential cross-section per atom can be written as [3, 4]:

$$\text{for spin 0} \quad \frac{d\sigma}{dT} = KZ \frac{Z_h^2}{\beta^2 T^2} \left[1 - \beta^2 \frac{T}{T_{max}} \right] \tag{12.31}$$

$$\text{for spin 1/2} \quad \frac{d\sigma}{dT} = KZ \frac{Z_h^2}{\beta^2 T^2} \left[1 - \beta^2 \frac{T}{T_{max}} + \frac{T^2}{2E^2} \right]$$

$$\text{for spin 1} \quad \frac{d\sigma}{dT} = KZ \frac{Z_h^2}{\beta^2 T^2} \left[\left(1 - \beta^2 \frac{T}{T_{max}} \right) \left(1 + \frac{T}{3Q_c} \right) + \frac{T^2}{3E^2} \left(1 + \frac{T}{2Q_c} \right) \right]$$

where Z is the atomic number, Z_h is the effective charge of the incident particle in units of positron charge, β is the relativistic velocity, and $Q_c = (Mc^2)^2/m_e c^2$. The factor K is expressed as $K = 2\pi r_e^2 m_e c^2$, where r_e is the classical electron radius. The integration of formula (12.29) gives the total

cross-section, which for particles with spin 0 and 1/2 are the following :

$$\text{for spin 0} \quad \sigma(Z, E, T_c) = KZ\frac{Z_h^2}{\beta^2}\left(\frac{1 - \tau + \beta^2\tau\ln\tau}{T_c}\right) \tag{12.32}$$

$$\text{for spin 1/2} \quad \sigma(Z, E, T_c) = KZ\frac{Z_h^2}{\beta^2}\left(\frac{1 - \tau + \beta^2\tau\ln\tau}{T_c} + \frac{T_{max} - T_c}{2E^2}\right)$$

where $\tau = T_c/T_{max}$.

The average energy transfer ΔE_δ of a particle with spin 0 to δ-electrons with $T > T_c$ can be expressed as:

$$\Delta E_\delta = N_{el}\frac{Z_h^2}{\beta^2}\left(-\ln\tau - \beta^2(1 - \tau)\right) \tag{12.33}$$

where N_{el} is the electron density of the medium. Using (12.31) one finds that the correction to (12.33) for particles with spin 1/2 is $(T_{max}^2 - T_c^2)/4E^2$. This value is very small for low energy and can be neglected. The same conclusion can be drawn for particles with spin 1.

The mean free path of the particle is tabulated during initialisation as a function of the material and of the energy for all the charged hadrons and static ions. Note, that for low energy $T_c = T_{max}$, cross-section is zero and the mean free path is set to infinity, compatible with the machine precision.

12.10.2 Energy Loss of Fast Hadrons

The energy lost in soft ionising collisions producing δ-rays below T_c are included in the continuous energy loss. The mean value of the energy loss is given by the restricted Bethe-Bloch formula [5, 3] :

$$\left.\frac{dE}{dx}\right]_{T<T_c} = KN_{el}\frac{Z_h^2}{\beta^2}L_0 \tag{12.34}$$

$$= KN_{el}\frac{Z_h^2}{\beta^2}\left[\ln\frac{2m_ec^2\beta^2\gamma^2T_{max}}{I^2} - \beta^2\left(1 + \frac{T_c}{T_{max}}\right) - \delta - \frac{2C_e}{Z}\right]$$

where N_{el} is the electron density of the medium, δ is the density correction term, and C_e/Z is the shell correction term.

The density effect becomes important at high energies because of the long-range polarisation of the medium by a relativistic charged particle. The shell correction term takes into account the fact that, at low energies for light elements, and at all energies for heavy ones, the probability of hadron interaction with inner atomic shells becomes small. The accuracy of the Bethe-Bloch formula with the correction terms mentioned above is estimated

247

as 1 % for energies between 6 MeV and 6 GeV [3]. Using (12.31) one can find out that the correction to L_0 for particles with the spin $1/2$ is $T_c^2/4E^2$. This value is very small and can be neglected.

There exists a variety of phenomenological approximations for parameters in the Bethe-Bloch formula. In Geant4 the tabulation of the ionisation potential from Ref.[6] is implemented for all the elements. For the density effect the formulation of Sternheimer [7] is used:

x is a kinetic variable of the particle : $\quad x = \log_{10}(\gamma\beta) = \ln(\gamma^2\beta^2)/4.606$, and $\delta(x)$ is defined by

$$
\begin{array}{lll}
\text{for} \quad x < x_0 : & \delta(x) = 0 & \\
\text{for} \quad x \in [x_0, \ x_1] : & \delta(x) = 4.606x - C + a(x_1 - x)^m & \qquad (12.35) \\
\text{for} \quad x > x_1 : & \delta(x) = 4.606x - C &
\end{array}
$$

where the matter-dependent constants are calculated as follows:

$$
\begin{array}{rcl}
h\nu_p & = & \text{plasma energy of the medium} = \sqrt{4\pi n_{el} r_e^3} \, mc^2/\alpha = \sqrt{4\pi n_{el} r_e} \, \hbar c \\
C & = & 1 + 2\ln(I/h\nu_p) \\
x_a & = & C/4.606 \\
a & = & 4.606(x_a - x_0)/(x_1 - x_0)^m \\
m & = & 3.
\end{array}
$$

$$(12.36)$$

For condensed media

$$
\begin{array}{ll}
I < 100\,\text{eV} & \left\{ \begin{array}{llll} \text{for } C \leq 3.681 & x_0 = 0.2 & & x_1 = 2 \\ \text{for } C > 3.681 & x_0 = 0.326C - 1.0 & x_1 = 2 \end{array} \right. \\
I \geq 100\,\text{eV} & \left\{ \begin{array}{llll} \text{for } C \leq 5.215 & x_0 = 0.2 & & x_1 = 3 \\ \text{for } C > 5.215 & x_0 = 0.326C - 1.5 & x_1 = 3 \end{array} \right.
\end{array}
$$

and for gaseous media

$$
\begin{array}{llll}
\text{for} & C < 10. & x_0 = 1.6 & x_1 = 4 \\
\text{for} & C \in [10.0, \ 10.5[& x_0 = 1.7 & x_1 = 4 \\
\text{for} & C \in [10.5, \ 11.0[& x_0 = 1.8 & x_1 = 4 \\
\text{for} & C \in [11.0, \ 11.5[& x_0 = 1.9 & x_1 = 4 \\
\text{for} & C \in [11.5, \ 12.25[& x_0 = 2. & x_1 = 4 \\
\text{for} & C \in [12.25, \ 13.804[& x_0 = 2. & x_1 = 5 \\
\text{for} & C \geq 13.804 & x_0 = 0.326C - 2.5 & x_1 = 5.
\end{array}
$$

The semi-empirical formula due to Barkas, which is applicable to all materials, is used for the shell correction term[8]:

$$
C_e(I, \beta\gamma) = \frac{a(I)}{(\beta\gamma)^2} + \frac{b(I)}{(\beta\gamma)^4} + \frac{c(I)}{(\beta\gamma)^6} \qquad (12.37)
$$

The functions a(I), b(I), c(I) can be found in the source code.

This formula breaks down at low energies, and it only applies for $\beta\gamma > 0.13$ (e.g. $T > 7.9$ MeV for a proton). For $\beta\gamma \leq 0.13$ the shell correction term is calculated as:

$$C_e(I, \beta\gamma)\Big|_{\beta\gamma \leq 0.13} = C_e(I, \beta\gamma = 0.13)\frac{\ln(T/T_{2l})}{\ln(7.9 \text{ MeV}/T_{2l})}$$

hence the correction becomes progressively smaller from $T = 7.9$ MeV to $T = T_{2l} = 2$ MeV.

Since $M \gg m_e$, the ionisation loss does not depend on the hadron mass, but on its velocity. Therefore the energy loss of a charged hadron with kinetic energy, T, is the same as the energy loss of a proton with the same velocity. The corresponding kinetic energy of the proton T_p is

$$T_{proton} = \frac{M_{proton}}{M}\,T. \tag{12.38}$$

At initialisation stage of Geant4 the dE/dx tables and range tables for all materials are calculated only for protons and antiprotons. During run time the energy loss and the range of any hadron or ion are recalculated using the scaling relation (12.38).

12.10.3   Barkas and Bloch effects

The accuracy of the Bethe-Bloch stopping power formula (12.38) can be improved if the higher order terms are taken into account:

$$-\frac{dE}{dx} = K\frac{Z_h^2}{\beta^2}(L_0 + Z_h L_1 + Z_h^2 L_2), \tag{12.39}$$

where L_1 is the Barkas term [9], describing the difference between ionisation of positively and negatively charged particles, and L_2 is the Bloch term.

The Barkas effect for kinetic energy of protons or antiprotons greater than $500 keV$ can be described as [10]:

$$L_1 = \frac{F\left(b/\sqrt{x}\right)}{\sqrt{Zx^3}}, \quad x = \frac{\beta^2 c^2}{Zv_0^2}, \quad b = 0.8Z^{\frac{1}{6}}\left(1 + 6.02Z^{-1.19}\right), \tag{12.40}$$

where v_0 is the Bohr velocity (corresponding to proton energy $T_p = 25 keV$), and the function F is tabulated according to [10].

The Bloch term [11] can be expressed in the following way:

$$Z_h^2 L_2 = -y^2 \sum_{j=1}^{\inf} \frac{1}{j(j^2 + y^2)}, \quad y = \frac{Z_h}{137\beta}. \tag{12.41}$$

Note, that for $y \ll 1$ the simplified expression $Z_h^2 L_2 = -1.202y^2$ can be used.

Both the Barkas and Bloch terms break scaling of ionisation losses if the absolute value of particle charge is different from unity, because the particle charge Z_h is not factorised in the formula (12.39). To take these terms into account correction is made at each step of the simulation for the value of dE/dx re-calculated from the proton or antiproton tables. There is the possibility to switch off the calculation of these terms.

12.10.4 Energy losses of slow positive hadrons

At low energies the total energy loss is usually described in terms of *electronic stopping power* $S_e = -dE/dx$. For charged hadron with velocity $\beta < 0.05$ (corresponding to 1 MeV for protons), formula (12.35) becomes inaccurate. In this case the velocity of the incident hadron is comparable to the velocity of atomic electrons. At very low energies, when $\beta < 0.01$, the model of a free electron gas [12] predicts the stopping power to be proportional to the hadron velocity, but it is not as accurate as the Bethe-Bloch formalism. The intermediate region $0.01 < \beta < 0.05$ is not covered by precise theories. In this energy interval the Bragg peak of ionisation loss occurs.

To simulate slow proton energy loss the following parametrisation from the review [13] was implemented:

$$
\begin{aligned}
S_e &= A_1 E^{1/2}, & 1 \ keV < T_p < 10 \ keV, \\
S_e &= \frac{S_{low} S_{high}}{S_{low} + S_{high}}, & 10 \ keV < T_p < 1 \ MeV, \\
S_{low} &= A_2 E^{0.45}, \\
S_{high} &= \frac{A_3}{E} \ln\left(1 + \frac{A_4}{E} + A_5 E\right), \\
S_e &= \frac{A_6}{\beta^2}\left[\ln\frac{A_7\beta^2}{1-\beta^2} - \beta^2 - \sum_{i=0}^{4} A_{i+8}(\ln E)^i\right], & 1 \ MeV < T_p < 100 \ MeV,
\end{aligned}
$$
(12.42)

where S_e is the stopping power in $[eV/10^{15}atoms/cm^2]$, $E = T_p/M_p[keV/amu]$, A_i are twelve fitting parameters found individually for each atom for atomic numbers from 1 to 92. This parametrisation is used in the interval of proton kinetic energy:

$$T_1 < T_p < T_2, \tag{12.43}$$

where $T_1 = 1 \ keV$ is the minimal kinetic energy of protons in the tables of Ref.[13], T_2 is an arbitrary value between 2 MeV and 100 MeV, since in this

Table 12.1: The list of parameterisations available.

Name	Particle	Source
Ziegler1977p	proton	J.F. Ziegler parameterisation [13]
Ziegler1977He	He^4	J.F. Ziegler parameterisation [15]
Ziegler1985p	proton	TRIM'85 parameterisation [16]
ICRU_R49p	proton	ICRU parameterisation [14]
ICRU_R49He	He^4	ICRU parameterisation [14]

range both the parametrisation (12.42) and the Bethe-Bloch formula (12.38) have practically the same accuracy and are close to each other. Currently the value $T_2 = 2\ MeV$ is chosen.

To avoid problems in computation and to provide a continuous dE/dx function, the factor

$$F = \left(1 + B\frac{T_2}{T_p}\right) \tag{12.44}$$

is multiplied by the value of dE/dx for $T_p > T_2$. The parameter B is determined for each element of the material in order to provide continuity at $T_p = T_2$. The value of B for all atoms is less than 0.01. For the simulation of the stopping power of very slow protons the model of a free electron gas [12] is used:

$$S_e = A\sqrt{T_p},\ \ T_p < T_1. \tag{12.45}$$

The parameter A is defined for each atom by requiring the stopping power to be continuous at $T_p = T_1$. Currently the value used is $T_1 = 1\ keV$.

Note that if the cut kinetic energy is small ($T_c < T_{max}$), then the average energy deposit giving rise to δ-electron production (12.33) is subtracted from the value of the stopping power S_e, which is calculated by formula (12.42).

Alternative parametrisations of proton energy loss are also available within Geant4 (Table 12.1). The parameterisation formulae in Ref.[14] are the same as in Ref.([13]) for the kinetic energy of protons $T_p < 1\ MeV$, but the values of the parameters are different. The type of parameterisation is optional and can be chosen by the user separately for each particle at the initialisation stage of Geant4.

12.10.5   Energy loss of alpha particles

The accuracy of the data for the ionisation losses of α-particles in all elements [14, 15] is comparable to the accuracy of the data for proton energy

loss [13, 14]. In the GEANT4 energy loss model for α-particles the Bethe-Bloch formula is used for kinetic energy $T > T_2$, where T_2 is the arbitrary parameter, currently set to 8 MeV. For lower energies a parameterisation is performed. In the energy range of the Bragg peak, 1 $keV < T < 10$ MeV, the parameterisation is:

$$
\begin{aligned}
S_e &= \frac{S_{low}S_{high}}{S_{low} + S_{high}}, \\
S_{low} &= A_1 T^{A_2}, \\
S_{high} &= \frac{A_3}{T} \ln\left(1 + \frac{A_4}{T} + A_5 T\right),
\end{aligned}
$$

(12.46)

where S_e is the electronic stopping power in $[eV/10^{15}atoms/cm^2]$, T is the kinetic energy of α-particles in MeV, A_i are the five fitting parameters fitted individually for each atom for atomic numbers from 1 to 92.

For higher energies $T > 10$ MeV, another parametrisation [15] is applied

$$
S_e = exp\left(A_6 + A_7 E + A_8 E^2 + A_9 E^3\right), \ E = ln(1/T). \tag{12.47}
$$

To ensure a continuous dE/dx function from the energy range of the Bethe-Bloch formula to the energy range of the parameterisation, the factor

$$
F = \left(1 + B\frac{T_2}{T}\right) \tag{12.48}
$$

is multiplied by the value of S_e as predicted by the Bethe-Bloch formula for $T > T_2$. The parameter B is determined for each element of the material in order to ensure continuity at $T_p = T_2$. The value of B for different atoms is usually less than 0.01.

For kinetic energies of α-particles $T < 1$ keV the model of free electron gas [12] is used

$$
S_e = A\sqrt{T}, \tag{12.49}
$$

The parameter A is defined for each atom by requiring the stopping power to be continuous at $T = 1$ keV.

12.10.6 Effective charge of ions

For hadrons or ions the scaling relation can be written as

$$
S_{ei}(T) = Z_{eff}^2 \cdot S_{ep}(T_p), \tag{12.50}
$$

where S_{ei} is the ion stopping power, S_{ep} is the proton stopping power at the energy scaled according (12.38), and Z_{eff} is effective charge of the particle, which has to be used in all expressions in place of Z_h. For fast particles it is equal to the particle charge Z_h, but for slow ions it differs significantly because a slow ion picks up electrons from the medium. The ion effective charge is expressed via the ion charge Z_h and the fractional effective charge of ion γ_i:

$$Z_{eff} = \gamma_i Z_h. \tag{12.51}$$

For helium ions fractional effective charge is parameterised for all elements with good accuracy [16] according to:

$$(\gamma_{He})^2 = \left(1 - \exp\left[-\sum_{j=0}^{5} C_j Q^j\right]\right)\left(1 + \frac{7 + 0.05Z}{1000}\exp(-(7.6 - Q)^2)\right)^2,$$
$$Q = \max(0, \ln T_p), \tag{12.52}$$

where the coefficients C_j are the same for all elements, and the helium ion kinetic energy is in keV/amu.

The following expression is used for heavy ions [17]:

$$\gamma_i = \left(q + \frac{1 - q}{2}\left(\frac{v_0}{v_F}\right)^2 \ln\left(1 + \Lambda^2\right)\right)\left(1 + \frac{(0.18 + 0.0015Z)\exp(-(7.6 - Q)^2)}{Z_i^2}\right), \tag{12.53}$$

where q is the fractional average charge of the ion, v_0 is the Bohr velocity, v_F is the Fermi velocity of the electrons in the target medium, and Λ is the term taking into account the screening effect. In Ref. [17], Λ is estimated to be:

$$\Lambda = 10\frac{v_F}{v_0}\frac{(1 - q)^{2/3}}{Z_i^{1/3}(6 + q)}. \tag{12.54}$$

The Fermi velocity of the medium is of the same order as the Bohr velocity, and its exact value depends on the detailed electronic structure of the medium. Experimental data on the Fermi velocity are taken from Ref.[16]. The expression for the fractional average charge of the ion is the following:

$$q = [1 - \exp(0.803y^{0.3} - 1.3167y^{0.6} - 0.38157y - 0.008983y^2)], \tag{12.55}$$

where y is a parameter that depends on the ion velocity v_i

$$y = \frac{v_i}{v_0 Z^{2/3}}\left(1 + \frac{v_F^2}{5v_i^2}\right). \tag{12.56}$$

The parametrisation described in this chapter is only valid if the reduced kinetic energy of the ion is higher than the lower limit of the energy:

$$T_p > \max\left(3.25\ keV, \frac{25\ keV}{Z^{2/3}}\right). \tag{12.57}$$

If the ion energy is lower, then the free electron gas model (12.49) is used to calculate the stopping power.

12.10.7 Energy losses of slow negative particles

At low energies, e.g. below a few MeV for protons/antiprotons, the Bethe-Bloch formula is no longer accurate in describing the energy loss of charged hadrons and higher Z terms should be taken in account. Odd terms in Z lead to a significant difference between energy loss of positively and negatively charged particles. The energy loss of negative hadrons is scaled from that of antiprotons. The antiproton energy loss is calculated in the following way:

- if the material is elemental, the quantum harmonic oscillator model is used, as described in [18] and references therein. The lower limit of applicability of the model is chosen for all materials at 50 keV. Below this value stopping power is set to constant equal to the dE/dx at 50 keV.

- if the material is not elemental, the energy loss is calculated down to 500 keV using the Barkas correction (12.48) and at lower energies fitting the proton energy loss curve.

12.10.8 Energy losses of hadrons in compounds

To obtain energy losses in a mixture or compound, the absorber can be thought of as made up of thin layers of pure elements with weights proportional to the electron density of the element in the absorber (Bragg's rule):

$$\frac{dE}{dx} = \sum_i \left(\frac{dE}{dx}\right)_i, \tag{12.58}$$

where the sum is taken over all elements of the absorber, i is the number of the element, $\left(\frac{dE}{dx}\right)_i$ is energy loss in the pure i-th element.

Bragg's rule is very accurate for relativistic particles when the interaction of electrons with a nucleus is negligible. But at low energies the accuracy of Bragg's rule is limited because the energy loss to the electrons in any material

depends on the detailed orbital and excitation structure of the material. In the description of Geant4 materials there is a special attribute: the chemical formula. It is used in the following way:

- if the data on the stopping power for a compound as a function of the proton kinetic energy is available (Table 12.2), then the direct parametrisation of the data for this material is performed;

- if the data on the stopping power for a compound is available for only one incident energy (Table 12.3), then the computation is performed based on Bragg's rule and the chemical factor for the compound is taken into account;

- if there are no data for the compound, the computation is performed based on Bragg's rule.

In the review [19] the parametrisation stopping power data are presented as

$$S_e(T_p) = S_{Bragg}(T_p) \left[1 + \frac{f(T_p)}{f(125 \ keV)} \left(\frac{S_{exp}(125 \ keV)}{S_{Bragg}(125 \ keV)} - 1 \right) \right], \quad (12.59)$$

where $S_{exp}(125 \ keV)$ is the experimental value of the energy loss for the compound for 125 keV protons or the reduced experimental value for He ions, $S_{Bragg}(T_p)$ is a value of energy loss calculated according to Bragg's rule, and $f(T_p)$ is a universal function, which describes the disappearance of deviations from Bragg's rule for higher kinetic energies according to:

$$f(T_p) = \frac{1}{1 + \exp\left[1.48\left(\frac{\beta(T_p)}{\beta(25 \ keV)} - 7.0 \right) \right]}, \quad (12.60)$$

where $\beta(T_p)$ is the relative velocity of the proton with kinetic energy T_p.

12.10.9 Nuclear stopping powers

Low energy ions transfer their energy not only to electrons of a medium but also to the nuclei of the medium due to the elastic Coulomb collisions. This contribution to the energy loss is called *nuclear stopping power*. It is parametrised [15, 16, 14] using a universal parameterisation for reduced ion energy, ϵ, which depends on ion parameters and on the charge, Z_t, and the mass, M_t, of the target nucleus:

$$\epsilon = \frac{32.536 T M_t}{Z_{eff} Z_t (M + M_t) \sqrt{Z_{eff}^{0.23} + Z_t^{0.23}}}. \quad (12.61)$$

Table 12.2: The list of chemical formulae of compounds for which parametrisation of stopping power as a function of kinetic energy is in Ref.[14].

Number	Chemical formula
1.	AlO
2.	C_2O
3.	CH_4
4.	(C_2H_4)_N-Polyethylene
5.	(C_2H_4)_N-Polypropylene
6.	(C_8H_8)_N
7.	C_3H_8
8.	SiO_2
9.	H_2O
10.	H_2O-Gas
11.	Graphite

The universal reduced nuclear stopping power, s_n, is determined by J. Moliere in the framework of Thomas-Fermi potential [20]. The corresponding tabulation from Ref.[14] is implemented. To transform the value of nuclear stopping power from reduced units to $[eV/10^{15}atoms/cm^2]$ the following formula is used:

$$S_n = s_n \frac{8.462 Z_i Z_t M_i}{(M_i + M_t)\sqrt{Z_i^{0.23} + Z_t^{0.23}}}.$$ (12.62)

The effect of nuclear stopping power is very small at high energies, but it is of the same order of magnitude as electronic stopping power for very slow ions (e.g. for protons, $T_p < 1keV$).

12.10.10 Fluctuations of energy losses of hadrons

The total continuous energy loss of charged particles is a stochastic quantity with a distribution described in terms of a straggling function. The straggling is partially taken into account by the simulation of energy loss by the production of δ-electrons with energy $T > T_c$. However, continuous energy loss also has fluctuations. Hence in the current GEANT4 implementation two different models of fluctuations are applied depending on the value of the parameter κ which is the lower limit of the number of interactions of the particle in the step. The default value chosen is $\kappa = 10$. To select a model

Table 12.3: The list of chemical formulae of compounds for which the *chemical factor* is calculated from the data of Ref.[19].

Number	Chemical formula	Number	Chemical formula
1.	H_2O	28.	C_2H_6
2.	C_2H_4O	29.	C_2F_6
3.	C_3H_6O	30.	C_2H_6O
4.	C_2H_2	31.	C_3H_6O
5.	C_H_3OH	32.	$C_4H_{10}O$
6.	C_2H_5OH	33.	C_2H_4
7.	C_3H_7OH	34.	C_2H_4O
8.	C_3H_4	35.	C_2H_4S
9.	NH_3	36.	SH_2
10.	$C_{14}H_{10}$	37.	CH_4
11.	C_6H_6	38.	$CCLF_3$
12.	C_4H_{10}	39.	CCl_2F_2
13.	C_4H_6	40.	$CHCl_2F$
14.	C_4H_8O	41.	$(CH_3)_2S$
15.	CCl_4	42.	N_2O
16.	CF_4	43.	$C_5H_{10}O$
17.	C_6H_8	44.	C_8H_6
18.	C_6H_{12}	45.	$(CH_2)_N$
19.	$C_6H_{10}O$	46.	$(C_3H_6)_N$
20.	C_6H_{10}	47.	$(C_8H_8)_N$
21.	C_8H_{16}	48.	C_3H_8
22.	C_5H_{10}	49.	C_3H_6-Propylene
23.	C_5H_8	50.	C_3H_6O
24.	C_3H_6-Cyclopropane	51.	C_3H_6S
25.	$C_2H_4F_2$	52.	C_4H_4S
26.	$C_2H_2F_2$	53.	C_7H_8
27.	$C_4H_8O_2$		

for thick absorbers the following boundary conditions are used:

$$\Delta E > T_c \kappa) \ \ or \ \ T_c < I\kappa, \tag{12.63}$$

where ΔE is the mean continuous energy loss in a track segment of length s, T_c is the cut kinetic energy of δ-electrons, and I is the average ionisation potential of the atom.

For long path lengths the straggling function approaches the Gaussian distribution with Bohr's variance [14]:

$$\Omega^2 = K N_{el} \frac{Z_h^2}{\beta^2} T_c s f \left(1 - \frac{\beta^2}{2} \right), \tag{12.64}$$

where f is a screening factor, which is equal to unity for fast particles, whereas for slow positively charged ions with $\beta^2 < 3Z(v_0/c)^2$ $f = a + b/Z_{eff}^2$, where parameters a and b are parametrised for all atoms [22, 23].

For short path lengths, when the condition 12.63 is not satisfied, the model described in the charter 7.2 is applied.

12.10.11 Sampling

At each step for a charged hadron or ion in an absorber, the step limit is calculated using range tables for protons or antiprotons depending on the particle charge. If the reduced particle energy $T_p < T_2$ the step limit is forced to be not longer than $\alpha R(T_2)$, where $R(T_2)$ is the range of the particle with the reduced energy T_2, α is an arbitrary coefficient, which is currently set to 0.05 in order to provide at least 20 steps for particles in the Bragg peak energy range. In each step continuous energy loss of the particle is calculated using loss tables for protons or antiprotons for $T_p > T_2$. For lower energies, continuous energy loss is calculated using the effective charge approach, chemical factors, and nuclear stopping powers. If the step of the particle is limited by the ionisation process the sampling of δ-electron production is performed. (A short overview of the method is given in Chapter 2.)

Apart from the normalisation, the cross-section (12.31) can be written as :

$$\frac{d\sigma}{dT} \sim f(T) \, g(T) \ \ with \ \ T \in [T_c, \ T_{max}] \tag{12.65}$$

with :

$$f(T) = \left(\frac{1}{T_c} - \frac{1}{T_{max}} \right) \frac{1}{T^2}$$

$$g(T) = 1 - \beta^2 \frac{T}{T_{max}} + S(T),$$

where $S(T)$ is a spin dependent term (12.31). For a spin-0 particle this term is zero, for a spin-$\frac{1}{2}$ particle $S(T) = T^2/2E^2$, whilst for spin-1 the expression is more complicated.

The energy, T, is sampled by :

1. Sample T from $f(T)$.

2. Calculate the rejection function $g(T)$ and accept the sampled T with a probability of $g(T)$.

After the successful sampling of the energy, the polar angles of the emitted electron are generated with respect to the direction of the incident particle. The azimuthal angle, ϕ, is generated isotropically; the polar angle θ is calculated from the energy momentum conservation. This information is used to calculate the energy and momentum of both particles and to transform them into the *global* coordinate system.

12.10.12 PIXE

PIXE is simulated by calculating cross-sections according to [24] and [25] to identify the primary ionised shell, and generating the subsequent atomic relaxation as described in 12.9. Sampling of excitations is carried out for both the continuous and the discrete parts of the process.

12.10.13 Status of this document

21.11.2000 Created by V.Ivanchenko
30.05.2001 Modified by V.Ivanchenko
23.11.2001 Modified by M.G. Pia to add PIXE section.
19.01.2002 Minor corrections (mma)
13.05.2002 Minor corrections (V.Ivanchenko)
28.08.2002 Minor corrections (V.Ivanchenko)

Bibliography

[1] V.N. Ivanchenko et al., GEANT4 Simulation of Energy Losses of Slow Hadrons, CERN-99-121, INFN/AE-99/20, (September 1999).

[2] S. Giani et al., GEANT4 Simulation of Energy Losses of Ions, CERN-99-300, INFN/AE-99/21, (November 1999).

[3] D.E. Groom et al., Eur. Phys. Jour. C15 (2000) 1.

[4] B. Rossi, High Energy Particles, Pretice-Hall, Inc., Englewood Cliffs, NJ, 1952.

[5] H. Bethe, Ann. Phys. 5 (1930) 325.

[6] (A. Allisy et al), Stopping Powers for Electrons and Positrons, ICRU Report 37, 1984.

[7] R.M. Sternheimer. Phys.Rev. B3 (1971) 3681.

[8] W.H. Barkas. Technical Report 10292,UCRL, August 1962.

[9] W.H. Barkas, W. Birnbaum, F.M. Smith, Phys. Rev. 101 (1956) 778.

[10] J.C. Ashley, R.H. Ritchie and W. Brandt, Phys. Rev. B5 (1972) 1.

[11] F. Bloch, Ann. Phys. 16 (1933) 285.

[12] J. Linhard and A. Winther, Mat. Fys. Medd. Dan. Vid. Selsk. 34, No 10 (1963).

[13] H.H. Andersen and J.F. Ziegler, The Stopping and Ranges of Ions in Matter. Vol.3, Pergamon Press, 1977.

[14] ICRU (A. Allisy et al), Stopping Powers and Ranges for Protons and Alpha Particles, ICRU Report 49, 1993.

[15] J.F. Ziegler, The Stopping and Ranges of Ions in Matter. Vol.4, Pergamon Press, 1977.

[16] J.F. Ziegler, J.P. Biersack, U . Littmark, The Stopping and Ranges of Ions in Solids. Vol.1, Pergamon Press, 1985.

[17] W. Brandt and M. Kitagawa, Phys. Rev. B25 (1982) 5631.

[18] P. Sigmund, Nucl. Instr. and Meth. B85 (1994) 541.

[19] J.F. Ziegler and J.M. Manoyan, Nucl. Instr. and Meth. B35 (1988) 215.

[20] G. Moliere, Theorie der Streuung schneller geladener Teilchen I; Einzelstreuungam abbgeschirmten Coulomb-Feld, Z. f. Naturforsch, A2 (1947) 133.

[21] GEANT3 manual, CERN Program Library Long Writeup W5013 (October 1994).

[22] Q. Yang, D.J. O'Connor, Z. Wang, Nucl. Instr. and Meth. B61 (1991) 149.

[23] W.K. Chu, in: Ion Beam Handbook for Material Analysis, edt. J.W. Mayer and E. Rimini, Academic Press, NY, 1977.

[24] M. Gryzinski, Phys. Rev. A 135 (1965) 305.

[25] M. Gryzinski, Phys. Rev. A 138 (1965) 322.

12.11 Penelope physics

12.11.1 Introduction

A new set of physics processes for photons, electrons and positrons is implemented in Geant4: it includes Compton scattering, photoelectric effect, Rayleigh scattering, gamma conversion, bremsstrahlung, ionization (to be released) and positron annihilation (to be released). These processes are the Geant4 implementation of the physics models developed for the PENELOPE code (PENetration and Energy LOss of Positrons and Electrons), version 2001, that are described in detail in Ref. [1]. The Penelope models have been specifically developed for Monte Carlo simulation and great care was given to the low energy description (i.e. atomic effects, etc.). Hence, these implementations provide reliable results for energies down to a few hundred eV and can be used up to ~1 GeV [1, 2]. For this reason, they may be used in Geant4 as an alternative to the Low Energy processes. For the same physics processes, the user now has more alternative descriptions from which to choose, including the cross section calculation and the final state sampling.

12.11.2 Compton scattering

Total cross section

The total cross section of the Compton scattering process is determined from an analytical parameterization. For γ energy E greater than 5 MeV, the usual Klein-Nishina formula is used for $\sigma(E)$. For $E < 5$ MeV a more accurate parameterization is used, which takes into account atomic binding effects and Doppler broadening [3]:

$$\sigma(E) = 2\pi \int_{-1}^{1} \frac{r_e^2}{2} \frac{E_C^2}{E^2} \left(\frac{E_C}{E} + \frac{E}{E_C} - \sin^2\theta \right) \cdot \sum_{shells} f_i \Theta(E - U_i) n_i(p_z^{max}) \, d(\cos\theta) \tag{12.66}$$

where:
r_e = classical radius of the electron;
m_e = mass of the electron;
θ = scattering angle;
E_C = Compton energy

$$= \frac{E}{1 + \frac{E}{m_e c^2}(1 - \cos\theta)}$$

f_i = number of electrons in the i-th atomic shell;

U_i = ionisation energy of the i-th atomic shell;

Θ = Heaviside step function;

p_z^{max} = highest possible value of p_z (projection of the initial momentum of the electron in the direction of the scattering angle)

$$= \frac{E(E - U_i)(1 - \cos\theta) - m_e c^2 U_i}{c\sqrt{2E(E - U_i)(1 - \cos\theta) + U_i^2}}.$$

Finally,

$$n_i(x) =$$

$$\begin{cases} \frac{1}{2}e^{[\frac{1}{2}-(\frac{1}{2}-\sqrt{2}J_{i0}x)^2]} & \text{if } x < 0 \\ 1 - \frac{1}{2}e^{[\frac{1}{2}-(\frac{1}{2}+\sqrt{2}J_{i0}x)^2]} & \text{if } x > 0 \end{cases} \qquad (12.67)$$

where J_{i0} is the value of the p_z-distribution profile $J_i(p_z)$ for the i-th atomic shell calculated in $p_z = 0$. The values of J_{i0} for the different shells of the different elements are tabulated from the Hartree-Fock atomic orbitals of Ref. [4].

The integration of Eq.(12.66) is performed numerically using the 20-point Gaussian method. For this reason, the initialization of the Penelope Compton process is somewhat slower than the Low Energy process.

Sampling of the final state

The polar deflection $\cos\theta$ is sampled from the probability density function

$$P(\cos\theta) = \frac{r_e^2}{2}\frac{E_C^2}{E^2}\left(\frac{E_C}{E} + \frac{E}{E_C} - \sin^2\theta\right)\sum_{shells} f_i\Theta(E - U_i)n_i(p_z^{max}) \quad (12.68)$$

(see Ref. [1] for details on the sampling algorithm). Once the direction of the emerging photon has been set, the active electron shell i is selected with relative probability equal to $Z_i\Theta(E - U_i)n_i[p_z^{max}(E,\theta)]$. A random value of p_z is generated from the analytical Compton profile [4]. The energy of the emerging photon is

$$E' = \frac{E\tau}{1 - \tau t}\left[(1 - \tau t \cos\theta) + \frac{p_z}{|p_z|}\sqrt{(1 - \tau t \cos\theta)^2 - (1 - t\tau^2)(1 - t)}\right],$$
$$(12.69)$$

where

$$t = \left(\frac{p_z}{m_e c}\right)^2 \quad \text{and} \quad \tau = \frac{E_C}{E}. \qquad (12.70)$$

The azimuthal scattering angle ϕ of the photon is sampled uniformly in the interval $(0,2\pi)$. It is assumed that the Compton electron is emitted with

263

energy $E_e = E - E' - U_i$, with polar angle θ_e and azimuthal angle $\phi_e = \phi + \pi$, relative to the direction of the incident photon. In this case $\cos\theta_e$ is given by

$$\cos\theta_e = \frac{E - E'\cos\theta}{\sqrt{E^2 + E'^2 - 2EE'\cos\theta}}. \tag{12.71}$$

Since the active electron shell is known, characteristic x-rays and electrons emitted in the de-excitation of the ionized atom can also be followed. The de-excitation is simulated as described in section 12.9. For further details see [1].

12.11.3 Rayleigh scattering

Total cross section

The total cross section of the Rayleigh scattering process is determined from an analytical parameterization. The atomic cross section for coherent scattering is given approximately by [5]

$$\sigma(E) = \pi r_e^2 \int_{-1}^{1} \frac{1 + \cos^2\theta}{2} [F(q,Z)]^2 \, d\cos\theta, \tag{12.72}$$

where $F(q,Z)$ is the atomic form factor, Z is the atomic number and q is the magnitude of the momentum transfer, i.e.

$$q = 2\,\frac{E}{c}\,\sin\left(\frac{\theta}{2}\right). \tag{12.73}$$

In the numerical calculation the following analytical approximations are used for the form factor:

$$F(q,Z) = f(x,Z) =$$
$$\begin{cases} Z\,\frac{1+a_1 x^2 + a_2 x^3 + a_3 x^4}{(1+a_4 x^2 + a_5 x^4)^2} & \text{or} \\ \max[f(x,Z), F_K(x,Z)] & \text{if } Z > 10 \text{ and } f(x,Z) < 2 \end{cases} \tag{12.74}$$

where

$$F_K(x,Z) = \frac{\sin(2b\arctan Q)}{bQ(1+Q^2)^b}, \tag{12.75}$$

with

$$x = 20.6074\frac{q}{m_e c}, \quad Q = \frac{q}{2m_e ca}, \quad b = \sqrt{1-a^2}, \quad a = \alpha\left(Z - \frac{5}{16}\right), \tag{12.76}$$

where α is the fine-structure constant. The function $F_K(x,Z)$ is the contribution to the atomic form factor due to the two K-shell electrons (see [6]).

264

The parameters of expression $f(x, Z)$ have been determined in Ref. [6] for Z=1 to 92 by numerically fitting the atomic form factors tabulated in Ref. [7]. The integration of Eq.(12.72) is performed numerically using the 20-point Gaussian method. For this reason the initialization of the Penelope Rayleigh process is somewhat slower than the Low Energy process.

Sampling of the final state

The angular deflection $\cos\theta$ of the scattered photon is sampled from the probability distribution function

$$P(\cos\theta) \;=\; \frac{1 + \cos^2\theta}{2}[F(q, Z)]^2.\qquad(12.77)$$

For details on the sampling algorithm (which is quite heavy from the computational point of view) see Ref. [1]. The azimuthal scattering angle ϕ of the photon is sampled uniformly in the interval $(0,2\pi)$.

12.11.4   Gamma conversion

Total cross section

The total cross section of the γ conversion process is determined from the data [8], as described in section 12.1.4.

Sampling of the final state

The energies E_- and E_+ of the secondary electron and positron are sampled using the Bethe-Heitler cross section with the Coulomb correction, using the semiempirical model of Ref. [6]. If

$$\epsilon \;=\; \frac{E_- + m_e c^2}{E}\qquad(12.78)$$

is the fraction of the γ energy E which is taken away from the electron,

$$\kappa \;=\; \frac{E}{m_e c^2}\quad\text{and}\quad a = \alpha Z,\qquad(12.79)$$

the differential cross section, which includes a low-energy correction and a high-energy radiative correction, is

$$\frac{d\sigma}{d\epsilon} \;=\; r_e^2 a(Z + \eta)C_r\frac{2}{3}\Big[2\Big(\frac{1}{2} - \epsilon\Big)^2\phi_1(\epsilon) + \phi_2(\epsilon)\Big],\qquad(12.80)$$

where:

$$\phi_1(\epsilon) = \frac{7}{3} - 2\ln(1+b^2) - 6b\arctan(b^{-1})$$
$$-b^2[4 - 4b\arctan(b^{-1}) - 3\ln(1+b^{-2})]$$
$$+4\ln(Rm_ec/\hbar) - 4f_C(Z) + F_0(\kappa, Z) \qquad (12.81)$$

and

$$\phi_2(\epsilon) = \frac{11}{6} - 2\ln(1+b^2) - 3b\arctan(b^{-1})$$
$$+\frac{1}{2}b^2[4 - 4b\arctan(b^{-1}) - 3\ln(1+b^{-2})]$$
$$+4\ln(Rm_ec/\hbar) - 4f_C(Z) + F_0(\kappa, Z), \qquad (12.82)$$

with

$$b = \frac{Rm_ec}{\hbar}\frac{1}{2\kappa}\frac{1}{\epsilon(1-\epsilon)}. \qquad (12.83)$$

In this case R is the screening radius for the atom Z (tabulated in [10] for Z=1 to 92) and η is the contribution of pair production in the electron field (rather than in the nuclear field). The parameter η is approximated as

$$\eta = \eta_\infty(1 - e^{-v}), \qquad (12.84)$$

where

$$v = (0.2840 - 0.1909a)\ln(4/\kappa) + (0.1095 + 0.2206a)\ln^2(4/\kappa)$$
$$+(0.02888 - 0.04269a)\ln^3(4/\kappa)$$
$$+(0.002527 + 0.002623)\ln^4(4/\kappa) \quad (12.85)$$

and η_∞ is the contribution for the atom Z in the high-energy limit and is tabulated for Z=1 to 92 in Ref. [10]. In the Eq.(12.80), the function $f_C(Z)$ is the high-energy Coulomb correction of Ref. [9], given by

$$f_C(Z) = a^2[(1+a^2)^{-1} + 0.202059 - 0.03693a^2 + 0.00835a^4$$
$$-0.00201a^6 + 0.00049a^8 - 0.00012a^{10} + 0.00003a^{12}]; \quad (12.86)$$

$C_r = 1.0093$ is the high-energy limit of Mork and Olsen's radiative correction (see Ref. [10]); $F_0(\kappa, Z)$ is a Coulomb-like correction function, which has been analytically approximated as [1]

$$F_0(\kappa, Z) = (-0.1774 - 12.10a + 11.18a^2)(2/\kappa)^{1/2}$$
$$+(8.523 + 73.26a - 44.41a^2)(2/\kappa)$$
$$-(13.52 + 121.1a - 96.41a^2)(2/\kappa)^{3/2}$$
$$+(8.946 + 62.05a - 63.41a^2)(2/\kappa)^2. \qquad (12.87)$$

The kinetic energy E_+ of the secondary positron is obtained as

$$E_+ \;=\; E - E_- - 2m_e c^2. \tag{12.88}$$

The polar angles θ_- and θ_+ of the directions of movement of the electron and the positron, relative to the direction of the incident photon, are sampled from the leading term of the expression obtained from high-energy theory (see Ref. [11])

$$p(\cos\theta_\pm) \;=\; a(1 - \beta_\pm \cos\theta_\pm)^{-2}, \tag{12.89}$$

where a is the a normalization constant and $\beta_\pm$ is the particle velocity in units of the speed of light. As the directions of the produced particles and of the incident photon are not necessarily coplanar, the azimuthal angles ϕ_- and ϕ_+ of the electron and of the positron are sampled independently and uniformly in the interval $(0,2\pi)$.

12.11.5 Photoelectric effect

Total cross section

The total photoelectric cross section at a given photon energy E is calculated from the data [12], as described in section 12.1.4.

Sampling of the final state

The incident photon is absorbed and one electron is emitted. The direction of the electron is sampled according to the Sauter distribution [13]. Introducing the variable $\nu = 1 - \cos\theta_e$, the angular distribution can be expressed as

$$p(\nu) \;=\; (2 - \nu)\Big[\frac{1}{A+\nu} + \frac{1}{2}\beta\gamma(\gamma-1)(\gamma-2)\Big]\frac{\nu}{(A+\nu)^3}, \tag{12.90}$$

where

$$\gamma = 1 + \frac{E_e}{m_e c^2}, \quad A = \frac{1}{\beta} - 1, \tag{12.91}$$

E_e is the electron energy, m_e its rest mass and β its velocity in units of the speed of light c. Though the Sauter distribution, strictly speaking, is adequate only for ionisation of the K-shell by high-energy photons, in many practical simulations it does not introduce appreciable errors in the description of any photoionisation event, irrespective of the atomic shell or of the photon energy.
The subshell from which the electron is emitted is randomly selected according to the relative cross sections of subshells, determined at the energy E

by interpolation of the data of Ref. [11]. The electron kinetic energy is the difference between the incident photon energy and the binding energy of the electron before the interaction in the sampled shell. The interaction leaves the atom in an excited state; the subsequent de-excitation is simulated as described in section 12.9.

12.11.6 Bremsstrahlung

Introduction

The class `G4PenelopeBremsstrahlung` calculates the continuous energy loss due to soft γ emission and simulates the photon production by electrons and positrons. As usual, the gamma production threshold T_c for a given material is used to separate the continuous and the discrete parts of the process.

Electrons

The total cross sections are calculated from the data [15], as described in sections 12.1.4 and 12.7.

The energy distribution $\frac{d\sigma}{dW}(E)$, i.e. the probability of the emission of a photon with energy W given an incident electron of kinetic energy E, is generated according to the formula

$$\frac{d\sigma}{dW}(E) \;=\; \frac{F(\kappa)}{\kappa}, \quad \kappa \;=\; \frac{W}{E}. \qquad (12.92)$$

The functions $F(\kappa)$ describing the energy spectra of the outgoing photons are taken from Ref. [14]. For each element Z from 1 to 92, 32 points in κ, ranging from 10^{-12} to 1, are used for the linear interpolation of this function. $F(\kappa)$ is normalized using the condition $F(10^{-12}) = 1$. The energy distribution of the emitted photons is available in the library [14] for 57 energies of the incident electron between 1 keV and 100 GeV. For other primary energies, logarithmic interpolation is used to obtain the values of the function $F(\kappa)$.

The direction of the emitted bremsstrahlung photon is determined by the polar angle θ and the azimuthal angle ϕ. For isotropic media, with randomly oriented atoms, the bremsstrahlung differential cross section is independent of ϕ and can be expressed as

$$\frac{d^2\sigma}{dW\,d\cos\theta} \;=\; \frac{d\sigma}{dW}p(Z,E,\kappa;\cos\theta). \qquad (12.93)$$

Numerical values of the "shape function" $p(Z,E,\kappa;\cos\theta)$, calculated by partial-wave methods, have been published in Ref. [16] for the following

benchmark cases: $Z=$ 2, 8, 13, 47, 79 and 92; $E=$ 1, 5, 10, 50, 100 and 500 keV; $\kappa=$ 0, 0.6, 0.8 and 0.95. It was found in Ref. [1] that the benchmark partial-wave shape function of Ref. [16] can be closely approximated by the analytical form (obtained in the Lorentz-dipole approximation)

$$
p(\cos\theta) = A\frac{3}{8}\Big[1 + \Big(\frac{\cos\theta - \beta'}{1 - \beta'\cos\theta}\Big)^2\Big]\frac{1 - \beta'^2}{(1 - \beta'\cos\theta)^2}
$$
$$
+ (1 - A)\frac{3}{4}\Big[1 - \Big(\frac{\cos\theta - \beta'}{1 - \beta'\cos\theta}m\Big)^2\Big]\frac{1 - \beta'^2}{(1 - \beta'\cos\theta)^2}, \tag{12.94}
$$

with $\beta' = \beta(1 + B)$, if one considers A and B as adjustable parameters. The parameters A and B have been determined, by least squares fitting, for the 144 combinations of atomic numbers, electron energies and reduced photon energies corresponding to the benchmark shape functions tabulated in [16]. The quantities $\ln(AZ\beta)$ and $B\beta$ vary smoothly with Z, β and κ and can be obtained by cubic spline interpolation of their values for the benchmark cases. This permits the fast evaluation of the shape function $p(Z, E, \kappa; \cos\theta)$ for any combination of Z, β and κ.

The stopping power $\frac{dE}{dx}$ due to soft bremsstrahlung is calculated by interpolating in E and κ the numerical data of scaled cross sections of Ref. [17]. The energy and the direction of the outgoing electron are determined by using energy-momentum balance.

Positrons

The radiative differential cross section $\frac{d\sigma^+}{dW}(E)$ for positrons reduces to that for electrons in the high-energy limit, but is smaller for intermediate and low energies. Owing to the lack of more accurate calculations, the differential cross section for positrons is obtained by multiplying the electron differential cross section $\frac{d\sigma^-}{dW}(E)$ by a $\kappa-$indendent factor, i.e.

$$
\frac{d\sigma^+}{dW} = F_p(Z, E)\frac{d\sigma^-}{dW}. \tag{12.95}
$$

The factor $F_p(Z, E)$ is set equal to the ratio of the radiative stopping powers for positrons and electrons, which has been calculated in Ref. [18]. For the actual calculation, the following analytical approximation is used:

$$
F_p(Z, E) = 1 - \exp(-1.2359 \cdot 10^{-1}t + 6.1274 \cdot 10^{-2}t^2 - 3.1516 \cdot 10^{-2}t^3
$$
$$
+ 7.7446 \cdot 10^{-3}t^4 - 1.0595 \cdot 10^{-3}t^5 + 7.0568 \cdot 10^{-5}t^6
$$
$$
- 1.8080 \cdot 10^{-6}t^7) \tag{12.96}
$$

where

$$t = \ln\left(1 + \frac{10^6}{Z^2} \frac{E}{m_e c^2}\right).$$ (12.97)

Because the factor $F_p(Z, E)$ is independent on κ, the energy distribution of the secondary γ's has the same shape as electron bremsstrahlung. Similarly, owing to the lack of numerical data for positrons, it is assumed that the shape of the angular distribution $p(Z, E, \kappa; \cos\theta)$ of the bremsstrahlung photons for positrons is the same as for the electrons.

The energy and direction of the outgoing positron are determined from energy-momentum balance.

12.11.7 Ionisation

The `G4PenelopeIonisation` class calculates the continuous energy loss due to electron and positron ionisation and simulates the δ-ray production by electrons and positrons. The electron production threshold T_c for a given material is used to separate the continuous and the discrete parts of the process.

The simulation of inelastic collisions of electrons and positrons is performed on the basis of a Generalized Oscillation Strength (GOS) model (see Ref. [1] for a complete description). It is assumed that GOS splits into contributions from the different atomic electron shells.

Electrons

The total cross section $\sigma^-(E)$ for the inelastic collision of electrons of energy E is calculated analytically. It can be split into contributions from distant longitudinal, distant transverse and close interactions,

$$\sigma^-(E) = \sigma_{dis,l} + \sigma_{dis,t} + \sigma_{clo}^-.$$ (12.98)

The contributions from distant longitudinal and transverse interactions are

$$\sigma_{dis,l} = \frac{2\pi e^4}{m_e v^2} \sum_{shells} f_k \frac{1}{W_k} \ln\left(\frac{W_k}{Q_k^{min}} \frac{Q_k^{min} + 2m_e c^2}{W_k + 2m_e c^2}\right)\Theta(E - W_k)$$ (12.99)

and

$$\sigma_{dis,t} = \frac{2\pi e^4}{m_e v^2} \sum_{shells} f_k \frac{1}{W_k}\left[\ln\left(\frac{1}{1 - \beta^2}\right) - \beta^2 - \delta_F\right]\Theta(E - W_k)$$ (12.100)

respectively, where:
m_e = mass of the electron;

v = velocity of the electron;

β = velocity of the electron in units of c;

f_k = number of electrons in the k-th atomic shell;

Θ = Heaviside step function;

W_k = resonance energy of the k-th atomic shell oscillator;

Q_k^{min} = minimum kinematically allowed recoil energy for energy transfer W_k

$$= \sqrt{\left[\sqrt{E(E + 2m_ec^2)} - \sqrt{(E - W_k)(E - W_k + 2m_ec^2)}\right]^2 + m_e^2c^4} - m_ec^2;$$

δ_F = Fermi density effect correction, computed as described in Ref. [19].

The value of W_k is calculated from the ionisation energy U_k of the k-th shell as $W_k = 1.65\, U_k$. This relation is derived from the hydrogenic model, which is valid for the innermost shells. In this model, the shell ionisation cross sections are only roughly approximated; nevertheless the ionisation of inner shells is a low-probability process and the approximation has a weak effect on the global transport properties[1].

The integrated cross section for close collisions is the Møller cross section

$$\sigma_{clo}^- = \frac{2\pi e^4}{m_ev^2} \sum_{shells} f_k \int_{W_k}^{\frac{E}{2}} \frac{1}{W^2} F^-(E, W)\, dW, \qquad (12.101)$$

where

$$F^-(E, W) = 1 + \left(\frac{W}{E - W}\right)^2 - \frac{W}{E - W} + \left(\frac{E}{E + m_ec^2}\right)^2 \left(\frac{W}{E - W} + \frac{W^2}{E^2}\right). \qquad (12.102)$$

The integral of Eq.(12.101) can be evaluated analytically. In the final state there are two indistinguishable free electrons and the fastest one is considered as the "primary"; accordingly, the maximum allowed energy transfer in close collisions is $\frac{E}{2}$.

The GOS model also allows evaluation of the spectrum $\frac{d\sigma^-}{dW}$ of the energy W lost by the primary electron as the sum of distant longitudinal, distant transverse and close interaction contributions,

$$\frac{d\sigma^-}{dW} = \frac{d\sigma_{clo}^-}{dW} + \frac{d\sigma_{dis,l}}{dW} + \frac{d\sigma_{dis,t}}{dW}. \qquad (12.103)$$

---

[1]In cases where inner-shell ionisation is directly observed, a more accurate description of the process should be used.

In particular,

$$\frac{d\sigma_{dis,l}}{dW} = \frac{2\pi e^4}{m_e v^2} \sum_{shells} f_k \frac{1}{W_k} \ln\left(\frac{W_k}{Q_-} \frac{Q_- + 2m_e c^2}{W_k + 2m_e c^2}\right) \delta(W - W_k)\Theta(E - W_k),$$

(12.104)

where

$$Q_- = \sqrt{\left[\sqrt{E(E + 2m_e c^2)} - \sqrt{(E-W)(E-W+2m_e c^2)}\right]^2 + m_e^2 c^4} - m_e c^2,$$

(12.105)

$$\frac{d\sigma_{dis,t}}{dW} = \frac{2\pi e^4}{m_e v^2} \sum_{shells} f_k \frac{1}{W_k}\left[\ln\left(\frac{1}{1-\beta^2}\right) - \beta^2 - \delta_F\right]$$
$$\Theta(E - W_k)\delta(W - W_k) \qquad (12.106)$$

and

$$\frac{d\sigma_{clo}^-}{dW} = \frac{2\pi e^4}{m_e v^2} \sum_{shells} f_k \frac{1}{W^2} F^-(E, W)\Theta(W - W_k). \qquad (12.107)$$

Eqs. (12.99), (12.100) and (12.101) derive respectively from the integration in dW of Eqs. (12.104), (12.106) and (12.107) in the interval $[0, W_{max}]$, where $W_{max} = E$ for distant interactions and $W_{max} = \frac{E}{2}$ for close. The analytical GOS model provides an accurate *average* description of inelastic collisions. However, the continuous energy loss spectrum associated with single distant excitations of a given atomic shell is approximated as a single resonance (a δ distribution). As a consequence, the simulated energy loss spectra show unphysical narrow peaks at energy losses that are multiples of the resonance energies. These spurious peaks are automatically smoothed out after multiple inelastic collisions.

The explicit expression of $\frac{d\sigma^-}{dW}$, Eq. (12.103), allows the analytic calculation of the partial cross sections for soft and hard ionisation events, i.e.

$$\sigma_{soft}^- = \int_0^{T_c} \frac{d\sigma^-}{dW}dW \quad \text{and} \quad \sigma_{hard}^- = \int_{T_c}^{W_{max}} \frac{d\sigma^-}{dW}dW. \qquad (12.108)$$

The first stage of the simulation is the selection of the active oscillator k and the oscillator branch (distant or close).

In distant interactions with the k-th oscillator, the energy loss W of the primary electron corresponds to the excitation energy W_k, i.e. $W = W_k$. If the interaction is transverse, the angular deflection of the projectile is neglected, i.e. $\cos\theta = 1$. For longitudinal collisions, the distribution of the recoil energy

Q is given by

$$P_k(Q) = \begin{cases} \dfrac{1}{Q[1+Q/(2m_ec^2)]} & \text{if } Q_- < Q < W_{max} \\ 0 & \text{otherwise} \end{cases} \tag{12.109}$$

Once the energy loss W and the recoil energy Q have been sampled, the polar scattering angle is determined as

$$\cos\theta = \frac{E(E+2m_ec^2)+(E-W)(E-W+2m_ec^2)-Q(Q+2m_ec^2)}{2\sqrt{E(E+2m_ec^2)(E-W)(E-W+2m_ec^2)}}. \tag{12.110}$$

The azimuthal scattering angle ϕ is sampled uniformly in the interval $(0,2\pi)$. For close interactions, the distributions for the reduced energy loss $\kappa \equiv W/E$ for electrons are

$$P_k^-(\kappa) = \left[\frac{1}{\kappa^2}+\frac{1}{(1-\kappa)^2}-\frac{1}{\kappa(1-\kappa)}+\left(\frac{E}{E+m_ec^2}\right)^2\left(1+\frac{1}{\kappa(1-\kappa)}\right)\right]$$

$$\Theta(\kappa-\kappa_c)\Theta(\frac{1}{2}-\kappa) \tag{12.111}$$

with $\kappa_c = \max(W_k,T_c)/E$. The maximum allowed value of κ is $1/2$, consistent with the indistinguishability of the electrons in the final state. After the sampling of the energy loss $W = \kappa E$, the polar scattering angle θ is obtained as

$$\cos^2\theta = \frac{E-W}{E}\frac{E+2m_ec^2}{E-W+2m_ec^2}. \tag{12.112}$$

The azimuthal scattering angle ϕ is sampled uniformly in the interval $(0,2\pi)$. According to the GOS model, each oscillator W_k corresponds to an atomic shell with f_k electrons and ionisation energy U_k. In the case of ionisation of an inner shell i (K or L), a secondary electron (δ-ray) is emitted with energy $E_s = W - U_i$ and the residual ion is left with a vacancy in the shell (which is then filled with the emission of fluorescence x-rays and/or Auger electrons). In the case of ionisation of outer shells, the simulated δ-ray is emitted with kinetic energy $E_s = W$ and the target atom is assumed to remain in its ground state. The polar angle of emission of the secondary electron is calculated as

$$\cos^2\theta_s = \frac{W^2/\beta^2}{Q(Q+2m_ec^2)}\left[1+\frac{Q(Q+2m_ec^2)-W^2}{2W(E+m_ec^2)}\right]^2 \tag{12.113}$$

(for close collisions $Q = W$), while the azimuthal angle is $\phi_s = \phi + \pi$. In this model, the Doppler effects on the angular distribution of the δ rays are

neglected.

The stopping power due to soft interactions of electrons, which is used for the computation of the continuous part of the process, is analytically calculated as

$$S_{in}^- = N \int_0^{T_c} W \frac{d\sigma^-}{dW} dW \qquad (12.114)$$

from the expression (12.103), where N is the number of scattering centers (atoms or molecules) per unit volume.

Positrons

The total cross section $\sigma^+(E)$ for the inelastic collision of positrons of energy E is calculated analytically. As in the case of electrons, it can be split into contributions from distant longitudinal, distant transverse and close interactions,

$$\sigma^+(E) = \sigma_{dis,l} + \sigma_{dis,t} + \sigma_{clo}^+. \qquad (12.115)$$

The contributions from distant longitudinal and transverse interactions are the same as for electrons, Eq. (12.99) and (12.100), while the integrated cross section for close collisions is the Bhabha cross section

$$\sigma_{clo}^+ = \frac{2\pi e^4}{m_e v^2} \sum_{shells} f_k \int_{W_k}^E \frac{1}{W^2} F^+(E,W) dW, \qquad (12.116)$$

where

$$F^+(E,W) = 1 - b_1 \frac{W}{E} + b_2 \frac{W^2}{E^2} - b_3 \frac{W^3}{E^3} + b_4 \frac{W^4}{E^4}; \qquad (12.117)$$

the Bhabha factors are

$$b_1 = \left(\frac{\gamma-1}{\gamma}\right)^2 \frac{2(\gamma+1)^2 - 1}{\gamma^2 - 1} \qquad b_2 = \left(\frac{\gamma-1}{\gamma}\right)^2 \frac{3(\gamma+1)^2 + 1}{(\gamma+1)^2},$$

$$b_3 = \left(\frac{\gamma-1}{\gamma}\right)^2 \frac{2(\gamma-1)\gamma}{(\gamma+1)^2}, \qquad b_4 = \left(\frac{\gamma-1}{\gamma}\right)^2 \frac{(\gamma-1)^2}{(\gamma+1)^2}, \qquad (12.118)$$

$$(12.119)$$

and γ is the Lorentz factor of the positron. The integral of Eq. (12.116) can be evaluated analytically. The particles in the final state are not undistinguishable so the maximum energy transfer W_{max} in close collisions is E.

As for electrons, the GOS model allows the evaluation of the spectrum $\frac{d\sigma^+}{dW}$ of

the energy W lost by the primary positron as the sum of distant longitudinal, distant transverse and close interaction contributions,

$$\frac{d\sigma^+}{dW} = \frac{d\sigma^+_{clo}}{dW} + \frac{d\sigma_{dis,l}}{dW} + \frac{d\sigma_{dis,t}}{dW}, \qquad (12.120)$$

where the distant terms $\frac{d\sigma_{dis,l}}{dW}$ and $\frac{d\sigma_{dis,t}}{dW}$ are those from Eqs. (12.104) and (12.106), while the close contribution is

$$\frac{d\sigma^+_{clo}}{dW} = \frac{2\pi e^4}{m_e v^2} \sum_{shells} f_k \frac{1}{W^2} F^+(E,W)\Theta(W - W_k). \qquad (12.121)$$

Also in this case, the explicit expression of $\frac{d\sigma^+}{dW}$, Eq. (12.120), allows an analytic calculation of the partial cross sections for soft and hard ionisation events, i.e.

$$\sigma^+_{soft} = \int_0^{T_c} \frac{d\sigma^+}{dW} dW \quad \text{and} \quad \sigma^+_{hard} = \int_{T_c}^E \frac{d\sigma^+}{dW} dW. \qquad (12.122)$$

The sampling of the final state in the case of distant interactions (transverse or longitudinal) is performed in the same way as for primary electrons, see section 12.11.7. For close positron interactions with the k-th oscillator, the distribution for the reduced energy loss $\kappa \equiv W/E$ is

$$P^+_k(\kappa) = \left[\frac{1}{\kappa^2} - \frac{b_1}{\kappa} + b_2 - b_3\kappa + b_4\kappa^2\right]\Theta(\kappa - \kappa_c)\Theta(1 - \kappa) \qquad (12.123)$$

with $\kappa_c = \max(W_k, T_c)/E$. In this case, the maximum allowed reduced energy loss κ is 1. After sampling the energy loss $W = \kappa E$, the polar angle θ and the azimuthal angle ϕ are obtained using the equations introduced for electrons in section 12.11.7. Similarly, the generation of δ rays is performed in the same way as for electrons.

Finally, the stopping power due to soft interactions of positrons, which is used for the computation of the continuous part of the process, is analytically calculated as

$$S^+_{in} = N \int_0^{T_c} W \frac{d\sigma^+}{dW} dW \qquad (12.124)$$

from the expression (12.120), where N is the number of scattering centers per unit volume.

12.11.8 Positron Annihilation

Total Cross Section

The total cross section (per target electron) for the annihilation of a positron of energy E into two photons is evaluated from the analytical formula [20, 21]

$$\sigma(E) = \frac{\pi r_e^2}{(\gamma + 1)(\gamma^2 - 1)} \times$$
$$\left\{ (\gamma^2 + 4\gamma + 1) \ln \left[\gamma + \sqrt{\gamma^2 - 1} \right] - (3 + \gamma) \sqrt{\gamma^2 - 1} \right\}. \quad (12.125)$$

where
r_e = classical radius of the electron, and
γ = Lorentz factor of the positron.

Sampling of the Final State

The target electrons are assumed to be free and at rest: binding effects, that enable one-photon annihilation [20], are neglected. When the annihilation occurs in flight, the two photons may have different energies, say E_- and E_+ (the photon with lower energy is denoted by the superscript "−"), whose sum is $E + 2m_e c^2$. Each annihilation event is completely characterized by the quantity

$$\zeta = \frac{E_-}{E + 2m_e c^2}, \quad (12.126)$$

which is in the interval $\zeta_{min} \leq \zeta \leq \frac{1}{2}$, with

$$\zeta_{min} = \frac{1}{\gamma + 1 + \sqrt{\gamma^2 - 1}}. \quad (12.127)$$

The parameter ζ is sampled from the differential distribution

$$P(\zeta) = \frac{\pi r_e^2}{(\gamma + 1)(\gamma^2 - 1)} [S(\zeta) + S(1 - \zeta)], \quad (12.128)$$

where γ is the Lorentz factor and

$$S(\zeta) = -(\gamma + 1)^2 + (\gamma^2 + 4\gamma + 1)\frac{1}{\zeta} - \frac{1}{\zeta^2}. \quad (12.129)$$

From conservation of energy and momentum, it follows that the two photons are emitted in directions with polar angles

$$\cos \theta_- = \frac{1}{\sqrt{\gamma^2 - 1}} \left(\gamma + 1 - \frac{1}{\zeta} \right) \quad (12.130)$$

276

and

$$\cos\theta_+ = \frac{1}{\sqrt{\gamma^2 - 1}}\Big(\gamma + 1 - \frac{1}{1 - \zeta}\Big) \qquad (12.131)$$

that are completely determined by ζ; in particuar, when $\zeta = \zeta_{min}$, $\cos\theta_- = -1$. The azimuthal angles are ϕ_- and $\phi_+ = \phi_- + \pi$; owing to the axial symmetry of the process, the angle ϕ_- is uniformly distributed in $(0, 2\pi)$.

12.11.9 Status of the document

09.06.2003 created by L. Pandola
20.06.2003 spelling and grammar check by D.H. Wright
07.11.2003 Ionisation and Annihilation section added by L. Pandola
01.06.2005 Added text in the PhotoElectric effect section, L. Pandola

Bibliography

[1] *Penelope - A Code System for Monte Carlo Simulation of Electron and Photon Transport*, Workshop Proceedings Issy-les-Moulineaux, France, 5−7 November 2001, AEN-NEA;

[2] J.Sempau *et al.*, *Experimental benchmarks of the Monte Carlo code PENELOPE*, submitted to NIM B (2002);

[3] D.Brusa *et al.*, *Fast sampling algorithm for the simulation of photon Compton scattering*, NIM A379,167 (1996);

[4] F.Biggs *et al.*, *Hartree-Fock Compton profiles for the elements*, At.Data Nucl.Data Tables 16,201 (1975);

[5] M.Born, *Atomic physics*, Ed. Blackie and Sons (1969);

[6] J.Baró *et al.*, *Analytical cross sections for Monte Carlo simulation of photon transport*, Radiat.Phys.Chem. 44,531 (1994);

[7] J.H.Hubbel *et al.*, *Atomic form factors, incoherent scattering functions and photon scattering cross sections*, J. Phys.Chem.Ref.Data 4,471 (1975). Erratum: *ibid.* 6,615 (1977);

[8] M.J.Berger and J.H.Hubbel, *XCOM: photom cross sections on a personal computer*, Report NBSIR 87-3597 (National Bureau of Standards) (1987);

[9] H.Davies *et al.*, *Theory of bremsstrahlung and pair production. II.Integral cross section for pair production*, Phys.Rev. 93,788 (1954);

[10] J.H.Hubbel *et al.*, *Pair, triplet and total atomic cross sections (and mass attenuation coefficients) for 1 MeV − 100 GeV photons in element Z=1 to 100*, J.Phys.Chem.Ref.Data 9,1023 (1980);

[11] J.W.Motz *et al.*, *Pair production by photons*, Rev.Mod.Phys 41,581 (1969);

[12] D.E.Cullen *et al.*, *Tables and graphs of photon-interaction cross sections from 10 eV to 100 GeV derived from the LLNL evaluated photon data library (EPDL)*, Report UCRL-50400 (Lawrence Livermore National Laboratory) (1989);

[13] , F. Sauter, Ann. Phys. 11 (1931) 454

[14] S.M.Seltzer and M.J.Berger, *Bremsstrahlung energy spectra from electrons with kinetic energy 1 keV - 100 GeV incident on screened nuclei and orbital electrons of neutral atoms with Z=1-100*, At.Data Nucl.Data Tables 35,345 (1986);

[15] D.E.Cullen *et al.*, *Tables and graphs of electron-interaction cross sections from 10 eV to 100 GeV derived from the LLNL evaluated photon data library (EEDL)*, Report UCRL-50400 (Lawrence Livermore National Laboratory) (1989);

[16] L.Kissel *et al.*, *Shape functions for atomic-field bremsstrahlung from electron of kinetic energy $1-500$ keV on selected neutral atoms $1 \leq Z \leq 92$*, At.Data Nucl.Data.Tab. 28,381 (1983);

[17] M.J.Berger and S.M.Seltzer, *Stopping power of electrons and positrons*, Report NBSIR 82-2550 (National Bureau of Standards) (1982);

[18] L.Kim *et al.*, *Ratio of positron to electron bremsstrahlung energy loss: an approximate scaling law*, Phys.Rev.A 33,3002 (1986);

[19] U.Fano, *Penetration of protons, alpha particles and mesons*, Ann.Rev.Nucl.Sci. 13,1 (1963);

[20] W.Heitler, *The quantum theory of radiation*, Oxford University Press, London (1954);

[21] W.R.Nelson *et al.*, *The EGS4 code system*, Report SLAC-265 (1985).

12.12 Very Low Energy Extensions (the Geant4 DNA project)

12.12.1 Introduction

Geant4 low energy electromagnetic Physics processes have been extended down to energies of a few electronVolts suitable for the simulation of radiation effects in liquid water for applications at the cellular and sub-cellular level. These developments take place in the framework of the Geant4 DNA project [http://www.ge.infn.it/geant4/dna].

We summarize hereafter the Physics processes available in this very low energy extension. A more detailed description of these models is available in [1].

12.12.2 Processes for the interactions of electrons

Electron interactions involve elastic scattering, excitation and ionisation.

Elastic scattering

The current implementation of this process provides one model for the calculation of the total cross section and two complementary models for the final state generation.

The total cross section is calculated from the integrated screened Rutherford formula; this approach has been demonstrated to be valid down to the scale of a few electronvolts [7].

The angular distribution of the scattered electron is derived from two models of the differential cross section, respectively valid in the energy range from 7.4 eV to 200 eV and above 200 eV. The lower energy model is based on a semi-empirical calculation [2], while the higher energy one implements the screened Rutherford differential cross section [3], where the calculation of the screening correction term [4], [5] is based on the modified treatment described in [6].

Excitation

This process takes into account five excitation levels of the water molecule: A1 B1, B1A1, Ryd A+B, Ryd C+D and diffuse bands [8].

The total cross sections for excitation are calculated analytically for each discrete transition taking into account a low energy adjustment function [9].

Ionisation

The ionisation by incident electrons adopts a semi-empirical model [8], which is based on the dielectric formalism for the valence shells (1b1, 3a1, 1b2 and 2a1) responsible for condensed-phase effects, and on the binary encounter approximation for the K-shell (1a1).

The angular distribution of the outgoing electron is calculated from kinematical constraints.

12.12.3   Processes for the interaction of protons

The interactions of protons include excitation, ionisation and charge transfer.

Excitation

Two complementary approaches [10] are used to calculate the excitation cross section: a semi-empirical model covers the energy range from 10 eV to 500 keV, while a calculation based on the Born theory is used from 500 keV up to 10 MeV. The semi-empirical model [10] adopts a method based on electron excitation cross sections, following an approach developed by [11]; the parameters of the model are chosen to ensure the agreement with the results of the first Born approximation in the higher energy limit. The five excitation levels of the water molecule are taken into account as mentioned for the electron excitation process.

The incident proton direction is not modified in the generation of the final state.

Ionisation

The calculation of the cross sections [10] is based on two complementary models: a semi-empirical analytical approach derived from [12], [13] in the energy range between 100 eV and 500 keV and a model based on the Born theory for energies above 500 keV up to 10 MeV. The parameters of the lower energy model are calculated for interactions with liquid water.

The generation of the energy spectrum of the secondary electrons adopts a singly differential cross section model [14] based on a modified binary encounter approach; this model is consistent with calculations in the first Born approximation at higher energies and with the model in [15] at lower energies.

Charge transfer

The calculation of the charge transfer cross section adopts a semi-empirical approach [10] : the cross section is described by an analytical formula, whose parameters were optimized according to the experimental data in [16]-[18].

12.12.4 Processes for the interaction of hydrogen

The ionisation differential cross section is modelled [10] by applying an energy dependent scaling factor with respect to the proton ionisation differential cross section. The total cross section is evaluated accordingly.

The cross section for charge increase (stripping) is modelled according to a semi-empirical formula [13] with parameters adjusted to experimental data [10] similarly to the method used for proton charge transfer.

12.12.5 Processes for the interaction of helium ions

The processes relevant to helium ions are the same as for protons: ionization, excitation and charge transfer. They are modelled by applying an effective charge scaling [19] to the corresponding models for protons. The models take into account the particle's electron screening.

12.12.6 Status of the document

29.11.2007 Text created by S. Incerti
12.12.2007 Converted to latex by K. Amako

Bibliography

[1] S.Chauvie, Z.Francis, S.Guatelli, S.Incerti, B.Mascialino, P.Moretto, P.Nieminen and M.G.Pia, *Geant4 physics processes for microdosimetry simulation: design foun dation and implementation of the first set of models*, to be published in IEEE Trans. Nucl. Sci., Dec. 2007;

[2] D.J.Brenner and M.Zaider, *A computationally convenient parameterization of experim ental angular distributions of low energy electrons elastically scattered off water vapour*, Phys. Med. Biol. 29 (4) (1983) 443-447;

[3] H.Bethe, *Moliere theory of multiple scattering,*, Phys. Rev. 89 (1953) 1256-1266;

[4] G.Moliere, *Theorie der Streuung schneller geladener Teilchen. I. Einzel-streuung am a bgeschirmten Coulomb-Feld*, Z. Naturf. A 2 (1947) 133-145;

[5] G.Moliere, *Theorie der Streuung schneller geladener Teilchen. II. Mehrfach- und Viel fachstreuung*, Z. Naturf A 3 (1948) 78-97;

[6] B.Grosswendt and E.Waibel, *Transport of low energy electrons in nitrogen and air*, Nucl. Instrum. Meth. 155 (1978) 145-156,;

[7] B.Senger, S.Fall, and R.V.Rechenmann, *Semi-empirical expressions describing the elastic scattering of slow electrons by molecules*, Rad. Prot. Dosim. 31 (1990) 37-42;

[8] D.Emfietzoglou and M.Moscovitch, *Inelastic collision characteristics of electrons in liquid water*, Nucl. Instrum. Meth. B 193 (2002) 71-78;

[9] D.Emfietzoglou, K.Karava, G.Papamichael, and M.Moscovitch,
Monte Carlo simulation of the energy loss of low-energy electrons in liquid water, Phys. Med. Biol. 48 (2003) 2355-2371,;

[10] M.Dingfelder, M.Inokuti, and H.G.Paretzke,
Inelastic-collision cross sections of liquid water for interactions of energetic protons, Radiat. Phys. Chem. 59 (2000) 255-275;

[11] J.H.Miller and A.E.S.Green, *Proton Energy Degradation in Water Vapor*, Radiat. Res. 54 (1973) 343-363;

[12] M.E.Rudd, T.V.Goffe, R.D.DuBois, and L.H.Toburen, *Cross sections for ionisat ion of water vapor by 7-4000 keV protons*, Phys. Rev. A 31 (1985) 492-494;

[13] M.E.Rudd, Y.K.Kim, D.H.Madison, and. J.W.Gallagher, *Electron production in proton collisions: total cross sections*, Rev. Mod. Phys. 57 (4) (1985) 965-994;

[14] M.E.Rudd, *User-friendly model for the energy distribution of electrons from proton or electron collisions*, Nucl. Tracks Rad. Meas. 16 (2-3) (1989) 213-218;

[15] M.E.Rudd, *Energy and angular distributions of secondary electrons from 5-100 keV proton collisions with hydrogen and nitrogen molecules*, Phys. Rev. A 20 (1979) 787-796;

[16] B.G.Lindsay, D.R.Sieglaff, K.A.Smith, and R.F.Stebbings, *Charge transfer of 0.5-, 1.5-, and 5-keV protons with H2O: absolute differential and integral cross sections*, Phys. Rev. A 55 (5) (1997) 3945-3946,;

[17] R.Dagnac, D.Blanc, and D.Molina, *A study on the collision of hydrogen ions H1+, H2+ and H3+ with a water-vapour target*, J. Phys. B 3 (1970) 1239-1251;

[18] L.H.Toburen, M.Y.Nakai, and R.A.Langley, *Measurement of high-energy charge transfer cross sections for incident protons and atomic hydrogen in various gases*, Phys. Rev. 171 (1) (1968) 114-122;

[19] M.Dingfelder, H.G.Paretzke, and L.H.Toburen, *An effective charge scaling model for ionization of partially dressed helium ions with liquid water*, Proc. of Monte Carlo 2005, Chattanooga, Tennessee, USA (2005),;

Chapter 13

Optical Photons

13.1 Interactions of optical photons

Optical photons are produced when a charged particle traverses:

1. a dielectric material with velocity above the Čerenkov threshold;

2. a scintillating material.

13.1.1 Physics processes for optical photons

A photon is called optical when its wavelength is much greater than the typical atomic spacing, for instance when $\lambda \geq 10nm$ which corresponds to an energy $E \leq 100eV$. Production of an optical photon in a HEP detector is primarily due to:

1. Čerenkov effect;

2. Scintillation.

Optical photons undergo three kinds of interactions:

1. Elastic (Rayleigh) scattering;

2. Absorption;

3. Medium boundary interactions.

Rayleigh scattering

For optical photons Rayleigh scattering is usually unimportant. For $\lambda = .2\mu m$ we have $\sigma_{Rayleigh} \approx .2b$ for N_2 or O_2 which gives a mean free path of $\approx 1.7km$ in air and $\approx 1m$ in quartz. Two important exceptions are aerogel, which is used as a Čerenkov radiator for some special applications and large water Čerenkov detectors for neutrino detection.

The differential cross section in Rayleigh scattering, $d\sigma/d\Omega$, is proportional to $\cos^2\theta$, where θ is the polar angle of the new polarization with respect to the old polarization.

Absorption

Absorption is important for optical photons because it determines the lower λ limit in the window of transparency of the radiator. Absorption competes with photo-ionization in producing the signal in the detector, so it must be treated properly in the tracking of optical photons.

Medium boundary effects

When a photon arrives at the boundary of a dielectric medium, its behaviour depends on the nature of the two materials which join at that boundary:

- Case dielectric → dielectric.
  The photon can be transmitted (refracted ray) or reflected (reflected ray). In case where the photon can only be reflected, total internal reflection takes place.

- Case dielectric → metal.
  The photon can be absorbed by the metal or reflected back into the dielectric. If the photon is absorbed it can be detected according to the photoelectron efficiency of the metal.

- Case dielectric → black material.
  A black material is a tracking medium for which the user has not defined any optical property. In this case the photon is immediately absorbed undetected.

13.1.2 Photon polarization

The photon polarization is defined as a two component vector normal to the direction of the photon:

$$\begin{pmatrix} a_1 e^{i\Phi_1} \\ a_2 e^{i\Phi_2} \end{pmatrix} = e^{\Phi_o} \begin{pmatrix} a_1 e^{i\Phi_c} \\ a_2 e^{-i\Phi_c} \end{pmatrix}$$

where $\Phi_c = (\Phi_1 - \Phi_2)/2$ is called circularity and $\Phi_o = (\Phi_1 + \Phi_2)/2$ is called overall phase. Circularity gives the left- or right-polarization characteristic of the photon. RICH materials usually do not distinguish between the two polarizations and photons produced by the Čerenkov effect and scintillation are linearly polarized, that is $\Phi_c = 0$.

The overall phase is important in determining interference effects between coherent waves. These are important only in layers of thickness comparable with the wavelength, such as interference filters on mirrors. The effects of such coatings can be accounted for by the empirical reflectivity factor for the surface, and do not require a microscopic simulation. GEANT4 does not keep track of the overall phase.

Vector polarization is described by the polarization angle $\tan \Psi = a_2/a_1$. Reflection/transmission probabilities are sensitive to the state of linear polarization, so this has to be taken into account. One parameter is sufficient to

describe vector polarization, but to avoid too many trigonometrical transformations, a unit vector perpendicular to the direction of the photon is used in GEANT4. The polarization vector is a data member of `G4DynamicParticle`.

13.1.3 Tracking of the photons

Optical photons are subject to in flight absorption, Rayleigh scattering and boundary action. As explained above, the status of the photon is defined by two vectors, the photon momentum ($\vec{p} = \hbar\vec{k}$) and photon polarization ($\vec{e}$). By convention the direction of the polarization vector is that of the electric field. Let also $\vec{u}$ be the normal to the material boundary at the point of intersection, pointing out of the material which the photon is leaving and toward the one which the photon is entering. The behaviour of a photon at the surface boundary is determined by three quantities:

1. refraction or reflection angle, this represents the kinematics of the effect;

2. amplitude of the reflected and refracted waves, this is the dynamics of the effect;

3. probability of the photon to be refracted or reflected, this is the quantum mechanical effect which we have to take into account if we want to describe the photon as a particle and not as a wave.

As said above, we distinguish three kinds of boundary action, dielectric → black material, dielectric → metal, dielectric → dielectric. The first case is trivial, in the sense that the photon is immediately absorbed and it goes undetected.

To determine the behaviour of the photon at the boundary, we will at first treat it as an homogeneous monochromatic plane wave:

$$\vec{E} = \vec{E}_0 e^{i\vec{k}\cdot\vec{x} - i\omega t}$$

$$\vec{B} = \sqrt{\mu\epsilon}\frac{\vec{k}\times\vec{E}}{k}$$

Case dielectric → dielectric

In the classical description the incoming wave splits into a reflected wave (quantities with a double prime) and a refracted wave (quantities with a single prime). Our problem is solved if we find the following quantities:

$$\vec{E}' = \vec{E}'_0 e^{i\vec{k}'\cdot\vec{x} - i\omega t}$$

$$\vec{E}'' = \vec{E}_0'' e^{i\vec{k}'' \cdot \vec{x} - i\omega t}$$

For the wave numbers the following relations hold:

$$|\vec{k}| = |\vec{k}''| = k = \frac{\omega}{c}\sqrt{\mu\epsilon}$$

$$|\vec{k}'| = k' = \frac{\omega}{c}\sqrt{\mu'\epsilon'}$$

Where the speed of the wave in the medium is $v = c/\sqrt{\mu\epsilon}$ and the quantity $n = c/v = \sqrt{\mu\epsilon}$ is called refractive index of the medium. The condition that the three waves, refracted, reflected and incident have the same phase at the surface of the medium, gives us the well known Fresnel law:

$$(\vec{k} \cdot \vec{x})_{surf} = (\vec{k}' \cdot \vec{x})_{surf} = (\vec{k}'' \cdot \vec{x})_{surf}$$

$$k \sin i = k' \sin r = k'' \sin r'$$

where i, r, r' are, respectively, the angle of the incident, refracted and reflected ray with the normal to the surface. From this formula the well known condition emerges:

$$i = r'$$

$$\frac{\sin i}{\sin r} = \sqrt{\frac{\mu'\epsilon'}{\mu\epsilon}} = \frac{n'}{n}$$

The dynamic properties of the wave at the boundary are derived from Maxwell's equations which impose the continuity of the normal components of $\vec{D}$ and $\vec{B}$ and of the tangential components of $\vec{E}$ and $\vec{H}$ at the surface boundary. The resulting ratios between the amplitudes of the the generated waves with respect to the incoming one are expressed in the two following cases:

1. a plane wave with the electric field (polarization vector) perpendicular to the plane defined by the photon direction and the normal to the boundary:

$$\frac{E_0'}{E_0} = \frac{2n\cos i}{n\cos i = \frac{\mu}{\mu'}n'\cos r} = \frac{2n\cos i}{n\cos i + n'\cos r}$$

$$\frac{E_0''}{E_0} = \frac{n\cos i - \frac{\mu}{\mu'}n'\cos r}{n\cos i + \frac{\mu}{\mu'}n'\cos r} = \frac{n\cos i - n'\cos r}{n\cos i + n'\cos r}$$

where we suppose, as it is legitimate for visible or near-visible light, that $\mu/\mu' \approx 1$;

2. a plane wave with the electric field parallel to the above surface:

$$\frac{E_0'}{E_0} = \frac{2n\cos i}{\frac{\mu}{\mu'}n'\cos i + n\cos r} = \frac{2n\cos i}{n'\cos i + n\cos r}$$

$$\frac{E_0''}{E_0} = \frac{\frac{\mu}{\mu'}n'\cos i - n\cos r}{\frac{\mu}{\mu'}n'\cos i + n\cos r} = \frac{n'\cos i - n\cos r}{n'\cos i + n\cos r}$$

with the same approximation as above.

We note that in case of photon perpendicular to the surface, the following relations hold:

$$\frac{E_0'}{E_0} = \frac{2n}{n'+n} \qquad \frac{E_0''}{E_0} = \frac{n'-n}{n'+n}$$

where the sign convention for the parallel field has been adopted. This means that if $n' > n$ there is a phase inversion for the reflected wave.

Any incoming wave can be separated into one piece polarized parallel to the plane and one polarized perpendicular, and the two components treated accordingly.

To maintain the particle description of the photon, the probability to have a refracted or reflected photon must be calculated. The constraint is that the number of photons be conserved, and this can be imposed via the conservation of the energy flux at the boundary, as the number of photons is proportional to the energy. The energy current is given by the expression:

$$\vec{S} = \frac{1}{2}\frac{c}{4\pi}\sqrt{\mu\epsilon}\vec{E} \times \vec{H} = \frac{c}{8\pi}\sqrt{\frac{\epsilon}{\mu}}E_0^2\hat{k}$$

and the energy balance on a unit area of the boundary requires that:

$$\vec{S}\cdot\vec{u} = \vec{S}'\cdot\vec{u} - \vec{S}''\cdot\vec{u}$$

$$S\cos i = S'cosr + S''cosi$$

$$\frac{c}{8\pi}\frac{1}{\mu}nE_0^2\cos i = \frac{c}{8\pi}\frac{1}{\mu'}n'E_0'^2\cos r + \frac{c}{8\pi}\frac{1}{\mu}nE_0''^2\cos i$$

If we set again $\mu/\mu' \approx 1$, then the transmission probability for the photon will be:

$$T = (\frac{E_0'}{E_0})^2\frac{n'\cos r}{n\cos i}$$

and the corresponding probability to be reflected will be $R = 1 - T$.

In case of reflection, the relation between the incoming photon $(\vec{k}, \vec{e})$, the refracted one $(\vec{k}', \vec{e}')$ and the reflected one $(\vec{k}'', \vec{e}'')$ is given by the following relations:

$$\vec{q} = \vec{k} \times \vec{u}$$

$$\vec{e}_\perp = \left(\frac{\vec{e} \cdot \vec{q}}{|\vec{q}|}\right)\frac{\vec{q}}{|\vec{q}|}$$

$$\vec{e}_\parallel = \vec{e} - \vec{e}_\perp$$

$$e'_\parallel = e_\parallel \frac{2n \cos i}{n' \cos i + n \cos r}$$

$$e'_{\perp|} = e_\perp \frac{2n \cos i}{n \cos i + n' \cos r}$$

$$e''_\parallel = \frac{n'}{n} e'_\parallel - e_\parallel$$

$$e''_\perp = e'_\perp - e_\perp$$

After transmission or reflection of the photon, the polarization vector is re-normalized to 1. In the case where $\sin r = n \sin i / n' > 1$ then there cannot be a refracted wave, and in this case we have a total internal reflection according to the following formulas:

$$\vec{k}'' = \vec{k} - 2(\vec{k} \cdot \vec{u})\vec{u}$$

$$\vec{e}'' = -\vec{e} + 2(\vec{e} \cdot \vec{u})\vec{u}$$

Case dielectric → metal

In this case the photon cannot be transmitted. So the probability for the photon to be absorbed by the metal is estimated according to the table provided by the user. If the photon is not absorbed, it is reflected.

Bibliography

[1] J.D. Jackson, *Classical Electrodynamics*, J. Wiley & Sons Inc., New York, 1975.

Chapter 14

Shower Parameterizations

14.1 Gflash Shower Parameterizations

The computing time needed for the simulation of high energy electromagnetic showers can become very large, since it increases approximately linearly with the energy absorbed in the detector. Using parameterizations instead of individual particle tracking for electromagnetic (sub)showers can speed up the simulations considerably without sacrificing much precision. The Gflash package allows the parameterization of electron and positron showers in homogeneous (for the time being) calorimeters and is based on the parameterization described in Ref. [1] .

14.1.1 Parameterization Ansatz

The spatial energy distribution of electromagnetic showers is given by three probability density functions (pdf),

$$dE(\vec{r}) = E f(t)dt f(r)dr f(\phi)d\phi, \tag{14.1}$$

describing the longitudinal, radial, and azimuthal energy distributions. Here t denotes the longitudinal shower depth in units of radiation length, r measures the radial distance from the shower axis in Molière units, and ϕ is the azimuthal angle. The start of the shower is defined by the space point where the electron or positron enters the calorimeter, which is different from the original Gflash. A gamma distribution is used for the parameterization of the longitudinal shower profile, $f(t)$. The radial distribution $f(r)$, is described by a two-component ansatz. In ϕ, it is assumed that the energy is distributed uniformly: $f(\phi) = 1/2\pi$.

14.1.2 Longitudinal Shower Profiles

The average longitudinal shower profiles can be described by a gamma distribution [2]:

$$\left\langle \frac{1}{E}\frac{dE(t)}{dt} \right\rangle = f(t) = \frac{(\beta t)^{\alpha-1}\beta \exp(-\beta t)}{\Gamma(\alpha)}. \tag{14.2}$$

The center of gravity, $\langle t \rangle$, and the depth of the maximum, T, are calculated from the shape parameter α and the scaling parameter β according to:

$$\langle t \rangle = \frac{\alpha}{\beta} \tag{14.3}$$

$$T = \frac{\alpha - 1}{\beta}. \tag{14.4}$$

In the parameterization all lengths are measured in units of radiation length (X_0), and energies in units of the critical energy ($E_c = 2.66 \left(X_0 \frac{Z}{A}\right)^{1.1}$). This allows material independence, since the longitudinal shower moments are equal in different materials, according to Ref. [3]. The following equations are used for the energy dependence of T_{hom} and (α_{hom}), with $y = E/E_c$ and $t = x/X_0$, x being the longitudinal shower depth:

$$T_{hom} = \ln y + t_1 \tag{14.5}$$
$$\alpha_{hom} = a_1 + (a_2 + a_3/Z) \ln y. \tag{14.6}$$

The y-dependence of the fluctuations can be described by:

$$\sigma = (s_1 + s_2 \ln y)^{-1}. \tag{14.7}$$

The correlation between $\ln T_{hom}$ and $\ln \alpha_{hom}$ is given by:

$$\rho(\ln T_{hom}, \ln \alpha_{hom}) \equiv \rho = r_1 + r_2 \ln y. \tag{14.8}$$

From these formulae, correlated and varying parameters α_i and β_i are generated according to

$$\begin{pmatrix} \ln T_i \\ \ln \alpha_i \end{pmatrix} = \begin{pmatrix} \langle \ln T \rangle \\ \langle \ln \alpha \rangle \end{pmatrix} + C \begin{pmatrix} z_1 \\ z_2 \end{pmatrix} \tag{14.9}$$

with

$$C = \begin{pmatrix} \sigma(\ln T) & 0 \\ 0 & \sigma(\ln \alpha) \end{pmatrix} \begin{pmatrix} \sqrt{\frac{1+\rho}{2}} & \sqrt{\frac{1-\rho}{2}} \\ \sqrt{\frac{1+\rho}{2}} & -\sqrt{\frac{1-\rho}{2}} \end{pmatrix}$$

$\sigma(\ln \alpha)$ and $\sigma(\ln T)$ are the fluctuations of T_{hom} and (α_{hom}. The values of the coefficients can be found in Ref. [1].

14.1.3 Radial Shower Profiles

For the description of average radial energy profiles,

$$f(r) = \frac{1}{dE(t)} \frac{dE(t,r)}{dr}, \tag{14.10}$$

a variety of different functions can be found in the literature. In Gflash the following two-component ansatz, an extension of that in Ref.[4], was used:

$$f(r) = p f_C(r) + (1 - p) f_T(r) \tag{14.11}$$
$$= p \frac{2r R_C^2}{(r^2 + R_C^2)^2} + (1 - p) \frac{2r R_T^2}{(r^2 + R_T^2)^2}$$

with
$$0 \le p \le 1.$$

Here R_C (R_T) is the median of the core (tail) component and p is a probability giving the relative weight of the core component. The variable $\tau = t/T$, which measures the shower depth in units of the depth of the shower maximum, is used in order to generalize the radial profiles. This makes the parameterization more convenient and separates the energy and material dependence of various parameters. The median of the core distribution, R_C, increases linearly with τ. The weight of the core, p, is maximal around the shower maximum, and the width of the tail, R_T, is minimal at $\tau \approx 1$.

The following formulae are used to parameterize the radial energy density distribution for a given energy and material:

$$R_{C,hom}(\tau) = z_1 + z_2\tau \tag{14.12}$$

$$R_{T,hom}(\tau) = k_1\{\exp(k_3(\tau - k_2)) + \exp(k_4(\tau - k_2))\} \tag{14.13}$$

$$p_{hom}(\tau) = p_1 \exp\left\{\frac{p_2 - \tau}{p_3} - \exp\left(\frac{p_2 - \tau}{p_3}\right)\right\} \tag{14.14}$$

The parameters $z_1 \cdots p_3$ are either constant or simple functions of $\ln E$ or Z.

Radial shape fluctuations are also taken into account. A detailed explanation of this procedure, as well as a list of all the parameters used in Gflash, can be found in Ref. [1].

14.1.4 Gflash Performance

The parameters used in this Gflash implementation were extracted from full simulation studies with Geant 3. They also give good results inside the Geant4 fast shower framework when compared with the full electromagnetic shower simulation. However, if more precision or higher particle energies are required, retuning may be necessary. For the longitudinal profiles the difference between full simulation and Gflash parameterization is at the level of a few percent. Because the radial profiles are slightly broader in Geant3 than in Geant4, the differences may reach $> 10\%$. The gain in speed, on the other hand, is impressive. The simulation of a 1 TeV electron in a $PbWO_4$ cube is 160 times faster with Gflash. Gflash can also be used to parameterize electromagnetic showers in sampling calorimeters. So far, however, only homogeneous materials are supported.

14.1.5 Status of this document

02.12.04 created by J.Weng
03.12.04 grammar check and minor re-wording by D.H. Wright

Bibliography

[1] G. Grindhammer, S. Peters, *The Parameterized Simulation of Electromagnetic Showers in Homogeneous and Sampling Calorimeters, hep-ex/0001020* (1993).

[2] E. Longo and I. Sestili,*Nucl. Instrum. Meth. 128, 283* (1975).

[3] Rossi *rentice Hall, New York* (1952).

[4] G. Grindhammer, M. Rudowicz, and S. Peters, *Nucl. Instrum. Meth. A290, 469* (1990).

Part IV

Hadronic Interactions

Chapter 15

Lepton Hadron Interactions

The photonuclear interaction of muons is currently the only process treated in this category.

15.1 *G4MuonNucleusProcess*

This class simulates the photonuclear interaction of muons in a material. The muon interacts electromagnetically with a nucleus, exchanging a virtual photon. At energies above a few GeV, the photon interacts hadronically with the nucleus, producing hadronic secondaries.

    The outcome of the simulation depends heavily upon the interaction model chosen. Hence the model-dependent part of the process is implemented in the *G4MuonNucleusInteractionModel* class, which can be easily replaced by another model.

    G4MuonNucleusInteractionModel calculates the cross section and final states of the muon and hadronic secondaries. The final muon momentum is given by a double-differential cross section which depends on the photoabsorption cross sections for longitudinally and transversely polarized photons. The final hadronic state is determined by replacing the virtual photon with a charged pion of the same Q^2 and then allowing the pion to interact with the nucleus. The charge of the pion is chosen at random. The pion interactions with the nucleus are modeled by processes derived from the GHEISHA [1] package. These processes are:

      G4LEPionPlusInelastic, G4LEPionMinusInelastic $E \leq 25$ GeV
      G4HEPionPlusInelastic, G4HEPionMinusInelastic $E > 25$ GeV

15.1.1 Cross Section Calculation

The cross section for the above process in a material is given roughly by

$$\sigma_{\mu A} = A\sigma_{\mu N}$$

where A is the atomic mass number of the material and $\sigma_{\mu N}$ is the cross section for the process on a single nucleon:

$$\sigma_{\mu N} = \begin{cases} 0.3 & (E \leq 30 GeV) \\ 0.3(E/30)^{0.25} & (E > 30 GeV) \end{cases} \; [\mu b].$$

The differential cross section, in terms of muon energy E and emission solid angle Ω, can be expressed as:

$$\frac{d\sigma}{d\Omega dE} = \Gamma\left(\sigma_T + \epsilon\sigma_L\right)$$

where σ_L and σ_T are the photoabsorption cross sections for longitudinal and transverse photons, respectively. Γ is the transverse photon flux and ϵ is the polarization of the intermediate photon. The photoabsorption cross sections are parameterized as:

$$\sigma_L = 0.3\left(1 - \frac{1}{1.868}Q^2\nu\right)\sigma_T$$
$$\sigma_T \sim const = 0.12mb$$

while the flux and polarization are given by

$$\Gamma = \frac{K\alpha}{2\pi}\frac{E'}{E}\frac{1}{1-\epsilon}$$
$$\epsilon = \left[1 + 2\frac{Q^2+\nu^2}{Q^2}tan^2\frac{\theta}{2}\right]^{-1}.$$

E and E' are the initial and final muon energies, Q^2 and ν are the scaling variables

$$Q^2 = -q^2 = 2(EE' - PP'cos\theta - m_\mu^2)$$
$$\nu = E - E',$$

and K is given using the Gilman convention

$$K = \nu + \frac{Q^2}{2\nu}.$$

15.2 Status of this document

20.04.02 re-written by D.H. Wright
23.10.98 created by M.Takahata

Bibliography

[1] H.Fesefeldt *GHEISHA The Simulation of Hadronic Showers* 149 *RWTH/PITHA 85/02* (1985)

Chapter 16

Cross-sections in Photonuclear and Electronuclear Reactions

16.1 Approximation of Photonuclear Cross Sections.

The photonuclear cross sections parameterized in the `G4PhotoNuclearCrossSection` class cover all incident photon energies from the hadron production threshold upward. The parameterization is subdivided into five energy regions, each corresponding to the physical process that dominates it.

- The Giant Dipole Resonance (GDR) region, depending on the nucleus, extends from 10 Mev up to 30 MeV. It usually consists of one large peak, though for some nuclei several peaks appear.

- The "quasi-deuteron" region extends from around 30 MeV up to the pion threshold and is characterized by small cross sections and a broad, low peak.

- The Δ region is characterized by the dominant peak in the cross section which extends from the pion threshold to 450 MeV.

- The Roper resonance region extends from roughly 450 MeV to 1.2 GeV. The cross section in this region is not strictly identified with the real Roper resonance because other processes also occur in this region.

- The Reggeon-Pomeron region extends upward from 1.2 GeV.

In the GEANT4 photonuclear data base there are about 50 nuclei for which the photonuclear absorption cross sections have been measured in the above

energy ranges. For low energies this number could be enlarged, because for heavy nuclei the neutron photoproduction cross section is close to the total photo-absorption cross section. Currently, however, 14 nuclei are used in the parameterization: ^{1}H, ^{2}H, ^{4}He, ^{6}Li, ^{7}Li, ^{9}Be, ^{12}C, ^{16}O, ^{27}Al, ^{40}Ca, Cu, Sn, Pb, and U. The resulting cross section is a function of A and $e = log(E_\gamma)$, where E_γ is the energy of the incident photon. This function is the sum of the components which parameterize each energy region.

The cross section in the GDR region can be described as the sum of two peaks,

$$GDR(e) = th(e, b_1, s_1) \cdot exp(c_1 - p_1 \cdot e) + th(e, b_2, s_2) \cdot exp(c_2 - p_2 \cdot e). \quad (16.1)$$

The exponential parameterizes the falling edge of the resonance which behaves like a power law in E_γ. This behavior is expected from the CHIPS model, which includes the nonrelativistic phase space of nucleons to explain evaporation. The function

$$th(e, b, s) = \frac{1}{1 + exp(\frac{b-e}{s})}, \quad (16.2)$$

describes the rising edge of the resonance. It is the nuclear-barrier-reflection function and behaves like a threshold, cutting off the exponential. The exponential powers p_1 and p_2 are

$$p_1 = 1, p_2 = 2 \text{ for } \quad A < 4$$
$$p_1 = 2, p_2 = 4 \text{ for } \quad 4 \le A < 8$$
$$p_1 = 3, p_2 = 6 \text{ for } 8 \le A < 12$$
$$p_1 = 4, p_2 = 8 \text{ for } \quad A \ge 12.$$

The A-dependent parameters b_i, c_i and s_i were found for each of the 14 nuclei listed above and interpolated for other nuclei.

The Δ isobar region was parameterized as

$$\Delta(e, d, f, g, r, q) = \frac{d \cdot th(e, f, g)}{1 + r \cdot (e - q)^2}, \quad (16.3)$$

where d is an overall normalization factor. q can be interpreted as the energy of the Δ isobar and r can be interpreted as the inverse of the Δ width. Once again th is the threshold function. The A-dependence of these parameters is as follows:

- $d = 0.41 \cdot A$ (for ^{1}H it is 0.55, for ^{2}H it is 0.88), which means that the Δ yield is proportional to A;

- $f = 5.13 - .00075 \cdot A$. $exp(f)$ shows how the pion threshold depends on A. It is clear that the threshold becomes 140 MeV only for uranium; for lighter nuclei it is higher.

- $g = 0.09$ for $A \geq 7$ and 0.04 for $A < 7$;

- $q = 5.84 - \frac{.09}{1+.003 \cdot A^2}$, which means that the "mass" of the Δ isobar moves to lower energies;

- $r = 11.9 - 1.24 \cdot log(A)$. r is 18.0 for ^{1}H. The inverse width becomes smaller with A, hence the width increases.

The A-dependence of the f, q and r parameters is due to the $\Delta + N \rightarrow N + N$ reaction, which can take place in the nuclear medium below the pion threshold.

The quasi-deuteron contribution was parameterized with the same form as the Δ contribution but without the threshold function:

$$QD(e, v, w, u) = \frac{v}{1 + w \cdot (e - u)^2}. \tag{16.4}$$

For ^{1}H and ^{2}H the quasi-deuteron contribution is almost zero. For these nuclei the third baryonic resonance was used instead, so the parameters for these two nuclei are quite different, but trivial. The parameter values are given below.

- $v = \frac{exp(-1.7 + a \cdot 0.84)}{1 + exp(7 \cdot (2.38 - a))}$, where $a = log(A)$. This shows that the A-dependence in the quasi-deuteron region is stronger than $A^{0.84}$. It is clear from the denominator that this contribution is very small for light nuclei (up to ^{6}Li or ^{7}Li). For ^{1}H it is 0.078 and for ^{2}H it is 0.08, so the delta contribution does not appear to be growing. Its relative contribution disappears with A.

- $u = 3.7$ and $w = 0.4$. The experimental information is not sufficient to determine an A-dependence for these parameters. For both ^{1}H and ^{2}H $u = 6.93$ and $w = 90$, which may indicate contributions from the $\Delta(1600)$ and $\Delta(1620)$.

The transition Roper contribution was parameterized using the same form as the quasi-deuteron contribution:

$$Tr(e, v, w, u) = \frac{v}{1 + w \cdot (e - u)^2}. \tag{16.5}$$

Using $a = log(A)$, the values of the parameters are

- $v = exp(-2. + a \cdot 0.84)$. For ^{1}H it is 0.22 and for ^{2}H it is 0.34.

- $u = 6.46 + a \cdot 0.061$ (for ^{1}H and for ^{2}H it is 6.57), so the "mass" of the Roper moves higher with A.

- $w = 0.1 + a \cdot 1.65$. For ^{1}H it is 20.0 and for ^{2}H it is 15.0).

The Regge-Pomeron contribution was parametrized as follows:

$$RP(e, h) = h \cdot th(7., 0.2) \cdot (0.0116 \cdot exp(e \cdot 0.16) + 0.4 \cdot exp(-e \cdot 0.2)), \tag{16.6}$$

where $h = A \cdot exp(-a \cdot (0.885 + 0.0048 \cdot a))$ and, again, $a = log(A)$. The first exponential in Eq. 16.6 describes the Pomeron contribution while the second describes the Regge contribution.

16.2 Electronuclear Cross Sections and Reactions

Electronuclear reactions are so closely connected with photonuclear reactions that they are sometimes called "photonuclear" because the one-photon exchange mechanism dominates in electronuclear reactions. In this sense electrons can be replaced by a flux of equivalent photons. This is not completely true, because at high energies the Vector Dominance Model (VDM) or diffractive mechanisms are possible, but these types of reactions are beyond the scope of this discussion.

16.2.1 Common Notation for Different Approaches to Electronuclear Reactions

The Equivalent Photon Approximation (EPA) was proposed by E. Fermi [1] and developed by C. Weizsacker and E. Williams [2] and by L. Landau and E. Lifshitz [3]. The covariant form of the EPA method was developed in Refs. [4] and [5]. When using this method it is necessary to take into account that real photons are always transversely polarized while virtual photons may

be longitudinally polarized. In general the differential cross section of the electronuclear interaction can be written as

$$\frac{d^2\sigma}{dydQ^2} = \frac{\alpha}{\pi Q^2}(S_{TL} \cdot (\sigma_T + \sigma_L) - S_L \cdot \sigma_L), \qquad (16.7)$$

where

$$S_{TL} = y\frac{1 - y + \frac{y^2}{2} + \frac{Q^2}{4E^2} - \frac{m_e^2}{Q^2}(y^2 + \frac{Q^2}{E^2})}{y^2 + \frac{Q^2}{E^2}}, \qquad (16.8)$$

$$S_L = \frac{y}{2}(1 - \frac{2m_e^2}{Q^2}). \qquad (16.9)$$

The differential cross section of the electronuclear scattering can be rewritten as

$$\frac{d^2\sigma_{eA}}{dydQ^2} = \frac{\alpha y}{\pi Q^2}\left(\frac{(1 - \frac{y}{2})^2}{y^2 + \frac{Q^2}{E^2}} + \frac{1}{4} - \frac{m_e^2}{Q^2}\right)\sigma_{\gamma^*A}, \qquad (16.10)$$

where $\sigma_{\gamma^*A} = \sigma_{\gamma A}(\nu)$ for small Q^2 and must be approximated as a function of ϵ, ν, and Q^2 for large Q^2. Interactions of longitudinal photons are included in the effective σ_{γ^*A} cross section through the ϵ factor, but in the present GEANT4 method, the cross section of virtual photons is considered to be ϵ-independent. The electronuclear problem, with respect to the interaction of virtual photons with nuclei, can thus be split in two. At small Q^2 it is possible to use the $\sigma_\gamma(\nu)$ cross section. In the $Q^2 >> m_e^2$ region it is necessary to calculate the effective $\sigma_{\gamma^*}(\epsilon, \nu, Q^2)$ cross section.

Following the EPA notation, the differential cross section of electronuclear scattering can be related to the number of equivalent photons $dn = \frac{d\sigma}{\sigma_{\gamma^*}}$. For $y << 1$ and $Q^2 < 4m_e^2$ the canonical method [6] leads to the simple result

$$\frac{ydn(y)}{dy} = -\frac{2\alpha}{\pi}ln(y). \qquad (16.11)$$

In [7] the integration over Q^2 for $\nu^2 >> Q_{max}^2 \simeq m_e^2$ leads to

$$\frac{ydn(y)}{dy} = -\frac{\alpha}{\pi}\left(\frac{1 + (1 - y)^2}{2}ln(\frac{y^2}{1 - y}) + (1 - y)\right). \qquad (16.12)$$

In the $y << 1$ limit this formula converges to Eq.(16.11). But the correspondence with Eq.(16.11) can be made more explicit if the exact integral

$$\frac{ydn(y)}{dy} = \frac{\alpha}{\pi}\left(\frac{1 + (1 - y)^2}{2}l_1 - (1 - y)l_2 - \frac{(2 - y)^2}{4}l_3\right), \qquad (16.13)$$

304

where $l_1 = ln\left(\frac{Q^2_{max}}{Q^2_{min}}\right)$, $l_2 = 1 - \frac{Q^2_{max}}{Q^2_{min}}$, $l_3 = ln\left(\frac{y^2 + Q^2_{max}/E^2}{y^2 + Q^2_{min}/E^2}\right)$, $Q^2_{min} = \frac{m_e^2 y^2}{1-y}$, is calculated for

$$Q^2_{max(m_e)} = \frac{4m_e^2}{1-y}. \tag{16.14}$$

The factor $(1-y)$ is used arbitrarily to keep $Q^2_{max(m_e)} > Q^2_{min}$, which can be considered as a boundary between the low and high Q^2 regions. The full transverse photon flux can be calculated as an integral of Eq.(16.13) with the maximum possible upper limit

$$Q^2_{max(max)} = 4E^2(1-y). \tag{16.15}$$

The full transverse photon flux can be approximated by

$$\frac{y dn(y)}{dy} = -\frac{2\alpha}{\pi}\left(\frac{(2-y)^2 + y^2}{2}ln(\gamma) - 1\right), \tag{16.16}$$

where $\gamma = \frac{E}{m_e}$. It must be pointed out that neither this approximation nor Eq.(16.13) works at $y \simeq 1$; at this point $Q^2_{max(max)}$ becomes smaller than Q^2_{min}. The formal limit of the method is $y < 1 - \frac{1}{2\gamma}$.

In Fig. 16.1(a,b) the energy distribution for the equivalent photons is shown. The low-Q^2 photon flux with the upper limit defined by Eq.(16.14)) is compared with the full photon flux. The low-Q^2 photon flux is calculated using Eq.(16.11) (dashed lines) and using Eq.(16.13) (dotted lines). The full photon flux is calculated using Eq.(16.16) (the solid lines) and using Eq.(16.13) with the upper limit defined by Eq.(16.15) (dash-dotted lines, which differ from the solid lines only at $\nu \approx E_e$). The conclusion is that in order to calculate either the number of low-Q^2 equivalent photons or the total number of equivalent photons one can use the simple approximations given by Eq.(16.11) and Eq.(16.16), respectively, instead of using Eq.(16.13), which cannot be integrated over y analytically. Comparing the low-Q^2 photon flux and the total photon flux it is possible to show that the low-Q^2 photon flux is about half of the the total. From the interaction point of view the decrease of $\sigma_{\gamma*}$ with increasing Q^2 must be taken into account. The cross section reduction for the virtual photons with large Q^2 is governed by two factors. First, the cross section drops with Q^2 as the squared dipole nucleonic form-factor

$$G_D^2(Q^2) \approx \left(1 + \frac{Q^2}{(843\ MeV)^2}\right)^{-2}. \tag{16.17}$$

Second, all the thresholds of the γA reactions are shifted to higher ν by a factor $\frac{Q^2}{2M}$, which is the difference between the K and ν values. Following the
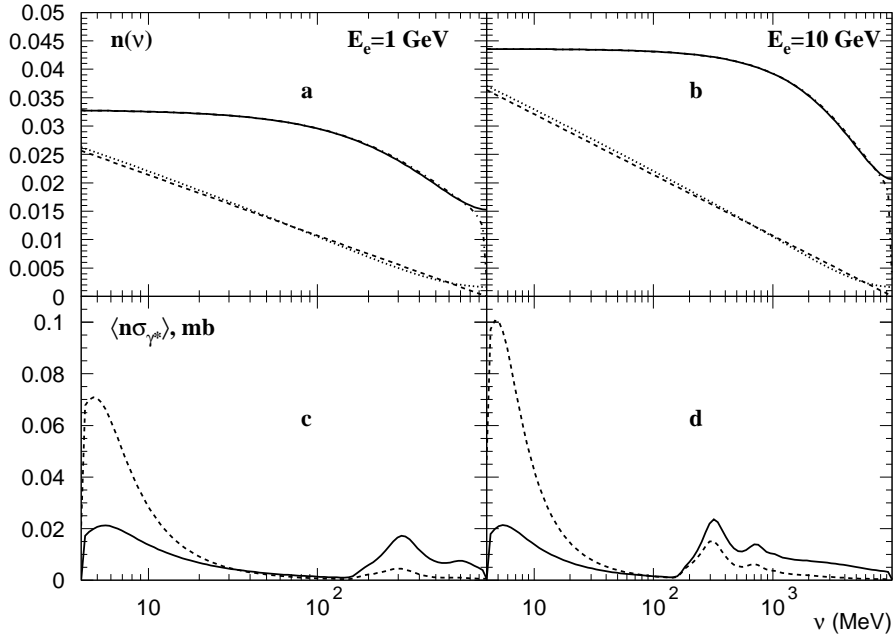
Figure 16.1: Relative contribution of equivalent photons with small Q^2 to the total "photon flux" for (a) 1 GeV electrons and (b) 10 GeV electrons. In figures (c) and (d) the equivalent photon distribution $dn(\nu, Q^2)$ is multiplied by the photonuclear cross section $\sigma_{\gamma*}(K, Q^2)$ and integrated over Q^2 in two regions: the dashed lines are integrals over the low-Q^2 equivalent photons (under the dashed line in the first two figures), and the solid lines are integrals over the high-Q^2 equivalent photons (above the dashed lines in the first two figures).

306

method proposed in [8] the $\sigma_{\gamma*}$ at large Q^2 can be approximated as

$$\sigma_{\gamma*} = (1 - x)\sigma_\gamma(K)G_D^2(Q^2)e^{b(\epsilon,K)\cdot r + c(\epsilon,K)\cdot r^3}, \tag{16.18}$$

where $r = \frac{1}{2}ln(\frac{Q^2+\nu^2}{K^2})$. The ϵ-dependence of the $a(\epsilon, K)$ and $b(\epsilon, K)$ functions is weak, so for simplicity the $b(K)$ and $c(K)$ functions are averaged over ϵ. They can be approximated as

$$b(K) \approx \left(\frac{K}{185\ MeV}\right)^{0.85}, \tag{16.19}$$

and

$$c(K) \approx -\left(\frac{K}{1390\ MeV}\right)^3. \tag{16.20}$$

The result of the integration of the photon flux multiplied by the cross section approximated by Eq.(16.18) is shown in Fig. 16.1(c,d). The integrated cross sections are shown separately for the low-Q^2 region ($Q^2 < Q^2_{max(m_e)}$, dashed lines) and for the high-Q^2 region ($Q^2 > Q^2_{max(m_e)}$, solid lines). These functions must be integrated over $ln(\nu)$, so it is clear that because of the Giant Dipole Resonance contribution, the low-Q^2 part covers more than half the total $eA \rightarrow hadrons$ cross section. But at $\nu > 200\ MeV$, where the hadron multiplicity increases, the large Q^2 part dominates. In this sense, for a better simulation of the production of hadrons by electrons, it is necessary to simulate the high-Q^2 part as well as the low-Q^2 part.

Taking into account the contribution of high-Q^2 photons it is possible to use Eq.(16.16) with the over-estimated $\sigma_{\gamma*A} = \sigma_{\gamma A}(\nu)$ cross section. The slightly over-estimated electronuclear cross section is

$$\sigma_{eA}^* = (2ln(\gamma) - 1) \cdot J_1 - \frac{ln(\gamma)}{E_e}\left(2J_2 - \frac{J_3}{E_e}\right). \tag{16.21}$$

where

$$J_1(E_e) = \frac{\alpha}{\pi}\int^{E_e}\sigma_{\gamma A}(\nu)dln(\nu) \tag{16.22}$$

$$J_2(E_e) = \frac{\alpha}{\pi}\int^{E_e}\nu\sigma_{\gamma A}(\nu)dln(\nu), \tag{16.23}$$

and

$$J_3(E_e) = \frac{\alpha}{\pi}\int^{E_e}\nu^2\sigma_{\gamma A}(\nu)dln(\nu). \tag{16.24}$$

The equivalent photon energy $\nu = yE$ can be obtained for a particular random number R from the equation

$$R = \frac{(2ln(\gamma) - 1)J_1(\nu) - \frac{ln(\gamma)}{E_e}(2J_2(\nu) - \frac{J_3(\nu)}{E_e})}{(2ln(\gamma) - 1)J_1(E_e) - \frac{ln(\gamma)}{E_e}(2J_2(E_e) - \frac{J_3(E_e)}{E_e})}.\qquad(16.25)$$

Eq.(16.13) is too complicated for the randomization of Q^2 but there is an easily randomized formula which approximates Eq.(16.13) above the hadronic threshold ($E > 10~MeV$). It reads

$$\frac{\pi}{\alpha D(y)}\int_{Q^2_{min}}^{Q^2}\frac{ydn(y, Q^2)}{dydQ^2}dQ^2 = -L(y, Q^2) - U(y),\qquad(16.26)$$

where

$$D(y) = 1 - y + \frac{y^2}{2},\qquad(16.27)$$

$$L(y, Q^2) = ln\left(F(y) + (e^{P(y)} - 1 + \frac{Q^2}{Q^2_{min}})^{-1}\right),\qquad(16.28)$$

and

$$U(y) = P(y) \cdot \left(1 - \frac{Q^2_{min}}{Q^2_{max}}\right),\qquad(16.29)$$

with

$$F(y) = \frac{(2 - y)(2 - 2y)}{y^2} \cdot \frac{Q^2_{min}}{Q^2_{max}}\qquad(16.30)$$

and

$$P(y) = \frac{1 - y}{D(y)}.\qquad(16.31)$$

The Q^2 value can then be calculated as

$$\frac{Q^2}{Q^2_{min}} = 1 - e^{P(y)} + \left(e^{R \cdot L(y, Q^2_{max}) - (1-R) \cdot U(y)} - F(y)\right)^{-1},\qquad(16.32)$$

where R is a random number. In Fig. 16.2, Eq.(16.13) (solid curve) is compared to Eq.(16.26) (dashed curve). Because the two curves are almost indistinguishable in the figure, this can be used as an illustration of the Q^2 spectrum of virtual photons, which is the derivative of these curves. An alternative approach is to use Eq.(16.13) for the randomization with a three dimensional table $\frac{ydn}{dy}(Q^2, y, E_e)$.

After the ν and Q^2 values have been found, the value of $\sigma_{\gamma^* A}(\nu, Q^2)$ is calculated using Eq.(16.18). If $R \cdot \sigma_{\gamma A}(\nu) > \sigma_{\gamma^* A}(\nu, Q^2)$, no interaction occurs and the electron keeps going. This "do nothing" process has low probability and cannot shadow other processes.
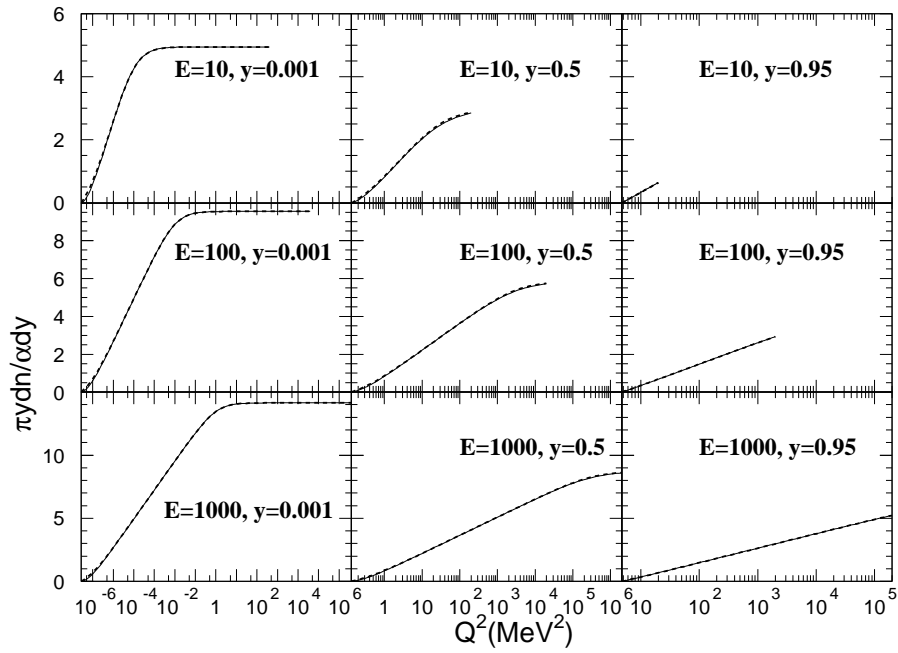
Figure 16.2: Integrals of Q^2 spectra of virtual photons for three energies 10 MeV, 100 MeV, and 1 GeV at $y = 0.001$, $y = 0.5$, and $y = 0.95$. The solid line corresponds to Eq.(16.13) and the dashed line (which almost everywhere coincides with the solid line) corresponds to Eq.(16.13).

16.3 Status of this document

created by ?
20.05.02 re-written by D.H. Wright
01.12.02 expanded section on electronuclear cross sections - H.P. Wellisch

Bibliography

[1] E. Fermi, Z. Physik **29**, 315 (1924).

[2] K. F. von Weizsacker, Z. Physik **88**, 612 (1934), E. J. Williams, Phys. Rev. **45**, 729 (1934).

[3] L. D. Landau and E. M. Lifshitz, Soc. Phys. **6**, 244 (1934).

[4] I. Ya. Pomeranchuk and I. M. Shmushkevich, Nucl. Phys. **23**, 1295 (1961).

[5] V. N. Gribov *et al.*, ZhETF **41**, 1834 (1961).

[6] L. D. Landau, E. M. Lifshitz, "Course of Theoretical Physics" v.4, part 1, "Relativistic Quantum Theory", Pergamon Press, p. 351, The method of equivalent photons.

[7] V. M. Budnev *et al.*, Phys. Rep. **15**, 181 (1975).

[8] F. W. Brasse *et al.*, Nucl. Phys. B **110**, 413 (1976).

Chapter 17

Total Reaction Cross Section in Nucleus-nucleus Reactions

The transportation of heavy ions in matter is a subject of much interest in several fields of science. An important input for simulations of this process is the total reaction cross section, which is defined as the total (σ_T) minus the elastic (σ_{el}) cross section for nucleus-nucleus reactions:

$$\sigma_R = \sigma_T - \sigma_{el}.$$

The total reaction cross section has been studied both theoretically and experimentally and several empirical parameterizations of it have been developed. In Geant4 the total reaction cross sections are calculated using four such parameterizations: the Sihver[1], Kox[2], Shen[3] and Tripathi[4] formulae. Each of these is discussed in order below.

17.1 Sihver Formula

Of the four parameterizations, the Sihver formula has the simplest form:

$$\sigma_R = \pi r_0^2 [A_p^{1/3} + A_t^{1/3} - b_0[A_p^{-1/3} + A_t^{-1/3}]]^2 \qquad (17.1)$$

where A_p and A_t are the mass numbers of the projectile and target nuclei, and

$$b_0 = 1.581 - 0.876(A_p^{-1/3} + A_t^{-1/3}),$$

$$r_0 = 1.36 fm.$$

It consists of a nuclear geometrical term $(A_p^{1/3} + A_t^{1/3})$ and an overlap or transparency parameter (b_0) for nucleons in the nucleus. The cross section is independent of energy and can be used for incident energies greater than 100 MeV/nucleon.

17.2   Kox and Shen Formulae

Both the Kox and Shen formulae are based on the strong absorption model. They express the total reaction cross section in terms of the interaction radius R, the nucleus-nucleus interaction barrier B, and the center-of-mass energy of the colliding system E_{CM}:

$$\sigma_R = \pi R^2 [1 - \frac{B}{E_{CM}}]. \tag{17.2}$$

Kox formula: Here B is the Coulomb barrier (B_c) of the projectile-target system and is given by

$$B_c = \frac{Z_t Z_p e^2}{r_C(A_t^{1/3} + A_p^{1/3})},$$

where $r_C = 1.3$ fm, e is the electron charge and Z_t, Z_p are the atomic numbers of the target and projectile nuclei. R is the interaction radius R_{int} which in the Kox formula is divided into volume and surface terms:

$$R_{int} = R_{vol} + R_{surf}.$$

R_{vol} and R_{surf} correspond to the energy-independent and energy-dependent components of the reactions, respectively. Collisions which have relatively small impact parameters are independent of both energy and mass number. These core collisions are parameterized by R_{vol}. Therefore R_{vol} can depend only on the volume of the projectile and target nuclei:

$$R_{vol} = r_0(A_t^{1/3} + A_p^{1/3}).$$

The second term of the interaction radius is a nuclear surface contribution and is parameterized by

$$R_{surf} = r_0[a\frac{A_t^{1/3}A_p^{1/3}}{A_t^{1/3} + A_p^{1/3}} - c] + D.$$

The first term in brackets is the mass asymmetry which is related to the volume overlap of the projectile and target. The second term c is

an energy-dependent parameter which takes into account increasing surface transparency as the projectile energy increases. D is the neutron-excess which becomes important in collisions of heavy or neutron-rich targets. It is given by

$$D = \frac{5(A_t - Z_t)Z_p}{A_p A_r}.$$

The surface component (R_{surf}) of the interaction radius is actually not part of the simple framework of the strong absorption model, but a better reproduction of experimental results is possible when it is used.

The parameters r_0, a and c are obtained using a χ^2 minimizing procedure with the experimental data. In this procedure the parameters r_0 and a were fixed while c was allowed to vary only with the beam energy per nucleon. The best χ^2 fit is provided by $r_0 = 1.1$ fm and $a = 1.85$ with the corresponding values of c listed in Table III and shown in Fig. 12 of Ref. [2] as a function of beam energy per nucleon. This reference presents the values of c only in chart and figure form, which is not suitable for Monte Carlo calculations. Therefore a simple analytical function is used to calculate c in Geant4. The function is:

$$c = -\frac{10}{x^5} + 2.0 \text{ for x} \geq 1.5$$

$$c = (-\frac{10}{1.5^5} + 2.0) \times (\frac{x}{1.5})^3 \text{ for x} < 1.5,$$

$$x = log(KE),$$

where KE is the projectile kinetic energy in units of MeV/nucleon in the laboratory system.

Shen formula: as mentioned earlier, this formula is also based on the strong absorption model, therefore it has a structure similar to the Kox formula:

$$\sigma_R = 10\pi R^2 [1 - \frac{B}{E_{CM}}]. \tag{17.3}$$

However, different parameterized forms for R and B are applied. The interaction radius R is given by

$$R = r_0 [A_t^{1/3} + A_p^{1/3} + 1.85 \frac{A_t^{1/3} A_p^{1/3}}{A_t^{1/3} + A_p^{1/3}} - C'(KE)]$$

$$+ \alpha \frac{5(A_t - Z_t)Z_p}{A_p A_r} + \beta E_{CM}^{-1/3} \frac{A_t^{1/3} A_p^{1/3}}{A_t^{1/3} + A_p^{1/3}}$$

313

where α, β and r_0 are

$$\alpha = 1 fm$$

$$\beta = 0.176 MeV^{1/3} \cdot fm$$

$$r_0 = 1.1 fm$$

In Ref. [3] as well, no functional form for $C'(KE)$ is given. Hence the same simple analytical function is used by Geant4 to derive c values.

The second term B is called the nuclear-nuclear interaction barrier in the Shen formula and is given by

$$B = \frac{1.44 Z_t Z_p}{r} - b\frac{R_t R_p}{R_t + R_p}(MeV)$$

where r, b, R_t and R_p are given by

$$r = R_t + R_p + 3.2 fm$$

$$b = 1 MeV \cdot fm^{-1}$$

$$R_i = 1.12 A_i^{1/3} - 0.94 A_i^{-1/3} \ (i = t, p)$$

The difference between the Kox and Shen formulae appears at energies below 30 MeV/nucleon. In this region the Shen formula shows better agreement with the experimental data in most cases.

17.3 Tripathi formula

Because the Tripathi formula is also based on the strong absorption model its form is similar to the Kox and Shen formulae:

$$\sigma_R = \pi r_0^2 (A_p^{1/3} + A_t^{1/3} + \delta_E)^2 [1 - \frac{B}{E_{CM}}], \tag{17.4}$$

where $r_0 = 1.1$ fm. In the Tripathi formula B and R are given by

$$B = \frac{1.44 Z_t Z_p}{R}$$

$$R = r_p + r_t + \frac{1.2(A_p^{1/3} + A_t^{1/3})}{E_{CM}^{1/3}}$$

where r_i is the equivalent sphere radius and is related to the $r_{rms,i}$ radius by

$$r_i = 1.29 r_{rms,i} \ (i = p, t).$$

δ_E represents the energy-dependent term of the reaction cross section which is due mainly to transparency and Pauli blocking effects. It is given by

$$\delta_E = 1.85S + (0.16S/E_{CM}^{1/3}) - C_{KE} + [0.91(A_t - 2Z_t)Z_p/(A_p A_t)],$$

where S is the mass asymmetry term given by

$$S = \frac{A_p^{1/3} A_t^{1/3}}{A_p^{1/3} + A_t^{1/3}}.$$

This is related to the volume overlap of the colliding system. The last term accounts for the isotope dependence of the reaction cross section and corresponds to the D term in the Kox formula and the second term of R in the Shen formula.

The term C_{KE} corresponds to c in Kox and $C'(KE)$ in Shen and is given by

$$C_E = D_{Pauli}[1 - \exp(-KE/40)] - 0.292 \exp(-KE/792) \times \cos(0.229 KE^{0.453}).$$

Here D_{Pauli} is related to the density dependence of the colliding system, scaled with respect to the density of the $^{12}C + ^{12}C$ colliding system:

$$D_{Pauli} = 1.75 \frac{\rho_{A_p} + \rho_{A_t}}{\rho_{A_C} + \rho_{A_C}}.$$

The nuclear density is calculated in the hard sphere model. D_{Pauli} simulates the modifications of the reaction cross sections caused by Pauli blocking and is being introduced to the Tripathi formula for the first time. The modification of the reaction cross section due to Pauli blocking plays an important role at energies above 100 MeV/nucleon. Different forms of D_{Pauli} are used in the Tripathi formula for alpha-nucleus and lithium-nucleus collisions. For alpha-nucleus collisions,

$$D_{Pauli} = 2.77 - (8.0 \times 10^{-3} A_t) + (1.8 \times 10^{-5} A_t^2)$$
$$-0.8/\{1 + \exp[(250 - KE)/75]\}$$

315

For lithium-nucleus collisions,

$$D_{Pauli} = D_{Pauli}/3.$$

Note that the Tripathi formula is not fully implemented in Geant4 and can only be used for projectile energies less than 1 GeV/nucleon.

17.4   Representative Cross Sections

Representative cross section results from the Sihver, Kox, Shen and Tripathi formulae in Geant4 are displayed in Table I and compared to the experimental measurements of Ref. [2].

17.5   Tripathi Formula for "light" Systems

For nuclear-nuclear interactions in which the projectile and/or target are light, Tripathi *et al* [6] propose an alternative algorithm for determining the interaction cross section (implemented in the new class G4TripathiLightCrossSection). For such systems, Eq.17.4 becomes:

$$\sigma_R = \pi r_0^2 [A_p^{1/3} + A_t^{1/3} + \delta_E]^2 (1 - R_C \frac{B}{E_{CM}}) X_m \qquad (17.5)$$

R_C is a Coulomb multiplier, which is added since for light systems Eq. 17.4 overestimates the interaction distance, causing B (in Eq. 17.4) to be underestimated. Values for R_C are given in Table 17.2.

$$X_m = 1 - X_1 \exp\left(-\frac{E}{X_1 S_L}\right) \qquad (17.6)$$

where:

$$X_1 = 2.83 - \left(3.1 \times 10^{-2}\right) A_T + \left(1.7 \times 10^{-4}\right) A_T^2 \qquad (17.7)$$

except for neutron interactions with ^{4}He, for which X_1 is better approximated to 5.2, and the function S_L is given by:

$$S_L = 1.2 + 1.6 \left[1 - \exp\left(-\frac{E}{15}\right)\right] \qquad (17.8)$$

For light nuclear-nuclear collisions, a slightly more general expression for C_E is used:

$$C_E = D \left[1 - \exp\left(-\frac{E}{T_1} \right) \right] - 0.292 \exp\left(-\frac{E}{792} \right) \cdot \cos\left(0.229 E^{0.453} \right) \quad (17.9)$$

D and T_1 are dependent on the interaction, and are defined in table 17.3.

17.6   Status of this document

25.11.03 created by Tatsumi Koi
28.11.03 grammar check and re-wording by D.H. Wright
18.06.04 light system section added by Peter Truscott

Bibliography

[1] L. Sihver et al., Phys. Rev. C47, 1225 (1993).

[2] Kox et al. Phys. Rev. C35, 1678 (1987).

[3] Shen et al. Nucl. Phys. A491, 130 (1989).

[4] Tripathi et al, NASA Technical Paper 3621 (1997).

[5] Jaros et al, Phys. Rev. C 18 2273 (1978).

[6] R K Tripathi, F A Cucinotta, and J W Wilson, "Universal parameterization of absorption cross-sections - Light systems," NASA Technical Paper TP-1999-209726, 1999.

Table 17.1: Representative total reaction cross sections

Proj.	Target	Elab [MeV/n]	Exp. Results [mb]	Sihver	Kox	Shen	Tripathi
^{12}C	^{12}C	30	1316±40	—	1295.04	1316.07	1269.24
		83	965±30	—	957.183	969.107	989.96
		200	864±45	868.571	885.502	893.854	864.56
		300	858±60	868.571	871.088	878.293	857.414
		870[1]	939±50	868.571	852.649	857.683	939.41
		2100[1]	888±49	868.571	846.337	850.186	936.205
	^{27}Al	30	1748±85	—	1801.4	1777.75	1701.03
		83	1397±40	—	1407.64	1386.82	1405.61
		200	1270±70	1224.95	1323.46	1301.54	1264.26
		300	1220±85	1224.95	1306.54	1283.95	1257.62
	^{89}Y	30	2724±300	—	2898.61	2725.23	2567.68
		83	2124±140	—	2478.61	2344.26	2346.54
		200	1885±120	2156.47	2391.26	2263.77	2206.01
		300	1885±150	2156.47	2374.17	2247.55	2207.01
^{16}O	^{27}Al	30	1724±80	—	1965.85	1935.2	1872.23
	^{89}Y	30	2707±330	—	3148.27	2957.06	2802.48
^{20}Ne	^{27}Al	30	2113±100	—	2097.86	2059.4	2016.32
		100	1446±120	1473.87	1684.01	1658.31	1667.17
		300	1328±120	1473.87	1611.88	1586.17	1559.16
	^{108}Ag	300	2407±200[2]	2730.69	3095.18	2939.86	2893.12

1. Data measured by Jaros et al. [5]
2. Natural silver was used in this measurement.

Table 17.2: Coulomb multiplier for light systems [6].

System	R_C
p + d	13.5
p + ^{3}He	21
p + ^{4}He	27
p + Li	2.2
d + d	13.5
d + ^{4}He	13.5
d + C	6.0
^{4}He + Ta	0.6
^{4}He + Au	0.6

Table 17.3: Parameters D and T1 for light systems [6].

System	T1 [MeV]	D	G [MeV] (^{4}He + X only)
p + X	23	$1.85 + \frac{0.16}{1+\exp\left(\frac{500-E}{200}\right)}$	(Not applicable)
n + X	18	$1.85 + \frac{0.16}{1+\exp\left(\frac{500-E}{200}\right)}$	(Not applicable)
d + X	23	$1.65 + \frac{0.1}{1+\exp\left(\frac{500-E}{200}\right)}$	(Not applicable)
^{3}He + X	40	1.55	(Not applicable)
^{4}He + ^{4}He	40	$D = 2.77 - 8.0 \times 10^{-3} A_T$ $+1.8 \times 10^{-5} A_T^2$ $-\frac{0.8}{1+\exp\left(\frac{250-E}{G}\right)}$	300
^{4}He + Be	25	(as for ^{4}He + ^{4}He)	300
^{4}He + N	40	(as for ^{4}He + ^{4}He)	500
^{4}He + Al	25	(as for ^{4}He + ^{4}He)	300
^{4}He + Fe	40	(as for ^{4}He + ^{4}He)	300
^{4}He + X (general)	40	(as for ^{4}He + ^{4}He)	75

Chapter 18

Coherent elastic scattering

18.1 Nucleon-Nucleon elastic Scattering

The classes G4LEpp and G4LEnp provide data-driven models for proton-proton (or neutron-neutron) and neutron-proton elastic scattering over the range 10-1200 MeV. Final states (primary and recoil particle) are derived by sampling from tables of the cumulative distribution function of the centre-of-mass scattering angle, tabulated for a discrete set of lab kinetic energies from 10 MeV to 1200 MeV. The CDF's are tabulated at 1 degree intervals and sampling is done using bi-linear interpolation in energy and CDF values. The data are derived from differential cross sections obtained from the SAID database, R. Arndt, 1998.

In class G4LEpp there are two data sets: one including Coulomb effects (for p-p scattering) and one with no Coulomb effects (for n-n scattering or p-p scattering with Coulomb effects suppressed). The method G4LEpp::SetCoulombEffects can be used to select the desired data set:

- SetCoulombEffects(0): No Coulomb effects (the default)

- SetCoulombEffects(1): Include Coulomb effects

The recoil particle will be generated as a new secondary particle. In class G4LEnp, the possiblity of a charge-exchange reaction is included, in which case the incident track will be stopped and both the primary and recoil particles will be generated as secondaries.

Chapter 19

Hadron-nucleus Elastic Scattering at Medium and High Energy

19.1 Method of Calculation

The Glauber model [1] is used as an alternative method of calculating differential cross sections for elastic and quasi-elastic hadron-nucleus scattering at high and intermediate energies.

For high energies this includes corrections for inelastic screening and for quasi-elastic scattering the exitation of a discrete level or a state in the continuum is considered.

The usual expression for the Glauber model amplitude for multiple scattering was used

$$F(q) = \frac{ik}{2\pi} \int d^2 b e^{\vec{q}\cdot\vec{b}} M(\vec{b}).$$

(19.1)

Here $M(\vec{b})$ is the hadron-nucleus amplitude in the impact parameter representation

$$M(\vec{b}) = 1 - [1 - e^{-A \int d^3 r \Gamma(\vec{b}-\vec{s})\rho(\vec{r})}]^A,$$

(19.2)

k is the incident particle momentum, $\vec{q} = \vec{k}' - \vec{k}$ is the momentum transfer, and $\vec{k}'$ is the scattered particle momentum. Note that $|\vec{q}|^2 = -t$ - invariant momentum transfer squared in the center of mass system. $\Gamma(\vec{b})$ is the hadron-nucleon amplitude of elastic scattering in the impact-parameter representation

$$\Gamma(\vec{b}) = \frac{1}{2\pi i k^{hN}} \int d\vec{q} e^{-\vec{q}\cdot\vec{b}} f(\vec{q}). \tag{19.3}$$

The exponential parameterization of the hadron-nucleon amplitude is usually used:

$$f(\vec{q}) = \frac{i k^{hN} \sigma^{hN}}{2\pi} e^{-0.5 q^2 B}. \tag{19.4}$$

Here $\sigma^{hN} = \sigma_{tot}^{hN}(1 - i\alpha)$, σ_{tot}^{hN} is the total cross section of a hadron-nucleon scattering, B is the slope of the diffraction cone and α is the ratio of the real to imaginary parts of the amplitude at $q = 0$. The value k^{hN} is the hadron momentum in the hadron-nucleon coordinate system.

The important difference of these calculations from the usual ones is that the two-gaussian form of the nuclear density was used

$$\rho(r) = C(e^{-(r/R_1)^2} - p e^{-(r/R_2)^2}), \tag{19.5}$$

where R_1, R_2 and p are the fitting parameters and C is a normalization constant.

This density representation allows the expressions for amplitude and differential cross section to be put into analytical form. It was earlier used for light [2, 3] and medium [4] nuclei. Described below is an extension of this method to heavy nuclei. The form 19.5 is not physical for a heavy nucleus, but nevertheless works rather well (see figures below). The reason is that the nucleus absorbs the hadrons very strongly, especially at small impact parameters where the absorption is full. As a result only the peripherial part of the nucleus participates in elastic scattering. Eq. 19.5 therefore describes only the edge of a heavy nucleus.

Substituting Eqs. 19.5 and 19.4 into Eqs. 19.1, 19.2 and 19.3 yields the following formula

$$F(q) = \frac{ik\pi}{2} \sum_{k=1}^{A} (-1)^k \binom{A}{k} [\frac{\sigma^{hN}}{2\pi(R_1^3 - pR_2^3)}]^k \sum_{m=0}^{k} (-1)^m \binom{k}{m} \left[\frac{R_1^3}{R_1^2 + 2B}\right]^{k-m}$$

$$\times \quad \left[\frac{pR_2^3}{R_2^2 + 2B}\right]^m \left(\frac{m}{R_2^2 + 2B} + \frac{k-m}{R_1^2 + 2B}\right)^{-1}$$

$$\times \quad \exp\left[-\frac{-q^2}{4}\left(\frac{m}{R_2^2 + 2B} + \frac{k-m}{R_1^2 + 2B}\right)^{-1}\right]. \tag{19.6}$$

An analogous procedure can be used to get the inelastic screening corrections to the hadron-nucleus amplitude $\Delta M(\vec{b})$ [5]. In this case an intermediate inelastic diffractive state is created which rescatters on the nucleons of the nucleus and then returns into the initial hadron. Hence it is nessesary to integrate the production cross section over the mass distribution of the exited system $\frac{d\sigma^{diff}}{dt dM_x^2}$. The expressions for the corresponding amplitude are quite long and so are not presented here. The corrections for the total cross-sections can be found in [5].

The full amplitude is the sum $M(\vec{b}) + \Delta M(\vec{b})$.

The differential cross section is connected with the amplitude in the following way

$$\frac{d\sigma}{d\Omega_{CM}} = |F(q)|^2, \qquad \frac{d\sigma}{|dt|} = \frac{d\sigma}{dq_{CM}^2} = \frac{\pi}{k_{CM}^2} |F(q)|^2. \qquad (19.7)$$

The main energy dependence of the hadron-nucleus elastic scattering cross section comes from the energy dependence of the parameters of hadron-nucleon scattering ($\sigma_{tot}^{hN} \alpha$, B and $\frac{d\sigma^{diff}}{dt dM_x^2}$). At interesting energies these parameters were fixed at their well-known values. The fitting of the nuclear density parameters was performed over a wide range of atomic numbers ($A = 4 - 208$) using experimental data on proton-nuclei elastic scattering at a kinetic energy of $T_p = 1 GeV$.

The fitting was perfomed both for individual nuclei and for the entire set of nuclei at once.

It is necessary to note that for every nucleus an optimal set of density parameters exists and it differs slightly from the one derived for the full set of nuclei.

A comparision of the phenomenological cross sections [6] with experiment is presented in Figs. 19.1 - 19.9

In this comparison, the individual nuclei parameters were used. The experimental data were obtained in Gatchina (Russia) and in Saclay (France) [6]. The horizontal axis is the scattering angle in the center of mass system Θ_{CM} and the vertical axis is $\frac{d\sigma}{d\Omega_{CM}}$ in $\frac{mb}{Ster}$.

Comparisions were also made for p^4He elastic scatering at $T_=1GeV$[7], $45GeV$ and $301GeV$ [3]. The resulting cross sections $\frac{d\sigma}{d|t|}$ are shown in the Figs. 19.10 - 19.12.

In order to generate events the distribution function $\mathcal{F}$ of a corresponding process must be known. The differential cross section is proportional to the density distribution. Therefore to get the distribution function it is sufficient to integrate the differential cross section and normalize it:

$$\mathcal{F}(q^2) = \frac{\int\limits_{0}^{q^2} d(q^2)\dfrac{d\sigma}{d(q^2)}}{\int\limits_{0}^{q_{max}^2} d(q^2)\dfrac{d\sigma}{d(q^2)}}.$$

(19.8)

Expressions 19.6 and 19.7 allow analytic integration in Eq. 19.8 but the result is too long to be given here.

For light and medium nuclei the analytic expression is more convenient for calculations than the numerical integration of Eq. 19.8, but for heavy nuclei the latter is preferred due to the large number of terms in the analytic expression.

19.2 Status of this document

18.06.04 created by Nikolai Starkov
19.06.04 re-written for spelling and grammar by D.H. Wright

Bibliography

[1] R.J. Glauber, in "High Energy Physics and Nuclear Structure", edited by S. Devons (Plenum Press, NY 1970).

[2] R. H. Bassel, W. Wilkin, Phys. Rev., 174, p. 1179, 1968;
T. T. Chou, Phys. Rev., 168, 1594, 1968;
M. A. Nasser, M. M. Gazzaly, J. V. Geaga et al., Nucl. Phys., A312, pp. 209-216, 1978.

[3] Bujak, P. Devensky, A. Kuznetsov et al., Phys. Rev., D23, N 9, pp. 1895-1910, 1981.

[4] V. L. Korotkikh, N. I. Starkov, Sov. Journ. of Nucl. Phys., v. 37, N 4, pp. 610-613, 1983;
N. T. Ermekov, V. L. Korotkikh, N. I. Starkov, Sov. Journ. of Nucl. Phys., 33, N 6, pp. 775-777, 1981.

[5] R.A. Nam, S. I. Nikol'skii, N. I. Starkov et al., Sov. Journ. of Nucl. Phys., v. 26, N 5, pp. 550-555, 1977.

[6] G.D. Alkhazov et al., Phys. Rep., 1978, C42, N 2, pp. 89-144;

[7] J. V. Geaga, M. M. Gazzaly, G. J. Jgo et al., Phys. Rev. Lett. 38, N
22, pp. 1265-1268;
S. J. Wallace. Y. Alexander, Phys. Rev. Lett. 38, N 22, pp. 1269-1272.

Figure 19.1: Elastic proton scattering on ^{9}Be at 1 GeV

Figure 19.2: Elastic proton scattering on ^{11}B at 1 GeV

Figure 19.3: Elastic proton scattering on ^{12}C at 1 GeV

Figure 19.4: Elastic proton scattering on ^{16}O at 1 GeV
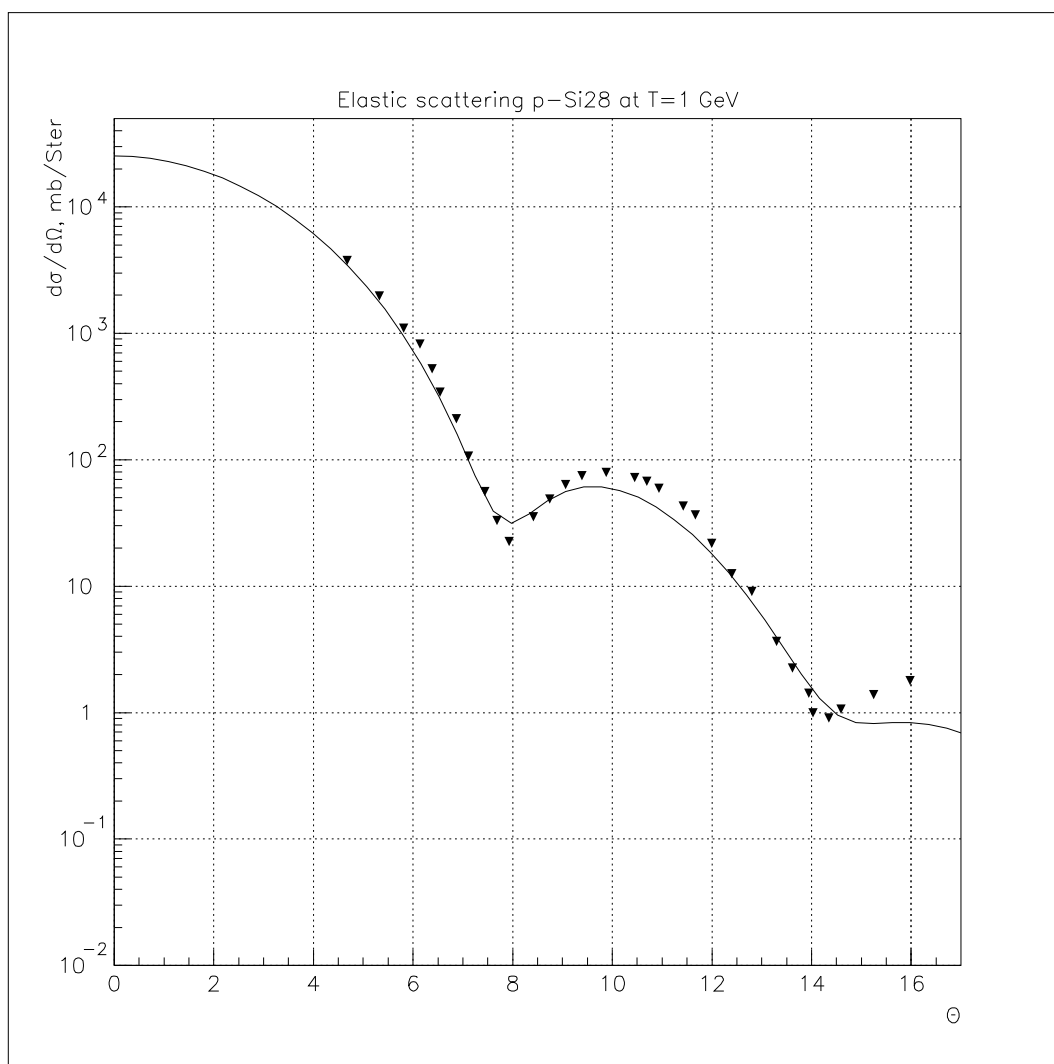
Figure 19.5: Elastic proton scattering on ^{28}Si at 1 GeV
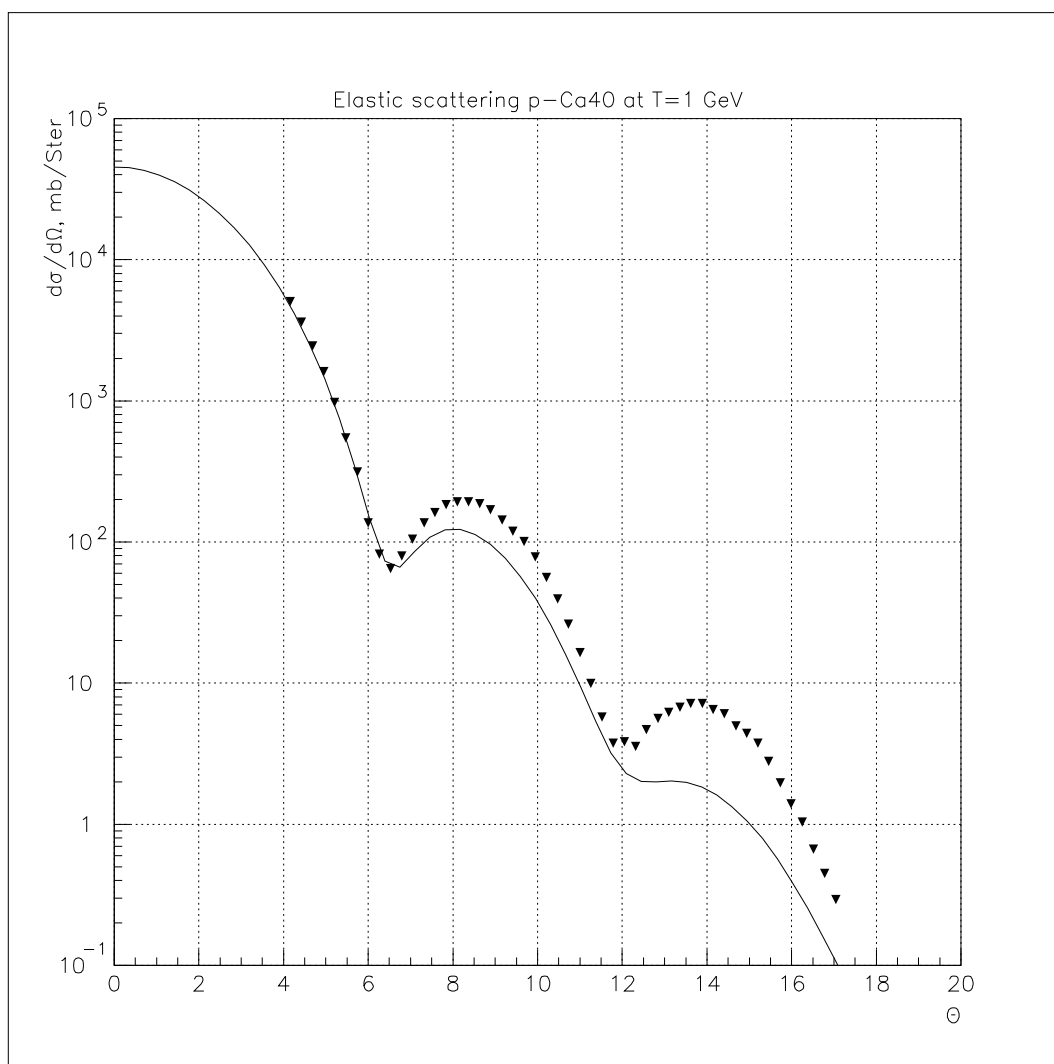
Figure 19.6: Elastic proton scattering on ^{40}Ca at 1 GeV
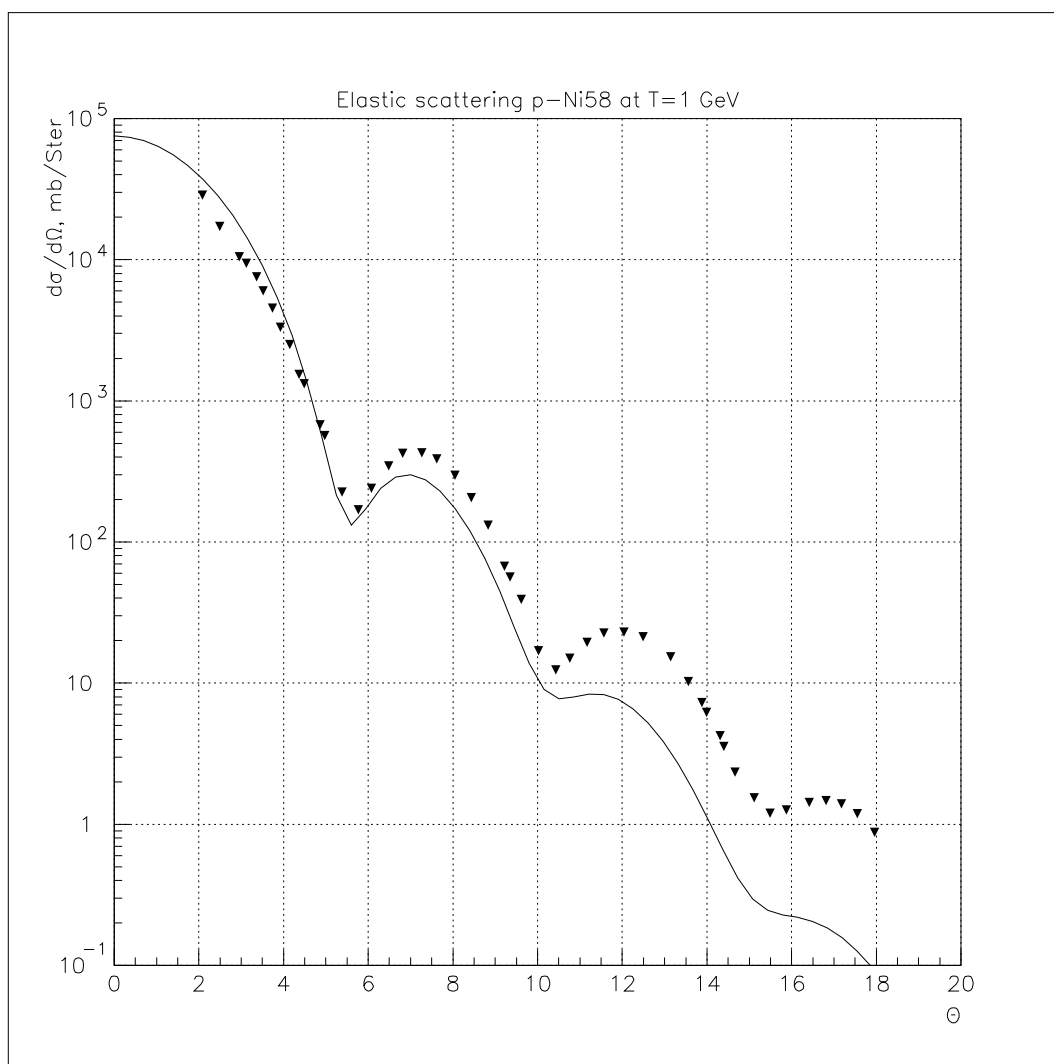
Figure 19.7: Elastic proton scattering on ^{58}Ni at 1 GeV
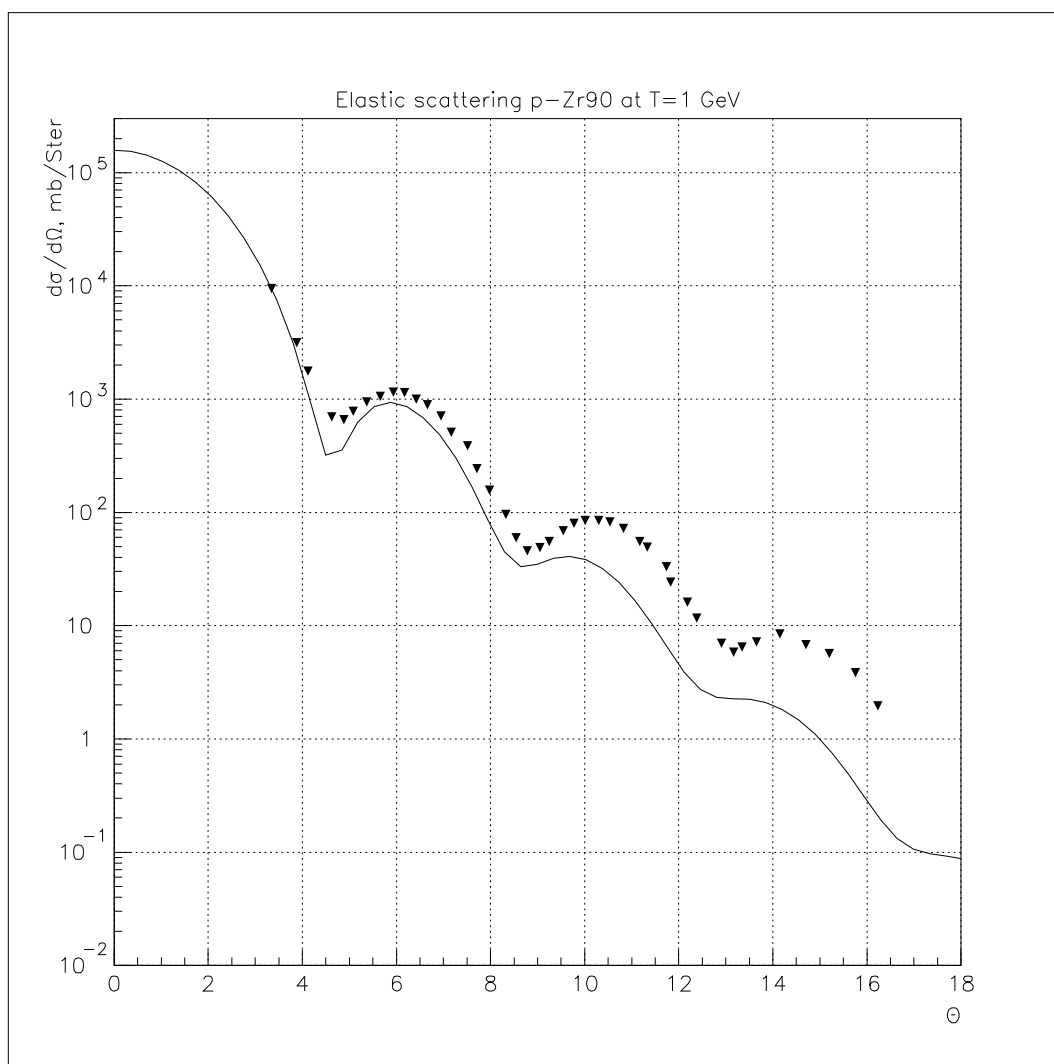
Figure 19.8: Elastic proton scattering on ^{90}Zr at 1 GeV
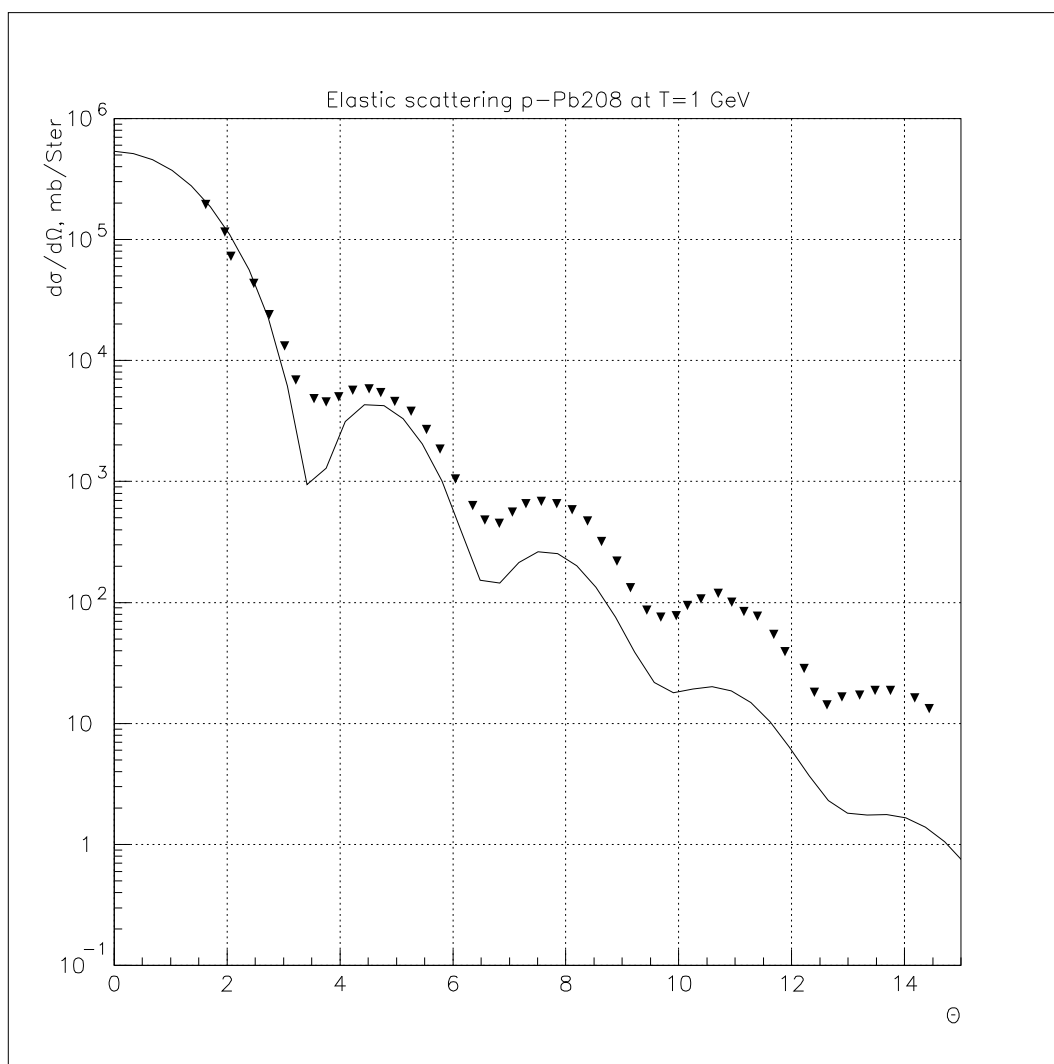
Figure 19.9: Elastic proton scattering on ^{208}Pb at 1 GeV
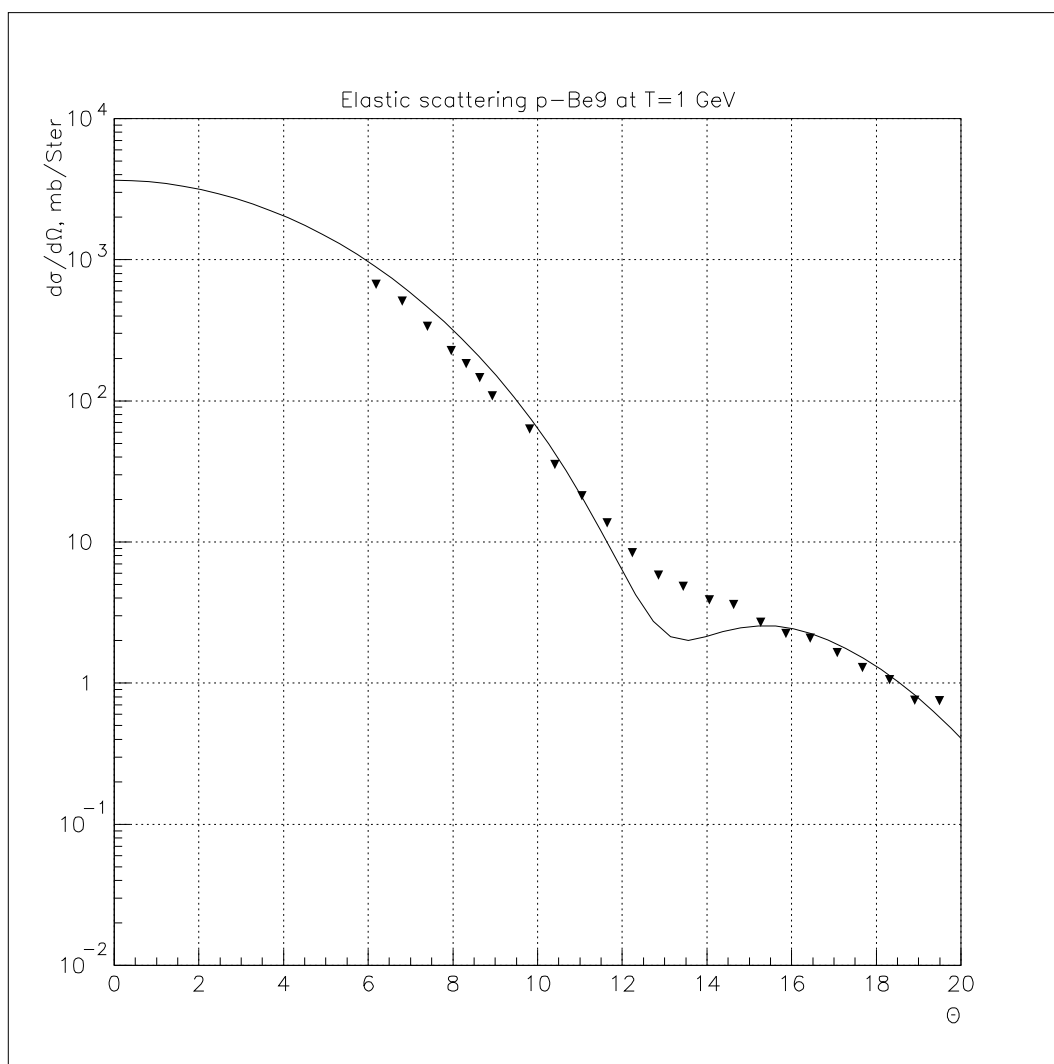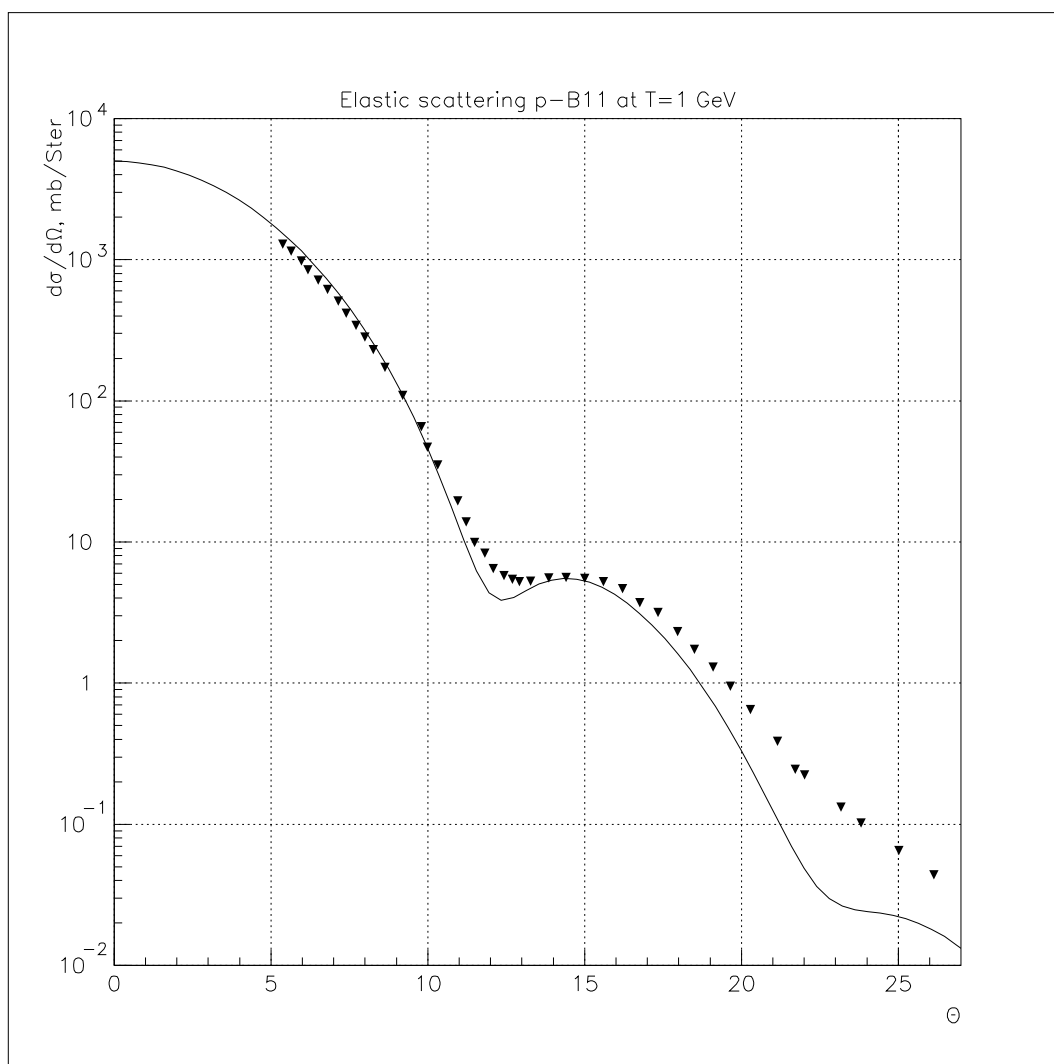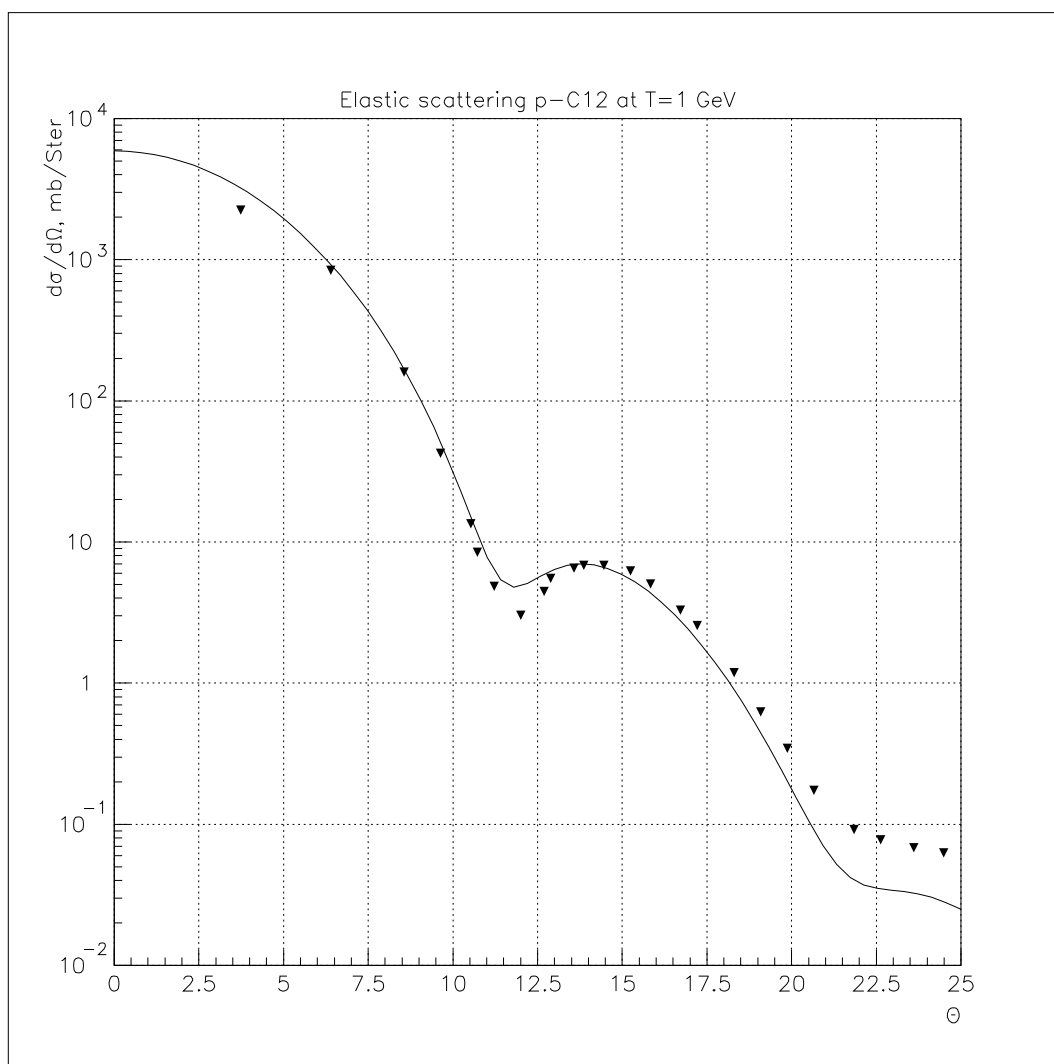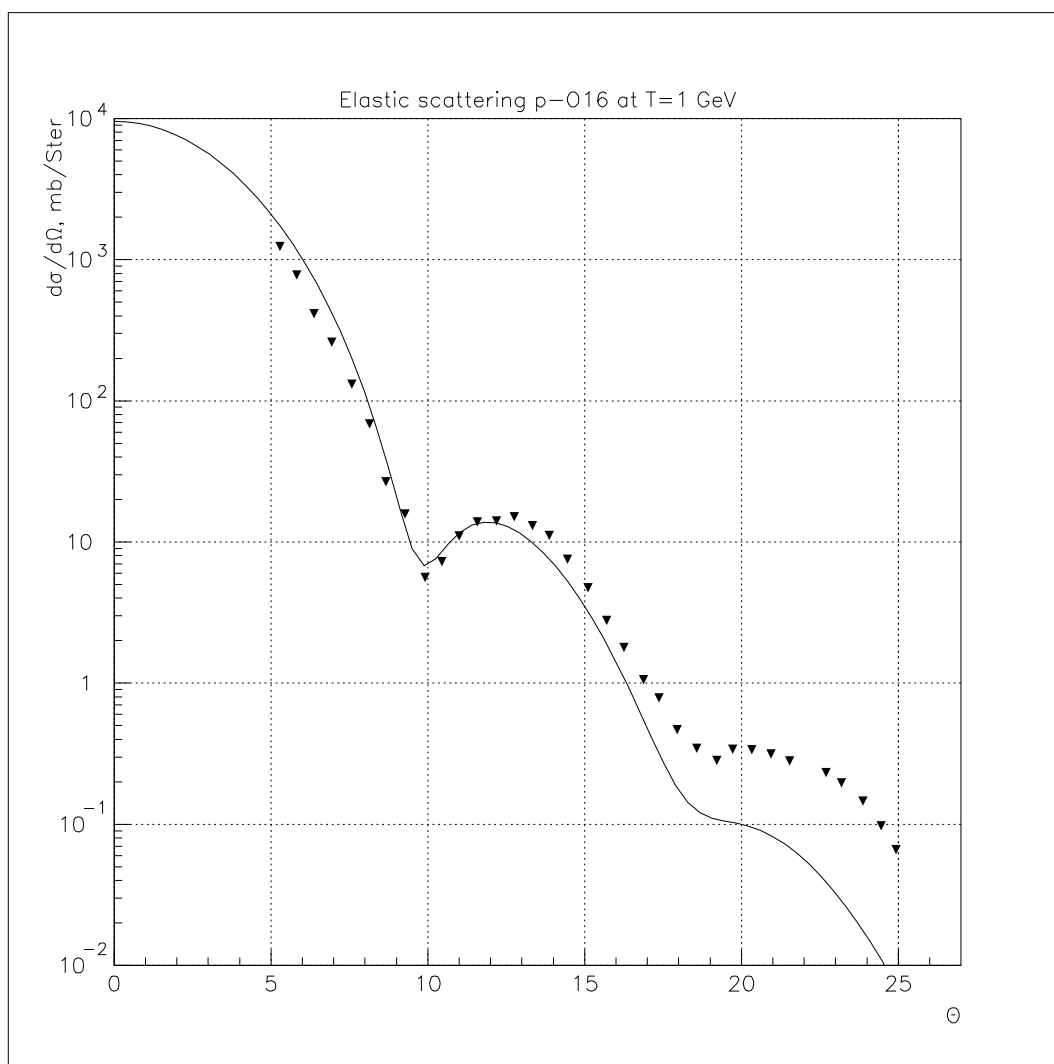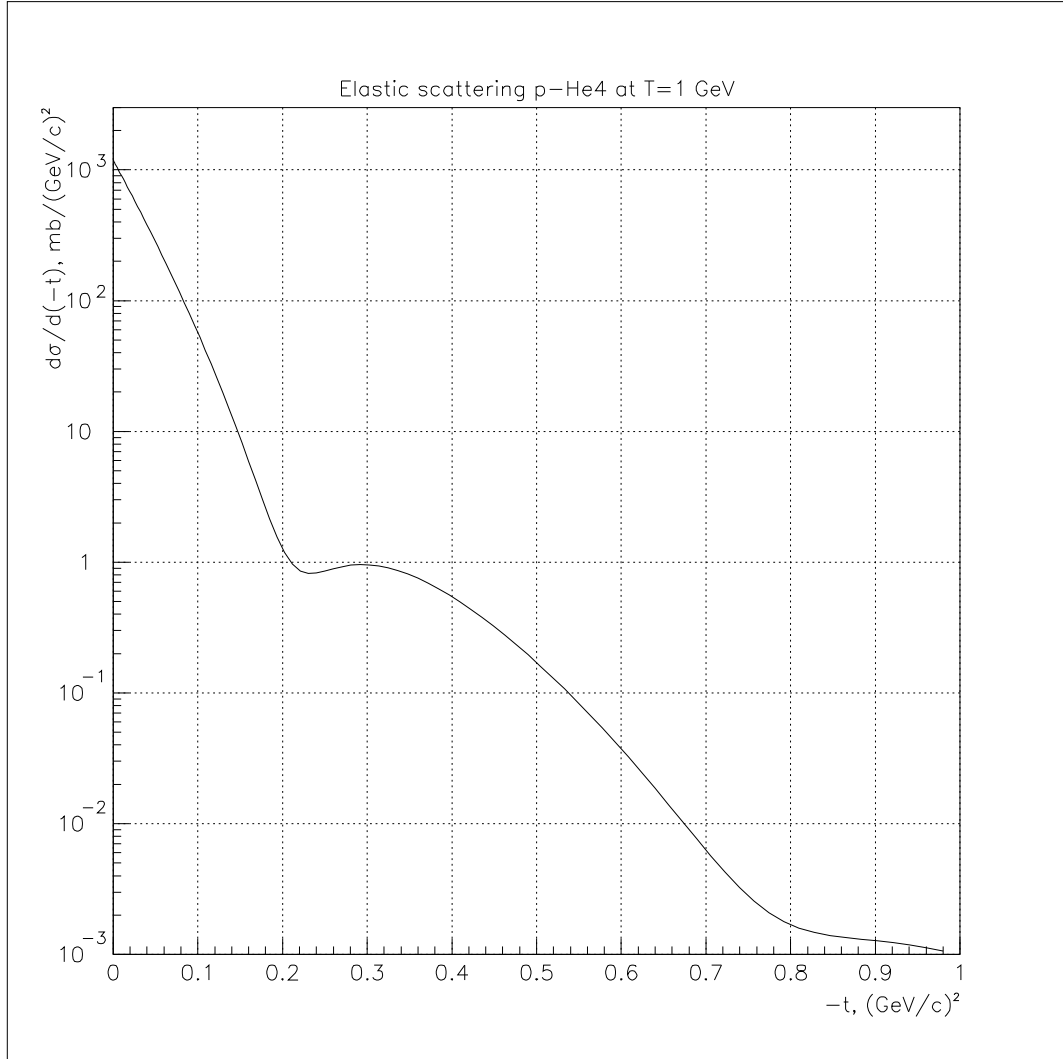
Figure 19.10: Elastic proton scattering on ^{4}He at 1 GeV
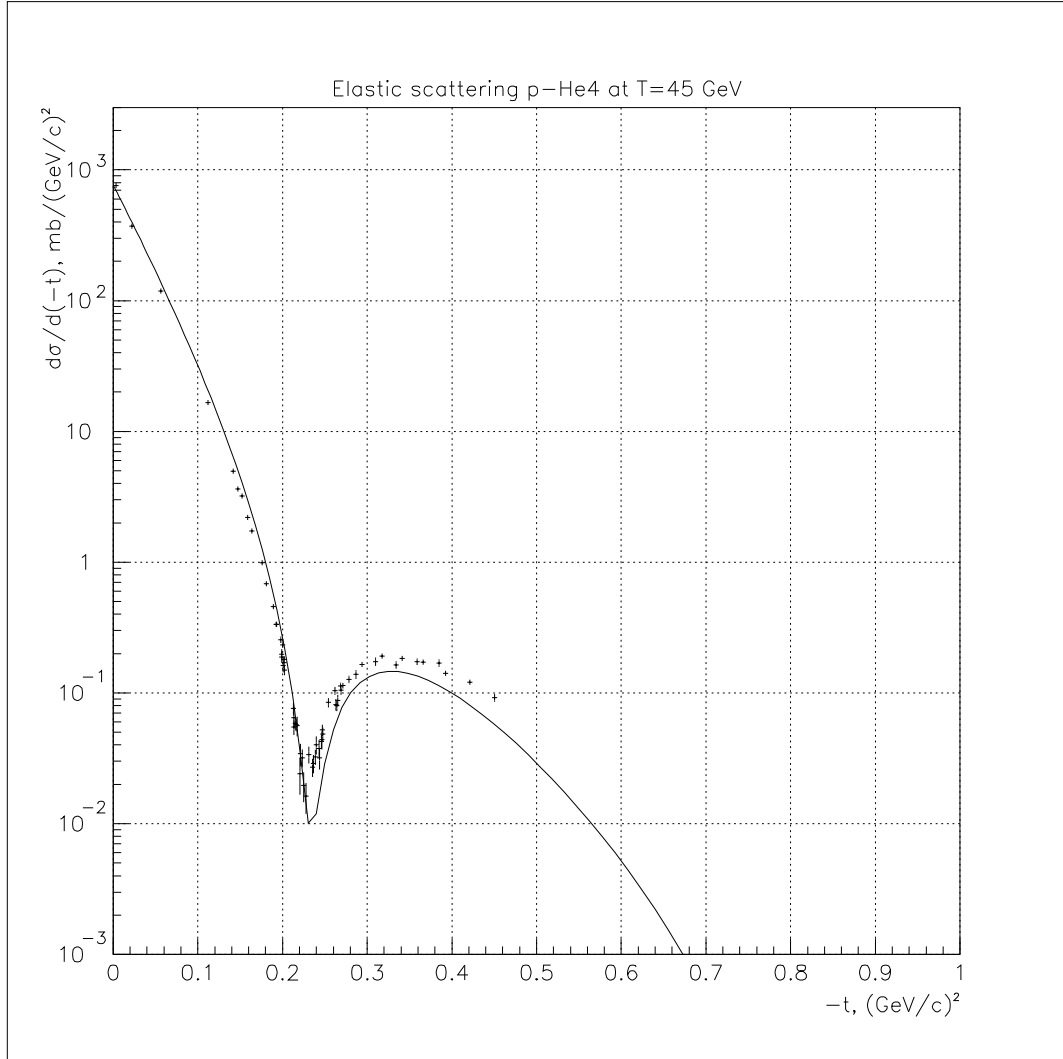
Figure 19.11: Elastic proton scattering on ^{4}He at 45 GeV
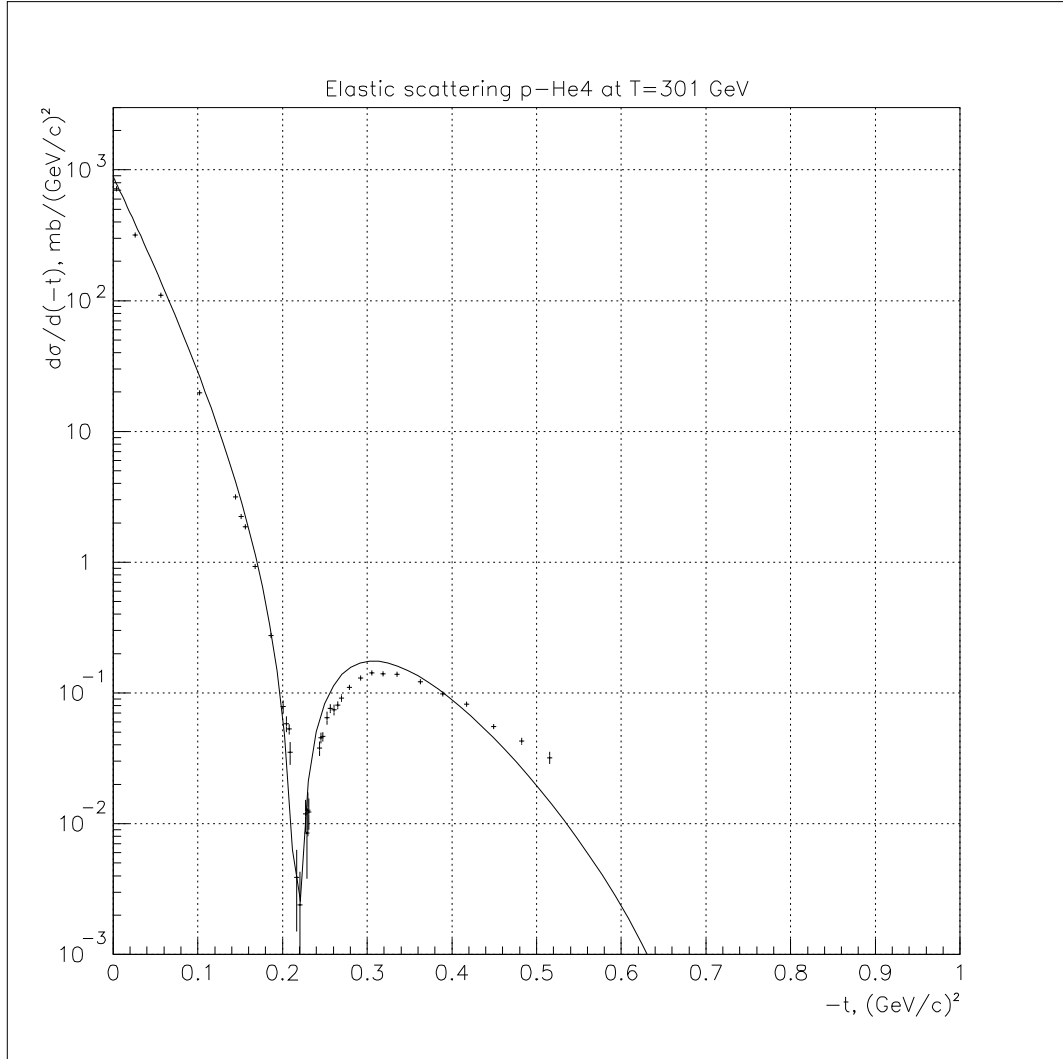
Figure 19.12: Elastic proton scattering on ^{4}He at 301 GeV

338

Chapter 20

Interactions of Stopping Particles

20.1 Complementary parameterised and theoretical treatment

Absorption of negative pions and kaons at rest from a nucleus is described in literature [1], [2], [3], [4] as consisting of two main components:

- a primary absorption process, involving the interaction of the incident stopped hadron with one or more nucleons of the target nucleus;

- the deexcitation of the remnant nucleus, left in an excited state as a result of the occurrence of the primary absorption process.

This interpretation is supported by several experiments [5], [6], [7], [8], [9], [10], [11], that have measured various features characterizing these processes. In many cases the experimental measurements are capable to distinguish the final products originating from the primary absorption process and those resulting from the nuclear deexcitation component.

A set of stopped particle absorption processes is implemented in GEANT4, based on this two-component model (PiMinusAbsorptionAtRest and KaonMinusAbsorptionAtRest classes, for π^- and K^- respectively. Both implementations adopt the same approach: the primary absorption component of the process is parameterised, based on available experimental data; the nuclear deexcitation component is handled through the theoretical models described elsewhere in this Manual.

20.1.1 Pion absorption at rest

The absorption of stopped negative pions in nuclei is interpreted [1], [2], [3], [4] as starting with the absorption of the pion by two or more correlated nucleons; the total energy of the pion is transferred to the absorbing nucleons, which then may leave the nucleus directly, or undergo final-state interactions with the residual nucleus. The remaining nucleus de-excites by evaporation of low energetic particles.

G4PiMinusAbsorptionAtRest generates the primary absorption component of the process through the parameterisation of existing experimental data; the primary absorption component is handled by class G4PiMinusStopAbsorption. In the current implementation only absorption on a nucleon pair is considered, while contributions from absorption on nucleon clusters are neglected; this approximation is supported by experimental results [1], [13] showing that it is the dominating contribution.

Several features of stopped pion absorption are known from experimental measurements on various materials [5], [6], [7], [8], [9], [10], [11], [12]:

- the average number of nucleons emitted, as resulting from the primary absorption process;

- the ratio of nn vs np as nucleon pairs involved in the absorption process;

- the energy spectrum of the resulting nucleons emitted and their opening angle distribution.

The corresponding final state products and related distributions are generated according to a parameterisation of the available experimental measurements listed above. The dependence on the material is handled by a strategy pattern: the features pertaining to material for which experimental data are available are treated in G4PiMinusStopX classes (where X represents an element), inheriting from G4StopMaterial base class. In case of absorption on an element for which experimental data are not available, the experimental distributions for the elements closest in Z are used.

The excitation energy of the residual nucleus is calculated by difference between the initial energy and the energy of the final state products of the primary absorption process.

Another strategy handles the nucleus deexcitation; the current default implementation consists in handling the deexcitatoin component of the process through the evaporation model described elsewhere in this Manual.

Bibliography

[1] E. Gadioli and E. Gadioli Erba *Phys. Rev. C 36* 741 (1987)

[2] H.C. Chiang and J. Hufner *Nucl. Phys. A352* 442 (1981)

[3] D. Ashery and J. P. Schiffer *Ann. Rev. Nucl. Part. Sci. 36* 207 (1986)

[4] H. J. Weyer *Phys. Rep. 195* 295 (1990)

[5] R. Hartmann et al., *Nucl. Phys. A300* 345 (1978)

[6] R. Madley et al., *Phys. Rev. C 25* 3050 (1982)

[7] F. W. Schleputz et al., *Phys. Rev. C 19* 135 (1979)

[8] C.J. Orth et al., *Phys. Rev. C 21* 2524 (1980)

[9] H.S. Pruys et al., *Nucl. Phys. A316* 365 (1979)

[10] P. Heusi et al., *Nucl. Phys. A407* 429 (1983)

[11] H.P. Isaak et al., *Nucl. Phys. A392* 368 (1983)

[12] H.P. Isaak et al., *Helvetica Physica Acta 55* 477 (1982)

[13] H. Machner *Nucl. Phys. A395* 457 (1983)

Chapter 21

Parametrization Driven Models

21.1 Introduction

Two sets of parameterized models are provided for the simulation of high energy hadron-nucleus interactions. The so-called "low energy model" is intended for hadronic projectiles with incident energies between 1 GeV and 25 GeV, while the "high energy model" is valid for projectiles between 25 GeV and 10 TeV. Both are based on the well-known GHEISHA package of GEANT3. The physics underlying these models comes from an old-fashioned multi-chain model in which the incident particle collides with a nucleon inside the nucleus. The final state of this interaction consists of a recoil nucleon, the scattered incident particle, and possibly many hadronic secondaries. Hadron production is approximated by the formation zone concept, in which the interacting quark-partons require some time and therefore some range to hadronize into real particles. All of these particles are able to re-interact within the nucleus, thus developing an intra-nuclear cascade.

In these models only the first hadron-nucleon collision is simulated in detail. The remaining interactions within the nucleus are simulated by generating additional hadrons and treating them as secondaries from the initial collision. The numbers, types and distributions of the extra hadrons are determined by functions which were fitted to experimental data or which reproduce general trends in hadron-nucleus collisions. Numerous tunable parameters are used throughout these models to obtain reasonable physical behavior. This restricts the use of these models as generators for hadron-nucleus interactions because it is not always clear how the parameters relate to physical quantities. On the other hand a precise simulation of minimum bias events is possible, with significant predictive power for calorimetry.

21.2   Low Energy Model

In the low energy parameterized model the mean number of hadrons produced in a hadron-nucleus collision is given by

$$N_m = C(s)A^{1/3}N_{ic} \tag{21.1}$$

where A is the atomic mass, $C(s)$ is a function only of the center of mass energy s, and N_{ic} is approximately the number of hadrons generated in the initial collision. Assuming that the collision occurs at the center of the nucleus, each of these hadrons must traverse a distance roughly equal to the nuclear radius. They may therefore potentially interact with a number of nucleons proportional to $A^{1/3}$. If the energy-dependent cross section for interaction in the nuclear medium is included in C then Eq. 21.1 can be interpreted as the number of target nucleons excited by the initial collision. Some of these nucleons are added to the intra-nuclear cascade. The rest, especially at higher momenta where nucleon production is suppressed, are replaced by pions and kaons.

Once the mean number of hadrons, N_m is calculated, the total number of hadrons in the intra-nuclear cascade is sampled from a Poisson distribution about the mean. Sampling from additional distribution functions provides

- the combined multiplicity $w(\vec{a}, n_i)$ for all particles i, $i = \pi^+, \pi^0, \pi^-, p, n, ...,$ including the correlations between them,

- the additive quantum numbers E (energy), Q (charge), S (strangeness) and B (baryon number) in the entire phase space region, and

- the reaction products from nuclear fission and evaporation.

A universal function $f(\vec{b}, x/p_T, m_T)$ is used for the distribution of the additive quantum numbers, where x is the Feynman variable, p_T is the transverse momentum and m_T is the transverse mass. $\vec{a}$ and $\vec{b}$ are parameter vectors, which depend on the particle type of the incoming beam and the atomic number A of the target. Any dependence on the beam energy is completely restricted to the multiplicity distribution and the available phase space.

The low energy model can be applied to the π^+, π^-, K^+, K^-, K^0 and $\overline{K^0}$ mesons. It can also be applied to the baryons p, n, Λ, Σ^+, Σ^-, Ξ^0, Ξ^-, Ω^-, and their anti-particles, as well as the light nuclei, d, t and α. The model can in principal be applied down to zero projectile energy, but the assumptions used to develop it begin to break down in the sub-GeV region.

21.3 High Energy Model

The high energy model is valid for incident particle energies from 10-20 GeV up to 10-20 TeV. Individual implementations of the model exist for π^+, π^-, K^+, K^-, K^0_S and K^0_L mesons, and for p, n, Λ, Σ^+, Σ^-, Ξ^0, Ξ^-, and Ω^- baryons and their anti-particles.

21.3.1 Initial Interaction

In a given implementation, the generation of the final state begins with the selection of a nucleon from the target nucleus. The pion multiplicities resulting from the initial interaction of the incident particle and the target nucleon are then calculated. The total pion multiplicity is taken to be a function of the log of the available energy in the center of mass of the incident particle and target nucleon, and the π^+, π^- and π^0 multiplicities are given by the KNO distribution.

From this initial set of particles, two are chosen at random to be replaced with either a kaon-anti-kaon pair, a nucleon-anti-nucleon pair, or a kaon and a hyperon. The relative probabilities of these options are chosen according to a logarithmically interpolated table of strange-pair and nucleon-anti-nucleon pair cross sections. The particle types of the pair are chosen according to averaged, parameterized cross sections typical at energies of a few GeV. If the increased mass of the new pair causes the total available energy to be exceeded, particles are removed from the initial set as necessary.

21.3.2 Intra-nuclear Cascade

The cascade of these particles through the nucleus, and the additional particles generated by the cascade are simulated by several models. These include high energy cascading, high energy cluster production, medium energy cascading and medium energy cluster production. For each event, high energy cascading is attempted first. If the available energy is sufficient, this method will likely succeed in producing the final state and the interaction will have been completely simulated. If it fails due to lack of energy or other reasons, the remaining models are called in succession until the final state is produced. If none of these methods succeeds, quasi-elastic scattering is attempted and finally, as a last resort, elastic scattering is performed. These models are responsible for assigning final state momenta to all generated particles, and for checking that, on average, energy and momentum are conserved.

21.3.3 High Energy Cascading

As particles from the initial collision cascade through the nucleus more particles will be generated. The number and type of these particles are parameterized in terms of the CM energy of the initial particle-nucleon collision. The number of particles produced from the cascade is given roughly by

$$N_m = C(s)[A^{1/3} - 1]N_{ic} \tag{21.2}$$

where A is the atomic mass, $C(s)$ is a function only of s, the square of the center of mass energy, and N_{ic} is approximately the number of hadrons generated in the initial collision. This can be understood qualitatively by assuming that the collision occurs, on average, at the center of the nucleus. Then each of the N_{ic} hadrons must traverse a distance roughly equal to the nuclear radius. They may therefore potentially interact with a number of nucleons proportional to $A^{1/3}$. If the energy-dependent cross section for interaction in the nuclear medium is included in $C(s)$ then Eq. 21.2 can be interpreted as the number of target nucleons excited by the initial collision and its secondaries.

Some of these nucleons are added to the intra-nuclear cascade. The rest, especially at higher momenta where nucleon production is suppressed, are replaced by pions, kaons and hyperons. The mean of the total number of hadrons generated in the cascade is partitioned into the mean number of nucleons, N_n, pions, N_π and strange particles, N_s. Each of these is used as the mean of a Poisson distribution which produces the randomized number of each type of particle.

The momenta of these particles are generated by first dividing the final state phase space into forward and backward hemispheres, where forward is in the direction of the original projectile. Each particle is assigned to one hemisphere or the other according to the particle type and origin:

- the original projectile, or its substitute if charge or strangeness exchange occurs, is assigned to the forward hemisphere and the target nucleon is assigned to the backward hemisphere;

- the remainder of the particles from the initial collision are assigned at random to either hemisphere;

- pions and strange particles generated in the intra-nuclear cascade are assigned 80% to the backward hemisphere and 20% to the forward hemisphere;

- nucleons generated in the intra-nuclear cascade are all assigned to the backward hemisphere.

It is assumed that energy is separately conserved for each hemisphere. If too many particles have been added to a given hemisphere, randomly chosen particles are deleted until the energy budget is met. The final state momenta are then generated according to two different algorithms, a cluster model for the backward nucleons from the intra-nuclear cascade, and a fragmentation model for all other particles. Several corrections are then applied to the final state particles, including momentum re-scaling, effects due to Fermi motion, and binding energy subtraction. Finally the de-excitation of the residual nucleus is treated by adding lower energy protons, neutrons and light ions to the final state particle list.

Fragmentation Model. This model simulates the fragmentation of the highly excited hadrons formed in the initial projectile-nucleon collision. Particle momenta are generated by first sampling the average transverse momentum p_T from an exponential distribution:

$$exp[-ap_T{}^b] \tag{21.3}$$

where

$$1.70 \leq a \leq 4.00; \ 1.18 \leq b \leq 1.67. \tag{21.4}$$

The values of a and b depend on particle type and result from a parameterization of experimental data. The value selected for p_T is then used to set the scale for the determination of x, the fraction of the projectile's momentum carried by the fragment. The sampling of x assumes that the invariant cross section for the production of fragments can be given by

$$E\frac{d^3\sigma}{dp^3} = \frac{K}{(M^2x^2 + p_T{}^2)^{3/2}} \tag{21.5}$$

where E and p are the energy and momentum, respectively, of the produced fragment, and K is a proportionality constant. M is the average transverse mass which is parameterized from data and varies from 0.75 GeV to 0.10 GeV, depending on particle type. Taking m to be the mass of the fragment and noting that

$$p_z \simeq xE_{proj} \tag{21.6}$$

in the forward hemisphere and

$$p_z \simeq xE_{targ} \tag{21.7}$$

in the backward hemisphere, Eq. 21.5 can be re-written to give the sampling function for x:

$$\frac{d^3\sigma}{dp^3} = \frac{K}{(M^2x^2 + p_T{}^2)^{3/2}} \frac{1}{\sqrt{m^2 + p_T{}^2 + x^2E_i^2}}, \tag{21.8}$$

346

where $i = proj$ or $targ$.

x-sampling is performed for each fragment in the final-state candidate list. Once a fragment's momentum is assigned, its total energy is checked to see if it exceeds the energy budget in its hemisphere. If so, the momentum of the particle is reduced by 10%, as is p_T and the integral of the x-sampling function, and the momentum selection process is repeated. If the offending particle starts out in the forward hemisphere, it is moved to the backward hemisphere, provided the budget for the backward hemisphere is not exceeded. If, after six iterations, the particle still does not fit, it is removed from the candidate list and the kinetic energies of the particles selected up to this point are reduced by 5%. The entire procedure is repeated up to three times for each fragment.

The incident and target particles, or their substitutes in the case of charge- or strangeness-exchange, are guaranteed to be part of the final state. They are the last particles to be selected and the remaining energy in their respective hemispheres is used to set the p_z components of their momenta. The p_T components selected by x-sampling are retained.

Cluster Model. This model groups the nucleons produced in the intra-nuclear cascade together with the target nucleon or hyperon, and treats them as a cluster moving forward in the center of mass frame. The cluster disintegrates in such a way that each of its nucleons is given a kinetic energy

$$40 < T_{nuc} < 600 \text{MeV} \tag{21.9}$$

if the kinetic energy of the original projectile, T_{inc}, is 5 GeV or more. If T_{inc} is less than 5 GeV,

$$40(T_{inc}/5\text{GeV})^2 < \text{T}_{\text{nuc}} < 600(\text{T}_{\text{inc}}/5\text{GeV})^2. \tag{21.10}$$

In each range the energy is sampled from a distribution which is skewed strongly toward the high energy limit. In addition, the angular distribution of the nucleons is skewed forward in order to simulate the forward motion of the cluster.

Momentum Re-scaling. Up to this point, all final state momenta have been generated in the center of mass of the incident projectile and the target nucleon. However, the interaction involves more than one nucleon as evidenced by the intra-nuclear cascade. A more correct center of mass should then be defined by the incident projectile and all of the baryons generated by the cascade, and the final state momenta already calculated must be re-scaled to reflect the new center of mass.

This is accomplished by correcting the momentum of each particle in the final state candidate list by the factor T_1/T_2. T_2 is the total kinetic energy in the lab frame of all the final state candidates generated assuming a projectile-nucleon center of mass. T_1 is the total kinetic energy in the lab frame of the same final state candidates, but whose momenta have been calculated by the phase space decay of an imaginary particle. This particle has the total CM energy of the original projectile and a cluster consisting of all the baryons generated from the intra-nuclear cascade.

Corrections. Part of the Fermi motion of the target nucleons is taken into account by smearing the transverse momentum components of the final state particles. The Fermi momentum is first sampled from an average distribution and a random direction for its transverse component is chosen. This component, which is proportional to the number of baryons produced in the cascade, is then included in the final state momenta.

Each final state particle must escape the nucleus, and in the process reduce its kinetic energy by the nuclear binding energy. The binding energy is parameterized as a function of A:

$$E_B = 25\text{MeV} \left(\frac{A - 1}{120} \right) \text{e}^{-(A-1)/120}.$$ (21.11)

Another correction reduces the kinetic energy of final state π^0s when the incident particle is a π^+ or π^-. This reduction increases as the log of the incident pion energy, and is done to reproduce experimental data. In order to conserve energy on average, the energy removed from the π^0s is re-distributed among the final state π^+s, π^-s and π^0s.

Nuclear De-excitation. After the generation of initial interaction and cascade particles, the target nucleus is left in an excited state. De-excitation is accomplished by evaporating protons, neutrons, deuterons, tritons and alphas from the nucleus according to a parameterized model. The total kinetic energy given to these particles is a function of the incident particle kinetic energy:

$$T_{evap} = 7.716\text{GeV} \left(\frac{A - 1}{120} \right) \text{F(T)} \text{e}^{-\text{F(T)}-(A-1)/120},$$ (21.12)

where

$$F(T) = \max[0.35 + 0.1304\text{ln(T)}, 0.15],$$ (21.13)

and

$$T = 0.1\text{GeV} \quad \text{for} \quad \text{T}_{\text{inc}} < 0.1\text{GeV} \tag{21.14}$$

$$T = T_{inc} \quad \text{for} \quad 0.1\text{GeV} \leq \text{T}_{\text{inc}} \leq 4\text{GeV} \tag{21.15}$$

$$T = 4\text{GeV} \quad \text{for} \quad \text{T}_{\text{inc}} > 4\text{GeV}. \tag{21.16}$$

The mean energy allocated for proton and neutron emission is $\overline{T_{pn}}$ and that for deuteron, triton and alpha emission is $\overline{T_{dta}}$. These are determined by partitioning T_{evap} :

$$\overline{T_{pn}} = T_{evap}R \quad , \quad \overline{T_{dta}} = T_{evap}(1 - R) \quad \text{with}$$

$$R = \max[1 - (\text{T}/4\text{GeV})^2, 0.5]. \tag{21.17}$$

The simulated values of T_{pn} and T_{dta} are sampled from normal distributions about $\overline{T_{pn}}$ and $\overline{T_{dta}}$ and their sum is constrained not to exceed the incident particle's kinetic energy, T_{inc}.

The number of proton and neutrons emitted, N_{pn}, is sampled from a Poisson distribution about a mean which depends on R and the number of baryons produced in the intranuclear cascade. The average kinetic energy per emitted particle is then $T_{av} = T_{pn}/N_{pn}$. T_{av} is used to parameterize an exponential which qualitatively describes the nuclear level density as a function of energy. The simulated kinetic energy of each evaporated proton or neutron is sampled from this exponential. Next, the nuclear binding energy is subtracted and the final momentum is calculated assuming an isotropic angular distribution. The number of protons and neutrons emitted is $(Z/A)N_{pn}$ and $(N/A)N_{pn}$, respectively.

A similar procedure is followed for the deuterons, tritons and alphas. The number of each species emitted is $0.6N_{dta}$, $0.3N_{dta}$ and $0.1N_{dta}$, respectively.

Tuning of the High Energy Cascade The final stage of the high energy cascade method involves adjusting the momenta of the produced particles so that they agree better with data. Currently, five such adjustments are performed, the first three of which apply only to charged particles incident upon light and medium nuclei at incident energies above $\simeq 65$ GeV.

- If the final state particle is a nucleon or light ion with a momentum of less than 1.5 GeV/c, its momentum will be set to zero some fraction of the time. This fraction increases with the logarithm of the kinetic energy of the incident particle and decreases with $log_{10}(A)$.

349

- If the final state particle with the largest momentum happens to be a π^0, its momentum is exchanged with either the π^+ or π^- having the largest momentum, depending on whether the incident particle charge is positive or negative.

- If the number of baryons produced in the cascade is a significant fraction (> 0.3) of A, about 25% of the nucleons and light ions already produced will be removed from the final particle list, provided their momenta are each less than 1.2 GeV/c.

- The final state of the interaction is of course heavily influenced by the quantum numbers of the incident particle, particularly in the forward direction. This influence is enforced by compiling, for each forward-going final state particle, the sum

$$S_{forward} = \Delta_M + \Delta_Q + \Delta_S + \Delta_B, \qquad (21.18)$$

where each Δ corresponds to the absolute value of the difference of the quantum number between the incident particle and the final state particle. M, Q, S, and B refer to mass, charge, strangeness and baryon number, respectively. For final state particles whose character is significantly different from the incident particle (S is large), the momentum component parallel to the incident particle momentum is reduced. The transverse component is unchanged. As a result, large-S particles are driven away from the axis of the hadronic shower. For backward-going particles, a similar procedure is followed based on the calculation of $S_{backward}$.

- Conservation of energy is imposed on the particles in the final state list in one of two ways, depending on whether or not a leading particle has been chosen from the list. If all the particles differ significantly from the incident particle in momentum, mass and other quantum numbers, no leading particle is chosen and the kinetic energy of each particle is scaled by the same correction factor. If a leading particle is chosen, its kinetic energy is altered to balance the total energy, while all the remaining particles are unaltered.

21.3.4   High Energy Cluster Production

As in the high energy cascade model, the high energy cluster model randomly assigns particles from the initial collision to either a forward- or backward-going cluster. Instead of performing the fragmentation process, however,

the two clusters are treated kinematically as the two-body final state of the hadron-nucleon collision. Each cluster is assigned a kinetic energy T which is sampled from a distribution

$$exp[-aT^{1/b}] \qquad (21.19)$$

where both a and b decrease with the number of particles in a cluster. If the combined total energy of the two clusters is larger than the center of mass energy, the energy of each cluster is reduced accordingly. The center of mass momentum of each cluster can then be found by sampling the 4-momentum transfer squared, t, from the distribution

$$exp[t(4.0 + 1.6ln(p_{inc}))] \qquad (21.20)$$

where $t < 0$ and p_{inc} is the incident particle momentum. Then,

$$cos\theta = 1 + \frac{t - (E_c - E_i)^2 + (p_c - p_i)^2}{2p_c p_i}, \qquad (21.21)$$

where the subscripts c and i refer to the cluster and incident particle, respectively. Once the momentum of each cluster is calculated, the cluster is decomposed into its constituents. The momenta of the constituents are determined using a phase space decay algorithm.

The particles produced in the intra-nuclear cascade are grouped into a third cluster. They are treated almost exactly as in the high energy cascade model, where Eq. 21.2 is used to estimate the number of particles produced. The main difference is that the cluster model does not generate strange particles from the cascade. Nucleon suppression is also slightly stronger, leading to relatively higher pion production at large incident momenta. Kinetic energy and direction are assigned to the cluster as described in the cluster model paragraph in the previous section.

The remaining steps to produce the final state particle list are the same as those in high energy cascading:

- re-scaling of the momenta to reflect a center of mass which involves the cascade baryons,

- corrections due to Fermi motion and binding energy,

- reduction of final state π^0 energies,

- nuclear de-excitation and

- high energy tuning.

21.3.5 Medium Energy Cascading

The medium energy cascade algorithm is very similar to the high energy cascade algorithm, but it may be invoked for lower incident energies (down to 1 GeV). The primary difference between the two codes is the parameterization of the fragmentation process. The medium energy cascade samples larger transverse momenta for pions and smaller transverse momenta for kaons and baryons.

A second difference is in the treatment of the cluster consisting of particles generated in the cascade. Instead of parameterizing the kinetic energies and angles of the outgoing particles, the phase space decay approach is used.

Another difference is that the high energy tuning of the final state distribution is not performed.

21.3.6 Medium Energy Cluster Production

The medium energy cluster algorithm is nearly identical to the high energy cluster algorithm, but it may be invoked for incident energies down to 10 MeV. There are three significant differences at medium energy: less nucleon suppression, fewer particles generated in the intra-nuclear cascade, and no high energy tuning of the final state particle distributions.

21.3.7 Elastic and Quasi-elastic Scattering

When no additional particles are produced in the initial interaction, either elastic or quasi-elastic scattering is performed. If there is insufficient energy to induce an intra-nuclear cascade, but enough to excite the target nucleus, quasi-elastic scattering is performed. The final state is calculated using two-body scattering of the incident particle and the target nucleon, with the scattering angle in the center of mass sampled from an exponential:

$$exp[-2bp_{in}p_{cm}(1 - cos\theta)]. \tag{21.22}$$

Here p_{in} is the incident particle momentum, p_{cm} is the momentum in the center of mass, and b is a logarithmic function of the incident momentum in the lab frame as parameterized from data. As in the cascade and cluster production models, the residual nucleus is then de-excited by evaporating nucleons and light ions.

If the incident energy is too small to excite the nucleus, elastic scattering is performed. The angular distribution of the scattered particle is sampled from the sum of two exponentials whose parameters depend on A.

21.4 Status of this document

7.10.02 re-written by D.H. Wright
1.11.04 new section on high energy model by D.H. Wright

Chapter 22

Leading Particle Bias

22.1 Overview

G4Mars5GeV is an inclusive event generator for hadron (photon) interactions with nuclei, and translated from the MARS code system (MARS13 (98)). To construct a cascade tree, only a fixed number of particles are generated at each vertex. A corresponding statistical weight is assigned to each secondary particle according to its type and phase-space. Rarely-produced particles or interesting phase-space region can be enhanced.

N.B. This inclusive simulation is implemented in Geant4 partially for the moment, not completed yet.

MARS Code System
MARS is a set of Monte Carlo programs for inclusive simulation of particle interactions, and high multiplicity or rare events can be simulated fast with its sophisticated biasing techniques. For the details on the MARS code system, see [1, 2].

22.2 Method

In *G4Mars5GeV*, three secondary hadrons are generated in the final state of an hadron(photon)-nucleus inelastic interaction, and a statistical weight is assigned to each particle according to its type, energy and emission angle. In this code, energies, momenta and weights of the secondaries are sampled, and the primary particle is simply terminated at the vertex. The allowed projectile kinetic energy is $E_0 \leq 5$ GeV, and following particles can be sim-

ulated;

$$p, \ n, \ \pi^+, \ \pi^-, \ K^+, \ K^-, \ \gamma, \ \bar{p} \ .$$

Prior to a particle generation, a Coulomb barrier is considered for projectile charged hadrons $(p, \ \pi^+, \ K^+$ and $\bar{p})$ with kinetic energy of less than 200 MeV. The coulomb potential V_{coulmb} is given by

$$V_{\mathrm{columb}} = 1.11 \times 10^{-3} \times Z/A^{1/3} \quad \text{(GeV)}, \tag{22.1}$$

where Z and A are atomic and mass number, respectivelly.

22.2.1 Inclusive hadron production

The following three steps are carried out in a sequence to produce secondary particles:

- nucleon production,

- charged pion/kaon production and

- neutral pion production.

These processes are performed independently, i.e. the energy and momentum conservation law is broken at each event, however, fulfilled on the average over a number of events simulated.

nucleon production
Projectiles $K^\pm$ and $\bar{p}$ are replaced with $\pi^\pm$ and p, individually to generate the secondary nucleon. Either of neutron or proton is selected randomly as the secondary except for the case of gamma projectiling. The gamma is handled as a pion.

charged pion/kaon production
If the incident nucleon does not have enough energy to produce the pion $(>$ 280 MeV$)$, charged and neutral pions are not produced. A charged pion is selected with the equal probability, and a bias is eliminated with the appropriate weight which is assigned taking into account the difference between π^+ and π^- both for production probability and for inclusive spectra. It is replaced with a charged kaon a certain fraction of the time, that depends on

the projectile energy if $E_0 > 2.1$ GeV. The ratio of kaon replacement is given by

$$R_{\text{kaon}} = 1.3 \times \left\{ C_{\min} + (C - C_{\min}) \frac{\log(E_0/2)}{\log(100/2)} \right\} \qquad (2.1 \leq E_0 \leq 5.2 \text{ GeV}),$$
$$(22.2)$$

where $C_{\min}$ is $0.03\,(0.08)$ for nucleon (others) projectiling, and

$$\qquad\qquad \textit{Produced particle} \qquad \textit{Projectile particle}$$

$$C = \left\{ \begin{array}{ll} 0.071 & (\ \pi^+ \ ) \\ 0.083 & (\ \pi^- \ ) \end{array} \right\} \times \left\{ \begin{array}{ll} 1.3 & (\ \pi^\pm \ ) \\ 2.0 & (\ K^\pm \ ) \\ 1.0 & (\ \text{others} \ ) \end{array} \right\} \qquad (22.3)$$

A similar strangeness replacement is not considered for nucleon production.

22.2.2 Sampling of energy and emission angle of the secondary

The energy and emission angle of the secondary particle depends on projectile energy. There are formulae depending on whether or not the interaction particle (IP) is identical to the secondary (JP).

For IP $\neq$ JP, the secondary energy E_2 is simply given by

$$E_2 = E_{\text{th}} \times \left(\frac{E_{\max}}{E_{\text{th}}} \right)^\epsilon \qquad (\text{MeV}) , \qquad (22.4)$$

where $E_{\max} = max\,(E_0, 0.5\,\text{MeV})$, $E_{\text{th}} = 1$ MeV, and ϵ is a uniform random between 0 and 1.

For IP $=$ JP,

$$E_2 = \left\{ \begin{array}{ll} E_{\text{th}} + \epsilon\,(E_{\max} - E_{\text{th}}) & E_0 < 100\,E_{\text{th}}\ \text{MeV} \\ E_{\text{th}} \times e^{\epsilon\,(\beta+99)} & (\text{MeV}) \quad E_0 \geq 100\,E_{\text{th}}\ \text{and}\ \epsilon < \eta \\ E_0 \times \left(\beta\,(\epsilon - 1) + 1 + 99\epsilon \right)/100 & E_0 \geq 100\,E_{\text{th}}\ \text{and}\ \epsilon \geq \eta \end{array} \right.$$
$$(22.5)$$

Here, $\beta = \log(E_0/100\,E_{\text{th}})$ and $\eta = \beta/(99 + \beta)$. If resulting E_2 is less than 0.5 MeV, nothing is generated.

Angular distribution

The angular distribution is mainly determined by the energy ratio of the secondary to the projectile (i.e. the emission angle and probability of the

occurrence increase as the energy ratio decreases). The emission angle of the secondary particle with respect to the incident direction is given by

$$\theta = -\log\big(1 - \epsilon(1 - e^{-\pi\tau})\big)/\tau \; , \qquad (22.6)$$

where $\tau = E_0/5(E_0 + 1/2)$.

22.2.3 Sampling statistical weight

The kinematics of the secondary particle are determined randomly using the above formulae (22.5,22.6). A statistical weight is calculated and assigned to each generated particle to reproduce a true inclusive spectrum in the event. The weight is given by

$$D2N = V10(\text{JP}) \times DW\,(E) \times DA\,(\theta) \times V1\,(E, \theta, \text{JP}), \qquad (22.7)$$

where
• $V10$ is the statistical weight for the production rate based on neutral pion production $(V10 = 1)$.

$$V10 = \begin{cases} 2.0\,(2.5) & \text{nucleon production (the case of gamma projectile)} \\ 2.1 & \text{charged pion/kaon production} \end{cases}$$

$$(22.8)$$

• DW and DA are dominantly determined by the secondary energy and emission angle, individually.

• V1 is a true double-differential production cross-section (divided by the total inelastic cross-section) [1], calculated in $G4Mars5GeV::D2N2$ according to the projectile type and energy, target atomic mass, and simulated secondary energy, emission angle and particle type.

22.3 Status of this document

11.06.2002 created by N. Kanaya.
20.06.2002 modified by N.V.Mokhov.

Bibliography

[1] N.V. Mokhov, *The MARS Code System User's Guide, Version 13(98)*, Fermilab-FN-628.

[2] *http://www-ap.fnal.gov/MARS/*

358

Chapter 23

Parton string model.

23.1 Reaction initial state simulation.

23.1.1 Allowed projectiles and bombarding energy range for interaction with nucleon and nuclear targets

The GEANT4 parton string models are capable to predict final states (produced hadrons which belong to the scalar and vector meson nonets and the baryon (antibaryon) octet and decuplet) of reactions on nucleon and nuclear targets with nucleon, pion and kaon projectiles. The allowed bombarding energy $\sqrt{s} > 5$ GeV is recommended. Two approaches, based on diffractive excitation or soft scattering with diffractive admixture according to cross-section, are considered.   Hadron-nucleus collisions in the both approaches (diffractive and parton exchange) are considered as a set of the independent hadron-nucleon collisions. However, the string excitation procedures in these approaches are rather different.

23.1.2 MC initialization procedure for nucleus.

The initialization of each nucleus, consisting from A nucleons and Z protons with coordinates $\mathbf{r}_i$ and momenta $\mathbf{p}_i$, where $i = 1, 2, ..., A$ is performed. We use the standard initialization Monte Carlo procedure, which is realized in the most of the high energy nuclear interaction models:

- Nucleon radii r_i are selected randomly in the rest of nucleus according to proton or neutron density $\rho(r_i)$. For heavy nuclei with $A > 16$ [1] nucleon density is

$$\rho(r_i) = \frac{\rho_0}{1 + \exp\left[(r_i - R)/a\right]} \qquad (23.1)$$

359

where

$$\rho_0 \approx \frac{3}{4\pi R^3}(1 + \frac{a^2\pi^2}{R^2})^{-1}. \tag{23.2}$$

Here $R = r_0 A^{1/3}$ fm and $r_0 = 1.16(1 - 1.16A^{-2/3})$ fm and $a \approx 0.545$ fm. For light nuclei with $A < 17$ nucleon density is given by a harmonic oscillator shell model [2], e. g.

$$\rho(r_i) = (\pi R^2)^{-3/2} \exp{(-r_i^2/R^2)}, \tag{23.3}$$

where $R^2 = 2/3 < r^2 >= 0.8133A^{2/3}$ fm². To take into account nucleon repulsive core it is assumed that internucleon distance $d > 0.8$ fm;

- The initial momenta of the nucleons are randomly choosen between 0 and p_F^{max}, where the maximal momenta of nucleons (in the local Thomas-Fermi approximation [3]) depends from the proton or neutron density ρ according to

$$p_F^{max} = \hbar c (3\pi^2\rho)^{1/3} \tag{23.4}$$

with $\hbar c = 0.197327$ GeV fm;

- To obtain coordinate and momentum components, it is assumed that nucleons are distributed isotropicaly in configuration and momentum spaces;

- Then perform shifts of nucleon coordinates $\mathbf{r'_j} = \mathbf{r_j} - 1/A \sum_i \mathbf{r_i}$ and momenta $\mathbf{p'_j} = \mathbf{p_j} - 1/A \sum_i \mathbf{p_i}$ of nucleon momenta. The nucleus must be centered in configuration space around $\mathbf{0}$, i. e. $\sum_i \mathbf{r}_i = \mathbf{0}$ and the nucleus must be at rest, i. e. $\sum_i \mathbf{p_i} = \mathbf{0}$;

- We compute energy per nucleon $e = E/A = m_N + B(A, Z)/A$, where m_N is nucleon mass and the nucleus binding energy $B(A, Z)$ is given by the Bethe-Weizsäcker formula[4]:

$$B(A, Z) =$$
$$= -0.01587A + 0.01834A^{2/3} + 0.09286(Z - \tfrac{A}{2})^2 + 0.00071Z^2/A^{1/3}, \tag{23.5}$$

and find the effective mass of each nucleon $m_i^{eff} = \sqrt{(E/A)^2 - p_i^{2'}}$.

23.1.3 Random choice of the impact parameter.

The impact parameter $0 \leq b \leq R_t$ is randomly selected according to the probability:

$$P(\mathbf{b})d\mathbf{b} = bd\mathbf{b}, \qquad (23.6)$$

where R_t is the target radius, respectively. In the case of nuclear projectile or target the nuclear radius is determined from condition:

$$\frac{\rho(R)}{\rho(0)} = 0.01. \qquad (23.7)$$

23.2 Sample of collision participants in nuclear collisions.

23.2.1 MC procedure to define collision participants.

The inelastic hadron–nucleus interactions at ultra–relativistic energies are considered as independent hadron–nucleon collisions. It was shown long time ago [5] for the hadron–nucleus collision that such a picture can be obtained starting from the Regge–Gribov approach [6], when one assumes that the hadron-nucleus elastic scattering amplitude is a result of reggeon exchanges between the initial hadron and nucleons from target–nucleus. This result leads to simple and efficient MC procedure [7] to define the interaction cross sections and the number of the nucleons participating in the inelastic hadron–nucleus collision:

- We should randomly distribute B nucleons from the target-nucleus on the impact parameter plane according to the weight function $T([\vec{b}_j^B])$. This function represents probability density to find sets of the nucleon impact parameters $[\vec{b}_j^B]$, where $j = 1, 2, ..., B$.

- For each pair of projectile hadron i and target nucleon j with choosen impact parameters $\vec{b}_i$ and $\vec{b}_j^B$ we should check whether they interact inelastically or not using the probability $p_{ij}(\vec{b}_i - \vec{b}_j^B, s)$, where $s_{ij} = (p_i + p_j)^2$ is the squared total c.m. energy of the given pair with the 4–momenta p_i and p_j, respectively.

In the Regge–Gribov approach[6] the probability for an inelastic collision of pair of i and j as a function at the squared impact parameter difference $b_{ij}^2 = (\vec{b}_i - \vec{b}_j^B)^2$ and s is given by

$$p_{ij}(\vec{b}_i - \vec{b}_j^B, s) = c^{-1}[1 - \exp\{-2u(b_{ij}^2, s)\}] = \sum_{n=1}^{\infty} p_{ij}^{(n)}(\vec{b}_i - \vec{b}_j^B, s), \quad (23.8)$$

where

$$p_{ij}^{(n)}(\vec{b}_i - \vec{b}_j^B, s) = c^{-1} \exp\left\{-2u(b_{ij}^2, s)\right\} \frac{[2u(b_{ij}^2, s)]^n}{n!}. \qquad (23.9)$$

is the probability to find the n cut Pomerons or the probability for $2n$ strings produced in an inelastic hadron-nucleon collision. These probabilities are defined in terms of the (eikonal) amplitude of hadron–nucleon elastic scattering with Pomeron exchange:

$$u(b_{ij}^2, s) = \frac{z(s)}{2} \exp(-b_{ij}^2/4\lambda(s)). \qquad (23.10)$$

The quantities $z(s)$ and $\lambda(s)$ are expressed through the parameters of the Pomeron trajectory, $\alpha_P' = 0.25 \ GeV^{-2}$ and $\alpha_P(0) = 1.0808$, and the parameters of the Pomeron-hadron vertex R_P and γ_P:

$$z(s) = \frac{2c\gamma_P}{\lambda(s)}(s/s_0)^{\alpha_P(0)-1} \qquad (23.11)$$

$$\lambda(s) = R_P^2 + \alpha_P' \ln(s/s_0), \qquad (23.12)$$

respectively, where s_0 is a dimensional parameter.

In Eqs. (23.8,23.9) the so–called shower enhancement coefficient c is introduced to determine the contribution of diffractive dissociation[6]. Thus, the probability for diffractive dissociation of a pair of nucleons can be computed as

$$p_{ij}^d(\vec{b}_i - \vec{b}_j^B, s) = \frac{c-1}{c}[p_{ij}^{tot}(\vec{b}_i - \vec{b}_j^B, s) - p_{ij}(\vec{b}_i - \vec{b}_j^B, s)], \qquad (23.13)$$

where

$$p_{ij}^{tot}(\vec{b}_i - \vec{b}_j^B, s) = (2/c)[1 - \exp\{-u(b_{ij}^2, s)\}]. \qquad (23.14)$$

The Pomeron parameters are found from a global fit of the total, elastic, differential elastic and diffractive cross sections of the hadron–nucleon interaction at different energies.

For the nucleon-nucleon, pion-nucleon and kaon-nucleon collisions the Pomeron vertex parameters and shower enhancement coefficients are found: $R_P^{2N} = 3.56 \ GeV^{-2}$, $\gamma_P^N = 3.96 \ GeV^{-2}$, $s_0^N = 3.0 \ GeV^2$, $c^N = 1.4$ and $R_P^{2\pi} = 2.36 \ GeV^{-2}$, $\gamma_P^\pi = 2.17 \ GeV^{-2}$, and $R_P^{2K} = 1.96 \ GeV^{-2}$, $\gamma_P^K = 1.92 \ GeV^{-2}$, $s_0^K = 2.3 \ GeV^2$, $c^\pi = 1.8$.

23.2.2 Separation of hadron diffraction excitation.

For each pair of target hadron i and projectile nucleon j with choosen impact parameters $\vec{b}_i$ and $\vec{b}_j^B$ we should check whether they interact inelastically or not using the probability

$$p_{ij}^{in}(\vec{b}_i - \vec{b}_j^B, s) = p_{ij}(\vec{b}_i - \vec{b}_j^B, s) + p_{ij}^d(\vec{b}_i^A - \vec{b}_j^B, s). \qquad (23.15)$$

If interaction will be realized, then we have to consider it to be diffractive or nondiffractive with probabilities

$$\frac{p_{ij}^d(\vec{b}_i - \vec{b}_j^B, s)}{p_{ij}^{in}(\vec{b}_i^A - \vec{b}_j^B, s)} \tag{23.16}$$

and

$$\frac{p_{ij}(\vec{b}_i - \vec{b}_j^B, s)}{p_{ij}^{in}(\vec{b}_i^A - \vec{b}_j^B, s)}. \tag{23.17}$$

23.3   Longitudinal string excitation

23.3.1   Hadron–nucleon inelastic collision

Let us consider collision of two hadrons with their c. m. momenta $P_1 = \{E_1^+, m_1^2/E_1^+, \mathbf{0}\}$ and $P_2 = \{E_2^-, m_2^2/E_2^-, \mathbf{0}\}$, where the light-cone variables $E_{1,2}^\pm = E_{1,2} \pm P_{z1,2}$ are defined through hadron energies $E_{1,2} = \sqrt{m_{1,2}^2 + P_{z1,2}^2}$, hadron longitudinal momenta $P_{z1,2}$ and hadron masses $m_{1,2}$, respectively. Two hadrons collide by two partons with momenta $p_1 = \{x^+ E_1^+, 0, \mathbf{0}\}$ and $p_2 = \{0, x^- E_2^-, \mathbf{0}\}$, respectively.

23.3.2   The diffractive string excitation

In the diffractive string excitation (the Fritiof approach [9]) only momentum can be transferred:

$$\begin{aligned} P_1' &= P_1 + q \\ P_2' &= P_2 - q, \end{aligned} \tag{23.18}$$

where

$$q = \{-q_t^2/(x^- E_2^-), q_t^2/(x^+ E_1^+), \mathbf{q_t}\} \tag{23.19}$$

is parton momentum transferred and $\mathbf{q_t}$ is its transverse component. We use the Fritiof approach to simulate the diffractive excitation of particles.

23.3.3   The string excitation by parton exchange

For this case the parton exchange (rearrangement) and the momentum exchange are allowed [10],[11],[7]:

$$\begin{aligned} P_1' &= P_1 - p_1 + p_2 + q \\ P_2' &= P_2 + p_1 - p_2 - q, \end{aligned} \tag{23.20}$$

where $q = \{0, 0, \mathbf{q_t}\}$ is parton momentum transferred, i. e. only its transverse components $\mathbf{q_t} = 0$ is taken into account.

23.3.4 Transverse momentum sampling

The transverse component of the parton momentum transferred is generated according to probability

$$P(\mathbf{q_t})d\mathbf{q_t} = \sqrt{\frac{a}{\pi}}\exp\left(-aq_t^2\right)d\mathbf{q_t}, \tag{23.21}$$

where parameter $a = 0.6$ GeV^{-2}.

23.3.5 Sampling x-plus and x-minus

Light cone parton quantities x^+ and x^- are generated independently and according to distribution:

$$u(x) \sim x^\alpha(1-x)^\beta, \tag{23.22}$$

where $x = x^+$ or $x = x^-$. Parameters $\alpha = -1$ and $\beta = 0$ are chosen for the FRITIOF approach [9]. In the case of the QGSM approach [7] $\alpha = -0.5$ and $\beta = 1.5$ or $\beta = 2.5$. Masses of the excited strings should satisfy the kinematical constraints:

$$P_1'^+P_1'^- \geq m_{h1}^2 + q_t^2 \tag{23.23}$$

and

$$P_2'^+P_2'^- \geq m_{h2}^2 + q_t^2, \tag{23.24}$$

where hadronic masses m_{h1} and m_{h2} (model parameters) are defined by string quark contents. Thus, the random selection of the values x^+ and x^- is limited by above constraints.

23.3.6 The diffractive string excitation

In the diffractive string excitation (the FRITIOF approach [9]) for each inelastic hadron–nucleon collision we have to select randomly the transverse momentum transferred $\mathbf{q_t}$ (in accordance with the probability given by Eq. (23.21)) and select randomly the values of $x^\pm$ (in accordance with distribution defined by Eq. (23.22)). Then we have to calculate the parton momentum transferred q using Eq. (23.19) and update scattered hadron and nucleon or scatterred nucleon and nucleon momenta using Eq. (23.20). For each collision we have to check the constraints (23.23) and (23.24), which can be written more explicitly:

$$[E_1^+ - \frac{q_t^2}{x^-E_2^-}][\frac{m_1^2}{E_1^+} + \frac{q_t^2}{x^+E_1^+}] \geq m_{h1}^2 + q_t^2 \tag{23.25}$$

and

$$[E_2^- + \frac{q_t^2}{x^- E_2^-}][\frac{m_2^2}{E_2^-} - \frac{q_t^2}{x^+ E_1^+}] \geq m_{h1}^2 + q_t^2. \qquad (23.26)$$

23.3.7   The string excitation by parton rearrangement

In this approach [7] strings (as result of parton rearrangement) should be spanned not only between valence quarks of colliding hadrons, but also between valence and sea quarks and between sea quarks. The each participant hadron or nucleon should be splitted into set of partons: valence quark and antiquark for meson or valence quark (antiquark) and diquark (antidiquark) for baryon (antibaryon) and additionaly the $(n-1)$ sea quark-antiquark pairs (their flavours are selected according to probability ratios $u : d : s = 1 : 1 : 0.35$), if hadron or nucleon is participating in the n inelastic collisions. Thus for each participant hadron or nucleon we have to generate a set of light cone variables x_{2n}, where $x_{2n} = x_{2n}^+$ or $x_{2n} = x_{2n}^-$ according to distribution:

$$f^h(x_1, x_2, ..., x_{2n}) = f_0 \prod_{i=1}^{2n} u_{q_i}^h(x_i)\delta(1 - \sum_{i=1}^{2n} x_i), \qquad (23.27)$$

where f_0 is the normalization constant. Here, the quark structure functions $u_{q_i}^h(x_i)$ for valence quark (antiquark) q_v, sea quark and antiquark q_s and valence diquark (antidiquark) qq are:

$$u_{q_v}^h(x_v) = x_v^{\alpha_v}, \ u_{q_s}^h(x_s) = x_s^{\alpha_s}, \ u_{qq}^h(x_{qq}) = x_{qq}^{\beta_{qq}}, \qquad (23.28)$$

where $\alpha_v = -0.5$ and $\alpha_s = -0.5$ [10] for the non-strange quarks (antiquarks) and $\alpha_v = 0$ and $\alpha_s = 0$ for strange quarks (antiquarks), $\beta_{uu} = 1.5$ and $\beta_{ud} = 2.5$ for proton (antiproton) and $\beta_{dd} = 1.5$ and $\beta_{ud} = 2.5$ for neutron (antineutron). Usualy x_i are selected between $x_i^{min} \leq x_i \leq 1$, where model parameter x^{min} is a function of initial energy, to prevent from production of strings with low masses (less than hadron masses), when whole selection procedure should be repeated. Then the transverse momenta of partons $\mathbf{q_{it}}$ are generated according to the Gaussian probability Eq. (23.21) with $a = 1/4\Lambda(s)$ and under the constraint: $\sum_{i=1}^{2n} \mathbf{q_{it}} = 0$. The partons are considered as the off-shell partons, i. e. $m_i^2 \neq 0$.

23.4   Longitudinal string decay.

23.4.1   Hadron production by string fragmentation.

A string is stretched between flying away constituents: quark and anti-quark or quark and diquark or diquark and antidiquark or antiquark and antidiquark. From knowledge of the constituents longitudinal $p_{3i} = p_{zi}$ and transversal $p_{1i} = p_{xi}$, $p_{2i} = p_{yi}$ momenta as well as their energies $p_{0i} = E_i$, where $i = 1, 2$, we can calculate string mass squared:

$$M_S^2 = p^\mu p_\mu = p_0^2 - p_1^2 - p_2^2 - p_3^2, \qquad (23.29)$$

where $p_\mu = p_{\mu 1} + p_{\mu 2}$ is the string four momentum and $\mu = 0, 1, 2, 3$.

The fragmentation of a string follows an iterative scheme:

$$string \Rightarrow hadron + new\ string, \qquad (23.30)$$

i. e. a quark-antiquark (or diquark-antidiquark) pair is created and placed between leading quark-antiquark (or diquark-quark or diquark-antidiquark or antiquark-antidiquark) pair.

The values of the strangeness suppression and diquark suppression factors are

$$u : d : s : qq = 1 : 1 : 0.35 : 0.1. \qquad (23.31)$$

A hadron is formed randomly on one of the end-points of the string. The quark content of the hadrons determines its species and charge. In the chosen fragmentation scheme we can produce not only the groundstates of baryons and mesons, but also their lowest excited states. If for baryons the quark-content does not determine whether the state belongs to the lowest octet or to the lowest decuplet, then octet or decuplet are choosen with equal probabilities. In the case of mesons the multiplet must also be determined before a type of hadron can be assigned. The probability of choosing a certain multiplet depends on the spin of the multiplet.

The zero transverse momentum of created quark-antiquark (or diquark-antidiquark) pair is defined by the sum of an equal and opposite directed transverse momenta of quark and antiquark.

The transverse momentum of created quark is randomly sampled according to probability (23.21) with the parameter $a = 0.25$ GeV^{-2}. Then a hadron transverse momentum $\mathbf{p_t}$ is determined by the sum of the transverse momenta of its constituents.

The fragmentation function $f^h(z, p_t)$ represents the probability distribution for hadrons with the transverse momenta $\mathbf{p_t}$ to aquire the light cone momentum fraction $z = z^\pm = (E^h \pm p_z^h / (E^q \pm p_z^q)$, where E^h and E^q

are the hadron and fragmented quark energies, respectively and p_z^h and p_z^q are hadron and fragmented quark longitudinal momenta, respectively, and $z_{min}^{\pm} \leq z^{\pm} \leq z_{max}^{\pm}$, from the fragmenting string. The values of $z_{min,max}^{\pm}$ are determined by hadron m_h and constituent transverse masses and the available string mass. One of the most common fragmentation function is used in the LUND model [12]:

$$f^h(z, p_t) \sim \frac{1}{z}(1-z)^a \exp\left[-\frac{b(m_h^2 + p_t^2)}{z}\right]. \tag{23.32}$$

One can use this fragmentation function for the decay of the excited string.

One can use also the fragmentation functions are derived in [13]:

$$f_q^h(z, p_t) = [1 + \alpha_q^h(<p_t>)](1-z)^{\alpha_q^h(<p_t>)}. \tag{23.33}$$

The advantage of these functions as compared to the LUND fragmentation function is that they have correct three–reggeon behaviour at $z \to 1$ [13].

23.4.2 The hadron formation time and coordinate.

To calculate produced hadron formation times and longitudinal coordinates we consider the $(1 + 1)$-string with mass M_S and string tension κ, which decays into hadrons at string rest frame. The i-th produced hadron has energy E_i and its longitudinal momentum p_{zi}, respectively. Introducing light cone variables $p_i^{\pm} = E_i \pm p_{iz}$ and numbering string breaking points consecutively from right to left we obtain $p_0^+ = M_S$, $p_i^+ = \kappa(z_{i-1}^+ - z_i^+)$ and $p_i^- = \kappa x_i^-$.

We can identify the hadron formation point coordinate and time as the point in space-time, where the quark lines of the quark-antiquark pair forming the hadron meet for the first time (the so-called 'yo-yo' formation point [12]):

$$t_i = \frac{1}{2\kappa}\left[M_S - 2\sum_{j=1}^{i-1} p_{zj} + E_i - p_{zi}\right] \tag{23.34}$$

and coordinate

$$z_i = \frac{1}{2\kappa}\left[M_S - 2\sum_{j=1}^{i-1} E_j + p_{zi} - E_i\right]. \tag{23.35}$$

23.5 Status of this document

05.12.05 corrected units on hbarc in section 1 - D.H. Wright
00.00.00 created by ??

Bibliography

[1] Grypeos M. E., Lalazissis G. A., Massen S. E., Panos C. P., J. Phys. **G17** 1093 (1991).

[2] Elton L. R. B., Nuclear Sizes, Oxford University Press, Oxford, 1961.

[3] DeShalit A., Feshbach H., Theoretical Nuclear Physics, Vol. 1: Nuclear Structure, Wyley, 1974.

[4] Bohr A., Mottelson B. R., Nuclear Structure, W. A. Benjamin, New York, Vol. 1, 1969.

[5] Capella A. and Krzywicki A., Phys. Rev. **D18** (1978) 4120.

[6] Baker M. and Ter–Martirosyan K. A., Phys. Rep. **28C** (1976) 1.

[7] Amelin N. S., Gudima K. K., Toneev V. D., Sov. J. Nucl. Phys. **51** (1990) 327; Amelin N. S., JINR Report **P2-86-56** (1986).

[8] Abramovskii V. A., Gribov V. N., Kancheli O. V., Sov. J. Nucl. Phys. **18** (1974) 308.

[9] Andersson B., Gustafson G., Nielsson-Almquist, Nucl. Phys. **281** 289 (1987).

[10] Kaidalov A. B., Ter-Martirosyan K. A., Phys. Lett. **B117** 247 (1982).

[11] Capella A., Sukhatme U., Tan C. I., Tran Thanh Van. J., Phys. Rep. **236** 225 (1994).

[12] Andersson B., Gustafson G., Ingelman G., Sjöstrand T., Phys. Rep. **97** 31 (1983).

[13] Kaidalov A. B., Sov. J. Nucl. Phys. **45** 1452 (1987).

Chapter 24

Chiral Invariant Phase Space Decay.

24.1   Introduction

The CHIPS computer code is a quark-level event generator for the fragmentation of hadronic systems into hadrons. In contrast to other parton models [1] CHIPS is nonperturbative and three-dimensional. It is based on the Chiral Invariant Phase Space (ChIPS) model [2, 3, 4] which employs a 3D quark-level SU(3) approach. Thus Chiral Invariant Phase Space refers to the phase space of massless partons and hence only light (u, d, s) quarks can be considered. The c, b, and t quarks are not implemented in the model directly, while they can be created in the model as a result of the gluon-gluon or photo-gluon fusion. The main parameter of the CHIPS model is the critical temperature $T_c \approx 200~MeV$. The probability of finding a quark with energy E drops with the energy approximately as $e^{-E/T}$, which is why the heavy flavors of quarks are suppressed in the Chiral Invariant Phase Space. The s quarks, which have masses less then the critical temperature, have an effective suppression factor in the model.

The critical temperature T_c defines the number of 3D partons in the hadronic system with total energy W. If masses of all partons are zero then the number of partons can be found from the equation $W^2 = 4T_c^2(n-1)n$. The mean squared total energy can be calculated for any "parton" mass (partons are usually massless). The corresponding formula can be found in [5]. In this treatment the masses of light hadrons are fitted better than by the chiral bag model of hadrons [6] with the same number of parameters. In both models any hadron consists of a few quark-partons, but in the CHIPS model the critical temperature defines the mass of the hadron, consisting of

N quark-partons, while in the bag model the hadronic mass is defined by the balance between the quark-parton internal pressure (which according to the uncertainty principle increases when the radius of the "bag" decreases) and the external pressure (B) of the nonperturbative vacuum, which has negative energy density.

In CHIPS the interactions between hadrons are defined by the Isgur quark-exchange diagrams, and the decay of excited hadronic systems in vacuum is treated as the fusion of quark-antiquark or quark-diquark partons. An important feature of the model is the homogeneous distribution of asymptotically free quark-partons over the invariant phase space, as applied to the fragmentation of various types of excited hadronic systems. In this sense the CHIPS model may be considered as a generalization of the well-known hadronic phase space distribution [7] approach, but it generates not only angular and momentum distributions for a given set of hadrons, but also the multiplicity distributions for different kinds of hadrons, which is defined by the multistep energy dissipation (decay) process.

The CHIPS event generator may be applied to nucleon excitations, hadronic systems produced in e^+e^- and $p\bar{p}$ annihilation, and high energy nuclear excitations, among others. Despite its quark nature, the nonperturbative CHIPS model can also be used successfully at very low energies. It is valid for photon and hadron projectiles and for hadron and nuclear targets. Exclusive event generation models multiple hadron production, conserving energy, momentum, and other quantum numbers. This generally results in a good description of particle multiplicities, inclusive spectra, and kinematic correlations in multihadron fragmentation processes. Thus, it is possible to use the CHIPS event generator in exclusive modeling of hadron cascades in materials.

In the CHIPS model, the result of a hadronic or nuclear interaction is the creation of a quasmon which is essentially an intermediate state of excited hadronic matter. When the interaction occurs in vacuum the quasmon can dissipate energy by radiating particles according to the quark fusion mechanism [2] described in section 24.4. When the interaction occurs in nuclear matter, the energy dissipation of a quasmon can be the result of quark exchange with surrounding nucleons or clusters of nucleons [3] (section 24.5), in addition to the vacuum quark fusion mechanism.

In this sense the CHIPS model can be a successful competitor of the cascade models, because it does not break the projectile, instead it captures it, creating a quasmon, and then decays the quasmon in nuclear matter. The perturbative mechanisms in deep inelastic scattering are in some sense similar to the cascade calculations, while the parton splitting functions are used instead of interactions. The nonperturbative CHIPS approach is making a "short cut" for the perturbative calculations too. Similar to the time-like
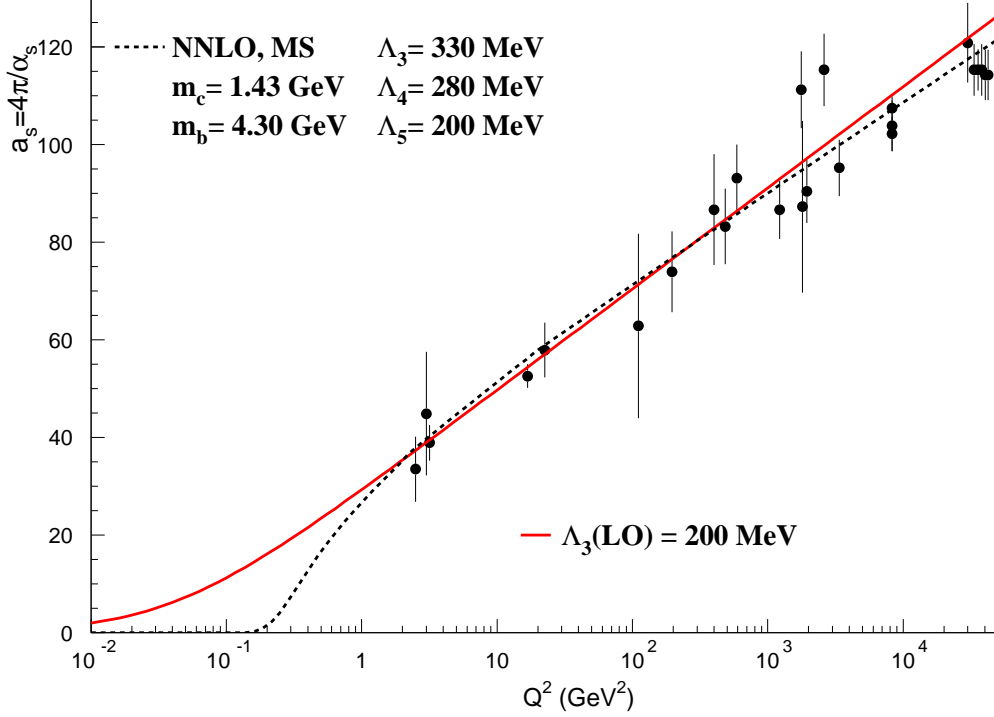
Figure 24.1: The CHIPS fit of the α_s measurements.

$s = W^2$ evolution of the number of partons in the nonperturbative chiral phase space (mentioned above) the space-like Q^2 evolution of the number of partons is given by $N(Q^2) = n_V + \frac{1}{2\alpha_s(Q^2)}$, where n_V is the number of valence quark-partons. The running $\alpha_s(Q^2)$ value is calculated in CHIPS as $\alpha_s(Q^2) = \frac{4\pi}{\beta_0 ln(1+Q^2/T_c^2)}$, where $\beta_0^{n_f=3)=9}$. In other words, the critical temperature T_c plays the role of $\Lambda_Q CD$ and still cuts out heavy flavors of quark-partons and high orders of the QCD calculation (NLO, NNLO, N^{3}LO, etc.), substituting for them the effective LO "short cut". This simple approximation of α_s fits all the present measurements of this value (Fig. 24.1). It is very important that α_s is defined in CHIPS for any Q^2, and that the number of partons at $Q^2 = 0$ converges to the number of valence quarks.

The effective α_s is defined for all Q^2, but at $Q^2 = 0$ it is infinite. In other words at $Q^2 = 0$ the number of the virtual interacting partons goes to infinity. This means that on the boundary between perturbative and non-perturbative vacuums a virtual "thermostate" of gluons with an effective temperature T_c exists. This "virtual thermostate" defines the phase space

distribution of partons, and the "thermalization" can happen very quickly. On the other hand, the CHIPS nonperturbative approach can be used below $Q^2 = 1\ GeV^2$. This was done for the neutrino-nuclear interactions (section 24.8).

24.2   Fundamental Concepts

The CHIPS model is an attempt to use a set of simple rules which govern microscopic quark-level behavior to model macroscopic hadronic systems with a large number of degrees of freedom. The invariant phase space distribution as a paradigm of thermalized chaos is applied to quarks, and simple kinematic mechanisms are used to model the hadronization of quarks into hadrons. Along with relativistic kinematics and the conservation of quantum numbers, the following concepts are used:

- **Quasmon:** in the CHIPS model, a quasmon is any excited hadronic system; it can be viewed as a continuous spectrum of a generalized hadron. At the constituent level, a quasmon may be thought of as a bubble of quark-parton plasma in which the quarks are massless and the quark-partons in the quasmon are homogeneously distributed over the invariant phase space. It may also be considered as a bubble of the three-dimensional Feynman-Wilson [8] parton gas. The traditional hadron is a particle defined by quantum numbers and a fixed mass or a mass with a width. The quark content of the hadron is a secondary concept constrained by the quantum numbers. The quasmon, however, is defined by its quark content and its mass, and the concept of a well defined particle with quantum numbers (a discrete spectrum) is of secondary importance. A given quasmon hadronic state with fixed mass and quark content can be considered as a superposition of traditional hadrons, with the quark content of the superimposed hadrons being the same as the quark content of the quasmon.

- **Quark fusion:** the quark fusion hypothesis determines the rules of final state hadron production, with energy spectra reflecting the momentum distribution of the quarks in the system. Fusion occurs when a quark-parton in a quasmon joins with another quark-parton from the same quasmon and forms a new white hadron, which can be radiated. If a neighboring nucleon (or the nuclear cluster) is present, quark-partons may also be exchanged between the quasmon and the neighboring nucleon (cluster). The kinematic condition applied to these mechanisms is that the resulting hadrons are produced on their mass shells. The

model assumes that the u, d and s quarks are effectively massless, which allows the integrals of the hadronization process to be done easily and the modeling decay algorithm to be accelerated. The quark mass is taken into account indirectly in the masses of outgoing hadrons. The type of the outgoing hadron is selected using combinatoric and kinematic factors consistent with conservation laws. In the present version of CHIPS all mesons with three-digit PDG Monte Carlo codes [9] up to spin 4, and all baryons with four-digit PDG codes up to spin $\frac{7}{2}$ are implemented.

- **Critical temperature** the only non-kinematic concept of the model is the hypothesis of the critical temperature of the quasmon. This has a 40-year history, starting with Ref. [10] and is based on the experimental observation of regularities in the inclusive spectra of hadrons produced in different reactions at high energies. Qualitatively, the hypothesis of a critical temperature assumes that the quark-gluon hadronic system (quasmon) cannot be heated above a certain temperature. Adding more energy to the hadronic system increases only the number of constituent quark-partons while the temperature remains constant. The critical temperature is the principal parameter of the model and is used to calculate the number of quark-partons in a quasmon. In an infinite thermalized system, for example, the mean energy of partons is $2T$ per particle, the same as for the dark body radiation.

24.3   Code Development

Because the CHIPS event generator was originally developed only for final state hadronic fragmentation, the initial interaction of projectiles with targets requires further development. Hence, the first applications of CHIPS described interactions at rest, for which the interaction cross section is not important [2], [3], and low energy photonuclear reactions [4], for which the interaction cross section can be calculated easily [11]. With modification of the first interaction algorithm the CHIPS event generator can be used for all kinds of hadronic interaction. The Geant4 String Model interface to the CHIPS generator [12], [13] also makes it possible to use the CHIPS code for nuclear fragmentation at extremely high energies.

In the first published versions of the CHIPS event generator the class `G4Quasmon` was the head of the model and all initial interactions were hidden in its constructor. More complicated applications of the model such as anti-proton nuclear capture at rest and the Geant4 String Model interface to

CHIPS led to the multi-quasmon version of the model. This required a change in the structure of the CHIPS event generator classes. In the case of at-rest anti-proton annihilation in a nucleus, for example, the first interaction occurs on the nuclear periphery. After this initial interaction, a fraction (defined by a special parameter of the model) of the secondary mesons independently penetrate the nucleus. Each of these mesons can create a separate quasmon in the interior of the nucleus. In this case the class `G4Quasmon` can no longer be the head of the model. A new head class, `G4QEnvironment`, was developed which can adopt a vector of projectile hadrons (`G4QHadronVector`) and create a vector of quasmons, `G4QuasmonVector`. All newly created quasmons then begin the energy dissipation process in parallel in the same nucleus. The `G4QEnvironment` instance can be used both for vacuum and for nuclear matter. If `G4QEnvironment` is created in vacuum, it is practically identical to the `G4Quasmon` class, because in this case only one instance of `G4Quasmon` is allowed. This leaves the model unchanged for hadronic interactions.

The convention adopted for the CHIPS model requires all its class names to use the prefix `G4Q` in order to distinguish them from other Geant4 classes, most of which use the `G4` prefix. The intent is that the `G4Q` prefix will not be used by other Geant4 projects.

24.4 Nucleon-Antinucleon Annihilation at Rest

In order to generate hadron spectra from the annihilation of a proton with an anti-proton at rest, the number of partons in the system must be found. For a finite system of N partons with a total center-of-mass energy M, the invariant phase space integral, Φ_N, is proportional to M^{2N-4}. According to the dimensional counting rule, $2N$ comes from $\prod_{i=1}^{N} \frac{d^3 p_i}{E_i}$, and 4 comes from the energy and momentum conservation function, $\delta^4(\underline{P} - \sum \underline{p}_i)$. At a temperature T the statistical density of states is proportional to $e^{-\frac{M}{T}}$ so that the probability to find a system of N quark-partons in a state with mass M is $dW \propto M^{2N-4} e^{-\frac{M}{T}} dM$. For this kind of probability distribution the mean value of M^2 is

$$< M^2 >= 4N(N-1) \cdot T^2. \tag{24.1}$$

When N goes to infinity one obtains for massless particles the well-known $< M > \equiv \sqrt{< M^2 >} = 2NT$ result.

After a nucleon absorbs an incident quark-parton, such as a real or virtual photon, for example, the newly formed quasmon has a total of N quark-partons, where N is determined by Eq. 24.1. Choosing one of these quark-partons with energy k in the center of mass system (CMS) of N partons, the

spectrum of the remaining $N - 1$ quark-partons is given by

$$\frac{dW}{kdk} \propto (M_{N-1})^{2N-6},\tag{24.2}$$

where M_{N-1} is the effective mass of the $N - 1$ quark-partons. This result was obtained by applying the above phase-space relation ($\Phi_N \propto M^{2N-4}$) to the residual $N - 1$ quarks. The effective mass is a function of the total mass M,

$$M_{N-1}^2 = M^2 - 2kM,\tag{24.3}$$

so that the resulting equation for the quark-parton spectrum is:

$$\frac{dW}{kdk} \propto (1 - \frac{2k}{M})^{N-3}.\tag{24.4}$$

24.4.1 Meson Production

In this section, only the quark fusion mechanism of hadronization is considered. The quark exchange mechanism can take place only in nuclear matter where a quasmon has neighboring nucleons. In order to decompose a quasmon into an outgoing hadron and a residual quasmon, one needs to calculate the probability of two quark-partons combining to produce the effective mass of the outgoing hadron. This requires that the spectrum of the second quark-parton be calculated. This is done by following the same argument used to determine Eq. 24.4. One quark-parton is chosen from the residual $N - 1$. It has an energy q in the CMS of the $N - 1$ quark-partons. The spectrum is obtained by substituting $N - 1$ for N and M_{N-1} for M in Eq. 24.4 and then using Eq. 24.3 to get

$$\frac{dW}{qdq} \propto \left(1 - \frac{2q}{M\sqrt{1 - \frac{2k}{M}}}\right)^{N-4}.\tag{24.5}$$

Next, one of the residual quark-partons must be selected from this spectrum such that its fusion with the primary quark-parton makes a hadron of mass μ. This selection is performed by the mass shell condition for the outgoing hadron,

$$\mu^2 = 2\frac{k}{\sqrt{1 - \frac{2k}{M}}} \cdot q \cdot (1 - \cos\theta).\tag{24.6}$$

Here θ is the angle between the momenta, $\mathbf{k}$ and $\mathbf{q}$ of the two quark-partons in the CMS of $N - 1$ quarks. Now the kinematic quark fusion probability

can be calculated for any primary quark-parton with energy k:

$$P(k, M, \mu) = \int \left(1 - \frac{2q}{M\sqrt{1 - \frac{2k}{M}}}\right)^{N-4}$$

$$\times \delta \left(\mu^2 - \frac{2kq(1 - \cos\theta)}{\sqrt{1 - \frac{2k}{M}}}\right) q dq d\cos\theta. \qquad (24.7)$$

Using the δ-function[1] to perform the integration over q one gets:

$$P(k, M, \mu) = \int \left(1 - \frac{\mu^2}{Mk(1 - \cos\theta)}\right)^{N-4}$$

$$\times \left(\frac{\mu^2\sqrt{1 - \frac{2k}{M}}}{2k(1 - \cos\theta)}\right)^2 d\left(\frac{1 - \cos\theta}{\mu^2}\right), \qquad (24.8)$$

or

$$P(k, M, \mu) = \frac{M - 2k}{4k} \int \left(1 - \frac{\mu^2}{Mk(1 - \cos\theta)}\right)^{N-4}$$

$$\times d\left(1 - \frac{\mu^2}{Mk(1 - \cos\theta)}\right). \qquad (24.9)$$

After the substitution $z = 1 - \frac{2q}{M_{N-1}} = 1 - \frac{\mu^2}{Mk(1-\cos\theta)}$, this becomes

$$P(k, M, \mu) = \frac{M - 2k}{4k} \int z^{N-4} dz, \qquad (24.10)$$

where the limits of integration are 0 when $\cos\theta = 1 - \frac{\mu^2}{M \cdot k}$, and

$$z_{\max} = 1 - \frac{\mu^2}{2Mk}, \qquad (24.11)$$

when $\cos\theta = -1$. The resulting range of θ is therefore $-1 < \cos\theta < 1 - \frac{\mu^2}{M \cdot k}$. Integrating from 0 to z yields

$$\frac{M - 2k}{4k \cdot (N - 3)} \cdot z^{N-3}, \qquad (24.12)$$

---

[1] If $g(x_0){=}0$, $\int f(x)\delta\left[g(x)\right] dx = \int \frac{f(x)\delta[g(x)]}{g'(x)} dg(x) = \frac{f(x_0)}{g'(x_0)}$

and integrating from 0 to z_{max} yields the total kinematic probability for hadronization of a quark-parton with energy k into a hadron with mass μ:

$$\frac{M - 2k}{4k \cdot (N - 3)} \cdot z_{\max}^{N-3}. \tag{24.13}$$

The ratio of expressions 24.12 and 24.13 can be treated as a random number, R, uniformly distributed on the interval [0,1]. Solving for z then gives

$$z = \sqrt[N-3]{R} \cdot z_{\max}. \tag{24.14}$$

In addition to the kinematic selection of the two quark-partons in the fusion process, the quark content of the quasmon and the spin of the candidate final hadron are used to determine the probability that a given type of hadron is produced. Because only the relative hadron formation probabilities are necessary, overall normalization factors can be dropped. Hence the relative probability can be written as

$$P_h(k, M, \mu) = (2s_h + 1) \cdot z_{\max}^{N-3} \cdot C_Q^h. \tag{24.15}$$

Here, only the factor $z_{\max}^{N-3}$ is used since the other factors in equation 24.13 are constant for all candidates for the outgoing hadron. The factor $2s_h + 1$ counts the spin states of a candidate hadron of spin s_h, and C_Q^h is the number of ways the candidate hadron can be formed from combinations of the quarks within the quasmon. In making these combinations, the standard quark wave functions for pions and kaons were used. For η and η' mesons the quark wave functions $\eta = \frac{\bar{u}u + \bar{d}d}{2} - \frac{\bar{s}s}{\sqrt{2}}$ and $\eta' = \frac{\bar{u}u + \bar{d}d}{2} + \frac{\bar{s}s}{\sqrt{2}}$ were used. No mixing was assumed for the ω and ϕ meson states, hence $\omega = \frac{\bar{u}u + \bar{d}d}{\sqrt{2}}$ and $\varphi = \bar{s}s$.

A final model restriction is applied to the hadronization process: after a hadron is emitted, the quark content of the residual quasmon must have a quark content corresponding to either one or two real hadrons. When the quantum numbers of a quasmon, determined by its quark content, cannot be represented by the quantum numbers of a real hadron, the quasmon is considered to be a virtual hadronic molecule such as $\pi^+\pi^+$ or $K^+\pi^+$, in which case it is defined in the CHIPS model to be a Chipolino pseudo-particle.

To fuse quark-partons and create the decay of a quasmon into a hadron and residual quasmon, one needs to generate randomly the residual quasmon mass m, which in fact is the mass of the residual $N - 2$ quarks. Using an equation similar to 24.3) one finds that

$$m^2 = z \cdot (M^2 - 2kM). \tag{24.16}$$

Using Eqs. 24.14 and 24.11, the mass of the residual quasmon can be expressed in terms of the random number R:

$$m^2 = (M - 2k) \cdot (M - \frac{\mu^2}{2k}) \cdot \sqrt[N-3]{R}. \tag{24.17}$$

At this point, the decay of the original quasmon into a final state hadron and a residual quasmon of mass m has been simulated. The process may now be repeated on the residual quasmon.

This iterative hadronization process continues as long as the residual quasmon mass remains greater than $m_{\min}$, whose value depends on the type of quasmon. For hadron-type residual quasmons

$$m_{\min} = m_{\min}^{QC} + m_{\pi^0}, \tag{24.18}$$

where $m_{\min}^{QC}$ is the minimum hadron mass for the residual quark content (QC). For Chipolino-type residual quasmons consisting of hadrons h_1 and h_2,

$$m_{\min} = m_{h_1} + m_{h_2}. \tag{24.19}$$

These conditions insure that the quasmon always has enough energy to decay into at least two final state hadrons, conserving four-momentum and charge.

If the remaining CMS energy of the residual quasmon falls below $m_{\min}$, then the hadronization process terminates with a final two-particle decay. If the parent quasmon is a Chipolino consisting of hadrons h_1 and h_2, then a binary decay of the parent quasmon into m_{h_1} and m_{h_2} takes place. If the parent quasmon is not a Chipolino then a decay into $m_{\min}^{QC}$ and m_h takes place. The decay into $m_{\min}^{QC}$ and m_π^0 is always possible in this case because of condition 24.18.

If the residual quasmon is not Chipolino-type, and $m > m_{\min}$, the hadronization loop can still be finished by the resonance production mechanism, which is modeled following the concept of parton-hadron duality [14]. If the residual quasmon has a mass in the vicinity of a resonance with the same quark content (ρ or K^* for example), there is a probability for the residual quasmon to convert to this resonance.[2] In the present version of the CHIPS event generator the probability of convert to the resonance is given by

$$P_{\text{res}} = \frac{m_{\min}^2}{m^2}. \tag{24.20}$$

Hence the resonance with the mass-squared value m_r^2 closest to m^2 is selected, and the binary decay of the quasmon into m_h and m_r takes place.

---

[2]When comparing quark contents, the quark content of the quasmon is reduced by canceling quark-antiquark pairs of the same flavor.

With more detailed experimental data, it will be possible to take into account angular momentum conservation, as well as C-, P- and G-parity conservation. In the present version of the generator, η and η' are suppressed by a factor of 0.3. This factor was tuned using data from experiments on antiproton annihilation at rest in liquid hydrogen and can be different for other hadronic reactions. It is possible to vary it when describing other reactions.

Another parameter, s/u, controls the suppression of heavy quark production [15]. For proton-antiproton annihilation at rest the strange quark-antiquark sea was found to be suppressed by the factor $s/u = 0.1$. In the JETSET [15] event generator, the default value for this parameter is $s/u = 0.3$. The lower value may be due to quarks and anti-quarks of colliding hadrons initially forming a non-strange sea, with the strange sea suppressed by the OZI rule [16]. This question is still under discussion [17] and demands further experimental measurements. The s/u parameter may differ for other reactions. In particular, for e$^+$e$^-$ reactions it can be closer to 0.3.

Finally, the temperature parameter has been fixed at $T = 180$ MeV. In earlier versions of the model it was found that this value successfully reproduced spectra of outgoing hadrons in different types of medium-energy reactions.

The above parameters were used to fit not only the spectrum of pions Fig. 24.2,a and the multiplicity distribution for pions Fig. 24.2,b but also branching ratios of various measured [18, 19] exclusive channels as shown in Figs. 24.3, 24.4, 24.5. In Fig. 24.5 one can see many decay channels with higher meson resonances. The relative contribution of events with meson resonances produced in the final state is 30 - 40 percent, roughly in agreement with experiment. The agreement between the model and experiment for particular decay modes is within a factor of 2-3 except for the branching ratios to higher resonances. In these cases it is not completely clear how the resonance is defined in a concrete experiment. In particular, for the $a_2\omega$ channel the mass sum of final hadrons is 2100 MeV with a full width of about 110 MeV while the total initial energy of the p$\bar{\text{p}}$ annihilation reaction is only 1876.5 MeV. This decay channel can be formally simulated by an event generator using the tail of the Breit-Wigner distribution for the a_2 resonance, but it is difficult to imagine how the a_2 resonance can be experimentally identified 2Γ away from its mean mass value.

24.4.2   Baryon Production

To model fragmentation into baryons the POPCORN idea [20] was used, which assumes the existence of diquark-partons. The assumption of massless
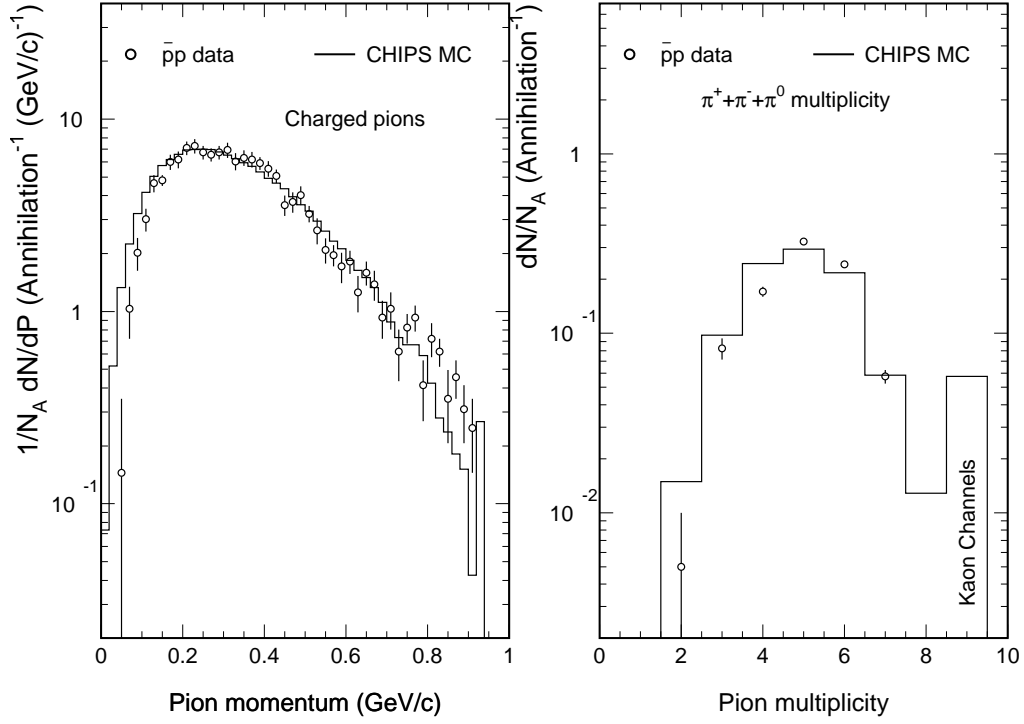
Figure 24.2: (a) (left): momentum distribution of charged pions produced in proton-antiproton annihilation at rest. The experimental data are from [18], and the histogram was produced by the CHIPS Monte Carlo. The experimental spectrum is normalized to the measured average charged pion multiplicity, 3.0. (b) (right): pion multiplicity distribution. Data points were taken from compilations of experimental data [19], and the histogram was produced by the CHIPS Monte Carlo. The number of events with kaons in the final state is shown in pion multiplicity bin 9, where no real 9-pion events are generated or observed experimentally. In the model, the percentage of annihilation events with kaons is close to the experimental value of 6% [19].
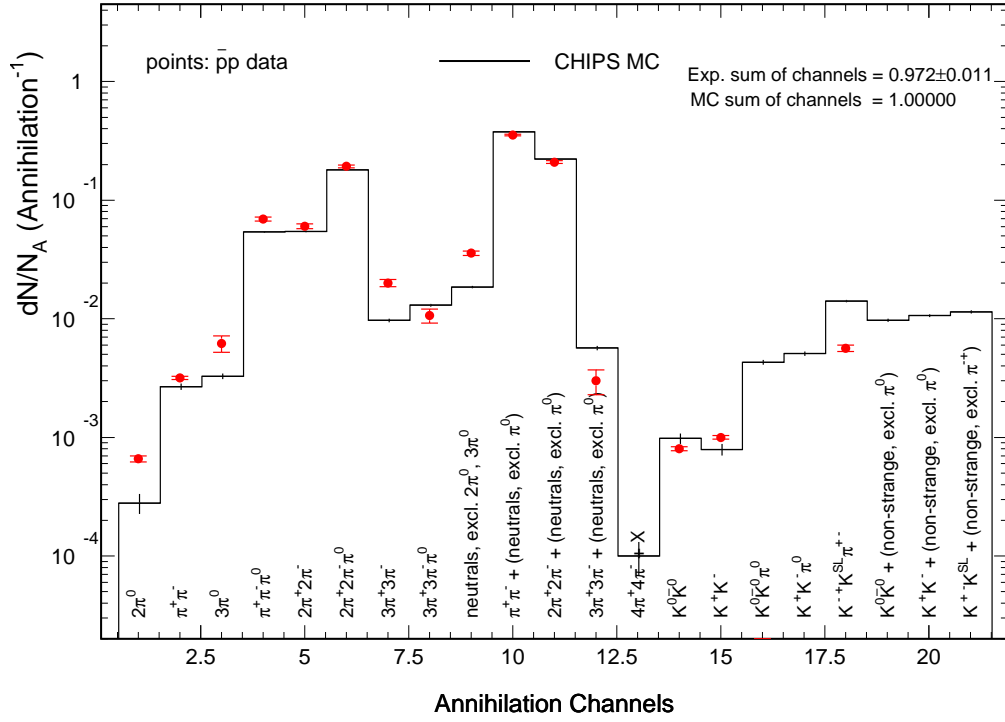
380

Figure 24.3: Branching probabilities for different channels in proton-antiproton annihilation at rest. The experimental data are from [19], and the histogram was produced by the CHIPS Monte Carlo.
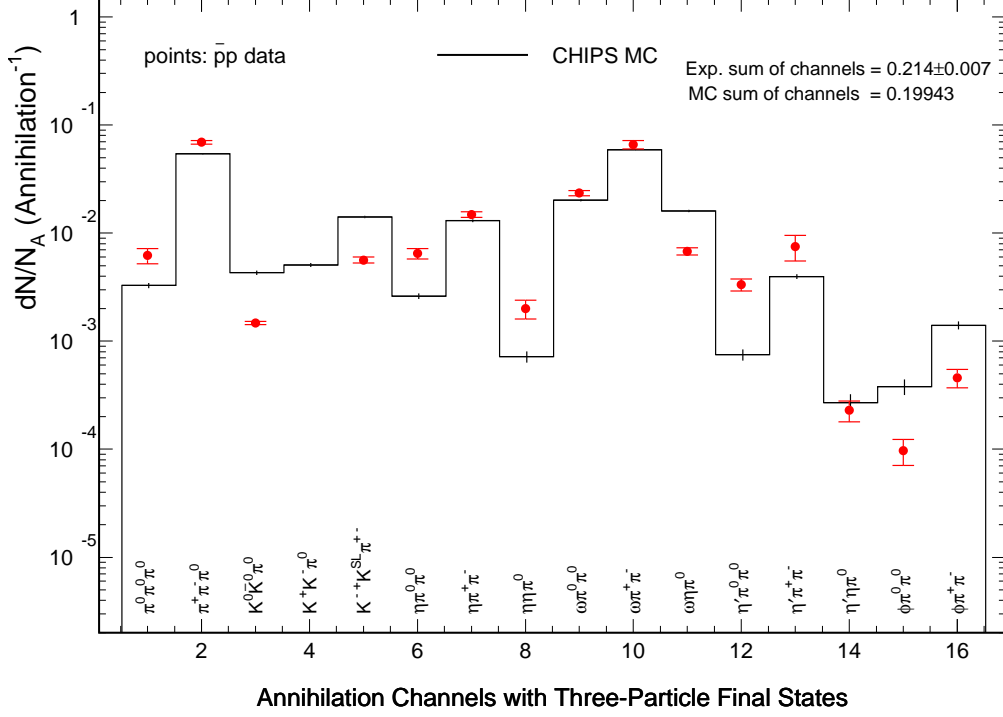
Figure 24.4: Branching probabilities for different channels with three-particle final states in proton-antiproton annihilation at rest. The points are experimental data [19] and the histogram is from the CHIPS Monte Carlo.

diquarks is somewhat inconsistent at low energies, as is the assumption of massless s-quarks, but it is simple and it helps to generate baryons in the same way as mesons.

Baryons are heavy, and the baryon production in $p\bar{p}$ annihilation reactions at medium energies is very sensitive to the value of the temperature. If the temperature is low, the baryon yield is small, and the mean multiplicity of pions increases very noticeably with center-of-mass energy as seen in Fig. 24.6. For higher temperature values the baryon yield reduces the pion multiplicity at higher energies. The existing experimental data [21], shown in Fig. 24.6, can be considered as a kind of "thermometer" for the model. This thermometer confirms that the critical temperature is about 200 MeV.

It can be used as a tool for the Monte Carlo simulation of a wide variety of hadronic reactions. The CHIPS event generator can be used not only for "phase-space background" calculations in place of the standard GENBOD
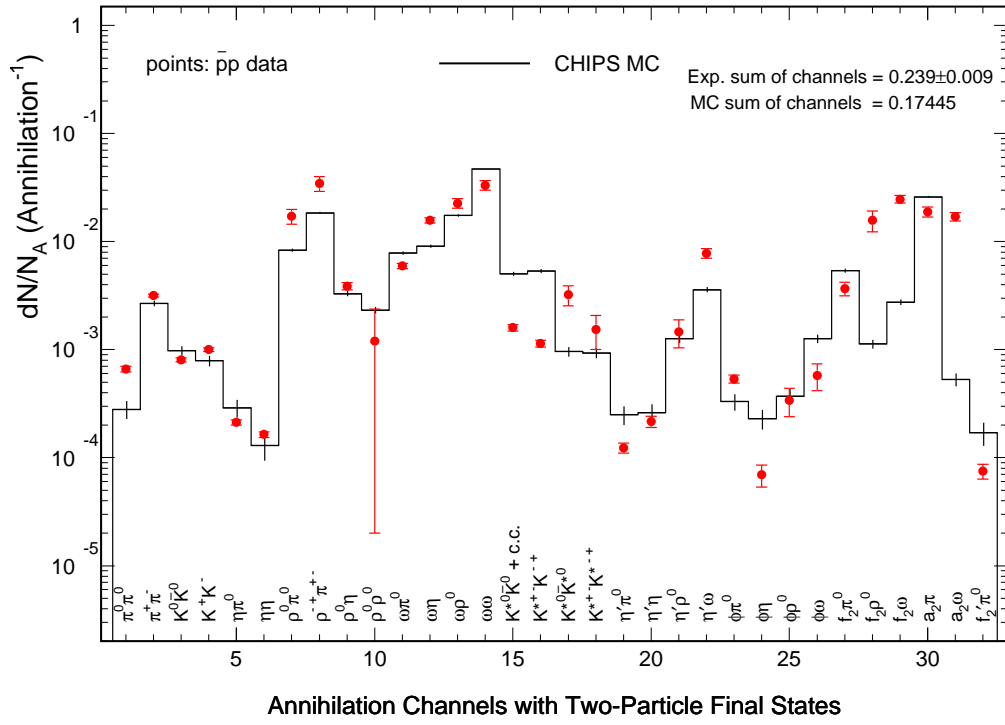
Figure 24.5: Branching probabilities for different channels with two-particle final states in proton-antiproton annihilation at rest. The points are experimental data [19] and the histogram is from the CHIPS Monte Carlo.
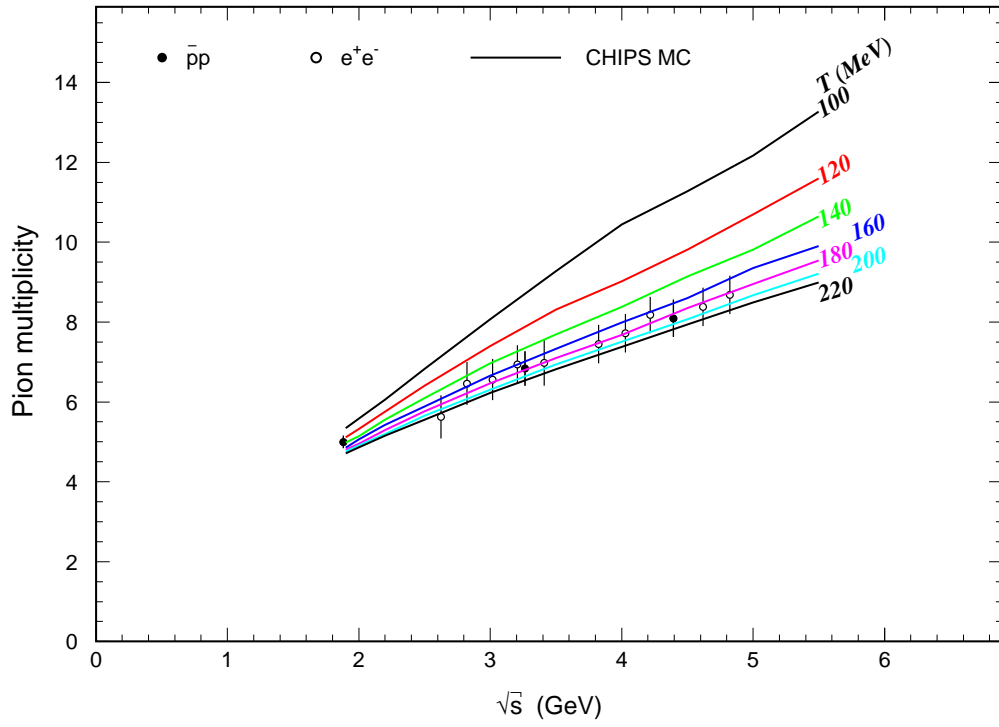
Figure 24.6: Average meson multiplicities in proton-antiproton and in electron-positron annihilation, as a function of the center-of-mass energy of the interacting hadronic system. The points are experimental data [21] and the lines are CHIPS Monte Carlo calculations at several values of the critical temperature parameter T.

routine [7], but even for taking into account the reflection of resonances in connected final hadron combinations. Thus it can be useful for physics analysis too, even though its main range of application is the simulation of the evolution of hadronic and electromagnetic showers in matter at medium energies.

## 24.5 Nuclear Pion Capture at Rest and Photonuclear Reactions Below the Delta(3,3) Resonance

When compared with the first "in vacuum" version of the model, described in Section 24.4, modeling hadronic fragmentation in nuclear matter is more complicated because of the much greater number of possible secondary fragments. However, the hadronization process itself is simpler in a way. In vacuum, the quark-fusion mechanism requires a quark-parton partner from the external (as in JETSET [15]) or internal (the quasmon itself, Section 24.4) quark-antiquark sea. In nuclear matter, there is a second possibility: quark exchange with a neighboring hadronic system, which could be a nucleon or multinucleon cluster.

In nuclear matter the spectra of secondary hadrons and nuclear fragments reflect the quark-parton energy spectrum within a quasmon. In the case of inclusive spectra that are decreasing steeply with energy, and correspondingly steeply decreasing spectra of the quark-partons in a quasmon, only those secondary hadrons which get the maximum energy from the primary quark-parton of energy k contribute to the inclusive spectra. This extreme situation requires the exchanged quark-parton with energy q, coming toward the quasmon from the cluster, to move in a direction opposite to that of the primary quark-parton. As a result the hadronization quark exchange process becomes one-dimensional along the direction of k. If a neighboring nucleon or nucleon cluster with bound mass $\tilde{\mu}$ absorbs the primary quark-parton and radiates the exchanged quark-parton in the opposite direction, then the energy of the outgoing fragment is $E = \tilde{\mu} + k - q$, and the momentum is $p = k + q$. Both the energy and the momentum of the outgoing nuclear fragment are known, as is the mass $\tilde{\mu}$ of the nuclear fragment in nuclear matter, so the momentum of the primary quark-parton can be reconstructed using the approximate relation

$$k = \frac{p + E - B \cdot m_N}{2}.$$ (24.21)

385

Here B is the baryon number of the outgoing fragment ($\tilde{\mu} \approx B \cdot m_N$) and m_N is the nucleon mass. In Ref. [22] it was shown that the invariant inclusive spectra of pions, protons, deuterons, and tritons in proton-nucleus reactions at 400 GeV [23] not only have the same exponential slope but almost coincide when they are plotted as a function of $k = \frac{p+E_{\text{kin}}}{2}$. Using data at 10 GeV [24], it was shown that the parameter k, defined by Eq. 24.21, is also appropriate for the description of secondary anti-protons produced in high energy nuclear reactions. This means that the extreme assumption of one-dimensional hadronization is a good approximation.

The same approximation is also valid for the quark fusion mechanism. In the one-dimensional case, assuming that q is the momentum of the second quark fusing with the primary quark-parton of energy k, the total energy of the outgoing hadron is $E = q + k$ and the momentum is $p = k - q$. In the one-dimensional case the secondary quark-parton must move in the opposite direction with respect to the primary quark-parton, otherwise the mass of the outgoing hadron would be zero. So, for mesons $k = \frac{p+E}{2}$, in accordance with Eq. 24.21. In the case of anti-proton radiation, the baryon number of the quasmon is increased by one, and the primary antiquark-parton will spend its energy to build up the mass of the antiproton by picking up an anti-diquark. Thus, the energy conservation law for antiproton radiation looks like $E + m_N = q + k$ and $k = \frac{p+E+m_N}{2}$, which is again in accordance with Eq. 24.21.

The one-dimensional quark exchange mechanism was proposed in 1984 [22]. Even in its approximate form it was useful in the analysis of inclusive spectra of hadrons and nuclear fragments in hadron-nuclear reactions at high energies. Later the same approach was used in the analysis of nuclear fragmentation in electro-nuclear reactions [25]. Also in 1984 the quark-exchange mechanism developed in the framework of the non-relativistic quark model was found to be important for the explanation of the short distance features of NN interactions [26]. Later it was successfully applied to K^-p interactions [27]. The idea of the quark exchange mechanism between nucleons was useful even for the explanation of the EMC effect [28]. For the non-relativistic quark model, the quark exchange technique was developed as an alternative to the Feynman diagram technique at short distances [29].

The CHIPS event generator models quark exchange processes, taking into account kinematic and combinatorial factors for asymptotically free quark-partons. In the naive picture of the quark-exchange mechanism, one quark-parton tunnels from the asymptotically free region of one hadron to the asymptotically free region of another hadron. To conserve color, another quark-parton from the neighboring hadron must replace the first quark-parton in the quasmon. This makes the tunneling mutual, and the resulting
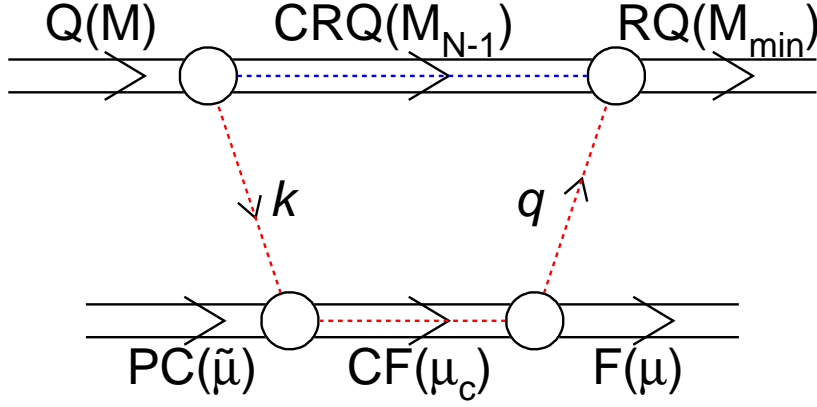
386

Figure 24.7: Diagram of the quark exchange mechanism.

process is quark exchange.

The experimental data available for multihadron production at high energies show regularities in the secondary particle spectra that can be related to the simple kinematic, combinatorial, and phase space rules of such quark exchange and fusion mechanisms. The CHIPS model combines these mechanisms consistently.

Fig. 24.7 shows a quark exchange diagram which helps to keep track of the kinematics of the process. It was shown in Section 24.4 that a quasmon, Q is kinematically determined by a few asymptotically free quark-partons homogeneously distributed over the invariant phase space. The quasmon mass M is related to the number of quark-partons N through

$$< M^2 >= 4N(N-1) \cdot T^2, \tag{24.22}$$

where T is the temperature of the system.

The spectrum of quark partons can be calculated as

$$\frac{dW}{k^*dk^*} \propto \left(1 - \frac{2k^*}{M}\right)^{N-3}, \tag{24.23}$$

where k^* is the energy of the primary quark-parton in the center-of-mass system of the quasmon. After the primary quark-parton is randomized and the neighboring cluster, or parent cluster, PC, with bound mass $\tilde{\mu}$ is selected, the quark exchange process begins. To follow the process kinematically one should imagine a colored, compound system consisting of a stationary, bound parent cluster and the primary quark. The primary quark has energy k in the lab system,

$$k = k^* \cdot \frac{E_N + p_N \cdot \cos(\theta_k)}{M_N}, \tag{24.24}$$

387

where M_N, E_N and p_N are the mass, energy, and momentum of the quasmon in the lab frame. The mass of the compound system, CF, is $\mu_c = \sqrt{(\tilde{\mu} + k)^2}$, where $\tilde{\mu}$ and k are the corresponding four-vectors. This colored compound system decays into a free outgoing nuclear fragment, F, with mass μ and a recoiling quark with energy q. q is measured in the CMS of $\tilde{\mu}$, which coincides with the lab frame in the present version of the model because no cluster motion is considered. At this point one should recall that a colored residual quasmon, CRQ, with mass M_{N-1} remains after the radiation of k. CRQ is finally fused with the recoil quark q to form the residual quasmon RQ. The minimum mass of RQ should be greater than $M_{\min}$, which is determined by the minimum mass of a hadron (or Chipolino double-hadron as defined in Section 24.4) with the same quark content.

All quark-antiquark pairs with the same flavor should be canceled in the minimum mass calculations. This imposes a restriction, which in the center-of-mass system of μ_c, can be written as

$$2q \cdot (E - p \cdot \cos\theta_{qCQ}) + M_{N-1}^2 > M_{\min}^2, \qquad (24.25)$$

where E is the energy and p is the momentum of the colored residual quasmon with mass M_{N-1} in the CMS of μ_c. The restriction for $\cos\theta_{qCQ}$ then becomes

$$\cos\theta_{qCQ} < \frac{2qE - M_{\min}^2 + M_{N-1}^2}{2qp}, \qquad (24.26)$$

which implies

$$q > \frac{M_{N-1}^2 - M_{\min}^2}{2 \cdot (E + p)}. \qquad (24.27)$$

A second restriction comes from the nuclear Coulomb barrier for charged particles. The Coulomb barrier can be calculated in the simple form:

$$E_{CB} = \frac{Z_F \cdot Z_R}{A_F^{\frac{1}{3}} + A_R^{\frac{1}{3}}} \; (\text{MeV}), \qquad (24.28)$$

where Z_F and A_F are the charge and atomic weight of the fragment, and Z_R and A_R are the charge and atomic weight of the residual nucleus. The obvious restriction is

$$q < k + \tilde{\mu} - \mu - E_{CB}. \qquad (24.29)$$

In addition to 24.27 and 24.29, the quark exchange mechanism imposes restrictions which are calculated below. The spectrum of recoiling quarks is similar to the k^* spectrum in the quasmon (24.23):

$$\frac{dW}{q \, dq \, d\cos\theta} \propto \left(1 - \frac{2q}{\tilde{\mu}}\right)^{n-3}, \qquad (24.30)$$

where n is the number of quark-partons in the nucleon cluster. It is assumed that $n = 3A_C$, where A_C is the atomic weight of the parent cluster. The tunneling of quarks from one nucleon to another provides a common phase space for all quark-partons in the cluster.

An additional equation follows from the mass shell condition for the outgoing fragment,

$$\mu^2 = \tilde{\mu}^2 + 2\tilde{\mu} \cdot k - 2\tilde{\mu} \cdot q - 2k \cdot q \cdot (1 - \cos\theta_{kq}), \qquad (24.31)$$

where θ_{kq} is the angle between quark-parton momenta in the lab frame. From this equation q can be calculated as

$$q = \frac{\tilde{\mu} \cdot (k - \Delta)}{\tilde{\mu} + k \cdot (1 - \cos\theta_{kq})}, \qquad (24.32)$$

where Δ is the covariant binding energy of the cluster $\Delta = \frac{\mu^2 - \tilde{\mu}^2}{2\tilde{\mu}}$. The quark exchange probability integral can be then written in the form:

$$P(k, \tilde{\mu}, \mu) =$$
$$\int \delta\left[\mu^2 - \tilde{\mu}^2 - 2\tilde{\mu} \cdot k + 2\tilde{\mu} \cdot q + 2k \cdot q \cdot (1 - \cos\theta_{kq})\right]$$
$$\times \left(1 - \frac{2q}{\tilde{\mu}}\right)^{n-3} q\, dq \cdot d\cos\theta_{kq}. \qquad (24.33)$$

Using the δ-function to perform the integration over q one obtains

$$P(k, \tilde{\mu}, \mu) = \int \left(1 - \frac{2(k - \Delta)}{\tilde{\mu} + k(1 - \cos\theta_{kq})}\right)^{n-3}$$
$$\times \frac{\tilde{\mu}(k - \Delta)}{2[\tilde{\mu} + k(1 - \cos\theta_{kq})]^2} d\cos\theta_{kq} \qquad (24.34)$$

or

$$P(k, \tilde{\mu}, \mu) = \int \left(1 - \frac{2(k - \Delta)}{\tilde{\mu} + k(1 - \cos\theta_{kq})}\right)^{n-3}$$
$$\times \left(\frac{\tilde{\mu}(k - \Delta)}{\tilde{\mu} + k(1 - \cos\theta_{kq})}\right)^2$$
$$\times d\left(\frac{\tilde{\mu} + k(1 - \cos\theta_{kq})}{\tilde{\mu}(k - \Delta)}\right). \qquad (24.35)$$

The result of the integration is

$$P(k, \tilde{\mu}, \mu) = \frac{\tilde{\mu}}{4k(n-2)}$$
$$\times \left[\left(1 - \frac{2(k - \Delta)}{\tilde{\mu} + 2k}\right)^{n-2}_{\text{high}} - \left(1 - \frac{2(k - \Delta)}{\tilde{\mu}}\right)^{n-2}_{\text{low}}\right]. \qquad (24.36)$$

For randomization it is convenient to make z a random parameter

$$z = 1 - \frac{2(k - \Delta)}{\tilde{\mu} + k(1 - \cos\theta_{kq})} = 1 - \frac{2q}{\tilde{\mu}}. \tag{24.37}$$

From (24.36) one can find the high and the low limits of the randomization. The first limit is for k: $k > \Delta$. It is similar to the restriction for quasmon fragmentation in vacuum: $k^* > \frac{\mu^2}{2M}$. The second limit is $k = \frac{\mu^2}{2\tilde{\mu}}$, when the low limit of randomization becomes equal to zero. If $k < \frac{\mu^2}{2\tilde{\mu}}$, then $-1 < \cos\theta_{kq} < 1$ and $z_{\text{low}} = 1 - \frac{2(k - \Delta)}{\tilde{\mu}}$. If $k > \frac{\mu^2}{2\tilde{\mu}}$, then the range of $\cos\theta_{kq}$ is $-1 < \cos\theta_{kq} < \frac{\mu^2}{k\tilde{\mu}} - 1$ and $z_{\text{low}} = 0$. This value of z_{low} should be corrected using the Coulomb barrier restriction (24.29), and the value of z_{high} should be corrected using the minimum residual quasmon restriction (24.27). In the case of a quasmon with momentum much less than k it is possible to impose tighter restrictions than (24.27) because the direction of motion of the CRQ is opposite to k. So $\cos\theta_{qCQ} = -\cos\theta_{kq}$, and from (24.32) one can find that

$$\cos\theta_{qCQ} = 1 - \frac{\tilde{\mu} \cdot (k - \Delta - q)}{k \cdot q}. \tag{24.38}$$

So in this case the equation (24.27) can be replaced by the more stringent one:

$$q > \frac{M_{N-1}^2 - M_{\min}^2 + 2\frac{p \cdot \tilde{\mu}}{k}(k - \Delta)}{2 \cdot (E + p + \frac{p \cdot \tilde{\mu}}{k})}. \tag{24.39}$$

The integrated kinematical quark exchange probability (in the range from z_{low} to z_{high}) is

$$\frac{\tilde{\mu}}{4k(n-2)} \cdot z^{n-2}, \tag{24.40}$$

and the total kinematic probability of hadronization of the quark-parton with energy k into a nuclear fragment with mass μ is

$$\frac{\tilde{\mu}}{4k(n-2)} \cdot \left(z_{\text{high}}^{n-2} - z_{\text{low}}^{n-2}\right). \tag{24.41}$$

This can be compared with the vacuum probability of the quark fusion mechanism from Section 24.4:

$$\frac{M - 2k}{4k(N-3)} z_{\max}^{N-3}. \tag{24.42}$$

The similarity is very important, as the absolute probabilities define the competition between vacuum and nuclear channels.

Equations (24.40) and (24.41) can be used for randomization of z:

$$z = z_{\text{low}} + \sqrt[n-2]{R} \cdot (z_{\text{high}} - z_{\text{low}}), \qquad (24.43)$$

where R is a random number, uniformly distributed in the interval (0,1).

Eq. (24.41) can be used to control the competition between different nuclear fragments and hadrons in the hadronization process, but in contrast to the case of "in vacuum" hadronization it is not enough to take into account only the quark combinatorics of the quasmon and the outgoing hadron. In the case of hadronization in nuclear matter, different parent bound clusters should be taken into account as well. For example, tritium can be radiated as a result of quark exchange with a bound tritium cluster or as a result of quark exchange with a bound ^{3}He cluster.

To calculate the yield of fragments it is necessary to calculate the probability to find a cluster with certain proton and neutron content in a nucleus. One could consider any particular probability as an independent parameter, but in such a case the process of tuning the model would be difficult. We proposed the following scenario of clusterization. A gas of quasi-free nucleons is close to the phase transition to a liquid bound by strong quark exchange forces. Precursors of the liquid phase are nuclear clusters, which may be considered as "drops" of the liquid phase within the nucleus. Any cluster can meet another nucleon and absorb it (making it bigger), or it can release one of the nucleons (making it smaller). The first parameter ε_1 is the percentage of quasi-free nucleons not involved in the clusterization process. The rest of the nucleons $(1 - \varepsilon_1)$ clusterize. We assume that since on the periphery of the nucleus the density is lower, one can consider only dibaryon clusters, and neglect triple-baryon clusters. Still we denote the number of nucleons clusterized in dibaryons on the periphery by the parameter ε_2. In the dense part of the nucleus, strong quark exchange forces make clusters out of quasi-free nucleons with high probability. To characterize the distribution of clusters the clusterization probability parameter ω was used.

If the number of nucleons involved in clusterization is $a = (1 - \varepsilon_1 - \varepsilon_2) \cdot A$, then the probability to find a cluster consisting of ν nucleons is defined by the distribution

$$P_\nu \propto C_\nu^a \cdot \omega^{\nu-1}, \qquad (24.44)$$

where C_ν^a is the corresponding binomial coefficient. The coefficient of proportionality can be found from the equation

$$a = b \cdot \sum_{\nu=1}^{a} \nu \cdot C_\nu^a \cdot \omega^{\nu-1} = b \cdot a \cdot (1 + \omega)^{a-1}. \qquad (24.45)$$

Thus, the number of clusters consisting of ν nucleons is

$$P_\nu = \frac{C_\nu^a \cdot \omega^{\nu-1}}{(1+\omega)^{a-1}}.$$

(24.46)

For clusters with an even number of nucleons we used only isotopically symmetric configurations ($\nu = 2n$, n protons and n neutrons) and for odd clusters ($\nu = 2n + 1$) we used only two configurations: n neutrons with $n + 1$ protons and $n + 1$ neutrons with n protons. This restriction, which we call "isotopic focusing", can be considered an empirical rule of the CHIPS model which helps to describe data. It is applied in the case of nuclear clusterization (isotopically symmetric clusters) and in the case of hadronization in nuclear matter. In the hadronization process the quasmon is shifted from the isotopic symmetric state (e.g., by capturing a negative pion) and transfers excess charge to the outgoing nuclear cluster. This tendency is symmetric with respect to the quasmon and the parent cluster.

The temperature parameter used to calculate the number of quark-partons in a quasmon (see equation 24.22) was chosen to be $T = 180$ MeV, which is the same as in Section 24.4.

CHIPS is mostly a model of fragmentation, conserving energy, momentum, and charge. But to compare it with experimental data one needs to model also the first interaction of the projectile with the nucleus. For proton-antiproton annihilation this was easy, as we assumed that in the interaction at rest, a proton and antiproton always create a quasmon. In the case of pion capture the pion can be captured by different clusters. We assumed that the probability of capture is proportional to the number of nucleons in a cluster. After the capture the quasmon is formed, and the CHIPS generator produces fragments consecutively and recursively, choosing at each step the quark-parton four-momentum k, the type of parent and outgoing fragment, and the four-momentum of the exchange quark-parton q, to produce a final state hadron and the new quasmon with less energy.

In the CHIPS model we consider this process as a chaotic process with large number of degrees of freedom and do not take into account any final state interactions of outgoing hadrons. Nevertheless, when the excitation energy dissipates, and in some step the quasmon mass drops below the mass shell, the quark-parton mechanism of hadronization fails. To model the event exclusively, it becomes necessary to continue fragmentation at the hadron level. Such a fragmentation process is known as nuclear evaporation. It is modeled using the non-relativistic phase space approach. In the non-relativistic case the phase space of nucleons can be integrated as well as in the ultra-relativistic case of quark-partons.

392

The general formula for the non-relativistic phase space can be found starting with the phase space for two particles $\tilde{\Phi}_2$. It is proportional to the center-of-mass momentum:

$$\tilde{\Phi}_2(W_2) \propto \sqrt{W_2}, \tag{24.47}$$

where W_2 is a total kinetic energy of the two non-relativistic particles. If the phase space integral is known for $n-1$ hadrons then it is possible to calculate the phase space integral for n hadrons:

$$
\begin{aligned}
\tilde{\Phi}_n(W_n) &= \int \tilde{\Phi}_{n-1}(W_{n-1}) \cdot \delta(W_n - W_{n-1} - E_{\text{kin}}) \\
&\times \sqrt{E_{\text{kin}}} dE_{\text{kin}} dW_{n-1}.
\end{aligned} \tag{24.48}
$$

Using (24.47) and (24.48) one can find that

$$\tilde{\Phi}_n(W_n) \propto W_n^{\frac{3}{2}n - \frac{5}{2}} \tag{24.49}$$

and the spectrum of hadrons, defined by the phase space of residual $n - 1$ nucleons, can be written as

$$\frac{dN}{\sqrt{E_{\text{kin}}} dE_{\text{kin}}} \propto \left(1 - \frac{E_{\text{kin}}}{W_n}\right)^{\frac{3}{2}n - 4}. \tag{24.50}$$

This spectrum can be randomized. The only problem is from which level one should measure the thermal kinetic energy when most nucleons in nuclei are filling nuclear levels with zero temperature. To model the evaporation process we used this unknown level as a parameter U of the evaporation process. Comparison with experimental data gives $U = 1.7$ MeV. Thus, the total kinetic energy of A nucleons is

$$W_A = U \cdot A + E_{\text{ex}}, \tag{24.51}$$

where E_{ex} is the excitation energy of the nucleus.

To be radiated, the nucleon should overcome the threshold

$$U_{\text{thresh}} = U + U_{\text{bind}} + E_{CB}, \tag{24.52}$$

where U_{bind} is the separation energy of the nucleon, and E_{CB} is the Coulomb barrier energy which is non-zero only for positive particles and can be calculated using formula (24.28).

From several experimental investigations of nuclear pion capture at rest, four published results have been selected here, which constitute, in our opinion, a representative data set covering a wide range of target nuclei, types

of produced hadrons and nuclear fragments, and their energy range. In the first publication [47] the spectra of charged fragments (protons, deuterons, tritons, ^{3}He, ^{4}He) in pion capture were measured on 17 nuclei within one experimental setup. To verify the spectra we compared them for a carbon target with detailed measurements of the spectra of charged fragments given in Ref. [48]. In addition, we took ^{6}Li spectra for a carbon target from the same paper.

The neutron spectra were added from Ref. [49] and Ref. [50]. We present data and Monte Carlo distributions as the invariant phase space function $f = \frac{d\sigma}{pdE}$ depending on the variable $k = \frac{p+E_{\mathrm{kin}}}{2}$ as defined in equation (24.21).

Spectra on ^{9}Be, ^{12}C, ^{28}Si (^{27}Al for secondary neutrons), ^{59}Co (^{64}Cu for secondary neutrons), and ^{181}Ta are shown in Figs. 24.8 through 24.12. The data are well-described, including the total energy spent in the reaction to yield the particular type of fragments.

The evaporation process for nucleons is also well-described. It is exponential in k, and looks especially impressive for Si/Al and Co/Cu data, where the Coulomb barrier is low, and one can see proton evaporation as a continuation of the evaporation spectra from secondary neutrons. This way the exponential behavior of the evaporation process can be followed over 3 orders of magnitude. Clearly seen is the transition region at $k \approx 90$ MeV (kinetic energy $15 - 20$ MeV) between the quark-level hadronization process and the hadron-level evaporation process. For light target nuclei the evaporation process becomes much less prominent.

The ^{6}Li spectrum on a carbon target exhibits an interesting regularity when plotted as a function of k: it practically coincides with the spectrum of ^{4}He fragments, and shows exponential behavior in a wide range of k, corresponding to a few orders of magnitude in the invariant cross section. To keep the figure readable, the ^{6}Li spectrum generated by CHIPS was not plotted. It coincides with the ^{4}He spectrum at $k > 200$ MeV, and underestimates lithium emission at lower energies, similarly to the ^{3}He and tritium data.

Between the region where hadron-level processes dominate and the kinematic limit, all hadronic spectrum slopes become similar when plotted as a function of k. In addition to this general behavior there is the effect of strong proton-neutron splitting. For protons and neutrons it reaches almost an order of magnitude. To model such splitting in the CHIPS generator, the mechanism of "isotopic focusing" was used, which locally transfers the negative charge from the pion to the first radiated nuclear fragment.

Thus, the model qualitatively describes all typical features of the pion capture process. The question is what can be extracted from the experimental

Table 24.1: Clusterization parameters

	^{9}Be	^{12}C	^{28}Si	^{59}Co	^{181}Ta
ε_1	0.45	0.40	0.35	0.33	0.33
ε_2	0.15	0.15	0.05	0.03	0.02
ω	5.00	5.00	5.00	5.00	5.00

data with this tool. The clusterization parameters are listed in Table 24.1. No formal fitting procedure has been performed. A balanced qualitative agreement with all data was used to tune the parameters. The difference between the $\frac{\varepsilon_2}{\varepsilon_1}$ ratio and the parameter ω (which is the same for all nuclei) is an indication that there is a phase transition between the gas phase and the liquid phase of the nucleus. The large value of the parameter ω, determining the average size of a nuclear cluster, is critical in describing the model spectra at large k, where the fragment spectra approach the kinematic limits.

Using the same parameters of clusterization, the γ absorption data [51] on Al and Ca nuclei were compared in Fig. 24.13) to the CHIPS results. One can see that the spectra of secondary protons and deuterons are qualitatively described by the CHIPS model.

The CHIPS model covers a wide spectrum of hadronic reactions with a large number of degrees of freedom. In the case of nuclear reactions the CHIPS generator helps to understand phenomena such as the order-of-magnitude splitting of neutron and proton spectra, the high yield of energetic nuclear fragments, and the emission of nucleons which kinematically can be produced only if seven or more nucleons are involved in the reaction.

The CHIPS generator allows the extraction of collective parameters of a nucleus such as clusterization. The qualitative conclusion based on the fit to the experimental data is that most of the nucleons are clusterized, at least in heavy nuclei. The nuclear clusters can be considered as drops of a liquid nuclear phase. The quark exchange makes the phase space of quark-partons of each cluster common, stretching the kinematic limits for particle production.

The hypothetical quark exchange process is important not only for nuclear clusterization, but also for the nuclear hadronization process. The quark exchange between the excited cluster (quasmon) and a neighboring nuclear cluster, even at low excitation level, operates with quark-partons at energies comparable with the nucleon mass. As a result it easily reaches the kinematic limits of the reaction, revealing the multi-nucleon nature of the process.

Up to now the most under-developed part of the model has been the initial interaction between projectile and target. That is why we started with
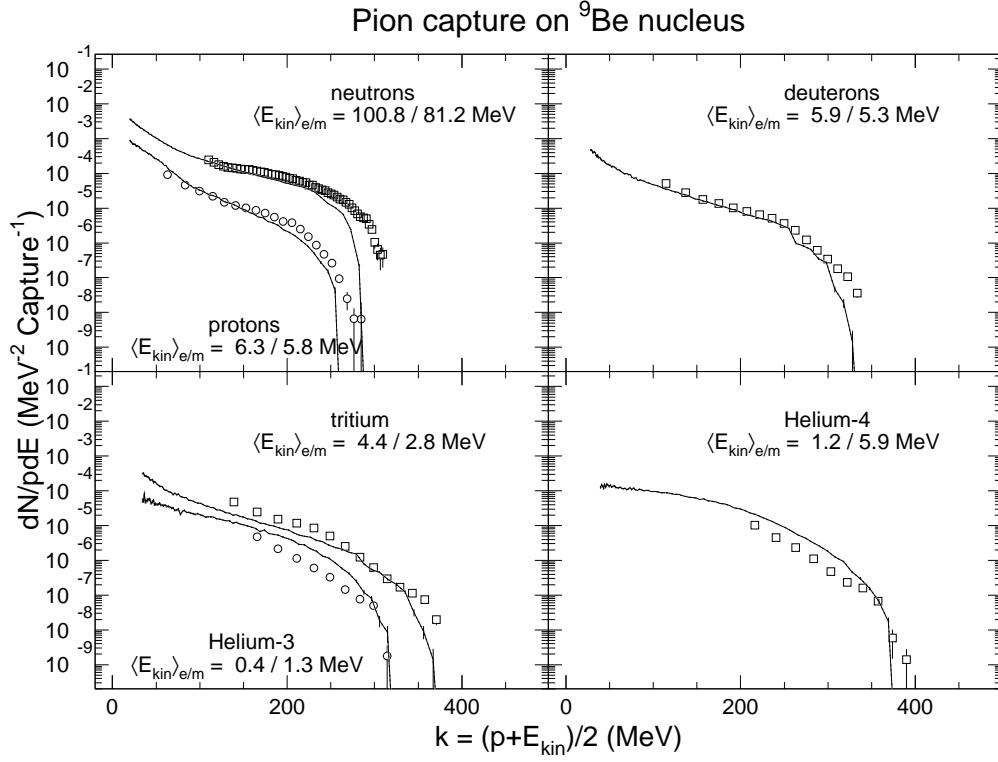
Figure 24.8: Comparison of the CHIPS model results with experimental data on proton, neutron, and nuclear fragment production in the capture of negative pions on ^{9}Be. Proton [47] and neutron [49] experimental spectra are shown in the upper left panel by open circles and open squares, respectively. The model calculations are shown by the two corresponding solid lines. The same arrangement is used to present ^{3}He [47] and tritium [47] spectra in the lower left panel. Deuterium [47] and ^{4}He [47] spectra are shown in the right panels of the figure by open squares and lines (CHIPS model). The average kinetic energy carried away by each nuclear fragment is shown in the panels by the two numbers: first is the average calculated using the experimental data shown; second is the model result.

Figure 24.9: Same as in Figure 24.8, for pion capture on ^{12}C. The experimental neutron spectrum is taken from [50]. In addition, the detailed data on charged particle production, including the ^{6}Li spectrum, taken from Ref. [48], are superimposed on the plots as a series of dots.

Figure 24.10: Same as in Figure 24.8, for pion capture on ^{28}Si nucleus. The experimental neutron spectrum is taken from [50], for the reaction on ^{27}Al.
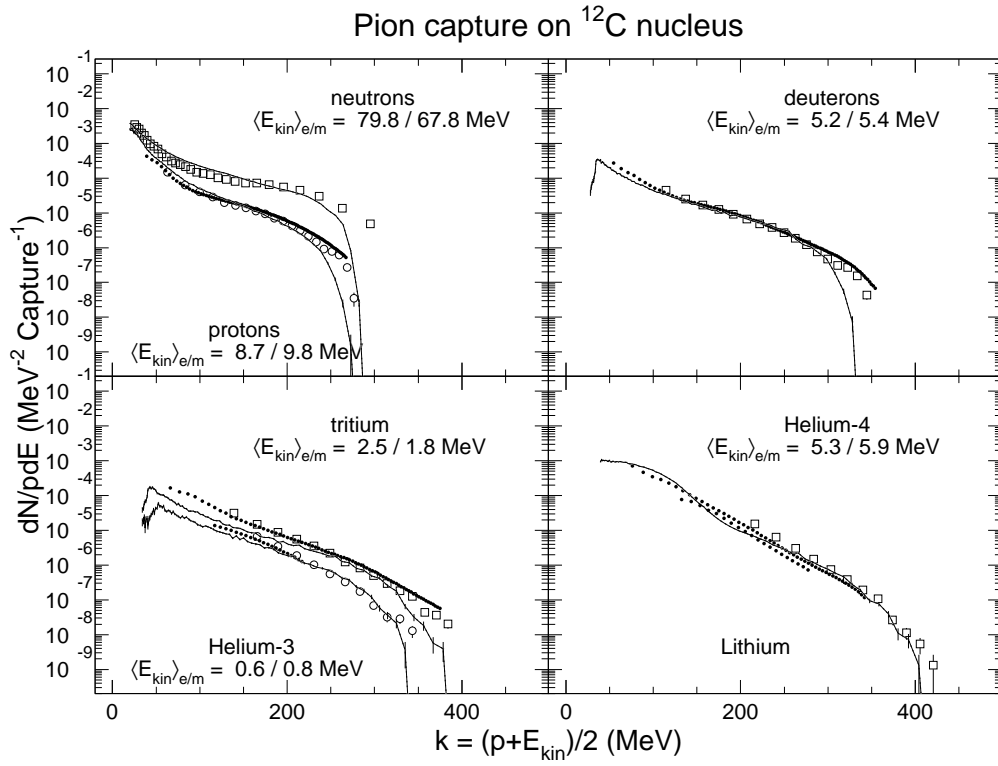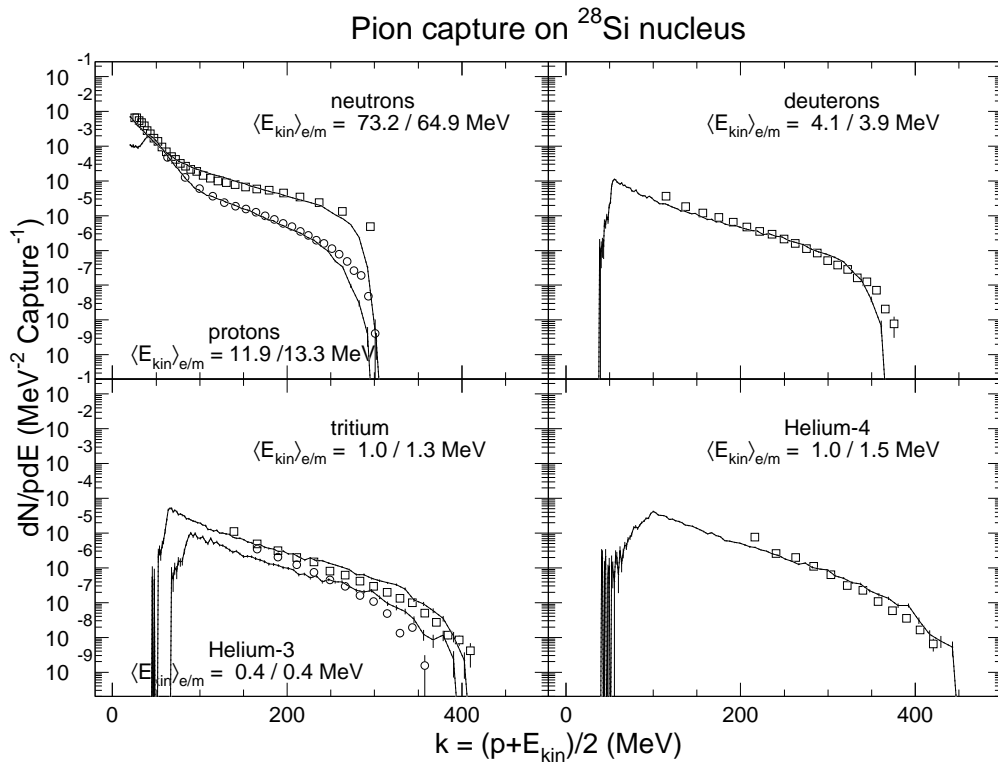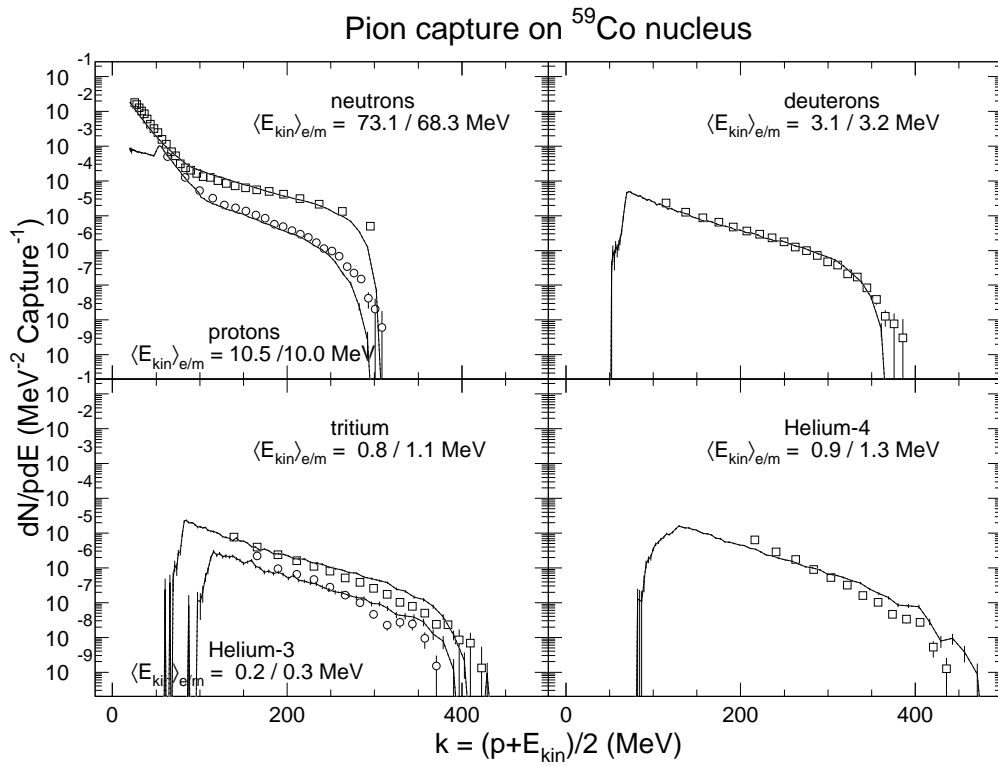
Figure 24.11: Same as in Figure 24.8, for pion capture on ^{59}Co. The experimental neutron spectrum is taken from [50], for the reaction on ^{64}Cu.
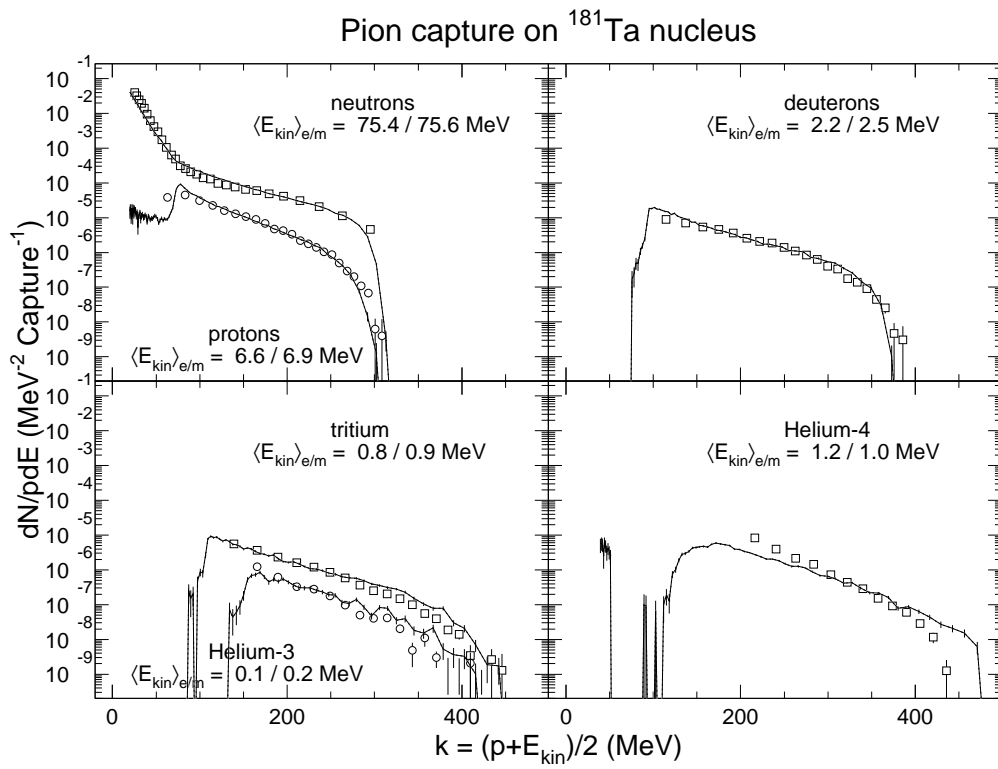
Figure 24.12: Same as in Figure 24.8, for pion capture on [181]Ta. The experimental neutron spectrum is taken from [50].
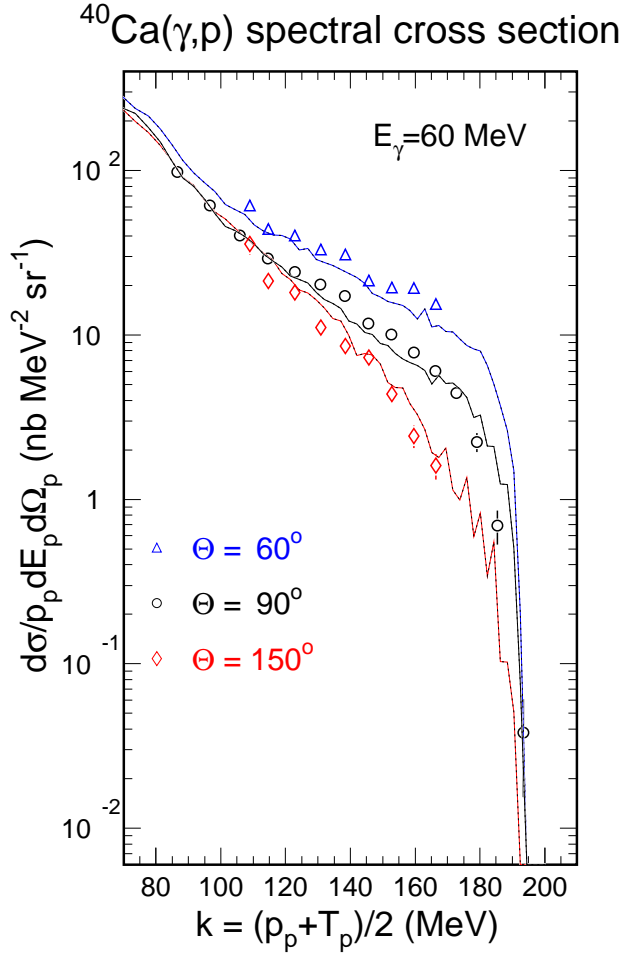
Figure 24.13: Comparison of CHIPS model with experimental data [51] on proton and deuteron production at 90° in photonuclear reactions on ^{27}Al and ^{40}Ca at 59 – 65 MeV. Open circles and solid squares represent the experimental proton and deuteron spectra, respectively. Solid and dashed lines show the results of the corresponding CHIPS model calculation. Statistical errors in the CHIPS results are not shown and can be judged by the point-to-point variations in the lines. The comparison is absolute, using the values of total photonuclear cross section 3.6 mb for Al and 5.4 mb for Ca, as given in Ref. [52].

proton-antiproton annihilation and pion capture on nuclei at rest, because the interaction cross section is not involved. The further development of the model will require a better understanding of the mechanism of the first interaction. However, we believe that even the basic model will be useful in the understanding the nature of multi-hadron fragmentation. Because of the model's features, it is a suitable candidate for the hadron production and hadron cascade parts of the newly developed event generation and detector simulation Monte Carlo computer codes.

24.6 Modeling of real and virtual photon interactions with nuclei below pion production threshold

In the example of the photonuclear reaction discussed in the Appendix D, namely the description of 90° proton and deuteron spectra in $A(\gamma, X)$ reactions at $E_\gamma = 59 - 65$ MeV, the assumption on the initial Quasmon excitation mechanism was the same. The description of the 90° data was satisfactory, but the generated data showed very little angular dependence, because the velocity of the quasmons produced in the initial state was small, and the fragmentation process was almost isotropic. Experimentally, the angular dependence of secondary protons in photo-nuclear reactions is quite strong even at low energies (see, for example, Ref. [53]). This is a challenging experimental fact which is difficult to explain in any model. It's enough to say that if the angular dependence of secondary protons in the γ^{40}Ca interaction at 60 MeV is analyzed in terms of relativistic boost, then the velocity of the source should reach $0.33c$; hence the mass of the source should be less than pion mass. The main point of this discussion is to show that the quark-exchange mechanism used in the CHIPS model can not only model the clusterization of nucleons in nuclei and hadronization of intranuclear excitations into nuclear fragments, but it can also model complicated mechanisms of the interaction of photons and hadrons in nuclear matter.

In Ref. Appendix D a quark-exchange diagram was defined which helps to keep track of the kinematics of the quark-exchange process (see Fig. 1 in Apendix D). To apply the same diagram to the first interaction of a photon with a nucleus, it is necessary to assume that the quark-exchange process takes place in nuclei continuously, even without any external interaction. Nucleons with high momenta do not leave the nucleus because of the lack of excess energy. The hypothesis of the CHIPS model is that the quark-exchange forces between nucleons [26] continuously create clusters in normal

nuclei. Since a low-energy photon (below the pion production threshold) cannot be absorbed by a free nucleon, other absorption mechanisms involving more than one nucleon have to be used.

The simplest scenario is photon absorption by a quark-parton in the nucleon. At low energies and in vacuum this does not work because there is no corresponding excited baryonic state. But in nuclear matter it is possible to exchange this quark with a neighboring nucleon or a nuclear cluster. The diagram for the process is shown in Fig. 24.14. In this case the photon is absorbed by a quark-parton from the parent cluster PC$_1$, and then the secondary nucleon or cluster PC$_2$ absorbs the entire momentum of the quark and photon. The exchange quark-parton q restores the balance of color, producing the final-state hadron F and the residual Quasmon RQ. The process looks like a knockout of a quasi-free nucleon or cluster out of the nucleus. It should be emphasized that in this scenario the CHIPS event generator produces not only "quasi-free" nucleons but "quasi-free" fragments as well. The yield of these quasi-free nucleons or fragments is concentrated in the forward direction.

The second scenario which provides for an angular dependence is the absorption of the photon by a colored fragment (CF$_2$ in Fig. 24.15). In this scenario, both the primary quark-parton with momentum k and the photon with momentum q_γ are absorbed by a parent cluster (PC$_2$ in Fig. 24.15), and the recoil quark-parton with momentum q cannot fully compensate the momentum $k + q_\gamma$. As a result the radiation of the secondary fragment in the forward direction becomes more probable.

In both cases the angular dependence is defined by the first act of hadronization. Further fragmentation of the residual quasmon is almost isotropic.

It was shown in Section 24.4 that the energy spectrum of quark partons in a quasmon can be calculated as

$$\frac{dW}{k^* dk^*} \propto \left(1 - \frac{2k^*}{M}\right)^{N-3}, \qquad (24.53)$$

where k^* is the energy of the primary quark-parton in the center-of-mass system of the quasmon, M is the mass of the quasmon. The number N of quark-partons in the quasmon can be calculated from the equation

$$< M^2 >= 4 \cdot N \cdot (N - 1) \cdot T^2. \qquad (24.54)$$

Here T is the temperature of the system.

In the first scenario of the γA interaction (Fig. 24.14), because both interacting particles are massless, we assumed that the cross section for the interaction of a photon with a particular quark-parton is proportional to the
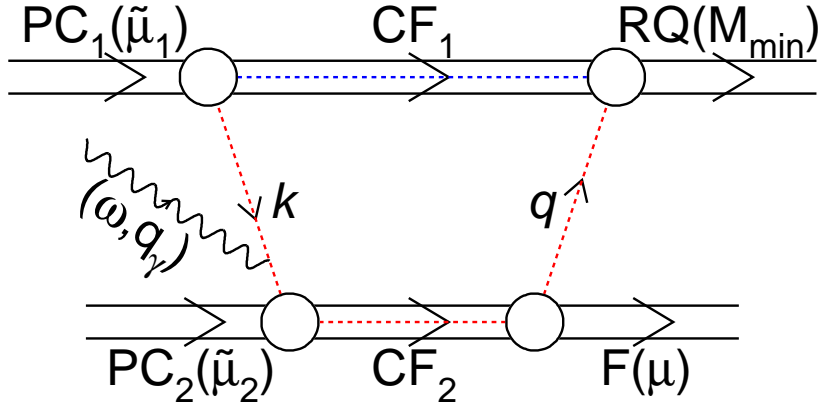
Figure 24.14: Diagram of photon absorption in the quark exchange mechanism. $PC_{1,2}$ stand for parent clusters with bound masses $\tilde{\mu}_{1,2}$, participating in the quark-exchange. $CF_{1,2}$ stand for the colored nuclear fragments in the process of quark exchange. $F(\mu)$ denotes the outgoing hadron with mass μ in the final state. RQ is the residual Quasmon which carries the rest of the excitation energy and momentum. M_{min} characterizes its minimum mass defined by its quark content. Dashed lines indicate colored objects. The photon is absorbed by a quark-parton k from the parent cluster PC_1.
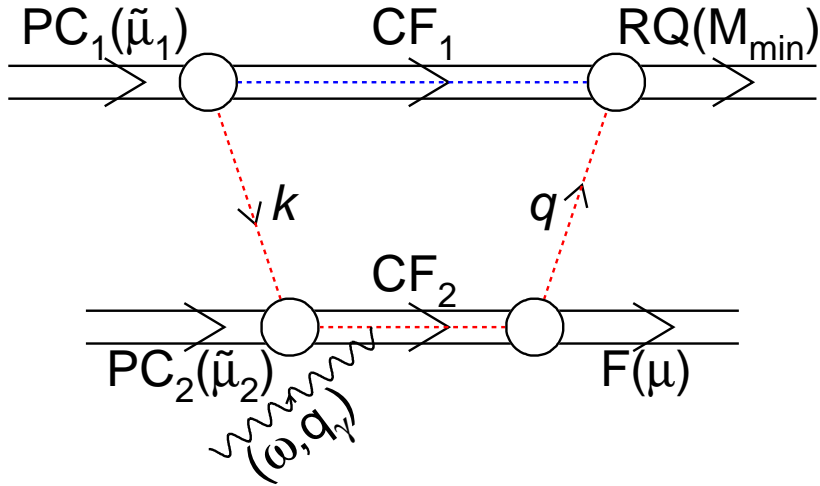

Figure 24.15: Diagram of photon absorption in the quark-exchange mechanism. The notation is the same as in Fig. 24.14. The photon is absorbed by the colored fragment CF_2.

charge of the quark-parton squared, and inversely proportional to the mass of the photon-parton system s, which can be calculated as

$$s = 2\omega k(1 - \cos(\theta_k)). \tag{24.55}$$

Here ω is the energy of the photon, and k is the energy of the quark-parton in the laboratory system (LS):

$$k = k^* \cdot \frac{E_N + p_N \cdot \cos(\theta_k)}{M_N}. \tag{24.56}$$

For a virtual photon, equation (24.55) can be written as

$$s = 2k(\omega - q_\gamma \cdot \cos(\theta_k)), \tag{24.57}$$

where q_γ is the momentum of the virtual photon. In both cases equation (24.53) transforms into

$$\frac{dW}{dk^*} \propto \left(1 - \frac{2k^*}{M}\right)^{N-3}, \tag{24.58}$$

and the angular distribution in $\cos(\theta_k)$ converges to a δ-function. In the case of a real photon $\cos(\theta_k) = 1$, and in the case of a virtual photon $\cos(\theta_k) = \frac{\omega}{q_\gamma}$.

In the second scenario for the photon interaction (Fig. 24.15) we assumed that both the photon and the primary quark-parton, randomized according to Eq. (24.53), enter the parent cluster PC_2, and after that the normal procedure of quark exchange continues, in which the recoiling quark-parton q returns to the first cluster.

An additional parameter in the model is the relative contribution of both mechanisms. As a first approximation we assumed equal probability, but in the future, when more detailed data are obtained, this parameter can be adjusted.

We begin the comparison with the data on proton production in the $^{40}\text{Ca}(\gamma, X)$ reaction at 90° and 59–65 MeV [51], and at 60° and 150° and 60 MeV [54]. We analyzed these data together to compare the angular dependence generated by CHIPS with experimental data. The data are presented as a function of the invariant inclusive cross section $f = \frac{d\sigma}{p_p dE_p}$ depending on the variable $k = \frac{T_p + p_p}{2}$, where T_p and p_p are the kinetic energy and momentum of the secondary proton. As one can see from Fig. 24.16, the angular dependence of the proton yield in photoproduction on ^{40}Ca at 60 MeV is reproduced quite well by the CHIPS event generator.

The second set of measurements that we use for the benchmark comparison deals with the secondary proton yields in $^{12}\text{C}(\gamma, X)$ reactions at 123 and
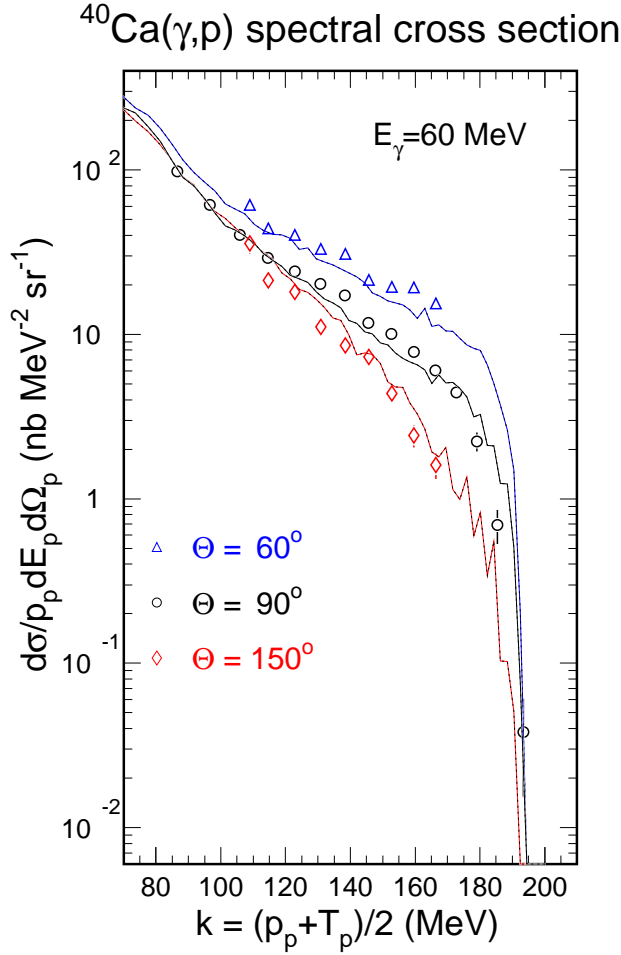
Figure 24.16: Comparison of the CHIPS model results (lines) with the experimental data [51] on proton spectra at 90° in the photonuclear reactions on ^{40}Ca at 59–65 MeV (open circles), and proton spectra at 60° (triangles) and 150° (diamonds). Statistical errors in the CHIPS results are not shown but can be judged by the point-to-point variations in the lines. The comparison is absolute, using the value of the total photonuclear cross section of 5.4 mb for Ca, as given in Ref. [52].
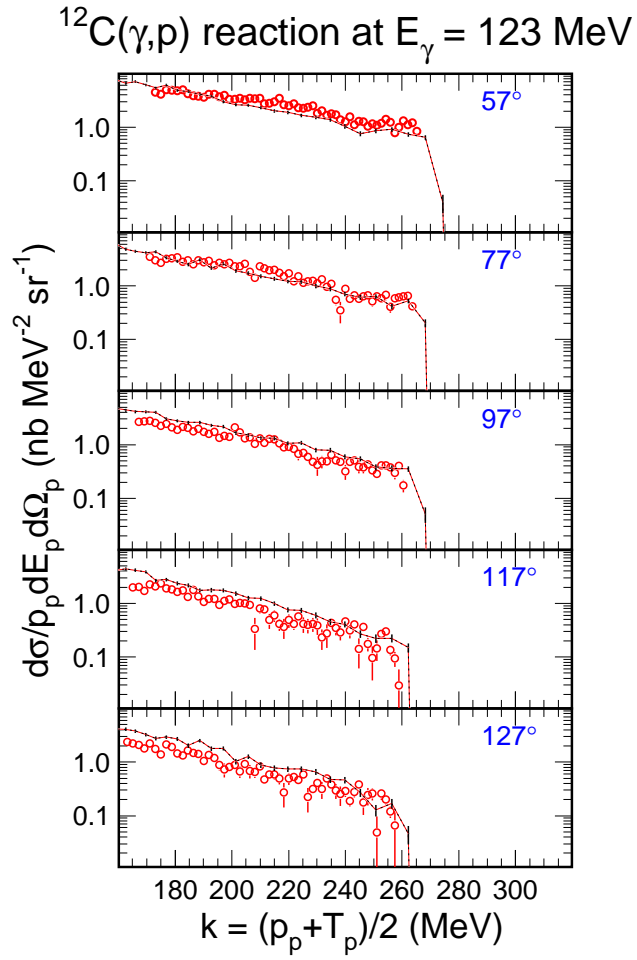
Figure 24.17: Comparison of the CHIPS model results (lines) with the experimental data [55] on proton spectra at 57°, 77°, 97°, 117°, and 127° in the photonuclear reactions on ^{12}C at 123 MeV (open circles). The value of the total photonuclear cross section was set to 1.8 mb.
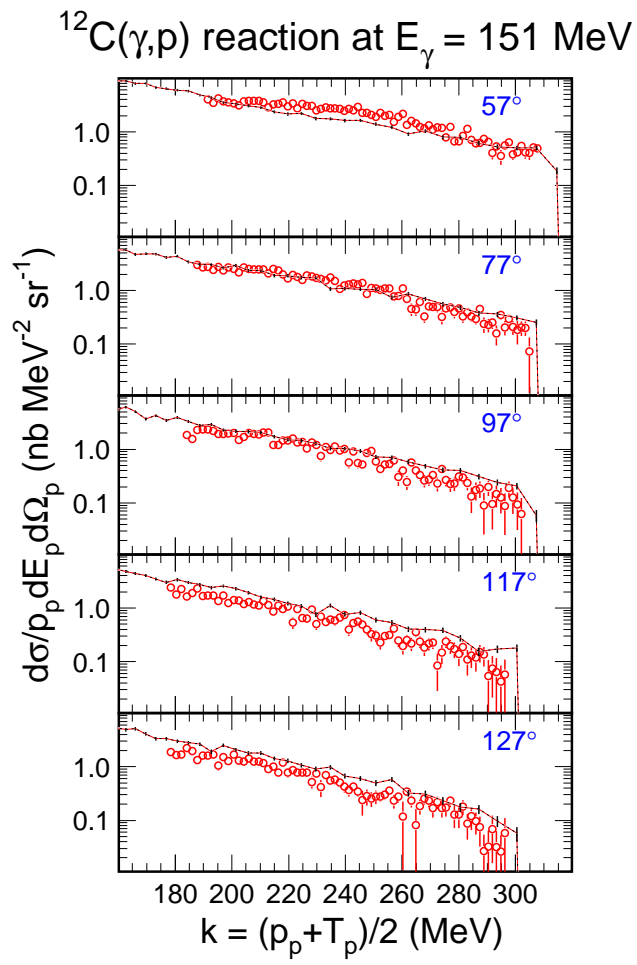
Figure 24.18: Same as in Fig. 24.17, for the photon energy 151 MeV.
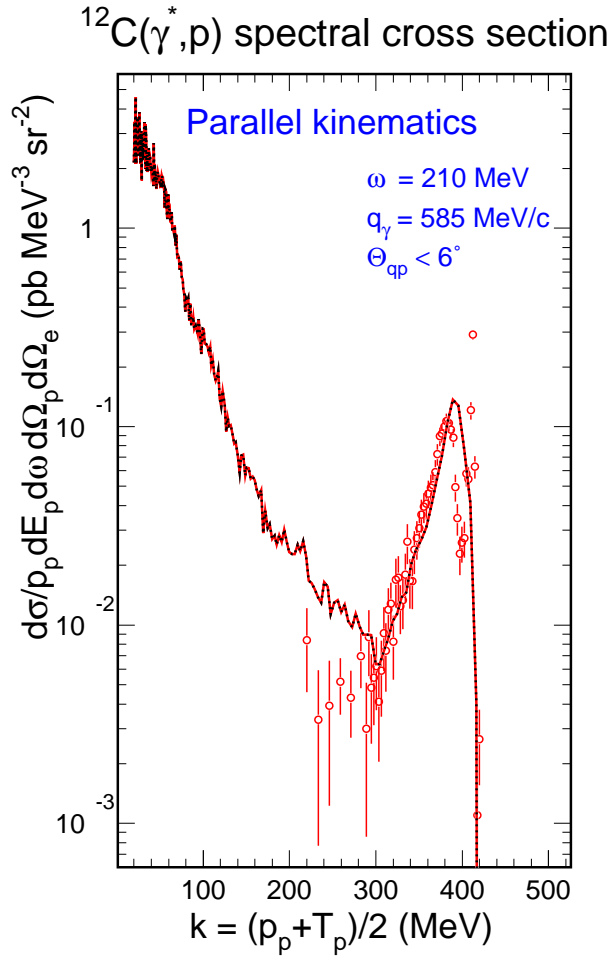
Figure 24.19: Comparison of the CHIPS model results (line) with the experimental data [56] (open circles) on the proton spectrum measured in parallel kinematics in the ^{12}C(e,e$'$p) reaction at an energy transfer equal to 210 MeV and momentum transfer equal to 585 MeV/c. Statistical errors in the CHIPS result are not shown but can be judged by the point-to-point variations in the line. The relative normalization is arbitrary.

151 MeV [55], which is still below the pion production threshold on a free nucleon. Inclusive spectra of protons have been measured in γ^{12}C reactions at 57°, 77°, 97°, 117°, and 127°. Originally, these data were presented as a function of the missing energy. We present the data in Figs. 24.17 and 24.18 together with CHIPS calculations in the form of the invariant inclusive cross section dependent on k. All parameters of the model such as temperature T and parameters of clusterization for the particular nucleus were the same as in Appendix D, where pion capture spectra were fitted. The agreement between the experimental data and the CHIPS model results is quite remarkable. Both data and calculations show significant strength in the proton yield cross section up to the kinematic limits of the reaction. The angular distribution in the model is not as prominent as in the experimental data, but agrees well qualitatively.

Using the same parameters, we applied the CHIPS event generator to the ^{12}C(e,e′p) reaction measured in Ref.[56]. The proton spectra were measured in parallel kinematics in the interaction of virtual photons with energy $\omega = 210$ MeV and momentum $q_\gamma = 585$ MeV/c. To account for the experimental conditions in the CHIPS event generator, we have selected protons generated in the forward direction with respect to the direction of the virtual photon, with the relative angle $\Theta_{qp} < 6°$. The CHIPS generated distribution and the experimental data are shown in Fig. 24.19 in the form of the invariant inclusive cross section as a function of k. The CHIPS event generator works only with ground states of nuclei so we did not expect any narrow peaks for $^1p_{3/2}$-shell knockout or for other shells. Nevertheless we found that the CHIPS event generator fills in the so-called "$^1s_{1/2}$-shell knockout" region, which is usually artificially smeared by a Lorentzian [57]. In the regular fragmentation scenario the spectrum of protons below $k = 300$ MeV is normal; it falls down to the kinematic limit. The additional yield at $k > 300$ MeV is a reflection of the specific first act of hadronization with the quark exchange kinematics. The slope increase with momentum is approximated well by the model, but it is obvious that the yield close to the kinematic limit of the $2 \to 2$ reaction can only be described in detail if the excited states of the residual nucleus are taken into account.

The angular dependence of the proton yield in low-energy photo-nuclear reactions is described in the CHIPS model and event generator. The most important assumption in the description is the hypothesis of a direct interaction of the photon with an asymptotically free quark in the nucleus, even at low energies. This means that asymptotic freedom of QCD and dispersion sum rules [46] can in some way be generalized for low energies. The knockout of a proton from a nuclear shell or the homogeneous distributions of nuclear evaporation cannot explain significant angular dependences at low energies.

The same mechanism appears to be capable of modeling proton yields in such reactions as the ^{16}C(e,e$'$p) reaction measured at MIT Bates [56], where it was shown that the region of missing energy above 50 MeV reflects "two-or-more-particle knockout" (or the "continuum" in terms of the shell model). The CHIPS model may help to understand and model such phenomena.

24.7 Chiral invariant phase-space decay in high energy hadron nuclear reactions

Chiral invariant phase-space decay can be used to de-excite an excited hadronic system. This possibility can be exploited to replace the intra-nuclear cascading after a high energy primary interaction takes place. The basic assumption in this is that the energy loss of the high energy hadron in nuclear matter is approximately constant per unit path length (about 1 GeV/fm). This energy is extracted from the soft part of the particle spectrum of the primary interaction, and from particles with formation times that place them within the nuclear boundaries.

Several approaches of transfering this energy into quasmons were studied, and comparisons with energy spectra of particles emitted in the backward hemisphere were made for a range of materials. Best results were achieved with a model that creates one quasmon per particle absorbed in the nucleus.

24.8 Neutrino-nuclear interactions

The simulation of DIS reactions includes reactions with high Q^2. The first approximation of the Q^2-dependent photonuclear cross-sections at high Q^2 was made in [11], where the modified photonuclear cross sections of virtual photons [34] were used. The structure functions of protons and deuterons have been approximated in CHIPS by the sum of non-perturbative multi-peripheral and non-perturbative direct interactions of virtual photons with hadronic partons:

$$F_2(x, Q^2) = [A(Q^2) \cdot x^{-\Delta(Q^2)} + B(Q^2) \cdot x] \cdot (1-x)^{N(Q^2)-2}, \qquad (24.59)$$

where $A(Q^2) = \bar{e}_S^2 \cdot D \cdot U$, $B(Q^2) = \bar{e}_V^2 \cdot (1-D) \cdot V$, $\bar{e}^2{}_{V(p)} = \frac{1}{3}$, $\bar{e}^2{}_{V(d)} = \frac{5}{18}$, $\bar{e}_S^2 = \frac{1}{3} - \frac{\frac{1}{3} - \frac{5}{18}}{1 + m_\phi^2/Q^2} + \frac{\frac{1}{3} - \frac{5}{18}}{1 + m_{J/\psi}^2/Q^2} - \frac{\frac{1}{3} - \frac{19}{63}}{1 + m_\Upsilon^2/Q^2}$, $N = 3 + \frac{0.5}{\alpha_s(Q^2)}$, $\alpha_s(Q^2) = \frac{4\pi}{\beta_0 ln(1 + \frac{Q^2}{\Lambda^2})}$, $\beta_0^{(n_f=3)} = 9$, $\Lambda = 200\ MeV$, $U = \frac{(3\ C(Q^2) + N - 3) \cdot \Gamma(N-\Delta)}{N \cdot \Gamma(N-1) \cdot \Gamma(1-\Delta)}$, $V = 3(N-1)$, $D(Q^2) = H \cdot S(Q^2) \left(1 - \frac{1}{2} S(Q^2) \frac{\bar{e}_V^2}{\bar{e}_S^2}\right)$, $S = \left(1 + \frac{m_\rho^2}{Q^2}\right)^{-\alpha_P(Q^2)}$, $\alpha_P = 1 + \Delta(Q^2)$,
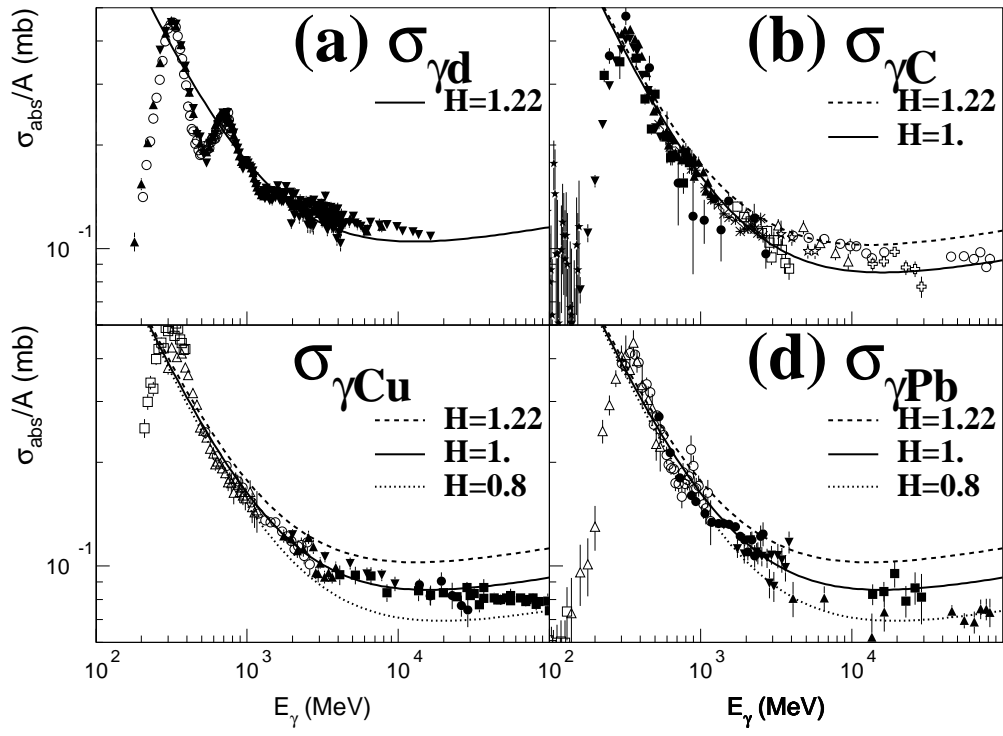
Figure 24.20: Fit of γA cross sections with different H values. Data are from [11].
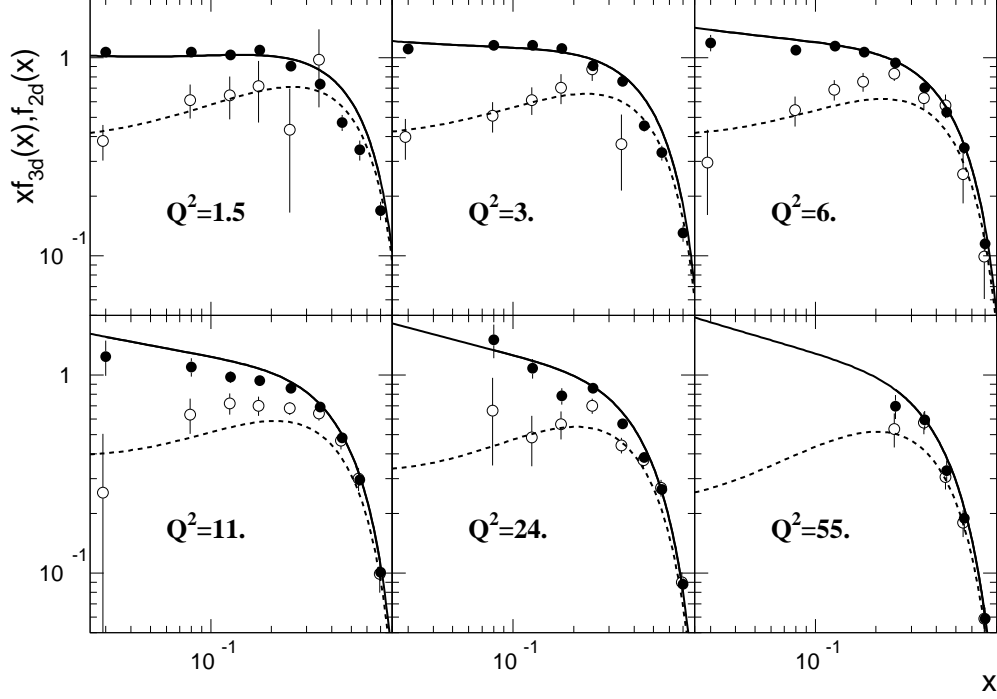
Figure 24.21: Fit of $f_{2d}(x, Q^2)$ (filled circles, solid lines) and $f_{3d}(x, Q^2)$ (open circles, dashed lines) structure functions measured by the WA25 experiment [35].

$\Delta = \frac{1+r}{12.5+2r}$, $r = \left(\frac{Q^2}{1.66}\right)^{1/2}$, $C = \frac{1+f}{g \cdot (1+f/.24)}$, $f = \left(\frac{Q^2}{0.08}\right)^2$, $g = 1 + \frac{Q^2}{21.6}$. The parton distributions are normalized to the unit total momentum fraction.

The photonuclear cross sections are calculated by the eikonal formula:

$$\sigma_\gamma^{tot} = \left[\frac{4\pi\alpha}{Q^2} F_2 \left(\frac{Q^2}{2M\nu}, Q^2 \right) \right]_{Q^2=0}^{\nu=E}, \qquad (24.60)$$

An example of the approximation is shown in Fig. 24.20. One can see that the hadronic resonances are "melted" in nuclear matter and the multi-peripheral part of the cross section (high energy) is shadowed.

The differential cross section of the (ν, μ) reaction was approximated as

$$\frac{y d^2 \sigma^{\nu,\bar{\nu}}}{dy dQ^2} = \frac{G_F^2 \cdot M_W^4}{4\pi \cdot (Q^2 + M_W^2)^2} \left[c_1(y) \cdot f_2(x, Q^2) \pm c_2(y) \cdot x f_3(x, Q^2) \right], \quad (24.61)$$

413
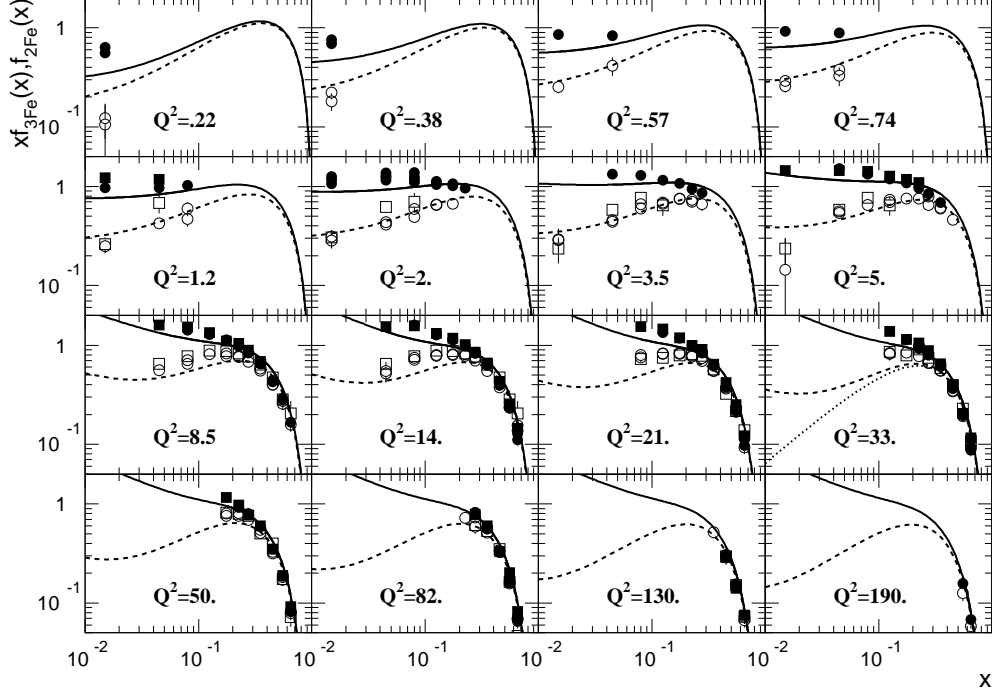
Figure 24.22: Fit of $f_{2Fe}(x, Q^2)$ (filled markers, solid lines) and $f_{3Fe}(x, Q^2)$ (open markers, dashed lines) structure functions measured by the CDHSW [36] (circles) and CCFR [37] (squares) experiments.

where $c_1(y) = 2 - 2y + \frac{y^2}{1+R}$, $R = \frac{\sigma_L}{\sigma_T}$, $c_2(y) = y(2 - y)$. As $e_V^{\bar{2}} = e_S^{\bar{2}} = 1$ in Eq.24.59, hence $f_2(x, Q^2) = \left[D \cdot U \cdot x^{-\Delta} + (1 - D) \cdot V \cdot x \right] \cdot (1 - x)^{N-2}$, $x f_3(x, Q^2) = \left[D \cdot U_{f3} \cdot x^{-\Delta} + (1 - D) \cdot V \cdot x \right] \cdot (1 - x)^{N-2}$, with $D = H \cdot S(Q^2) \cdot \left(1 - \frac{1}{2}S(Q^2) \right)$ and $U_{f3} = \frac{3 \cdot C(Q^2) \cdot \Gamma(N-\Delta)}{N \cdot \Gamma(N-1)\Gamma(1-\Delta)}$. The approximation is compared with data in Fig.24.21 for deuterium [35] and in Fig.24.22 for iron [36, 37]. It must be emphasized that the CHIPS parton distributions are the same as for electromagnetic reactions.

For the (ν, μ) amplitudes one can not apply the optical theorem, To calculate the total cross sections, it is therefore necessary to integrate the differential cross sections first over x and then over Q^2. For the (ν, μ) reactions the differential cross section can be integrated with good accuracy even for low energies because it does not have the $\frac{1}{Q^4}$ factor of the boson propagator. The quasi-elastic part of the total cross-section can be calculated for $W < m_N + m_\pi$. The total (ν, μ) cross-sections are shown in Fig.24.23(a,b).

414
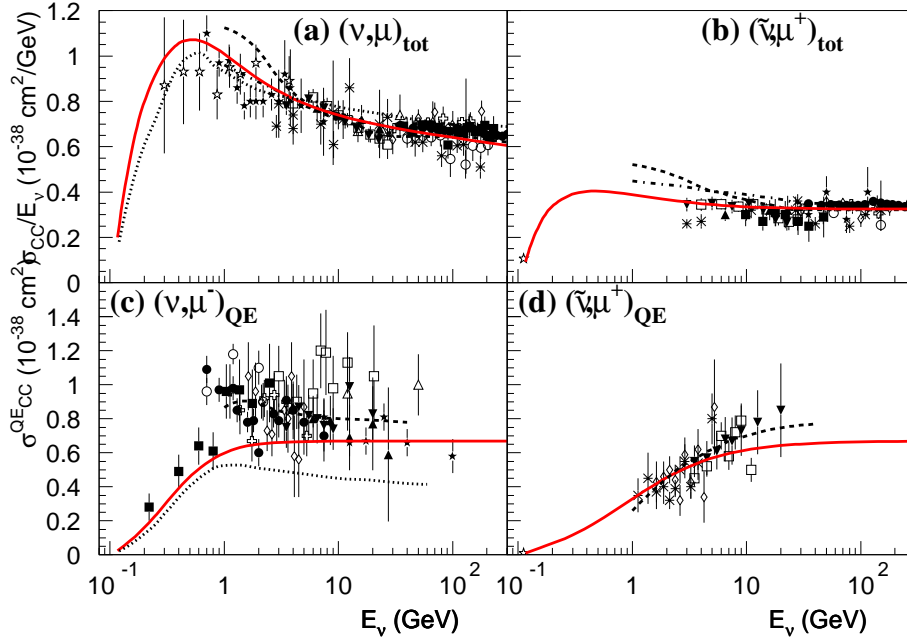
Figure 24.23: Fit of total (a,b) and quasi-elastic (c,d) cross-sections of (ν, μ) reactions (Geant4 database). The solid line is the CHIPS approximation (for other lines see text).

The dashed curve corresponds to the GRV [38] approximation of parton distributions and the dash-dotted curves correspond to the KMRS [39] approximation. Neither approximation fits low energies, because the perturbative calculations give parton distributions only for $Q^2 > 1$ GeV^2. In [40] an attempt was made to freeze the DIS parton distributions at $Q^2 = 1$ and to use them at low Q^2. The $W < 1.4$ GeV part of DIS was replaced by the quasi-elastic and one pion production contributions, calculated on the basis of the low energy models. The results of [40] are shown by the dotted lines. The nonperturbative CHIPS approximation (solid curves) fits both total and quasi-elastic cross sections even at low energies.

The quasi-elastic (ν, μ) cross sections are shown in Fig.24.23(c,d). The CHIPS approximation (solid line) is compared with calculations made in [40] (the dotted line) and the best fit of the $V - A$ theory was made in [41] (the dashed lines). One can see that CHIPS gives reasonable agreement.

The Q^2 spectra for each energy are known as an intermediate result of the calculation of total or quasi-elastic cross sections. For the quasi-elastic interactions ($W < m_N + m_\pi$) one can use $x = 1$ and simulate a binary reaction. In the final state the recoil nucleon has some probability of interacting with the nucleus. If $W > m_N + m_\pi$ the Q^2 value is randomized and therefore the Q^2 dependent coefficients (the number of partons in non-perturbative phase space N, the Pomeron intercept α_P, the fraction of the direct interactions, etc.) can be calculated. Then for fixed energy and Q^2 the neutrino interaction with quark-partons (directly or through the Pomeron ladder) can be randomized and the secondary parton distribution can be calculated. In vacuum or in nuclear matter the secondary partons are creating quasmons [2, 3] which decay to secondary hadrons.

24.9   Conclusion.

For users who would like to improve the interaction part of the CHIPS event generator for their own specific reactions, some advice concerning data presentation is useful.

It is a good idea to use a normalized invariant function $\rho(k)$

$$\rho = \frac{2E \cdot d^3\sigma}{\sigma_{tot} \cdot d^3p} \propto \frac{d\sigma}{\sigma_{tot} \cdot pdE},$$

where σ_{tot} is the total cross section of the reaction. The simple rule, then, is to divide the distribution over the hadron energy E by the momentum and by the reaction cross section. The argument k can be calculated for any outgoing hadron or fragment as

$$k = \frac{E + p - B \cdot m_N}{2},$$

which is the energy of the primary quark-parton. Because the spectrum of the quark-partons is universal for all the secondary hadrons or fragments, the distributions over this parameter have a similar shape for all the secondaries. They should differ only when the kinematic limits are approached or in the evaporation region. This feature is useful for any analysis of experimental data, independent of the CHIPS model.

Some concluding remarks should be made about the parameters of the model. The main parameter, the critical temperature T_c, should not be varied. A large set of data confirms the value **180 MeV** while from the mass spectrum of hadrons it can be found more precisely as 182 MeV. The clusterization parameter is **4.** which is just about $4\pi/3$. If the quark exchange

starts at the mean distance between baryons in the dense part of the nucleus, then the radius of the clusterization sphere is twice the "the radius of the space occupied by the baryon". It gives 8 for the parameter, but the space occupied by the baryon can not be spherical; only cubic subdivision of space is possible so the factor $\pi/6$ appears. But this is a rough estimate, so **4** or even **5** can be tried. The surface parameter fD varies slightly with A, growing from 0 to 0.04. For the present CHIPS version the recommended parameters for low energies are:

A	T	s/u	eta	noP	fN	fD	Cp	rM	sA
Li	180.	0.1	0.3	223	.4	.00	4.	1.0	0.4
Be	180.	0.1	0.3	223	.4	.00	4.	1.0	0.4
C	180.	0.1	0.3	223	.4	.00	4.	1.0	0.4
O	180.	0.1	0.3	223	.4	.02	4.	1.0	0.4
F	180.	0.1	0.3	223	.4	.03	4.	1.0	0.4
Al	180.	0.1	0.3	223	.4	.04	4.	1.0	0.4
Ca	180.	0.1	0.3	223	.4	.04	4.	1.0	0.4
Cu	180.	0.1	0.3	223	.4	.04	4.	1.0	0.4
Ta	180.	0.1	0.3	223	.4	.04	4.	1.0	0.4
U	180.	0.1	0.3	223	.4	.04	4.	1.0	0.4

The vacuum hadronization weight parameter can be bigger for light nuclei and smaller for heavy nuclei, but 1.0 is a good guess. The s/u parameter is not yet tuned, as it demands strange particle production data. A guess is that if there are as many $u\bar{u}$ and $d\bar{d}$ pairs in the reaction as in the $p\bar{p}$ interaction, the parameter can be 0.1. In other cases it is closer to 0.3 as in other event generators. But it is bestnot to touch any parameters for the first experience with the CHIPS event generator. Only the incident momentum, the PDG code of the projectile, and the CHIPS style PDG code of the target need be changed.

24.10 Status of this document

02.12.05 neutrino interactions section and figures added by M.V. Kossov
26.04.03 first four sections re-written by D.H. Wright
01.01.01 created by M.V. Kossov and H.P. Wellisch

Bibliography

[1] B. Andersson, G. Gustafson, G. Ingelman, T. Sjöstrand, Phys. Rep. **97** (1983) 31

[2] P. V. Degtyarenko, M. V. Kossov, and H.P. Wellisch, Chiral invariant phase space event generator, I. Nucleon-antinucleon annihilation at rest, Eur. Phys. J. A 8 (2000) 217.

[3] P. V. Degtyarenko, M. V. Kossov, and H. P. Wellisch, Chiral invariant phase space event generator, II.Nuclear pion capture at rest, Eur. Phys. J. A 9 (2000) 411.

[4] P. V. Degtyarenko, M. V. Kossov, and H. P. Wellisch, Chiral invariant phase space event generator, III Photonuclear reactions below $\Delta(3,3)$ excitation, Eur. Phys. J. A 9, (2000) 421.

[5] M. V. Kossov, Chiral invariant phase space model, I Masses of hadrons, Eur. Phys. J. A 14 (2002) 265.

[6] C.A.Z. Vasconcellos et al., Eur. Phys. J. C **4** (1998) 115; G.A. Miller, A.W. Thomas, S. Theberge, Phys. Lett. B **91** (1980) 192; C.E. de Tar, Phys. Rev. D **24** (1981) 752; M.A.B. Bég, G.T. Garvey, Comments Nucl. Part. Phys. **18** (1988) 1

[7] F. James, *Monte Carlo Phase Space*, CERN 68-15 (1968)

[8] K.G. Wilson, Proc. Fourteenth Scottish Universities Summer School in Physics (1973), eds R. L. Crawford, R. Jennings (Academic Press, New York, 1974)

[9] Monte Carlo particle numbering scheme, in: Particle Data Group, *Review of Particle Physics*, Eur. Phys. J. C **3** (1998) 180

[10] R. Hagedorn, Nuovo Cimento Suppl. **3** (1965) 147

[11] M. V. Kossov, Approximation of photonuclear interaction cross-sections, Eur. Phys. J. A 14 (2002) 377.

[12] S. Giani et al., Geant4: Object Oriented Toolkit for Simulation in HEP, LCB status report CERN/LHCC/98-44, November 1998.

[13] J. P. Wellisch, On hadronic models in GEANT4, Program and Book of Abstracts.International Conference on Advanced Monte Carlo for Radiation Physics, Particle Transport Simulation and Applications, 23-26 October 2000, IST,Lisbon, Portugal, p. 330.

[14] Yu.L. Dokshitzer, V.S. Fadin and V.A. Khoze, Phys. Lett. **115B** (1982) 242L

[15] T. Sjöstrand, Comp. Phys. Comm. **92** (1994) 74

[16] S. Ocubo, Phys. Lett. **5** (1963) 165; G. Zweig, CERN Preprint 8419/TH-412 (1964); I. Iizuka, Progr. Theor. Phys. Suppl. **37** (1966) 21

[17] V.E. Markushin, M.P. Locher, Eur. Phys. J. A **1** (1998) 91

[18] J. Sedlak and V. Simak, Sov. J. Part. Nucl. **19** (1988) 191

[19] C. Amsler, Rev.Mod.Phys. **70** (1998) 1293; C. Amsler and F. Myher, Annu. Rev. Nucl. Part. Sci. **41** (1991) 219

[20] B. Andersson, G. Gustafson, T. Sjöstrand, Nucl. Phys. B **197**(1982) 45; B. Andersson, G. Gustafson, T. Sjöstrand, Physica Scripta **32** (1985) 574

[21] P. Gregory et al., Nucl. Phys. B **102** (1976) 189

[22] M.V. Kossov and L.M. Voronina, Preprint ITEP 165-84, Moscow (1984)

[23] V.I. Efremenko et al., Phys. Rev. C **22** (1980) 700.

[24] S.V Boyarinov et al., Phys. At. Nucl. **56** (1993) 72.

[25] P.V. Degtyarenko et al., Phys. Rev. C **50** (1994) R541

[26] K. Maltman and N. Isgur, Phys. Rev. D **29** (1984) 952.

[27] K. Maltman and N. Isgur, Phys. Rev. D **34** (1986) 1372.

[28] P. Hoodbhoy and R. J. Jaffe, Phys. Rev. D **35** (1987) 113.

[29] N. Isgur, Nucl. Phys. **A497** (1989) 91.

[30] M. V. Kossov, CHIPS: masses of hadrons. (be published).

[31] L. D. Landau, E. M. Lifshitz, "Course of Theoretical Physics" v.4, part 1, "Relativistic Quantum Theory", Pergamon Press, paragraph 96, The method of equivalent photons.

[32] J. Eickmeyer et al. Phys. Rev. Letters **36** (1976) 289-291.

[33] D'Agostini, Hard Scattering Process in High Energy Gamma-Induced Reactions, DESY 94-169, September 1994.

[34] F. W. Brasse et al. Nuclear Physics **B39** (1972) 421-431.

[35] D. Allasia *et al*, Z. Phys C **28**, 321 (1985)

[36] P. Berg *et al*, Z. Phys C **49**, 187 (1991)

[37] E. Oltman *et al*, Z. Phys C **53**, 51 (1992)

[38] M. Glück *et al*, Z. Phys. C **48**, 471 (1990)

[39] J. Kviecinski *et al*, Phys. Rev. D **42**, 3645 (1990)

[40] P. Lipari *et al*, Phys. Rev. Let. **74**, 4384 (1995)

[41] S.V. Belikov *et al*, Z. Phys. A **320**, 625 (1985)

[42] A. Lepretre et al. Nuclear Physics **A390** (1982) 221-239.

[43] P.V. Degtyarenko and M.V. Kossov, Preprint ITEP 11-92, Moscow (1992)

[44] P.V. Degtyarenko et al., Z. Phys. A - Atomic Nuclei, **335** (1990) 231

[45] P.V. Degtyarenko, *Applications of the photonuclear fragmentation model to radiation protection problems*, in: Proceedings of Second Specialist's Meeting on Shielding Aspects of Accelerators, Targets and Irradiation Facilities (SATIF-2), CERN, Geneva, Switzerland, 12-13 October 1995, published by Nuclear Energy Agency, Organization for Economic Co-operation and Development, pages 67 - 91 (1996)

[46] C. Bernard, A. Duncan, J. LoSecco, and S. Weinberg, Phys. Rev. D **12** (1975) 792;

E. Poggio, H. Quinn, and S. Weinberg, Phys. Rev. D **13** (1976) 1958

[47] A. I. Amelin et al., "Energy spectra of charged particles in the reaction of π^- absorption at rest by ^{6,7}Li, ^{9}Be, ^{10,11}B, ^{12}C, ^{28}Si, ^{40}Ca, ^{59}Co, ^{93}Nb, ^{114,117,120,124}Sn, ^{169}Tm, ^{181}Ta and ^{209}Bi nuclei", Moscow Physics and Engineering Institute Preprint No. 034-90, Moscow, 1990.

[48] G. Mechtersheimer et al., Nucl. Phys. **A324** (1979) 379.

[49] C. Cernigoi et al., Nucl. Phys. **A456** (1986) 599.

[50] R. Madey et al., Phys. Rev. C **25** (1982) 3050.

[51] D. Ryckbosch et al., Phys. Rev. C **42** (1990) 444.

[52] J. Ahrens et al., Nucl. Phys. **A446** (1985) 229c.

[53] Jan Ryckebusch et al., Phys. Rev. C **49** (1994) 2704.

[54] C. Van den Abeele; private communication cited in the reference: Jan Ryckebusch et al., Phys. Rev. C **49** (1994) 2704.

[55] P.D. Harty et al. (unpublished); private communication cited in the reference: Jan Ryckebusch et al., Phys. Rev. C **49** (1994) 2704.

[56] L.B. Weinstein et al., Phys. Rev. Lett. **64** (1990) 1646.

[57] J.P. Jeukenne and C. Mahaux, Nucl. Phys. A **394** (1983) 445.

Chapter 25

Bertini Intranuclear Cascade Model in GEANT4

25.1 Introduction

This model is based on a re-engineering of the INUCL code and includes the Bertini intra-nuclear cascade model with excitons, a pre-equilibrium model, a nucleus explosion model, a fission model, and an evaporation model. Intermediate energy nuclear reactions from 100 MeV to 5 GeV are treated for protons, neutrons, pions, photons and nuclear isotopes. We present an overview of the models, review results achieved from simulations and make comparisons with experimental data.

The intranuclear cascade model (INC) was was first proposed by Serber in 1947 [19]. He noticed that in particle-nuclear collisions the deBroglie wavelength of the incident particle is comparable (or shorter) than the average intra-nucleon distance. Hence, a description of interactions in terms of particle-particle collisions is justified.

The INC has been used succesfully in Monte Carlo simulations at intermediate energies since Goldberger made the first hand-calculations in 1947 [9]. The first computer simulations were done by Metropolis et al. in 1958 [16]. Standard methods in INC implementations were developed when Bertini published his results in 1968 [3]. An important addition to INC was the exciton model introduced by Griffin in 1966 [10].

The current presentation describes the implementation of the Bertini INC model within the GEANT4 hadronic physics framework [8]. This framework is flexible and allows for the modular implementation of various kinds of hadronic interactions. It is based on the concepts of physics processes and models. While the process is a general concept, models may be restricted ac-

cording to process type, material, element and energy range. Several models can be utilized by one process class; for instance, a process class for inelastic collisions can use a different model for each energy range.

The process classes use model classes to determine the secondaries produced in the interaction and to calculate the momenta of the particles. Here we present a collection of such models which describe a medium-energy intranuclear cascade.

25.2 The Geant4 Cascade Model

Inelastic particle-nucleus collisions are characterized by both fast and slow components. The fast $(10^{-23} - 10^{-22}s)$ intra-nuclear cascade results in a highly excited nucleus which may decay by fission or pre-equilibrium emission. The slower $(10^{-18} - 10^{-16}s)$ compound nucleus phase follows with evaporation. A Boltzmann equation must be solved to treat the collision process in detail.

The intranuclear cascade (INC) model developed by Bertini [3, 4] solves the Boltzmann equation on average. This model has been implemented in several codes such as HETC [1]. Our model, which is based on a re-engineering of the INUCL code [20], includes the Bertini intranuclear cascade model with excitons, a pre-equilibrium model, a simple nucleus explosion model, a fission model, and an evaporation model.

The target nucleus is modeled as a three-region approximation to the continuously changing density distribution of nuclear matter within nuclei. The cascade begins when the incident particle strikes a nucleon in the target nucleus and produces secondaries. The secondaries may in turn interact with other nucleons or be absorbed. The cascade ends when all particles, which are kinematically able to do so, escape the nucleus. At that point energy conservation is checked. Relativistic kinematics is applied throughout the cascade.

25.2.1 Model Limits

The model is valid for incident protons, neutrons and pions. Particles treated in the model include protons, neutrons, pions, photons and nuclear isotopes. All types of targets are allowed.

The necessary condition of validity of the INC model is $\lambda_B/v << \tau_c <<$ Δt, where δ_B is the deBroglie wavelenth of the nucleons, v is the average relative velocity between two nucleons and Δt is the time interval between collisions. At energies below $200MeV$, this condition is no longer strictly

valid, and a pre-quilibrium model must be invoked. At energies greater than ≈ 10 GeV) the INC picture breaks down. This model has been tested against experimental data at incident kinetic energies between 100 MeV and 5 GeV.

25.2.2 Intranuclear Cascade Model

The basic steps of the INC model are summarized as follows:

1. the space point at which the incident particle enters the nucleus is selected uniformly over the projected area of the nucleus,

2. the total particle-particle cross sections and region-depenent nucleon densities are used to select a path length for the projectile,

3. the momentum of the struck nucleon, the type of reaction and the four-momenta of the reaction products are determined, and

4. the exciton model is updated as the cascade proceeds.

5. If the Pauli exclusion principle allows and $E_{particle} > E_{cutoff} = 2$ MeV, step (2) is performed to transport the products.

After the intra-nuclear cascade, the residual excitation energy of the resulting nucleus is used as input for non-equilibrium model.

25.2.3 Nuclear Model

Some of the basic features of the nuclear model are:

- the nucleons are assumed to have a Fermi gas momentum distribution. The Fermi energy is calculated in a local density approximation i.e. the Fermi energy is made radius-dependent with Fermi momentum $p_F(r) = \left(\frac{3\pi^2 \rho(r)}{2}\right)^{\frac{1}{3}}$.

- Nucleon binding energies (BE) are calculated using the mass formula. A parameterization of the nuclear binding energy uses a combination of the Kummel mass formula and experimental data. Also, the asymptotic high temperature mass formula is used if it is impossible to use experimental data.

Initialization

The initialization phase fixes the nuclear radius and momentum according to the Fermi gas model.

If the target is hydrogen (A = 1) a direct particle-particle collision is performed, and no nuclear modeling is required.

If $1 < A < 4$, a nuclear model consisting of one layer with a radius of 8.0 fm is created.

For $4 < A < 11$, the nuclear model is composed of three concentric spheres $i = \{1, 2, 3\}$ with radius

$$r_i(\alpha_i) = \sqrt{C_1^2(1 - \frac{1}{A}) + 6.4}\sqrt{-log(\alpha_i)}$$

.

Here $\alpha_i = \{0.01, 0.3, 0.7\}$ and $C_1 = 3.3836A^{1/3}$.

If $A > 11$, a nuclear model with three concentric spheres is also used. The sphere radius is now defined as

$$r_i(\alpha_i) = C_2 \log(\frac{1 + e^{-\frac{C_1}{C_2}}}{\alpha_i} - 1) + C_1, \tag{25.1}$$

where $C_2 = 1.7234$.

The potential energy V for nucleon N is

$$V_N = \frac{p_F^2}{2m_N} + BE_N(A, Z), \tag{25.2}$$

where p_f is the Fermi momentum and BE is the binding energy.

The momentum distribution in each region follows the Fermi distribution with zero temperature.

$$f(p) = cp^2 \tag{25.3}$$

where

$$\int_0^{p_F} f(p)dp = n_p \text{orn}_n \tag{25.4}$$

where n_p and n_n are the number of protons or neutrons in the region. P_f is the momentum corresponding to the Fermi energy

$$E_f = \frac{p_F^2}{2m_N} = \frac{\hbar^2}{2m_N}(\frac{3\pi^2}{v})^{\frac{2}{3}}, \tag{25.5}$$

which depends on the density n/v of particles, and which is different for each particle and each region.

Pauli Exclusion Principle

The Pauli exclusion principle forbids interactions where the products would be in occupied states. Following the assumption of a completely degenerate Fermi gas, the levels are filled from the lowest level. The minimum energy allowed for the products of a collision correspond to the lowest unfilled level of the system, which is the Fermi energy in the region. So in practice, the Pauli exclusion principle is taken into account by accepting only secondary nucleons which have $E_N > E_f$.

Cross Sections and Kinematics

Path lengths of nucleons in the nucleus are sampled according to the local density and the free $N - N$ cross sections. Angles after the collision are sampled from experimental differential cross sections. Tabulated total reaction cross sections are calculated by Letaw's formulation [14, 15, 17]. For $N - N$ cross sections the parameterizations are based on the experimental energy and isospin dependent data. The parameterization described in [2] is used.

For pions the intra-nuclear cross sections are provided to treat elastic collisions and the following inelastic channels: $\pi^-p \to \pi^0n$, $\pi^0p \to \pi^+n$, $\pi^0n \to \pi^-p$, and $\pi^+n \to \pi^0p$. Multiple particle production is also implemented.

The pion absorption channels are $\pi^+nn \to pn$, $\pi^+pn \to pp$, $\pi^0nn \to nn$, $\pi^0pn \to pn$, $\pi^0pp \to pp$, $\pi^-pn \to nn$, and $\pi^-pp \to pn$.

25.2.4   Pre-equilibrium Model

The GEANT4 cascade model implements the exciton model proposed by Griffin [10, 11]. In this model, nucleon states are characterized by the number of excited particles and holes (the excitons). Intra-nuclear cascade collisions give rise to a sequence of states characterized by increasing exciton number, eventually leading to an equilibrated nucleus. For a practical implementation of the exciton model we use parameters from [18], (level densities) and [13] (matrix elements).

In the exciton model the possible selection rules for particle-hole configurations in the source of the cascade are: $\Delta p = 0, \pm 1$ $\Delta h = 0, \pm 1$ $\Delta n = 0, \pm 2$, where p is the number of particles, h is number of holes and $n = p + h$ is the number of excitons.

The cascade pre-equilibrium model uses target excitation data and the exciton configurations for neutrons and protons to produce non-equilibrium evaporation. The angular distribution is isotropic in the rest frame of the exciton system.

Parameterizations of the level density are tabulated as functions of A and Z, and with high temperature behavior (the nuclear binding energy using the smooth liquid high energy formula).

25.2.5 Break-up models

Fermi break-up is allowed only in some extreme cases, i.e. for light nuclei ($A < 12$ and $3(A - Z) < Z < 6$) and $E_{excitation} > 3E_{binding}$. A simple explosion model decays the nucleus into neutrons and protons and decreases exotic evaporation processes.

The fission model is phenomenological, using potential minimization. A binding energy paramerization is used and some features of the fission statistical model are incorporated [7].

25.2.6 Evaporation Model

A statistical theory for particle emission of the excited nucleus remaining after the intra-nuclear cascade was originally developed by Weisskopf [21]. This model assumes complete energy equilibration before particle emission, and re-equilibration of excitation energies between successive evaporations. As a result the angular distribution of emitted particles is isotropic.

The GEANT4 evaporation model for the cascade implementation adapts the often-used computational method developed by Dostrowski [5, 6]. The emission of particles is computed until the excitation energy falls below some specific cutoff. If a light nucleus is highly excited, the Fermi break-up model is executed. Also, fission is performed if that channel is open. The main chain of evaporation is followed until $E_{excitation}$ falls below $E_{cutoff} = 0.1$ MeV. The evaporation model ends with an emission chain which is followed until $E_{excitation} < E_{cutoff}^{\gamma} = 10^{-15}$ MeV.

An example of Bertini evaporation model in action is shown in Fig. 25.1.

25.3 Interfacing Bertini implementation

Typically Bertini models are used through physics lists, with 'BERT' in their name. User should consult these validated physics model collection to understand the inclusion mechanisms before using directly the actual Bertini cascade interfaces:

G4CascadeInterface *All the Bertini cascade submodels* in integrated fashion, can be used collectively through this interface using method *Apply-*
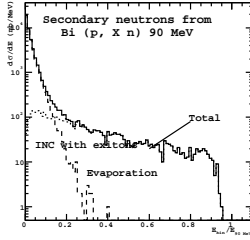
Figure 25.1: Secondary neutrons generated by Bertini INC with exitons and evaporation model.

> *Yourself.* A GEANT4 track (*G4Track*) and a nucleus (*G4Nucleus*) are given as parameters.

G4ElasticCascadeInterface provides an access to elastic hadronic scattering. Particle treated are the same as in case for *G4CascadeInterface* but only elastic scattering is modeled.

G4PreCompoundCascadeInterface provides an interface to INUCL intra nuclear cascade with exitons. Subsequent evaporation phase is *not* modeled.

G4InuclEvaporation provides an interface to INUCL evaporation model. This interface with method *BreakItUp* inputs an exited nuclei *G4Fragment* to model evaporation phase.

25.4   Status of this document

01.12.02 created by Aatos Heikkinen, Nikita Stepanov and Hans-Peter Wellisch
14.06.05 grammar, spelling check and list of pion absorption channels corrected by D.H. Wright
30.05.07 New interfaces documented Aatos Heikkinen

Bibliography

[1] R.G. Alsmiller and F.S. Alsmiller and O.W. Hermann, The high-energy transport code HETC88 and comparisons with experimental data, Nuclear Instruments and Methods in Physics Research A 295, (1990), 337–343,

[2] V.S. Barashenkov and V.D. Toneev, High Energy interactions of particles and nuclei with nuclei (In russian), (1972)

[3] M. P. Guthrie, R. G. Alsmiller and H. W. Bertini, Nucl. Instr. Meth, 66, 1968, 29.

[4] H. W. Bertini and P. Guthrie, Results from Medium-Energy Intranuclear-Cascade Calculation, Nucl. Phys.A169, (1971).

[5] I. Dostrovsky, Z. Zraenkel and G. Friedlander, Monte carlo calculations of high-energy nuclear interactions. III. Application to low-lnergy calculations, Physical Review, 1959, 116, 3, 683-702.

[6] I. Dostrovsky and Z. Fraenkel and P. Rabinowitz, Monte Carlo Calculations of Nuclear Evaporation Processes. V. Emission of Particles Heavier Than ^4He, Physical Review, 1960.

[7] P. Fong, Statistical Theory of Fission, 1969, Gordon and Breach, New York.

[8] Geant4 collaboration, Geant4 general paper (to be published), Nuclear Instruments and Methods A, (2003).

[9] M. Goldberger, The Interaction of High Energy Neutrons and Hevy Nuclei, Phys. Rev. 74, (1948), 1269.

[10] J. J. Griffin, Statistical Model of Intermediate Structure, Physical Review Letters 17, (1966), 478-481.

[11] J. J. Griffin, Statistical Model of Intermediate Structure, Physics Letters 24B, 1 (1967), 5-7.

[12] A. S. Iljonov et al., Intermediate-Energy Nuclear Physics, CRC Press 1994.

[13] C. Kalbach, Exciton Number Dependence of the Griffin Model Two-Body Matrix Element, Z. Physik A 287, (1978), 319-322.

[14] J. R. Letaw et al., The Astrophysical Journal Supplements 51, (1983), 271f.

[15] J. R. Letaw et al., The Astrophysical Journal 414, 1993, 601.

[16] N. Metropolis, R. Bibins, M. Storm, Monte Carlo Calculations on Intranuclear Cascades. I. Low-Energy Studies, Physical Review 110, (1958), 185ff.

[17] S. Pearlstein, Medium-energy nuclear data libraries: a case study, neutron- and proton-induced reactions in ^{5}6Fe, The Astrophysical Journal 346, (1989), 1049-1060.

[18] I. Ribansky et al., Pre-equilibrium decay and the exciton model, Nucl. Phys. A 205, (1973), 545-560.

[19] R. Serber, Nuclear Reactions at High Energies, Phys. Rev. 72, (1947), 1114.

[20] Experimental and Computer Simulations Study of Radionuclide Production in Heavy Materials Irradiated by Intermediate Energy Protons, Yu. E. Titarenko et al., nucl-ex/9908012, (1999).

[21] V. Weisskopf, Statistics and Nuclear Reactions, Physical Review 52, (1937), 295–302.

Chapter 26

The GEANT4 Binary Cascade

26.1 Modeling overview

The Geant4 Binary Cascade is an intranuclear cascade propagating primary and secondary particles in a nucleus. Interactions are between a primary or secondary particle and an individual nucleon of the nucleus, leading to the name Binary Cascade. Cross section data are used to select collisions. Where available, experimental cross sections are used by the simulation. Propagating of particles is the nuclear field is done by numerically solving the equation of motion. The cascade terminates when the average and maximum energy of secondaries is below threshold. The remaining fragment is treated by precompound and de-excitation models documented in the corresponding chapters.

26.1.1 The transport algorithm

For the primary particle an impact parameter is chosen random in a disk outside the nucleus perpendicular to a vector passing through the center of the nucleus coordinate system an being parallel to the momentum direction. Using a straight line trajectory, the distance of closest approach d_i^{min} to each target nucleon i and the corresponding time-of-flight t_i^d is calculated. In this calculation the momentum of the target nucleons is ignored, i.e. the target nucleons do not move. The interaction cross section σ_i with target nucleons is calculated using total inclusive cross-sections described below. For calculation of the cross-section the momenta of the nucleons are taken into account. The primary particle may interact with those target nucleons where the distance of closest approach d_i^{min} is smaller than $d_i^{min} < \sqrt{\frac{\sigma_i}{\pi}}$. These candidate interactions are called collisions, and these collisions are

431

stored ordered by time-of-flight t_i^d. In the case no collision is found, a new impact parameter is chosen.

The primary particle is tracked the time-step given by the time to the first collision. As long a particle is outside the nucleus, that is a radius of the outermost nucleon plus $3 fm$, particles travel along straight line trajectories. Particles entering the nucleus have their energy corrected for Coulomb effects. Inside the nucleus particles are propagated in the scalar nuclear field. The equation of motion in the field is solved for a given time-step using a Runge-Kutta integration method.

At the end of the step, the primary and the nucleon interact suing the scattering term. The resulting secondaries are checked for the Fermi exclusion principle. If any of the two particles has a momentum below Fermi momentum, the interaction is suppressed, and the original primary is tracked to the next collision. In case interaction is allowed, the secondaries are treated like the primary, that is, all possible collisions are calculated like above, with the addition that these new primary particles may be short-lived and may decay. A decay is treated like others collisions, the collision time being the time until the decay of the particle. All secondaries are tracked until they leave the nucleus, or the until the cascade stops.

26.1.2   The description of the target nucleus and fermi motion

The nucleus is constructed from A nucleons and Z protons with nucleon coordinates $\mathbf{r}_i$ and momenta $\mathbf{p}_i$, with $i = 1, 2, ..., A$. We use a common initialization Monte Carlo procedure, which is realized in the most of the high energy nuclear interaction models:

- Nucleon radii r_i are selected randomly in the nucleus rest frame according to nucleon density $\rho(r_i)$. For heavy nuclei with $A > 16$ [2] nucleon density is

$$\rho(r_i) = \frac{\rho_0}{1 + \exp\left[(r_i - R)/a\right]} \tag{26.1}$$

  where

$$\rho_0 \approx \frac{3}{4\pi R^3}(1 + \frac{a^2\pi^2}{R^2})^{-1}. \tag{26.2}$$

  Here $R = r_0 A^{1/3}$ fm and $r_0 = 1.16(1 - 1.16A^{-2/3})$ fm and $a \approx 0.545$ fm. For light nuclei with $A < 17$ nucleon density is given by a harmonic oscillator shell model [3], e. g.

$$\rho(r_i) = (\pi R^2)^{-3/2} \exp\left(-r_i^2/R^2\right), \tag{26.3}$$

where $R^2 = 2/3 < r^2 >= 0.8133 A^{2/3}$ fm^2. To take into account nucleon repulsive core it is assumed that internucleon distance $d > 0.8$ fm;

- The nucleus is assumed to be isotropic, i.e. we place each nucleon using a random direction and the previously determined radius r_i.

- The initial momenta of the nucleons p_i are randomly choosen between 0 and $p_F^{max}(r)$, where the maximal momenta of nucleons (in the local Thomas-Fermi approximation [4]) depends from the proton or neutron density ρ according to

$$p_F^{max}(r) = \hbar c (3\pi^2 \rho(r))^{1/3} \qquad (26.4)$$

- To obtain momentum components, it is assumed that nucleons are distributed isotropic in momentum space; i.e. the momentum direction is chosen at random.

- The nucleus must be centered in momentum space around $\mathbf{0}$, *i. e.* the nucleus must be at rest, i. e. $\sum_i \mathbf{p_i} = \mathbf{0}$; To achieve this, we choose one nucleon to compensate the sum the remaining nucleon momenta $p_r est = \sum_{i=1}^{i=A-1}$. If this sum is larger than maximum momentum $p_F^{max}(r)$, we change the direction of the momentum of a few nucleons. If this does not lead to a possible momentum value, than we repeat the procedure with a different nucleon having a larger maximum momentum $p_F^{max}(r)$. In the rare case this fails as well, we choose new momenta for all nucleons.

  This procedure gives special for hydrogen ^{1}H, where the proton has momentum $p = 0$, and for deuterium ^{2}H, where the momenta of proton and neutron are equal, and in opposite direction.

- We compute energy per nucleon $e = E/A = m_N + B(A, Z)/A$, where m_N is nucleon mass and the nucleus binding energy $B(A, Z)$ is given by the tabulation of [5]: and find the effective mass of each nucleon $m_i^{eff} = \sqrt{(E/A)^2 - p_i^{2\prime}}$.

26.1.3 Optical and phenomenological potentials

The effect of collective nuclear elastic interaction upon primary and secondary particles is approximated by a nuclear potential.

For projectile protons and neutrons this scalar potential is given by the local Fermi momentum $p_F(r)$

$$V(r) = \frac{p_F^2(r)}{2m} \qquad (26.5)$$

where m is the mass of the neutron m_n or the mass of proton m_p.

For pions the potential is given by the lowest order optical potential [6]

$$V(r) = \frac{-2\pi(\hbar c)^2 A}{\overline{m}_\pi}(1 + \frac{m_\pi}{M})b_0\rho(r) \qquad (26.6)$$

where A is the nuclear mass number, m_π, M are the pion and nucleon mass, $\overline{m}_\pi$ is the reduced pion mass $\overline{m}_\pi = (m_\pi m_N)/(m_\pi + m_N)$, with m_N is the mass of the nucleus, and $\rho(r)$ is the nucleon density distribution. The parameter b_0 is the effective $s-$wave scattering length and is obtained from analysis to pion atomic data to be about $-0.042 fm$.

26.1.4   Pauli blocking simulation

The cross sections used in this model are cross sections for free particles. In the nucleus these cross sections are reduced to effective cross sections by Pauli-blocking due to Fermi statistics.

For nucleons created by a collision, ie. an inelastic scattering or from decay, we check that all secondary nucleons occupy a state allowed by Fermi statistics. We assume that the nucleus in its ground state and all states below Fermi energy are occupied. All secondary nucleons therefore must have a momentum p_i above local Fermi momentum $p_F(r)$, i.e.

$$p_i > p_F^{max}(r). \qquad (26.7)$$

If any of the nucleons of the collision has a momentum below the local Fermi momentum, then the collision is Pauli blocked. The reaction products are discarded, and the original particles continue the cascade.

26.1.5   The scattering term

The basis of the description of the reactive part of the scattering amplitude are two particle binary collisions (hence binary cascade), resonance production, and decay. Based on the cross-section described later in this paper, collisions will occur when the transverse distance d_t of any projectile target pair becomes smaller than the black disk radium corresponding to the total cross-section σ_t

$$\frac{\sigma_t}{\pi} > d_t^2$$

In case of a collision, all particles will be propagated to the estimated time of the collision, i.e. the time of closest approach, and the collision final state is produced.

26.1.6   Total inclusive cross-sections

Experimental data are used in the calculation of the total, inelastic and elastic cross-section wherever available.

hadron-nucleon scattering

For the case of proton-proton(pp) and proton-neutron(pn) collisions, as well as $\pi^=$ and π^- nucleon collisions, experimental data are readily available as collected by the Particle Data Group (PDG) for both elastic and inelastic collisions. We use a tabulation based on a sub-set of these data for $\sqrt{S}$ below 3 GeV. For higher energies, parametrizations from the CERN-HERA collection are included.

26.1.7   Channel cross-sections

A large fraction of the cross-section in individual channels involving meson nucleon scattering can be modeled as resonance excitation in the s-channel. This kind of interactions show a resonance structure in the energy dependency of the cross-section, and can be modeled using the Breit-Wigner function

$$\sigma_{res}(\sqrt{s}) = \sum_{FS} \frac{2J+1}{(2S_1+1)(2S_2+1)} \frac{\pi}{k^2} \frac{\Gamma_I S \Gamma_F S}{(\sqrt{s}-M_R)^2 + \Gamma/4},$$

Where $S1$ and $S2$ are the spins of the two fusing particles, J is the spin of the resonance, $\sqrt{(s)}$ the energy in the center of mass system, k the momentum of the fusing particles in the center of mass system, $\Gamma_I S$ and $\Gamma)FS$ the partial width of the resonance for the initial and final state respectively. M_R is the nominal mass of the resonance.

The initial states included in the model are pion and kaon nucleon scattering. The product resonances taken into account are the Delta resonances with masses 1232, 1600, 1620, 1700, 1900, 1905, 1910, 1920, 1930, and 1950 MeV, the excited nucleons with masses of 1440, 1520, 1535, 1650, 1675, 1680, 1700, 1710, 1720, 1900, 1990, 2090, 2190, 2220, and 2250 MeV, the Lambda, and its excited states at 1520, 1600, 1670, 1690, 1800, 1810, 1820, 1830, 1890, 2100, and 2110 MeV, and the Sigma and its excited states at 1660, 1670, 1750, 1775, 1915, 1940, and 2030 MeV.

26.1.8 Mass dependent resonance width and partial width

During the cascading, the resonances produced are assigned reall masses, with values distributed according to the production cross-section described above. The concrete (rather than nominal) masses of these resonances may be small compared to the PDG value, and this implies that some channels may not be open for decay. In general it means, that the partial and total width will depend on the concrete mass of the resonance. We are using the UrQMD[13][14] approach for calculating these actual width,

$$\Gamma_{R \to 12}(M) = (1 + r) \frac{\Gamma_{R \to 12}(M_R)}{p(M_R)^{(2l+1)}} \frac{M_R}{M} \frac{p(M)^{(2l+1)}}{1 + r(p(M)/p(M_R))^{2l}}. \tag{26.8}$$

Here M_R is the nominal mass of the resonance, M the actual mass, p is the momentum in the center of mass system of the particles, L the angular momentum of the final state, and r=0.2.

26.1.9 Resonance production cross-section in the t-channel

In resonance production in the t-channel, single and double resonance excitation in nucleon-nucleon collisions are taken into account. The resonance production cross-sections are as much as possible based on parametrizations of experimental data[15] for proton proton scattering. The basic formula used is motivated from the form of the exclusive production cross-section of the Δ_{1232} in proton proton collisions:

$$\sigma_{AB} = 2\alpha_{AB}\beta_{AB} \frac{\sqrt{s} - \sqrt{s_0}}{(\sqrt{s} - \sqrt{s_0})^2 + \beta_{AB}^2} \left(\frac{\sqrt{s0} + \beta_{AB}}{\sqrt{s}} \right)^{\gamma_{AB}}$$

The parameters of the description for the various channels are given in table26.1. For all other channels, the parametrizations were derived from these by adjusting the threshold behavior.

The reminder of the cross-section are derived from these, applying detailed balance. Iso-spin invariance is assumed. The formalism used to apply detailed balance is

$$\sigma(cd \to ab) = \sum_{J,M} \frac{\langle j_c m_c j_d m_d \| JM \rangle^2}{\langle j_a m_a j_b m_b \| JM \rangle^2} \frac{(2S_a + 1)(2S_b + 1)}{(2S_c + 1)(2S_d + 1)} \frac{\langle p_{ab}^2 \rangle}{\langle p_{cd}^2 \rangle} \sigma(ab \to cd) \tag{26.9}$$

Reaction	α	β	γ
pp → pΔ_{1232}	25 mbarn	0.4 GeV	3
pp → $\Delta_{1232}\Delta_{1232}$	1.5 mbarn	1 GeV	1
pp → pp*	0.55 mbarn	1 GeV	1
pp → pΔ_*	0.4 mbarn	1 GeV	1
pp → $\Delta_{1232}\Delta^*$	0.35 mbarn	1 GeV	1
pp → Δ_{1232}N*	0.55 mbarn	1 GeV	1

Table 26.1: Values of the parameters of the cross-section formula for the individual channels.

26.1.10 Nucleon Nucleon elastic collisions

Angular distributions for elastic scattering of nucleons are taken as closely as possible from experimental data, i.e. from the result of phase-shift analysis. They are derived from differential cross sections obtained from the SAID database, R. Arndt, 1998.

Final states are derived by sampling from tables of the cumulative distribution function of the centre-of-mass scattering angle, tabulated for a discrete set of lab kinetic energies from 10 MeV to 1200 MeV. The CDF's are tabulated at 1 degree intervals and sampling is done using bi-linear interpolation in energy and CDF values. Coulomb effects are taken into consideration for pp scattering.

26.1.11 Generation of transverse momentum

Angular distributions for final states other than nucleon elastic scattering are calculated analytically, derived from the collision term of the in-medium relativistic Boltzmann-Uehling-Uhlenbeck equation, absed on the nucleon nucleon elastic scattering cross-sections:

$$\sigma_{NN\to NN}(s,t) = \frac{1}{(2\pi)^2 s}\left(D(s,t) + E(s,t) + (invertedt,u)\right)$$

Here s, t, u are the Mandelstamm variables, $D(s,t)$ is the direct term, and $E(s,t)$ is the exchange term, with

$$D(s,t) = \frac{(g_{NN}^\sigma)^4(t-4m^{*2})^2}{2(t-m_\sigma^2)^2} + \frac{(g_{NN}^\omega)^4(2s^2+2st+t^2-8m^{*2}s+8m^{*4})}{(t-m_\omega^2)^2} + \frac{24(g_{NN}^\pi)^4 m^{*2}t^2}{(t-m_\pi^2)^2} - \frac{4(g_{NN}^\sigma g_{NN}^\omega)^2(2s+t-4m^{*2})m^{*2}}{(t-m_\sigma^2)(t-m_\omega^2)},$$

and

$$E(s,t) = \frac{(g_{NN}^\sigma)^4\big(t(t+s)+4m^{*2}(s-t)\big)}{8(t-m_\sigma^2)(u-m_\sigma^2)} + \frac{(g_{NN}^\omega)^4(s-2m^{*2})(s-6m^{*2}))}{2(t-m_\omega^2)(u-m_\omega^2)} -$$
$$\frac{6(g_{NN}^\pi)^4(4m^{*2}-s-t)m^{*4}t}{(t-m_\pi^2)(u=m_p i^2)} + \frac{3(g_{NN}^\sigma g_{NN}^\pi)^2 m^{*2}(4m^{*2}-s-t)(4m^{*2}-t)}{(t-m_\sigma^2)(u-m_\pi^2)} +$$
$$\frac{3(g_{NN}^\sigma g_{NN}^\pi)^2 t(t+s)m^{*2}}{2(t-m_\pi^2)(u-m_\sigma^2)} + \frac{(g_{NN}^\sigma g_{NN}^\omega)^2 t^2 - 4m^{*2}s - 10m^{*2}t + 24m^{*4}}{4(t-m_\sigma^2)(u-m_\omega^2)} +$$
$$\frac{(g_{NN}^\sigma g_{NN}^\omega)^2(t+s)^2 - 2m^{*2}s + 2m^{*2}t}{4(t-m_\omega^2)(u-m_\sigma^2)} + \frac{3(g_{NN}^\omega g_{NN}^\pi)^2(t+s-4m^{*2})(t+s-2m^{*2})}{(t-m_\omega^2)(u-m_\pi^2)} +$$
$$\frac{3(g_{NN}^\omega g_{NN}^\pi)^2 m^{*2}(t^2-2m^{*2}t)}{(t-m_\pi^2)(u-m_\omega^2)}. \tag{26.10}$$

$$\tag{26.11}$$

Here, in this first release, the in-medium mass was set to the free mass, and the nucleon nucleon coupling constants used were 1.434 for the π, 7.54 for the ω, and 6.9 for the σ. This formula was used for elementary hadron-nucleon differential cross-sections by scaling teh center of mass energy squared accordingly.

Finite size effects were taken into account at the meson nucleon vertex, using a phenomenological form factor (cut-off) at each vertex.

26.1.12 Decay

In the simulation of decay of strong resonances, we use the nominal decay branching ratios from the particle data book. The stochastic mass of a individual resonance created is sampled at creation time from the Breit-Wigner form, under the mass constraints posed by center of mass energy of the scattering, and the mass in the lightest decay channel. The decay width from the particle data book are then adjusted according to equation 26.8, to take the stochastic mass value into account.

All decay channels with nominal branching ratios greater than 1% are simulated.

26.1.13 The escaping particle and coherent effects

When a nucleon other than the incident particle leaves the nucleus, the ground state of the nucleus changes. The energy of the outgoing particle cannot be such that the total mass of the new nucleus would be below its ground state mass. To avoid this, we reduce the energy of an outgoing nucleons by the mass-difference of old and new nucleus.

Furthermore, the momentum of the final exited nucleus derived from energy momentum balance may be such that its mass is below its ground

state mass. In this case, we arbitrarily scale the momenta of all outgoing particles by a factor derived from the mass of the nucleus and the mass of the system of outgoing particles.

26.1.14 Light ion reactions

In simulating light ion reactions, the initial state of the cascade is prepared in the form of two nuclei, as described in the above section on the nuclear model.

The lighter of the collision partners is selected to be the projectile. The nucleons in the projectile are then entered, with position and momenta, into the initial state of the cascade. Note that before the first scattering of an individual nucleon, a projectile nucleon's Fermi-momentum is not taken into account in the tracking inside the target nucleus. The nucleon distribution inside the projectile nucleus is taken to be a representative distribution of its nucleons in configuration space, rather than an initial state in the sense of QMD. The Fermi momentum and the local field are taken into account in the calculation of the collision probabilities and final states of the binary collisions.

26.1.15 Transition to pre-compound modeling

Eventually, the cascade assumptions will break down at low energies, and the state of affairs has to be treated by means of evaporation and pre-equilibrium decay. This transition is not at present studied in depth, and an interesting approach which uses the tracking time, as in the Liege cascade code, remains to be studied in our context.

For this first release, the following algorithm is used to determine when cascading is stopped, and pre-equilibrium decay is called: As long as there are still particles above the kinetic energy threshold (75 MeV), cascading will continue. Otherwise, when the mean kinetic energy of the participants has dropped below a second threshold (15 MeV), the cascading is stopped.

The residual participants, and the nucleus in its current state are then used to define the initial state, i.e. excitation energy, number of excitons, number of holes, and momentum of the exciton system, for pre-equilibrium decay.

In the case of light ion reactions, the projectile excitation is determined from the binary collision participants (P) using the statistical approach towards excitation energy calculation in an adiabatic abrasion process, as de-

scribed in [12]:

$$E_{ex} = \sum_P (E^P_{fermi} - E^P)$$

Given this excitation energy, the projectile fragment is then treated by the evaporation models described previously.

26.1.16 Calculation of excitation energies and residuals

At the end of the cascade, we form a fragment for further treatment in precompound and nuclear de-excitation models ([16]).

These models need information about the nuclear fragment created by the cascade. The fragment is characterized by the number of nucleons in the fragment, the charge of the fragment, the number of holes, the number of all excitons, and the number of charged excitons, and the four momentum of the fragment.

The number of holes is given by the difference of the number of nucleons in the original nucleus and the number of non-excited nucleons left in the fragment. An exciton is a nucleon captured in the fragment at the end of the cascade.

The momentum of the fragment calculated by the difference between the momentum of the primary and the outgoing secondary particles must be split in two components. The first is the momentum acquired by coherent elastic effects, and the second is the momentum of the excitons in the nucleus rest frame. Only the later part is passed to the de-excitation models. Secondaries arising from de-excitation models, including the final nucleus, are transformed back the frame of the moving fragment.

26.2 Comparison with experiments

We add here a set of preliminary results produced with this code, focusing on neutron and pion production. Given that we are still in the process of writing up the paper, we apologize for the at release time still less then publication quality plots.

Bibliography

[1] J. Cugnon, C. Volant, S. Vuillier DAPNIA-SPHN-97-01, Dec 1996. 62pp. Submitted to Nucl.Phys.A,

Figure 26.1: Double differential cross-section for neutrons produced in proton scattering off Aluminum. Proton incident energy was 113 MeV.

Figure 26.2: Double differential cross-section for neutrons produced in proton scattering off Aluminum. Proton incident energy was 256 MeV. The points are data, the histogram is Binary Cascade prediction.

Figure 26.3: Double differential cross-section for neutrons produced in proton scattering off Aluminum. Proton incident energy was 597 MeV. The points are data, the histogram is Binary Cascade prediction.

Figure 26.4: Double differential cross-section for neutrons produced in proton scattering off Aluminum. Proton incident energy was 800 MeV. The points are data, the histogram is Binary Cascade prediction.

Figure 26.5: Double differential cross-section for neutrons produced in proton scattering off Iron. Proton incident energy was 113 MeV. The points are data, the histogram is Binary Cascade prediction.

Figure 26.6: Double differential cross-section for neutrons produced in proton scattering off Iron. Proton incident energy was 256 MeV. The points are data, the histogram is Binary Cascade prediction.

Figure 26.7: Double differential cross-section for neutrons produced in proton scattering off Iron. Proton incident energy was 597 MeV. The points are data, the histogram is Binary Cascade prediction.
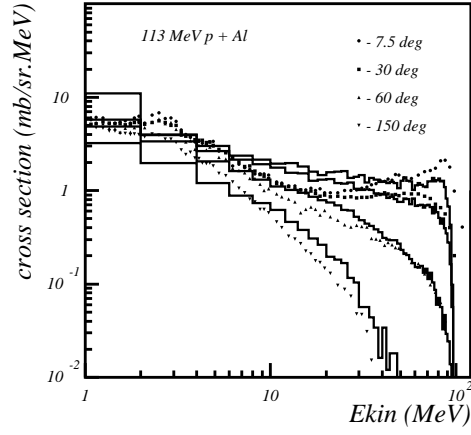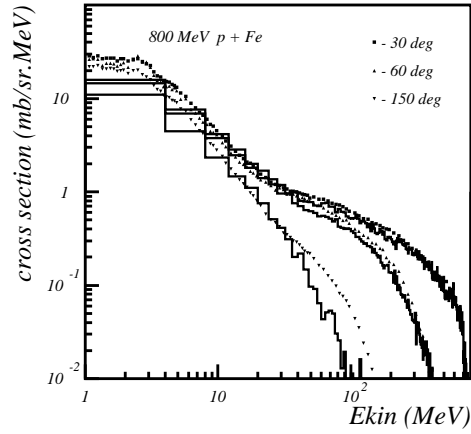

Figure 26.8: Double differential cross-section for neutrons produced in proton scattering off Iron. Proton incident energy was 800 MeV. The points are data, the histogram is Binary Cascade prediction.
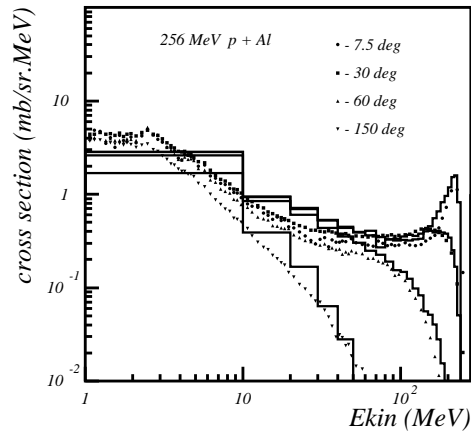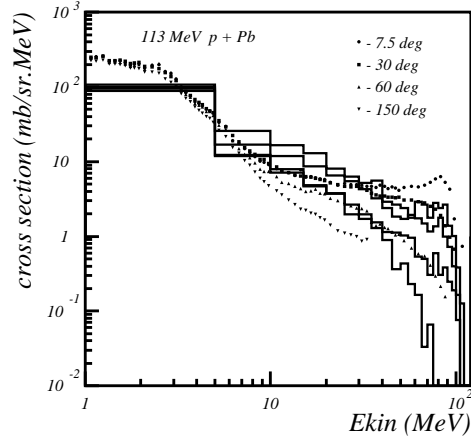
Figure 26.9: Double differential cross-section for neutrons produced in proton scattering off Lead. Proton incident energy was 113 MeV. The points are data, the histogram is Binary Cascade prediction.
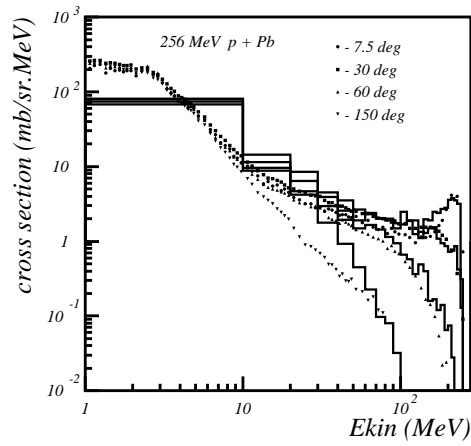
Figure 26.10: Double differential cross-section for neutrons produced in proton scattering off Lead. Proton incident energy was 256 MeV. The points are data, the histogram is Binary Cascade prediction.
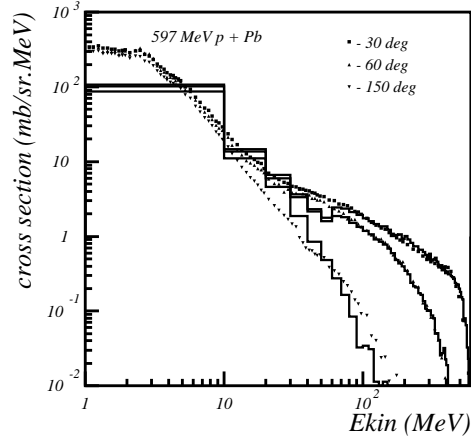
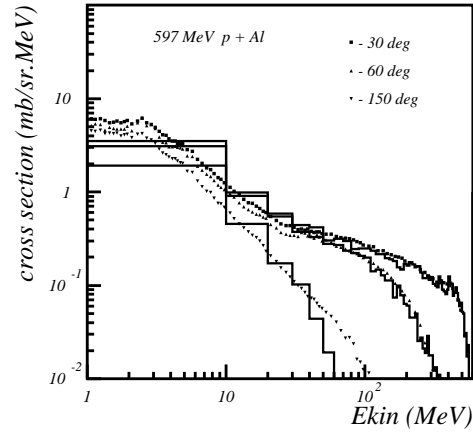Figure 26.11: Double differential cross-section for neutrons produced in proton scattering off Lead. Proton incident energy was 597 MeV. The points are data, the histogram is Binary Cascade prediction.
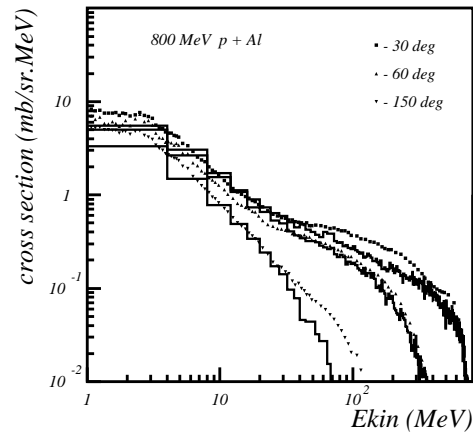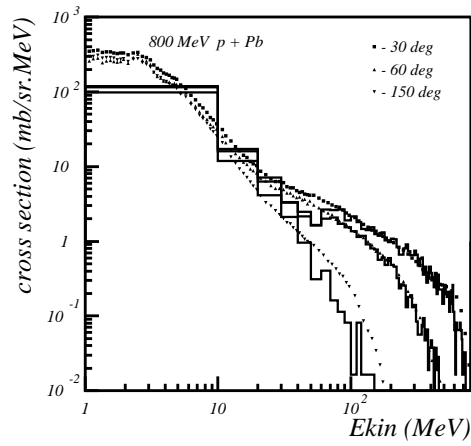

Figure 26.12: Double differential cross-section for neutrons produced in proton scattering off Lead. Proton incident energy was 800 MeV. The points are data, the histogram is Binary Cascade prediction.
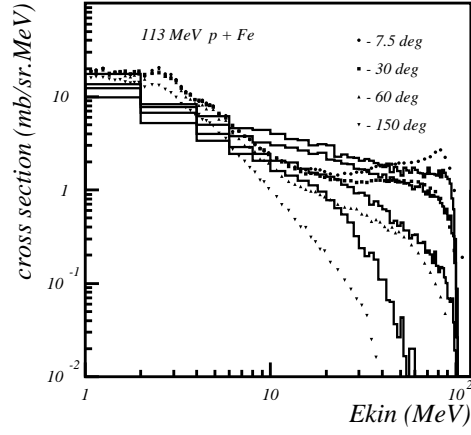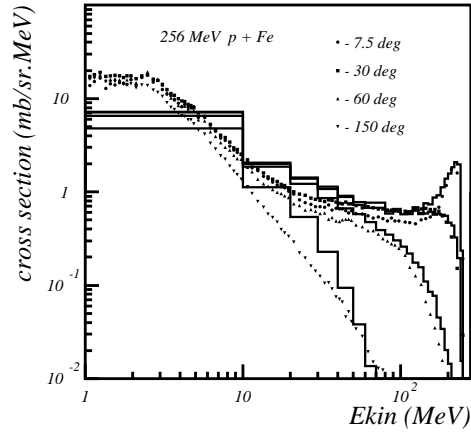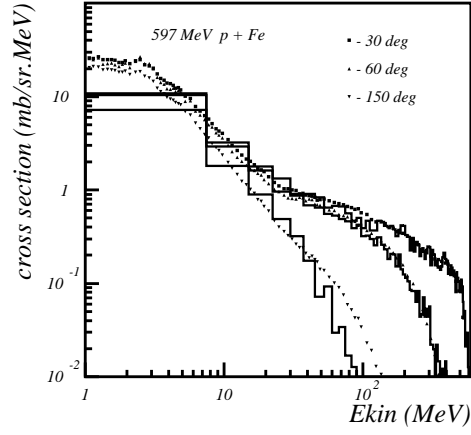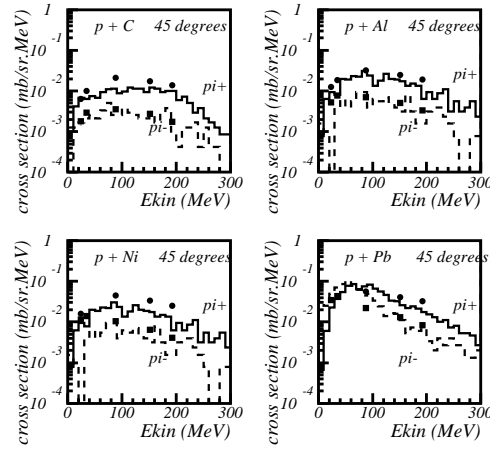
Figure 26.13: Double differential cross-section for pions produced at 45° in proton scattering off various materials. Proton incident energy was 597 MeV in each case. The points are data, the histogram is Binary Cascade prediction.

G. Peter, D. Behrens, C.C. Noack Phys.Rev. C49, 3253, (1994),
Hai-Qiao Wang, Xu Cai, Yong Liu High Energy Phys.Nucl.Phys. 16, 101, (1992),
A.S. Ilinov, A.B. Botvina, E.S. Golubeva, I.A. Pshenichnov, Sov. J. Nucl. Phys. 55, 734, (1992),
and citations therein.

[2] Grypeos M. E., Lalazissis G. A., Massen S. E., Panos C. P., J. Phys. **G17** 1093 (1991).

[3] Elton L. R. B., Nuclear Sizes, Oxford University Press, Oxford, 1961.

[4] DeShalit A., Feshbach H., Theoretical Nuclear Physics, Vol. 1: Nuclear Structure, Wyley, 1974.

[5] reference to be completed

[6] K. Stricker, H. McManus, J. A. Carr Nuclear scattering of low energy pions, Phys. Rev. C **19**, 929, (1979)

[7] M. M. Meier et al., Differential neutron production cross sections and neutron yields from stopping-length targets for 113-MeV protons, Nucl. Scien. Engin. **102**, 310, (1989)

[8] M. M. Meier et al., Differential neutron production cross sections for 256-MeV protons, Nucl. Scien. Engin. **110**, 289, (1992)

[9] W. B. Amian et al., Differential neutron production cross sections for 597-MeV protons, Nucl. Scien. Engin. **115**, 1, (1993)

[10] W. B. Amian et al., Differential neutron production cross sections for 800-MeV protons, Nucl. Scien. Engin. **112**, 78, (1992)

[11] J. F. Crawford et al., Measurement of cross sections and asymmetry parameters for the production of charged pions from various nuclei by 585-MeV protons, Phys. Rev. **C 22**, 1184, (1980)

[12] J. J. Gaimard and K. H. Schmidt, "A Reexamination of the abrasion - ablation model for the description of the nuclear fragmentation reaction," Nucl. Phys. A **531** (1991) 709.

[13] reference to be completed.

[14] reference to be completed

[15] reference to be completed

[16] reference to be completed

Chapter 27

Abrasion-ablation Model

27.1 Introduction

The abrasion model is a simplified macroscopic model for nuclear-nuclear interactions based largely on geometric arguments rather than detailed consideration of nucleon-nucleon collisions. As such the speed of the simulation is found to be faster than models such as G4BinaryCascade, but at the cost of accuracy. The version of the model implemented is interpreted from the so-called abrasion-ablation model described by Wilson *et al* [1],[2] together with an algorithm from Cucinotta to approximate the secondary nucleon energy spectrum [3]. By default, instead of performing an ablation process to simulate the de-excitation of the nuclear pre-fragments, the Geant4 implementation of the abrasion model makes use of existing and more detailed nuclear de-excitation models within Geant4 (G4Evaporation, G4FermiBreakup, G4StatMF) to perform this function (see section 27.5). However, in some cases cross sections for the production of fragments with large ΔA from the pre-abrasion nucleus are more accurately determined using a Geant4 implementation of the ablation model (see section 27.6).

The abrasion interaction is the initial fast process in which the overlap region between the projectile and target nuclei is sheered-off (see figure 27.1) The spectator nucleons in the projectile are assumed to undergo little change in momentum, and likewise for the spectators in the target nucleus. Some of the nucleons in the overlap region do suffer a change in momentum, and are assumed to be part of the original nucleus which then undergoes de-excitation.

Less central impacts give rise to an overlap region in which the nucleons can suffer significant momentum change, and zones in the projectile and target outside of the overlap where the nucleons are considered as spectators to the

initial energetic interaction.

The initial description of the interaction must, however, take into consideration changes in the direction of the projectile and target nuclei due to Coulomb effects, which can then modify the distance of closest approach compared with the initial impact parameter. Such effects can be important for low-energy collisions.

27.2 Initial nuclear dynamics and impact parameter

For low-energy collisions, we must consider the deflection of the nuclei as a result of the Coulomb force (see figure 27.2). Since the dynamics are non-relativistic, the motion is governed by the conservation of energy equation:

$$E_{tot} = \frac{1}{2}\mu\dot{r}^2 + \frac{l^2}{2\mu r^2} + \frac{Z_P Z_T e^2}{r} \tag{27.1}$$

where:

E_{tot} = total energy in the centre of mass frame;
$r, \dot{r}$ = distance between nuclei, and rate of change of distance;
l = angular momentum;
μ = reduced mass of system *i.e.* $m_1 m_2/(m_1 + m_2)$;
e = electric charge (units dependent upon the units for E_{tot} and r);
Z_P, Z_T = charge numbers for the projectile and target nuclei.

The angular momentum is based on the impact parameter between the nuclei when their separation is large, *i.e.*

$$E_{tot} = \frac{1}{2}\frac{l^2}{\mu b^2} \ \Rightarrow \ l^2 = 2E_{tot}\mu b^2 \tag{27.2}$$

At the point of closest approach, $\dot{r}=0$, therefore:

$$E_{tot} = \frac{E_{tot}b^2}{r^2} + \frac{Z_P Z_T e^2}{r}$$
$$r^2 = b^2 + \frac{Z_P Z_T e^2}{E_{tot}}r \tag{27.3}$$

Rearranging this equation results in the expression:

$$b^2 = r(r - r_m) \tag{27.4}$$

where:

$$r_m = \frac{Z_P Z_T e^2}{E_{tot}} \tag{27.5}$$

In the implementation of the abrasion process in Geant4, the square of the far-field impact parameter, b, is sampled uniformly subject to the distance of closest approach, r, being no greater than $r_P + r_T$ (the sum of the projectile and target nuclear radii).

27.3   Abrasion process

In the abrasion process, as implemented by Wilson *et al* [1] it is assumed that the nuclear density for the projectile is constant up to the radius of the projectile (r_P) and zero outside. This is also assumed to be the case for the target nucleus. The amount of nuclear material abraded from the projectile is given by the expression:

$$\Delta_{abr} = F A_P \left[1 - \exp\left(-\frac{C_T}{\lambda} \right) \right] \tag{27.6}$$

where F is the fraction of the projectile in the interaction zone, λ is the nuclear mean-free-path, assumed to be:

$$\lambda = \frac{16.6}{E^{0.26}} \tag{27.7}$$

E is the energy of the projectile in MeV/nucleon and C_T is the chord-length at the position in the target nucleus for which the interaction probability is maximum. For cases where the radius of the target nucleus is greater than that of the projectile (*i.e.* $r_T > r_P$):

$$C_T = \begin{cases} 2\sqrt{r_T^2 - x^2} & : x > 0 \\ 2\sqrt{r_T^2 - r^2} & : x \leq 0 \end{cases} \tag{27.8}$$

where:

$$x = \frac{r_P^2 + r^2 - r_T^2}{2r} \tag{27.9}$$

In the event that $r_P > r_T$ then C_T is:

$$C_T = \begin{cases} 2\sqrt{r_T^2 - x^2} & : x > 0 \\ 2r_T & : x \leq 0 \end{cases} \tag{27.10}$$

where:

$$x = \frac{r_T^2 + r^2 - r_P^2}{2r} \tag{27.11}$$

The projectile and target nuclear radii are given by the expression:

$$r_P \approx 1.29 \sqrt{r_{RMS,P}^2 - 0.84^2}$$
$$r_T \approx 1.29 \sqrt{r_{RMS,T}^2 - 0.84^2}$$
(27.12)

The excitation energy of the nuclear fragment formed by the spectators in the projectile is assumed to be determined by the excess surface area, given by:

$$\Delta S = 4\pi r_P^2 \left[1 + P - (1 - F)^{2/3} \right]$$
(27.13)

where the functions P and F are given in section 27.7. Wilson *et al* equate this surface area to the excitation to:

$$E_S = 0.95 \Delta S$$
(27.14)

if the collision is peripheral and there is no significant distortion of the nucleus, or

$$E_S = 0.95 \left\{ 1 + 5F + \Omega F^3 \right\} \Delta S$$
$$\Omega = \begin{cases} 0 & : A_P > 16 \\ 1500 & : A_P < 12 \\ 1500 - 320 \left(A_P - 12 \right) & : 12 \leq A_P \leq 16 \end{cases}$$
(27.15)

if the impact separation is such that $r << r_P + r_T$. E_S is in MeV provided ΔS is in fm^2.

For the abraded region, Wilson *et al* assume that fragments with a nucleon number of five are unbounded, 90% of fragments with a nucleon number of eight are unbound, and 50% of fragments with a nucleon number of nine are unbound. This was not implemented within the Geant4 version of the abrasion model, and disintegration of the pre-fragment was only simulated by the subsequent de-excitation physics models in the G4DeexcitationHandler (evaporation, *etc.* or G4WilsonAblationModel) since the yields of lighter fragments were already underestimated compared with experiment.

In addition to energy as a result of the distortion of the fragment, some energy is assumed to be gained from transfer of kinetic energy across the boundaries of the nuclei. This is approximated to the average energy transferred to a nucleon per unit intersection pathlength (assumed to be 13 MeV/fm) and the longest chord-length, C_l, and for half of the nucleon-nucleon collisions it is assumed that the excitation energy is:

$$E_X^* = \begin{cases} 13 \cdot \left[1 + \frac{C_t - 1.5}{3} \right] C_l & : C_t > 1.5\text{fm} \\ 13 \cdot C_l & : C_t \leq 1.5\text{fm} \end{cases}$$
(27.16)

where:

$$C_l = \begin{cases} 2\sqrt{r_P^2 + 2rr_T - r^2 - r_T^2} & r > r_T \\ 2r_P & r \leq r_T \end{cases} \qquad (27.17)$$

$$C_t = 2\sqrt{r_P^2 - \frac{(r_P^2 + r^2 - r_T^2)^2}{4r^2}} \qquad (27.18)$$

For the remaining events, the projectile energy is assumed to be unchanged. Wilson *et al* assume that the energy required to remove a nucleon is 10MeV, therefore the number of nucleons removed from the projectile by ablation is:

$$\Delta_{abl} = \frac{E_S + E_X}{10} + \Delta_{spc} \qquad (27.19)$$

where Δ_{spc} is the number of loosely-bound spectators in the interaction region, given by:

$$\Delta_{spc} = A_P F \exp\left(-\frac{C_T}{\lambda}\right) \qquad (27.20)$$

Wilson *et al* appear to assume that for half of the events the excitation energy is transferred into one of the nuclei (projectile or target), otherwise the energy is transferred in to the other (target or projectile respectively).
The abrasion process is assumed to occur without preference for the nucleon type, *i.e.* the probability of a proton being abraded from the projectile is proportional to the fraction of protons in the original projectile, therefore:

$$\Delta Z_{abr} = \Delta_{abr} \frac{Z_P}{A_P} \qquad (27.21)$$

In order to calculate the charge distribution of the final fragment, Wilson *et al* assume that the products of the interaction lie near to nuclear stability and therefore can be sampled according to the Rudstam equation (see section 27.6). The other obvious condition is that the total charge must remain unchanged.

27.4   Abraded nucleon spectrum

Cucinotta has examined different formulae to represent the secondary protons spectrum from heavy ion collisions [3]. One of the models (which has been implemented to define the final state of the abrasion process) represents the momentum distribution of the secondaries as:

$$\psi(p) \propto \sum_{i=1}^{3} C_i \exp\left(-\frac{p^2}{2p_i^2}\right) + d_0 \frac{\gamma p}{\sinh(\gamma p)} \qquad (27.22)$$

where:

$\psi(p)$ = number of secondary protons with momentum p per unit of momentum phase space [c^3/MeV^3];

p = magnitude of the proton momentum in the rest frame of the nucleus from which the particle is projected [MeV/c];

$C1$, $C2$, $C3$ = 1.0, 0.03, and 0.0002;

$p1$, $p2$, $p3$ = $\sqrt{\frac{2}{5}}p_F$, $\sqrt{\frac{6}{5}}p_F$, 500 [MeV/c]

p_F = Momentum of nucleons in the nuclei at the Fermi surface [MeV/c]

d_0 = 0.1

$\frac{1}{\gamma}$ = 90 [MeV/c];

G4WilsonAbrasionModel approximates the momentum distribution for the neutrons to that of the protons, and as mentioned above, the nucleon type sampled is proportional to the fraction of protons or neutrons in the original nucleus.

The angular distribution of the abraded nucleons is assumed to be isotropic in the frame of reference of the nucleus, and therefore those particles from the projectile are Lorentz-boosted according to the initial projectile momentum.

27.5 De-excitation of the projectile and target nuclear pre-fragments by standard Geant4 de-excitation physics

Unless specified otherwise, G4WilsonAbrasionModel will instantiate the following de-excitation models to treat subsequent particle emission of the excited nuclear pre-fragments (from both the projectile and the target):

1 G4Evaporation, which will perform nuclear evaporation of (α-particles, ^{3}He, ^{3}H, ^{2}H, protons and neutrons, in competition with photo-evaporation and nuclear fission (if the nucleus has sufficiently high A).

2 G4FermiBreakUp, for nuclei with $A \leq 12$ and $Z \leq 6$.

3 G4StatMF, for multi-fragmentation of the nucleus (minimum energy for this process set to 5 MeV).

As an alternative to using this de-excitation scheme, the user may provide to the G4WilsonAbrasionModel a pointer to her own de-excitation handler, or invoke instantiation of the ablation model (G4WilsonAblationModel).

27.6 De-excitation of the projectile and target nuclear pre-fragments by nuclear ablation

A nuclear ablation model, based largely on the description provided by Wilson *et al* [1], has been developed to provide a better approximation for the final nuclear fragment from an abrasion interaction. The algorithm implemented in G4WilsonAblationModel uses the same approach for selecting the final-state nucleus as NUCFRG2 and determining the particles evaporated from the pre-fragment in order to achieve that state. However, use is also made of classes in Geant4's evaporation physics to determine the energies of the nuclear fragments produced.

The number of nucleons ablated from the nuclear pre-fragment (whether as nucleons or light nuclear fragments) is determined based on the average binding energy, assumed by Wilson *et al* to be 10 MeV, *i.e.*:

$$A_{abl} = \begin{cases} Int\left(\frac{E_x}{10MeV}\right) & : A_{PF} > Int\left(\frac{E_x}{10MeV}\right) \\ A_{PF} & : otherwise \end{cases} \qquad (27.23)$$

Obviously, the nucleon number of the final fragment, A_F, is then determined by the number of remaining nucleons. The proton number of the final nuclear fragment (Z_F) is sampled stochastically using the Rudstam equation:

$$\sigma(A_F, Z_F) \propto \exp\left(-R\left|Z_F - SA_F - TA_F^2\right|^{3\!/2}\right) \qquad (27.24)$$

Here R=11.8/$AF^{0.45}$, S=0.486, and T=3.8·10^{-4}. Once Z_F and A_F have been calculated, the species of the ablated (evaporated) particles are determined again using Wilson's algorithm. The number of α-particles is determined first, on the basis that these have the greatest binding energy:

$$N_\alpha = \begin{cases} Int\left(\frac{Z_{abl}}{2}\right) & : Int\left(\frac{Z_{abl}}{2}\right) < Int\left(\frac{A_{abl}}{4}\right) \\ Int\left(\frac{A_{abl}}{4}\right) & : Int\left(\frac{Z_{abl}}{2}\right) \geq Int\left(\frac{A_{abl}}{4}\right) \end{cases} \qquad (27.25)$$

Calculation of the other ablated nuclear/nucleon species is determined in a similar fashion in order of decreasing binding energy per nucleon of the ablated fragment, and subject to conservation of charge and nucleon number. Once the ablated particle species are determined, use is made of the Geant4 evaporation classes to sample the order in which the particles are ejected (from G4AlphaEvaporationProbability, G4He3EvaporationProbability, G4TritonEvaporationProb G4DeuteronEvaporationProbability, G4ProtonEvaporationProbability and G4NeutronEvaporatio

and the energies and momenta of the evaporated particle and the residual nucleus at each two-body decay (using G4AlphaEvaporationChannel, G4He3EvaporationChannel, G4TritonEvaporationChannel, G4DeuteronEvaporationChannel, G4ProtonEvaporationChannel and G4NeutronEvaporationChannel). If at any stage the probability for evaporation of any of the particles selected by the ablation process is zero, the evaporation is forced, but no significant momentum is imparted to the particle/nucleus. Note, however, that any particles ejected from the projectile will be Lorentz boosted depending upon the initial energy per nucleon of the projectile.

27.7 Definition of the functions P and F used in the abrasion model

In the first instance, the form of the functions P and F used in the abrasion model are dependent upon the relative radii of the projectile and target and the distance of closest approach of the nuclear centres. Four radius condtions are treated.

$r_T > r_P$ **and** $r_T - r_P \leq r \leq r_T + r_P$:

$$P = 0.125\sqrt{\mu\nu}\left(\frac{1}{\mu} - 2\right)\left(\frac{1-\beta}{\nu}\right)^2 - 0.125\left[0.5\sqrt{\mu\nu}\left(\frac{1}{\mu} - 2\right) + 1\right]\left(\frac{1-\beta}{\nu}\right)^3 \tag{27.26}$$

$$F = 0.75\sqrt{\mu\nu}\left(\frac{1-\beta}{\nu}\right)^2 - 0.125\left[3\sqrt{\mu\nu} - 1\right]\left(\frac{1-\beta}{\nu}\right)^3 \tag{27.27}$$

where:

$$\nu = \frac{r_P}{r_P + r_T} \tag{27.28}$$

$$\beta = \frac{r}{r_P + r_T} \tag{27.29}$$

$$\mu = \frac{r_T}{r_P} \tag{27.30}$$

$r_T > r_P$ **and** $r < r_T - r_P$:

$$P = -1 \tag{27.31}$$

456

$$F = 1 \tag{27.32}$$

$\underline{r_P > r_T \text{ and } r_P - r_T \leq r \leq r_P + r_T}$:

$$P = 0.125\sqrt{\mu\nu}\left(\frac{1}{\mu} - 2\right)\left(\frac{1-\beta}{\nu}\right)^2 \tag{27.33}$$

$$- 0.125\left\{0.5\sqrt{\frac{\nu}{\mu}}\left(\frac{1}{\mu} - 2\right) - \left[\frac{\sqrt{1-\mu^2}}{\nu} - 1\right]\sqrt{\frac{2-\mu}{\mu^5}}\right\}\left(\frac{1-\beta}{\nu}\right)^3$$

$$F = 0.75\sqrt{\mu\nu}\left(\frac{1-\beta}{\nu}\right)^2 \tag{27.34}$$

$$- 0.125\left[3\sqrt{\frac{\nu}{\mu}} - \frac{\left[1 - (1-\mu^2)^{3/2}\right]\sqrt{1-(1-\mu)^2}}{\mu^3}\right]\left(\frac{1-\beta}{\nu}\right)^3$$

$\underline{r_P > r_T \text{ and } r < r_T - r_P}$:

$$P = \left[\frac{\sqrt{1-\mu^2}}{\nu} - 1\right]\sqrt{1 - \left(\frac{\beta}{\nu}\right)^2} \tag{27.35}$$

$$F = \left[1 - (1-\mu^2)^{3/2}\right]\sqrt{1 - \left(\frac{\beta}{\nu}\right)^2} \tag{27.36}$$

27.8 Status of this document

18.06.04 created by Peter Truscott

Bibliography

[1] J W Wilson, R K Tripathi, F A Cucinotta, J K Shinn, F F Badavi, S Y Chun, J W Norbury, C J Zeitlin, L Heilbronn, and J Miller, "NUCFRG2: An evaluation of the semiempirical nuclear fragmentation database," NASA Technical Paper 3533, 1995.
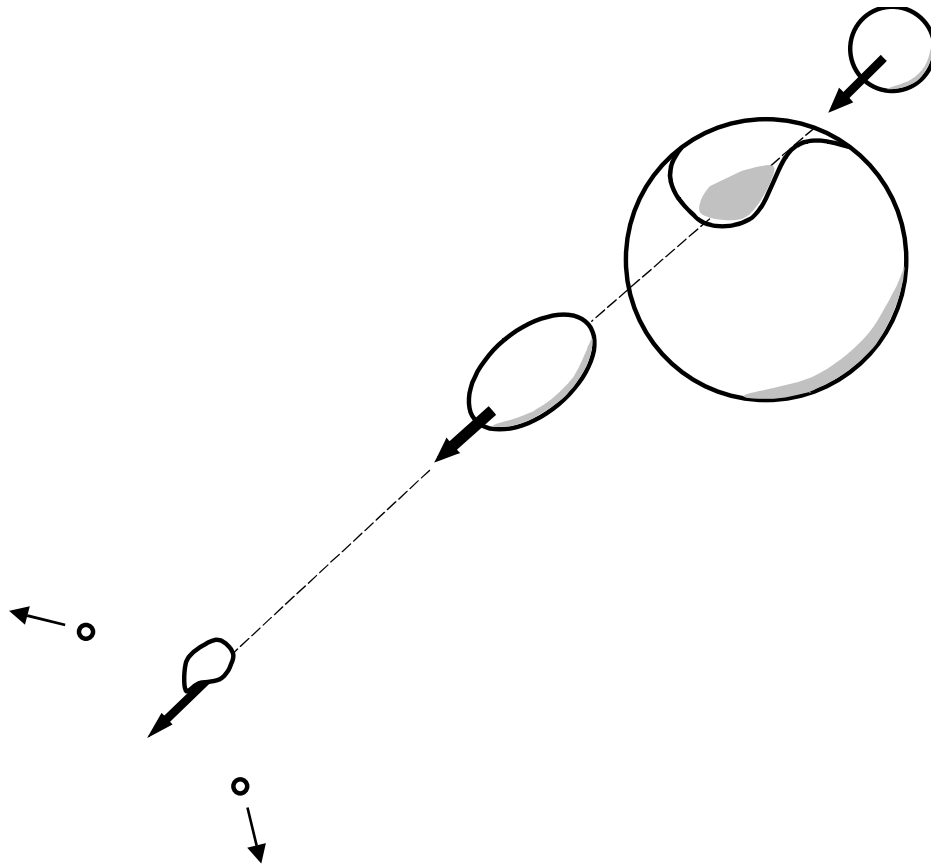
Figure 27.1: In the abrasion process, a fraction of the nucleons in the projectile and target nucleons interact to form a fireball region with a velocity between that of the projectile and the target. The remaining spectator nucleons in the projectile and target are not initially affected (although they do suffer change as a result of longer-term de-excitation).
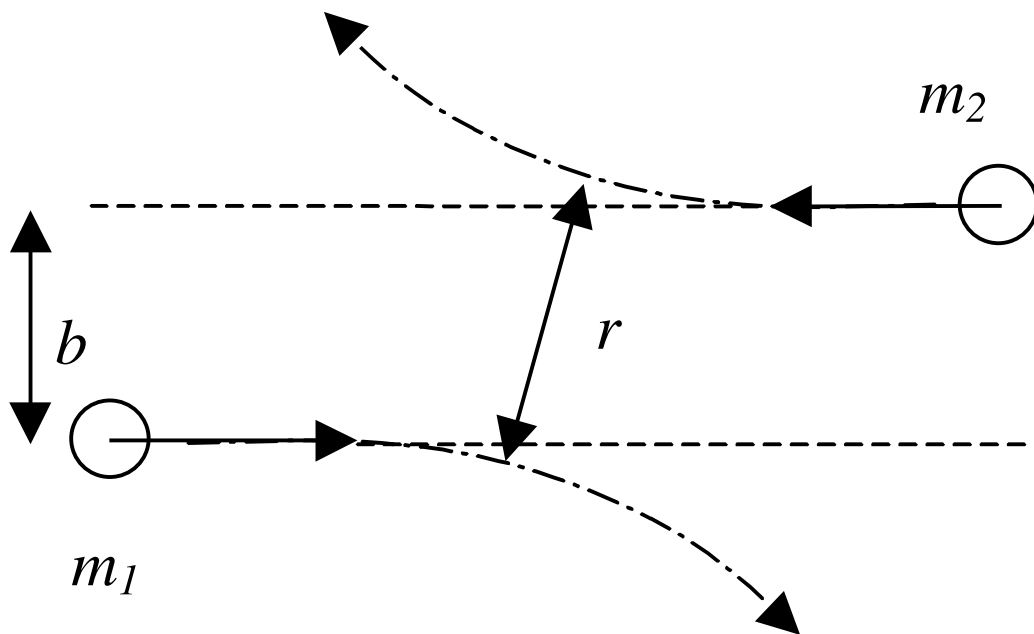
Figure 27.2: Illustration clarifying impact parameter in the far-field (b) and actual impact parameter (r).

[2] Lawrence W Townsend, John W Wilson, Ram K Tripathi, John W Norbury, Francis F Badavi, and Ferdou Khan, "HZEFRG1, An energy-dependent semiempirical nuclear fragmentation model," NASA Technical Paper 3310, 1993.

[3] Francis A Cucinotta, "Multiple-scattering model for inclusive proton production in heavy ion collisions," NASA Technical Paper 3470, 1994.

Chapter 28

Electromagnetic Dissociation Model

28.1 The Model

The relative motion of a projectile nucleus travelling at relativistic speeds with respect to another nucleus can give rise to an increasingly hard spectrum of virtual photons. The excitation energy associated with this energy exchange can result in the liberation of nucleons or heavier nuclei (*i.e.* deuterons, α-particles, *etc.*). The contribution of this source to the total inelastic cross section can be important, especially where the proton number of the nucleus is large. The electromagnetic dissociation (ED) model is implemented in the classes G4EMDissociation, G4EMDissociationCrossSection and G4EMDissociationSpectrum, with the theory taken from Wilson *et al* [1], and Bertulani and Baur [2].

The number of virtual photons $N(E_\gamma, b)$ per unit area and energy interval experienced by the projectile due to the dipole field of the target is given by the expression [2]:

$$N\left(E_\gamma, b\right) = \frac{\alpha Z_T^2}{\pi^2 \beta^2 b^2 E_\gamma} \left\{ x^2 k_1^2(x) + \left(\frac{x^2}{\gamma^2}\right) k_0^2(x) \right\} \tag{28.1}$$

where x is a dimensionless quantity defined as:

$$x = \frac{bE_\gamma}{\gamma\beta\hbar c} \tag{28.2}$$

and:

α = fine structure constant
β = ratio of the velocity of the projectile in the laboratory frame to the velocity of light

γ = Lorentz factor for the projectile in the laboratory frame
b = impact parameter
c = speed of light
$\bar{h}$ = quantum constant
E_γ = energy of virtual photon
k_0 and k_1 = zeroth and first order modified Bessel functions of the second kind
Z_T = atomic number of the target nucleus

Integrating Eq. 28.1 over the impact parameter from b_{min} to ∞ produces the virtual photon spectrum for the dipole field of:

$$N_{E1}\left(E_\gamma\right) = \frac{2\alpha Z_T^2}{\pi\beta^2 E_\gamma}\left\{\xi k_0(\xi)k_1(\xi) - \frac{\xi^2\beta^2}{2}\left(k_1^2(\xi) - k_0^2(\xi)\right)\right\} \qquad (28.3)$$

where, according to the algorithm implemented by Wilson *et al* in NUCFRG2 [1]:

$$\xi = \frac{E_\gamma b_{\min}}{\gamma\beta hc}$$

$$b_{\min} = (1 + x_d)b_c + \frac{\pi\alpha_0}{2\gamma}$$

$$\alpha_0 = \frac{Z_P Z_T e^2}{\mu\beta^2 c^2} \qquad (28.4)$$

$$b_c = 1.34\left[A_P^{1/3} + A_T^{1/3} - 0.75\left(A_P^{-1/3} + A_T^{-1/3}\right)\right]$$

and μ is the reduced mass of the projectile/target system, $x_d = 0.25$, and A_P and A_T are the projectile and target nucleon numbers. For the last equation, the units of b_c are fm. Wilson *et al* state that there is an equivalent virtual photon spectrum as a result of the quadrupole field:

$$N_{E2}\left(E_\gamma\right) = \frac{2\alpha Z_T^2}{\pi\beta^4 E_\gamma}\left\{2\left(1 - \beta^2\right)k_1^2(\xi) + \xi\left(2 - \beta^2\right)^2 k_0(\xi)k_1(\xi) - \frac{\xi^2\beta^4}{2}\left(k_1^2(\xi) - k_0^2(\xi)\right)\right\}$$
$$(28.5)$$

The cross section for the interaction of the dipole and quadrupole fields is given by:

$$\sigma_{ED} = \int N_{E1}\left(E_\gamma\right)\sigma_{E1}\left(E_\gamma\right)dE_\gamma + \int N_{E2}\left(E_\gamma\right)\sigma_{E2}\left(E_\gamma\right)dE_\gamma \qquad (28.6)$$

Wilson *et al* assume that $\sigma_{E1}(E_\gamma)$ and $\sigma_{E2}(E_\gamma)$ are sharply peaked at the giant dipole and quadrupole resonance energies:

$$E_{GDR} = \bar{h}c \left[\frac{m^* c^2 R_0^2}{8J} \left(1 + u - \frac{1+\varepsilon+3u}{1+\varepsilon+u}\varepsilon \right) \right]^{-\frac{1}{2}}$$

$$E_{GQR} = \frac{63}{A_P^{1/3}} \tag{28.7}$$

so that the terms for N_{E1} and N_{E2} can be taken out of the integrals in Eq. 28.6 and evaluated at the resonances.

In Eq. 28.7:

$$u = \frac{3J}{Q'} A_P^{-1/3}$$

$$R_0 = r_0 A_P^{1/3} \tag{28.8}$$

$\epsilon = 0.0768$, $Q' = 17\text{MeV}$, $J = 36.8\text{MeV}$, $r_0 = 1.18\text{fm}$, and m^* is 7/10 of the nucleon mass (taken as 938.95 MeV/c^2). (The dipole and quadrupole energies are expressed in units of MeV.)

The photonuclear cross sections for the dipole and quadrupole resonances are assumed to be given by:

$$\int \sigma_{E1}(E_\gamma)\, dE_\gamma = 60\frac{N_P Z_P}{A_P} \tag{28.9}$$

in units of MeV-mb (N_P being the number of neutrons in the projectile) and:

$$\int \sigma_{E2}(E_\gamma) \frac{dE_\gamma}{E_\gamma^2} = 0.22 f Z_P A_P^{2/3} \tag{28.10}$$

in units of μb/MeV. In the latter expression, f is given by:

$$f = \begin{cases} 0.9 & A_P > 100 \\ 0.6 & 40 < A_P \leq 100 \\ 0.3 & 40 \leq A_P \end{cases} \tag{28.11}$$

The total cross section for electromagnetic dissociation is therefore given by Eq. 28.6 with the virtual photon spectra for the dipole and quadrupole fields calculated at the resonances:

$$\sigma_{ED} = N_{E1}\left(E_{GDR}\right)\int \sigma_{E1}\left(E_\gamma\right)dE_\gamma + N_{E2}\left(E_{GQR}\right)E_{GQR}^2 \int \frac{\sigma_{E2}\left(E_\gamma\right)}{E_\gamma^2}dE_\gamma$$
(28.12)

where the resonance energies are given by Eq. 28.7 and the integrals for the photonuclear cross sections given by Eq. 28.9 and Eq. 28.10.

The selection of proton or neutron emission is made according to the following prescription from Wilson *et al.*

$$\sigma_{ED,p} = \sigma_{ED} \times \begin{cases} 0.5 & Z_P < 6 \\ 0.6 & 6 \le Z_P \le 8 \\ 0.7 & 8 < Z_P < 14 \\ \min\left[\frac{Z_P}{A_P}, 1.95\exp(-0.075Z_P)\right] & Z_P \ge 14 \end{cases}$$

$$\sigma_{ED,n} = \sigma_{ED} - \sigma_{ED,p}$$

(28.13)

Note that this implementation of ED interactions only treats the ejection of single nucleons from the nucleus, and currently does not allow emission of other light nuclear fragments.

28.2   Status of this document

19.06.04 created by Peter Truscott

Bibliography

[1] J. W. Wilson, R. K. Tripathi, F. A. Cucinotta, J. K. Shinn, F. F. Badavi, S. Y. Chun, J. W. Norbury, C. J. Zeitlin, L. Heilbronn, and J. Miller, "NUCFRG2: An evaluation of the semiempirical nuclear fragmentation database," NASA Technical Paper 3533, 1995.

[2] C. A. Bertulani, and G. Baur, Electromagnetic processes in relativistic heavy ion collisions, Nucl Phys, A458, 725-744, 1986.

Chapter 29

Precompound model.

29.1 Reaction initial state.

The GEANT4 precompound model is considered as an extension of the hadron kinetic model. It gives a possibility to extend the low energy range of the hadron kinetic model for nucleon-nucleus inelastic collision and it provides a "smooth" transition from kinetic stage of reaction described by the hadron kinetic model to the equilibrium stage of reaction described by the equilibrium deexcitation models.

The initial information for calculation of pre-compound nuclear stage consists from the atomic mass number A, charge Z of residual nucleus, its four momentum P_0, excitation energy U and number of excitons n equals the sum of number of particles p (from them p_Z are charged) and number of holes h.

At the preequilibrium stage of reaction, we following the [1] approach, take into account all possible nuclear transition the number of excitons n with $\Delta n = +2, -2, 0$ [1], which defined by transition probabilities. Only emmision of neutrons, protons, deutrons, thritium and helium nuclei are taken into account.

29.2 Simulation of pre-compound reaction

The precompound stage of nuclear reaction is considered until nuclear system is not an equilibrium state. Further emission of nuclear fragments or photons from excited nucleus is simulated using an equilibrium model.

29.2.1 Statistical equilibrium condition

In the state of statistical equilibrium, which is characterized by an eqlibrium number of excitons n_{eq}, all three type of transitions are equiprobable. Thus n_{eq} is fixed by $\omega_{+2}(n_{eq}, U) = \omega_{-2}(n_{eq}, U)$. From this condition we can get

$$n_{eq} = \sqrt{2gU}. \tag{29.1}$$

29.2.2 Level density of excited (n-exciton) states

To obtain Eq. (29.1) it was assumed an equidistant scheme of single-particle levels with the density $g \approx 0.595aA$, where a is the level density parameter, when we have the level density of the n-exciton state as

$$\rho_n(U) = \frac{g(gU)^{n-1}}{p!h!(n-1)!}. \tag{29.2}$$

29.2.3 Transition probabilities

The partial transition probabilities changing the exciton number by Δn is determined by the squared matrix element averaged over allowed transitions $<|M|^2>$ and the density of final states $\rho_{\Delta n}(n, U)$, which are really accessible in this transition. It can be defined as following:

$$\omega_{\Delta n}(n, U) = \frac{2\pi}{h} <|M|^2> \rho_{\Delta n}(n, U). \tag{29.3}$$

The density of final states $\rho_{\Delta n}(n, U)$ were derived in paper [2] using the Eq. (29.2) for the level density of the n-exciton state and later corrected for the Pauli principle and indistinguishability of identical excitons in paper [3]:

$$\rho_{\Delta n=+2}(n, U) = \frac{1}{2}g\frac{[gU - F(p+1, h+1)]^2}{n+1}[\frac{gU - F(p+1, h+1)}{gU - F(p, h)}]^{n-1}, \tag{29.4}$$

$$\rho_{\Delta n=0}(n, U) = \frac{1}{2}g\frac{[gU - F(p, h)]}{n}[p(p-1) + 4ph + h(h-1)] \tag{29.5}$$

and

$$\rho_{\Delta n=-2}(n, U) = \frac{1}{2}gph(n-2), \tag{29.6}$$

where $F(p, h) = (p^2 + h^2 + p - h)/4 - h/2$ and it was taken to be equal zero. To avoid calculation of the averaged squared matrix element $<|M|^2>$ it was assumed [1] that transition probability $\omega_{\Delta n=+2}(n, U)$ is the same as the

probability for quasi-free scattering of a nucleon above the Fermi level on a nucleon of the target nucleus, i. e.

$$\omega_{\Delta n=+2}(n, U) = \frac{< \sigma(v_{rel})v_{rel} >}{V_{int}}. \tag{29.7}$$

In Eq. (29.7) the interaction volume is estimated as $V_{int} = \frac{4}{3}\pi(2r_c + \lambda/2\pi)^3$, with the De Broglie wave length $\lambda/2\pi$ corresponding to the relative velocity $< v_{rel} >= \sqrt{2T_{rel}/m}$, where m is nucleon mass and $r_c = 0.6$ fm.

The averaging in $< \sigma(v_{rel})v_{rel} >$ is further simplified by

$$< \sigma(v_{rel})v_{rel} >=< \sigma(v_{rel}) >< v_{rel} > . \tag{29.8}$$

For $\sigma(v_{rel})$ we take approximation:

$$\sigma(v_{rel}) = 0.5[\sigma_{pp}(v_{rel}) + \sigma_{pn}(v_{rel}]P(T_F/T_{rel}), \tag{29.9}$$

where factor $P(T_F/T_{rel})$ was introduced to take into account the Pauli principle. It is given by

$$P(T_F/T_{rel}) = 1 - \frac{7}{5}\frac{T_F}{T_{rel}} \tag{29.10}$$

for $\frac{T_F}{T_{rel}} \leq 0.5$ and

$$P(T_F/T_{rel}) = 1 - \frac{7}{5}\frac{T_F}{T_{rel}} + \frac{2}{5}\frac{T_F}{T_{rel}}(2 - \frac{T_{rel}}{T_F})^{5/2} \tag{29.11}$$

for $\frac{T_F}{T_{rel}} > 0.5$.

The free-particle proton-proton $\sigma_{pp}(v_{rel})$ and proton-neutron $\sigma_{pn}(v_{rel})$ interaction cross sections are estimated using the equations [4]:

$$\sigma_{pp}(v_{rel}) = \frac{10.63}{v_{rel}^2} - \frac{29.93}{v_{rel}} + 42.9 \tag{29.12}$$

and

$$\sigma_{pn}(v_{rel}) = \frac{34.10}{v_{rel}^2} - \frac{82.2}{v_{rel}} + 82.2, \tag{29.13}$$

where cross sections are given in mbarn.

The mean relative kinetic energy T_{rel} is needed to calculate $< v_{rel} >$ and the factor $P(T_F/T_{rel})$ was computed as $T_{rel} = T_p + T_n$, where mean kinetic energies of projectile nucleons $T_p = T_F + U/n$ and target nucleons $T_N = 3T_F/5$, respecively.

Combining Eqs. (29.3) - (29.7) and assuming that $< |M|^2 >$ are the same for transitions with $\Delta n = 0$ and $\Delta n = \pm 2$ we obtain for another transition probabilities:

$$\omega_{\Delta n=0}(n, U) =$$
$$= \frac{<\sigma(v_{rel})v_{rel}>}{V_{int}} \frac{n+1}{n} \left[\frac{gU-F(p,h)}{gU-F(p+1,h+1)}\right]^{n+1} \frac{p(p-1)+4ph+h(h-1)}{gU-F(p,h)} \tag{29.14}$$

and

$$\omega_{\Delta n=-2}(n, U) =$$
$$= \frac{<\sigma(v_{rel})v_{rel}>}{V_{int}} \left[\frac{gU-F(p,h)}{gU-F(p+1,h+1)}\right]^{n+1} \frac{ph(n+1)(n-2)}{[gU-F(p,h)]^2}. \tag{29.15}$$

29.2.4 Emission probabilities for nucleons

Emission process probability has been choosen similar as in the classical equilibrium Weisskopf-Ewing model [5]. Probability to emit nucleon b in the energy interval $(T_b, T_b + dT_b)$ is given

$$W_b(n, U, T_b) = \sigma_b(T_b) \frac{(2s_b + 1)\mu_b}{\pi^2 h^3} R_b(p, h) \frac{\rho_{n-b}(E^*)}{\rho_n(U)} T_b, \tag{29.16}$$

where $\sigma_b(T_b)$ is the inverse (absorption of nucleon b) reaction cross section, s_b and m_b are nucleon spin and reduced mass, the factor $R_b(p, h)$ takes into account the condition for the exciton to be a proton or neutron, $\rho_{n-b}(E^*)$ and $\rho_n(U)$ are level densities of nucleus after and before nucleon emission are defined in the evaporation model, respectively and $E^* = U - Q_b - T_b$ is the excitation energy of nucleus after fragment emission.

29.2.5 Emission probabilities for complex fragments

It was assumed [1] that nucleons inside excited nucleus are able to "condense" forming complex fragment. The "condensation" probability to create fragment consisting from N_b nucleons inside nucleus with A nucleons is given by

$$\gamma_{N_b} = N_b^3 (V_b/V)^{N_b-1} = N_b^3 (N_b/A)^{N_b-1}, \tag{29.17}$$

where V_b and V are fragment b and nucleus volumes, respectively. The last equation was estimated [1] as the overlap integral of (constant inside a volume) wave function of independent nucleons with that of the fragment.

During the prequilibrium stage a "condense" fragment can be emitted. The probability to emit a fragment can be written as [1]

$$W_b(n, U, T_b) = \gamma_{N_b} R_b(p, h) \frac{\rho(N_b, 0, T_b + Q_b)}{g_b(T_b)} \sigma_b(T_b) \frac{(2s_b + 1)\mu_b}{\pi^2 h^3} \frac{\rho_{n-b}(E^*)}{\rho_n(U)} T_b, \tag{29.18}$$

where

$$g_b(T_b) = \frac{V_b(2s_b + 1)(2\mu_b)^{3/2}}{4\pi^2 h^3}(T_b + Q_b)^{1/2} \qquad (29.19)$$

is the single-particle density for complex fragment b, which is obtained by assuming that complex fragment moves inside volume V_b in the uniform potential well whose depth is equal to be Q_b, and the factor $R_b(p, h)$ garantees correct isotopic composition of a fragment b.

29.2.6 The total probability

This probability is defined as

$$W_{tot}(n, U) = \sum_{\Delta n=+2,0,-2} \omega_{\Delta n}(n, U) + \sum_{b=1}^{6} W_b(n, U), \qquad (29.20)$$

where total emission $W_b(n, U)$ probabilities to emit fragment b can be obtained from Eqs. (29.16) and (29.18) by integration over T_b:

$$W_b(n, U) = \int_{V_b}^{U-Q_b} W_b(n, U, T_b)dT_b. \qquad (29.21)$$

29.2.7 Calculation of kinetic energies for emitted particle

The equations (29.16) and (29.18) are used to sample kinetic energies of emitted fragment.

29.2.8 Parameters of residual nucleus.

After fragment emission we update parameter of decaying nucleus:

$$\begin{aligned} A_f &= A - A_b; Z_f = Z - Z_b; P_f = P_0 - p_b; \\ E_f^* &= \sqrt{E_f^2 - \vec{P}_f^2} - M(A_f, Z_f). \end{aligned} \qquad (29.22)$$

Here p_b is the evaporated fragment four momentum.

29.3 Status of this document

00.00.00 created by Vicente Lara

Bibliography

[1] K.K. Gudima, S.G. Mashnik, V.D. Toneev, Nucl. Phys. **A401** 329 (1983).

[2] F. C. Williams, Phys. Lett. **B31** 180 (1970).

[3] I. Ribanský, P. Obložinský, E. Bétaǩ, Nucl. Phys. **A205** 545 (1973).

[4] N. Metropolis *et al.*, Phys. Rev. **100** 185 (1958).

[5] V.E. Weisskopf, D.H. Ewing, Phys. Rev. 57 472 (1940).

Chapter 30

Evaporation Model

30.1   Introduction.

At the end of the pre-equilibrium stage, or a thermalizing process, the
residual nucleus is supposed to be left in an equilibrium state, in which the
excitation energy E^* is shared by a large number of nucleons. Such an equili-
brated compound nucleus is characterized by its mass, charge and excitation
energy with no further memory of the steps which led to its formation. If
the excitation energy is higher than the separation energy, it can still eject
nucleons and light fragments (d, t, ^{3}He, α). These constitute the low energy
and most abundant part of the emitted particles in the rest system of the
residual nucleus. The emission of particles by an excited compound nucleus
has been successfully described by comparing the nucleus with the evapora-
tion of molecules from a fluid [1]. The first statistical theory of compound
nuclear decay is due to Weisskopf and Ewing[2].

30.2   Model description.

The Weisskopf treatment is an application of the detailed balance principle
that relates the probabilities to go from a state i to another d and viceversa
through the density of states in the two systems:

$$P_{i \to d}\rho(i) = P_{d \to i}\rho(d) \tag{30.1}$$

where $P_{d \to i}$ is the probability per unit of time of a nucleus d captures a particle
j and form a compound nucleus i which is proportional to the compound
nucleus cross section σ_{inv}. Thus, the probability that a parent nucleus i with
an excitation energy E^* emits a particle j in its ground state with kinetic

energy ε is

$$P_j(\varepsilon)\mathrm{d}\varepsilon = g_j\sigma_{\mathrm{inv}}(\varepsilon)\frac{\rho_d(E_{\max} - \varepsilon)}{\rho_i(E^*)}\varepsilon\mathrm{d}\varepsilon \qquad (30.2)$$

where $\rho_i(E^*)$ is the level density of the evaporating nucleus, $\rho_d(E_{\max}-\varepsilon)$ that of the daugther (residual) nucleus after emission of a fragment j and $E_{\max}$ is the maximum energy that can be carried by the ejectile. With the spin s_j and the mass m_j of the emitted particle, g_j is expressed as $g_j = (2s_j+1)m_j/\pi^2\hbar^2$.

This formula must be implemented with a suitable form for the level density and inverse reaction cross section. We have followed, like many other implementations, the original work of Dostrovsky *et al.* [3] (which represents the first Monte Carlo code for the evaporation process) with slight modifications. The advantage of the Dostrovsky model is that it leds to a simple expression for equation 30.2 that can be analytically integrated and used for Monte Carlo sampling.

30.2.1 Cross sections for inverse reactions.

The cross section for inverse reaction is expressed by means of empirical equation [3]

$$\sigma_{\mathrm{inv}}(\varepsilon) = \sigma_g\alpha\left(1 + \frac{\beta}{\varepsilon}\right) \qquad (30.3)$$

where $\sigma_g = \pi R^2$ is the geometric cross section.

In the case of neutrons, $\alpha = 0.76 + 2.2A^{-\frac{1}{3}}$ and $\beta = (2.12A^{-\frac{2}{3}} - 0.050)/\alpha$ MeV. This equation gives a good agreement to those calculated from continuum theory [4] for intermediate nuclei down to $\varepsilon \sim 0.05$ MeV. For lower energies $\sigma_{\mathrm{inv},n}(\varepsilon)$ tends toward infinity, but this causes no difficulty because only the product $\sigma_{\mathrm{inv},n}(\varepsilon)\varepsilon$ enters in equation 30.2. It should be noted, that the inverse cross section needed in 30.2 is that between a neutron of kinetic energy ε and a nucleus in an excited state.

For charged particles (p, d, t, ^{3}He and α), $\alpha = (1 + c_j)$ and $\beta = -V_j$, where c_j is a set of parameters calculated by Shapiro [5] in order to provide a good fit to the continuum theory [4] cross sections and V_j is the Coulomb barrier.

30.2.2 Coulomb barriers.

Coulomb repulsion, as calculated from elementary electrostatics are not directly applicable to the computation of reaction barriers but must be corrected in several ways. The first correction is for the quantum mechanical

phenomenoon of barrier penetration. The proper quantum mechanical expressions for barrier penetration are far too complex to be used if one wishes to retain equation 30.2 in an integrable form. This can be approximately taken into account by multiplying the electrostatic Coulomb barrier by a coefficient k_j designed to reproduce the barrier penetration approximately whose values are tabulated [5].

$$V_j = k_j \frac{Z_j Z_d e^2}{R_c} \qquad (30.4)$$

The second correction is for the separation of the centers of the nuclei at contact, R_c. We have computed this separation as $R_c = R_j + R_d$ where $R_{j,d} = r_c A_{j,d}^{1/3}$ and r_c is given [6] by

$$r_c = 2.173 \frac{1 + 0.006103 Z_j Z_d}{1 + 0.009443 Z_j Z_d} \qquad (30.5)$$

30.2.3 Level densities.

The simplest and most widely used level density based on the Fermi gas model are those of Weisskopf [7] for a completely degenerate Fermi gas. We use this approach with the corrections for nucleon pairing proposed by Hurwitz and Bethe [8] which takes into account the displacements of the ground state:

$$\rho(E) = C \exp\left(2\sqrt{a(E - \delta)} \right) \qquad (30.6)$$

where C is considered as constant and does not need to be specified since only ratios of level densities enter in equation 30.2. δ is the pairing energy correction of the daughter nucleus evaluated by Cook *et al.* [9] and Gilbert and Cameron [10] for those values not evaluated by Cook *et al.*. The level density parameter is calculated according to:

$$a(E, A, Z) = \tilde{a}(A) \left\{ 1 + \frac{\delta}{E}[1 - \exp(-\gamma E)] \right\} \qquad (30.7)$$

and the parameters calculated by Iljinov *et al.* [11] and shell corrections of Truran, Cameron and Hilf [12].

30.2.4 Maximum energy available for evaporation.

The maximum energy avilable for the evaporation process (*i.e.* the maximum kinetic energy of the outgoing fragment) is usually computed like $E^* - \delta - Q_j$ where is the separation energy of the fragment j: $Q_j =$

$M_i - M_d - M_j$ and M_i, M_d and M_j are the nclear masses of the compound, residual and evporated nuclei respectively. However, that expression does not consider the recoil energy of the residual nucleus. In order to take into account the recoil energy we use the expression

$$\varepsilon_j^{\max} = \frac{(M_i + E^* - \delta)^2 + M_j^2 - M_d^2}{2(M_i + E^* - \delta)} - M_j \tag{30.8}$$

30.2.5 Total decay width.

The total decay width for evaporation of a fragment j can be obtained by integrating equation 30.2 over kinetic energy

$$\Gamma_j = \hbar \int_{V_j}^{\varepsilon_j^{\max}} P(\varepsilon_j) \mathrm{d}\varepsilon_j \tag{30.9}$$

This integration can be performed analiticaly if we use equation 30.6 for level densities and equation 30.3 for inverse reaction cross section. Thus, the total width is given by

$$\Gamma_j = \frac{g_j m_j R_d^2}{2\pi\hbar^2} \frac{\alpha}{a_d^2} \times \left[\left\{ \left(\beta a_d - \frac{3}{2} \right) + a_d(\varepsilon_j^{\max} - V_j) \right\} \exp\left\{ -\sqrt{a_i(E^* - \delta_i)} \right\} + \right.$$

$$\left\{ (2\beta a_d - 3)\sqrt{a_d(\varepsilon_j^{\max} - V_j)} + 2a_d(\varepsilon_j^{\max} - V_j) \right\} \times$$

$$\left. \exp\left\{ 2\left[\sqrt{a_d(\varepsilon_j^{\max} - V_j)} - \sqrt{a_i(E^* - \delta_i)} \right] \right\} \right] \tag{30.10}$$

where $a_d = a(A_d, Z_d, \varepsilon_j^{\max})$ and $a_i = a(A_i, Z_i, E^*)$.

30.3 GEM Model

As an alternative model we have implemented the generalized evaporation model (GEM) by Furihata [13]. This model considers emission of fragments heavier than α particles and uses a more accurate level density function for total decay width instead of the approximation used by Dostrovsky. We use the same set of parameters but for heavy ejectiles the parameters determined by Matsuse *et al.* [14] are used.

Based on the Fermi gas model, the level density function is expressed as

$$\rho(E) = \begin{cases} \frac{\sqrt{\pi}}{12} \frac{e^{2\sqrt{a(E-\delta)}}}{a^{1/4}(E-\delta)^{5/4}} & \text{for} \quad E \geq E_x \\ \frac{1}{T} e^{(E-E_0)/T} & \text{for} \quad E < E_x \end{cases} \tag{30.11}$$

473

where $E_x = U_x + \delta$ and $U_x = 150/M_d + 2.5$ (M_d is the mass of the daughter nucleus). Nuclear temperature T is given as $1/T = \sqrt{a/U_x} - 1.5 U_x$, and E_0 is defined as $E_0 = E_x - T(\log T - \log a/4 - (5/4)\log U_x + 2\sqrt{aU_x})$.

By substituting equation 30.11 into equation 30.2 and integrating over kinetic energy can be obtained the following expression

$$\Gamma_j = \frac{\sqrt{\pi} g_j \pi R_d^2 \alpha}{12 \rho(E^*)} \times \begin{cases} \{I_1(t,t) + (\beta + V)I_0(t)\} & \text{for} \quad \varepsilon_j^{\max} - V_j < E_x \\ \{I_1(t,t_x) + I_3(s,s_x)e^s + & \\ (\beta + V)(I_0(t_x) + I_2(s,s_x)e^s)\} & \text{for} \quad \varepsilon_j^{\max} - V_j \geq E_x. \end{cases}$$
(30.12)

$I_0(t)$, $I_1(t,t_x)$, $I_2(s,s_x)$, and $I_3(s,s_x)$ are expressed as:

$$I_0(t) = e^{-E_0/T}(e^t - 1) \tag{30.13}$$

$$I_1(t,t_x) = e^{-E_0/T}T\{(t - t_x + 1)e^{t_x} - t - 1\} \tag{30.14}$$

$$I_2(s,s_x) = 2\sqrt{2}\Big\{ s^{-3/2} + 1.5 s^{-5/2} + 3.75 s^{-7/2} -$$

$$(s_x^{-3/2} + 1.5 s_x^{-5/2} + 3.75 s_x^{-7/2}) \Big\} \tag{30.15}$$

$$I_3(s,s_x) = \frac{1}{2\sqrt{2}}\Big[2s^{-1/2} + 4s^{-3/2} + 13.5 s^{-5/2} + 60.0 s^{-7/2} +$$

$$325.125 s^{-9/2} - \Big\{ (s^2 - s_x^2)s_x^{-3/2} + (1.5 s^2 + 0.5 s_x^2)s_x^{-5/2} +$$

$$(3.75 s^2 + 0.25 s_x^2)s_x^{-7/2} + (12.875 s^2 + 0.625 s_x^2)s_x^{-9/2} +$$
$$(59.0625 s^2 + 0.9375 s_x^2)s_x^{-11/2} +$$

$$(324.8 s^2 + 3.28 s_x^2)s_x^{-13/2} + \Big\} \Big] \tag{30.16}$$

where $t = (\varepsilon_j^{\max} - V_j)/T$, $t_x = E_x/T$, $s = 2\sqrt{a(\varepsilon_j^{\max} - V_j - \delta_j)}$ and $s_x = 2\sqrt{a(E_x - \delta)}$.

Besides light fragments, 60 nuclides up to ^{28}Mg are considered, not only in their ground states but also in their exited states, are considered. The excited state is assumed to survive if its lifetime $T_{1/2}$ is longer than the decay time, i. e., $T_{1/2}/\ln 2 > \hbar/\Gamma_j^*$, where Γ_j^* is the emission width of the resonance calculated in the same manner as for ground state particle emission. The total emission width of an ejectile j is summed over its ground state and all its excited states which satisfy the above condition.

30.4 Fission probability calculation.

The fission decay channel (only for nuclei with $A > 65$) is taken into account as a competitor for fragment and photon evaporation channels.

30.4.1 The fission total probability.

The fission probability (per unit time) W_{fis} in the Bohr and Wheeler theory of fission [15] is proportional to the level density $\rho_{fis}(T)$ (approximation Eq. (30.6) is used) at the saddle point, i.e.

$$W_{fis} = \frac{1}{2\pi\hbar\rho_{fis}(E^*)} \int_0^{E^*-B_{fis}} \rho_{fis}(E^* - B_{fis} - T)dT =$$
$$= \frac{1 + (C_f - 1)\exp{(C_f)}}{4\pi a_{fis}\exp{(2\sqrt{aE^*})}}, \qquad (30.17)$$

where B_{fis} is the fission barrier height. The value of $C_f = 2\sqrt{a_{fis}(E^* - B_{fis})}$ and a, a_{fis} are the level density parameters of the compound and of the fission saddle point nuclei, respectively.

The value of the level density parameter is large at the saddle point, when excitation energy is given by initial excitation energy minus the fission barrier height, than in the ground state, i. e. $a_{fis} > a$. $a_{fis} = 1.08a$ for $Z < 85$, $a_{fis} = 1.04a$ for $Z \geq 89$ and $a_f = a[1.04 + 0.01(89. - Z)]$ for $85 \leq Z < 89$ is used.

30.4.2 The fission barrier.

The fission barrier is determined as difference between the saddle-point and ground state masses.

We use simple semiphenomenological approach was suggested by Barashenkov and Gereghi [16]. In their approach fission barrier $B_{fis}(A, Z)$ is approximated by

$$B_{fis} = B_{fis}^0 + \Delta_g + \Delta_p. \qquad (30.18)$$

The fission barrier height $B_{fis}^0(x)$ varies with the fissility parameter $x = Z^2/A$. $B_{fis}^0(x)$ is given by

$$B_{fis}^0(x) = 12.5 + 4.7(33.5 - x)^{0.75} \qquad (30.19)$$

for $x \leq 33.5$ and

$$B_{fis}^0(x) = 12.5 - 2.7(x - 33.5)^{2/3} \qquad (30.20)$$

for $x > 33.5$. The $\Delta_g = \Delta M(N) + \Delta M(Z)$, where $\Delta M(N)$ and $\Delta M(Z)$ are shell corrections for Cameron's liquid drop mass formula [17] and the pairing energy corrections: $\Delta_p = 1$ for odd-odd nuclei, $\Delta_p = 0$ for odd-even nuclei, $\Delta_p = 0.5$ for even-odd nuclei and $\Delta_p = -0.5$ for even-even nuclei.

30.5 The Total Probability for Photon Evaporation

As the first approximation we assume that dipole $E1$–transitions is the main source of γ–quanta from highly–excited nuclei [11]. The probability to evaporate γ in the energy interval $(\epsilon_\gamma, \epsilon_\gamma + d\epsilon_\gamma)$ per unit of time is given

$$W_\gamma(\epsilon_\gamma) = \frac{1}{\pi^2(\hbar c)^3}\sigma_\gamma(\epsilon_\gamma)\frac{\rho(E^* - \epsilon_\gamma)}{\rho(E^*)}\epsilon_\gamma^2, \qquad (30.21)$$

where $\sigma_\gamma(\epsilon_\gamma)$ is the inverse (absorption of γ) reaction cross section, ρ is a nucleus level density is defined by Eq. (30.6).

The photoabsorption reaction cross section is given by the expression

$$\sigma_\gamma(\epsilon_\gamma) = \frac{\sigma_0\epsilon_\gamma^2\Gamma_R^2}{(\epsilon_\gamma^2 - E_{GDP}^2)^2 + \Gamma_R^2\epsilon_\gamma^2}, \qquad (30.22)$$

where $\sigma_0 = 2.5A$ mb, $\Gamma_R = 0.3E_{GDP}$ and $E_{GDP} = 40.3A^{-1/5}$ MeV are empirical parameters of the giant dipole resonance [11]. The total radiation probability is

$$W_\gamma = \frac{3}{\pi^2(\hbar c)^3}\int_0^{E^*}\sigma_\gamma(\epsilon_\gamma)\frac{\rho(E^* - \epsilon_\gamma)}{\rho(E^*)}\epsilon_\gamma^2 d\epsilon_\gamma. \qquad (30.23)$$

The integration is performed numericaly.

30.5.1 Energy of evaporated photon

The energy of γ-quantum is sampled according to the Eq. (30.21) distribution.

30.6 Discrete photon evaporation

The last step of evaporation cascade consists of evaporation of photons with discrete energies. The competition between photons and fragments as well as giant resonance photons is neglected at this step. We consider the discrete E1, M1 and E2 photon transitions from tabulated isotopes. There are large number of isotopes [18] with the experimentally measured exited level energies, spins, parities and relative transitions probabilities. This information is implemented in the code.

30.7 Internal conversion electron emission

An important conpetitive channel to photon emission is internal conversion. To take this into account, the photon evaporation data-base was entended to include internal conversion ceffficients.

The above constitute the first six columns of data in the photon evaporation files. The new version of the data base adds eleven new columns corresponding to:

7. ratio of internal conversion to gamma-ray emmission probability

8. - 17. internal conversion coefficients for shells K, L1, L2, L3, M1, M2, M3, M4, M5 and N+ respectively. These coefficients are normalised to 1.0

The calculation of the Internal Conversion Coefficients (ICCs) is done by a cubic spline interpolation of tabulalted data for the corresponding transition energy. These ICC tables, which we shall label Band [19], Rösel [20] and Hager-Seltzer [21], are widely used and were provided in electronic format by staff at LBNL. The reliability of these tabulated data has been reviewed in Ref. [22]. From tests carried out on these data we find that the ICCs calculated from all three tables are comparable within a 10% uncertainty, which is better than what experimetal measurements are reported to be able to achive.

The range in atomic number covered by these tables is Band: $1 <= Z <= 80$; Rösel: $30 <= Z <= 104$ and Hager-Seltzer: $3, 6, 10, 14 <= Z <= 103$. For simplicity and taking into account the completeness of the tables, we have used the Band table for $Z <= 80$ and Rösel for $81 <= Z <= 98$.

The Band table provides a higher resolution of the ICC curves used in the interpolation and covers ten multipolarities for all elements up to $Z = 80$, but it only includes ICCs for shells up to M5. In order to calculate the ICC of the N+ shell, the ICCs of all available M shells are added together and the total divided by 3. This is the scheme adopted in the LBNL ICC calculation code when using the Band table. The Rösel table includes ICCs for all shells in every atom and for $Z > 80$ the N+ shell ICC is calculated by adding together the ICCs of all shells above M5. In this table only eight multipolarities have ICCs calculated for.

30.7.1 Multipolarity

The ENSDF data provides information on the multipolarity of the transition. The ICCs included in the photon evaporation data base refer to the multipolarity indicated in the ENSDF file for that transition. Only one type of

mixed mulltipolarity is considered (M1+E2) and whenever the mixing ratio is provided in the ENSDF file, it is used to calculate the ICCs corresponding to the mixed multipolarity according the the formula:

- fraction in $M1 = 1/(1 + \delta^2)$
- fraction in $E2 = \delta^2/(1 + \delta^2)$

where δ is the mixing ratio.

30.7.2 Binding energy

For the production of an internal conversion electron, the energy of the transition must be at least the binding energy of the shell the electron is being released from. The binding energy corresponding to the various shells in all isotopes used in the ICC calculation has been taken from the Geant4 file G4AtomicShells.hh.

30.7.3 Isotopes

The list of isotopes included in the photon evaporation data base has been extended from $A <= 240$ to $A <= 250$. The highest atomic number included is $Z = 98$ (this ensures that Americium sources can now be simulated).

Bibliography

[1] I. Frenkel. *Sov. Phys.* **9** 533 (1936).

[2] V. E. Weisskopf and D. H. Ewing. *Phys. Rev.* **57** 472 (1940).

[3] I. Dostrovsky, Z. Fraenkel, G. Friedlander. *Phys. Rev.* **116** 683 (1959).

[4] J. Blatt and V. F. Weisskopf, *Theoretical Nuclear Physics* (John Wiley & Sons, Inc., New York, 1952)

[5] M. M. Shapiro. *Phys. Rev.* **90**, 171 (1953).

[6] A. S. Iljinov, M. V. Kazarnovsky and E. Ya. Paryev. *Intermediate–Energy Nuclear Physics* (CRC Press, 1994).

[7] V. F. Weisskopf. *Phys. Rev.* **52**, 295 (1937)

[8] H. Hurwitz and H. A. Bethe. *Phys. Rev.* **81**, (1951)

[9] J.L. Cook, H. Ferguson and A. R. L. Musgrove. *Aust. J. Phys.*, **20**, 477 (1967)

[10] A. Gilbert and A.G.W. Cameron, *Can. J. Phys.*, **43**, 1446 (1965)

[11] A. S. Iljinov, M. V. Mevel *et al.. Nucl. Phys.* **A543**, 517 (1992).

[12] J. W. Truran, A. G. W. Cameron, and E. Hilf. *Proc. Int. Conf. on the Properties of Nuclei Far From the Beta-Stability* Leysin, Switzerland, August 31 - September 4, 1970, Vol.1, p. 275

[13] S. Furihata. *Nucl. Instr. and Meth. in Phys. Res.* **B171**, 251 (2000)

[14] T. Matsuse, A. Arima, and S. M. Lee. *Phys. Rev. C* **26**, 2338 (1982)

[15] Bohr N., Wheeler J. W., Phys. Rev., **56** 426 (1939).

[16] Barashenkov V. S., Iljinov A. S., Toneev V. D., Gereghi F. G, Nucl. Phys. **A206** 131 (1973).

[17] Cameron A. G. W. Canad. J. Phys., **35** 1021 (1957), **36** 1040 (1958).

[18] Evaluated Nuclear Structure Data File (ENSDF) - a computer file of evaluated experimental nuclear structure data maintained by the National Nuclear Data Center, Brookhaven National Laboratory (http://www.nndc.bnl.gov/nndc/nudat/).

[19] I.M. Band and M.B. Trzhaskovskaya, Tables of the Gamma-ray Internal Conversion Coefficients for the K, L, M Shells, for $1 <= Z <= 80$, Leningrad: Nuclear Physics Institute (1978).

[20] F. Rösel, H.M. Fries, K. Alder and H.C. Pauli, At. Data Nucl. Data Tables 21 (1978).

[21] R.S. Hager and E.C. Seltzer, Nucl. Data A4 (1968).

[22] M. Rysavy and O. Dragoun, On the Reliability of the Theoretical Internal Conversion Coefficients, J. Phys. G: Nucl. Part. Phys., 2000, v.26, N. 12, pp 1859-72.

Chapter 31

Fission model.

31.1 Reaction initial state.

The GEANT4 fission model is capable to predict final excited fragments as result of an excited nucleus symmetric or asymmetric fission. The fission process (only for nuclei with atomic number $A \geq 65$) is considered as a competitor for evaporation process, when nucleus transits from an excited state to the ground state. Here we describe the final state generation. The calculation of the relative probability of fission with respect to the evaporation channels are described in the chapter concerning evaporation.

The initial information for calculation of fission decay consists from the atomic mass number A, charge Z of excited nucleus, its four momentum P_0 and excitation energy U.

31.2 Fission process simulation.

31.2.1 Atomic number distribution of fission products.

As follows from experimental data [1] mass distribution of fission products consists of the symmetric and the asymmetric components:

$$F(A_f) = F_{sym}(A_f) + \omega F_{asym}(A_f), \tag{31.1}$$

where $\omega(U, A, Z)$ defines relative contribution of each component and it depends from excitation energy U and A, Z of fissioning nucleus. It was found in [2] that experimental data can be approximated with a good accuracy, if one take

$$F_{sym}(A_f) = \exp\left[-\frac{(A_f - A_{sym})^2}{2\sigma_{sym}^2}\right] \tag{31.2}$$

and

$$F_{asym}(A_f) = \exp\left[-\frac{(A_f - A_2)^2}{2\sigma_2^2}\right] + \exp\left[-\frac{A_f - (A - A_2)^2}{2\sigma_2^2}\right] +$$
$$+ C_{asym}\left\{\exp\left[-\frac{(A_f - A_1)^2}{2\sigma_1^2}\right] + \exp\left[-\frac{A_f - (A - A_1)^2}{2\sigma_2^2}\right]\right\}, \tag{31.3}$$

where $A_{sym} = A/2$, A_1 and A_2 are the mean values and σ_{sim}^2, σ_1^2 and σ_2^2 are dispersions of the Gaussians respectively. From an analysis of experimental data [2] the parameter $C_{asym} \approx 0.5$ was defined and the next values for dispersions:

$$\sigma_{sym}^2 = \exp\left(0.00553U + 2.1386\right), \tag{31.4}$$

where U in MeV,

$$2\sigma_1 = \sigma_2 = 5.6 \ MeV \tag{31.5}$$

for $A \leq 235$ and

$$2\sigma_1 = \sigma_2 = 5.6 + 0.096(A - 235) \ MeV \tag{31.6}$$

for $A > 235$ were found.

The weight $\omega(U, A, Z)$ was approximated as follows

$$\omega = \frac{\omega_a - F_{asym}(A_{sym})}{1 - \omega_a F_{sym}((A_1 + A_2)/2)}. \tag{31.7}$$

The values of ω_a for nuclei with $96 \geq Z \geq 90$ were approximated by

$$\omega_a(U) = \exp\left(0.538U - 9.9564\right) \tag{31.8}$$

for $U \leq 16.25$ MeV,

$$\omega_a(U) = \exp\left(0.09197U - 2.7003\right) \tag{31.9}$$

for $U > 16.25$ MeV and

$$\omega_a(U) = \exp\left(0.09197U - 1.08808\right) \tag{31.10}$$

for $z = 89$. For nuclei with $Z \leq 88$ the authors of [2] constructed the following approximation:

$$\omega_a(U) = \exp\left[0.3(227 - a)\right] \exp\left\{0.09197[U - (B_{fis} - 7.5)] - 1.08808\right\}, \tag{31.11}$$

where for $A > 227$ and $U < B_{fis} - 7.5$ the corresponding factors occuring in exponential functions vanish.

31.2.2 Charge distribution of fission products.

At given mass of fragment A_f the experimental data [1] on the charge Z_f distribution of fragments are well approximated by Gaussian with dispertion $\sigma_z^2 = 0.36$ and the average $< Z_f >$ is described by expression:

$$< Z_f >= \frac{A_f}{A} Z + \Delta Z, \qquad (31.12)$$

when parameter $\Delta Z = -0.45$ for $A_f \geq 134$, $\Delta Z = -0.45(A_f - A/2)/(134 - A/2)$ for $A - 134 < A_f < 134$ and $\Delta Z = 0.45$ for $A \leq A - 134$.

After sampling of fragment atomic masses numbers and fragment charges, we have to check that fragment ground state masses do not exceed initial energy and calculate the maximal fragment kinetic energy

$$T^{max} < U + M(A, Z) - M_1(A_{f1}, Z_{f1}) - M_2(A_{f2}, Z_{f2}), \qquad (31.13)$$

where U and $M(A, Z)$ are the excitation energy and mass of initial nucleus, $M_1(A_{f1}, Z_{f1})$, and $M_2(A_{f2}, Z_{f2})$ are masses of the first and second fragment, respectively.

31.2.3 Kinetic energy distribution of fission products.

We use the empiricaly defined [3] dependence of the average kinetic energy $< T_{kin} >$ (in MeV) of fission fragments on the mass and the charge of a fissioning nucleus:

$$< T_{kin} >= 0.1178 Z^2/A^{1/3} + 5.8. \qquad (31.14)$$

This energy is distributed differently in cases of symmetric and asymmetric modes of fission. It follows from the analysis of data [2] that in the asymmetric mode, the average kinetic energy of fragments is higher than that in the symmetric one by approximately 12.5 MeV. To approximate the average numbers of kinetic energies $< T_{kin}^{sym}$ and $< T_{kin}^{asym} >$ for the symmetric and asymmetric modes of fission the authors of [2] suggested empirical expressions:

$$< T_{kin}^{sym} >=< T_{kin} > -12.5 W_{asim}, \qquad (31.15)$$

$$< T_{kin}^{asym} >=< T_{kin} > +12.5 W_{sim}, \qquad (31.16)$$

where

$$W_{sim} = \omega \int F_{sim}(A) dA / \int F(A) dA \qquad (31.17)$$

and

$$W_{asim} = \int F_{asim}(A) dA / \int F(A) dA, \qquad (31.18)$$

respectively. In the symmetric fission the experimental data for the ratio of the average kinetic energy of fission fragments $< T_{kin}(A_f) >$ to this maximum energy $< T_{kin}^{max} >$ as a function of the mass of a larger fragment A_{max} can be approximated by expressions

$$< T_{kin}(A_f) > / < T_{kin}^{max} >= 1 - k[(A_f - A_{max})/A]^2 \qquad (31.19)$$

for $A_{sim} \leq A_f \leq A_{max} + 10$ and

$$< T_{kin}(A_f) > / < T_{kin}^{max} >= 1 - k(10/A)^2 - 2(10/A)k(A_f - A_{max} - 10)/A$$
$$(31.20)$$

for $A_f > A_{max} + 10$, where $A_{max} = A_{sim}$ and $k = 5.32$ and $A_{max} = 134$ and $k = 23.5$ for symmetric and asymmetric fission respectively. For both modes of fission the distribution over the kinetic energy of fragments T_{kin} is choosen Gaussian with their own average values $< T_{kin}(A_f) >=< T_{kin}^{sym}(A_f) >$ or $< T_{kin}(A_f) >=< T_{kin}^{asym}(A_f) >$ and dispersions σ_{kin}^2 equal 8^2 MeV or 10^2 MeV^2 for symmetrical and asymmetrical modes, respectively.

31.2.4 Calculation of the excitation energy of fission products.

The total excitation energy of fragments U_{frag} can be defined according to equation:

$$U_{frag} = U + M(A, Z) - M_1(A_{f1}, Z_{f1}) - M_2(A_{f2}, Z_{f2}) - T_{kin}, \qquad (31.21)$$

where U and $M(A, Z)$ are the excitation energy and mass of initial nucleus, T_{kin} is the fragments kinetic energy, $M_1(A_{f1}, Z_{f1})$, and $M_2(A_{f2}, Z_{f2})$ are masses of the first and second fragment, respectively.

The value of excitation energy of fragment U_f determines the fragment temperature ($T = \sqrt{U_f/a_f}$, where $a_f \sim A_f$ is the parameter of fragment level density). Assuming that after disintegration fragments have the same temperature as initial nucleus than the total excitation energy will be distributed between fragments in proportion to their mass numbers one obtains

$$U_f = U_{frag}\frac{A_f}{A}. \qquad (31.22)$$

31.2.5 Excited fragment momenta.

Assuming that fragment kinetic energy $T_f = P_f^2/(2(M(A_f, Z_f + U_f))$ we are able to calculate the absolute value of fragment c.m. momentum

$$P_f = \frac{(M_1(A_{f1}, Z_{f1} + U_{f1})(M_2(A_{f2}, Z_{f2} + U_{f2})}{M_1(A_{f1}, Z_{f1}) + U_{f1} + M_2(A_{f2}, Z_{f2}) + U_{f2}}T_{kin}. \qquad (31.23)$$

and its components, assuming fragment isotropical distribution.

Bibliography

[1] Vandenbosch R., Huizenga J. R., Nuclear Fission, Academic Press, New York, 1973.

[2] Adeev G. D. *et al.* Preprint INR 816/93, Moscow, 1993.

[3] Viola V. E., Kwiatkowski K. and Walker M, Phys. Rev. **C31** 1550 (1985).

Chapter 32

Fermi break-up model.

32.1 Fermi break-up simulation for light nuclei.

The GEANT4 Fermi break-up model is capable to predict final states as result of an excited nucleus with atomic number $A < 17$ statistical break-up.

For light nuclei the values of excitation energy per nucleon are often comparable with nucleon binding energy. Thus a light excited nucleus breaks into two or more fragments with branching given by available phase space. To describe a process of nuclear disassembling the so-called Fermi break-up model is used [1], [2], [3]. This statistical approach was first used by Fermi [1] to describe the multiple production in high energy nucleon collision.

32.1.1 Allowed channel.

The channel will be allowed for decay, if the total kinetic energy E_{kin} of all fragments of the given channel at the moment of break-up is positive. This energy can be calculated according to equation:

$$E_{kin} = U + M(A, Z) - E_{Coulomb} - \sum_{b=1}^{n}(m_b + \epsilon_b), \qquad (32.1)$$

m_b and ϵ_b are masses and excitation energies of fragments, respectively, $E_{Coulomb}$ is the Coulomb barrier for a given channel. It is approximated by

$$E_{Coulomb} = \frac{3}{5}\frac{e^2}{r_0}(1 + \frac{V}{V_0})^{-1/3}(\frac{Z^2}{A^{1/3}} - \sum_{b=1}^{n}\frac{Z^2}{A_b^{1/3}}), \qquad (32.2)$$

where V_0 is the volume of the system corresponding to the normal nuclear matter density and $\kappa = \frac{V}{V_0}$ is a parameter ($\kappa = 1$ is used).

32.1.2 Break-up probability.

The total probability for nucleus to break-up into n componets (nucleons, deutrons, tritons, alphas etc) in the final state is given by

$$W(E, n) = (V/\Omega)^{n-1} \rho_n(E), \qquad (32.3)$$

where $\rho_n(E)$ is the density of a number of final states, V is the volume of decaying system and $\Omega = (2\pi\hbar)^3$ is the normalization volume. The density $\rho_n(E)$ can be defined as a product of three factors:

$$\rho_n(E) = M_n(E) S_n G_n. \qquad (32.4)$$

The first one is the phase space factor defined as

$$M_n = \int_{-\infty}^{+\infty} ... \int_{-\infty}^{+\infty} \delta(\sum_{b=1}^{n} \mathbf{p_b}) \delta(E - \sum_{b=1}^{n} \sqrt{p^2 + m_b^2}) \prod_{b=1}^{n} d^3 p_b, \qquad (32.5)$$

where $\mathbf{p_b}$ is fragment b momentum. The second one is the spin factor

$$S_n = \prod_{b=1}^{n} (2s_b + 1), \qquad (32.6)$$

which gives the number of states with different spin orientations. The last one is the permutation factor

$$G_n = \prod_{j=1}^{k} \frac{1}{n_j!}, \qquad (32.7)$$

which takes into account identity of components in final state. n_j is a number of components of j- type particles and k is defined by $n = \sum_{j=1}^{k} n_j$).

In non-relativistic case (Eq. (32.10) the integration in Eq. (32.5) can be evaluated analiticaly (see e. g. [5]). The probability for a nucleus with energy E disassembling into n fragments with masses m_b, where $b = 1, 2, 3, ..., n$ equals

$$W(E_{kin}, n) = S_n G_n (\frac{V}{\Omega})^{n-1} (\frac{1}{\sum_{b=1}^{n} m_b} \prod_{b=1}^{n} m_b)^{3/2} \frac{(2\pi)^{3(n-1)/2}}{\Gamma(3(n-1)/2)} E_{kin}^{3n/2-5/2}, \qquad (32.8)$$

where $\Gamma(x)$ is the gamma function.

32.1.3 Fermi break-up model parameter.

Thus the Fermi break-up model has only one free parameter V is the volume of decaying system, which can be calculated as follows:

$$V = 4\pi R^3/3 = 4\pi r_0^3 A/3, \tag{32.9}$$

where $r_0 = 1.4$ fm is used.

32.1.4 Fragment characteristics.

We take into account the formation of fragments in their ground and low-lying excited states, which are stable for nucleon emission. However, several unstable fragments with large lifetimes: ^5He, ^5Li, ^8Be, ^9B etc are also considered. Fragment characteristics A_b, Z_b, s_b and ϵ_b are taken from [6].

32.1.5 MC procedure.

The nucleus break-up is described by the Monte Carlo (MC) procedure. We randomly (according to probability Eq. (32.8) and condition Eq. (32.1)) select decay channel. Then for given channel we calculate kinematical quantities of each fragment according to n-body phase space distribution:

$$M_n = \int_{-\infty}^{+\infty} ... \int_{-\infty}^{+\infty} \delta(\sum_{b=1}^{n} \mathbf{p_b}) \delta(\sum_{b=1}^{n} \frac{p_b^2}{2m_b} - E_{kin}) \prod_{b=1}^{n} d^3 p_b. \tag{32.10}$$

The Kopylov's sampling procedure [7] is applied. The angular distributions for emitted fragments are considered to be isotropical.

Bibliography

[1] Fermi E., Prog. Theor. Phys. **5** 1570 (1950).

[2] Kretschmar M. Annual Rev. Nucl. Sci. **11** 1 (1961).

[3] Epherre M., Gradsztajn E., J. Physique **18** 48 (1967).

[4] Cameron A. G. W. Canad. J. Phys., **35** 1021 (1957), **36** 1040 (1958).

[5] Barashenkov V. S., Barbashov B. M., Bubelev E. G. Nuovo Cimento, **7** 117 (1958).

[6] Ajzenberg-Selone F., Nucl. Phys. 1 **360** (1981); **A375** (1982); **392** (1983); **A413** (1984); **A433** (1985).

[7] Kopylov G. I., Principles of resonance kinematics, Moscow, Nauka, 1970 (in Russian).

Chapter 33

Multifragmentation model.

33.1 Multifragmentation process simulation.

The GEANT4 multifragmentation model is capable to predict final states as result of an highly excited nucleus statistical break-up.

The initial information for calculation of multifragmentation stage consists from the atomic mass number A, charge Z of excited nucleus and its excitation energy U. At high excitation energies $U/A > 3$ MeV the multifragmentation mechanism, when nuclear system can eventually breaks down into fragments, becomes the dominant. Later on the excited primary fragments propagate independently in the mutual Coulomb field and undergo de-excitation. Detailed description of multifragmentation mechanism and model can be found in review [1].

33.1.1 Multifragmentation probability.

The probability of a breakup channel b is given by the expression (in the so-called microcanonical approach [1], [2]):

$$W_b(U, A, Z) = \frac{1}{\sum_b \exp[S_b(U, A, Z)]} \exp[S_b(U, A, Z)], \qquad (33.1)$$

where $S_b(U, A, Z)$ is the entropy of a multifragment state corresponding to the breakup channel b. The channels $\{b\}$ can be parametrized by set of fragment multiplicities N_{A_f, Z_f} for fragment with atomic number A_f and charge Z_f. All partitions $\{b\}$ should satisfy constraints on the total mass and charge:

$$\sum_f N_{A_f, Z_f} A_f = A \qquad (33.2)$$

and

$$\sum_f N_{A_f, Z_f} Z_f = Z. \tag{33.3}$$

It is assumed [2] that thermodynamic equilibrium is established in every channel, which can be characterized by the channel temperature T_b.

The channel temperature T_b is determined by the equation constraining the average energy $E_b(T_b, V)$ associated with partition b:

$$E_b(T_b, V) = U + E_{ground} = U + M(A, Z), \tag{33.4}$$

where V is the system volume, E_{ground} is the ground state (at $T_b = 0$) energy of system and $M(A, Z)$ is the mass of nucleus.

According to the conventional thermodynamical formulae the average energy of a partitition b is expressed through the system free energy F_b as follows

$$E_b(T_b, V) = F_b(T_b, V) + T_b S_b(T_b, V). \tag{33.5}$$

Thus, if free energy F_b of a partition b is known, we can find the channel temperature T_b from Eqs. (33.4) and (33.5), then the entropy $S_b = -dF_b/dT_b$ and hence, decay probability W_b defined by Eq. (33.1) can be calculated.

Calculation of the free energy is based on the use of the liquid-drop description of individual fragments [2]. The free energy of a partition b can be splitted into several terms:

$$F_b(T_b, V) = \sum_f F_f(T_b, V) + E_C(V), \tag{33.6}$$

where $F_f(T_b, V)$ is the average energy of an individual fragment including the volume

$$F_f^V = [-E_0 - T_b^2/\epsilon(A_f)]A_f, \tag{33.7}$$

surface

$$F_f^{Sur} = \beta_0[(T_c^2 - T_b^2)/(T_c^2 + T_b^2)]^{5/4} A_f^{2/3} = \beta(T_b) A_f^{2/3}, \tag{33.8}$$

symmetry

$$F_f^{Sim} = \gamma(A_f - 2Z_f)^2/A_f, \tag{33.9}$$

Coulomb

$$F_f^C = \frac{3}{5} \frac{Z_f^2 e^2}{r_0 A_f^{1/3}}[1 - (1 + \kappa_C)^{-1/3}] \tag{33.10}$$

and translational

$$F_f^t = -T_b \ln (g_f V_f/\lambda_{T_b}^3) + T_b \ln (N_{A_f, Z_f}!)/N_{A_f, Z_f} \tag{33.11}$$

490

terms and the last term

$$E_C(V) = \frac{3}{5}\frac{Z^2 e^2}{R} \qquad (33.12)$$

is the Coulomb energy of the uniformly charged sphere with charge Ze and the radius $R = (3V/4\pi)^{1/3} = r_0 A^{1/3}(1 + \kappa_C)^{1/3}$, where $\kappa_C = 2$ [2].

Parameters $E_0 = 16$ MeV, $\beta_0 = 18$ MeV, $\gamma = 25$ MeV are the coefficients of the Bethe-Weizsacker mass formula at $T_b = 0$. $g_f = (2S_f + 1)(2I_f + 1)$ is a spin S_f and isospin I_f degeneracy factor for fragment (fragments with $A_f > 1$ are treated as the Boltzmann particles), $\lambda_{T_b} = (2\pi h^2/m_N T_b)^{1/2}$ is the thermal wavelength, m_N is the nucleon mass, $r_0 = 1.17$ fm, $T_c = 18$ MeV is the critical temperature, which corresponds to the liquid-gas phase transition. $\epsilon(A_f) = \epsilon_0[1 + 3/(A_f - 1)]$ is the inverse level density of the mass A_f fragment and $\epsilon_0 = 16$ MeV is considered as a variable model parameter, whose value depends on the fraction of energy transferred to the internal degrees of freedom of fragments [2]. The free volume $V_f = \kappa V = \kappa \frac{4}{3}\pi r_0^4 A$ available to the translational motion of fragment, where $\kappa \approx 1$ and its dependence on the multiplicity of fragments was taken from [2]:

$$\kappa = [1 + \frac{1.44}{r_0 A^{1/3}}(M^{1/3} - 1)]^3 - 1. \qquad (33.13)$$

For $M = 1$ $\kappa = 0$.

The light fragments with $A_f < 4$, which have no excited states, are considered as elementary particles characterized by the empirical masses M_f, radii R_f, binding energies B_f, spin degeneracy factors g_f of ground states. They contribute to the translation free energy and Coulomb energy.

33.1.2 Direct simulation of the low multiplicity multi-fragment disintegration

At comparatively low excitation energy (temperature) system will disintegrate into a small number of fragments $M \leq 4$ and number of channel is not huge. For such situation a direct (microcanonical) sorting of all decay channels can be performed. Then, using Eq. (33.1), the average multiplicity value $< M >$ can be found. To check that we really have the situation with the low excitation energy, the obtained value of $< M >$ is examined to obey the inequality $< M > \leq M_0$, where $M_0 = 3.3$ and $M_0 = 2.6$ for $A \sim 100$ and for $A \sim 200$, respectively [2]. If the discussed inequality is fulfilled, then the set of channels under consideration is belived to be able for a correct description of the break up. Then using calculated according Eq. (33.1) probabilities we can randomly select a specific channel with given values of A_f and Z_f.

33.1.3 Fragment multiplicity distribution.

The individual fragment multiplicities N_{A_f,Z_f} in the so-called macrocanonical ensemble [1] are distributed according to the Poisson distribution:

$$P(N_{A_f,Z_f}) = \exp\left(-\omega_{A_f,Z_f}\right)\frac{\omega_{A_f,Z_f}^{N_{A_f,Z_f}}}{N_{A_f,Z_f}!} \tag{33.14}$$

with mean value $< N_{A_f,Z_f} >= \omega_{A_f,Z_f}$ defined as

$$< N_{A_f,Z_f} >= g_f A_f^{3/2}\frac{V_f}{\lambda_{T_b}^3}\exp\left[\frac{1}{T_b}(F_f(T_b,V) - F_f^t(T_b,V) - \mu A_f - \nu Z_f)\right], \tag{33.15}$$

where μ and ν are chemical potentials. The chemical potential are found by substituting Eq. (33.15) into the system of constraints:

$$\sum_f < N_{A_f,Z_f} > A_f = A \tag{33.16}$$

and

$$\sum_f < N_{A_f,Z_f} > Z_f = Z \tag{33.17}$$

and solving it by iteration.

33.1.4 Atomic number distribution of fragments.

Fragment atomic numbers $A_f > 1$ are also distributed according to the Poisson distribution [1] (see Eq. (33.14)) with mean value $< N_{A_f} >$ defined as

$$< N_{A_f} >= A_f^{3/2}\frac{V_f}{\lambda_{T_b}^3}\exp\left[\frac{1}{T_b}(F_f(T_b,V) - F_f^t(T_f,V) - \mu A_f - \nu < Z_f >)\right], \tag{33.18}$$

where calculating the internal free energy $F_f(T_b,V) - F_f^t(T_b,V)$ one has to substitute $Z_f \rightarrow < Z_f >$. The average charge $< Z_f >$ for fragment having atomic number A_f is given by

$$< Z_f(A_f) >= \frac{(4\gamma + \nu)A_f}{8\gamma + 2[1 - (1+\kappa)^{-1/3}]A_f^{2/3}}. \tag{33.19}$$

33.1.5   Charge distribution of fragments.

At given mass of fragment $A_f > 1$ the charge Z_f distribution of fragments are described by Gaussian

$$P(Z_f(A_f)) \sim \exp\left[-\frac{(Z_f(A_f) - < Z_f(A_f) >)^2}{2(\sigma_{Z_f}(A_f))^2}\right] \qquad (33.20)$$

with dispertion

$$\sigma_{Z_f(A_f)} = \sqrt{\frac{A_f T_b}{8\gamma + 2[1 - (1 + \kappa)^{-1/3}]A_f^{2/3}}} \approx \sqrt{\frac{A_f T_b}{8\gamma}}. \qquad (33.21)$$

and the average charge $< Z_f(A_f) >$ defined by Eq. (33.17).

33.1.6   Kinetic energy distribution of fragments.

It is assumed [2] that at the instant of the nucleus break-up the kinetic energy of the fragment T_{kin}^f in the rest of nucleus obeys the Boltzmann distribution at given temperature T_b:

$$\frac{dP(T_{kin}^f)}{dT_{kin}^f} \sim \sqrt{T_{kin}^f} \exp\left(-T_{kin}^f/T_b\right). \qquad (33.22)$$

Under assumption of thermodynamic equilibrium the fragment have isotropic velocities distribution in the rest frame of nucleus. The total kinetic energy of fragments should be equal $\frac{3}{2}MT_b$, where M is fragment multiplicity, and the total fragment momentum should be equal zero. These conditions are fullfilled by choosing properly the momenta of two last fragments.

The initial conditions for the divergence of the fragment system are determined by random selection of fragment coordinates distributed with equal probabilities over the break-up volume $V_f = \kappa V$. It can be a sphere or prolongated ellipsoid. Then Newton's equations of motion are solved for all fragments in the self-consistent time-dependent Coulomb field [2]. Thus the asymptotic energies of fragments determined as result of this procedure differ from the initial values by the Coulomb repulsion energy.

33.1.7   Calculation of the fragment excitation energies.

The temparature T_b determines the average excitation energy of each fragment:

$$U_f(T_b) = E_f(T_b) - E_f(0) = \frac{T_b^2}{\epsilon_0}A_f + [\beta(T_b) - T_b\frac{d\beta(T_b)}{dT_b} - \beta_0]A_f^{2/3}, \quad (33.23)$$

where $E_f(T_b)$ is the average fragment energy at given temperature T_b and $\beta(T_b)$ is defined in Eq. (33.8). There is no excitation for fragment with $A_f < 4$, for ^4He excitation energy was taken as $U_{^4He} = 4T_b^2/\epsilon_o$.

Bibliography

[1] Bondorf J. P., Botvina A. S., Iljinov A. S., Mishustin I. N., Sneppen K., Phys. Rep. **257** 133 (1995).

[2] Botvina A. S. *et al.*, Nucl. Phys. **A475** 663 (1987).

Chapter 34

INCL 4.2 Cascade and ABLA V3 Evaporation with Fission

34.1   Introduction

There is a renewed interest in the study of spallation reactions. This is largely due to new technological applications, such as Accelerator Driven Systems, consisting of sub-critical nuclear reactor and particle accelerator. These applications require optimized spallation targets or spallation sources. This type of problem has typically a large number of parameters and thus it cannot be solved by trial and error method. One has to rely on simulations, which implies that very accurate simulation tools need to be developed and their validity and accuracy needs also to be assessed.

Above the energy 200 MeV it is necessary to use reliable models due to the prohibitive number of open channels. The most appropriate modeling technique in this energy region is intranuclear cascade (INC) combined with evaporation model. One such pair of models is the Liège cascade model INCL4.2 coupled with ABLA evaporation model. The strategy adopted by the INCL4.2 cascade is to improve the quasi-classical treatment of physics without relying on too many free parameters.

This chapter introduces the physics provided by INCL4.2 and ABLA V3 codes as implemented in Geant4. Tables 34.1 and 34.3 will summarize the key features and provides references describing in detail the physics.

34.2   INCL4.2 cascade

INCL4.2 is a Monte Carlo simulation incorporating aforementioned cascade physics principles. INCL4.2 cascade algorithm consists of an initialization

495

stage and the actual data processing stage.

The INCL4.2 cascade can be used to simulate the collisions between bullet particles and nuclei. The supported bullet particles and the interface classes supporting them are presented in table 34.1.

The momenta and positions of the nucleons inside the nuclei are determined at the beginning of the simulation run by modeling the nucleus as a free fermi gas in a static potential well. The cascade is modeled by tracking the nucleons and their collisions. The collisions are assumed to be well separated in space and time.

The possible reactions inside the nucleus are

- $NN \rightarrow N\Delta$ and $N\Delta \rightarrow NN$

- $\Delta \rightarrow \pi N$ and $\pi N \rightarrow \Delta$

34.2.1 Model limits

The INCL4.2 model has certain limitations with respect to the bullet particle energy and target nucleus type. The supported energy range for bullets is: 200 MeV - 3 GeV. Acceptable target nuclei range from Carbon to Uranium.

34.2.2 Model principles

The INCL model uses only two external user defined parameters: the nuclear potential depth and scaling factor for time-step. All other parameters used during the calculation are obtained either from theory or experiments. In the actual simulation code good default values for these two parameters are predefined.

During the initialization the necessary Woods-Saxon potential calculations are made. The results of these calculations are used at the beginning of a cascade to determine the positions and momenta of the nucleons inside the nucleus. The nucleons are modeled as free Fermi gas in a static potential well. The principle for doing this is presented in the following equations 34.1 and 34.2.

The nucleon density in r-space is given by formula:

$$\rho(r) = \begin{cases} \frac{\rho_0}{1+exp(\frac{r-R_0}{a})} & \text{for } r < R_{max} \\ 0 & \text{for } r > R_{max} \end{cases} \qquad (34.1)$$

The nucleon positions r and momenta p are correlated in the following way:

$$\rho(p)p^2dp = -\frac{d\rho(p)}{dr}\frac{r^3}{3}dr. \qquad (34.2)$$

After the initialization a projectile particle, bullet, is shot towards the target nucleus. The impact parameter, i.e. the distance between the projectile particle and the center point of the projected nucleus surface is chosen at random. The value of the impact parameter determines the point where the bullet particle will hit the nucleus. After this the algorithm tracks the nucleons by determining the times at which an event will happen. The possible events are:

- collision

- decay of a delta resonance

- reflection from nuclear potential wall (only for nucleons)

The particles are assumed to propagate along straight line trajectories. The algorithm calculates the time at which events will happen and propagates the particles directly to their positions at that particular point in time. Practically this means that the length of the time step in simulation is not constant.

All particles in the model are labeled either as *participants* or *spectators*. Only collisions where participants are involved are taken into account.

The processes undergone by the nucleons, pions and delta resonances are as follows:

- $NN \rightarrow N\Delta$ and $N\Delta \rightarrow NN$

- $\Delta \rightarrow \pi N$ and $\pi N \rightarrow \Delta$

34.2.3 Conservation laws

During cascade INCL model conserves several quantities: energy, baryon number, charge number, energy, momentum and angular momentum. The conservation relations are:

$$A_{projectile} + A_{target} = A_{ejectiles} + A_{remnant} \qquad (34.3)$$

$$Z_{projectile} + Z_{target} = Z_{ejectiles} + Z_{remnant} \qquad (34.4)$$

$$T_{laboratory} = K_{ejectiles} + W_{\pi} + E_{recoil} + E_{excitation} + S \qquad (34.5)$$

$$\vec{p}_{laboratory} = \vec{p}_{ejectiles} + \vec{p}_{\pi} + \vec{p}_{remnant} \qquad (34.6)$$

$$\vec{l} = \vec{l}_{ejectiles} + \vec{l}_{\pi} + \vec{l}_{remnant} + \vec{l}_{excitation}, \qquad (34.7)$$

where A is baryon number, Z charge, T energy, K kinetic energy, E_{recoil} remnant recoil energy, $E_{excitation}$ remnant nucleus excitation energy, S separation energy, $\vec{p}$ momentum and $\vec{l}$ angular momentum.

34.2.4 Cascade stopping time

Stopping time is defined as the point in time when the cascade phase is finished and the excited nucleus remnant is given to evaporation model. In INCL model the stopping time, t_{stop}, is determined as:

$$t_{stop} = f_{stop}t_0(A_{target}/208)^{0.16}. \tag{34.8}$$

Here A_{target} is the target mass number and t_0 is a constant with default value 70 fm/c. Factor f_{stop} is the second of the two free parameters in the model. It is a scaling factor for the stopping time. Good default value for this factor is $f_{stop} = 1.0$.

34.2.5 Light ions

In addition to protons, neutrons and pions INCL4.2 supports also light ion projectiles: deuterons, tritons, He3 and alpha. In light of INCL physics modeling principles presented above, the extension to light ions is quite natural. Light ions are modeled in similar way to nucleus, except that ion potential is considered to be Gaussian instead of real Woods-Saxon shape. In table 34.2 the parameters for Gaussian forms used for distance and momentum distributions in light ions are presented.

34.3 ABLA V3 evaporation

The ABLA V3 evaporation model takes excited nucleus parameters, excitation energy, mass number, charge number and nucleus spin, as input. It calculates the probabilities for emitting proton, neutron or alpha particle and also probability for fission to occur. The summary of Geant4 ABLA V3 implementation is represented in Table 34.3.

The probabilities for emission of particle type j are calculated using formula:

$$W_j(N, Z, E) = \frac{\Gamma_j(N, Z, E)}{\sum_k \Gamma_k(N, Z, E)}, \tag{34.9}$$

where Γ_j is emission width for particle j, N is neutron number, Z charge number and E excitation energy. Possible emitted particles are *protons*, *neutrons* and *alphas*. Emission widths are calculated using the following formula:

$$\Gamma_j = \frac{1}{2\pi\rho_c(E)} \frac{4m_j R^2}{\hbar^2} T_j^2 \rho_j(E - S_j - B_j), \tag{34.10}$$

where $\rho_c(E)$ and $\rho_j(E - S_j - B_j)$ are the level densities of the compound nucleus and the exit channel, respectively. B_j is the height of the Coulomb barrier, S_j the separation energy, R is the radius and T_j the temperature of the remnant nucleus after emission and m_j the mass of the emitted particle.

The fission width is calculated from:

$$\Gamma_i = \frac{1}{2\pi\rho_c(E)} T_f \rho_f(E - B_f), \qquad (34.11)$$

where $\rho_f(E)$ is the level density of transition states in the fissioning nucleus, B_f the height of the fission barrier and T_f the temperature of the nucleus.

34.3.1 Level densities

Nuclear level densities are calculated using the following formula:

$$a = 0.073A[MeV^{-1}] + 0.095B_sA^{2/3}[MeV^{-2}], \qquad (34.12)$$

where A the nucleus mass number and B_s dimensionless surface area of the nucleus.

34.3.2 Fission

Fission barrier, used to calculate fission width 34.11, is calculated using a semi-empirical model fitting to data obtained from nuclear physics experiments.

34.4 External data file required

Both INCL4.2 and ABLA V3 need data files. These files contain ABLA V3 shell corrections and remnant nucleus masses for INCL4.2. To enable this data set, environment variable `G4ABLADATA` needs to be set, and the data downloaded from Geant4 web page. For Geant4 9.1 release use data file G4ABLA3.0

34.5 Implementation details

INCL4.2 and ABLA V3 are provided as alpha release for Geant4 9.1. In this first release design follows as closely as possibly the original codes, and class re-design is left for future Geant4 releases. Current simple design is shown in 34.1

Testing of INCL and ABLA models is based on ROOT [9] scripting.

Figure 34.1: Simplified UML class diagram of INCL and ABLA implementations in Geant4.

34.6 Physics Performance

INCL4.2 together with ABLA V3 provides an up to date modeling tool particularly for spallation studies for hadron projectile energy range 200 MeV - 3 GeV. It provides an detailed description of double differential energy spectrum of cascading particles (see 34.2) and remnants.

Models are validated against recent data and continually updated.

34.7 Status of this document

06.12.2007 Documentation for alpha release added. Pekka Kaitaniemi, HIP (translation); Alain Boudard, CEA (contact person INCL/ABLA); Joseph Cugnon, University of Liège (INCL physics modelling); Karl-Heintz Schmidt, GSI (ABLA); Christelle Schmidt, IPNL (fission code); Aatos Heikkinen, HIP (project coordination)

Bibliography

[1] A. Boudard et al *Phys. Rev. C66* (2002) 044615

[2] J. Cugnon et al *Nuc. Phys. A352* (1981) 505
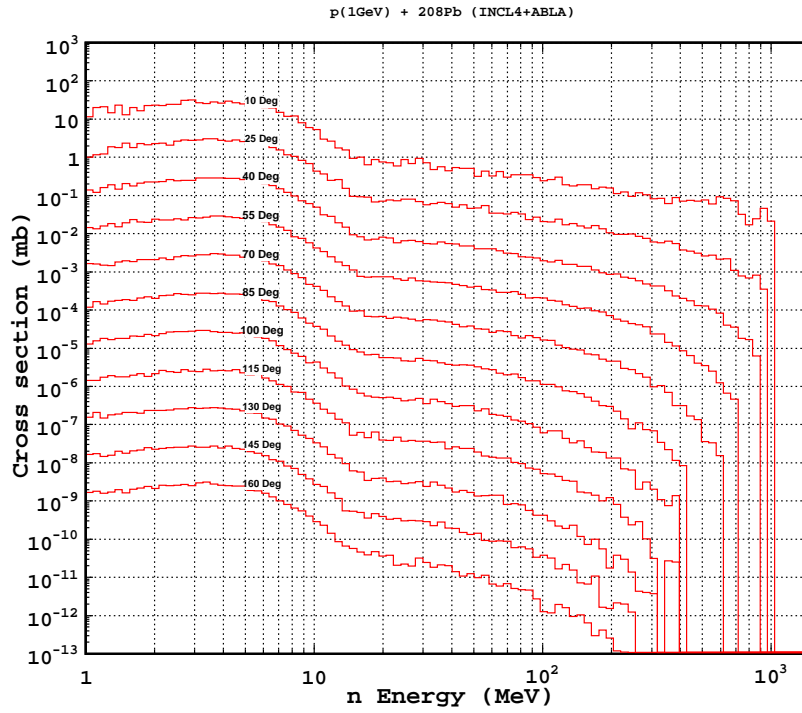
[3] J. Cugnon et al *Nuc. Phys. A462* (1987) 751

Figure 34.2: Geant4 implementation of INCL4.2 together with ABLA V3. Neutron double differential cross sections of reaction p(1GeV) + Pb For more detailed discussion on this subject see reference [1].

[4] J. Cugnon et al *Nuc. Phys. A500* (1989) 701

[5] J. Cugnon et al *Nuc. Phys. A620* (1997) 745

[6] A.R. Junghans et al *Nuc. Phys. A629* (1998) 635

[7] J. Benlliure et al *Nuc. Phys. A628* (1998) 458

[8] P. Kaitaniemi et al. *Implementation of INCL4 cascade and ABLA evaporation codes in Geant4* (To be published in the proceedings of CHEP 2007, September 2-6, Victoria, BC, Canada.)

[9] R. Brun, F. Rademakers *Nucl. Inst & Meth. in Phys. Res. A 389* (1997) 81

Table 34.1: INCL 4.2 (located in the Geant4 directory `source/processes/-hadronic/models/incl`) feature summary.

Requirements	
External data file	G4ABLA3.0 available at Geant4 site
Environment variable	`G4ABLADATA`
for external data	
Usage	
Physics list	Not yet implemented,
	instead use the interfaces directly.
Interfaces	
`G4InclCascadeInterface`	h–A
`G4InclLightIonInterface`	A–A
Projectile particles	proton, neutron
	pions (π^+, π^0, π^-)
	deuteron, triton
	α, ^{3}He
Energy range	200 MeV - 3 GeV
Target nuclei	
Lightest applicable	Carbon, C
Heaviest	Uranium, U
Features	No ad-hoc parameters
	Woods-Saxon nuclear potential
	Coulomb barrier
	Non-uniform time-step
	Pion and delta production cross sections
	Delta decay
	Pauli blocking
Misc.	5 classes (see fig. 34.1), 8k lines
	$0.9 <$ speed C++/F77 < 1.1
References	Key reference [1], see also [5, 2, 3, 4]

Table 34.2: The parameters for nucleon position and momentum distributions in light ions.

Particle	$\sqrt{(r_{mean})^2}$ [fm]	$\sqrt{(p_{mean})^2}$ [MeV/c]
Deuteron	1.91	77
Triton	1.8	110
He3	1.8	110
Alpha	1.63	153

Table 34.3: ABLA V3 (located in the Geant4 directory `source/processes/-hadronic/models/incl`) feature summary.

Requirements	
External data file	G4ABLA3.0 available at Geant4 site
Environment variable for external data	`G4ABLADATA`
Usage	
Physics list	Not yet implemented, instead use the interfaces directly.
Interfaces	
`G4InclAblaCascadeInterface`	h–A
`G4InclAblaLightIonInterface`	A–A
Supported input	Excited nuclei
Output particles	proton, neutron
	α
	fission products
	residual nuclei
Features	evaporation of proton, neutron and α
	fission
Misc.	5 classes, 5k lines
	$0.9 <$ speed C++/F77 < 1.1
References	Key reference: [6], see also [7]

Chapter 35

Low Energy Neutron Interactions

35.1 Introduction

The neutron transport class library described here simulates the interactions of neutrons with kinetic energies from thermal energies up to O(20 MeV). The upper limit is set by the comprehensive evaluated neutron scattering data libraries that the simulation is based on. The result is a set of secondary particles that can be passed on to the tracking sub-system for further geometric tracking within GEANT4.

The interactions of neutrons at low energies are split into four parts in analogy to the other hadronic processes in GEANT4. We consider radiative capture, elastic scattering, fission, and inelastic scattering as separate models. These models comply with the interface for use with the GEANT4 hadronic processes which enables their transparent use within the GEANT4 tool-kit together with all other GEANT4 compliant hadronic shower models.

35.2 Physics and Verification

35.2.1 Inclusive Cross-sections

All cross-section data are taken from the ENDF/B-VI[1] evaluated data library.

All inclusive cross-sections are treated as point-wise cross-sections for reasons of performance. For this purpose, the data from the evaluated data library have been processed, to explicitly include all neutron nuclear resonances in the form of point-like cross-sections rather than in the form of

parametrisations. The resulting data have been transformed into a linearly interpolable format, such that the error due to linear interpolation between adjacent data points is smaller than a few percent.

The inclusive cross-sections comply with the cross-sections data set interface of the GEANT4 hadronic design. They are, when registered with the tool-kit at initialisation, used to select the basic process. In the case of fission and inelastic scattering, point-wise semi-inclusive cross-sections are also used in order to decide on the active channel for an individual interaction. As an example, in the case of fission this could be first, second, third, or forth chance fission.

35.2.2 Elastic Scattering

The final state of elastic scattering is described by sampling the differential scattering cross-sections $\frac{d\sigma}{d\Omega}$. Two representations are supported for the normalised differential cross-section for elastic scattering. The first is a tabulation of the differential cross-section, as a function of the cosine of the scattering angle θ and the kinetic energy E of the incoming neutron.

$$\frac{d\sigma}{d\Omega} \;=\; \frac{d\sigma}{d\Omega}\,(\cos\theta,\; E)$$

The tabulations used are normalised by $\sigma/(2\pi)$ so the integral of the differential cross-sections over the scattering angle yields unity.

In the second representation, the normalised cross-section are represented as a series of legendre polynomials $P_l(\cos\theta)$, and the legendre coefficients a_l are tabulated as a function of the incoming energy of the neutron.

$$\frac{2\pi}{\sigma(E)}\frac{d\sigma}{d\Omega}\,(\cos\theta,\; E) \;=\; \sum_{l=0}^{n_l}\frac{2l+1}{2}a_l(E)P_l(\cos\theta)$$

Describing the details of the sampling procedures is outside the scope of this paper.

An example of the result we show in figure 35.1 for the elastic scattering of 15 MeV neutrons off Uranium a comparison of the simulated angular distribution of the scattered neutrons with evaluated data. The points are the evaluated data, the histogram is the Monte Carlo prediction.

In order to provide full test-coverage for the algorithms, similar tests have been performed for ^{72}Ge, ^{126}Sn, ^{238}U, ^{4}He, and ^{27}Al for a set of neutron kinetic energies. The agreement is very good for all values of scattering angle and neutron energy investigated.
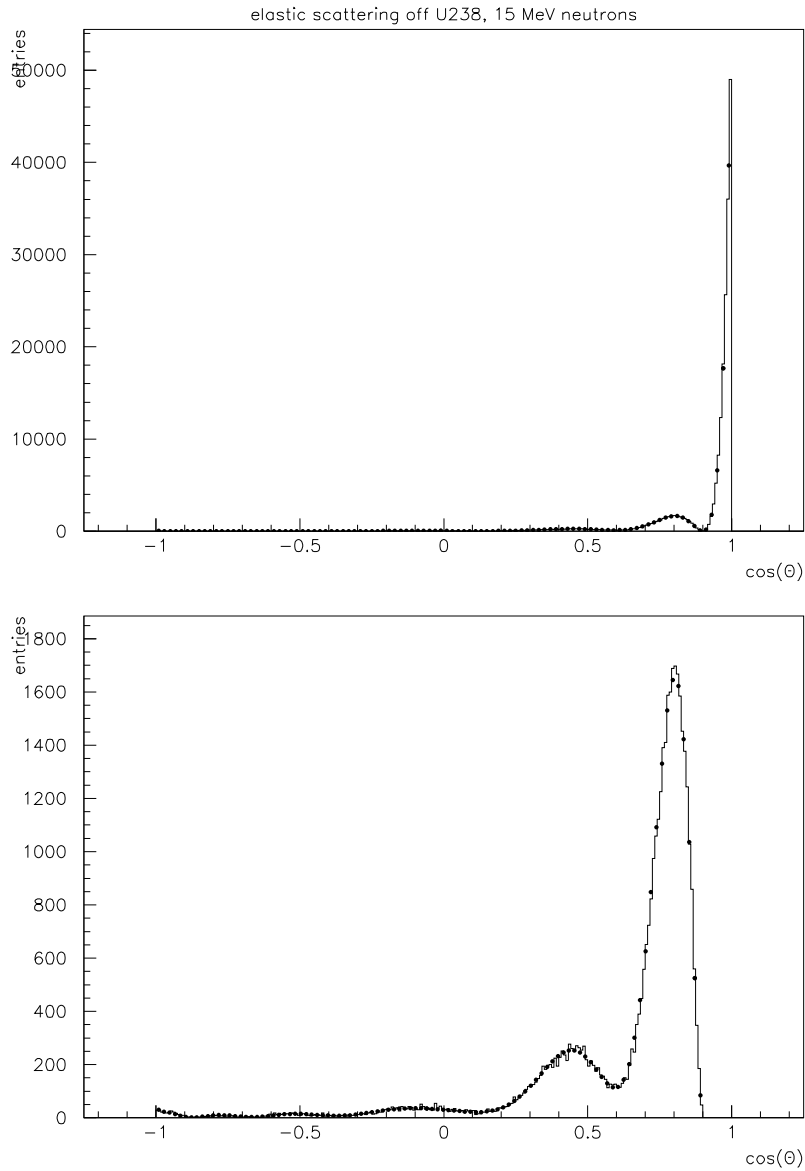
Figure 35.1: Comparison of data and Monte Carlo for the angular distribution of 15 MeV neutrons scattered elastically off Uranium (^{238}U). The points are evaluated data, and the histogram is the Monte Carlo prediction. The lower plot excludes the forward peak, to better show the Frenel structure of the angular distribution of the scattered neutron.

507

35.2.3 Radiative Capture

The final state of radiative capture is described by either photon multiplicities, or photon production cross-sections, and the discrete and continuous contributions to the photon energy spectra, along with the angular distributions of the emitted photons.

For the description of the photon multiplicity there are two supported data representations. It can either be tabulated as a function of the energy of the incoming neutron for each discrete photon as well as the eventual continuum contribution, or the full transition probability array is known, and used to determine the photon yields. If photon production cross-sections are used, only a tabulated form is supported.

The photon energies E_γ are associated to the multiplicities or the cross-sections for all discrete photon emissions. For the continuum contribution, the normalised emission probability f is broken down into a weighted sum of normalised distributions g.

$$f\left(E \to E_\gamma\right) \;=\; \sum_i p_i(E) g_i(E \to E_\gamma)$$

The weights p_i are tabulated as a function of the energy E of the incoming neutron. For each neutron energy, the distributions g are tabulated as a function of the photon energy. As in the ENDF/B-VI data formats[1], several interpolation laws are used to minimise the amount of data, and optimise the descriptive power. All data are derived from evaluated data libraries.

The techniques used to describe and sample the angular distributions are identical to the case of elastic scattering, with the difference that there is either a tabulation or a set of legendre coefficients for each photon energy and continuum distribution.

As an example of the results is shown in figure35.2 the energy distribution of the emitted photons for the radiative capture of 15 MeV neutrons on Uranium (^{238}U). Similar comparisons for photon yields, energy and angular distributions have been performed for capture on ^{238}U, ^{235}U, ^{23}Na, and ^{14}N for a set of incoming neutron energies. In all cases investigated the agreement between evaluated data and Monte Carlo is very good.

35.2.4 Fission

For neutron induced fission, we take first chance, second chance, third chance and forth chance fission into account.

Neutron yields are tabulated as a function of both the incoming and outgoing neutron energy. The neutron angular distributions are either tabulated,

or represented in terms of an expansion in legendre polynomials, similar to the angular distributions for neutron elastic scattering. In case no data are available on the angular distribution, isotropic emission in the centre of mass system of the collision is assumed.

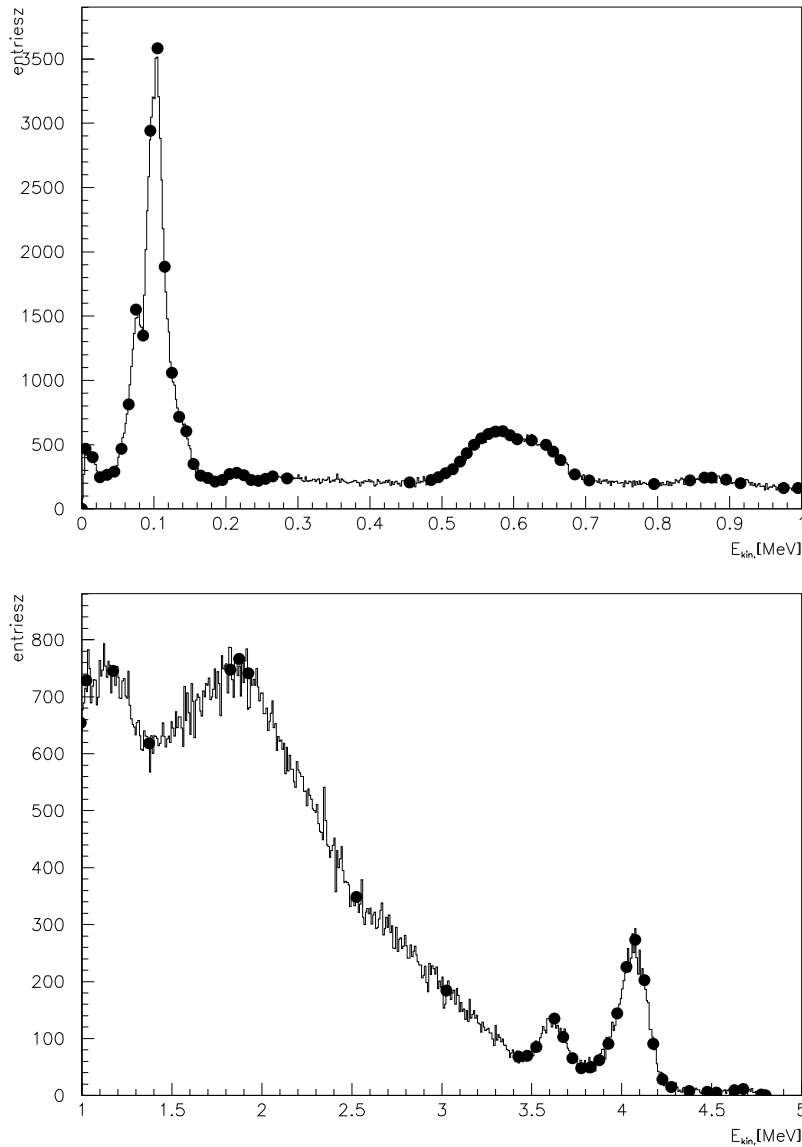There are six different possibilities implemented to represent the neu-

Figure 35.2: Comparison of data and Monte Carlo for photon energy distributions for radiative capture of 15 MeV neutrons on Uranium (^{238}U). The points are evaluated data, the histogram is the Monte Carlo prediction.

509

tron energy distributions. The energy distribution of the fission neutrons $f(E \rightarrow E')$ can be tabulated as a normalised function of the incoming and outgoing neutron energy, again using the ENDF/B-VI interpolation schemes to minimise data volume and maximise precision.

The energy distribution can also be represented as a general evaporation spectrum,

$$f(E \rightarrow E') \;=\; f\left(E'/\Theta(E)\right).$$

Here E is the energy of the incoming neutron, E' is the energy of a fission neutron, and $\Theta(E)$ is effective temperature used to characterise the secondary neutron energy distribution. Both the effective temperature and the functional behaviour of the energy distribution are taken from tabulations.

Alternatively energy distribution can be represented as a Maxwell spectrum,

$$f(E \rightarrow E') \;\propto\; \sqrt{E'}\mathrm{e}^{E'/\Theta(E)},$$

or a evaporation spectrum

$$f(E \rightarrow E') \;\propto\; E'\mathrm{e}^{E'/\Theta(E)}.$$

In both these cases, the temperature is tabulated as a function of the incoming neutron energy.

The last two options are the energy dependent Watt spectrum, and the Madland Nix spectrum. For the energy dependent Watt spectrum, the energy distribution is represented as

$$f(E \rightarrow E') \;\propto\; \mathrm{e}^{-E'/a(E)} \sinh \sqrt{b(E)E'}.$$

Here both the parameters a, and b are used from tabulation as function of the incoming neutron energy. In the case of the Madland Nix spectrum, the energy distribution is described as

$$f(E \rightarrow E') \;=\; \frac{1}{2}\left[g(E', <K_l>) \;+\; g(E', <K_h>)\right].$$

Here

$$g(E', <K>) \;=\; \frac{1}{3\sqrt{<K>\Theta}}\left[u_2^{3/2}E_1(u_2) - u_1^{3/2}E_1(u_1) + \gamma(3/2, u_2) - \gamma(3/2, u_1)\right],$$

$$u_1(E', <K>) = \frac{(\sqrt{E'} - \sqrt{<K>})^2}{\Theta}, \text{ and}$$

$$u_2(E', <K>) = \frac{(\sqrt{E'} + \sqrt{<K>})^2}{\Theta}.$$

510

Here K_l is the kinetic energy of light fragments and K_h the kinetic energy of heavy fragments, $E_1(x)$ is the exponential integral, and $\gamma(x)$ is the incomplete gamma function. The mean kinetic energies for light and heavy fragments are assumed to be energy independent. The temperature Θ is tabulated as a function of the kinetic energy of the incoming neutron.

Fission photons are describes in analogy to capture photons, where evaluated data are available. The measured nuclear excitation levels and transition probabilities are used otherwise, if available.

As an example of the results is shown in figure35.3 the energy distribution of the fission neutrons in third chance fission of 15 MeV neutrons on Uranium (^{238}U). This distribution contains two evaporation spectra and one Watt spectrum. Similar comparisons for neutron yields, energy and angular distributions, and well as fission photon yields, energy and angular distributions have been performed for ^{238}U, ^{235}U, ^{234}U, and ^{241}Am for a set of incoming neutron energies. In all cases the agreement between evaluated data and Monte Carlo is very good.

35.2.5 Inelastic Scattering

For inelastic scattering, the currently supported final states are (nA→) nγs (discrete and continuum), np, nd, nt, n^{3}He, nα, nd2α, nt2α, n2p, n2α, npα, n3α, 2n, 2np, 2nd, 2nα, 2n2α, nX, 3n, 3np, 3nα, 4n, p, pd, pα, 2p d, dα, d2α, dt, t, t2α, ^{3}He, α, 2α, and 3α.

The photon distributions are again described as in the case of radiative capture.

The possibility to describe the angular and energy distributions of the final state particles as in the case of fission is maintained, except that normally only the arbitrary tabulation of secondary energies is applicable.

In addition, we support the possibility to describe the energy angular correlations explicitly, in analogy with the ENDF/B-VI data formats. In this case, the production cross-section for reaction product n can be written as

$$\sigma_n(E, E', \cos(\theta)) = \sigma(E)Y_n(E)p(E, E', \cos(\theta)).$$

Here $Y_n(E)$ is the product multiplicity, $\sigma(E)$ is the inelastic cross-section, and $p(E, E', \cos(\theta))$ is the distribution probability. Azimuthal symmetry is assumed.

The representations for the distribution probability supported are isotropic emission, discrete two-body kinematics, N-body phase-space distribution, continuum energy-angle distributions, and continuum angle-energy distributions in the laboratory system.

The description of isotropic emission and discrete two-body kinematics is possible without further information. In the case of N-body phase-space distribution, tabulated values for the number of particles being treated by the law, and the total mass of these particles are used. For the continuum energy-angle distributions, several options for representing the angular dependence are available. Apart from the already introduced methods of expansion in terms of legendre polynomials, and tabulation (here in both the incoming neutron energy, and the secondary energy), the Kalbach-Mann systematic is available. In the case of the continuum angle-energy distributions in the laboratory system, only the tabulated form in incoming neutron energy, product energy, and product angle is implemented.

First comparisons for product yields, energy and angular distributions have been performed for a set of incoming neutron energies, but full test cov-
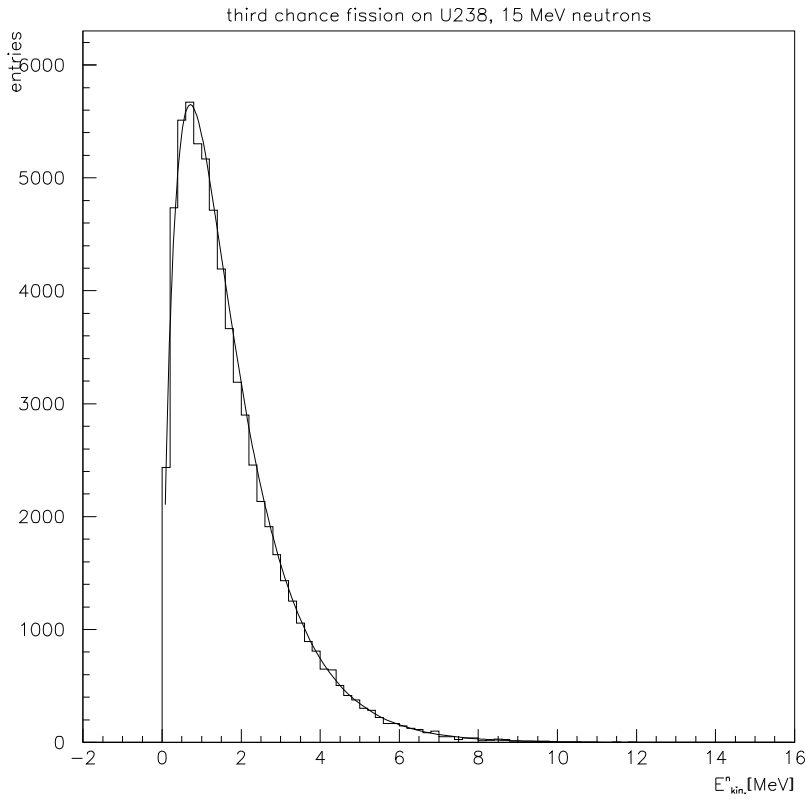

Figure 35.3: Comparison of data and Monte Carlo for fission neutron energy distributions for induced fission by 15 MeV neutrons on Uranium (^{238}U). The curve represents evaluated data and the histogram is the Monte Carlo prediction.

erage is still to be achieved. In all cases currently investigated, the agreement between evaluated data and Monte Carlo is very good.

35.3 High Precision Models and Low Energy Parameterized Models

The high precision neutron models discussed in the previous section depend on an evaluated neutron data library (G4NDL) for cross sections, angular distributions and final state information. However the library is not complete because there are no data for several key elements. In order to use the high precision models, users must develop their detectors using only elements which exist in the library. In order to avoid this difficulty, alternative models were developed which use the high precision models when data are found in the library, but use the low energy parameterized neutron models when data are missing.

The alternative models cover the same types of interaction as the originals, that is elastic and inelastic scattering, capture and fission. Because the low energy parameterized part of the models is independent of G4NDL, results will not be as precise as they would be if the relevant data existed.

35.4 Summary

By the way of abstraction and code reuse we minimised the amount of code to be written and maintained. The concept of container-sampling lead to abstraction and encapsulation of data representation and the corresponding random number generators. The Object Oriented design allows for easy extension of the cross-section base of the system, and the ENDF-B VI data evaluations have already been supplemented with evaluated data on nuclear excitation levels, thus improving the energy spectra of de-excitation photons. Other established data evaluations have been investigated, and extensions based on the JENDL[2], CENDL[4], and Brond[5] data libraries are foreseen for next year.

35.5 Status of this document

00.00.00 created by H.P. Wellisch
08.12.05 section on high precision and low energy parameterized model added

by T. Koi

Bibliography

[1] ENDF/B-VI: Cross Section Evaluation Working Group, *ENDF/B-VI Summary Document*, Report **BNL-NCS-17541 (ENDF-201)** (1991), edited by P.F. Rose, National Nuclear Data Center, Brookhave National Laboratory, Upton, NY, USA.

[2] JENDL-3: T. Nakagawa, et al., *Japanese Evaluated Nuclear Data Library, Version 3, Revision 2,* **J. Nucl. Sci. Technol. 32**, 1259 (1995).

[3] Jef-2: C. Nordborg, M. Salvatores, *Status of the JEF Evaluated Data Library*, **Nuclear Data for Science and Technology**, edited by J. K. Dickens (American Nuclear Society, LaGrange, IL, 1994).

[4] CENDL-2: Chinese Nuclear Data Center, *CENDL-2, The Chinese Evaluated Nuclear Data Library for Neutron Reaction Data*, Report **IAEA-NDS-61**, Rev. 3 (1996), International Atomic Energy Agency, Vienna, Austria.

[5] Brond-2.2: A.I Blokhin et al., *Current status of Russian Nuclear Data Libraries*, **Nuclear Data for Science and Technology**, Volume2, p.695. edited by J. K. Dickens (American Nuclear Society, LaGrange, IL, 1994)

Chapter 36

Radioactive Decay

36.1 The Radioactive Decay Module

G4RadioactiveDecay and associated classes are used to simulate the decay of radioactive nuclei by α, β^+, and β^- emission and by electron capture (EC). The simulation model is empirical and data-driven, and uses the Evaluated Nuclear Structure Data File (ENSDF) [1] for information on:

- nuclear half-lives,
- nuclear level structure for the parent or daughter nuclide,
- decay branching ratios, and
- the energy of the decay process.

If the daughter of a nuclear decay is an excited isomer, its prompt nuclear de-excitation is treated using the *G4PhotoEvaporation* class [2].

36.2 Sampling

Sampling of the β-spectrum, which includes the coordinated energies and momenta of the $\beta^\pm$, ν, or $\bar{\nu}$ and residual nucleus, is performed either from histogrammed data, or through a three-body decay algorithm. In the latter case, the effect of the Coulomb barrier on the probability of $\beta^\pm$-emission can also be taken into account using the Fermi function:

$$F(E_0) = \frac{\gamma}{1 - e^{-\gamma}} \left(\frac{Z^2(E_0 + 1)^2}{137^2} + \frac{E_0^2 + 2E_0}{4} \right)^{\sqrt{1 - \frac{Z^2}{137^2}} - 1}. \qquad (36.1)$$

Here E_0 is the energy of the β-particle given as a fraction of the end-point energy, Z is the atomic number of the nucleus, and γ is given by the expression:

$$\gamma = \frac{2\pi Z}{137} \frac{1 + E_0}{\sqrt{E_0^2 + 2E_0}}. \tag{36.2}$$

Due to the level of imprecision of the rest-mass energy of the nuclei generated by $G4IonTable :: GetNucleusMass$, the mass of the parent nucleus is modified to a minor extent just before performing the two- or three-body decay so that the Q for the transition process equals that identified in the ENSDF data.

36.2.1 Biasing Methods

By default, sampling of the times of radioactive decay and branching ratios is done according to standard, analogue Monte Carlo modeling. The user may switch on one or more of the following variance reduction schemes, which can provide significant improvement in the modelling efficiency:

1. The decays can be biased to occur more frequently at certain times, for example, corresponding to times when measurements are taken in a real experiment. The statistical weights of the daughter nuclides are reduced according to the probability of survival to the time of the event, t, which is determined from the decay rate. The decay rate of the nth nuclide in a decay chain is given by the recursive formulae:

$$R_n(t) = \sum_{i=1}^{n-1} A_{n:i} f(t, \tau_i) + A_{n:n} f(t, \tau_n) \tag{36.3}$$

where:

$$A_{n:i} = \frac{\tau_i}{\tau_i - \tau_n} A_{n:i} \quad \forall i < n \tag{36.4}$$

$$A_{n:n} = -\sum_{i=1}^{n-1} \frac{\tau_n}{\tau_i - \tau_n} A_{n:i} - y_n \tag{36.5}$$

$$f(t, \tau_i) = \frac{e^{-\frac{t}{\tau_i}}}{\tau_i} \int\limits_{-\inf}^{t} F(t') e^{\frac{t'}{\tau_i}} dt'. \tag{36.6}$$

The values τ_i are the mean life-times for the nuclei, y_i is the yield of the ith nucleus, and $F(t)$ is a function identifying the time profile of the source. The above expression for decay rate is simplified, since it assumes that the

i^{th} nucleus undergoes 100% of the decays to the $(i+1)^{th}$ nucleus. Similar expressions which allow for branching and merging of different decay chains can be found in Ref. [3].

A consequence of the form of equations 36.4 and 36.6 is that the user may provide a source time profile so that each decay produced as a result of a simulated source particle incident at time $t = 0$ is convolved over the source time profile to derive the actual decay rate for that source function.

This form of variance reduction is only appropriate if the radionuclei can be considered to be at rest with respect to the geometry when decay occurs.

2. For a given decay mode (α, $\beta^+ + EC$, or β^-) the branching ratios to the daughter nuclide can be sampled with equal probability, so that some low probability branches which may have a disproportionately greater effect on the measurement are sampled with increased probability.

3. Each parent nuclide can be split into a user-defined number of nuclides (of proportionally lower statistical weight) prior to treating decay in order t o increase the sampling of the effects of the daughter products.

36.3 Status of this document

00.00.00 created by ?
21.11.03 bibliography added, minor re-wording by D.H. Wright

Bibliography

[1] J. Tuli, *"Evaluated Nuclear Structure Data File,"* BNL-NCS-51655-Rev87, 1987.

[2] Chapter 25, Geant4 Physics Reference Manual.

[3] P.R. Truscott, PhD Thesis, University of London, 1996.